

Advanced Structured Materials

Lucas F. M. da Silva *Editor*

# Materials Design and Applications II

 Springer

# **Advanced Structured Materials**

Volume 98

## **Series editors**

Andreas Öchsner, Faculty of Mechanical Engineering, Esslingen University of Applied Sciences, Esslingen, Germany

Lucas F. M. da Silva, Department of Mechanical Engineering, Faculty of Engineering, University of Porto, Porto, Portugal

Holm Altenbach, Otto-von-Guericke University, Magdeburg, Sachsen-Anhalt, Germany

Common engineering materials reach in many applications their limits and new developments are required to fulfil increasing demands on engineering materials. The performance of materials can be increased by combining different materials to achieve better properties than a single constituent or by shaping the material or constituents in a specific structure. The interaction between material and structure may arise on different length scales, such as micro-, meso- or macroscale, and offers possible applications in quite diverse fields.

This book series addresses the fundamental relationship between materials and their structure on the overall properties (e.g. mechanical, thermal, chemical or magnetic etc.) and applications.

The topics of *Advanced Structured Materials* include but are not limited to

- classical fibre-reinforced composites (e.g. glass, carbon or Aramid reinforced plastics)
- metal matrix composites (MMCs)
- micro porous composites
- micro channel materials
- multilayered materials
- cellular materials (e.g. metallic or polymer foams, sponges, hollow sphere structures)
- porous materials
- truss structures
- nanocomposite materials
- biomaterials
- nano porous metals
- concrete
- coated materials
- smart materials

Advanced Structures Material is indexed in Google Scholar and Scopus.

More information about this series at <http://www.springer.com/series/8611>

Lucas F. M. da Silva  
Editor

# Materials Design and Applications II

 Springer

*Editor*

Lucas F. M. da Silva  
Department of Mechanical Engineering,  
Faculty of Engineering  
University of Porto  
Porto, Portugal

ISSN 1869-8433

ISSN 1869-8441 (electronic)

Advanced Structured Materials

ISBN 978-3-030-02256-3

ISBN 978-3-030-02257-0 (eBook)

<https://doi.org/10.1007/978-3-030-02257-0>

Library of Congress Control Number: 2018958956

© Springer Nature Switzerland AG 2019

This work is subject to copyright. All rights are reserved by the Publisher, whether the whole or part of the material is concerned, specifically the rights of translation, reprinting, reuse of illustrations, recitation, broadcasting, reproduction on microfilms or in any other physical way, and transmission or information storage and retrieval, electronic adaptation, computer software, or by similar or dissimilar methodology now known or hereafter developed.

The use of general descriptive names, registered names, trademarks, service marks, etc. in this publication does not imply, even in the absence of a specific statement, that such names are exempt from the relevant protective laws and regulations and therefore free for general use.

The publisher, the authors and the editors are safe to assume that the advice and information in this book are believed to be true and accurate at the date of publication. Neither the publisher nor the authors or the editors give a warranty, express or implied, with respect to the material contained herein or for any errors or omissions that may have been made. The publisher remains neutral with regard to jurisdictional claims in published maps and institutional affiliations.

This Springer imprint is published by the registered company Springer Nature Switzerland AG  
The registered company address is: Gewerbestrasse 11, 6330 Cham, Switzerland

# Preface

This volume of *Advanced Structured Materials* contains selected papers presented at the 2nd International Conference on Materials Design and Applications 2018 (MDA 2018), held in Porto, Portugal during 5–6 July 2018. The goal of the conference was to provide a unique opportunity to exchange information, present the latest results as well as to discuss issues relevant to materials design and applications. The focus is on fundamental research and application areas in the field of the design and application of engineering materials, predominantly within the context of mechanical engineering applications. This includes a wide range of materials engineering and technology, including metals, e.g. lightweight metallic materials, polymers, composites and ceramics. Advanced applications include manufacturing of new materials, testing methods, multi-scale experimental and computational aspects. Approximately 140 papers were presented by researchers from nearly 30 countries.

In order to disseminate the work presented in MDA 2018, selected papers were prepared which resulted in the present volume dedicated to ‘Materials Design and Applications II’. A wide range of topics are covered resulting in 34 papers dealing with: metals, ceramics, composites, design, power generation, additive manufacturing, machining, fracture mechanics, joining, tribology and forming. The book is a state-of-the-art of materials design and applications and also serves as a reference volume for researchers and graduate students working with advanced materials.

The organizer and editor wish to thank all the authors for their participation and cooperation, which made this volume possible. Finally, I would like to thank the team of Springer-Verlag, especially Dr. Christoph Baumann, for the excellent cooperation during the preparation of this volume.

Porto, Portugal  
September 2018

Lucas F. M. da Silva

# Contents

## Part I Metals

<b>Comparison of Artificial Neural Network and Adaptive Neuro Fuzzy Inference Systems for Predicting the Life of Blanking Punch</b> .....	3
Sachin Salunkhe, D. Rajamani and E. Balasubramanian	
<b>Comparison Between Hot Rolled and PM/HIP Processed Duplex Stainless Steel UNS S31803</b> .....	17
J. V. S. Matias, H. M. L. F. de Lima, W. S. Araujo, J. M. Pardal and Sérgio S. M. Tavares	
<b>Determination of Previous Austenite Grain Size 9%Ni Low Carbon Steel and Its Effect on Impact Toughness at <math>-196^{\circ}\text{C}</math></b> .....	29
Sérgio S. M. Tavares, Rachel P. C. da Cunha, Cássio Barbosa, Manoel R. Silva and Rafael A. Vinhos	
<b>Corrosion Study of Ti5Al4V and Ti6Al4V in Different Simulated Body Fluids</b> .....	39
M. P. Nikolova and E. H. Yankov	
<b>Inverse Methodology for Estimating the Heat Transfer Coefficient in a Duplex Stainless Steel Casting</b> .....	59
R. O. Sousa, I. Felde, P. J. Ferreira, A. M. Deus and L. M. M. Ribeiro	

## Part II Polymers

<b>Fluid Based Protective Structures</b> .....	73
Dawid Pacek	

### Part III Ceramics

<b>Synthesis of Mg–Zn–Ca Alloy by the Spark Plasma Sintering</b> . . . . .	85
Sabina Lesz, Joanna Kraczla and Ryszard Nowosielski	
<b>The Effect of Ceramic Application in Design of Ceramic-Based Plasters</b> . . . . .	97
M. Čáchová, L. Scheinherrová, M. Doleželová and M. Keppert	
<b>Visual Analysis of Ceramic Combinations with Educational Purposes for the Development of Artisan Products</b> . . . . .	107
H. D. Castaño and V. Suárez	
<b>Design of the Ternary Gypsum-Based Building Composite Using Simplex Optimization</b> . . . . .	119
M. Doleželová, J. Pokorný and A. Vimrová	
<b>Study of the Influence of Sintering Temperature on Water Absorption in the Manufacture of Porcelain Cups</b> . . . . .	129
T. P. Duarte, J. L. Alves and P. Pereira	

### Part IV Composites

<b>Design and Characterization of Porous Collagen/Gelatin/Hydroxyethyl Cellulose Matrices Containing Microspheres Based on <math>\kappa</math>-Carrageenan</b> . . . . .	151
J. Kozłowska, K. Pauter, J. Skopinska-Wisniewska and A. Sionkowska	
<b>Effects of Fiber Treatment on the Properties of Epoxy Curaua-Reinforced Composites</b> . . . . .	159
F. C. Amorim, J. F. B. Souza and J. M. L. Reis	

### Part V Design

<b>The Effect of the Position of Compression Screw in Plate-Screws Method Used in Fracture Treatment on Fatigue Strength of Joint</b> . . . . .	171
R. Cagri Kutlubay, Tezcan Sekercioglu and A. Cagdas Yorukoglu	
<b>Life Cycle Cost Assessment and the Optimum Design of Timber Roofs for Sustainable Construction</b> . . . . .	183
Kamil Krzywiński and Łukasz Sadowski	
<b>Analysis and Conceptual Development of a New Packaging Material—Air Pack</b> . . . . .	203
J. Silva and J. L. Alves	



**The Toy as a Factor of Better Children’s Integration in Hospitalization Context** ..... 215  
 T. Freitas, B. Rangel and J. Lino Alves

**Evaluation of Sustainability in the Development of Food Packaging** ..... 235  
 V. L. Suárez, G. Barrera and R. M. Naveiro

**Part VI Power Generation**

**Experimental Investigations of a MR Clutch for a Centrifugal Pump** ..... 253  
 A. I. Bosioc, T. Ardelean, R. Szakal, S. Muntean, I. Borbath and L. Vékás

**Experimental Investigations of a Magneto-Rheological Brake Embedded in a Swirl Generator Apparatus** ..... 265  
 R. A. Szakal, A. I. Bosioc, S. Muntean, D. Susan-Resiga and L. Vékás

**Part VII Additive Manufacturing**

**Orientation of the Digital Model for SLA 3D Printing and Its Influence on the Accuracy of the Manufactured Physical Objects for Micro- and Nano Technologies** ..... 283  
 E. H. Yankov and M. P. Nikolova

**Part VIII Machining**

**Effect of Additives on the Machinability of Glass Fiber Reinforced Polymer** ..... 295  
 Jean-François Chatelain, C. M. Ouellet-Plamondon, B. Lasseur and H. Kuate-Togue

**Influence of Surface Topography of HSS Edges Produced by Different Methods on Their Technological and Functional Properties** ..... 313  
 Maciej Jan Kupczyk and Jędrzej Komolka

**Comparative Investigations of Durability of Cutting Edges Made of Nanocrystalline Cemented Carbides with Different Growth Inhibitors** ..... 331  
 Maciej Jan Kupczyk, Jędrzej Komolka and Piotr Siwak

**Evaluation of Machining Defects in a Composite Laminate by Combining Non-destructive and Tensile Testing** ..... 341  
 Louis-Alexandre Généreux, Gilbert Lebrun, Martin Viens and Jean-François Chatelain

**The Effect of Machining on Surface Integrity of Gamma Titanium Aluminides Using Different Cemented Carbide Tools** ..... 363  
 S. D. Castellanos, J. Lino Alves, R. Neto and A. Cavaleiro

## Part IX Fracture Mechanics

<b>Analysis of the Semi-circular Bend (SCB) Specimen: Finite Element Method Determination of T-stress, <math>K_I</math> and <math>K_{II}</math> . . . . .</b>	<b>387</b>
---	------------

E. Shahabi and P. M. S. T. de Castro

<b>Analysis of Mode II and Mixed Mode I-II in Fracture and Fatigue: A Numerical and Experimental Study . . . . .</b>	<b>403</b>
--	------------

J. Baganha Marques, S. M. O. Tavares and P. M. S. T. de Castro

## Part X Joining

<b>The Friction Weldability of AA6063 Tube to AA6082 Tube Plates Using an External Tool . . . . .</b>	<b>427</b>
---	------------

E. Korkmaz, A. Gülsöz and C. Meran

## Part XI Tribology

<b>Study of the Texture Parameters Effects on the Anti-fingerprint Function . . . . .</b>	<b>441</b>
---	------------

M. Belhadjamor, S. Belghith and S. Mezlini

<b>Mechanical Characterization of Film/Substrate Materials Using Nanoindentation Technique . . . . .</b>	<b>453</b>
--	------------

Nadia Chakroun and Hedi Belhadjsalah

## Part XII Forming

<b>Limiting Drawing Ratio and Formability Behaviour of Dual Phase Steels—Experimental Analysis and Finite Element Modelling . . . . .</b>	<b>469</b>
---	------------

R. L. Amaral, A. D. Santos and S. S. Miranda

<b>Characterization and Formability Analysis of a Composite Sandwich Metal-Polymer Material . . . . .</b>	<b>487</b>
---	------------

S. S. Miranda, A. D. Santos, R. L. Amaral and L. T. Malheiro

<b>Study on Forming Tool Module with Variable Stiffness Blank-Holder for Applications in High Strength Steel and Laser Welding Parts. . . . .</b>	<b>509</b>
---	------------

C. Faria, J. Magalhães, V. Blanco, N. Peixinho and S. Costa

# **Part I**

## **Metals**

# Comparison of Artificial Neural Network and Adaptive Neuro Fuzzy Inference Systems for Predicting the Life of Blanking Punch



Sachin Salunkhe, D. Rajamani and E. Balasubramanian

**Abstract** Predicting the life of blanking punch is one of the major concerns in designing compound dies. Finite element analysis is performed to determine the maximum and minimum principal stresses through which fatigue limit of punch is estimated. The factors affecting the life of punch are examined and a mathematical model is established using artificial neural network (ANN) and adaptive neuro fuzzy inference systems (ANFIS). The developed model is utilized to evaluate the life of punch for varied load conditions. Comparative evaluation of ANN and ANFIS results suggested that the later model is superior in predicting the life of punch and it can be effectively utilized in machine tool applications.

**Keywords** Blanking punch · Compound die · Finite element analysis · ANN ANFIS

## 1 Introduction

Compound dies are extremely useful to stamping industries because of the following: (1) high dimensional accuracy (2) superior surface finish (3) adequate structural integrity and (4) reduction in material wastage. However, design of compound dies are considered to be challenging task due to the involvement of various components such as punches, die block, stripper, knockout bar, die gage, die-set, etc. in stamping industries to meet the functional requirement. Current market (stamping

---

S. Salunkhe (✉) · D. Rajamani · E. Balasubramanian  
Department of Mechanical Engineering, Vel Tech Rangarajan Dr. Sagunthala R & D  
Institute of Science and Technology, Chennai 600062, India  
e-mail: [drsalunkhesachin@veltech.edu.in](mailto:drsalunkhesachin@veltech.edu.in)

D. Rajamani  
e-mail: [rajamanitamil1991@gmail.com](mailto:rajamanitamil1991@gmail.com)

E. Balasubramanian  
e-mail: [esak.bala@gmail.com](mailto:esak.bala@gmail.com)

© Springer Nature Switzerland AG 2019  
L. F. M. da Silva (ed.), *Materials Design and Applications II*, Advanced  
Structured Materials 98, [https://doi.org/10.1007/978-3-030-02257-0\\_1](https://doi.org/10.1007/978-3-030-02257-0_1)

industries) demands that the blanking punch of compound die should produce more accurate sheet metal parts without any internal or external defects. Estimating the life of blanking punch is considered to be critical aspect in die design. The punch life of compound die mainly depends on punch force, sheet thickness and punch area. Generally, life of punch is predicted through experienced die designers with its performance characteristics and it can cause severe penalty when misjudgment occurs. In the last two decades, researchers have realized that ANN and ANFIS are most reliable techniques to provide viable solutions in sheet stamping. Di and Thomson [1] employed ANN model for identification of wrinkling behavior of formed sheet metal parts. Greska et al. [2] used neural networks and fourier descriptors to identify various categories of sheet metal parts. Inamdar et al. [3] developed an ANN model to study the behavior of bending parts and prediction of springback. Djurisic and Manic [4] proposed trained neural network for shape recognition of sheet metal parts. Yilbas et al. [5] formulated an ANN model for study of formed kerf surface of laser cutting corners in sheet metal parts. Process parameters and tool geometry of a springback of cylindrical deep drawing process [6] are constructed in ANN model. De and Klingenberg [7] used a combination of neural network for the detection of tool wear and blanking force measurement in sheet metal forming process. Babu et al. [8] incorporated ANN model and expert system to predict the behavior of deep drawing sheet metal parts. ANFIS and FEM method [9] is utilized to arrive an optimal shape of sheet metal bending die. Lin et al. [10] formulated ANFIS algorithm to measure the springback angle of forming parts. Ashhab et al. [11] investigated the combination of deep drawing and extrusion processes using an ANN model. Kashid and Kumar [12, 13] developed ANN model for predicting the life of compound die components. Liu et al. [14] evaluated the bending radius of sheet metal parts through back propagation ANN strategy. Kashid et al. [15] developed ANN to estimate the life of stripper. Zhou et al. [16] proposed convolutional neural network (CNN) to examine the defects on metal parts. Yaghoobi et al. [17] combined ANFIS and genetic algorithm of hydroforming process of cylindrical-spherical sheet parts. Radial Basis Function (RBF) neural network are effectively utilized by Wang et al. [18] to envisage and optimize the location layout of sheet metal fixtures. Panthi et al. [19] estimated the velocity of spring back using a backpropagation ANN model in straight flanging process. Naranje et al. [20] assessed the life of deep drawing die with an ANN model. Dilan et al. [21] examined the springback effect of sheet metal bending process through an ANN strategy. Aleyasin [22] proposed ANFIS algorithm to determine forming limit diagram (FLD) of sheet metals. Mekras [23] proposed ANN for modeling of aluminum based sheet metal tools. Kannadasan et al. [24] used ANN and ANFIS model to determine optimal strain factor of aluminum alloy sheet metal. It is evident from these review of literature that, estimating the life of blanking punch is not yet investigated. In particular, the development of ANFIS and ANN algorithms is useful to predict the life of punch in compound die effortlessly with less human intervention to save time and cost.

## 2 Analytical Model for Blanking Punches

Life of blanking punches of compound die is dependent on sheet material, thickness, shear strength of punch and number of parts to be produced on blanking punches. Initially, 3-D CAD model of blanking punch is designed in CATIA platform (Dassault Systèmes, Vélizy-Villacoublay, France). Further, finite element analysis (FEA) of blanking punch is performed in ANSYS workbench tool. From the output of FEA (maximum and minimum principal stress), S-N method is used to calculate number of mathematical cycles (one cycle means one parts can be manufactured). Mean stress ( $\sigma_m$ ) and amplitude stress ( $\sigma_a$ ) are an important equations to calculate number of mathematical cycles. They are calculated using the following relations which are,

$$\sigma_a = \frac{\sigma_{max} - \sigma_{min}}{2} \tag{1}$$

$$\sigma_m = \frac{\sigma_{max} + \sigma_{min}}{2} \tag{2}$$

Based on these two parameters ( $\sigma_m$ ) and ( $\sigma_a$ ), number of cycles of blanking punch is determined using Haigh diagram. Utilizing these approximations, a generalized S-N curve can be drawn as shown in Fig. 1. The endurance strength is calculated from following equation:

$$S_e = 0.5 \times S_u \tag{3}$$

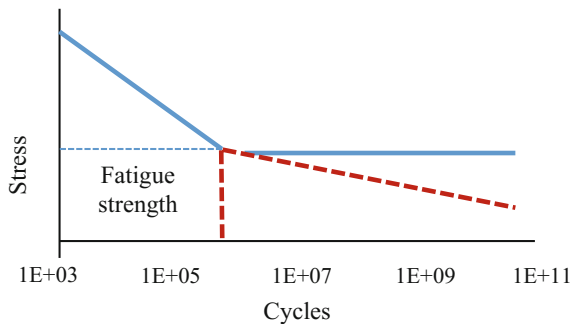
The number of cycles is calculated by using the following relation,

$$N = \left( \frac{S_n}{S_e} \right)^{\frac{1}{b}} \times 10^6 \tag{4}$$

where,

- N Number of cycles
- $S_n$  Fatigue strength (from Goodman equation)
- $S_e$  Endurance strength

**Fig. 1** S-N for tool steel [25]



$$b = -\frac{1}{3} \log\left(\frac{\sigma_a}{S_e}\right) \quad (5)$$

Goodman relationship is given as,

$$\left(\frac{\sigma_a}{S_n}\right) + \left(\frac{\sigma_m}{S_u}\right) = 1 \quad (6)$$

These empirical relations are utilized to construct the ANN and ANFIS model to estimate the fatigue limit of blanking punch and Fig. 2 depicts the framework of proposed ANN and ANFIS.

### 3 Proposed ANN and ANFIS Models to Estimate the Life of Blanking Punches

The relations given in Eqs. 4–6 are considered to perform initial calculations. Neural network toolbox in MATLAB™ is used for the development of proposed model. The ANN model of analytical data is divided into three sets (1) training the system (60%) (2) testing of data (20%) and (3) performing validation (20%). The weights of neural network are adjusted through set of training and testing data. A supervised ANN, Lavenberg-Marquardt backpropagation is used. In the present study, eight layers of neurons with four input parameters, three hidden layer and one output layer is utilized as depicted in Fig. 3.

The selection of input and output parameters are influencing the ANN framework and it depends upon the nature of a problem. The input parameters of proposed ANN model are maximum and minimum principal stress, amplitude stress and mean stress. Similarly, the output parameter is number of cycles. Based on input and output parameters of ANN, the neurons of hidden layer are chosen. The learning rate of proposed ANN model is set as 0.01. ANFIS is amalgamation of neural network and fuzzy logic for mapping the relationship between inputs and outputs. The fuzzy inference system contains the fuzzy sets and membership functions, fuzzy implication operators and linguistic if-then rules. There are several membership functions viz. Triangular (trimf), generalized bell (gbellmf), trapezoidal (trapmf), Gaussian (gaussmf), etc., used in fuzzy inference system. The ANFIS model consists of five layers, and each layer is connected through several nodes. The structure of ANFIS model is shown in Fig. 4.

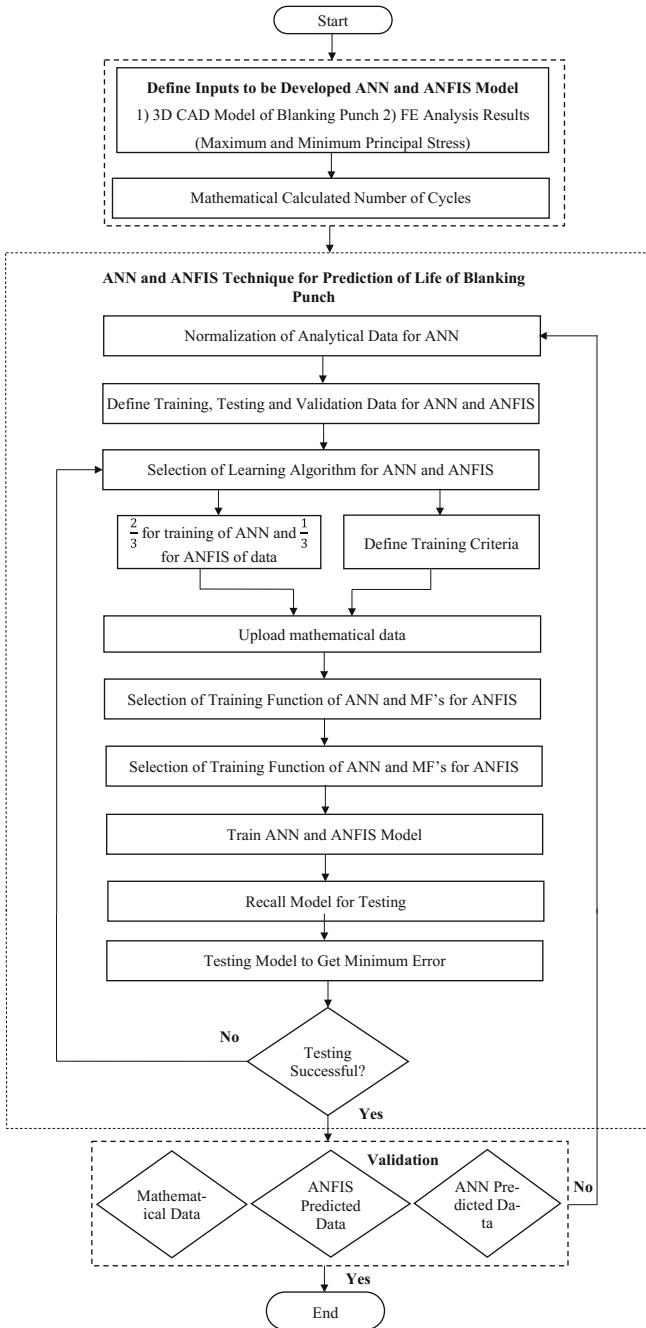


Fig. 2 Framework of proposed ANN and ANFIS model



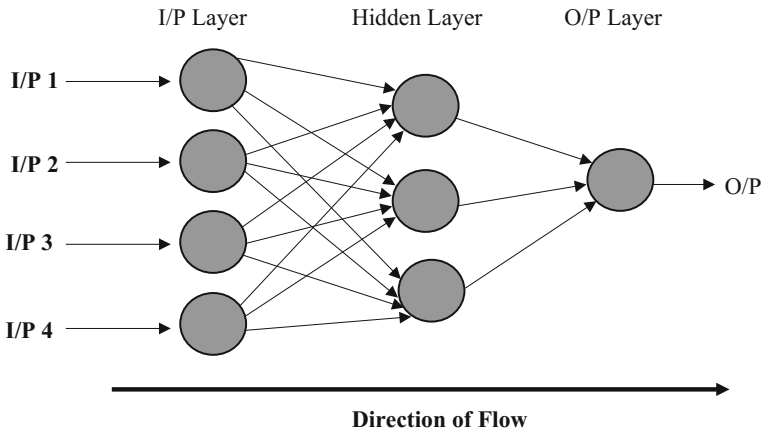


Fig. 3 Feed forward ANN structure

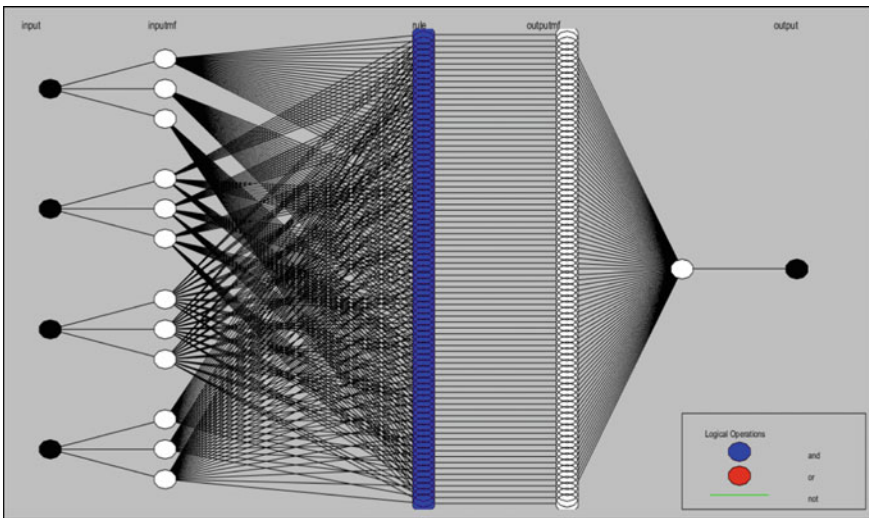


Fig. 4 ANFIS model structure

### 4 Testing of Proposed Models

The proposed ANN and ANFIS models are tested on various blanking punch of compound dies. The present study considers a blanking punch of compound die of sheet metal industry M/s Panchmahal Dies and Tools Pvt. Ltd. Vadodara, India. A sample 3D model of blanking punch is depicted in Fig. 5. FEA is performed and the results are shown in Figs. 6 and 7 and also summarized in Table 1.

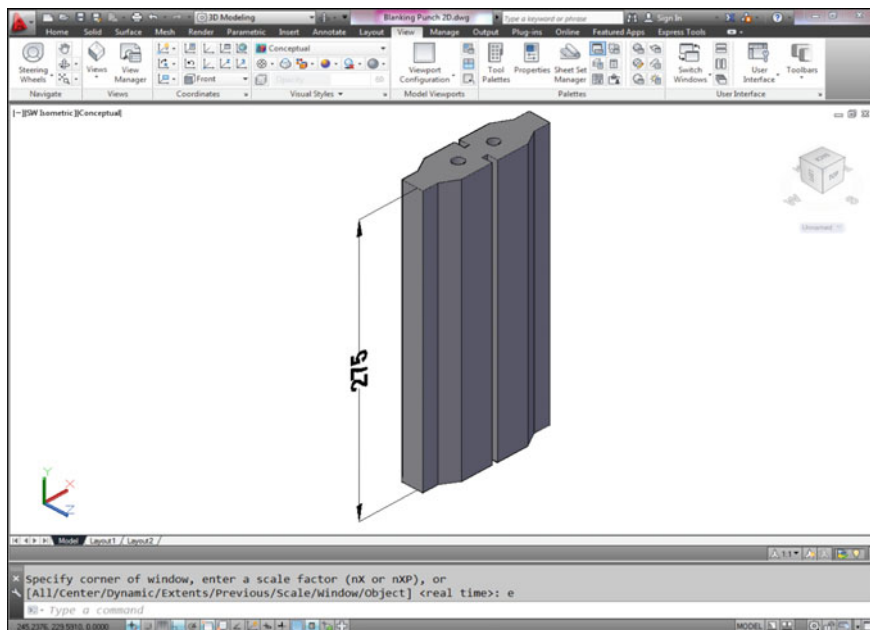


Fig. 5 CAD model of blanking punch

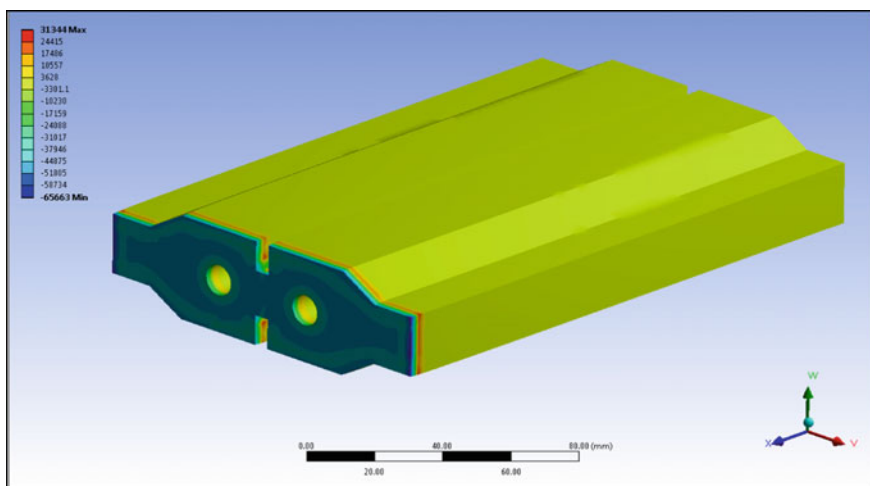


Fig. 6 Maximum principal stress

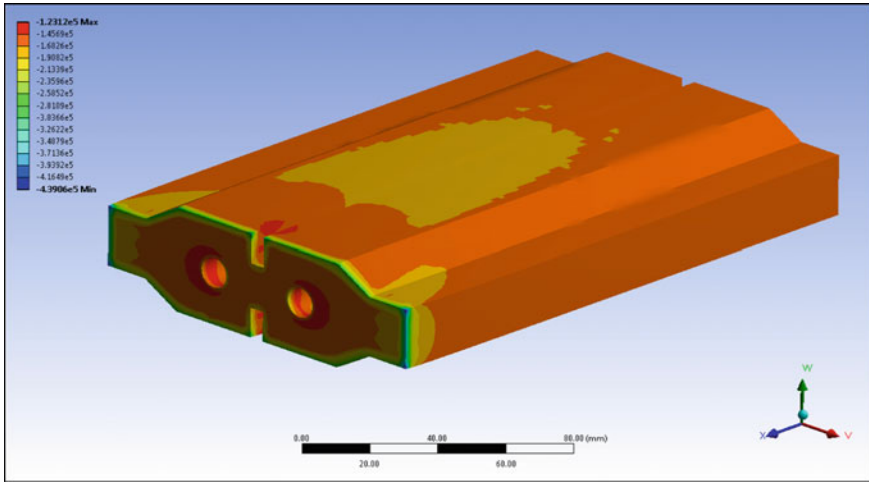


Fig. 7 Minimum principal stress

Table 1 Outputs of blanking punch

Blanking punch stresses in [MPa]							
Sr. no.	Max. principal stress	Min. principal stress	Amplitude stress ( $\sigma_a$ )	Mean stress ( $\sigma_m$ )	Analytical results (Cycles)	ANN predicted results (Cycles)	ANFIS predicted (Cycles)
1	-65,663	-439,060	187,187.5	-251,872.5	656,590	647,674	651,851
2	-64,685	-437,426	186,859.5	-250,566.5	654,112	646,001	649,714
3	-63,707	-435,792	186,531.5	-249,260.5	651,626	643,987	647,763
4	-62,729	-434,158	186,203.5	-247,954.5	649,131	641,126	644,725
5	-61,751	-432,524	185,875.5	-246,648.5	646,627	638,981	642,586
6	-60,773	-430,890	185,547.5	-245,342.5	644,115	636,125	640,358
7	-59,795	-429,256	185,219.5	-244,036.5	641,593	633,985	638,542
8	-58,817	-427,622	184,891.5	-242,730.5	639,062	631,009	634,461
9	-57,839	-425,988	184,563.5	-241,424.5	636,522	628,124	632,864
10	-56,861	-424,354	184,235.5	-240,118.5	633,974	625,983	630,251
11	-55,883	-422,720	183,907.5	-238,812.5	631,416	623,202	627,896
12	-54,905	-421,086	183,579.5	-237,506.5	628,849	620,126	625,486
13	-53,927	-419,452	183,251.5	-236,200.5	626,272	618,933	622,245
14	-52,949	-417,818	182,923.5	-234,894.5	623,687	615,037	619,827
15	-51,971	-416,184	182,595.5	-233,588.5	621,092	613,789	616,534
16	-50,993	-414,550	182,267.5	-232,282.5	618,489	610,748	615,238
17	-50,015	-412,916	181,939.5	-230,976.5	615,875	607,669	610,562
18	-49,037	-411,282	181,611.5	-229,670.5	613,253	605,741	607,543
19	-48,059	-409,648	181,283.5	-228,364.5	610,621	602,458	605,879
20	-47,081	-408,014	180,955.5	-227,058.5	607,979	599,764	602,358

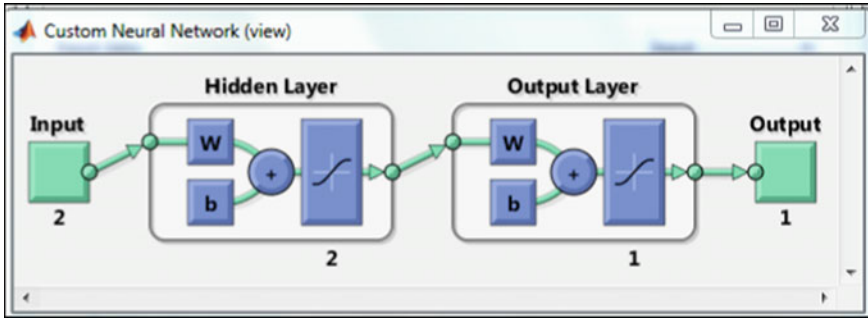


Fig. 8 Number of layers 2 and 3 neurons

### 5 Results and Discussion

After training the ANN (Fig. 8) and ANFIS model (Fig. 10), for a typical loading conditions, life of the punch is estimated as 647,674 and 651,851 cycles, respectively which is considerably higher than the manufacturer recommendation of about 600,000 cycles. Figure 9 shows the results of trained, validated, tested and best performance of the ANN model.

Predicting the life of blanking punch using ANFIS mainly consists of three stages: training and testing. In this study, 45 data set cited in analytical results have been selected for training the ANFIS network with 300 epochs. The trained network is tested with other 45 datasets which is not accounted during training. Further, ANFIS model is divided into three phases to predict the number of cycles effectively. The first phase is to define the type of fuzzy rules. Then the set of all fuzzy subsets of variables with membership functions (MFs) are formed. In the third phase, appropriate number of MFs have been selected for estimating the life of punch. Triangular membership (*trimf*) function is selected due to its low mean square error (MSE) in comparison to other MFs. The error tolerance during the training of ANFIS network is kept as 0.01 to obtain low error in prediction. For training, numerical results are loaded to the ANFIS model until a value reached  $<0.001$ . It is found that the 300 number of epoch with a 0.01 error shows that there is no further error reduction is pertinent. In addition, the trained ANFIS network is tested to validate the accuracy of prediction. Figure 9 shows the performance of testing and it has an average testing error of 10,495.39, which shows the accuracy of prediction. A total number of 81 fuzzy rules are generated which is shown in Fig. 11. From the ANFIS rule, the first four columns indicates the input parameters and last column represents the predictor variable. The ruler can move from minimum to maximum levels of selected variables to calculate the predictor variables.

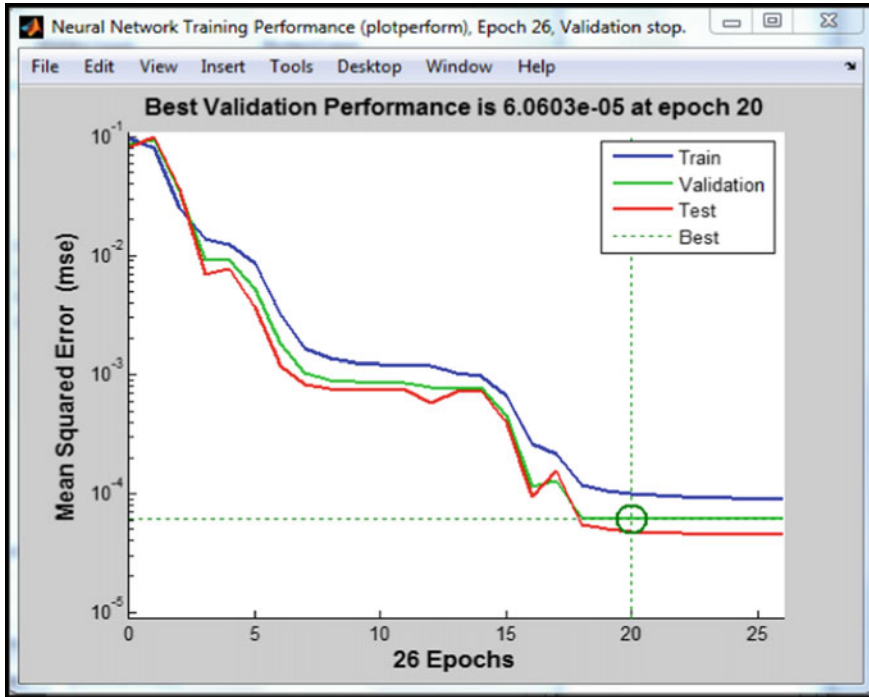


Fig. 9 Minimum error for 2 layers and 3 neurons

Finally, the ANN and ANFIS models predicted parameters are compared with analytical results as depicted in Fig. 12. It is observed that, the error difference between the mathematical with ANN and ANFIS are 1.26%, 0.66%, respectively. Therefore, it can be concluded that the ANFIS model performance is superior to the ANN model to predict the life of blanking punches of compound die.

## 6 Conclusions

In this paper, ANN and ANFIS models are developed to estimate the life of blanking punch of compound dies in which ANFIS model required less time than ANN model in prediction. The results of this developed model can be summarized as follows:

- (1) The results obtained from ANFIS model shown 99% confidence level. In addition to that, average percentage of error between the analytical and predicted ANFIS model is found to be 0.66%, whereas ANN model obtained an average error of 1.26%.

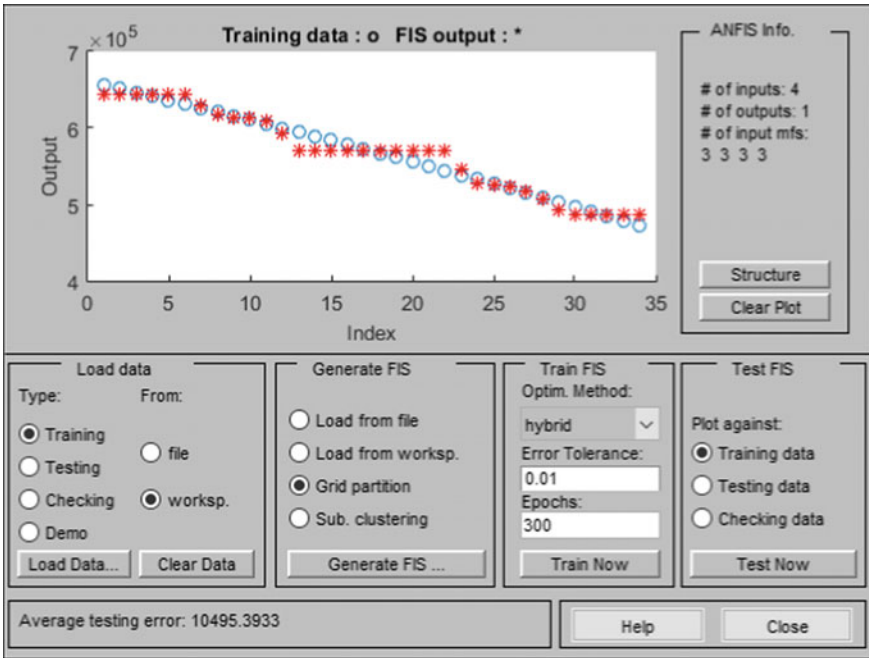


Fig. 10 Testing ANFIS model

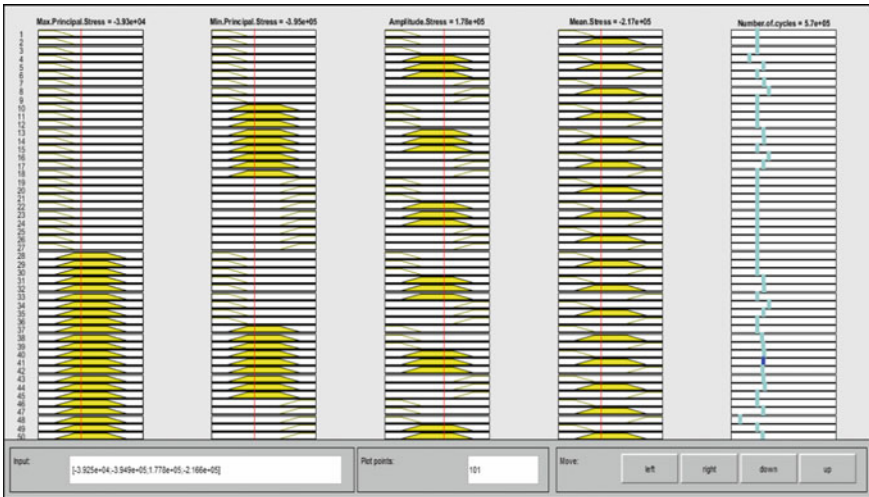
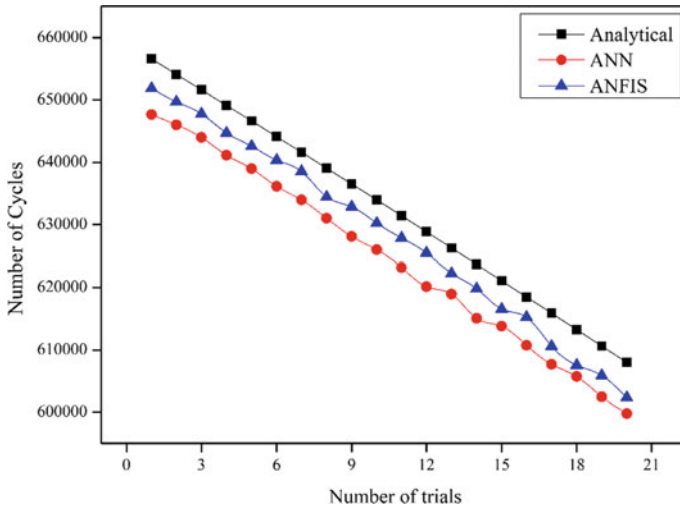


Fig. 11 Proposed ANFIS rules



**Fig. 12** Comparison of analytical result, ANN and ANFIS predicted

- (2) ANFIS model demonstrated better robustness compared to mathematical model. Hence, the proposed ANFIS model is effectively predicting the life of blanking punch of compound die compared to ANN model.
- (3) These results indicate that ANFIS technique is reliable to predict the life of various dies including bending and progressive.

## References

1. Di, S., Thomson, P.F.: Neural network approach for prediction of wrinkling limit in square metal sheet under diagonal tension. *J. Test. Eval.* **25**, 74–81 (1997)
2. Greska, W., Franke, V., Geiger, M.: Classification problems in manufacturing of sheet metal parts. *Comput. Ind.* **33**, 17–30 (1997)
3. Inamdar, M.V., Date, P.P., Desai, U.B.: Studies on the prediction of springback in air vee bending of metallic sheets using an artificial neural network. *J. Mater. Process. Technol.* **108**, 45–54 (2000)
4. Djuriscic, Z., Manic, M.: Intelligent nesting system. *Yugosl. J. Oper. Res.* **13**, 229–243 (2003)
5. Yilbas, B., Karatas, C., Keles, O., Uslan, I., Usta, Y., Ahsan, M., Yilbas, Z.: Laser cutting of corners: assessment of cutting quality. *Lasers Eng.* **16**, 157–171 (2006)
6. Crina, A.: Control the springback of metal sheets by using an artificial neural network. In: 10th Esaform Conference on Material Forming, Zaragoza Spain (2006)
7. De, B., Klingenberg, W.: Architecture for a neural expert system for condition-based maintenance of blanking. *Int. J. Mater. Prod. Technol.* **32**, 447–459 (2008)
8. Veera Babu, K., Ganesh Narayanan, R., Saravana Kumar, C.: An expert system for predicting the deep drawing behavior of tailor welded blanks. *Expert Syst. Appl.* **37**, 7802–7812 (2010)
9. Yeh, F., Li, C., Tsay, K.: Application of adaptive network fuzzy inference system to die shape optimal design in sheet metal bending process. *J. Appl. Sci. Eng.* **15**, 31–40 (2012)

10. Lin, B., Huang, K., Kuo, C.: An adaptive-network-based fuzzy inference system for predicting springback of U-Bending. *Appl. Mech. Mater.* **284–287**, 25–30 (2013)
11. Ashhab, M., Breitsprecher, T., Wartzack, S.: Neural network based modeling and optimization of deep drawing—extrusion combined process. *J. Intell. Manuf.* **25**, 77–84 (2014)
12. Kashid, S., Kumar, S.: Prediction of life of compound die using artificial neural network (ANN). *Key Eng. Mater.* **622–623**, 664–671 (2014)
13. Kashid, S., Kumar, S.: Prediction of life of die block using artificial neural network. *Appl. Mech. Mater.* **592–594**, 689–693 (2014)
14. Liu, N., Yang, H., Li, H., Yan, S., Zhang, H., Tang, W.: BP artificial neural network modeling for accurate radius prediction and application in incremental in-plane bending. *Int. J. Adv. Manuf. Technol.* **80**, 971–984 (2015)
15. Kashid, S., Kumar, S., Hussein, H.M.A.: *Key Eng. Mater.* **639**, 501–508 (2015)
16. Zhou, S., Chen, Y., Zhang, D., Xie, J., Zhou, Y.: Classification of surface defects on steel sheet using convolutional neural networks. *Mater. Technol.* **51**, 123–131 (2016)
17. Yaghoobi, A., Bakhshi-Jooybari, M., Gorji, A., Baseri, H.: Application of adaptive neuro fuzzy inference system and genetic algorithm for pressure path optimization in sheet hydroforming process. *Int. J. Adv. Manuf. Technol.* **86**, 2667–2677 (2016)
18. Wang, Z., Yang, B., Kang, Y., Yang, Y.: Development of a prediction model based on RBF neural network for sheet metal fixture locating layout design and optimization. *Comput. Intell. Neurosci.* (2016). <https://doi.org/10.1155/2016/7620438>
19. Panthi, S., Hora, M., Ahmed, M.: Artificial neural network and experimental study of effect of velocity on springback in straight flanging process. *Indian J. Eng. Mater. Sci.* **23**, 159–164 (2016)
20. Naranje, V., Kumar, S., Kashid, S., Ghodke, A., Hussein, H.M.A.: Prediction of life of deep drawing die using artificial neural network. *Adv. Mater. Process. Technol.* **2**, 132–142 (2016)
21. Dilan, R., Balkan, T., Platin, B.: An online intelligent algorithm pipeline for the elimination of springback effect during sheet metal bending. *Procedia Eng.* **207**, 1576–1581 (2017)
22. Aleyasin, H.: The prediction of forming limit diagram of low carbon steel sheets using adaptive fuzzy inference system identifier. *J. Solid Mech.* **9**, 472–489 (2017)
23. Mekras, N.: Using artificial neural networks to model aluminum based sheet forming processes and tools details. *J. Phys.* (2017). <https://doi.org/10.1088/1742-6596/896/1/012090>
24. Kannadasan, S., Senthil Kumar, A., Pandivelan, C., Sathiya Narayanan, C.: Modelling the forming limit diagram for aluminium alloy sheets using ANN and ANFIS. *Appl. Math. Inf. Sci.* **11**, 1435–1442 (2017)
25. Kazymyrovych, V.: Very high cycle fatigue of tool steels. Faculty of Technology and Science Materials Engineering, Karlstad University Studies, Karlstad, Sweden (2010)



# Comparison Between Hot Rolled and PM/HIP Processed Duplex Stainless Steel UNS S31803



J. V. S. Matias, H. M. L. F. de Lima, W. S. Araujo, J. M. Pardal  
and Sérgio S. M. Tavares

**Abstract** Duplex stainless steels (DSS) are corrosion resistant alloys (CRA) which became largely employed due to its excellent combination of high strength, pitting corrosion resistance and toughness. The steel with basic composition 21.0–23.0%Cr, 4.5–6.5%Ni, 2.5–3.5%Mo, 0.08–0.20%N was developed in the 1980s and became the most popular DSS used in the oil and gas industry. The mechanical properties and corrosion resistance are optimized with a microstructure containing equal parts of ferrite ( $\delta$ ) and austenite ( $\gamma$ ). This balanced microstructure is obtained by the chemical composition control and heat treatment. A solution treatment at 1050–1100 °C followed by water cooling is recommended. Although other heat treatments are not common in DSS, a significant hardening effect can be obtained by short duration exposition to 475 °C. Long thermal aging in the 350–550 °C interval has been extensively studied by many authors, and was proved to cause embrittlement and decrease of corrosion resistance, due to spinodal decomposition of ferrite into Cr-rich ( $\alpha'$ ) and Cr-depleted ( $\alpha''$ ) regions. However, a heat treatment at 475 °C for 4 h or 8 h may increase the yield and ultimate tensile strength without significant decrease of toughness and corrosion resistance, as observed previously. The goal of this work is to compare the microstructure, mechanical properties and corrosion resistance of two duplex stainless steels with similar composition, but produced by different methods: hot rolling and powder metallurgy PM/HIP. These two fabrication processes may be

---

J. V. S. Matias

Instituto Federal Fluminense, Campus São João da Barra, Núcleo de Ciência e Tecnologia dos Materiais, BR 356 - KM 181, Perigoso, São João da Barra, RJ CEP: 28200-000, Brazil

H. M. L. F. de Lima · W. S. Araujo

Departamento de Engenharia Metalúrgica, Universidade Federal do Ceará, Bloco 729 do Campus do Pici, Fortaleza, CE CEP: 60440-900, Brazil

J. M. Pardal · S. S. M. Tavares (✉)

Departamento de Engenharia Mecânica, Universidade Federal Fluminense, Rua Passo da Pátria, 156, Niterói CEP: 24210-240, Brazil

e-mail: [ssmtavares@terra.com.br](mailto:ssmtavares@terra.com.br)

J. M. Pardal · S. S. M. Tavares

Centro Federal de Educação Tecnológica Celso Suckow da Fonseca, Av. Maracanã, 229, Maracanã, Rio de Janeiro, RJ 20550-144, Brazil

© Springer Nature Switzerland AG 2019

L. F. M. da Silva (ed.), *Materials Design and Applications II*, Advanced Structured Materials 98, [https://doi.org/10.1007/978-3-030-02257-0\\_2](https://doi.org/10.1007/978-3-030-02257-0_2)

concurrent for some applications, such as manifolds in the oil and gas industry. The response of both materials to short duration aging at 475 °C was compared.

**Keywords** Duplex stainless steel · HIP process · 475 °C aging

## 1 Introduction

Duplex stainless steels (DSS) are Fe-Cr-Ni-Mo alloys, with extra low carbon contents, and are considered corrosion resistant alloys (CRA) which became largely employed due to its excellent combination of high strength, pitting resistance and toughness [1, 2]. The steel with basic composition 21.0–23.0%Cr, 4.5–6.5%Ni, 2.5–3.5%Mo, 0.08–0.20%N, designated UNS S31803, was developed in the 1980s and became the most popular DSS used in the oil and gas industry. The mechanical properties and corrosion resistance are optimized with a microstructure containing equal parts of ferrite ( $\delta$ ) and austenite ( $\gamma$ ). This balanced microstructure is obtained by the chemical composition control and heat treatment. The solution treatment at 1050–1100 °C followed by water cooling is recommended.

Although other heat treatments are not common in DSS, a significant hardening effect can be obtained by short duration exposition to 475 °C, where the precipitation kinetics is higher. Long term aging in the 350–550 °C interval has been extensively studied by many authors [3–6], and was proved to cause embrittlement and decrease of corrosion resistance, due to spinodal decomposition of ferrite into Cr-rich ( $\alpha'$ ) and Cr-depleted ( $\alpha''$ ) regions. However, a heat treatment at 475 °C for 4 h or 8 h may increase the yield and ultimate tensile strength without significant decrease of toughness and corrosion resistance, as observed previously [7, 8].

DSS components may be produced by different fabrication processes, such as casting, forging, hot and cold rolling, and powder metallurgy with hot isostatic pressing (HIP). Since these processes may be concurrent, it is useful to identify the advantages and limitations of each process. For instance, powder metallurgy with HIP is a near net shape process, i.e., the components are produced with shape and dimensions very close to the design. Just finishing machining operations are performed to obtain the final dimensions and rugosity. On the other hand, rolled products present excellent mechanical properties due to grain refinement by thermomechanical treatment. However, there is a tendency to obtain anisotropic microstructure and properties, due to the elongation of austenite and ferrite phases along the rolling direction.

Short duration heat treatments at 475 °C can be an interesting option to some DSS components, especially those in which thermomechanical treatment cannot be used to increase the mechanical resistance.

The goal of this work is to compare the microstructure, mechanical properties, such as hardness and toughness, and corrosion resistance of two duplex stainless steels with similar composition, but produced by different methods: hot rolling and powder metallurgy (PM) with HIP. These two fabrication processes may be concu-

rent for some applications, such as manifolds in the oil and gas industry. The response of both materials to short duration aging at 475 °C was compared.

## 2 Materials and Methods

The two UNS S31803 DSS, wrought (Hot rolled) and HIP, present chemical composition according to Table 1. C, S and N were analyzed by combustion method, while the other elements were analyzed by plasma spectroscopy.

The materials were solution treated at 1060 °C for 1 h and water quenched. After this treatment some specimens were cut and machined to the dimensions of sub-size Charpy impact specimens ( $55 \times 10 \times 7.5 \text{ mm}^3$ ) [9]. Specimens for the critical pitting temperature (CPT) tests were cut and machined with approximate dimensions  $15 \times 15 \times 10 \text{ mm}^3$ . Some specimens were subjected to aging heat treatments at 475 °C for 4, 8 and 12 h, followed by water cooling.

The microstructures were analyzed by optical microscopy. Specimens were prepared by grinding and etching with Behara's solution (80 ml H<sub>2</sub>O, 20 ml HCl, 0.3 g potassium metabissulfite). Vickers hardness with 10 kgf load and Charpy impact tests at -46 °C were performed in samples to evaluate the degree of embrittlement in each condition. After the tests some samples were selected to fractography in a scanning electron microscope (SEM).

The effects of the aging on the pitting corrosion resistance of each condition were evaluated by CPT and cyclic potentiodynamic polarization tests (CPP). The cyclic polarization tests were conducted in 3.5% NaCl solution at room temperature in a potentiostat-galvanostat AUTOLAB (Amsterdam, Netherlands) model PGSTAT 302 N. A conventional three-electrode electrochemical cell using a platinum (Pt) grid as the counter electrode, saturated KCl silver/silver chloride (Ag/AgCl) as the reference electrode and the working electrode was constructed using the steel samples embedded in epoxy resin. The working electrode area exposed to the test solution was approximately 0.5 cm<sup>2</sup>. The tests were started after a nearly steady-state open circuit potential ( $E_{ocp}$ ) had developed (60 min). After that, a potential sweep was applied in the anodic direction at 1 mV s<sup>-1</sup> until a current density of 1 mA/cm<sup>2</sup> was reached at which point the scanning direction was then reversed. Prior to each experiment, the specimens were abraded with silicon carbide paper up to 600 mesh, degreased with alcohol, washed with distilled water and dried with hot air. For each alloy in each experimental condition, at least three CPP curves were recorded.

The CPT tests were carried out using a conventional three electrode cell with working electrode, saturated calomel electrode (SCE) as reference and a Pt wire as counter-electrode. The test was controlled and the data were collected in a potentiostat-galvanostat  $\mu$ -AUTOLAB (Amsterdam, Netherlands). The test solution was 1 M NaCl, without prior deaeration, heated at a rate of 4 °C per minute, from the temperature of 10 °C. During the test, a 700 mV<sub>SCE</sub> constant potential was applied to the samples in relation to the reference electrode. Finally, the values of current density versus temperature are plotted. Thus, in accordance with ASTM G150 [10], CPT

**Table 1** Chemical composition (wt%) of the DSS investigated

DSS	Cr	Ni	Mo	Mn	Si	N	Cu	W	C	P	S
Hot rolled	21.64	5.29	2.832	1.155	0.552	0.133	0.177	0.223	0.028	0.007	0.000
HIP	21.57	5.23	2.938	1.416	0.686	0.140	0.171	0.160	0.038	0.017	0.005

**Fig. 1** Determination of the critical pitting temperature (CPT) of the hot rolled (W) DSS aged at 475 °C for 4 h

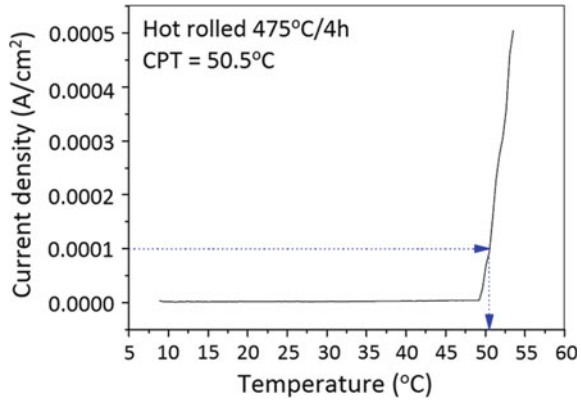


**Table 2** PREN values and volumetric fractions (%) of ferrite and austenite phases of the DSS analyzed

DSS	PREN	Ferrite ( $\delta$ )	Austenite ( $\gamma$ )
Wrought	33.5	60.9 $\pm$ 0.7	39.1 $\pm$ 0.7
HIP	33.4	54.8 $\pm$ 0.7	45.2 $\pm$ 0.7

is the temperature at which the current density ( $\delta i$ ) increases above 100  $\mu\text{A}/\text{cm}^2$ , remaining above this critical value for at least 60 s, as shown in Fig. 1 for the 4 h aged wrought DSS.

### 3 Results and Discussion

The chemical compositions of the two UNS S31803 DSS studied are shown in Table 1. The Pitting Resistant Equivalent Number (PREN) of the steels, calculated by the formulae  $\text{PREN} = (\%Cr) + 3.3(\%Mo + 0.5(\%W)) + 16(\%N)$ , and the volumetric fractions of the ferrite ( $\delta$ ) and austenite ( $\gamma$ ) phases are presented in Table 2. As observed, the PREN values are very close due to the similar chemical compositions of steels. Although the hot rolled DSS exhibits a more uneven balance of phases  $\delta/\gamma$  compared to the HIPped DSS, both steels are in an acceptable range according to Norsok M-601 standard [11], thus optimizing its properties [1, 2].

Figure 2 shows the microstructure of the materials after the solution treatment. Deleterious phases were not detected in the specimens under this condition. The morphological difference of microstructures presented evidences the variation of manufacturing processes by which these steels were submitted. As expected, the wrought DSS has elongated grains on the rolling direction (horizontal) and the HIPped has some equiaxial shaped grains due to isostatic pressing process.

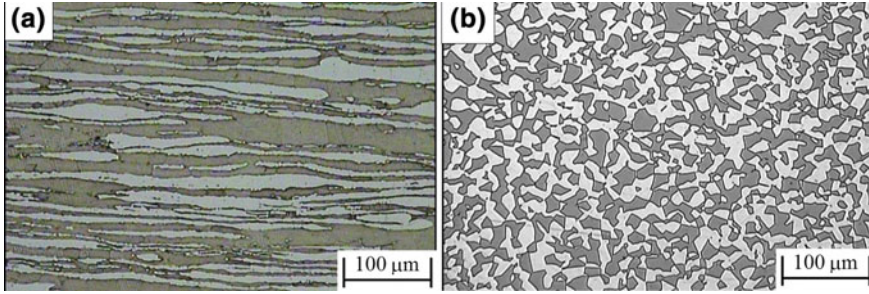


**Fig. 2** Microstructure of the hot rolled DSS (a) and HIP DSS (b), both solution treated. Austenite is light and ferrite is dark. Beraha's etching

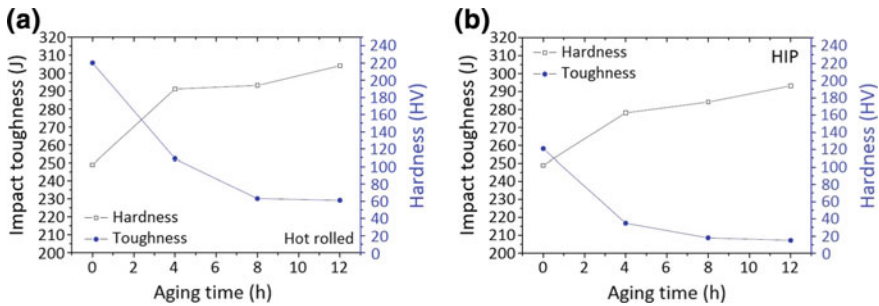


**Fig. 3** Curves of hardness and toughness at  $-46\text{ }^{\circ}\text{C}$  as function of aging time at  $475\text{ }^{\circ}\text{C}$  for a wrought (hot rolled) and b HIP DSS

Figure 3 shows the variation curves of hardness and impact toughness as function of aging time at  $475\text{ }^{\circ}\text{C}$  for the two materials. Both materials exhibit a similar behavior among themselves and in relation to the previously obtained results with duplex and super duplex stainless steels, with distinct designations, in different works [3–6]. As observed, the aging at  $475\text{ }^{\circ}\text{C}$  promotes a substantial increase in hardness accompanied by an unfortunate sharp decline in toughness, already in the first 4 h of heat treatment, due to the strong  $\alpha'$  precipitation kinetics resulting from spinoidal decomposition of the ferritic matrix ( $\delta$ ) [1–6]. However, the values found for 8 and 12 h of treatment were very close, showing no significant variations in the mechanical properties analyzed in these cases.

It should be noted that the impact toughness values obtained in the wrought DSS are higher compared to the HIPped material, in all conditions. This fact is probably due to the orientation of Charpy specimens, with the notch perpendicular to the elongated grains. This orientation gives a higher toughness because the crack's path is through finer austenite and ferrite grains. Likely, if the notches were positioned in the rolling direction, toughness values would be lower. This difference should not be high in the HIP, because there is no preferential direction of alignment (Fig. 2), as result of the manufacturing process.

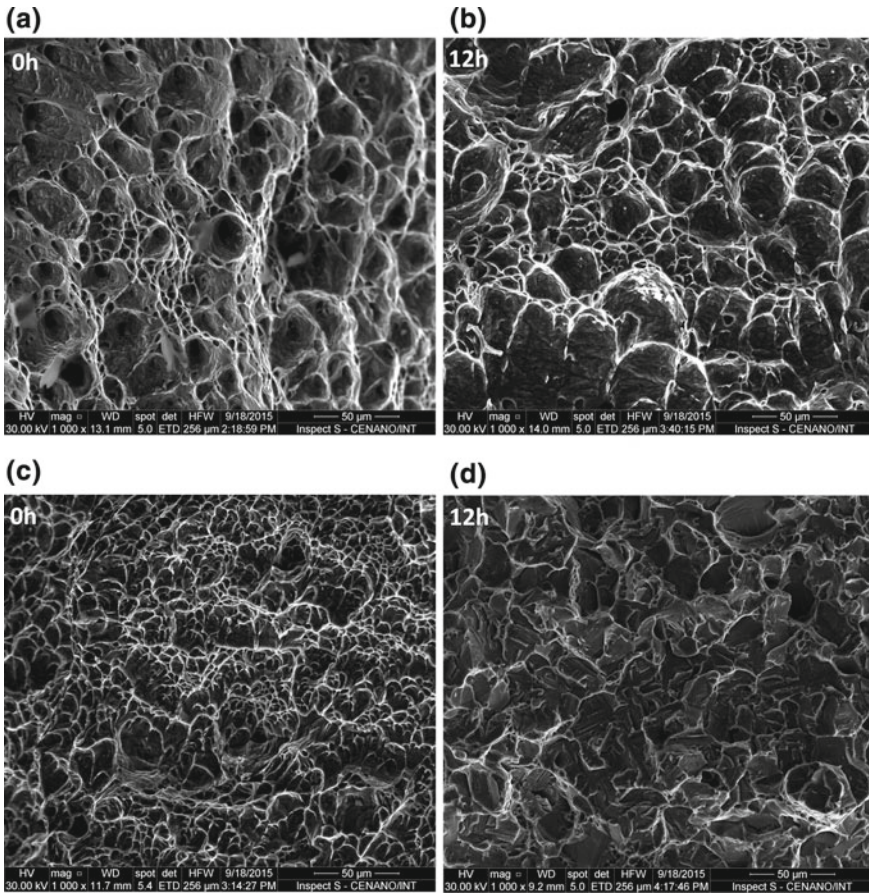


**Fig. 4** Fracture surfaces of Charpy specimens: Wrought (hot rolled) DSS, **a** solution treated and **b** 475 °C/12 h; HIP DSS, **c** solution treated and **d** 475 °C/12 h

When analyzing the fracture surfaces of the specimens, it was possible to display differences in the type of fracture between the two steels studied. The wrought DSS presented a predominantly ductile appearance, with dimples, under all conditions analyzed, even after 12 h of aging (Fig. 4b). However, the DSS produced by HIP presented ductile behavior only in the solution treated condition (Fig. 4c), showing an increasingly brittle aspect, with cleavage facets, with the increase of heat treatment time up to 12 h (Fig. 4d).

The more ductile behavior of the hot rolled steel can be attributed to the lower C and S contents in its chemical composition. It was possible to observe, in this same material, the occurrence of openings with de-lamination characteristics in specimens aged for 4, 8 and 12 h. Delaminations were not present in the solution condition of wrought DSS, neither in HIP DSS under any heat treatment conditions.

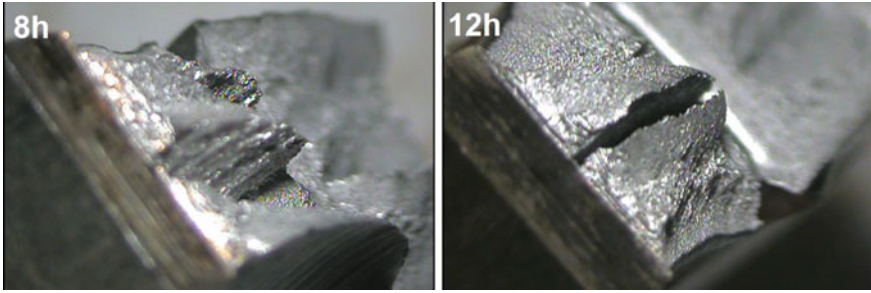
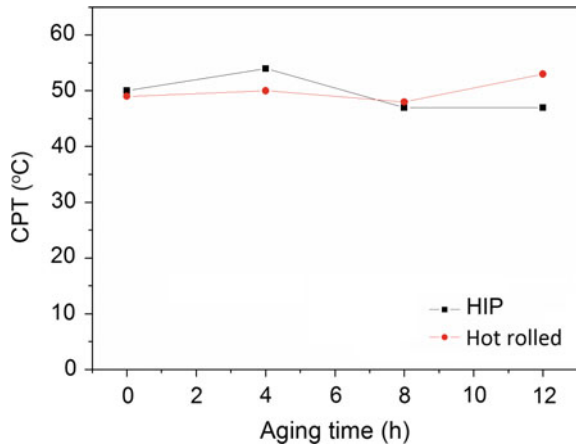


**Fig. 5** Presence of delaminations on fracture surfaces of wrought (hot rolled) DSS Charpy specimens aged at 475 °C for 8 and 12 h

**Fig. 6** Critical pitting temperature (CPT) as a function of aging time at 475 °C



According to Straffelini et al. [12] delaminations are formed due to the brittle cracking of ferrite lamellae at low temperatures and have the effect of deflecting the propagation of cracks, which justifies the high amount of energy absorbed under these conditions, besides the presence of the ductile phase austenite. The delaminations are more evident in mechanically worked materials. Regions with ductile fracture characteristics and areas with brittle fracture appearance, due to delamination, indicate that although the material presents good toughness at this temperature ( $-46$  °C), it is close to the ductile-brittle transition of ferrite phase ( $\delta$ ) [12]. Figure 5 shows the presence of delaminations in the specimens of wrought material under the conditions where they are more apparent: 8 and 12 h of aging.

Figure 6 shows the critical pitting temperature (CPT) as a function of aging time at 475 °C for the two DSS studied. Both materials showed no evident decrease on CPT as the aging time increased. Also, showing close values between the two steels, approximately 50 °C, under all conditions analyzed, in agreement with values found in other studies [1, 2, 13]. This can be explained by similar values of PREN.



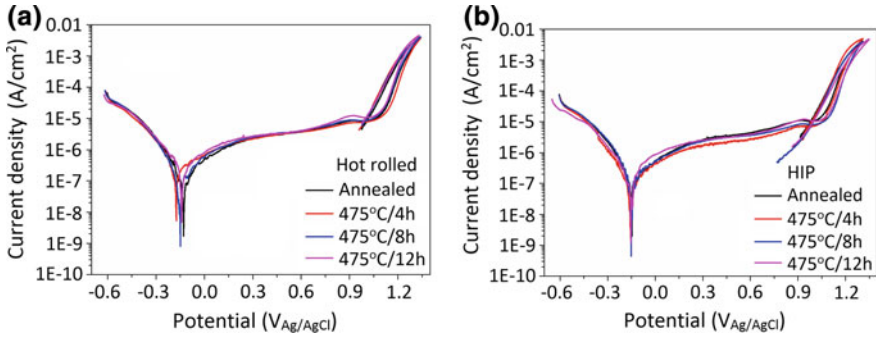
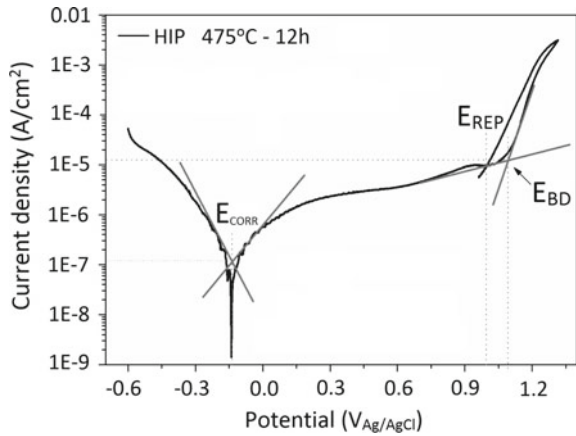


**Fig. 7** Cyclic polarization curves in 3.5% NaCl of **a** Hot rolled and **b** HIP DSS

**Fig. 8** Determination of electrochemical parameters by polarization curves



Therefore, there was no evidence of influence of  $\alpha'$  phase, up to 12 h exposure, on pitting corrosion resistance of these steels. However, the mechanical properties were more sensitive to this deleterious phase, evidencing changes already in the first 4 h of treatment.

Figure 7 shows the potentiodynamic polarization curves of duplex stainless steel under the different heat treatment conditions in 3.5% NaCl solution. Figure 8 gives an example of how the electrochemical parameters were obtained from these curves.

Typical anodic polarization behavior of a stainless steel in 3.5% NaCl solution consists of active dissolution (around the anodic peak), passivity, and a rapid increase of the current density. Table 3 shows the corrosion potential ( $E_{CORR}$ ), corrosion current density ( $I_{CORR}$ ), passivation current density ( $I_{PASS}$ ), breakdown potential ( $E_{BD}$ ) and repassivation potential ( $E_{REP}$ ) obtained through the polarization curves of Fig. 8. It is worth noting that no significant changes occur in the corrosion ( $E_{CORR}$ ), breakdown ( $E_{BD}$ ) and repassivation potentials ( $E_{REP}$ ). Samples annealed and aged presented a low current density, around a few  $\mu A cm^{-2}$  up to 1.0  $V_{Ag/AgCl}$ . The abrupt increase of current, for these samples, was felt in the potential range where oxygen evolution

**Table 3** Electrochemical parameters calculated by polarization curves of HIP and wrought (W) (hot rolled) DSS

DSS	$E_{CORR}$ ( $V_{Ag/AgCl}$ )	$I_{CORR}$ (A $cm^{-2}$ )	$E_{BD}$ ( $V_{Ag/AgCl}$ )	$I_{BD}$ (A $cm^{-2}$ )	$E_{REP}$ ( $V_{Ag/AgCl}$ )	$I_{REP}$ (A $cm^{-2}$ )
HIP_Annealed	-0.140	2.58E-07	1.030	1.08E-05	0.978	1.03E-05
HIP_475 °C_4 h	-0.147	1.16E-07	1.060	8.95E-06	0.970	7.22E-06
HIP_475 °C_8 h	-0.146	2.19E-07	1.103	9.97E-06	0.985	8.05E-06
HIP_475 °C_12 h	-0.166	2.15E-07	1.089	1.19E-05	1.00	1.06E-05
W_Annealed	-0.129	1.56E-07	1.101	9.00E-06	1.006	8.07E-06
W_475 °C_4 h	-0.140	1.82E-07	1.093	1.69E-05	1.001	1.82E-05
W_475 °C_8 h	-0.155	1.01E-07	1.070	9.49E-06	0.997	8.44E-06
W_475 °C_12 h	-0.129	1.79E-07	1.119	1.35E-05	1.001	1.07E-05

could already thermodynamically take place. At higher potentials, the oxygen anodic reaction seemed to participate in pitting nucleation through the formation of a triple interface between the metal, electrolyte, and oxygen bubbles [14]. Indeed, a previous measurement performed on a Pt electrode in this test solution had indicated that the evolution of  $O_2$  was about  $1.05 V_{Ag/AgCl}$  at  $25.0^\circ C$ . Therefore, the steep increase at  $\sim 1.0 V_{Ag/AgCl}$  ( $E_{BD}$  in Table 3) for these samples is likely due not to pitting corrosion but to the onset of oxygen evolution. These results are in accordance to the CPT values of Fig. 6.

## 4 Conclusions

The main conclusions about the effect of thermal aging at  $475^\circ C$  on two duplex stainless steels with similar composition, but produced by different methods (hot rolling and PM-HIP), are:

- There is a substantial increase on hardness of the analyzed steels in the first 4 h of thermal aging at  $475^\circ C$  as a consequence of the spinodal decomposition of the ferritic matrix;
- The impact toughness, in both materials, decreased considerably in the first 4 h of aging at  $475^\circ C$ , which means that these steels are very susceptible to  $\alpha'$  formation through the  $\delta$  spinoidal decomposition. The toughness values obtained for the wrought (hot rolled) DSS are higher than for HIPped steel, under all conditions, probably due to the orientation of Charpy test specimens notch, which was perpendicular to the rolling direction;

- The fracture surface of specimens of the hot rolled steel remained predominantly ductile even after 12 h of aging, being less influenced by the 475 °C embrittlement than the DSS produced by HIP;
- De-laminations appeared in wrought DSS specimens aged for 4, 8 and 12 h, not occurring in the solution condition of this material, neither in HIP DSS, under any conditions. This phenomenon, which is common in wrought materials, is due to brittle cracking of ferrite at low temperatures;
- Both materials showed critical pitting temperature (CPT) values close to each other, approximately 50 °C, under all conditions analyzed, due to their similar values of PREN. Besides, no evident decrease of CPT was observed with the increase of aging time at 475 °C;
- The results of potentiodynamic polarization tests in 3.5% NaCl solution at room temperature were in accordance to the CPT tests, i.e. the electrochemical parameters from both steels were similar and no deterioration was observed with aging at 475 °C. All breakdown potentials were slightly superior to 1.0 V<sub>Ag/AgCl</sub> and were attributed to the onset of oxygen evolution.
- The results show that, for both materials, mechanical properties, such as toughness and hardness, are more sensitive to aging at 475 °C, having been affected already in the first 4 h of heat treatment, whereas pitting corrosion resistance was not altered by the precipitation of  $\alpha'$  phase, even after 12 h of exposure.

**Acknowledgements** Authors are grateful to Brazilian Research Agencies CAPES, FAPERJ and CNPq.

## References

1. Gunn, R.N.: Duplex Stainless Steels. Microstructure, Properties and Applications. Abington Publishing, Cambridge (2003)
2. Alvarez-Armas, I., Degalliaix-Moreuil S.: Duplex Stainless Steels. ISTE Ltd and Wiley, London, England (2009)
3. Sahu, J.K., Krupp, U., Ghosh, R.N., Christ, H.-J.: Effect of 475 °C embrittlement on the mechanical properties of duplex stainless steel. *Mater. Sci. Eng. A* **508**, 1–14 (2009)
4. Hättestrand, M., Larsson, P., Chai, G., Nilsson, J.O., Odqvist, J.: Study of decomposition of ferrite in a duplex stainless steel cold worked and aged at 450–500 °C. *Mater. Sci. Eng. A* **499**, 489–492 (2009)
5. Tavares, S.S.M., Terra V.F., de Lima Neto, P., Matos D.E.: Corrosion resistance evaluation of the UNS S31803 duplex stainless steels aged at low temperatures (350 to 550 °C) using DLEPR tests. *J. Mater. Sci.* **40**, 4025–4028 (2005)
6. Weng, K.L., Chen, H.R., Yang, J.R.: The low-temperature aging embrittlement in a 2205 duplex stainless steel. *Mater. Sci. Eng. A* **379**, 119–132 (2004)
7. Loureiro, A., da Costa, V.C., Pardal, J.M., Montenegro, T.R., Tavares, S.S.M.: Influence of heat treatments at 475 °C and 400 °C on the pitting corrosion resistance and sensitization of UNS S32750 and UNS S32760 superduplex stainless steels. *Mater. Corros.* **63**, 522–526 (2012)
8. Tavares, S.S.M., Pardal, J.M., Abreu, H.F.G., Nunes, C.S., da Silva, M.R.: Tensile properties of duplex UNS S32205 and lean duplex UNS S32304 steels and the influence of short duration 475 °C aging. *Mater. Res.* **15**, 859–864 (2012)

9. ASTM International: ASTM G150—Standard Test Method for Electrochemical Critical Pitting Temperature Testing of Stainless Steels. West Conshohocken, PA (2013)
10. ASTM International: ASTM E23-16b—Standard Test Methods for Notched Bar Impact Testing of Metallic Materials. West Conshohocken, PA (2016)
11. Norsok Standard: Norsok Standard M-601—Welding Specification of piping. Standards Norway, Lysaker (2016)
12. Straffelini, G., Fontanari, V., Molinari, A.: Impact fracture toughness of porous alloys between room temperature and  $-60\text{ }^{\circ}\text{C}$ : *Mater. Sci. Eng. A* **272**, 389–397 (1999)
13. Nascimento, A.M., Ierardi, M.C.F., Kina, A.Y., Tavares, S.S.M.: Pitting corrosion resistance of cast duplex stainless steels in 3.5% NaCl solution. *Mater. Charact.* **59**, 1736–1740 (2008)
14. Alonso-Falleiros, N., Hakim, A., Wolyneć, S.: Comparison between potentiodynamic and potentiostatic tests for pitting potential measurement of duplex stainless steels. *Corrosion* **55**, 443–448 (1999)

# Determination of Previous Austenite Grain Size 9%Ni Low Carbon Steel and Its Effect on Impact Toughness at $-196\text{ }^{\circ}\text{C}$



Sérgio S. M. Tavares, Rachel P. C. da Cunha, Cássio Barbosa,  
Manoel R. Silva and Rafael A. Vinhosa

**Abstract** Low carbon steel with 9%Ni is used in cryogenic services, in which high toughness and strength are required. One of the main concepts of physical metallurgy is that the toughness and strength may be increased by grain refinement. In martensitic steels, the grain size that can be measured is the previous austenite grain size (PAGS). The goal of this work is to reveal and measure the PAGS's of different specimens of 9%Ni low carbon steel and correlate these results with hardness and low temperature toughness. The decrease of PAGS's improve the toughness of specimens quenched and quenched and tempered.

**Keywords** PAGS · Previous austenite grain size · 9%Ni low carbon steel

## 1 Introduction

One of the more solid concepts of physical metallurgy is that the grain refinement is a strengthening mechanism which also increases the impact and fracture toughness of metallic materials, including steels. This is the basis for many researches and

---

S. S. M. Tavares

Universidade Federal Fluminense, Rua Passo da Pátria, São Domingos, Niterói RJ  
156-209, Brazil

R. P. C. da Cunha (✉) · R. A. Vinhosa

Centro Federal de Educação Tecnológica Celso Suckow da Fonseca, Av. Maracanã,  
229 – Maracanã, Rio de Janeiro – RJ, Brazil  
e-mail: [rachel.pereira.cunha@gmail.com](mailto:rachel.pereira.cunha@gmail.com)

R. P. C. da Cunha · C. Barbosa

Instituto Nacional de Tecnologia, Centro de Nanomateriais, Av. Venezuela,  
82 – Praça Mauá, Rio de Janeiro – RJ, Brazil

M. R. Silva

Universidade Federal de Itajubá, Av. B P S, 1303 – Pinheirinho, Itajubá, MG, Brazil

© Springer Nature Switzerland AG 2019

L. F. M. da Silva (ed.), *Materials Design and Applications II*, Advanced  
Structured Materials 98, [https://doi.org/10.1007/978-3-030-02257-0\\_3](https://doi.org/10.1007/978-3-030-02257-0_3)

developments in high strength low alloys steels (HSLA) with ferritic or bainitic structures [1–5]. However, in quenched and tempered (Q&T) steels, the grain size that can be measured by metallographic techniques is the previous austenite grain size (PAGS). The toughness of the final product can be function of the PAGS, but is also strongly influenced by other microstructural features that are controlled by the tempering treatment.

Some previous works investigated the effect of PAGS on the toughness of high nickel alloys. The more common behavior is the increase of toughness with the decrease of average grain size, and this is also expected for PAGS refinement. However, exceptions to this behavior can be found in some specific materials. For instance, Sinha et al. [6] observed the increase of fracture toughness of a maraging steel solution treated. In a previous work, Tavares et al. [7] also observed the increase of impact toughness of maraging 300 with the increase of austenitizing temperature and PAGS. However, in aged specimens, the toughness was much lower, and the influence of PAGS could not be determined.

Steels with 9%Ni and low carbon are used in cryogenic services, in which high toughness and strength are required. According to ASTM A333 [8], standard, pipes and tubes of these steels must be quenched and tempered or double normalized and tempered. Tempering temperature must be in the 565–605 °C range. If the tempering is carried out some degrees above the  $A_1$  temperature of the steel, some austenite is formed and retained on cooling to room temperature. The high strengths of martensitic steels are attributed to high density dislocation martensite laths with body-centred cubic (BCC) structure, while their good ductility results from the retained austenite flakes with face-centred cubic (FCC) structure between laths [9]. A microstructure of tempered martensite with 6–10% of reverse austenite is so produced. On the other hand, the tempering at 400 °C may promote temper embrittlement of 9%Ni low carbon steels. Temper embrittlement may occur if these steels are subjected to tempering at 370–540 °C for prolonged periods [10].

The measurement of PAGS is an important issue. The careful metallographic preparation and the choice of the etching reagent and procedure are the main challenges for an accurate measurement. In this work, the previous austenite grains boundaries of a 9%Ni low carbon steel were revealed to obtain a reliable quantification of PAGS in function of the soaking (austenitizing) temperature in the quenching treatment. The correlation of impact toughness and PAGS was determined for specimens un-tempered and specimens tempered at 400–600 °C.

## 2 Materials and Methods

Specimens of a 9%Ni steel (composition shown in Table 1) were cut from a forged and machined to dimensions close to the sub-size Charpy specimen ( $11 \times 8.0 \times 56 \text{ mm}^3$ ). The pre-machined pieces were heat treated by quenching and tempering and then machined to final dimensions ( $10 \times 7.5 \times 55 \text{ mm}^3$ ) with V-notch.

**Table 1** Chemical composition of 9%Ni-low carbon steel studied (mass %)

C	Mn	Ni	Si	P	S	Ti	Al
0.062	0.64	9.54	0.259	0.01	0.01	0.014	0.023

**Table 2** Heat treatments performed and specimens identification

Austenitizing temperature (°C)	Tempering		
	Un-tempered	400 °C/1 h	600 °C/1 h
820	Q1	Q1-T400	Q1-T600
1000	Q2	Q2-T400	Q2-T600
1150	Q3	Q3-T400	Q3-T600

Heat treatments and specimens' identification are described in Table 2. Three soaking (austenitizing) temperatures were used in order to obtain different PAGS's. Specimens of each soaking temperature were tempered at 400–600 °C, or un-tempered.

Impact toughness was measured at  $-196$  °C with sub-size V-notched Charpy (7.5 mm) specimens. Two specimens were produced per each heat treatment and average results are presented. The fractured specimens were observed by scanning electron microscopy.

Charpy impact tests at  $-196$  °C were performed in an Universal Pendul, with maximum energy 300 J. After the tests the surfaces of fracture were collected and protected against corrosion for observation in the scanning electron microscope (SEM). Vickers hardness tests with load 10 kgf were performed in all specimens.

Previous austenite grain boundaries were revealed by immersion in a solution composed of 15 g picric acid, 5 ml of potassium chromate, 625 ml of distilled water and 275 ml of neutral detergent solution.

The optical microscope images were treated using software ImageJ [11]. The PAGS was quantified with the intercept method described in the ASTM E-112 standard [12].

Austenite formation was evaluated in small samples carefully cut from the un-deformed portion of fractured Charpy specimens. The austenite volume fraction was determined by the magnetization saturation method [13], using a vibrating sample magnetometer (VSM) with maximum applied field 1 T, at room temperature. A specimen quenched and deformed by cold rolling was produced to determine the value of the magnetization saturation intrinsic of martensite ( $m_{S(i)}$ ). This value was found to be 230.4 emu/g. The austenite volume fraction (AVF) was estimated by:

$$C_{\gamma} = 1 - \frac{m_S}{m_{S(i)}} \quad (1)$$

where  $m_S$  is the magnetization saturation of the specimen analyzed.

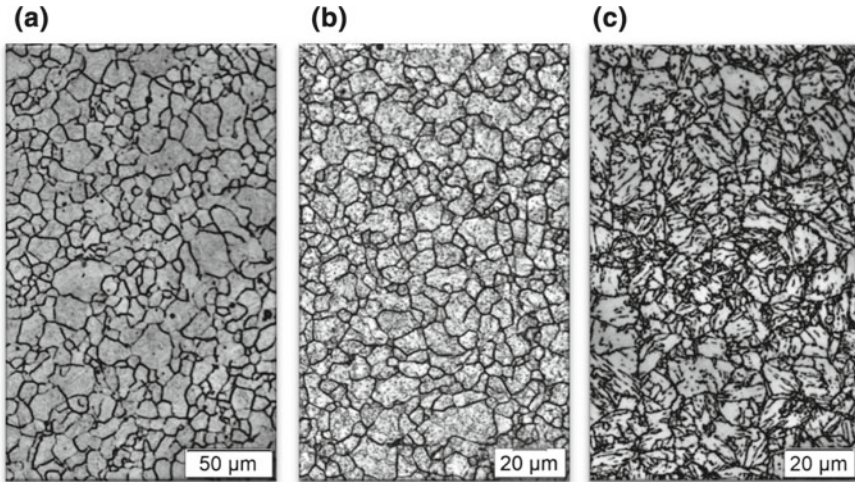


**Fig. 1** Optical microscope images after chemical solution—previous austenite grain size images **a** Q1 **b** Q1-T400 **c** Q1-T600

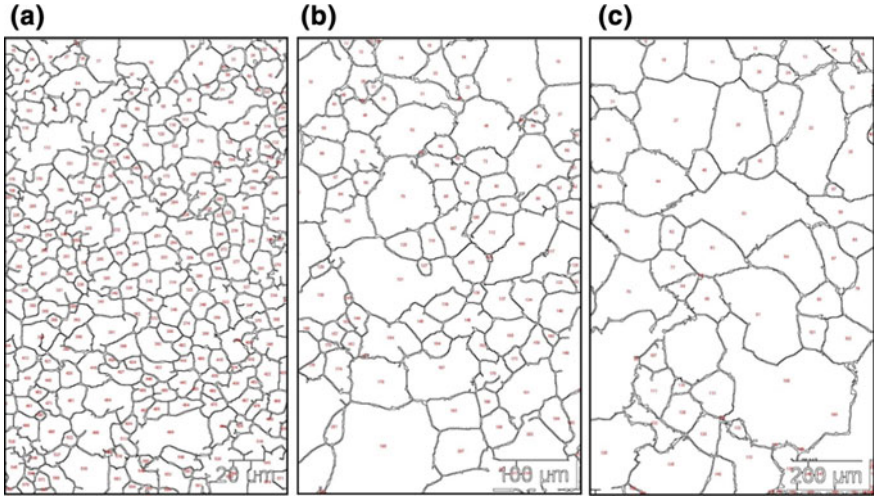
### 3 Results and Discussion

Figure 1a–c shows the micrographs of specimens Q1, Q1-T400 and Q1-T600, which were austenitized at 820 °C. Although all specimens were etched with picric acid and potassium chromate solution, the best results to reveal the PAGS were obtained in specimens tempered at 400 °C. The image of the quenched specimen shows that austenite grain boundaries were partially revealed (Fig. 1a). On the other hand, specimens tempered at 600 °C had new boundaries due to the tempering reactions, including recrystallization and reverse austenite formation. It is believed that the PAGS is not changed with tempering at 400 or 600 °C.

Images from Q1-T400, Q2-T400 and Q3-T400 were used to measure the PAGS by intercept method and mean Feret's diameter (the longest distance between any two points along the automatic selection boundary) after treatment with ImageJ. This software has the tool Automatic Particle counting, which was used to quantify the PAGS. Before application of this tool the images need to be cleaned to show only the grain boundaries. Three resources inside ImageJ [11] were used to improve the original images: the plugins Clahe, Threshold and Watershed. Figure 2a–c shows the images of specimens Q1-T400, Q2-T400 and Q3-T400, after cleaning.

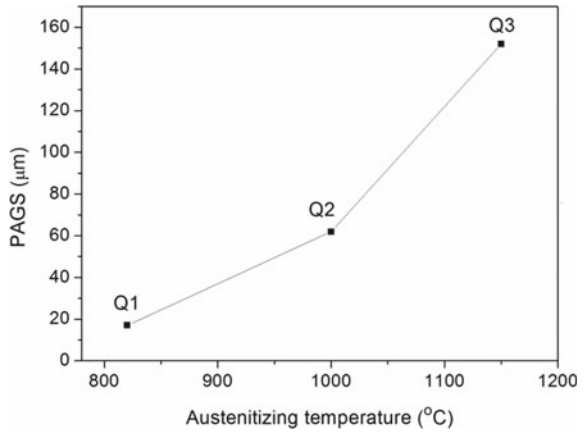
Figure 3 shows the variation of PAGS with austenitizing temperature before quenching Q1, Q2 and Q3. Figure 4 shows the impact toughness as function of heat treatment, with PAGS indicated. As can be seen, the increase of PAGS provokes a general decrease of toughness. Although this is an expected result, Cao et al.





**Fig. 2** Optical microscope images on software ImageJ, after treatment with ImageJ tools. **a** Q1-T400 **b** Q2-T400 **c** Q3-T400

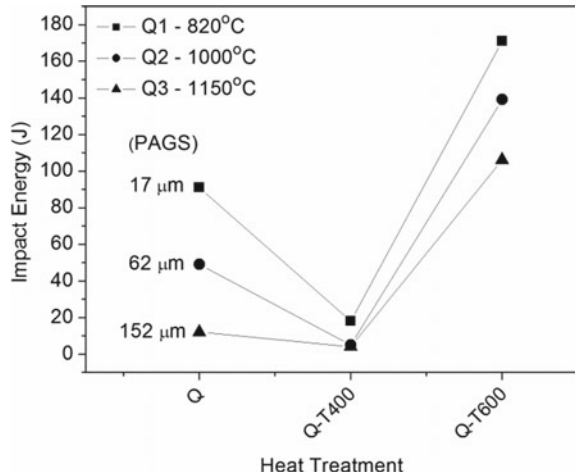
**Fig. 3** Variation of PAGS with austenitizing temperature



[14] reported that the coarse grained heat affected zone (CGHAZ) of a 8%Ni steel showed higher toughness than the fine grained region (FGHAZ). Possibly, other microstructural features exert influence on the HAZ toughness.

Very low toughness is obtained with tempering at 400 °C. At this tempering temperature the material shows a temper embrittlement effect [10]. This effect is enhanced with the increase of PAGS, as shown in Fig. 4.

**Fig. 4** Variation of toughness with heat treatments



The higher toughness values were obtained in specimens tempered at 600 °C, but the grain coarsening also decreased the impact toughness. Figure 5a–c, d–f and g–i compare the surface of fracture of specimens Q1-T600, Q2-T600 and Q3-T600, respectively. The main difference between the three specimens was noticed in the images taken from the center of fractured Charpy specimens, since near the surface they all showed ductile features. In the center region, specimen Q1-T600 showed a completely ductile fracture (Fig. 5a), while specimens Q2-T600 and Q3-T600 showed typical cleavage facets and rivers (Fig. 5d, g).

Figure 6 shows the variation of Vickers hardness with the heat treatment. Comparing the results of as quenched specimens, it was observed the decrease of the hardness with the increase of tempering temperature. After tempering at 400–600 °C the hardness values were very close.

Figure 7 shows the Austenite Volumetric Fraction (AVF) as a function of heat treatment temperature. In general, the specimen quenched from 1150 °C and tempered had less austenite than the specimens quenched from 1000 to 820 °C. In low alloys steels, such as SAE 4340, the increase of PAGS increases the harden ability but also results in a higher retained austenite content [13]. This was only observed when comparing specimens quenched from 820 °C (Q1) to 1000 °C (Q2). Also, according to some previous works [15, 16], the increase of reverse austenite formed in the tempering treatment improves the toughness of 9%Ni steels. This austenite formed during tempering is different from the retained austenite un-transformed in the quenching treatment. Specimens Q2 and Q3 have high contents of retained austenite, but it does not contribute to improve toughness.

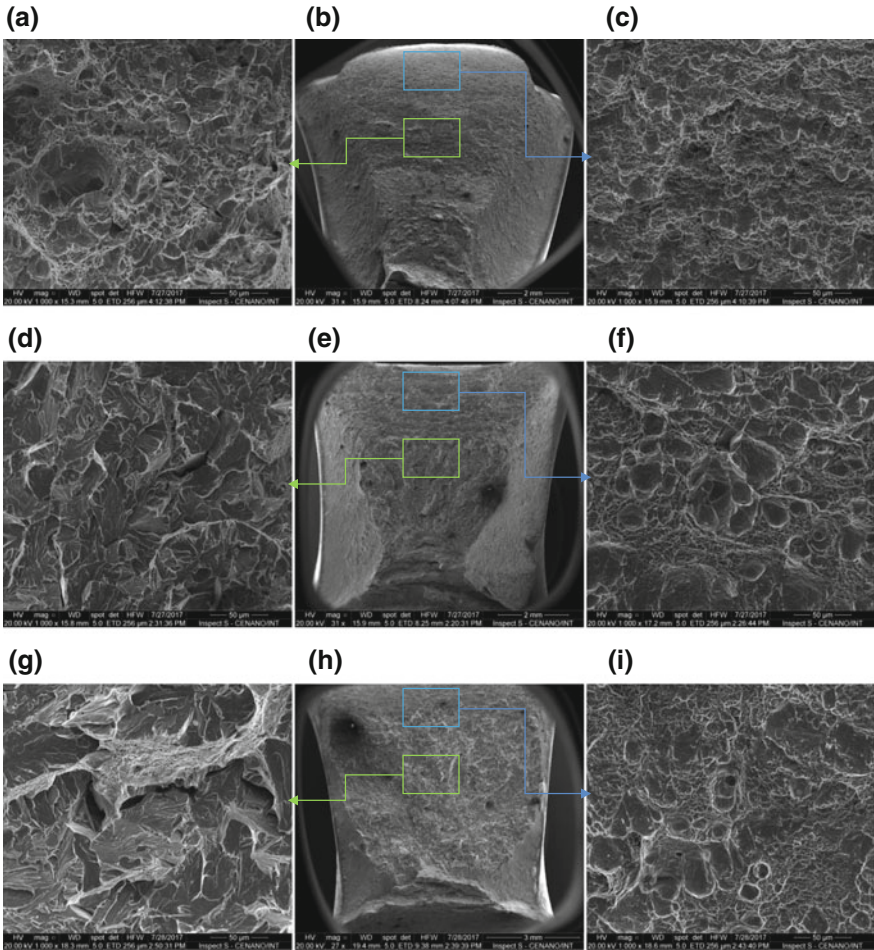


**Fig. 5** Scanning electron microscopy images of fractured Charpy specimens tested at  $-196\text{ }^{\circ}\text{C}$  a-c Q1-T600 d-f Q2-T600 g-i Q3-T600

## 4 Conclusions

Previous austenite grain sizes (PAGS) of specimens quenched and tempered of 9%Ni low carbon steel were determined by quantitative metallography. Three austenitizing temperatures (820, 1000 and 1150  $^{\circ}\text{C}$ ) were tested. Previous austenite grains were revealed by etching in a solution composed of 15 g picric acid, 5 ml of potassium chromate, 625 ml of distilled water and 275 ml of neutral detergent solution. The

**Fig. 6** Hardness as function of heat treatment temperature

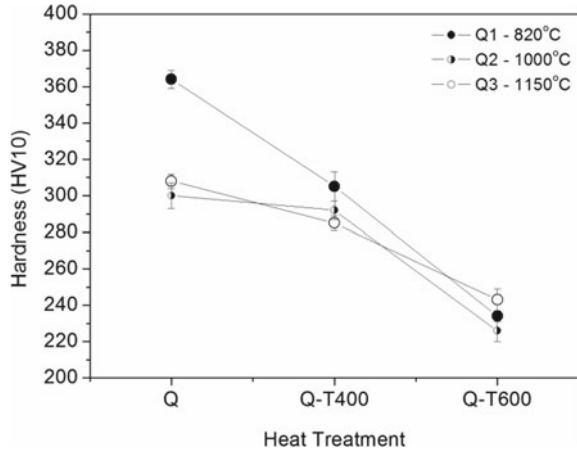
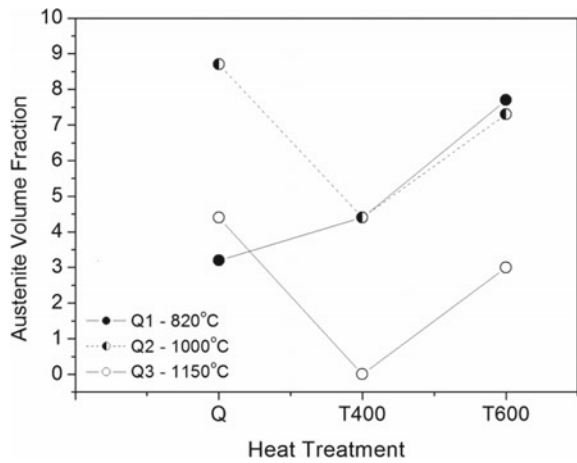


**Fig. 7** Austenite volumetric fraction as a function of heat treatment



images from specimens quenched and tempered at 400 °C were the most suitable for PAGES quantification. ImageJ software [11] was used to treat the images and determine the PAGES.

The increase of PAGES caused the decrease of toughness of specimens as quenched, quenched and tempered at 400 °C, and quenched and tempered at 600 °C.

**Acknowledgements** This work was conducted during a scholarship supported by the International Cooperation Program CAPES at the CEFET/RJ. Financed by CAPES—Brazilian Federal Agency for Support and Evaluation of Graduate Education within the Ministry of Education of Brazil.

## References

1. Lan, H.F., Du, L.X., Li, Q., Qiu, C.L., Misra, R.D.K.: Improvement of strength-toughness combination in austempered low carbon bainitic steel: The key role of refining prior austenite grain size. *J. Alloy. Compd.* **710**, 702–710 (2017)
2. Kang, J., Li, C., Yuan, G., Wang, G.: Improvement of strength and toughness for hot rolled low-carbon bainitic steel via grain refinement and crystallographic texture. *Mater. Lett.* **175**, 157–160 (2016)
3. Srivatsa, K., Srinivas, P., Balachandran, G., Balasubramanian, V.: Improvement of impact toughness by modified hot working and heat treatment in 13% Cr martensitic stainless steel. *Mater. Sci. Eng.* **677**, 240–251 (2016)
4. Calcagnotto, M., Ponge, D., Raabe, D.: Effect of grain refinement to 1  $\mu\text{m}$  on strength and toughness of dual-phase steels. *Mater. Sci. Eng. A* **527**, 7832–7840 (2010)
5. Ming, L., Wang, Q., Wang, H., Zhang C., Guo, A.: A remarkable role of niobium precipitation in refining microstructure and improving toughness of A QT-treated 20CrMo47NbV steel with ultrahigh strength. *Mater. Sci. Eng.* **613**, 240–259 (2014)
6. Sinha, P.P., Sreekumar, K., Babu, N.S., Pant, B., Natarajan, A., Nagarajan, K.V.: Development of heat treatment parameters to improve fracture toughness and grain size of an embrittled maraging steel. *J. Heat Treat.* **9**, 125–131 (1992)
7. Tavares, S.S.M., Pardal, J.M., Martins, T.R.B., Schmitt, V.M., Szejf, J.F.V.: Influence of austenitizing on the mechanical properties of maraging 300 and SAE 4340 steels—comparative study. *Mater. Res.* **20**(2) (2017)
8. ASTM A-333-15: Standard Specification for Seamless and Welded Steel Pipe for Low-Temperature Service and Other Applications with Required Notch Toughness. ASTM International, West Conshohocken, PA, USA (2015)
9. Wang, Y., Zhang, K., Guo, Z., Chen, N., Rong, Y.: A new effect of retained austenite on ductility enhancement in high strength bainitic steel. *Mater. Sci. Eng.* **552**, 288–295 (2012)
10. Ahsan, Q., Haseeb, A.S.M.A., Hussein, N.I.S.B.H., Chang, S.Y.: 9% Nickel steels and their welding behavior. *Compr. Mater. Process.* **6**, 135–149 (2014)
11. Rasband, W.S.: ImageJ, U.S. National Institutes of Health, Bethesda, Maryland, USA (1997–2016). <https://imagej.nih.gov/ij/>
12. ASTM E112-13: Standard Test Methods for Determining Average Grain Size. ASTM International, West Conshohocken, PA (2013)
13. Ajus, C., Tavares, S.S.M., Silva, M.R., Corte, R.R.A.: Magnetic properties and retained austenite quantification in SAE 4340 steel. *Rev. Matér.* **14**, 993–999 (2009)
14. Cao, R., Feng, W., Peng, Y., Du, W.S., Tian, Z.L., Chen, J.H.: Investigation of abnormal high impact toughness in simulated welding CGHAZ of a 8%Ni 980 MPa high strength steel. *Mater. Sci. Eng. A* **528**, 631–642 (2010)
15. Kim, K.J., Schwartz, L.H.: On the effects of intercritical tempering on the impact energy of Fe-9Ni-0.1C. *Mater. Sci. Eng.* **33**, 5–20 (1978)
16. Tavares, S.S.M., Rodrigues, C.R., Oliveira, C.A.S., Woyames, C.B., Dille, J.: Influence of heat treatments on microstructure and toughness of 9%Ni steel. *J. Mater. Eng. Perform.* **27**, 1530–1536 (2018)
17. Voort, G.F.V.: Revealing prior-austenite grain boundaries. *Microsc. Microanal.* **16**(2) (2010)

# Corrosion Study of Ti5Al4V and Ti6Al4V in Different Simulated Body Fluids



M. P. Nikolova and E. H. Yankov

**Abstract** The ( $\alpha + \beta$ ) Ti6Al4V alloy is widely used in different industrial applications and in medicine. The decrease in the content of the  $\alpha$ -strengthening element Al in Ti5Al4V as opposed to conventional Ti6Al4V alloy reduces the hardness as Al is a solid solution hardener but simultaneously, the alloy is expected to have lower cytotoxicity, improved plasticity and low precipitation hardening ability at precipitation temperature. The role of the alloying elements and the influence of heat treatment on corrosion resistance of Ti5Al4V and Ti6Al4V alloys have been studied after a short and long-term immersion in Ringer (RS), phosphate buffer saline (PBS) with and without the addition of H<sub>2</sub>O<sub>2</sub>, and 5 M HCl at  $37 \pm 0.1$  °C. It has been found out that lower pH and higher Cl<sup>-</sup> concentration in RS make the surface of the alloys more prone to pitting corrosion and showing nobler corrosion potentials at the same time, in contrast to PBS where salt films of insoluble products are formed on some pits. The potentiodynamic polarisation measurements show higher anodic reaction rate after a 30-days' period of immersion in PBS and H<sub>2</sub>O<sub>2</sub> for both alloys. The dissolution of Ti, Al, and V and oxidation in 5 M HCl are the highest for solution treated Ti6Al4V and Ti5Al4V alloys, while the corrosion rate for the 10-days' period in the acid was the lowest for the as-received Ti5Al4V.

**Keywords** Ti6Al4V · Heat treatment · Microstructure · Pits · SEM-EDS Corrosion behavior

## 1 Introduction

The most common  $\alpha + \beta$  titanium alloy is Ti6Al4V (Ti-64). It is widely used in medicine for implants and prosthesis replacing or stabilizing various parts of the body, such as joint replacements, dental implants, heart valves, surgical equipment,

---

M. P. Nikolova (✉) · E. H. Yankov  
Department of Material Science and Technology, University of Ruse "A. Kanchev",  
8 Studentska Str., Ruse, Bulgaria  
e-mail: [mpnikolova@uni-ruse.bg](mailto:mpnikolova@uni-ruse.bg)

© Springer Nature Switzerland AG 2019  
L. F. M. da Silva (ed.), *Materials Design and Applications II*, Advanced  
Structured Materials 98, [https://doi.org/10.1007/978-3-030-02257-0\\_4](https://doi.org/10.1007/978-3-030-02257-0_4)

etc. By using heat treatment the alloy could be straightened by  $\beta \rightarrow \alpha'$  diffusionless transformation and precipitation of intermetallics. Al is an  $\alpha$ -phase stabilizer although it has a significant solubility in  $\beta$  phase. The isomorphous with  $\beta$ -Ti V, Mo and Nb stabilize the  $\beta$ -phase. Nag et al. [1] discovered that the elastic modulus of Ti tends to increase with increasing the content of Al and with increasing the volume fraction of  $\alpha$ -phase in the alloy. The higher mismatch between the bone and the implant results in higher “stress shielding effect” [2] at their contact interface and substantial bone resorption. Therefore, the alloy having a lower Al content like Ti5Al4V (Ti-54) could be more favorable for mating with bone.

The interaction between the metallic implant and the body environment determines the service life of the component and is strongly dependent on the corrosion behavior of the alloy [3]. The properties of the surface oxides are essential for the corrosion behavior as they affect the ion exchange events, re-passivation processes, and fracture. The properties of the oxide film depend on the different kinds of point defects, dislocations, grain boundaries, etc. Therefore, not only the chemical composition but also the microstructure, along with the topography, could modify the electrochemical behavior of the implant material. The body fluids consist of different inorganic ions ( $\text{Na}^+$ ,  $\text{Ca}^{2+}$ ,  $\text{Cl}^-$ ,  $\text{PO}_3^{4-}$ , etc.), organic acids, proteins, enzymes, etc. and pH buffered at 7.15–7.35 [4]. During inflammatory reactions and wound healing, bacteria or inflammatory cells release hydrogen peroxide ( $\text{H}_2\text{O}_2$ ) or other superoxides into the extracellular environment in order to defend from foreign bodies [5, 6]. Dissemond [7] found out that in the context of wound healing the pH lowers down to pH 5 during the first two weeks and then shifts back to normal pH values of 7.4–7.6. The use of infusion or buffer saline may give insight to some aspects of passivation behavior of materials without the presence of enzymes and other reactive species which are expected to be present in vivo environment. Additionally, for a better understanding of the electrochemical behavior under inflammatory conditions, the processes have to be simulated in biologically relevant electrolyte solutions and conditions. Wang et al. [8] discussed that as the anodic currents for Ti alloys do not exhibit considerable densities, the high potentials ( $> +1$  V vs. SHE) are not considered as relevant because of the oxygen evolution. Therefore, more aggressive solutions could be used in the vicinity of open circuit potential. For that reason, in the particular study, except simulated body fluids, we use 5 M HCl to check the weight losses and changes in the surface chemical composition.

Examining the behavior of a Ti-64 alloy, Brunette [9] claimed that alumina presented mainly in the outer region of the oxide layer, while vanadium oxides are closer to the bulk material. Auger measurements show that the native passive film of Ti-64 alloy contains roughly 10 at. % Al( $\text{Al}_2\text{O}_3$ ) and small quantities of V [10]. Alumina forms at the outer oxide/electrolyte surface and tends to segregate above the  $\alpha$ -phase [11]. According to Metikoš-Hukovic et al. [12] the  $\text{Cl}^-$  ions deteriorate the passivity of the oxide film especially in the presence of V oxides that preferentially dissolve in contrast to  $\text{TiO}_2$ . Therefore, the phase distribution and their chemical composition will affect the corrosion behavior of Ti–Al–V alloys.

The Ti-64 alloy is most commonly used in wrought and cast form. The thermal processes are able to change the properties of these alloys by altering the amount,

distribution or type of the  $\beta$ -phase. The fast cooling (water quenching) within the  $\alpha + \beta$  range usually forms primary equiaxed  $\alpha$ -grains and acicular martensite acquired by the  $\beta$ -transformation. The ability of the alloy to age by separation of  $Ti_3Al$  phase could additionally increase the strengthening of titanium alloy. There have been no systematic investigations regarding the corrosion behavior of Ti-64 and Ti-54 in different heat-treated conditions. Therefore, in the present work, the corrosion behavior of the as-received and heat-treated Ti-64 and Ti-54 alloys in Ringer, PBS with and without added  $H_2O_2$  and 5 M HCl saline have been explored and compared.

## 2 Experimental Procedures

The chemical compositions of both materials (Etropole, Bulgaria) used for the experiment, determined by JEOL JXCA-733 Microprobe scanning electron microscope (SEM) equipped with wavelength dispersive spectrometers (WDS), were shown in Table 1. Samples with dimensions  $14 \times 14 \times 4$  and  $15 \times 15 \times 4$  mm were cut out using electro-erosion cutting method.

The variation in the composition of the modified Ti-54 alloy changes the temperature of the solution treatment and that of the decomposition of the quenched structures as opposed to the conventional Ti-64 alloy [13]. The temperature of the solution treatment and precipitation of both alloys was adapted to obtain bimodal microstructure with low volume fraction of primary  $\alpha$ -grains and high hardness. The as-received (AR) samples were single solution treated (ST) for 30 min at 920 and 950 °C for Ti54 and Ti64, respectively and water quenched. Half of the ST specimens were precipitated (P) for 4 h at 500 and 540 °C for Ti54 and Ti64, respectively and slowly cooled down. All treatments were carried out in  $\leq 1$  Pa vacuum. The surfaces of the samples were grounded with 220 up to 1500 grit SiC paper, polished, and ultrasonically cleaned in ethanol and deionized water for 5 min before the electrochemical tests.

A standard three-electrode cell was used for the electrochemical measurements with Ag/AgCl reference electrode and a large pure Pt foil—as a counter electrode. Both electrodes together with the working one with  $1 \text{ cm}^2$  exposed area were immersed in 70 ml naturally aerated solutions—Ringer solution (RS) (8.60 g/L NaCl, 0.3 g/L KCl, and 0.33 g/L  $CaCl_2 \cdot 2H_2O$  with pH 5.7 (infusion bank)) and PBS (8 g/L NaCl, 0.2 g/L KCl, 1.44 g/L  $Na_2HPO_4$ , 0.24  $KH_2PO_4$  (Sigma Aldrich)) with pH 7.4) maintained at body temperature ( $37 \pm 0.5$  °C). To assess the long-term stability of both alloys another set of experiments were conducted for the 30-days-immersed samples in RS and PBS solution, whereas the samples were kept at  $37 \pm 1$  °C. In order to simulate inflammatory conditions for another set of samples, the PBS solution was acidified to pH 5 and  $H_2O_2$  (37%) was added to the saline, up to reaching 150 mM peroxide concentration. After two weeks the peroxide solution was replaced by a fresh PBS solution which time corresponded to the inflammatory process and the experiments continued 16 days more.



**Table 1** Chemical composition (wt%) of the substrate material

Element	Al	V	Fe	Mn	Co	Mo	Pd	Nb	Hf	Ti
Ti54	5.21	4.40	0.14	0.11	0.06	0.17	0.15	0.36	0.04	Bal.
Ti64	5.80	4.67	0.16	–	0.09	0.07	0.02	–	0.14	Bal.

**Table 2** Hardness values (HRc) of Ti-54 and Ti-64 in AR, ST and ST+P conditions

Alloy	AR	ST	ST+P
Ti54	29.2 ± 1.1	36.7 ± 0.8	37.9 ± 0.4
Ti64	32.8 ± 0.7	40 ± 0.5	41.5 ± 0.6

The open circuit (OC) potentials for all samples were monitored for 30 min by using potentiostat EG&G Princeton Applied Research Model 173. Subsequently, the potentiodynamic measurements were carried out at a scan rate of 0.5 mV/s from  $-0.3$  V up to  $+0.5$  V versus Ag/AgCl electrode. All OC potentials and potentiodynamic measurements were repeated at least twice in order to ensure repeatability of the experimental results. Before and after the electrochemical tests, the specimens were cleaned with ethanol and the surface morphologies were observed by scanning electron microscopy (SEM—LYRA I XMU, Tescan) equipped with energy dispersive spectroscopy (EDX—Quantax 200, Bruker) under an accelerating beam voltage of 20 kV.

The corrosion resistance was also assessed by performing weight loss experiments in 5 M HCl at  $37 \pm 1$  °C. Three samples of each AR, ST, and ST+P condition of both alloys were used. After grinding all sides with 1500 grit SiC, the specimens were ultrasonically cleaned in ethanol and deionized water. During that experiment, the alloys were removed every 2 days over a 10-days' period, ultrasonically cleaned in deionized water for 5 min, dried weighed and then placed in a freshly prepared solution for the next 2 days. The weight losses were calculated from the initial weight  $w_i$  and the on-going dried weight value  $w_o$  using the Eq. 1:

$$\text{Weight loss(\%)} = \frac{w_i - w_o}{w_i} \cdot 100 \quad (1)$$

### 3 Results and Discussions

The secondary electron image of the AR Ti-54 alloy obtained in form of plate displays thermo-mechanically treated bi-phase coarse lamellar (basket wave) structure (Fig. 1a) as opposed to the more equiaxed  $\alpha$  and intercrystalline  $\beta$  within the AR Ti-64 microstructure (Fig. 1b). For ensuring the straightening, both alloys were quickly cooled down in water (solution treated (ST)) from temperatures high in the  $\alpha + \beta$  phase area but below the  $\beta$ -phase transformation temperature. The hardness values obtained are shown in Table 2. Consequently, in ST condition both Ti-54 and Ti-64 alloys contain elongated (Fig. 1c) or equiaxed (Fig. 1d) primary  $\alpha$  and acicular  $\alpha'$ -martensite formed by the diffusionless  $\beta \rightarrow \alpha'$  transformation. The martensite laths are thin, long and orthogonally orientated. The precipitation treatment produces fine  $\text{Ti}_3\text{Al}$  intermetallic compounds and disperse  $\beta$ -phases acting as age-hardening particles that are not clearly seen in Fig. 1e, f but proved by the measured slight increase in the hardness values.

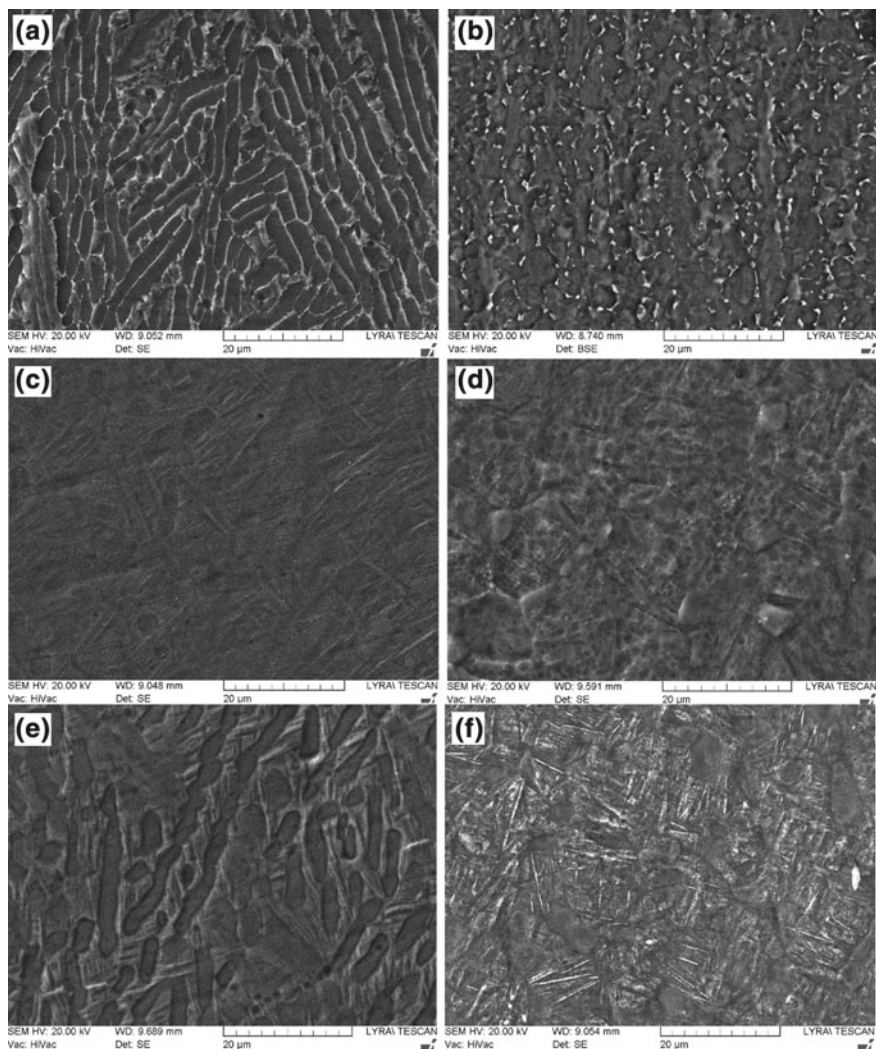


**Fig. 1** Secondary SEM images of the microstructure of **a** AR Ti-54; **b** AR Ti-64 ( $\alpha$  phase in dark gray and  $\beta$  phase in white); **c** ST Ti-54; **d** ST Ti-64; **e** ST+P Ti-54; **f** ST+P Ti-64 samples. The samples were etched with Kroll's reagent

The potentiodynamic polarization curves (PDCs) in Ringer solution (RS) for each alloy in AR, ST and ST+P condition are shown in Fig. 2. The last  $E_{OC}$  values of the 30 min test are plotted in Table 3. All OC potentials' plots (not shown) display an increase in the potentials towards the more positive values for all samples regardless of whether the samples have been initially immersed or not. This effect could be explained by the spontaneous passivation during the stay in the solutions.

**Table 3** The electrochemical parameters of the alloys in different solutions and immersion times

Sample	Solution	Time of immersion	$E_{\text{corr}}$ , mV <sub>Ag/AgCl</sub>	$I_{\text{corr}}$ , $\mu\text{A}/\text{cm}^2$	$E_{\text{OC}}$ , (mV) versus Ag/AgCl
AR Ti54	RS	30 min	-183.37	0.066	-113
AR Ti64			-259.55	0.059	-182
ST Ti54			-156.89	0.122	-139
ST Ti64			-81.02	0.140	-119
ST+P Ti54			-51.58	0.078	-118
ST+P Ti64			-61.08	0.144	-144
AR Ti54			RS	30 days	-35.49
AR Ti64	-41.35	0.116			-155
ST Ti54	-28.64	0.108			-147
ST Ti64	-32.19	0.129			-157
ST+P Ti54	-49.86	0.114			-153
ST+P Ti64	-45.74	0.130			-147
AR Ti54	PBS	30 min			-11.26
AR Ti64			-43.28	0.124	-125
ST Ti54			-58.33	0.135	-109
ST Ti64			-88.27	0.102	-138
ST+P Ti54			-98.87	0.091	-111
ST+P Ti64			-93.94	0.090	-204
AR Ti54			PBS	30 days	-60.82
AR Ti64	-85.95	0.101			-195
ST Ti54	-41.65	0.103			-145
ST Ti64	-67.37	0.104			-159
ST+P Ti54	-50.58	0.090			-144
ST+P Ti64	-70.10	0.126			-145
AR Ti54	PBS and H <sub>2</sub> O <sub>2</sub>	30 days			-37.71
AR Ti64			-56.23	0.114	-156
ST Ti54			-40.54	0.22	-132
ST Ti64			-79.92	0.13	-141
ST+P Ti54			-10.50	0.13	-139
ST+P Ti64			-40.57	0.11	-143

The anodic polarization behavior of the alloys in RS shows no breakdown potentials for most of the 30 min soaked samples except for the ST Ti-54 where this potential reaches a value of 0.27 V versus Ag/AgCl (Fig. 2a). The heat-treated samples of both alloys show nobler corrosion potentials after the short term immersion in RS. These results comply with those reported in [11, 14, 15]. The phenomenon could be explained by the higher localized breakdowns of the oxide layer of the AR samples because of micro-galvanic cells formation at  $\alpha/\beta$  interface. According to Hack [16]

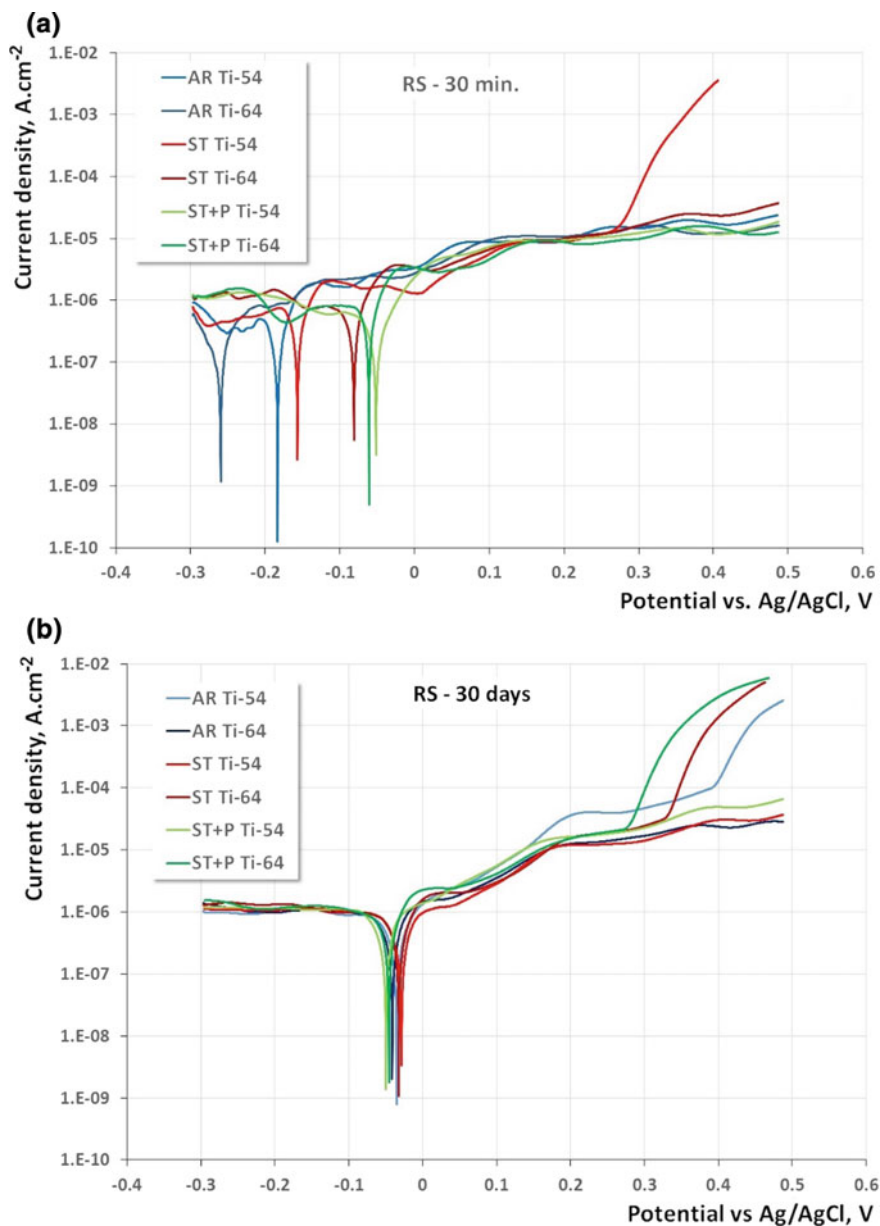


**Fig. 2** Potentiodynamic polarization curves in RS after 30 min (a) and 30 days (b) of immersion at 37 °C for the AR, ST, ST+P conditions of Ti-54 and Ti-64 alloys

the strength of the galvanic coupling that exists between  $\alpha$  and  $\beta$  phase, is mainly determined by the composition of the constituent phase and the effective interphase area between them. The spectroscopic characterizations of the oxides formed on the surface of a Ti-64 alloy [17] show that the oxide films consist predominantly of  $\text{TiO}_2$  and small amounts of  $\text{Ti}_2\text{O}_3$ , Al (in form of  $\text{Al}_2\text{O}_3$ ) and V oxides (in form of  $\text{V}_2\text{O}_5$ ,  $\text{VO}_2$ ,  $\text{V}_2\text{O}_3$  or  $\text{VO}_x$  (readily soluble in water)) with lower surface amounts. Milosev et al. [18] reported that in the presence of  $\text{Cl}^-$  ions, the V (IV) oxides form soluble complexes with chlorides containing vanadyl ions ( $\text{VO}^{2+}$ ). The same authors commented also that the presence of V is related to high cation vacancy diffusivity across the oxide layer which effect according to Macdonald [19] plays a central role in susceptibility to pitting. These V-rich oxides are formed over the  $\beta$ -phase of the AR structures that could destroy the passivity by proving conduction channels in the alloy. It is obvious that the bi-modal structure of the AR Ti-64 alloy with higher V and Al content is less stable in the solution when soaked for 30 min as compared to the AR Ti-54 alloy. However, the corrosion current densities of both AR alloys show lower values than those of the heat-treated samples (Table 3). In contrast, the unstable  $\alpha'$  microstructure has an increased number of surface defects but forms a more stable layer due to the uniform distribution of the alloying elements. The uniform distribution of the alloying elements suggests a more homogeneous oxide layer formation resulting from the finer structure which promotes better passivation and barrier protection along the interphase regions and phase boundaries. Additionally, the post heat treatment retains the laths structure but reduces surface defects.

In general, after 30 days of immersion, the shift of the anodic curve toward lower current densities up to about 0.2 V versus Ag/AgCl as compared to the 30 min soaked specimens evidences the more protective oxide film formed on the surface as it grows (Fig. 2 B). The nobleness of the  $E_{\text{corr}}$  potentials observed after a longer stay in the RS indicates better corrosion resistance for the soaked samples. The potentiodynamic polarization results indicate nearly identical behavior for all samples with well-defined passive-like regions with slowly increasing current densities. Critical potentials were observed after 0.28, 0.33 and 0.39 V versus Ag/AgCl for the ST+P Ti-64, ST Ti-64 and AR Ti-54 samples, respectively, indicating the formation of stable pits on their surfaces. That breakdown potential depends on the stability of the passive film. It follows that the oxide layers on the heat-treated Ti-64 samples and AR Ti-54 alloy have a high tendency of dissolution with pit formation. The estimated  $E_{\text{corr}}$  and  $I_{\text{corr}}$  values are given in Table 3. The measured low values ( $<1 \mu\text{A}/\text{cm}^2$ ) of the  $I_{\text{corr}}$  are typical for the passive metals and are also determine by other authors [20, 21]. Considering the expected  $E_{\text{corr}}$  scattering during the potentiodynamic test, one could conclude that after the 30 days of immersion in RS all specimens show similar corrosion potentials of around  $-28 \div -50$  mV versus Ag/AgCl. The similar values of the cathodic current densities of all samples after 30 days of immersion suggest that the slight differences in the alloying elements content and microstructure do not influence the cathodic reactions.

To characterize the re-passivation behavior of the Ti alloys the local breakdowns of the surface oxide layers were examined and shown in Fig. 3. The pit on the surface of the 30 min soaked ST Ti-54 alloy (Fig. 3a) displays that Ti, Al, and V were dissolved

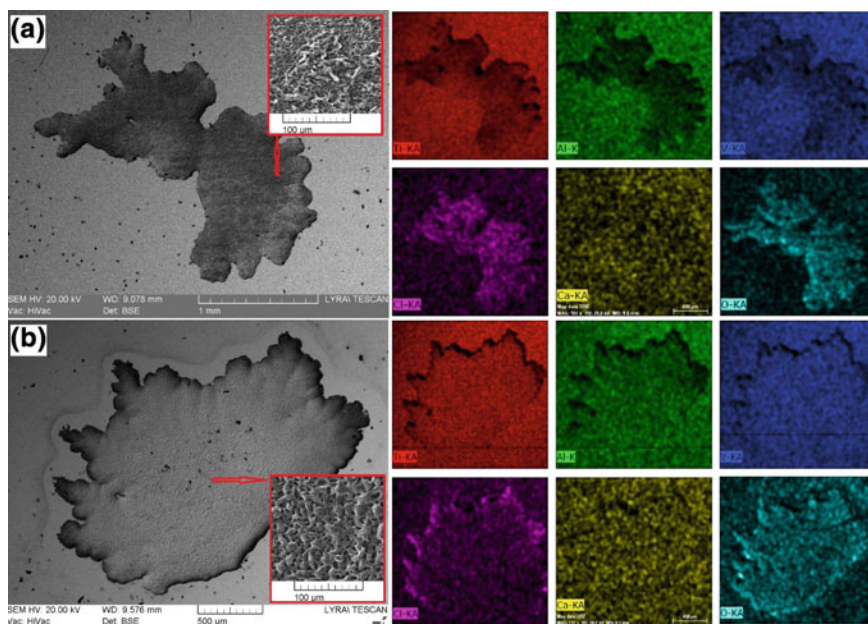


**Fig. 3** Micrograph of the pit on the surface and corresponding element mapping of **a** ST Ti54 after 30 min immersion in RS; **b** ST Ti64 after 30 days of immersion in RS at 37 °C and potentiodynamic tests

from the surface after the breakdown potential while chlorides and oxygen actively incorporate in the corroded place. Calcium was almost homogeneously distributed on the surface after the test. A smaller pit with less dissolved Ti, Al atoms and V but highly oxidized was seen on the surface of the ST Ti-64 sample tested after 30 days of immersion in RS at 37 °C (Fig. 3b). Metikos-Hukovic et al. [17] noticed that the adsorption of  $\text{Cl}^-$  to the surface oxygen vacancies enhances the flux of cation vacancies from the oxide/electrolyte towards the metal oxide interface where they annihilate. If the annihilation reaction does not consume the cation vacancies at the metal/oxide film interface, these excess vacancies coalesce and when the condensate formed reaches a critical size, localized breakdown occurs.

After the short time immersion in PBS solution (Fig. 4a) all samples show re-passivation at potentials from 0 up to 0.5 V versus Ag/AgCl. The passive current densities vary between  $6.2 \times 10^{-6} - 1.2 \times 10^{-5} \text{ A/cm}^{-2}$  except for the ST Ti64 alloy that shows higher values. After the longer stay in PBS (Fig. 4b) the variation in the  $E_{\text{corr}}$  values decreases and the process of passivation at the beginning shifts towards lower values ( $1.1 \times 10^{-6} - 2.16 \times 10^{-6} \text{ A/cm}^{-2}$ ). Subsequently, the protective properties of the formed oxides are worse following a monotonous increase of the current density with the increase of the potential. The increase in the passivation current density could be related to the presence of more vacancies and increased diffusivity of oxygen.

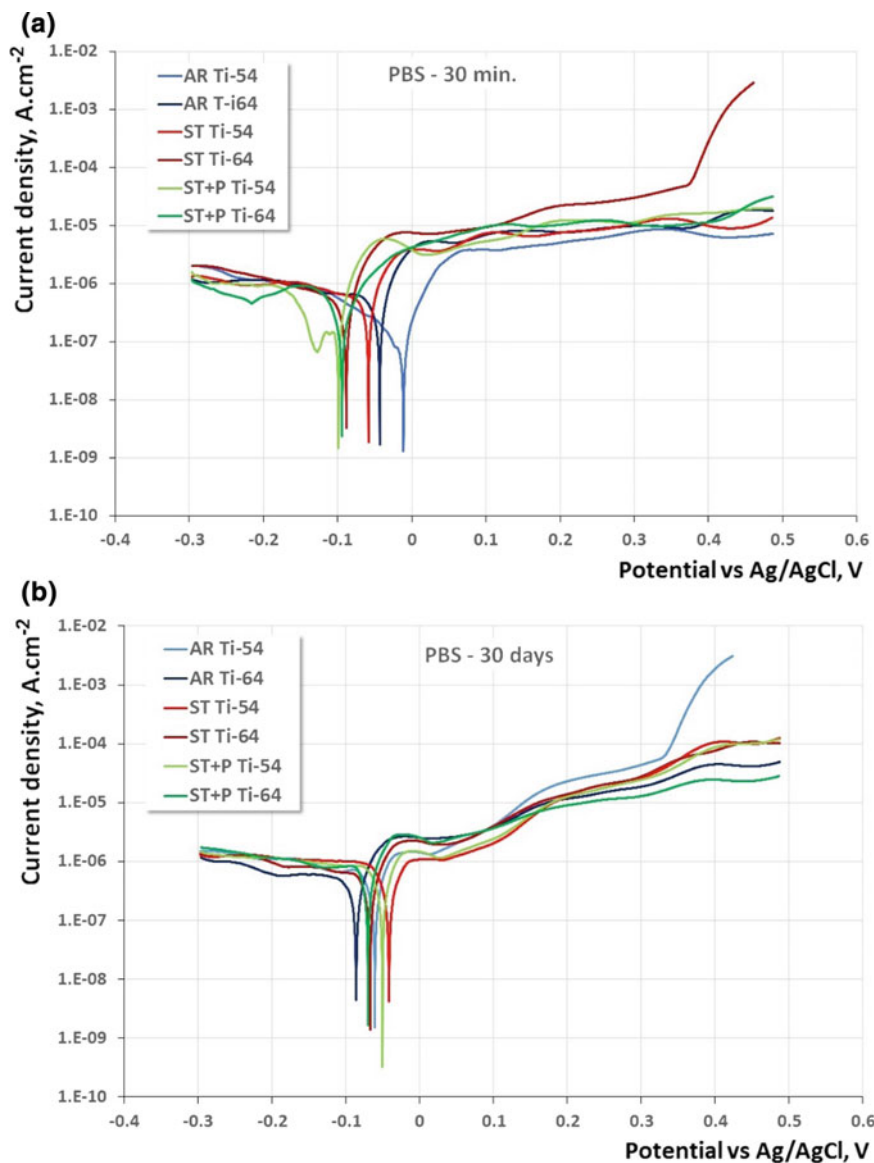


**Fig. 4** Potentiodynamic polarization curves in PBS after 30 min (a) and 30 days (b) of immersion at 37 °C for the AR, ST, ST+P conditions of Ti-54 and Ti-64 alloys

The precipitation of insoluble products on the nucleating pits could explain the hindered cathodic reaction and low values of the anodic current density of the AR Ti54 alloy immersed for 30 min in PBS. A change in the mechanism or kinetics of the oxygen reduction reaction could, therefore, occur in the PBS solution when soaking



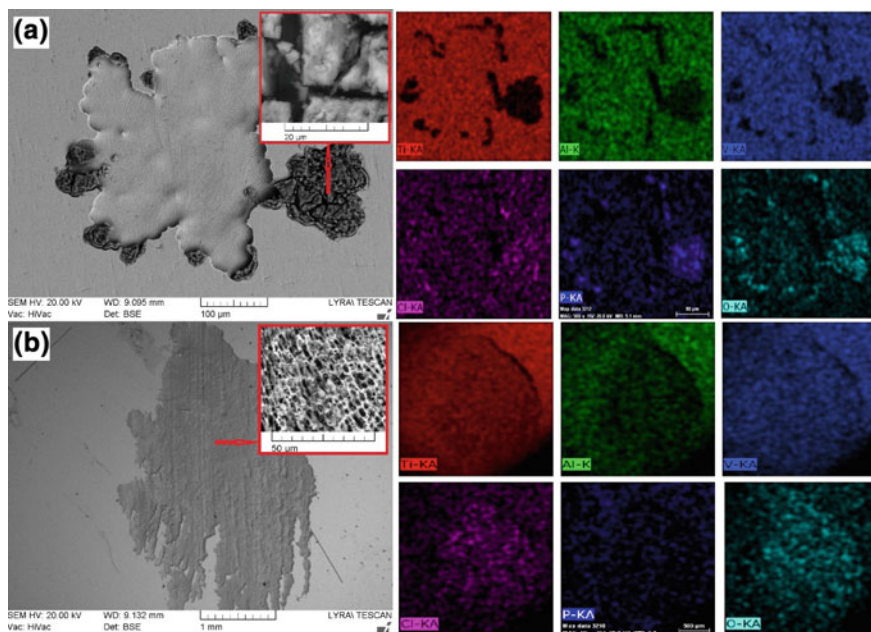
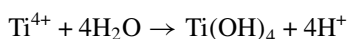


**Fig. 5** Micrograph of the pits on the surface of AR Ti54 alloy and corresponding element mapping after **a** 30 min and **b** 30 days of immersion in PBS at 37 °C and potentiodynamic tests

certain samples for shorter immersion times. The X-ray map of the corroded area indicates that these products have phosphate nature (Fig. 5a) mainly containing Ti and some additional Na, K, and Ca ions. The salt film formed on the pit surface limits the pit growth rate by a mass transport out of the working electrode [22]. For that reason, the pit looks hemispherical with polished surfaces. In that case, the healing of the breakdown is not inhibited by the chloride ions because the salt film forms at the pit surface at the very early stages of pit growth as suggested by Frankel [22].

After 30 days of immersion, the results from the elements mapping in the pits and the matrix (Fig. 5b) indicate that while the Ti and Al are decreasing, the oxygen and chloride concentrations are increasing within the pit. Hang et al. [23] suggested that in PBS solution hydrolysis could occur:



The hydrogen produced could lower the pH near the reaction sides, increasing the solubility of the oxide. Additionally, the  $\text{Cl}^-$  attacks the positively charged ions at the reaction sides and accelerates the dissolution of the oxide. The SEM images demonstrate much smaller pit formation on the surface of the AR Ti54 alloy after 30 min of immersion in PBS as opposed to that on the surface of the 30 days immersed sample. That effect can be correlated with the PDCs' character shown in Fig. 4. The

very similar behavior of all samples soaked in PBS for 30 days suggests higher unification of the corrosion potentials varying from about  $-40 \div -80$  mV versus Ag/AgCl for all samples.

It is obvious that the concentration of  $\text{Cl}^-$  ions and pH of the solution have a significant influence on the stability of the oxide films and the tendency for pits' formation—higher in RS than in PBS. The rupture of the oxide film could occur as a result of the formation of titanium chloride metal-oxide interface as well as the higher ionic radius of Na, Ca, K cations in the solution as compared to those of the Ti ions leading to vacancy condensate formation [24]. Not only the lower Al and V content, but also the presence of a slightly higher amount of Nb and Mo in the two-phase Ti-54 alloy could improve the stability of the passive film at lower potentials. The alloying additions such as Mo and Nb could reduce the active anodic dissolution rates of the Ti-54 alloy by enhancing atomic bond strength among Ti-Nb-Mo [2]. In contrast, Hack [16] found out that if  $\text{Al}^{3+}$  substitutes some  $\text{Ti}^{4+}$  ions in  $\text{TiO}_2$ , more anion vacancies will be formed in the passive film which increases the diffusivity of oxygen. The vacancy deficit may result in a reduction of the passivation current density [25], which effect is observed for most of the Ti-54 samples as opposed to the Ti-64 specimens in both RS and PBS. However, the higher Al and V content in the Ti-64 alloy has a positive influence on the resistance to pitting corrosion at higher potentials for the AR sample.

The  $\text{TiO}_2\text{-H}_2\text{O}_2$  interaction has been widely studied in the literature [26]. The  $\text{H}_2\text{O}_2$  is known to be strong oxidant modifying the surfaces of the Ti alloys. The  $\text{H}_2\text{O}_2$  concentration measured in the extracellular environment is in the  $\mu\text{M}$  range but in certain micro-environment created by immune cells and microbial biofilms the concentration could rise up to mM [27] together with acidification of the environment during inflammation process. The  $\text{H}_2\text{O}_2$  forms  $\text{Ti-H}_2\text{O}_2$  complexes with the Ti alloys which process increases the corrosion of the latter because of the formation of thicker but more porous oxide films [28]. As seen in Fig. 6, the addition of  $\text{H}_2\text{O}_2$  to the PBS solution and its acidification for 14-days period is associated with resultant higher anodic reaction rate. The large increase in the anodic current densities occurs because the oxide could not balance the potential difference across the film. The increased rate of the anodic reaction due to the presence of  $\text{H}_2\text{O}_2$  was observed also by [8, 29]. This fact the authors attribute to higher ion release and dissolution. Another explanation could be the reaction of  $\text{OH}^-$  with the oxide leading to the formation of hydroxide layer at lower pH with porous structure [30].

The surface micrograph of the ST+P Ti-54 sample indicates some cracks located close to the pit boundary as well as seen in the detailed microstructure from the central area of the pit (Fig. 7). The crack morphology of the corroded surface, as along with the higher oxygen concentration all over the surface, confirm the formation of a thicker corrosion oxide layer. The elements that decrease their concentration in the pit are Ti and Al, while V concentration is much lowered down to  $1.82 \pm 1.2$  wt% in the pit and  $1.95 \pm 1.3$  wt% on the surface (Fig. 7). Similar observations were reported by Yu et al. [31] and Shukla et al. [32] claiming that  $\text{H}_2\text{O}_2$  preferentially attacks the  $\beta$ -phase of the Ti-64 alloy. According to Ferraris et al. [33], the passive film of Ti-64 alloy contains a significant amount of  $\text{Al}_2\text{O}_3$  above the  $\alpha$ -phase, whereas the passive

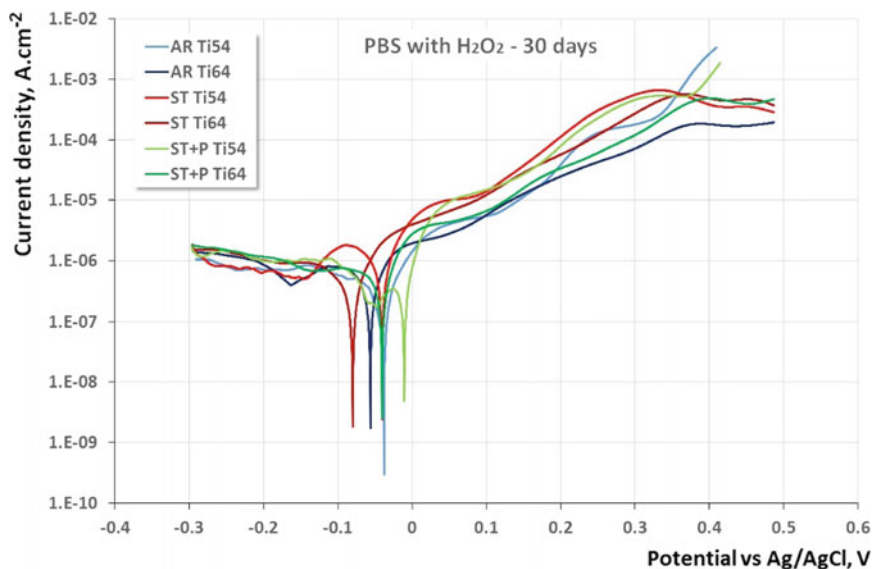


**Fig. 6** Potentiodynamic polarization curves in PBS and  $\text{H}_2\text{O}_2$  after 30 days of immersion at  $37\text{ }^\circ\text{C}$  for the AR, ST, ST+P conditions of Ti-54 and Ti-64 alloys

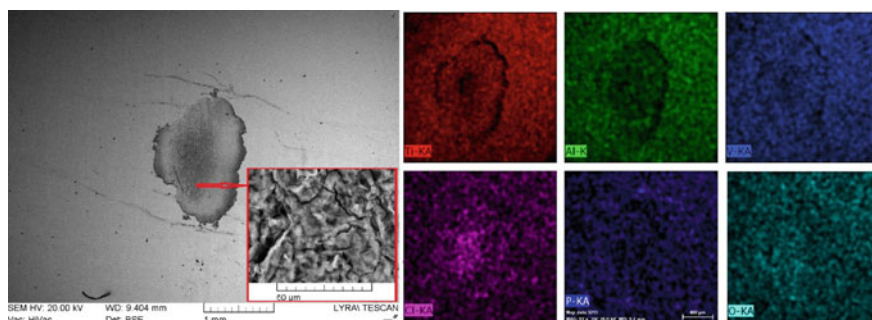


**Fig. 7** Backscattered SEM image and corresponding element mapping of the corroded ST+P Ti54 alloy after 14 days of immersion in PBS and  $\text{H}_2\text{O}_2$  with pH 5 and 16 days in PBS solution at  $37\text{ }^\circ\text{C}$  and potentiodynamic tests

film on the  $\beta$ -phase consists of almost pure  $\text{TiO}_2$  with which the  $\text{H}_2\text{O}_2$  forms Ti complexes.

According to the results from the potentiodynamic polarisation measurements in both solutions, it could be determined that without the presence of  $\text{H}_2\text{O}_2$  as the pH increase from 5.7 to 7.4 together with a decrease in  $\text{Cl}^-$  concentration, the potential dependent passivation of both Ti-54 and Ti-64 alloys decrease. Similar observations were reported by Khan et al. [34]. The authors explain that fact with the higher release of metal ions in the solution. As the corrosion potentials indicate the stability

**Table 4** The elements concentration on the surface of the alloys after the test in 5 M HCl

Element	Ti 54 alloy			Ti 64 alloy		
	AR	ST	ST+P	AR	ST	ST+P
Ti	91.17 ± 0.11	89.59 ± 0.68	90.97 ± 0.29	91.23 ± 0.09	87.98 ± 3.86	90.5 ± 0.72
Al	5.18 ± 0.05	5.05 ± 0.12	5.16 ± 0.36	5.65 ± 0.04	5.29 ± 0.44	5.48 ± 0.52
V	2.72 ± 0.08	2.56 ± 0.28	2.89 ± 0.15	2.83 ± 0.01	2.61 ± 0.32	2.86 ± 0.1
O	0.36 ± 0.01	2.58 ± 0.25	0.56 ± 0.32	0.12 ± 0.06	3.97 ± 4.35	0.997 ± 1.24

of the surface in the particular conditions, their more positive values as compared to the  $E_{OC}$  for almost all samples indicate a tendency of slow corrosion processes (Table 3). The ST Ti-64 sample immersed for 30 min in RS has the highest  $I_{CORR}$  values, while the AR Ti-54 soaked in PBS for 30 min shows the lowest  $I_{CORR}$  values. Since the corrosion current density is proportional to the corrosion rate of the system, the results suggest that ST Ti-64 immersed for 30 min in RS has a higher tendency of corrosion reaction.

The average measurements of the tested samples in 5 M HCl at 37 °C for each testing time (10-days' period) are presented in Fig. 8. For both alloys, the weight losses were almost linear suggesting that the corrosion rate was merely constant in time. The calculated average corrosion rate for the whole time period is 111.1, 131.08 and 124.12 mpy for the AR, ST and ST+P Ti-54 samples, respectively and 135.9, 137.9 and 146.67 mpy for the AR, ST and ST+P Ti-64 samples, respectively. Comparable results for the corrosion rate of the Ti-64 in 5 M HCl alloy at 37 °C were reported by Atapour et al. [3]. The similar slopes after approximately 8-days' period of exposure of the ST and ST+P Ti-54 and Ti-64 samples indicate a similar corrosion kinetic behavior.

Elmer et al. [35] reported that in equilibrium state the  $\alpha$  in Ti64 alloy contains 91.2 wt% Ti and 6.73% Al, while  $\beta$ -phase contains 80.7% Ti and 2.92% Al. From a microstructural point of view, after the fast cooling of the ST samples, the amount of  $\alpha$ -phase significantly decreases and the concentration of Al in the remaining phases drastically increases while that of the V, Nb, etc. in  $\alpha'$ -martensite is increased. Al and V atoms are trapped in the martensite structure because of the fast cooling of the ST materials. In 5 M HCl where the concentration of  $Cl^-$  ions is extremely high, the high concentration of defects above the  $\alpha$ - and  $\alpha'$ -phase and the depletion in  $\alpha$ -phase grains lead to a decreased stability of  $TiO_2$  in the acid. The ST structure of both alloys (Fig. 9c, d) is more prone to metal ion release (especially Al and V) in the 5 M HCl (Table 4) and more highly oxidized.

During the precipitation treatment,  $\alpha'$  is depleted in  $\beta$ -stabilizing element (V) and enriched in  $\alpha$ -stabilizing elements (Al). The precipitation process allows the transformation of  $\alpha'$ -martensite to  $\alpha' + Ti_3Al$  precipitates and the increase in  $\beta$ -phase content. The appearance of  $Ti_3Al$  due to partitioning could explain a local decrease in Ti concentration in the microstructure or enrichment in V content. The agglomeration

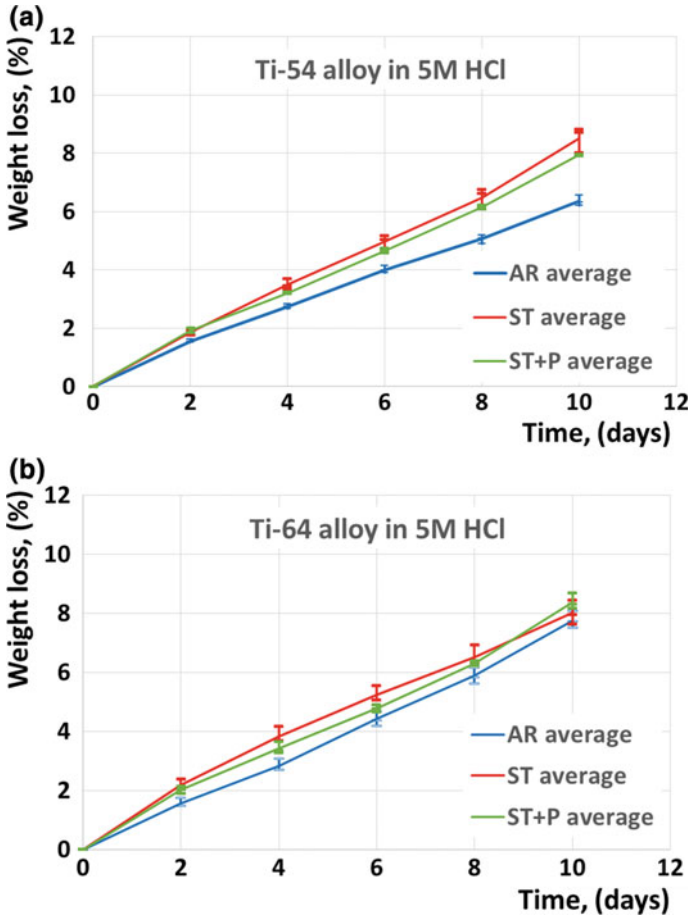


**Fig. 8** Weight losses in time on exposure in 5 M HCl at 37 °C of Ti-54 (a) and Ti-64 (b) alloy in different conditions: AR, ST and ST+P

of the phases leads to reducing the  $\alpha/\beta$  interface area and the sides of corrosion decrease. The increased  $\beta$ -phase percentage reduced  $\alpha/\beta$  interface and coarsening of  $\alpha$  laths (Fig. 9e, f) reduce the corrosion dissolution of the Al and V in the 5 M HCl solution. It was also reported by Yu et al. [36] that the V rich phases are less prone to corrosion reaction as compared to  $\alpha$ -phases. The temperature of precipitation and alloy composition will determine the extent to which the aforementioned processes has taken place. Despite the higher corrosion rate of the ST+P Ti-64 alloy, the ion release from its surface is comparable to that of the ST+P Ti-54 but showing a slightly higher oxygen content (Table 4). A comparable high content of Ti, Al, and V is determined on the surface of both AR Ti-54 and Ti-64 alloys on the account of low oxygen concentration and low weight losses as opposed to the heat-treated

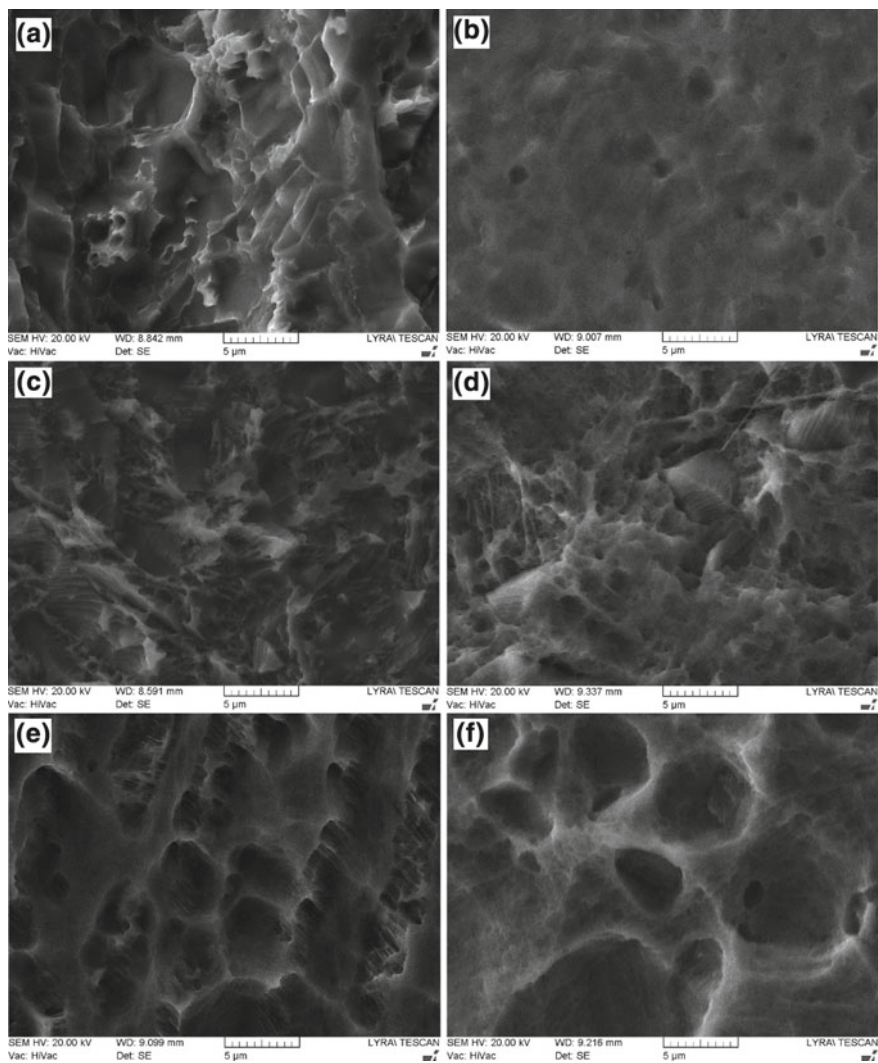


**Fig. 9** SEM micrographs of the corroded surface in 5 M HCl at 37 °C of: **a** AR Ti-54; **b** AR Ti-64; **c** ST Ti-54; **d** ST Ti-64; **e** ST+P Ti-54; **f** ST+P Ti-64 samples

samples of the same alloys. However, the weight losses are the lowest for the AR Ti54 alloys in 5 M HCl at 37 °C.

## 4 Conclusions

The corrosion behavior of two biomedical alloys in different conditions was investigated in Ringer, PBS, PBS and H<sub>2</sub>O<sub>2</sub> and 5 M HCl solution at 37 °C for different time periods. From the particular study is evident that not only the chemical composition, but also the fabrication method and heat treatment could influence the surface film formation, density, chemistry, stability or even oxide structure.

The lamellar structure of the Ti-54 alloy gives rise to a better corrosion resistance in the tested solution as compared to that of the Ti64 alloy with equiaxed grains but is more prone to pits formation at higher potentials. The comparison among the PDCs of the examined as-received and heat-treated samples reveals that the long-term stay in PBS with pH 7.4 causes slightly worse corrosion resistance than that in RS with pH 5.7 where, however, more samples become prone to pitting corrosion when the potential is increased to a higher value. The long-term stay in the PBS with H<sub>2</sub>O<sub>2</sub> has a negative effect on the re-passivation behavior of both alloys. The heat treatment deteriorates the corrosion resistance of the alloys in 5 M HCl solution. The average corrosion rate during the 10 days of exposure in the acid solution shows the lowest values for the AR Ti-54 sample and the highest—for the ST and ST+P Ti-64 alloy. The finer grained, thermodynamically unstable and more homogeneous structures of the ST and ST+P samples indicate increased dissolution kinetic in 5 M HCl as opposed to the AR samples of the same alloy.

This research highlights the need for examination not only of the time-dependent influence of the chemical composition of the implant alloys, but also that of the microstructural differences on the stability of the material, since there is a clear change in the corrosion behavior of the examined samples.

**Acknowledgements** The study was supported by contract of University of Ruse “Angel Kanchev”, № BG05M2OP001-2.009-0011-C01, “Support for the development of human resources for research and innovation at the University of Ruse “Angel Kanchev”. The project is funded with support from the Operational Program “Science and Education for Smart Growth 2014–2020” financed by the European Social Fund of the European Union.

## References

1. Nag, S., Banerjee, R., Stechschulte, J., Fraser, H.L.: Comparison of microstructural evolution in Ti-Mo-Zr-Fe and Ti-15Mo biocompatible alloys. *J. Mater. Sci. Mater. Med.* 679–85 (2005)
2. Manam, N.S., Harun, W.S.W., Shri, D.N.A., Ghani, S.A.C., Kurniawan, T., Ismail, M.H., Ibrahim, M.H.I.: Study of corrosion in biocompatible metals for implants: a review. *J Alloys Compnd.* **701**, 698–715 (2017)

3. Atapour, M., Pilchak, A.L., Frankel, G.S., Williams, J.C.: Corrosion behavior of  $\beta$  titanium alloys for biomedical applications. *Mater. Sci. Eng., C* **31**, 885–891 (2011)
4. Hiromoto, S.: Corrosion of metallic biomaterials in cell culture environments. *Electrochem. Soc. Interface* 41–44 (2008)
5. Höhn, S., Virtanen, S.: Effect of inflammatory conditions and  $H_2O_2$  on bare and coated Ti–6Al–4 V surfaces: Corrosion behavior, metal ion release and Ca-P formation under long-term immersion in DMEM. *Appl. Surf. Sci.* **357**, 101–111 (2015)
6. Beringer, J.P., Orme, C.A., Gilbert, J.L.: Effect of hydrogen peroxide on titanium surfaces: in situ imaging and step-polarization impedance spectroscopy of commercially pure titanium and titanium. 6-aluminum 4-vanadium. *J. Biomed. Mater. Res.* **67**, 702–712 (2003)
7. Dissemmond, J.: Die Bedeutung des pH-Wertes für die Wundheilung. *Hartmann Wund Forum* **1**, 15–19 (2006)
8. Wang, J.L., Liu, R.L., Majumdar, T., Mantri, S.A., Ravi, V.A., Banerjee, R., Birbilis, N.: A closer look at the in vitro electrochemical characterisation of titanium alloys for biomedical applications using in-situ methods. *Acta Biomater.* **54**, 469–478 (2017)
9. Brunette, D.M.: *Titanium in Medicine: Material Science, Surface Science, Engineering, Biological Responses, and Medical Applications*. Springer, Berlin, New York (2001)
10. Krawiec, H., Vignal, V., Loch, J., Erasmus-Vignal, P.: Influence of plastic deformation on the microstructure and corrosion behaviour of Ti–10Mo–4Zr and Ti–6Al–4 V alloys in the Ringer’s solution at 37 °C. *Corros. Sci.* **96**, 160–170 (2015)
11. Cvijovic´-Alagic´, I., Cvijovic´, Z., Bajat, J., Rakin, M.: Composition and processing effects on the electrochemical characteristics of biomedical titanium alloys. *Corros. Sci.* **83**, 245–254 (2014)
12. Metikoš-Hukovic´, M., Kwokal, A., Piljac, J.: The influence of niobium and vanadium on passivity of titanium-based implants in physiological solution. *Biomaterials* **24**, 3765–3775 (2003)
13. Nikolova, M.P., Yankov, E., Petrov P, Nikolov, D., Valkov, S., Zaharieva, V., Ormanova, M.: Phase and mechanical changes of Ti5AL4V alloy after heat treatment in vacuum. In: *METAL 2017–26th International Conference on Metallurgy and Materials, Conference Proceedings*, pp. 1899–1904 (2017)
14. Geetha, M., Mudali, U.K., Gogia, A.K., Asokamani, R., Raj, B.: Influence of microstructure and alloying elements on corrosion behavior of Ti–13Nb–13Zr alloy. *Corros. Sci.* **46**(4), 877–892 (2004)
15. Xu, Y., Lu, Y., Sundberg, K.L., Liang, J., Sisson Jr., R.D.: Effect of annealing treatments on the microstructure, mechanical properties and corrosion behavior of direct metal laser sintered Ti–6Al–4 V. *J. Mater. Eng. Perform.* **26**(6), 2572–2582 (2017)
16. Hack, H.P.: Evaluating galvanic corrosion. In: *ASM International 13(A). Corrosion: Fundamental Testing and Protection*, ASM International, Materials Park, OH, p. 563 (2003)
17. Metikos-Hukovic, M., Kwokal, A., Piljac, J.: The influence of niobium and vanadium on passivity of titanium-based implants in physiological solution. *Biomaterials* **24**, 3765–3775 (2003)
18. Milosev, I., Metikos-Hukovic, M., Strehblow, H.: Passive film on orthopaedic TiAlV alloy formed in physiological solution investigated by X-ray photoelectron spectroscopy. *Biomaterials* **21**, 2103–2113 (2000)
19. Macdonald, D.D.: Point defect model for passive state. *J. Electrochem. Soc.* **139**, 3434–3449 (1992)
20. Karimi, S.: Corrosion behavior of metallic bio-implant alloys. Ph.D. thesis, University of British Columbia, Vancouver, Canada, p. 206 (2014)
21. Barao, V.A.R., Mathew, M.T., Assuncao, W.G., Yuan, J.C., Wimmer, M.A., Sukotjo, C.: Stability of cp-Ti and Ti–6Al–4 V alloy for dental implants as a function of saliva pH—an electrochemical study. *Clin. Oral Impl. Res.* **23**, 1055–1062 (2012)
22. Frankel, G.S.: Pitting corrosion of metals a review of the critical factors. *J. Electrochem. Soc.* **145**(6), 2186–2198 (1998)



23. Hang, R., Ma, S., Ji, V., Chu, P.K.: Corrosion behavior of NiTi alloy in fetal bovine serum. *Electrochim. Acta* **55**, 5551–5560 (2010)
24. Munirathinam, B., Narayanan, R., Neelakantan, L.: Electrochemical and semiconducting properties of thin passive film formed on titanium in chloride medium at various pH conditions. *Thin Solid Films* **598**, 260–270 (2016)
25. Hong, S.B., Eliaz, N., Sachs, E.M., Allen, S.M., Latanision, R.M.: Corrosion behavior of advanced titanium-based alloys made by three-dimensional printing (3DP<sup>TM</sup>) for biomedical applications. *Corros. Sci.* **43**, 1781–1791 (2001)
26. Mao, C., Li, H., Fuzhai, C., Feng, Q.: Oriented growth of phosphates on polycrystalline titanium in a process mimicking biomineralization. *J. Cryst. Growth* **206**, 308–321 (1999)
27. Liu, X., Ramsey, M.M., Chen, X., Koley, D., Whiteley, M., Bard, A.J.: Real-time mapping of a hydrogen peroxide concentration profile across a polymicrobial bacterial biofilm using scanning electrochemical microscopy. *Proc. Natl. Acad. Sci. U.S.A.* **108**, 2668–2673 (2011)
28. Zhang, Y., Addison, O., Yu, F., Troconis, B.C.R., Scully, J.R., Davenport, A.J.: Time-dependent enhanced corrosion of Ti6Al4V in the presence of H<sub>2</sub>O<sub>2</sub> and albumin. *Sci. Rep.* **8**, 3185 (2018)
29. Fonseca, C., Barbosa, M.A.: Corrosion behaviour of titanium in biofluids containing H<sub>2</sub>O<sub>2</sub> studied by electrochemical impedance spectroscopy. *J. Corros. Sci.* **43**, 547–559 (2001)
30. Handzlik, P., Fitzner, K.: Corrosion resistance of Ti and Ti–Pd alloy in phosphate buffered saline solutions with and without H<sub>2</sub>O<sub>2</sub> addition. *Trans. Nonferrous Met. Soc. China* **23**, 866–875 (2013)
31. Yu, F., Addison, O., Davenport, A.J.: A synergistic effect of albumin and H<sub>2</sub>O<sub>2</sub> accelerates corrosion of Ti6Al4V. *Acta Biomater.* **26**, 355–365 (2015)
32. Shukla, A.K., Balasubramaniam, R., Bhargava, S.: Properties of passive film formed on CP titanium, Ti–6Al–4 V and Ti–13.4Al–29Nb alloys in simulated human body conditions. *Intermetallics* **13**, 631–637 (2005)
33. Ferraris, S., Spriano, S., Pan, G., Venturello, A., Bianchi, C.L., Chiesa, R., Faga, M.G., Maina, G., Vernè, E.: Surface modification of Ti–6Al–4 V alloy for biomineralization and specific biological response: Part I. Inorganic modification. *J. Mater. Sci. Mater. Med.* **22**, 533–545 (2011)
34. Khan, M.A., Williams, R.L., Williams, D.F.: The corrosion behaviour of Ti–6Al–4 V, Ti–6Al–7Nb and Ti–13Nb–13Zr in protein solutions. *Biomaterials* **20**, 631–637 (1999)
35. Elmer, J.W., Palmer, T.A., Babu, S.S., Zhang, W., DebRoy, T.: Phase transformation dynamics during welding of Ti–6Al–4V. *J. Appl. Phys.* **95**, 8327–8340 (2004)
36. Yu, C.Y., Yang, L.X., Shen, C.C., Luan, B., Perng, T.P.: Corrosion behavior of thermohydrogen processed Ti6Al4V. *Scripta Mater.* **56**(12), 1019–1022 (2007)

# Inverse Methodology for Estimating the Heat Transfer Coefficient in a Duplex Stainless Steel Casting



R. O. Sousa, I. Felde, P. J. Ferreira, A. M. Deus and L. M. M. Ribeiro

**Abstract** In sand casting of metallic alloys, the cooling rate is a key parameter that affects the microstructure and the appearance of defects and residual stresses in the end cast components. In this work, a numerical model was developed to simulate the cooling of a duplex stainless steel casting on a furan-bonded sand mold. The heat transfer coefficient (HTC) as a function of temperature was determined by an inverse method. A good agreement between experimental and numerical cooling curves was achieved, showing the importance of estimating HTC as a function of temperature. On the basis of these results, it is possible to calculate thermal residual stresses and model the microstructure of duplex stainless steel castings with complex geometries.

**Keywords** Finite element analysis · Inverse analysis · Heat transfer coefficient  
Duplex stainless steel · Furan-bonded sand

---

R. O. Sousa (✉) · L. M. M. Ribeiro  
Department of Metallurgical and Materials Engineering, University  
of Porto, Porto, Portugal  
e-mail: [rmsousa@fe.up.pt](mailto:rmsousa@fe.up.pt)

R. O. Sousa · L. M. M. Ribeiro  
INEGI, Institute of Science and Innovation in Mechanical and Industrial Engineering,  
Porto, Portugal

I. Felde  
John von Neumann Faculty of Informatics, Óbuda University, Budapest, Hungary

P. J. Ferreira  
Iberian Nanotechnology Laboratory, Braga, Portugal

P. J. Ferreira · A. M. Deus  
Mechanical Engineering Department and IDMEC, Instituto Superior Técnico,  
University of Lisbon, Lisbon, Portugal

P. J. Ferreira  
Materials Science and Engineering Program, University of Texas at Austin, Austin, TX, USA

A. M. Deus  
CeFEMA, University of Lisbon, Lisbon, Portugal

## 1 Introduction

During sand casting of metallic alloys, the cooling rate is a key parameter that affects the microstructure and the occurrence of defects (hot tears, shrinkage, porosity) and residual stresses in the final cast components. In the particular case of high alloy duplex stainless steels, the cooling from high temperatures promotes the precipitation of brittle intermetallic secondary phases. This problem becomes worse when the cast components have a complex geometry. In those cases, thermal cycles can vary significantly from point to point in the cast parts, inducing non-uniform precipitation, which in turn influences the fatigue behavior, fracture strength, and even the corrosion resistance of the component [1]. In extreme situations, residual stresses can result in distortions or even cracking, affecting the quality of near net shape cast components. In this context, the role of numerical simulation as a tool to predict the thermal residual stress distribution is very important, since time and costs can be reduced. However, to obtain meaningful simulations, it is absolutely necessary to employ accurate and reliable cooling curves [2]. In this respect, the knowledge of the heat transfer coefficient (HTC) as a function of temperature is essential, but such data is not easily obtained from the literature. Some authors [3–5] have reported HTC as a function of time in a particular setup, but this is not easily applicable to a different set of conditions. On the other hand, the HTC values are not easily determined by direct measurements. In fact, the experimental determination of the HTC is affected by several factors such as the component geometry, the formation of an air gap at the metal/mold interface, surface roughness, contact pressure and composition of both the metal and mold materials [4, 6]. The inverse heat transfer approach has been used before for the description of boundary conditions in thermal processing of metal alloys [7–10], thus it can be considered a valuable tool in the determination of the HTC.

In this work, an inverse methodology for the estimation of the heat transfer coefficient in the casting process is presented. The proposed approach consists first of generating a numerical model by finite element method. The two major inputs for this procedure are the geometry of the cast component and the thermal properties of the materials (duplex stainless steel and furan-bonded sand), which are known parameters. In this procedure, the temperature-dependent HTC is considered unknown, being adjusted in such a way so as to adequately simulate the temperature distribution in the cast component. For that purpose, in a second step, the simulation-generated data is compared with cooling curves obtained from experiment, in an iterative process where the HTC function is modified until a good fit between the numerical and experimental cooling curves is obtained.

## 2 Experimental Procedure

The casting material studied is a 25Cr-7Mo-Ni-N super duplex stainless steel cast in furan-bounded sand molds. The chemical composition of the alloy melted by induction is given in Table 1.

The heat transfer is strongly dependent on the alloy properties, specifically density, specific heat and thermal conductivity. Thus, the numerical analysis took into account the thermophysical properties of the duplex stainless steel obtained from the JMatPro™ software (Sente Software Ltd., Surrey, United Kingdom). Furthermore, the same properties of the furan-bounded sand were obtained by using the MPDB™ software (JAHM Software, Inc, North Reading, USA). All these properties were obtained as a function of temperature and are shown on Fig. 1.

**Table 1** Chemical composition of the 25Cr-7Mo-Ni-N (wt%)

C	Si	Mn	Ni	Mo	Cr	Cu	W	N
0.02	0.7	0.7	7.9	3.8	25.3	0.9	0.7	0.2

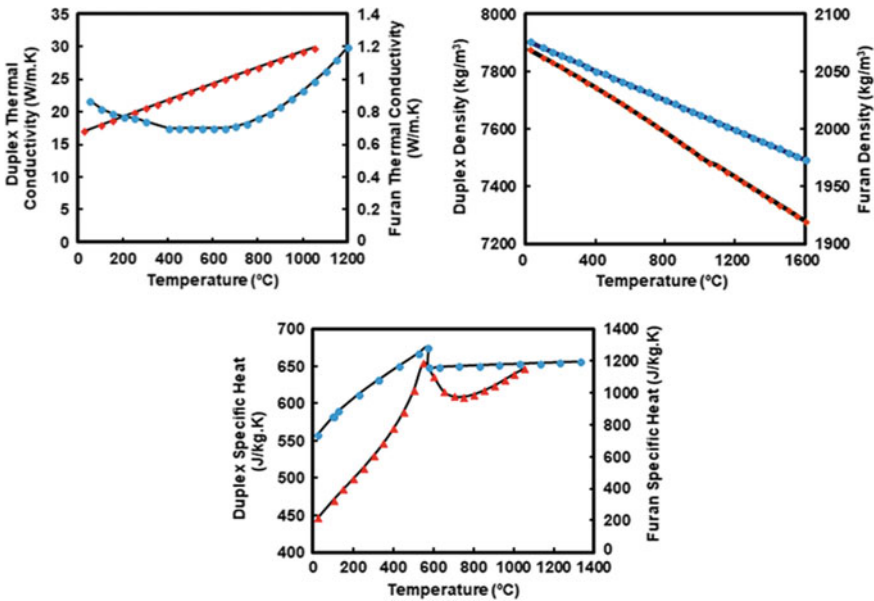


**Fig. 1** Thermophysical properties of the 25Cr-7Mo-Ni-N steel and furan-bounded sand (red: duplex stainless steel, blue: furan-bounded sand)

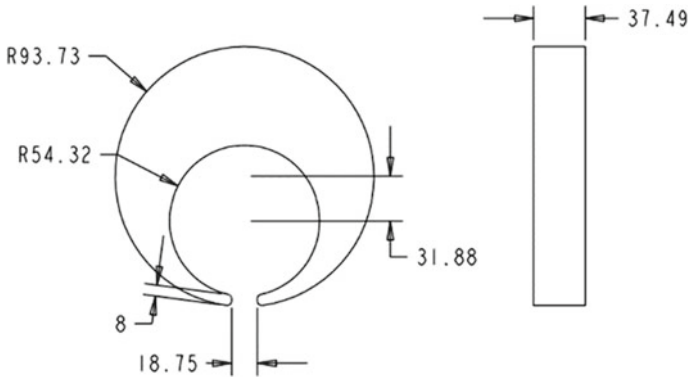


**Fig. 2** C-ring specimen (dimensions in mm)

### 3 Methods

#### a. Experimental cooling curves

The inverse analysis model was based on experimental cooling curves, which were applied to calibrate the numerical model. For this purpose, an experimental set up was built using a C-ring specimen as illustrated in Fig. 2. This geometry provides different cooling rates along the thickness gradient, thus simulating the real casting conditions of a complex component with a variable cross-section.

The holes for inserting thermocouples were drilled on specific positions of the furan-bonded sand molds. The C-ring temperature was measured for 6400 s with a frequency of 1.1 Hz, using R-type thermocouples on the thin and thick sections (see Fig. 3).

#### b. Numerical Model

The numerical model was generated in Abaqus<sup>TM</sup>/CAE (Dassault Systèmes, Vélizy-Villacoublay, France), which consisted of two assembled parts: a parallelepiped block with a cavity inside, representing the mold and the designed C-ring. The meshes were built from 4-node linear heat transfer tetrahedrons (DC3D4). The mold has 18052 elements, while the C-ring has 30316 elements. The meshes for both parts are shown on Fig. 4.

The initial condition for the thermal problem is the initial temperature for both C-ring and mold parts. Therefore, on C-ring it was two zones, with respect to the maximum values of temperatures observed in the thick and thin cross-sections: 1462 and 1106 °C, were considered. For the mold part, the initial temperature was set to 25 °C. Another necessary input was the initial estimate of HTC for duplex stainless steel and furan-bonded sand, which was obtained from the literature [11]. The time increments were controlled by the specification of the maximum allowable temperature variation of 10 °C for the heat transfer analysis. The inverse analysis is based

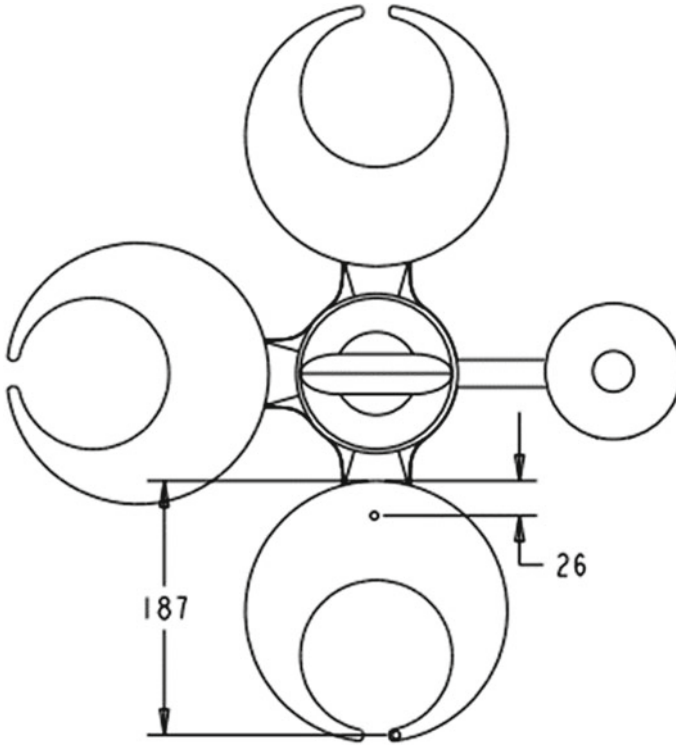


**Fig. 3** Position of thermocouples on C-ring specimen (dimensions in mm)

on the minimization of the difference between experimental and numerical cooling curves. Those curves were compared and, each time, if the agreement between the curves was not satisfactory, the parameters HTC for the thin and thick C-ring sections were modified. The cycle stops when the convergence among curves is verified. This inverse analysis is able to estimate the mold/metal interfacial HTC as a function of temperature and consequently to solve the thermal problem adequately.

## 4 Results and Discussion

### c. Experimental cooling curves

The cooling curves of the C-rings starting from the pouring are shown in Fig. 5. The maximum temperatures measured were 1462 and 1106 °C, for the thick and thin sections respectively. These values are below the peak temperature (1630 °C), which can be explained by the heating inertia of the thermocouples, due to the outer ceramic sheath that embeds the hot junction. Practically, the thermocouple response

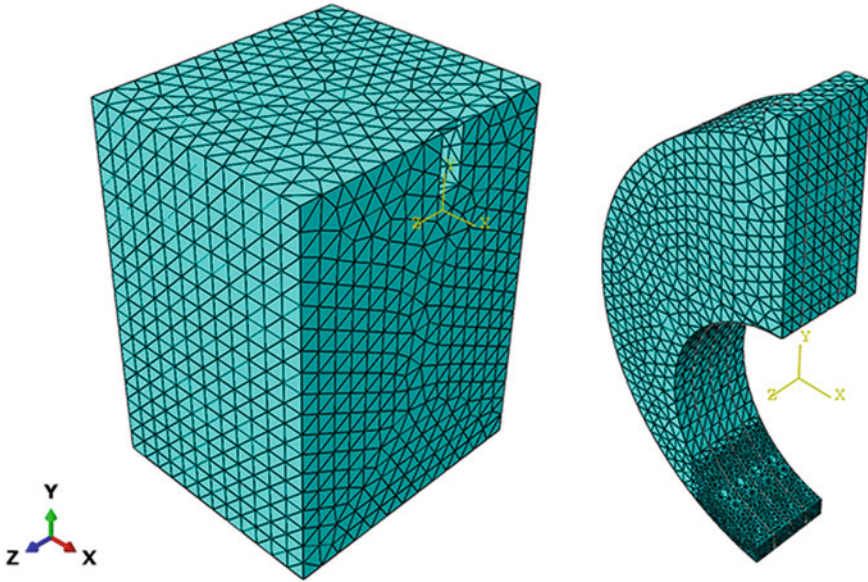


**Fig. 4** Finite element mesh for furan mold and C-ring. For computational cost saving, half of model was considered

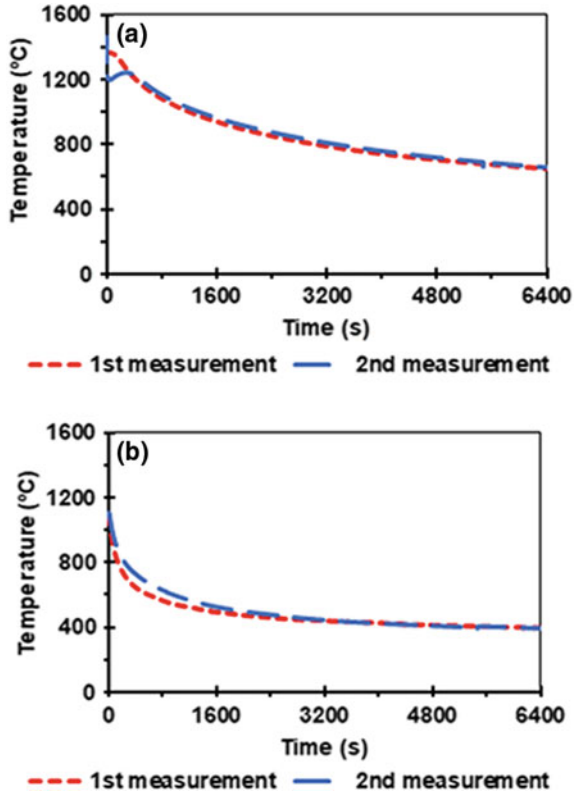
time is inadequate in the initial period of the casting. In our work, the time needed to reach the maximum temperature was 150 s, after the start of the pouring, for both sections.

Regarding the cooling curves of thick section (Fig. 5a), the agreement between the two measured curves is generally good, however, the second measurement shows a slight deviation on the first 300 s. This may be a consequence of an uneven displacement of the thermocouple caused by the liquid metal entering the mold cavity. Concerning the thin section (Fig. 5b), there is a small deviation of the cooling curves between the two cases, which we attribute to a small variation of the thermocouple position between experiments. Since the thin section is narrow compared to the thermocouple diameter, any slight variation on its position could result in a measured difference. Still, it can be concluded that there is a reasonable agreement between the results.

#### d. Numerical Model

As described in the “Methods” section, the HTC is estimated using an inverse analysis approach, on a model where the applied initial temperatures were the maximum temperatures measured for each section. For that purpose, the inverse analysis started with a direct heat transfer analysis, in which the HTC values for a similar system (a duplex stainless steel with a different geometry cast in a silica sand mold), were considered [11].

**Fig. 5** Cooling curves for the two measurements: **a** thick section and **b** thin section

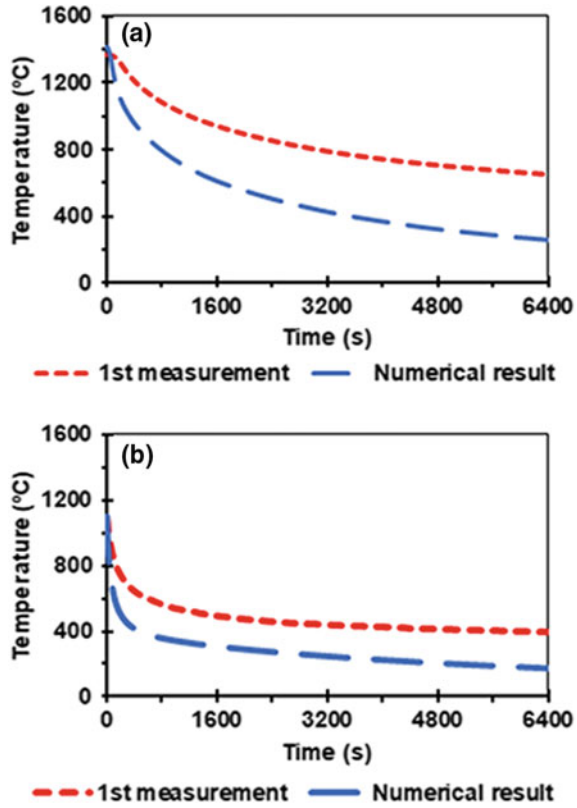


The results of considering those HTC functions as initial guesses are shown in Fig. 6, which underlines the differences between experimental and numerical curves. The direct approach using generic values available in the literature cannot be applied to solve a specific problem, particularly involving complex shapes. In this case, the numerical cooling curves display a faster cooling rate, than the measured curves. This difference could lead to errors regarding the calculation of residual stress distribution. For example, Kang et al. [12], discussed how faster and uniform cooling rates result on a decrease of residual stresses and solve the deformation issues during cooling of larger casting components. So, if the thermal model is inaccurate, the design engineers cannot properly solve the residual stresses problem and improve the castings quality.

Another issue is related with prediction of phase transformations, which is determined by the cooling rate. If this parameter varies along the casting thickness, the eventual formation of secondary phases is a function of geometry. If an incorrect thermal model is considered, the formation of secondary phases cannot be accurately predicted. In the literature there is research, which describes the formation of brittle intermetallic secondary phases in a duplex stainless steel, at temperatures ranging between 700 and 1000 °C [13, 14]. Hence, it is particularly important to



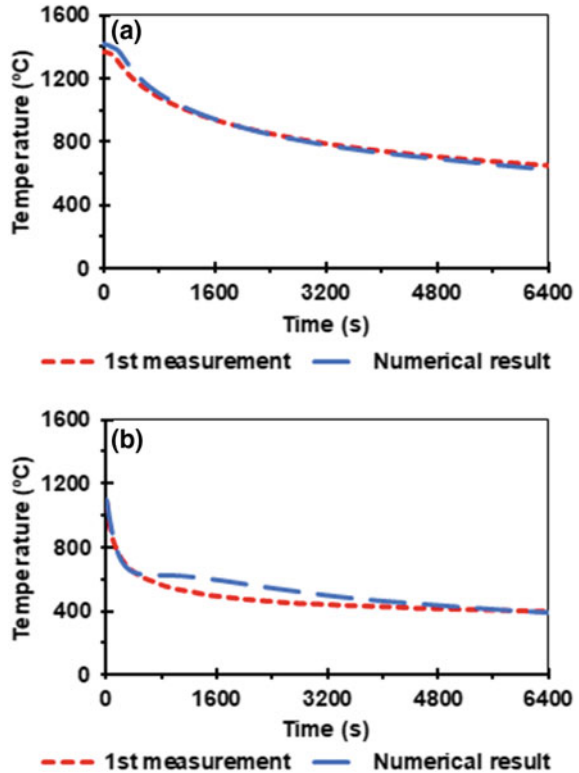
**Fig. 6** Experimental (red) and numerical (blue) cooling curves, using HTC from the literature: **a** thick section and **b** thin section



obtain accurate thermal results in that temperature range. However, to the authors best knowledge, it is not available in the literature a description of the HTC functions for the duplex stainless steel and furan-bonded sand system. The available work on the subject usually considers simple geometries, as plates [15, 16] and bars or cylinders [3, 11, 17]. For this reason, an inverse methodology is proposed, to determine the HTC function for this particular casting system, comprising the C-ring shape.

The inverse methodology allowed us to obtain a good correlation between numerical and experimental results, as shown on Fig. 7. The numerical results for the thick section (Fig. 7a) are very close to the experimental cooling curves, for the considered dwelling time. As for the thin section (Fig. 7b), the numerical result matches the real cooling curve, until the temperature of 680 °C is reached. For lower temperatures there is a slight deviation between the curves. However, in general, the agreement between the thermal model and expected behavior for the casting process is good. From a metallurgical point of view, the numerical model provides a good prediction for the formation of secondary phases, since a good correlation between numerical and experimental results is achieved until 700 °C.

**Fig. 7** Experimental (red) and numerical (blue) cooling curves in the context of the inverse analysis: **a** thick section and **b** thin section

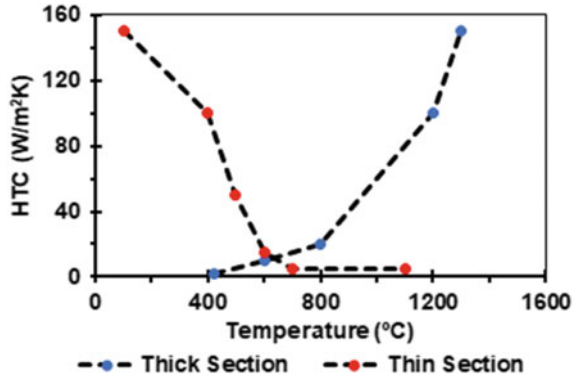


The results from the thermal model were obtained by the application of separate HTC functions on the thin and thick sections. Note that each function is affected by both experimental readings. The consideration of two functions, one for each region, instead of a single global function for the whole domain was considered adequate, as it leads to a better match with experimental data. Besides, the heat transfer regime is expected to be different in each of those sections, due to the geometric factors previously discussed, so it seems appropriate to have a separate HTC function for each one of those domains. If thermocouple data is available for more points, more functions (one for each respective section) can in principle be generated.

The resulting heat transfer coefficient functions, under the experimental conditions of this work, are shown in Fig. 8.

These results show that the casting geometry and other affected variables, such as shrinkage, deformation and interface clearance, may influence the heat transfer of the system that was investigated.

**Fig. 8** HTC as a function of temperature, for thick (blue) and thin (red) sections



## 5 Conclusions

In this work, an inverse analysis methodology has been used to estimate the heat transfer coefficient as a function of temperature for a duplex stainless steel cast in a furan-bonded sand. The major conclusions from this work are summarized below:

- The HTC functions cannot be generalized and must be determined for a particular casting geometry, alloy chemical composition and the composition of the mold sand mixture. The HTC functions available in the literature are not adequate to replicate experimental thermal data obtained for casting a complex shape, such as a C-ring.
- Inverse analysis can be used as a calibration process for a numerical model in order to determine the HTC for a particular setup. This is particularly critical if the temperature distribution is the main input for further studies such as residual stress calculations or the prediction of microstructure.

**Acknowledgements** We acknowledge the financial support of this work by the Hungarian State and the European Union under the EFOP-3.6.1-16-2016-00010 project and the Hungarian-Portuguese bilateral Scientific and Technological (TÉT\_16-1-2016-0097) project/Project 3883, Fundação para a Ciência e Tecnologia (FCT—Portugal) and Nemzeti Kutatási, Fejlesztési és Innovációs Hivatal (NKFIH—Hungary).

The authors also acknowledge FERESPE—Fundação Portuguesa de Ferro e Aço (Portugal) for providing the material and technical support.

## References

1. Honggang, Z., Xiangru, C., Lu, A., Qije, Z.: Effect of cooling rate on solidification structure and linear contraction of a duplex stainless steel. *China Foundry* **9**(3), 239–243 (2012)
2. Palumbo, G., Piccininni, A., Piglionico, V., Guglielmi, P., Sorgente, D., Tricarico, L.: Modelling residual stresses in sand-cast superduplex stainless steel. *J. Mater. Process. Technol.* **217**, 253–261 (2015)

3. Zhang, L., Tan, W., Hu, H.: Determination of the heat transfer coefficient at the metal–sand mold interface of lost foam casting process. *Heat Mass Transf.* **52**, 1131–1138 (2016)
4. Bohacek, J., Kharicha, A., Ludwig, A., Wu, M., Karimi-Sibaki, E.: Heat transfer coefficient at cast-mold interface during centrifugal casting: calculation of air gap. *Metall. Mater. Trans. B* **49B**, 1421–1433 (2018)
5. Hadala, B., Malinowski, Z., Szajding, A.: Solution strategy for the inverse determination of the specially varying heat transfer coefficient. *Int. J. Heat Mass Transf.* **104**, 993–1007 (2017)
6. Wang, D., Zhou, C., Xu, G., Huaiyuan, A.: Heat transfer behavior of top side-pouring twin-roll casting. *J. Mater. Process. Technol.* **214**(6), 1275–1284 (2014)
7. Prabhu, K.N., Ashish, A.A.: Inverse modeling of heat transfer with application to solidification and quenching. *Mater. Manuf. Process.* **17**(4), 469–481 (2002)
8. Felde, I., Fried, Z., Szénási, S.: Solution of 2-D inverse heat conduction problem with graphic accelerator. *Mater. Perform. Character.* **6**(5), 882–893 (2017)
9. Malinowski, Z., Cebo-Rudnicka, A., Telejko, T., Hadala, B., Szajding, A.: Inverse method implementation to heat transfer coefficient determination over the plate cooled by water spray. *Inverse Probl. Sci. Eng.* **23**(3), 518–556 (2014)
10. Wang, Z., Yao, M., Wang, X., Zhang, X., Yang, L., Lu, H., Wang, X.: Inverse problem-coupled heat transfer model for steel continuous casting. *J. Mater. Process. Technol.* **214**(1), 44–49 (2014)
11. Palumbo, G., Piglionico, V., Piccininni, A., Guglielmi, P., Sorgente, D., Tricarico, L.: Determination of interfacial heat transfer coefficients in a sand mould casting process using an optimised inverse analysis. *Appl. Therm. Eng.* **78**, 682–694 (2015)
12. Kang, J., Hao, X., Nie, G., Long, H., Liu, B.: Intensive riser cooling of castings after solidification. *J. Mater. Process. Technol.* **215**, 278–286 (2015)
13. Nilsson, J.-O., Kangas, P., Karlsson, T., Wilson, A.: Mechanical properties, microstructural stability and kinetics of sigma-phase formation in 29Cr-6Ni-2Mo-0.38 N superduplex stainless steel. *Metall. Mater. Trans. A* **31**(A), 35–45 (2000)
14. Elmer, J.W., Palmer, T.A., Specht, E.D.: Direct observations of sigma phase formation in duplex stainless steels using in situ synchrotron X-Ray diffraction. *Metall. Trans. A* **38**(A), 464–475 (2007)
15. Arunkumar, S., Rao, K.V.S., Kumar, T.S.P.: Spatial variation of heat flux at the metal—mold interface due to mold filling effects in gravity die-casting. *Int. J. Heat Mass Transf.* **51**, 2676–2685 (2008)
16. Chen, L., Wang, Y., Peng, L., Fu, P., Jiang, H.: Study on the interfacial heat transfer coefficient between AZ91D magnesium alloy and silica sand. *Exp. Thermal Fluid Sci.* **54**, 196–203 (2014)
17. Vacca, S., Martorano, M.A., Heringer, R., Bocalini Jr., M.: Determination of the heat transfer coefficient at the metal-mold interface during centrifugal casting. *Metall. Mater. Trans. A* **46**(A), 2238–2248 (2015)

# **Part II**

## **Polymers**



Dawid Pacek

**Abstract** This paper describes rheological tests, drop tests and bulletproof tests of materials which are planned to be used as elements of bulletproof vests as well as in high impact protective equipment. Rheological tests of a homogenous composition of methyl-, phenyl-, borosiloxane polymers (KM material) performed for variable values of stress and strain at a fixed frequency of 1 Hz showed that the loss modulus exceeds the storage modulus throughout the whole tested range of shear stress so that the energy is more dissipated than stored. In the drop tests, same-mass samples of three materials, i.e. the KM material, the shear thickening fluid STF1 and the commercial shear thickening polymer ZB were tested. For a given impact energy ( $E_i = 35$  J) and impact velocity ( $V_i = 1.9$  m/s), the ZB material shows the best protective capability. In the ballistic tests, the sample with the KM material was tested with the use of .44 Magnum SJHP (semi-jacketed hollow-point) bullet following NIJ Standard-0101.04 for IIIA bulletproof class. The results were compared to the bulletproof tests of the ZB material from previous works. Better protective capability was achieved in the case of a commercial material. However, the tested KM material also exhibited the energy dissipation capability. Further work is needed to investigate the effectiveness of the KM material in a different type of casing.

**Keywords** Body armor · Rheological test · Drop test · Ballistic test

## 1 Introduction

Since contemporary weapons are becoming more efficient, body armor needs to be improved accordingly. If we want to provide protection against increasingly dangerous threats, we have to take into consideration that high flexibility and low weight

---

ZB—Zoombang<sup>®</sup>—Manufacturer: ZB Products, LP (26947 Katy Freeway, Katy, TX 77494).

---

D. Pacek (✉)

Department of Armour Development, Military Institute of Armament Technology, 7  
Wyszynskiego St., 05-220 Zielonka, Poland  
e-mail: [pacekd@witu.mil.pl](mailto:pacekd@witu.mil.pl)

are particularly important, and consequently modern armor cannot be simply scaled by adding more layers of the same material or thickening it. It is necessary to work towards new solutions by designing new ballistic pads. Thus the concepts of flexible armor based on fluids are being developed.

So far, the most described has been the idea of using shear thickening fluids (STF). Results of ballistic tests, knife stab and puncture-resistant performance as well as numerical simulations were studied by University of Delaware in cooperation with the U.S. Army Research Laboratory (ARL) [1–6], NASA Johnson Space Center and the University of Texas [7–9], ARL and the University of Texas [10, 11], University of Rome [12], Seoul National University [13], University of Science and Technology of China [14], Military Institute of Armament Technology in Poland [15, 16].

The article [4] presents the results of firing standard fragment simulating projectiles FSP ( $m = 1.1$  g) at different variants of armor with STF and—for comparative purposes—at armor consisting solely of Kevlar® layers. When same-mass samples were tested, the best protective capability was obtained for impregnated layers. Taking into consideration that the mass and ballistic efficiency of 4 layers of impregnated Kevlar® were approximately the same as for 10 layers of non-impregnated Kevlar® as well as that 4-layered Kevlar® impregnated with STF is more flexible (deflection angle of  $51^\circ$ ) than 10-layered non-impregnated Kevlar® (deflection angle of  $13^\circ$ ), it has been concluded in [4] that impregnating Kevlar® with STF can be useful for improving its protective properties.

The other studies carried out by the University of Delaware and ARL concerned, for instance, the influence of carrier fluid viscosity as well as size and shape of the particles [2] in the impregnated Kevlar® layers on its protective properties (ballistic-penetration resistance). What was also examined was the possibility of applying softer particles [1] instead of hard silica particles that had been used before.

Experimental studies and numerical analyses focusing on the possibility of using STF in armor were also conducted by NASA Johnson Space Center and the University of Texas [7–9]. These studies concerned the hypervelocity impact of aluminum projectiles (2.8–3.2 mm in diameter) on multi-layer aluminum-Kevlar® armor. In this case, the impregnation of Kevlar® with STF has not improved its protective properties.

The properties of shear-thickening-fluid Kevlar® were also investigated by ARL in cooperation with the Department of Mechanical Engineering at the University of Texas [10, 11]. These studies aimed at developing the so-called soft wall containment system which would provide protection against fan blade off event in engines. In comparison to the previous experimental studies, projectiles used in this research were larger:

1. a steel disk with a diameter of 38.1 mm, height of 6.35 mm and mass of 56.7 g;
2. an aluminum cylinder with a diameter of 12.7 mm, height of 25.4 mm and mass of 8.69 g.

Samples consisting of 1–24 layers of STF-impregnated or neat Kevlar® were tested for two different boundary conditions:

1. all edges of the material fixed;
2. 2 edges of the material fixed, 2 edges free.

Three series of tests were carried out:

1. with projectile no. 1 and boundary condition no. 1;
2. with projectile no. 2 and boundary condition no. 1;
3. with projectile no. 2 and boundary condition no. 2.

When comparing same-mass samples of neat Kevlar<sup>®</sup> with shear-thickening-fluid Kevlar<sup>®</sup>, the following results have been obtained for the latter [11]:

1. in the first and second series of tests—decrease of protective capabilities;
2. in the third series, where samples were fixed along two edges—similar protective capabilities.

On the basis of the third series of tests, it can be concluded that adding STF to the material improves its protective capabilities owing to the fact that the absorption of projectile impact energy is largely influenced by friction between warp and weft of the material—although insufficient due to the mass increase.

In research described in paper [15], the ballistic resistance of armor samples to perforation by .44 Magnum SJHP (semi-jacketed hollow-point) bullet was examined. The tests were carried out following NIJ Standard-0101.04 [17] requirements for IIIA bulletproof class. Among all shear-thickening-fluid armor variants, the best energy absorption and the lowest backface signature with respect to the mass of a sample were achieved for the armor with the anti-trauma pad consisting of a foam produced with the addition of the STF1 (areal density  $A_d = 4.98 \text{ kg/m}^2$ ; average backface signature for impact angle of  $0^\circ$  from the surface normal— $BFS_{av} = 38.8 \text{ mm}$ ).

The capability to dampen the impact energy of high strain rates is also exhibited by a homogenous composition of methyl-, phenyl-, borosiloxane polymers with the addition of fillers and lubricating mediums—i.e. KM material which is used in railway dampers [15, 16]. The presented study aimed at comparing protective properties of this kind of material and shear thickening fluids.

## 2 Rheological Behavior of KM Material

Rheological tests were performed with a rotational rheometer operating in the stress-controlled mode. In plate-plate configuration (plate diameter –  $\varphi = 20 \text{ mm}$ ) in dynamic mode (oscillatory test for variable values of stress and strain at a fixed frequency of 1 Hz), storage modulus  $G'$ , loss modulus  $G''$  and complex modulus  $G^*$  were determined. This kind of test defines what properties (elastic or viscous) are predominant in the material for given loads. In the case of the KM material, the loss modulus exceeds the storage modulus throughout the whole tested range of shear stress (Fig. 1). Consequently, the viscous properties, characteristic of fluids, are predominant in this material. After initial fluctuations, from the complex stress



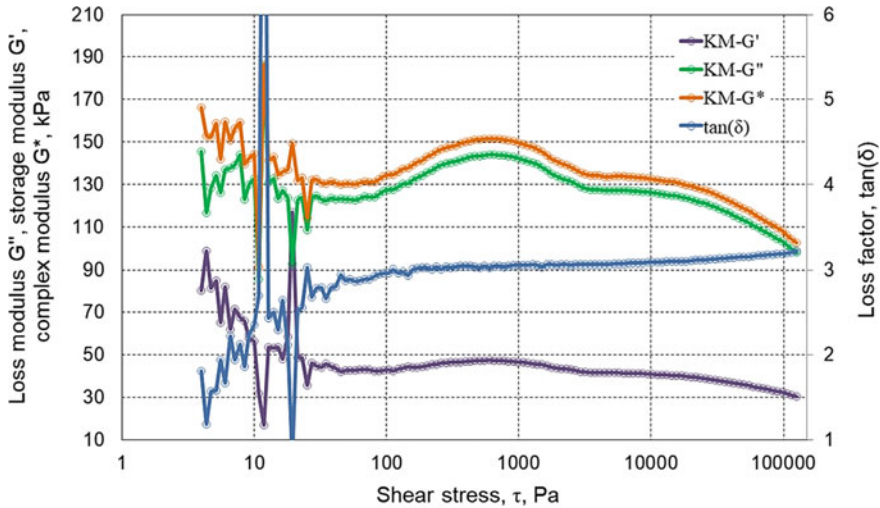


**Fig. 1** Dynamic test results for KM material

of approximately 45 Pa the ratio of loss modulus to storage modulus (loss factor) remains stable and falls within the following range:  $\tan(\delta) \in \langle 2.9, 3.2 \rangle$ . As shown on the graph, when the stress exceeds 600 Pa, for which the complex modulus is 152 kPa, a drop of  $G^*(\tau = 125 \text{ kPa}) = 102 \text{ kPa}$  can be observed until the limit value of stress is reached. It means that in this range the complex strain grows quicker than complex stress, which in turn indicates that the material is weakened.

### 3 Drop Tests

After investigating rheological properties of the KM material, samples ( $4.5 \text{ kg/m}^2$ ) with this material and two kinds of STF—one produced in Warsaw University of Technology (Poland) marked as STF1 and a commercial product (USA) marked as ZB—were examined in the drop tests with a free fall shock machine (Fig. 2a, b). The 20 kg carriage with accelerometer (Fig. 2d) was dropped onto samples placed on the pulse-shaping device (Fig. 2c). The height was adjusted to obtain the right amount of impact energy  $E_i = 35 \text{ J}$  (impact velocity  $V_i = 1.9 \text{ m/s}$ ). Carriage acceleration curves obtained for all materials and without a sample are presented in Fig. 3.

When impact on the base was tested for an uncovered sample, the average maximum acceleration was 921 g. Adding a sample with the KM material reduced the value by 74%. For STF1, a similar result was obtained. The smallest maximal acceleration of 80 g (mean of three drops) was obtained for the ZB material. In comparison to the test without a sample and with the KM material, the values were lower by 91% and 67% respectively.

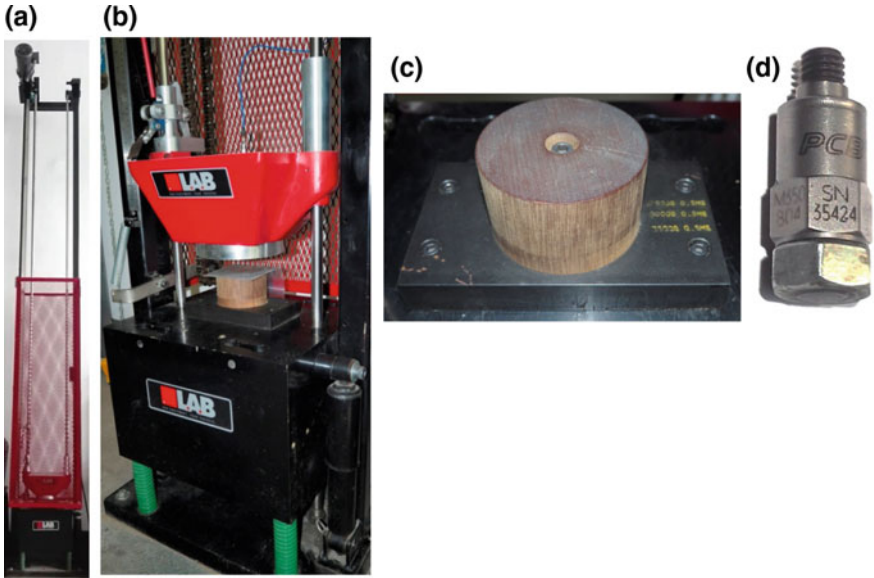


**Fig. 2** Drop tests: **a** free fall shock machine, **b** exemplary sample, **c** pulse shaping device, **d** accelerometer

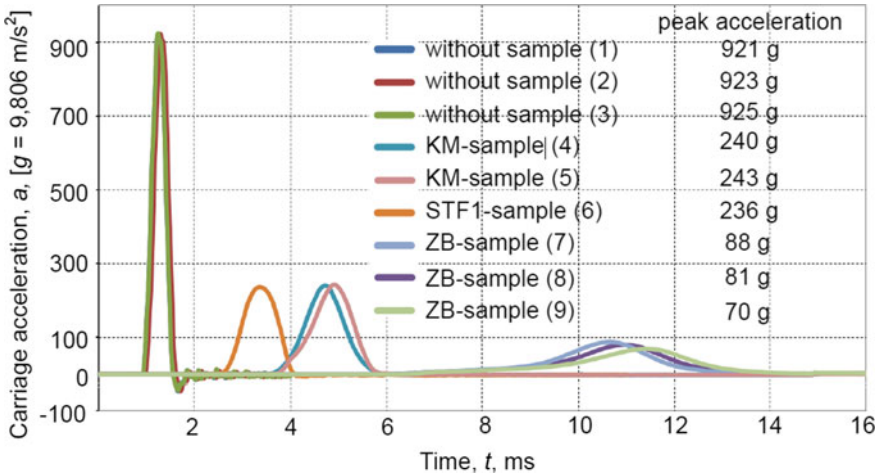


**Fig. 3** Carriage acceleration curves

For a given energy and impact speed, the commercial product marked as ZB proves most useful as a protective element. In further research, the free fall shock machine will be used to compare protective capabilities of materials for higher impact velocities.

## 4 Ballistic Testing of Anti-trauma Pads

In order to test the utility of the KM material in comparison to the ZB shear thickening polymer, an anti-trauma pad was formed with the KM material placed in the cover of the commercially available interlayer (ZB-7<sup>®</sup> ballistic pad) with the ZB material (Fig. 4). The commercial pad will be labeled as X. The polymer was removed from the cells of the interlayer X and then replaced in each cell with a same-mass sample of KM material. The interlayers were prepared to allow the removal of the polymer. The created incisions were glued after the addition of KM. A sample with this pad (which we now refer to as X') was constructed analogously to the sample previously tested with the original interlayer X (the same number and layering) [17].

A 400 × 400 mm sample was tested with the use of .44 SJHP (semi-jacket hollow-point) bullet following NIJ Standard-0101.04 for IIIA bulletproof class considering the boundary conditions, shot locations, bullet velocity ( $436 \pm 9$  m/s) and impact angles ( $0^\circ$  and  $30^\circ$  from the surface normal). Table 1 and Fig. 5 show the results of the ballistic tests of X'. For comparative purposes, Table 1 also shows the previous results of anti-trauma X interlayer firing. Detailed results from X are described in [17].

For the KM interlayer, the average deflection of a backing material (oil base modeling clay) was 23% higher than of the original interlayer and in two cases the backface signature exceeded the permissible value of NIJ 0101.04. This may be due to the lower energy absorption capacity of the KM compared to the ZB polymer, but also because the insert casing and the cell size were matched to a ZB polymer with a density 58% lower than KM.

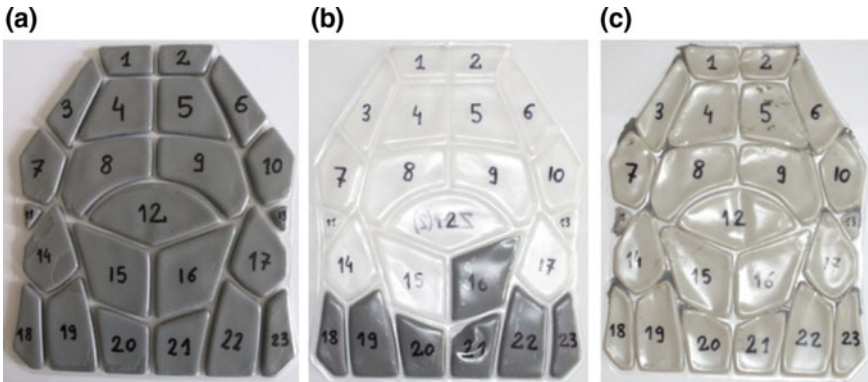


**Fig. 4** Filling the interlayer with KM material: **a** original interlayer ZB-7<sup>®</sup> filled with the ZB polymer; **b** the interlayer with partially removed polymer, **c** X interlayer filled with KM material

**Table 1** Results of ballistic tests of samples with X and X' interlayers

Sample construction	Areal density, $m_p$ (kg/m <sup>2</sup> )	Impact spot ( <sup>1</sup> angle)		Impact velocity, $V_i$ (m/s)	Backface signature, <i>BFS</i> (mm)	
19 l. Dyneema® SB71/X' = casing of X + KM/ 2 l. Dyneema® SB71	6.1	1	(0°)	451	<b>56</b>	41.3
		2	(0°)	437	41	
		3	(0°)	447	42	
		4	(30°)	433	30	
		5	(30°)	446	30	
		6	(0°)	443	<b>49</b>	
19 l. Dyneema® SB71/X/ 2 l. Dyneema® SB71	6.1	1	(0°)	445	38	33.7
		2	(0°)	440	34	
		3	(0°)	440	33	
		4	(30°)	439	28	
		5	(30°)	446	28	
		6	(0°)	444	41	

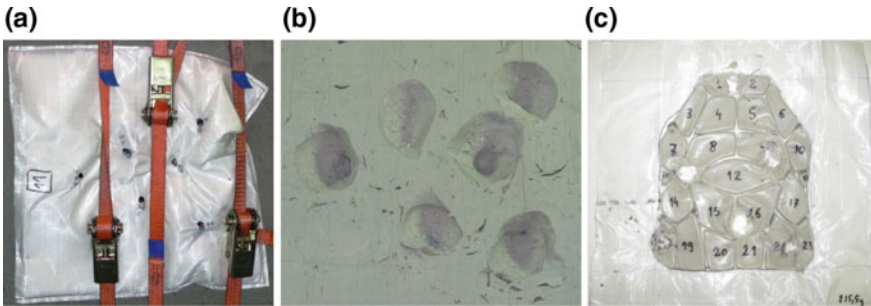


**Fig. 5** Base and sample with X cover filled with KM material after firing **a** sample; **b** base, **c** interlayer X' (filled with KM)

## 5 Conclusions

On the basis of carried out tests the following conclusions have been drawn:

1. In the case of the KM material, the loss modulus exceeds the storage modulus throughout the whole tested range of shear stress ( $\tan(\delta) < 2.9, 3.2 >$ )—energy is dissipated to a greater extent than stored.

2. In the case of the drop tests with  $E_i = 35 \text{ J}$  and  $V_i = 1.9 \text{ m/s}$  (same-mass samples), the smallest carriage peak acceleration is exhibited by the ZB material.
3. Replacing the ZB material with the KM material of the same mass in a commercial cover designed for the ZB material does not improve protective properties of the anti-trauma pad dedicated for bulletproof vests.
4. Both in the drop tests and the ballistic test described in this article, better protective capability (of the same-mass samples) was achieved in the case of a commercial material used for reference purposes. However, the tested KM material also exhibited the energy dissipation capability. In the research described in publication [16], which was conducted on a sample with a different structure, the KM material exceeded the effectiveness of the ZB material. Therefore the works focusing on the construction of a shield based on the KM material shall be continued.

## References

1. Kalman, D.P., Shein, J.B., Houghton, J.M., Laufer, C.H.N., Wetzel, E.D., Wagner, N.J.: Polymer dispersion based shear thickening fluid-fabrics for protective applications. In: Proceedings of Symposium and Exhibition of the Society for the Advancement of Material and Process Engineering SAMPE 2007, Baltimore (2007)
2. Wetzel, E.D., Lee, Y.S., Egres, R.G., Kirkwood, K.M., Kirkwood, J.E., Wagner, N.J.: The effect of rheological parameters on the ballistic properties of shear thickening fluid (STF)—Kevlar composites. In: Proceedings of 8th International Conference on Numerical Methods in Industrial Forming Processes NUMIFORM 2004, Columbus (2004)
3. Rosen, B.A., Laufer, C.H.N., Kalman, D.P., Wetzel, E.D., Wagner, N.J.: Multi-threat performance of kaolin-based shear thickening fluid (STF)-treated fabrics. In: Proceedings of Symposium and Exhibition of the Society for the Advancement of Material and Process Engineering SAMPE 2007, Baltimore (2007)
4. Lee, Y.S., Wetzel, E.D., Wagner, N.J.: The ballistic impact characteristics of Kevlar woven fabrics impregnated with a colloidal shear thickening fluid. *J. Mater. Sci.* **38**, 2825–2833 (2003)
5. Lee, Y.S., Wetzel, E.D., Egres Jr., R.G., Wagner, N.J.: Advanced body armor utilizing shear thickening fluids. In: Proceedings of 14th International Conference on Composite Materials, San Diego (2003)
6. Wetzel, E.D., Wagner, N.J.: Advanced body armor utilizing shear thickening fluids. In: Presentation from 23rd Army Science Conference, Orlando (2002)
7. Bohannan, A.L.: Hypervelocity impact simulation using membrane particle-elements. M.S. Thesis, Dept. of Mechanical Engineering, University of Texas, Austin, TX (2008)
8. Bohannan, A.L., Fahrenthold, E.P.: Hypervelocity impact simulation using membrane particle-elements. *Int. J. Impact Eng.* **35**(12) (2008)
9. Bohannan, A.L., Fahrenthold, E.P.: Simulation of STF Kevlar shielding performance in a stuffed Whipple configuration. In: 50th AIAA Structures, Structural Dynamics, and Materials Conference, AIAA Paper 2009-2400 (2009)
10. Rabb, R.J.: A mesomechanical particle-element model of impact dynamics in neat and shear thickening fluid Kevlar. Ph.D. thesis, The University of Texas at Austin (2007)
11. Rabb, R.J., Fahrenthold, E.P.: Evaluation of shear-thickening-fluid Kevlar for large-fragment-containment applications. *J. Aircr.* **48**(1), 230–234 (2011)

12. Pastore, R., Giannini, G., Morles, R., Marchetti, R., Micheli, D.: Impact response of nanofluid-reinforced antiballistic Kevlar fabrics, Chapter 9. In: Ebrahimi, F. (ed.) *Nanocomposites—New Trends and Developments*, pp. 215–238 (2012). ISBN 978-953-51-0762-0. [http://www.issp.ac.ru/eboks/books/open/Nano-composites\\_-\\_New\\_Trends\\_and\\_Developments.pdf](http://www.issp.ac.ru/eboks/books/open/Nano-composites_-_New_Trends_and_Developments.pdf)
13. Kang, J.T., Hong, K.H., Yoo, M.R.: Preparation and properties of fumed Sillica/Kevlar composite fabrics for application of stab resistant material. *Fibers Polym.* **11**(5), 719–724 (2010)
14. Gong, X., Xu, Y., Zhu, W., Xuan, S., Jiang, W.: Study of the knife stab and puncture-resistant performance for shear thickening fluid enhanced fabric. *J. Compos. Mater.* 1–17 (2011)
15. Pacek, D., Zochowski, P., Wisniewski A.: Anti-trauma pads based on non-newtonian materials for flexible bulletproof inserts. In: *Proceedings of 29th International Symposium on Ballistics*, pp. 2116–2126, Edinburgh (2016)
16. Pacek, D.: Flexible bulletproof armor with modular interlayer. In: *Proceedings of 30th International Symposium on Ballistics*, pp. 2034–2045, Long Beach (2017)
17. National Institute of Justice: *Ballistic Resistance of Personal Body Armor—NIJ Standard-0101.04*, June 2001

**Part III**  
**Ceramics**

# Synthesis of Mg–Zn–Ca Alloy by the Spark Plasma Sintering



Sabina Lesz, Joanna Kraczla and Ryszard Nowosielski

**Abstract** Mechanical alloying (MA) and spark plasma sintering (SPS) was employed to synthesize the  $\text{Mg}_{60}\text{Zn}_{35}\text{Ca}_5$  alloy. SPS, which is also known as the field-assisted sintering technique, plasma-activated sintering, pulsed electric current sintering, or plasma pressure-compaction, appears to be promising for manufacturing a biodegradable  $\text{Mg}_{60}\text{Zn}_{35}\text{Ca}_5$  alloy. SPS is a sintering technology that utilizes Joule heating via a pulsed electric current to achieve densification. SPS allows very fast heating and cooling rates, very short holding time, and the possibility of obtaining fully dense samples at comparatively low sintering temperatures, typically a few hundred degrees lower than normal hot pressing. The Joule heating could lead to further improved densification via localized plastic flow at the necks of connected particles during sintering. The structure and compressive strength of the  $\text{Mg}_{60}\text{Zn}_{35}\text{Ca}_5$  alloy were investigated. In the X-ray diffraction (XRD) patterns of the representative  $\text{Mg}_{60}\text{Zn}_{35}\text{Ca}_5$  powder after 13 h of MA, a broad diffraction peak corresponding to the amorphous phase is noticed. The results by XRD show that the  $\text{Mg}_{60}\text{Zn}_{35}\text{Ca}_5$  alloy after sintering has a multiphase structure. The investigated alloy shows a slightly higher compressive strength (264–300 MPa) compared to the crystalline Mg-based alloy (250 MPa) and exhibits properties appropriate for medical applications.

**Keywords** Magnesium alloy · Spark plasma sintering (SPS) · X-ray diffraction (XRD) · Scanning electron microscopy (SEM)

## 1 Introduction

Magnesium alloys have been widely studied as potential biomaterials. Since traditional metallic biomaterials are biocompatible but not biodegradable, the magnesium alloys have attracted the attention of biomaterial scientists [1–8]. Degradable bioma-

---

S. Lesz (✉) · J. Kraczla · R. Nowosielski  
Institute of Engineering Materials and Biomaterials, Silesian University of Technology, 18a  
Konarskiego Street, 44-100 Gliwice, Poland  
e-mail: [sabina.lesz@polsl.pl](mailto:sabina.lesz@polsl.pl)

© Springer Nature Switzerland AG 2019  
L. F. M. da Silva (ed.), *Materials Design and Applications II*, Advanced  
Structured Materials 98, [https://doi.org/10.1007/978-3-030-02257-0\\_7](https://doi.org/10.1007/978-3-030-02257-0_7)



materials should have sufficient strength, matching degradation rate with tissue healing rate and good biocompatibilities [9]. Magnesium is the fourth most abundant mineral found in the human body, with an estimated 25 g of magnesium stored in the human body and approximately half of the total content is stored in bone tissue. Magnesium is a cofactor for many enzymes and stabilized the structures of DNA (deoxyribonucleic acid) and RNA (ribonucleic acid) [4, 10, 11]. Magnesium has a standard electrode potential of  $-2.37$  V. From the perspective of mechanical features magnesium has good compatibility with human bone since Mg density of  $1.74$  g/cm<sup>3</sup>, Young's modulus of 41–45 GPa and compressive yield strength between 65 and 100 MPa are close to those of natural bone ( $1.8$ – $2.1$  g/cm<sup>3</sup>, 3–20 GPa and 130–180 MPa) [4]. The specific design of alloys intended for the repair of bone fractures is based on the introduction of biologically important elements such as Ca and Zn. The small addition of Ca to a magnesium alloy is an effective way to improve the mechanical properties and corrosion resistance [12, 13]. Zn enhances the strength of Mg by solid solution strengthening [14]. Binary Mg–Ca, Mg–Zn alloys and ternary Mg–Zn–Ca alloys, fully crystalline or amorphous, have been thoroughly studied and also show improvements on mechanical strength [15–19].

To achieve higher strengths of conventional crystalline magnesium alloys, rapid solidification (RS) and mechanical alloying (MA) methods have been successfully utilized to decrease grain size and to obtain amorphous matrix [20–22]. However, the glass forming ability (GFA) of Mg–Zn–Ca bulk metallic glasses (BMGs) is limited (critical size diameter ( $D_c$ )  $\approx 5$  mm) [23]. MA was used to produce binary Mg<sub>70</sub>Zn<sub>30</sub> [24], Mg<sub>50</sub>Ti<sub>50</sub> [25] and ternary Mg–Y–Cu [26] amorphous Mg-based alloys.

Most commercial magnesium alloys contain Al and impurities. Al is a neurotoxicant [27]. The presence of impurities in magnesium alloys can have dramatic effects on the properties of the material. In magnesium, the two most common impurities are intermetallic (containing iron, nickel, cobalt) and magnesium oxide inclusions. Even at low concentrations, intermetallics significantly reduce the corrosion resistance of magnesium and easily reduce the specifications to a sub-standard level [28, 29].

Therefore, another research highlight is the exploration of the new magnesium alloy system containing nontoxic or low toxic elements. High purity Mg-based alloys can be obtained by spark plasma sintering (SPS). SPS, which is also known as the field-assisted sintering technique, plasma-activated sintering, pulsed electric current sintering, or plasma pressure-compaction [30–32], appears to be promising for manufacture biodegradable Mg<sub>60</sub>Zn<sub>35</sub>Ca<sub>5</sub> alloy. SPS is a sintering technology that utilizes Joule heating via a pulsed electric current to achieve densification. SPS allows very fast heating and cooling rates, very short holding time, and the possibility to obtain fully dense samples at comparatively low sintering temperatures, typically a few hundred degrees lower than normal hot pressing [30]. Joule heating could lead to further improved densification via localized plastic flow at the necks of connected particles during sintering [31, 32].

The purpose of the paper was to investigate the structure, density and compressive strength of the Mg<sub>60</sub>Zn<sub>35</sub>Ca<sub>5</sub> alloy. Previous work reports the results of a study conducted to explore the influence of milling time on amorphization of Mg–Zn–Ca powders synthesized by MA method [33].

## 2 Materials and Methods

### 2.1 Material

Pure magnesium (99.8 wt%, –20+100 mesh), zinc (99.9 wt%, –100 mesh) and calcium (99.5 wt%, –16 mesh) powders were used as starting materials to the desired composition of  $\text{Mg}_{60}\text{Zn}_{35}\text{Ca}_5$  (60 at.% Mg–35 at.% Zn–5 at.% Ca) alloy.

Samples were prepared by a mechanical alloying (MA) process. SPEX 8000 (Metuchen, U.S.A.) high energy shaker ball mill was used for MA at room temperature. The milling was performed in an Ar atmosphere. Milling was carried out with a ball to powder weight ratio of 10:1 in a stainless steel vial using 10 mm stainless steel balls for 13 h milling time. The MA process was performed with 0.5 h intervals. The powders and the milling balls were loaded into a stainless steel vial under an argon atmosphere and all the powder handling was performed in a glove box.

Then the powder mixture was sintered by spark plasma sintering (SPS) using the equipment of FCT firm (Frankenblick, Germany). The mixed powders to be consolidated were poured into a cylindrical graphite die (10 mm inside diameter). A graphite foil between the sample and the internal surface of the die was placed in order to facilitate sample extraction after the SPS process. In addition, the die was covered with a layer of graphite felt to minimize heat loss by thermal radiation. The pressure level on the compacts was kept constant at 51 MPa throughout the sintering process. The samples were heated (with a heating rate of 100 K/min) to the temperature of 573 K. The vacuum level of the sintering chamber was <1 hPa. After a hold time of 15 min, the  $\text{Mg}_{60}\text{Zn}_{35}\text{Ca}_5$  bulks were cooled to room temperature for 10 min.

The morphology with EDS spectrum of the elemental metal of Mg, Zn, Ca and blended  $\text{Mg}_{60}\text{Zn}_{35}\text{Ca}_5$  powders after 13 h of high energy MA was examined by scanning electron microscope (SEM) and is shown in Fig. 1a–d.

### 2.2 Experimental Procedure

The following experimental techniques were used: X-ray diffraction (XRD) phase analysis method to test the structure [34], density measurements and compression test. The morphological characterization of the powder and sintered samples were made by scanning electron microscopy (SEM).

X-ray phase analysis was conducted on a PANalytical X-Pert PRO (Almelo, The Netherlands) diffractometer using  $\text{Co-K}\alpha$  radiation. The result of the analysis consists of an identified phase list with experimentally observed X-ray patterns and known diffraction patterns from various sources. The sources and the notation describing the quality of data are maintained by the International Centre for Diffraction Data (ICDD) [35].

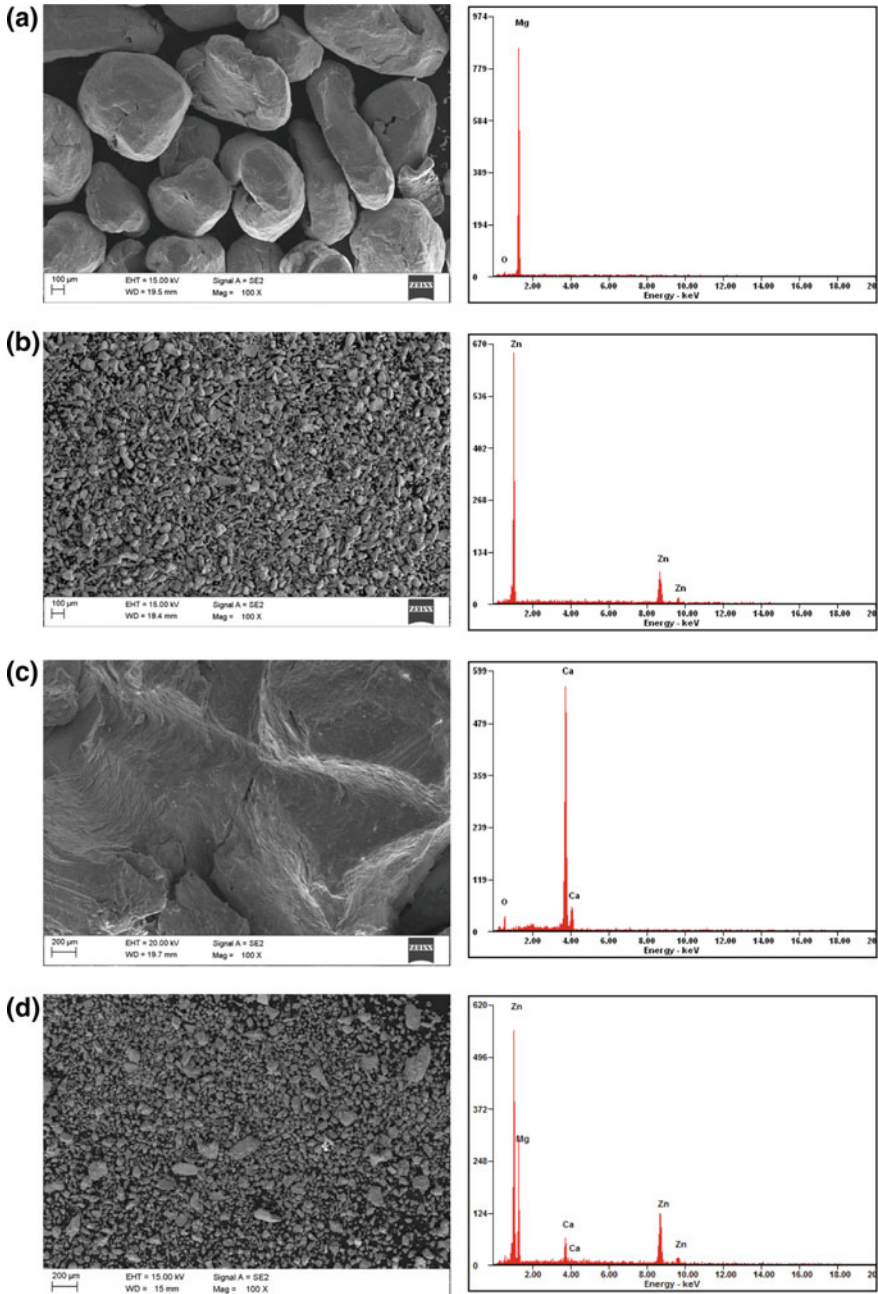


**Fig. 1** The morphology with EDS spectrum of the elemental metal powders of Mg (a), Zn (b) shots of Ca (c) and blended Mg<sub>60</sub>Zn<sub>35</sub>Ca<sub>5</sub> powders after 13 h of high energy mechanical alloying (MA), (d) SEM

Density measurements were carried out using the helium pycnometer Micromeritics AccuPyc II 1340 (Norcross, U.S.A.). The density determined by helium pycnometer is termed the absolute ( $\rho_a$ ), real and helium density. In order to limit measure error, measurements were repeated five times. The value of porosity of three sintered Mg–Zn–Ca sample was measured based on the following Eq. (1):

$$P = \left(1 - \frac{\rho_c}{\rho_a}\right) \cdot 100\% \quad (1)$$

where  $\rho_c$  was the calculated value of density and  $\rho_a$  was an absolute density of the sample. The calculated value of density  $\rho_c$  of samples were determined from weight and dimensional measurements, which were accurate to within  $\pm 0.001$  g and  $\pm 0.001$  mm, respectively.

The deformation behaviour of the Mg<sub>60</sub>Zn<sub>35</sub>Ca<sub>5</sub> sintered alloy was investigated using compression test. The compression tests were carried out according to the PN-H-04320 standard [36] at a displacement rate of 0.5 mm min<sup>-1</sup> using a Zwick/Roell multifunctional Z100 testing machine (Ulm, Germany). Compression force was 2 kN. Three samples were taken in the form of rolls with a base-to-height ratio of approximately 1:1.5.

The morphological characterization of the powder and the sintered samples were made by scanning electron microscope (SEM) SUPRA 25, Carl Zeiss (Jena, Germany), equipped with an energy-dispersive X-ray spectroscopy (EDS). Fractography investigations was carried out by SEM on the failure surfaces of sintered samples after decohesion in compression test, to determine the character of fracture.

### 3 Results and Discussion

Examination of blended Mg<sub>60</sub>Zn<sub>35</sub>Ca<sub>5</sub> powders after 13 h of high energy MA by X-ray method shows a broad peak corresponding to the amorphous phase (Fig. 2a). The X-ray diffraction (XRD) pattern in Fig. 2a and previous results of our work [33] verify the amorphous nature of blended Mg<sub>60</sub>Zn<sub>35</sub>Ca<sub>5</sub> powders after 13 h of high energy MA. Figure 2b shows XRD pattern of the Mg<sub>60</sub>Zn<sub>35</sub>Ca<sub>5</sub> alloy sintered by SPS at temperature of 573 K for 10 min. The Mg<sub>60</sub>Zn<sub>35</sub>Ca<sub>5</sub> alloy has a crystalline structure, as demonstrated by a strong intensities Bragg peaks obtained in the diffraction pattern (Fig. 2b). The Mg<sub>60</sub>Zn<sub>35</sub>Ca<sub>5</sub> alloy presented characteristic diffraction spectra of a hexagonal close-packed Mg phase. For the samples sintered at 573 K for 10 min besides the Mg phase, a few of Bragg peaks of MgZn<sub>2</sub>, Mg<sub>2</sub>Zn<sub>3</sub>, Mg<sub>7</sub>Zn<sub>3</sub>, MgZn, Ca<sub>2</sub>Mg<sub>5</sub>Zn<sub>13</sub> phases have been detected. No peaks correspond to any metal oxides were detected from XRD for samples sintered in SPS method at 573 K.

Table 1 shows the calculated and absolute density and porosity values of three sintered Mg–Zn–Ca samples. Results of the compression test of three sintered Mg–Zn–Ca samples are shown in Table 1, too.

**Fig. 2** XRD patterns of  $Mg_{60}Zn_{35}Ca_5$  powders with different states: **a** blended powders after 13 h of high energy mechanical alloying (MA), **b** alloy sintered by SPS at temperature of 573 K for 10 min

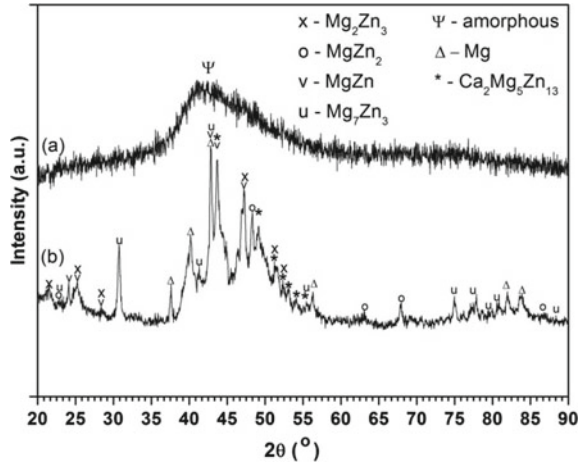


**Table 1** The calculated ( $\rho_c$ ) absolute density ( $\rho_a$ ) porosity ( $P$ ) and compressive strength ( $\sigma_c$ ) values of three sintered Mg–Zn–Ca samples

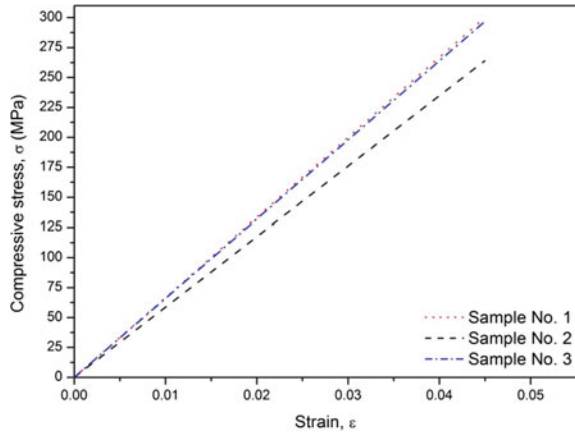
Samples No.	Calculated density $\rho_c$ (g/cm <sup>3</sup> )	Absolute density $\rho_a$ (g/cm <sup>3</sup> )	Porosity $P$ (%)	Compressive strength $\sigma_c$ (MPa)	Young’s modulus $E$ (MPa)
1	3.2102	3.3365	4	300	6605
2	2.9792	3.3406	11	264	7042
3	3.1941	3.3327	4	297	6728

As it can be seen in Table 1, little change is observed in the density of sintered samples. It can be observed that the calculated density value have a greater spread in relation to the absolute density value.

However, the calculated density value is based on the geometry of the sample, not taking into account the presence of the pores and void spaces within the bulk sample. Therefore, the absolute value of sintered particles is higher than the calculated density value. The porosity value between samples was not significantly different. Only sample No. 2 has the higher value of porosity equal 11%.

The compressive curves of the  $Mg_{60}Zn_{35}Ca_5$  alloy samples are shown in Fig. 3. The typical compressive curves for a brittle material were observed. The compressive strength ( $\sigma_c$ ) of the samples exhibited increasing tendency with the increase of the strain. The mechanical parameters obtained on compression testing of the  $Mg_{60}Zn_{35}Ca_5$  alloy are from 264 to 300 MPa (compressive strength) and from 6605 to 7042 MPa (Young’s modulus). The results of compression test show that the highest compressive strength ( $\sigma_c = 300$  MPa) and lowest elasticity ( $E = 6605$  MPa) is found in the Mg–Zn–Ca sinter for sample No. 1. The highest elasticity is found in the Mg–Zn–Ca sintered sample No. 2. For this material the longitudinal elastic modulus  $E$  was 7042 MPa.

**Fig. 3** Compressive curves of the  $\text{Mg}_{60}\text{Zn}_{35}\text{Ca}_5$  alloy samples Nos. 1, 2 and 3 sintered by SPS at the temperature of 573 K for 10 min



The correlation between porosity ( $P$ ) and compressive strength ( $\sigma_c$ ) was observed. While the porosity ( $P$ ) decreased from 11 to 4%, the compressive strength ( $\sigma_c$ ) increased from 264 to 300 MPa. The relationship between porosity and strength are in good agreement with those obtained by Dewidar [37] for porous 316L stainless steel. The high elasticity of the sample No. 2 is attributed to the porosity which phenomena was also confirmed by the Zhang and Zhang [38]. For comparison, the highest values of compressive strength ( $\sigma_c$ ) and Young's modulus ( $E$ ) of Mg-rich alloys was found in the bulk metallic glasses (BMGs) by Zberg et al. [39]. For the  $\text{Mg}_{66}\text{Zn}_{30}\text{Ca}_4$ , ranges from 716 to 854 MPa and  $E$  ranges to 48 GPa. Similar mechanical parameters was obtained by Zhao et al. [23] for the more Mg-rich bulk BMGs. Our earlier research showed that the  $\text{Mg}_{60}\text{Zn}_{35}\text{Ca}_5$  alloy produced in MA process and sintered at temperature 523 K by conventional powder metallurgy and SPS method get lower values of compressive strength ( $\sigma_c$ ) equal 50 MPa and 80 MPa, respectively [40]. Our earlier research showed that with the Gd addition is possible to improve the mechanical properties Mg–Zn–Ca sintered alloy [41].

The value obtained for the density ( $\sim 3.33 \text{ g/cm}^3$ ) of the samples correlates well with bone density and shows only slight differences. The density of selected bones of the human skeleton is in the range of  $1.8\text{--}2.1 \text{ g/cm}^3$  [4, 42]. In light of such results, it can be concluded that the tested of the  $\text{Mg}_{60}\text{Zn}_{35}\text{Ca}_5$  sintered alloy exhibits slightly higher mechanical properties ( $\sigma_c$  from 264 to 300 MPa) than the human bone (strength of 130–180 MPa) [4, 42]. Although in the case of medical applications of these materials, attention should be paid to the closest approximation of material properties and mechanical parameters to the tissues of the organism, so that the implants made of such biomaterials would not generate additional stress and provide negative affect on the host's body [42].

Fractographic investigations of failure surfaces after decohesion in compression test showed, in all samples sintered at temperature 573 K, the same morphology (Fig. 4a–f).

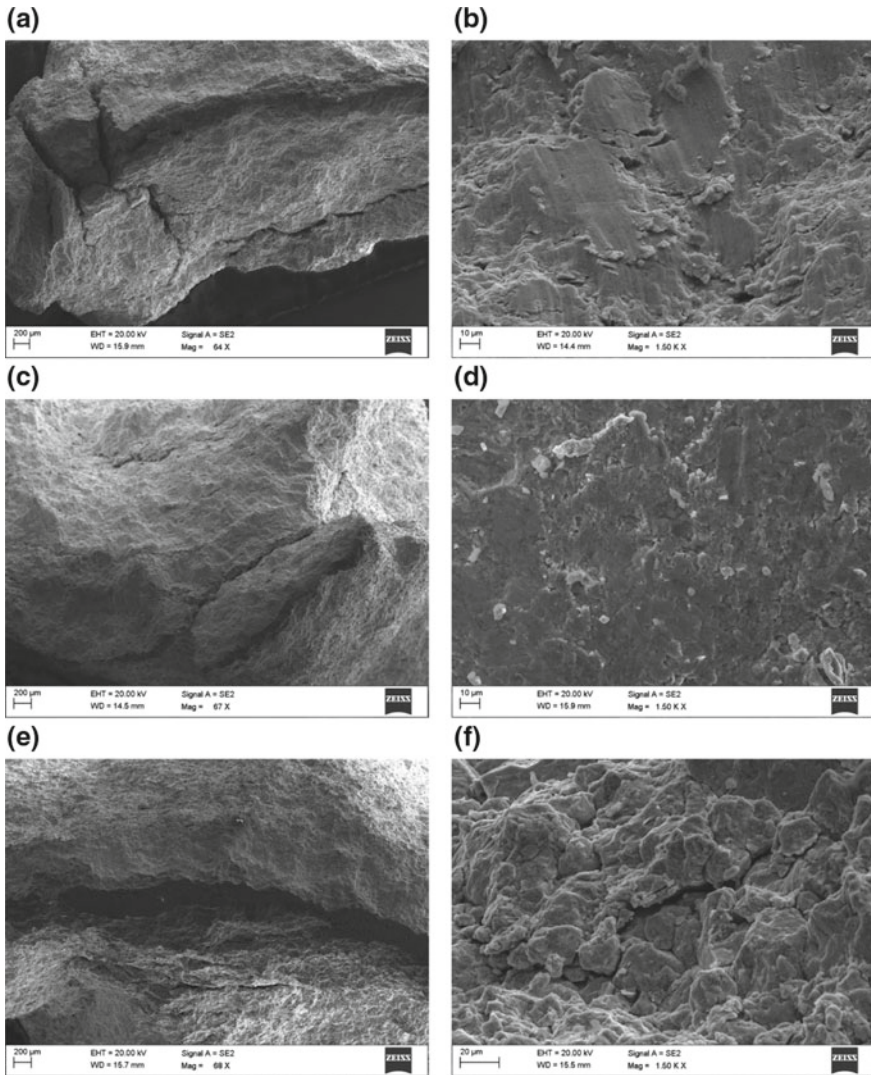


**Fig. 4** Morphology of the fracture section after a compression test of samples of the  $Mg_{60}Zn_{35}Ca_5$  alloy in different magnification: sample No. 1 (a, b), No. 2 (c, d) and No. 3 (e, f)

The SEM fractographs of the fractured surface revealed that cleavage fracture are presented (Fig. 4a–f). The nearly closed sintered sample surface with no pores is observed. The SEM image (Fig. 4a, c, e) shows a large cracks in compression test sample surface. Besides the cracks, generated during compression test, the material is nearly perfectly sintered, showing a suitable choice of sintering parameters.

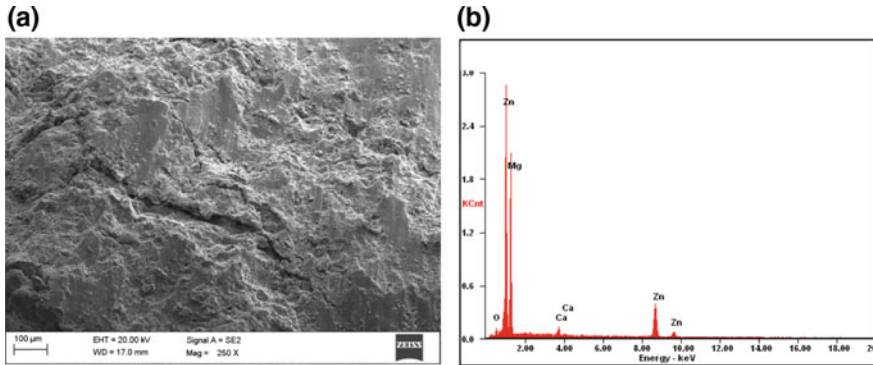


**Fig. 5** SEM images of representative sintered sample of the Mg<sub>60</sub>Zn<sub>35</sub>Ca<sub>5</sub> alloy (250× magnification) (a) and corresponding elemental composition observed by energy dispersive X-ray (EDS) analysis (b)

The elemental composition of sintered samples, determined by microanalysis using energy dispersive X-ray spectroscopy (Fig. 5) indicates the presence of Mg, Zn, Ca and O. The presence of oxygen was also reported by other researchers [43]. In this case oxygen may be introduced during preparation of samples to SEM study.

## 4 Conclusions

Based on the results of the investigations aiming at the determination of the structure, density and compressive strength of the Mg<sub>60</sub>Zn<sub>35</sub>Ca<sub>5</sub> alloy, obtained by MA and SPS methods, it can be concluded that:

- The Mg<sub>60</sub>Zn<sub>35</sub>Ca<sub>5</sub> has been successfully synthesized by MA and SPS methods. High energy MA and SPS methods eliminate the potential environmental risks of Mg-based alloys production via liquid metallurgy route with high production volumes of powder viable for mass production of parts for biomedical applications.
- On the basis of the XRD it is concluded that the structure of samples after 13 h of high energy MA process is amorphous. The Mg<sub>60</sub>Zn<sub>35</sub>Ca<sub>5</sub> alloy after the SPS process has a crystalline structure, consisting of a hexagonal Mg phase and MgZn<sub>2</sub>, Mg<sub>2</sub>Zn<sub>3</sub>, Mg<sub>7</sub>Zn<sub>3</sub>, MgZn, Ca<sub>2</sub>Mg<sub>5</sub>Zn<sub>13</sub> phases.
- The average density between the samples was not significantly different. The density of the sintered samples (~3.33 g/cm<sup>3</sup>) is similar to that of a human bone.
- The mechanical properties that can be achieved using SPS of the Mg<sub>60</sub>Zn<sub>35</sub>Ca<sub>5</sub> alloy are very promising. The compressive strength (~300 MPa) of the samples with the lower porosity (4%) is higher than the compressive strength (264 MPa) of the samples with the higher porosity (11%). Therefore, the improvement of compressive strength is determined by porosity.



- Fracture morphology of the  $Mg_{60}Zn_{35}Ca_5$  alloy is characteristic for brittle crystalline materials.
- Future works will be focused on investigating corrosion resistance of the  $Mg_{60}Zn_{35}Ca_5$  alloy.

**Acknowledgements** This work was financially supported with statutory funds of Faculty of Mechanical Engineering of Silesian University of Technology in 2018.

## References

1. Persaud-Sharma, D., McGoron, A.: Biodegradable magnesium alloys: a review of material development and applications. *J. Biomim. Biomater. Tissue Eng.* **12**, 25–39 (2012)
2. Plaass, C., Falck, C., Ettinger, S., Sonnow, L., Calderone, F., Weizbauer, A., Reifenrath, J., Claassen, L., Waizy, H., Daniilidis, K., Stukenborg-Colsman, C., Windhagen, H.: Bioabsorbable magnesium versus standard titanium compression screws for fixation of distal metatarsal osteotomies—3 year results of a randomized clinical trial. *J. Orthop. Sci.* **23**(2), 321–327 (2018)
3. Babilas, R., Bajorek, A., Simka, W., Babilas, D.: Study on corrosion behavior of Mg-based bulk metallic glasses in NaCl solution. *Electrochim. Acta* **209**, 632–642 (2016)
4. Staiger, M.P., Pietak, A.M., Huadmai, J., Dias, G.: Magnesium and its alloys as orthopedic biomaterials. *Biomaterials* **27**, 1728–1734 (2006)
5. Zheng, Y.F., Gu, X.N., Witte, F.: Biodegradable metals. *Mater. Sci. Eng. Rep.* **77**, 1–34 (2014)
6. Zheng, Y.F., Gu, X.N., Xi, Y.L., Chai, D.L.: In vitro degradation and cytotoxicity of Mg/Ca composites produced by powder metallurgy. *Acta Biomater.* **6**, 1783–1791 (2010)
7. Nowosielski, R., Cesarz-Andraczke, K., Sakiewicz, P., Maciej, A., Jakóbiak-Kolon, A., Babilas, R.: Corrosion of biocompatible  $Mg_{66+x}Zn_{30-x}Ca_4$  ( $x=0.2$ ) bulk metallic glasses. *Arch. Metall. Mater.* **61**(2), 807–810 (2016)
8. Brar, H.S., Platt, M.O., Sarntinoranont, M., Martin, P.I., Manuel, M.V.: Magnesium as a biodegradable and bioabsorbable material for medical implants. *JOM* **61**(9), 31–34 (2009)
9. Gu, X.N., Zheng, Y.F.: A review on magnesium alloys as biodegradable materials. *Front. Mater. Sci. China* **4**(2), 111–115 (2010)
10. Hartwig, A.: Role of magnesium in genomic stability. *Mutat. Res.* **475**, 113–121 (2001)
11. Saris, N.E., Mervaala, E., Karppanen, H., Khawaja, J.A., Lewenstam, A.: Magnesium: an update on physiological, clinical and analytical aspects. *Clin. Chim. Acta* **294**(1–2), 1–26 (2000)
12. Lavernia, E.J., Gomez, E., Grant, N.J.: The structures and properties of Mg–Al–Zr and Mg–Zn–Zr alloys produced by liquid dynamic compaction. *Mater. Sci. Eng.* **95**, 225–236 (1987)
13. Luo, A., Pekguleryuz, M.O.: Cast magnesium alloys for elevated temperature applications. *J. Mater. Sci.* **29**, 5259–5271 (1994)
14. Witte, F., Hort, N., Vogt, C., Cohen, S., Kainer, K.U., Willumeit, R., Feyerabend, F.: Degradable biomaterials based on magnesium corrosion. *Curr. Opin. Solid State Mater. Sci.* **12**(5–6), 63–72 (2008)
15. Zhang, S., Li, J., Song, Y., Zhao, C., Zhang, X., Xie, C., Bian, Y.: In vitro degradation, hemolysis and MC3T3-E1 cell adhesion of biodegradable Mg–Zn alloy. *Mater. Sci. Eng. C* **29**(6), 1907–1912 (2009)
16. Zhang, S., Zhang, X., Zhao, C., Li, J., Song, Y., Xie, C., Bian, Y.: Research on an Mg–Zn alloy as a degradable biomaterial. *Acta Biomater.* **6**(2), 626–640 (2010)
17. Wang, Y.B., Xie, X.H., Li, H.F., Wang, X.L., Zhao, M.Z., Zhang, E.W., Qin, L.: Biodegradable CaMgZn bulk metallic glass for potential skeletal application. *Acta Biomater.* **7**(8), 3196–3208 (2011)

18. Gonzalez, S., Pellicer, E., Fornell, J., Blanquer, A., Barrios, L., Ibanez, E., Sort, J.: Improved mechanical performance and delayed corrosion phenomena in biodegradable Mg–Zn–Ca alloys through Pd-alloying. *J. Mech. Behav. Biomed. Mater.* **6**, 53–62 (2012)
19. Hänzi, A.C., Dalla Torre, F.H., Sologubenko, A.S., Gunde, P., Schmid-Fetzer, R., Kuehlein, M., Löffler, J.F., Uggowitzer, P.J.: Design strategy for microalloyed ultra-ductile magnesium alloys. *Philos. Mag. Lett.* **89**, 377–390 (2009)
20. Inoue, A.: Stabilization of metallic supercooled liquid and bulk amorphous alloys. *Acta Mater.* **48**, 279–306 (2000)
21. Fousova, M., Capek, J., Vojtech, D.: Magnesium-Zinc alloy prepared by mechanical alloying and spark plasma sintering. In: *Metal Conference, Brno, Czech Republic, 21–23 May 2014*
22. Suryanarayana, C.: Mechanical alloying and milling. *Prog. Mater. Sci.* **46**, 1–184 (2001)
23. Zhao, Y.Y., Ma, E., Xu, J.: Reliability of compressive fracture strength of Mg–Zn–Ca bulk metallic glasses: flaw sensitivity and Weibull statistics. *Scr. Mater.* **58**, 496–499 (2008)
24. Calka, A., Radlinski, A.P.: Amorphization of MgZn alloys by mechanical alloying. *Mater. Sci. Eng. A* **118**, 131–135 (1989)
25. Rousselot, S., Bichat, M.P., Guay, D., Roue, L.: Structure and electrochemical behaviour of metastable Mg<sub>50</sub>Ti<sub>50</sub> alloy prepared by ball milling. *J. Power Sources* **175**, 621–624 (2008)
26. Lee, P.Y., Kao, M.C., Lin, C.K., Huang, J.C.: Mg–Y–Cu bulk metallic glass prepared by mechanical alloying and vacuum hot-pressing. *Intermetallics* **14**, 994–999 (2006)
27. El-Rahman, S.S.: Neuropathology of aluminum toxicity in rats (glutamate and GABA impairment). *Pharmacol. Res.* **47**(3), 189–194 (2003)
28. Bell, S., Davis, B., Javaid, A., Essadiqi, E.: Final report on effect of impurities in magnesium. Technical Report No. 2005–29(CF) (2006). <https://doi.org/10.13140/rg.2.2.35126.50248>
29. Südholza, A.D., Kirkland, N.T., Buchheit, R.G., Birbilis, N.: Electrochemical properties of intermetallic phases and common impurity elements in magnesium alloys. *Electrochem. Solid-State Lett.* **14**(2), C5–C7 (2011)
30. Nygren, M., Shen, Z.: On the preparation of bio, nano and structural ceramics and composites by spark plasma sintering. *Solid State Sci.* **5**, 125–131 (2003)
31. Tokita, M.: Trends in advanced SPS spark plasma sintering systems and technology. *J. Soc. Powder Technol. Jpn.* **30**, 790–804 (1993)
32. Groza, J.R., Zavaliangos, A.: Sintering activation by external electrical field. *Mater. Sci. Eng. A* **287**, 171–177 (2000)
33. Lesz, S., Kremzer, M., Gołombek, K., Nowosielski, R.: Influence of milling time on amorphization of Mg–Zn–Ca powders synthesized by mechanical alloying technique. *Arch. Metall. Mater.* **63**(2), 839–845 (2018)
34. Hanawalt, J.D., Rinn, H.W.: Identification of crystalline materials: classification and use of X-ray diffraction patterns. *Powder Diffr.* **1**, 2–6 (1986)
35. Hanawalt, J.D.: Manual search/match methods for powder diffraction in 1986. *Powder Diffr.* **1**, 7–13 (1986)
36. PN-H-04320: Static test of metal compression (1957)
37. Dewidar, M.: Influence of processing parameters and sintering atmosphere on the mechanical properties and microstructure of porous 316L stainless steel for possible hard-tissue applications. *Int. J. Mech. Mechatron. Eng. IJMME-IJENS* **12**(1), 10–24 (2012)
38. Zhang, Y., Zhang, M.: Three-dimensional macroporous calcium phosphate bioceramics with nested chitosan sponges for load-bearing bone implants. *J. Biomed. Mater. Res.* **61**(1), 1–8 (2002)
39. Zberg, B., Uggowitzer, P.J., Löffler, J.F.: MgZnCa glasses without clinically observable hydrogen evolution for biodegradable implants. *Nat. Mater.* **8**, 887–891 (2009)
40. Nowosielski, R., Babilas, R., Cesarz-Andreczke, K., Gawlas-Mucha, A., Lesz, S., Sakiewicz, P.: *Resorbable Materials for Medical Implants*. Silesian University of Technology Press, Gliwice (2017). (in Polish)
41. Lesz, S., Kraczla, J., Nowosielski, R.: Structure and compression strength characteristics of the sintered Mg–Zn–Ca–Gd alloy for medical applications. *Arch. Civ. Mech. Eng.* **18**(4), 1288–1299 (2018)

42. DeGarmo, P.E.: *Materials and Processes in Manufacturing*, 5th edn. Collin Macmillan, New York (1979)
43. Sunil, B.R., Ganapathy, C., Kumar, T.S., Chakkingal, U.: Processing and mechanical behavior of lamellar structured degradable magnesium-hydroxyapatite implants. *J. Mech. Behav. Biomed. Mater.* **40**, 178–189 (2014)

# The Effect of Ceramic Application in Design of Ceramic-Based Plasters



M. Čáchová, L. Scheinherrová, M. Doleželová and M. Keppert

**Abstract** The main aim of this article is to find a progressive composition of plaster mixture consisting of lime hydrate, siliceous aggregates and a waste material admixture. Recycled finely ground brick powder appears to be a suitable material for lime or cement plasters. It exhibits good pozzolanic characteristics and actively participates in creation of bonds within the material structure. The brick dust primarily comes from the production of thermal insulating brick blocks. Therefore, recycling of this waste leads to improvement of ecological and economic aspects. In our previous studies, the effect of ceramic waste on properties of ceramic-based plasters has been studied and it was found out that the most promising solution is to partially replace fine aggregates and lime hydrate by ceramic powder as it can participate in pozzolanic reactions and it also plays a role of a filler. Ceramic powder significantly improved all studied material parameters presented in this article. Therefore, this article is an extension of previous studies and brings new insights to the topic, for example time horizon of the study. The first part of this article is focused on the analysis of the pozzolanic reaction. The effectivity of the ceramic waste on pozzolanic reactions was studied on pastes prepared only from lime hydrate with different amounts of ceramic powder replacement (from 10 to 70 mass% of ceramic waste). The pastes were stored in a climatic chamber under constant temperature and humidity conditions. The pozzolanic reactions were studied after 28 and 360 days of hydration using selected experimental measurements, namely characteristics of the pore system, mechanical properties and thermal analysis (DSC/TG). Based on the obtained results, the best paste was selected for the design of the plaster mixture

---

M. Čáchová (✉) · L. Scheinherrová · M. Doleželová · M. Keppert  
Czech Technical University in Prague, Thákurova 7, Prague 166 29, Czech Republic  
e-mail: [monika.cachova@fsv.cvut.cz](mailto:monika.cachova@fsv.cvut.cz)

L. Scheinherrová  
e-mail: [lenka.scheinherrova@fsv.cvut.cz](mailto:lenka.scheinherrova@fsv.cvut.cz)

M. Doleželová  
e-mail: [magdalena.dolezelova@fsv.cvut.cz](mailto:magdalena.dolezelova@fsv.cvut.cz)

M. Keppert  
e-mail: [martin.keppert@fsv.cvut.cz](mailto:martin.keppert@fsv.cvut.cz)

enriched by siliceous sand. The same properties of the newly designed plaster were studied to confirm the effectivity of this mixture.

**Keywords** Pozzolana · Ceramic waste · Pore system · Mechanical properties  
DSC/TG

## 1 Introduction

Nowadays days, there is a wide variety of plasters, which are used either for external or internal walls. The binder material can be clay, gypsum, gypsum-lime, magnesium, quicklime, hydraulic lime, lime-pozzolana, lime-cement or cement. Cement, which started to be utilized in plasters in 1920s, gives the material higher hardness and strength, on the other hand the diffusion properties are worsened, which is, besides its less original appearance the reason why they are not recommended for use on historical buildings. Lime plasters are commonly the most popular form of surface finishing. They have good diffusion properties, but they are less resistant to weathering and other external harmful influences. We are able to see progressive redirection from classic building techniques and therefore alternative financial and ecological advantageous solutions are looked for [1, 2].

Pozzolanic materials have been used as a part of binder since ancient times. Their presence in a mixture is beneficial in many ways, which was known already in the era of Roman Empire. The Romans used natural pozzolanas such as volcanic ash, tuff, spongolite or burnt clays. Nowadays, many natural pozzolanic materials and even pozzolanas of technogenic origin are frequently utilized. Investigation attempts are mainly focused on ternary systems; which means binder consists of three different components. The paper deals with possibility of recycling ceramic dust as a component in lime plasters. Many studies proved suitability of finely crushed bricks for plaster mixtures. Finely crushed brick dust contains pozzolanic-active particles, which help with formation of better binding bonds. Waste material from brickyards could become common part of plasters. The problematic issue is an appropriate ratio to reach the desired properties of a certain plaster, which request a well elaborated design [1, 3].

As a first step, it is very important for research to understand the emerging links and chemical reactions between the basic materials. The combination of lime hydrate and pozzolanic material has also been confirmed from a historical perspective [3]. Therefore, it is important to determine the degree of the pozzolan activity at the beginning of the research. Any material with a pozzolanic presumption may not be suitable for usage in a final plaster mix. This is due to the lack of the pozzolanic reactivity between input basic materials. This knowledge is also the conclusion of the article from Matias et al. [4]. In the article mentioned before, authors studied many pozzolanic materials in combination with lime hydrate. The values of the mechanical properties of the selected materials with good pozzolanic characteristics have been increased; this is the fundamental trend and conclusion of this research, too.

There are many methods that determine the pozzolanic activity of the substances. It is divided into direct and indirect methods. Navrátilová and Rovnaníková tried combinations of the tests (direct and indirect methods) [5]. They studied mainly pozzolan activity and assessed the strength characteristics on these samples. The strength properties were comparable as in the case of indirect methods.

Hydration reactions and carbonation of the hydraulic lime can be studied in detail. These properties are also important for a future plaster development. Currently, it is also very important to use the modern methods to determine the pozzolan activity, for example by thermal analysis. Cizer and colleagues [6] have used this method in the lime-pozzolan system. They performed thermal analysis (DTG—diffraction scanning analysis) for their research. Moropoulou et al. [7] studied the determination of the pozzolan activity by the thermal analysis of malts made of natural and artificial pozzolan. Diffraction thermal analysis and thermogravimetry (DTA and TG) were used. Their pastes were also studied at the same time (simultaneously). The conclusion stated that determining the pozzolanic activity with DTA/TG may be a good alternative for the future.

In this article, pozzolanic activity was studied by the lime-brick power system with indirect methods. This easier process proves that we can find the effective compensation for the lime, which leads to an improvement of ecological and economic aspects. As indirect methods were employed the mechanical measurement, pore system and thermal analysis.

## 2 Studied Material

An influence of ceramic waste on pozzolanic reactions was studied on pastes prepared only from lime hydrate with different amounts of ceramic powder replacement (Table 1). This effectivity was observed at the results of the pore system and the carbonation and hydration. The used pastes consist of the lime CL 90 S (by company Čertovy schody a. s., Tmaň, Czech Republic), brick dust (by company Heluz cihlářský průmysl, v. o. s., Hevlín, Czech Republic) and water. The pastes were labeled by the marks MP10 up to MP90. The digits in the names represented the percentage of the brick dust in the mixtures. The reference paste was labeled as MPR (only pure lime). The Table 1 shows amount of water, which was needed to ensure the constant flow by flow table—140/140 mm (ČSN EN 1015-3) [8]. Some plasters were selected with respect to the mechanical properties. The pastes mentioned in the bracket were studied in detail (MPR, MP10, MP50 and MP70).

**Table 1** Materials composition of studied pastes

Material	Lime (%)	Brick powder (%)	Water/Dry material
<b>MPR</b>	100	0	1.23
<b>MP10</b>	90	10	0.95
MP20	80	20	0.73
MP30	70	30	0.67
MP40	60	40	0.66
<b>MP50</b>	50	50	0.63
MP60	40	60	0.53
<b>MP70</b>	30	70	0.50
MP80	20	80	0.44
MP90	10	90	0.42

### 3 Experimental Measurements and Results

#### 3.1 Mechanical Properties

The first step in the design of the mixture was the production of samples (dimensions  $40 \times 40 \times 160$  mm) submitted to tests of the mechanical properties. Compressive and bending strengths were measured according to standard methods using loading devices EU 40 and MTS 100 [9]. The first experiment was measured on all ten samples (Table 1) at 28 days (Table 2). The paste MP10 with the lowest percentage of the brick powder expressed the lowest value of the strength. The pastes showed an increasing trend with the increasing content of used pozzolana. However, sample with the 70% compensation (MP70) decreased in the strength characteristics. This decrease was caused because the pozzolanic reaction was no longer effective. In the mixture, there was excess amount of the pozzolan and little calcium hydroxide. The pastes MPR, MP10, MP50 and MP70 were studied in more detail. Purposes for detailed study were following: MPR was the reference sample, MP10 contained the minimum ceramic powder, MP70 as the sample with the highest strength and MP50 as the sample of “mean mix”.

The following experiments were carried out in varying times (up to 1 year) to allow longer evolution of the compressive strength due to the presence of pozzolana and its prolonged pozzolanic reaction. The results of the compressive strength are presented in Fig. 1. Stefanidou and Papayianni [10] have investigated pastes and pozzolanas plasters and their study confirmed the increasing strength after the addition of the pozzolanic active ingredients.

**Table 2** The mechanical properties of the studied pastes (28 days)

Material	Bending strength (MPa)	Compressive strength (MPa)
<b>MPR</b>	0.40	1.25
<b>MP10</b>	0.39	1.20
MP20	0.52	1.23
MP30	0.59	1.72
MP40	0.80	3.55
<b>MP50</b>	0.81	3.71
MP60	0.82	5.83
<b>MP70</b>	1.21	9.61
MP80	0.78	8.49
MP90	0.77	8.07

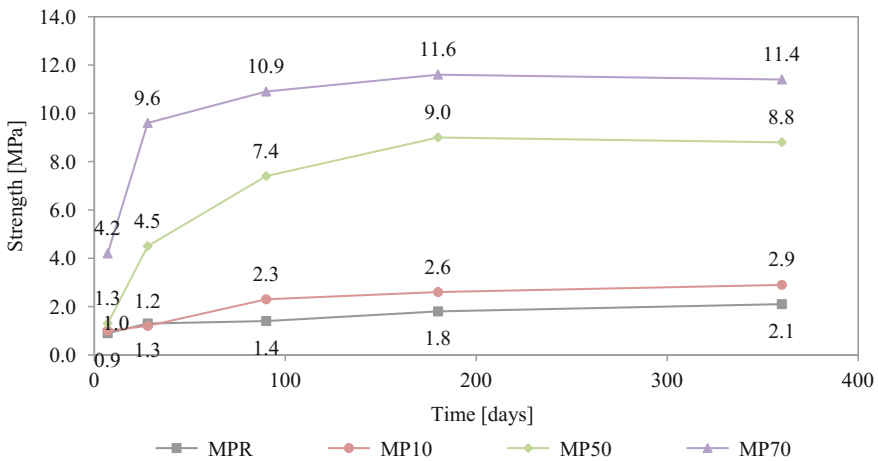


**Fig. 1** The compressive strength of selected pastes over time

### 3.2 Pore System

The most influencing property is indisputably porosity of the studied material. However, more detailed description than just value of porosity is required for better comprehension. The pore structure of studied plasters was determined by using mercury intrusion porosimetry. For this experiment, measurement apparatus PASCAL 140+440 was used. Results are presented in Figs. 2 and 3. In these pictures, the pore system of the special pastes in 28 and 360 days are shown.

The sample MP70 contains more pores with smaller size than pastes MP50, MP10 and reference MPR. In the Fig. 3, we can see that the paste MP10 contains the highest pore size of about 0.3 μm, sample MP50 about 0.45 μm and material MP70 about 0.65 μm. It is an apparent trend—with the increasing amount of the



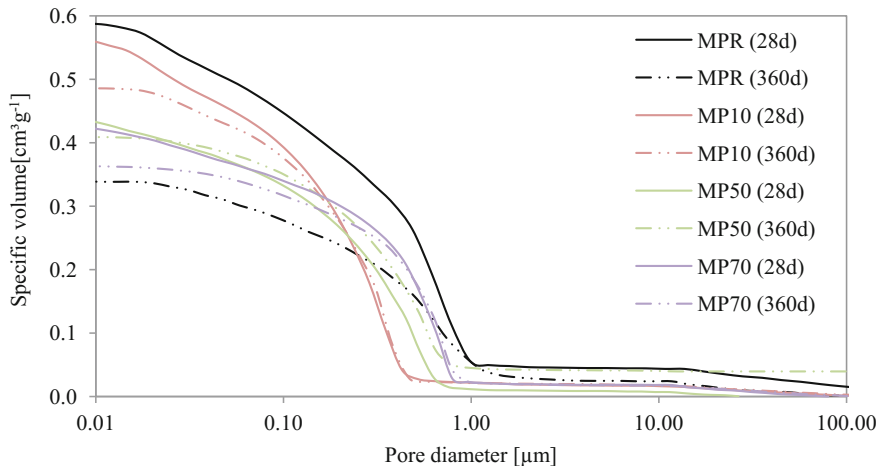


**Fig. 2** Cumulative curves of the studied pastes

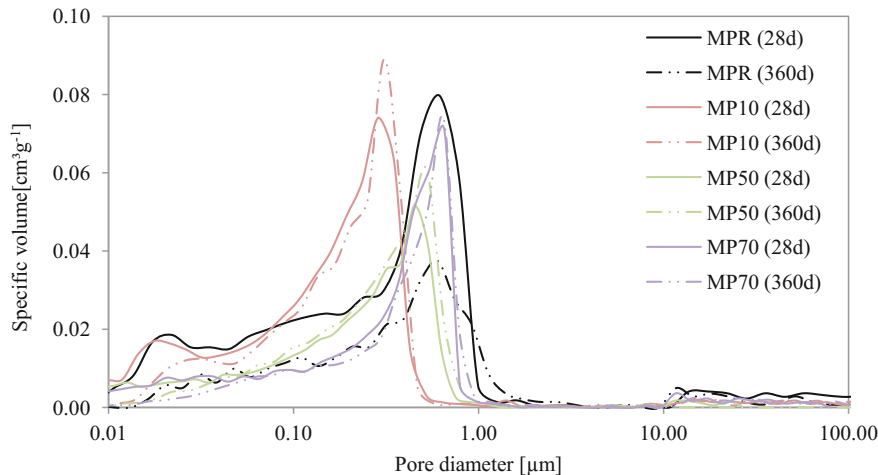


**Fig. 3** Distribution curves of the studied pastes

brick powder in paste the volume with the bigger pores increases. The special paste MP10 after 360 days showed only a slight increase in the peak (represent the pore size). The paste MP50 after 360 days increased the pore size to 0.55 μm. We have observed slight decrease in pore volume at sample MP70.

Similar results were obtained by Nežerka et al. The authors studied very similar brick dust pastes but only after 28 days [11]. This fact affects studied characteristics which were confirmed by Mary [12]. Arandigoyen and Sharman proved that pore sizes depend on the amount of water [13]; which was also taken into account in the proposed mixtures.

### 3.3 Thermal Analysis (DSC/TG)

This issue was verified by using a differential scanning calorimetry (DSC) coupled with thermogravimetry (TG). Both analyses were performed simultaneously using a Labsys Evo (Setaram, France) instrument. Before analyses, all studied materials were dried. All measurements were executed in the temperature range from 25 to 1000 °C with a heating rate of 5 °C/min in an argon atmosphere (40 mL/min) [14, 15].

The DSC/TG results of the lime-pozzolana paste over the time are summarized in Figs. 4 and 5. The endothermic reaction and dehydration of portlandite (calcium hydroxide) was observed at the temperature approximately 450 °C by all samples (Fig. 4). The associated mass loss, calcium oxide and water emerge were detected. The second observed reaction refers to the decomposition of the calcite (CaCO<sub>3</sub>). This reaction arose at the temperature about 750 °C. This effect was accompanied by a change in mass and heat flows, the difference was lower. The DTG curve as of 820 °C temperature by the samples MP50 and MP70 are increased—It is exothermic process in which the crystallization arises. Differences in the heatflow values between time dependencies are increasing. Moropoulou have provided a very similar study [7].

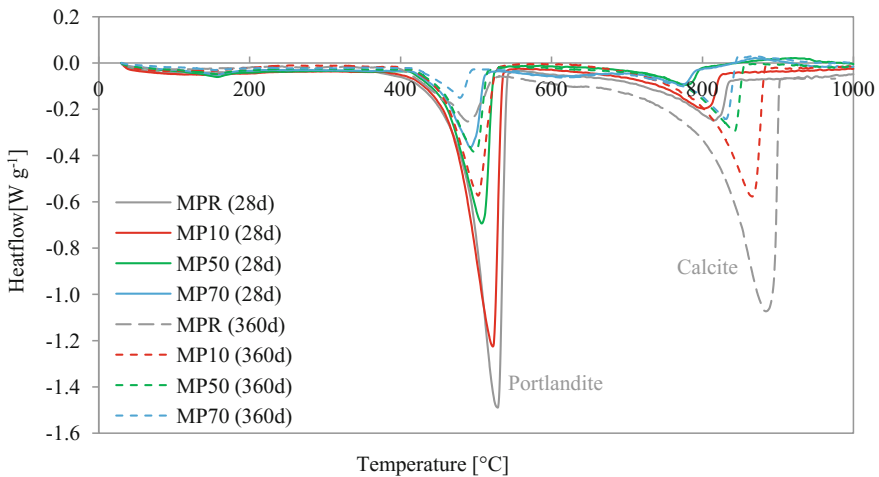


**Fig. 4** Heatflow of the studied pastes

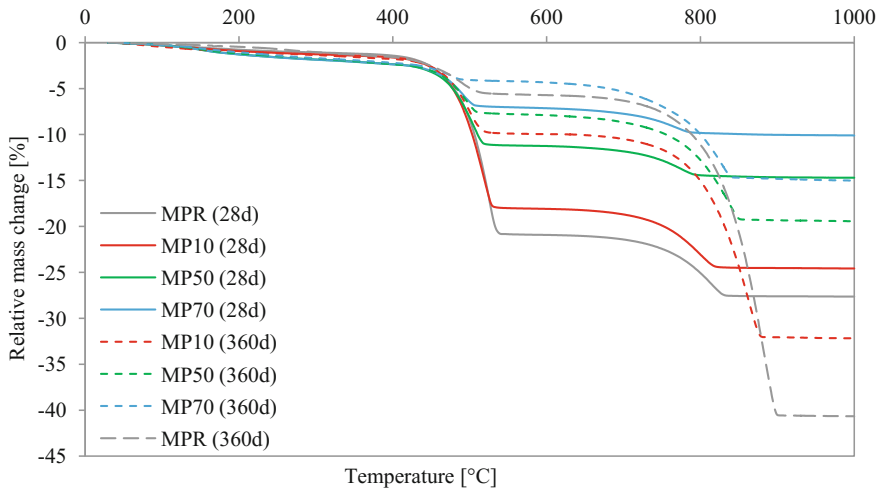


Fig. 5 Relative mass change of the studied pastes

## 4 Conclusion

The studied pastes were researched for better understanding of the lime-pozzolana system and for effective compensation of the lime in the future plaster mixtures. Particularly, the lime hydrate of the designed materials was replaced by 10, 50 and 70% brick powder. The following list show the results measured on the studied lime-pozzolanic pastes within the experimental program mentioned before.

- When we have studied the characterization of the pore system, there was a difference between MP10 and other pastes containing brick powder. Material MP10 showed significantly more pores with the smaller size than the other studied pastes, which had the higher percentage of the brick dust. A clear trend that increasing amount of the pozzolanic admixture in the pastes increased the volume of the larger pores can be seen from the distribution and cumulative pore curves. These trends were evident at all time ranges (28 and 360 days). Only gel pores have been found in this studied material (MP10).
- The MPR reference paste achieved the lowest values of the strength characteristics during the 28-day tests. The pastes presented an increasing trend coupled with an increasing amount of the brick powder (up to 70% of the replacement MP70). A significant decrease in the strength characteristics was observed. This decrease occurred due to presence of excess amount of pozzolan and a little amount of lime hydrate. The reaction loss efficiency and therefore pozzolana have served more as filler than binder. It has been shown, in more detailed study of the compressive strengths values with respect to the time, that the increasing volume of powder brick in the pastes also increases the strength.

- The largest relative mass change showed by the thermal analysis (DSC) at the reference material MPR and at the material with the smallest content of the brick dust MP10. These mass decreases have been rising and showed the highest values in the last range (360 days). This trend was observed in all studied pastes. The weight-loss was also increasing. The trend of significant changes in the heatflow of the material MP10 was evident, while the other studied paste MP70 with the highest percentage of pozzolan showed the smallest changes. This phenomenon can be seen in the graphs of heatflow (Figs. 4 and 5). The pastes MP50 and MP70, 28 days old, showed an exothermic process at the temperature 820 °C—crystalization. For the pastes with the lowest amount of pozzolan MP10 and reference material MPR, no similar reaction was recorded. The reaction at 800 °C gradually began to change to an endothermic process. After 360 days, these peaks had the same size as the sample MP10.

The influence of brick powder in lime hydrate can be observed from the measured and presented results of the lime-pozzolanic paste. By the mechanical tests it has also been confirmed that the lime-pozzolanic paste is able to effectively replacing the lime hydrate. It has been found, at the porous system, that pastes contain only gel pores and that the content and size of pores is changing over time. Thermal analysis has shown influence of the time and brick dust amount on the reactions occurring in this system.

**Acknowledgements** This research has been supported in the Czech Republic under project SGS16/199/OHK1/3T/11.

## References

1. Rovnaníková, P.: Omítky. Chemické a Technologické vlastnosti. STOP, Praha (2002)
2. Kočí, J., Maděra, J., Rovnaníková, P., Černý, R.: Hygrothermal performance of innovative renovation renders used for different types of historical masonry. *WIT Trans. Built Environ.* **118**, 683–693 (2011)
3. Walker, R., Pavía, S.: Physical properties and reactivity of pozzolans, and their influence on the properties of lime-pozzolan pastes. *Mater. Struct.* **44**, 1139–1150 (2011)
4. Matias, G., Faria, P., Torres, I.: Lime mortars with ceramic wastes: characterization of components and their influence on the mechanical behaviour. *Constr. Build. Mater.* **73**, 523–534 (2014)
5. Navrátilová, E., Rovnaníková, P.: Reactivity of brick powder in lime mortars. *Adv. Mater. Res.* **897**, 103210 (2013)
6. Cizer, Ö., Van Balen, K., Van Gemert, D.: Competition between hydration and carbonation in hydraulic lime and lime-pozzolana mortars. *Adv. Mater. Res.* **133–134**, 241–246 (2010)
7. Moropoulou, A., Bakolas, A., Aggelakopoulou, E.: Evaluation of pozzolanic activity of natural and artificial pozzolans by thermal analysis. *Thermochim. Acta* **420**, 135–140 (2004)
8. ČSN EN 1015-3: Methods of test for mortar for masonry—Part 3: Determination of consistence of fresh mortar (by flow table) (1999)
9. ČSN EN 1015-11: Methods of test for mortar for masonry—Part 11: Determination of flexural and compressive strength of hardened mortar (2000)
10. Stefanidou, M., Papayianni, I.: The role of aggregates on the structure and properties of lime mortars. *Cem. Concr. Compos.* **27**, 914–919 (2005)

11. Nežerka, V., Slížková, Z., Tesárek, P., Plachý, T., Frankeová, D., Petráňová, V.: Comprehensive study on mechanical properties of lime-based pastes with additions of metakaolin and brick dust. *Cem. Concr. Res.* **64**, 17–29 (2014)
12. Maria, S.: Methods for porosity measurement in lime-based mortars, construction and building materials. *Constr. Build. Mater.* **24**, 2572–2578 (2010)
13. Panday, S.P., Sharma, R.L.: Influence of mineral additives on the strength and porosity of OPC mortar. *Cem. Concr. Res.* **30**, 19–23 (2000)
14. Kloužková, A., Zemanová, P., Kloužek, J., Pabst, W.: Termická analýza. <http://tresen.vscht.cz/sil/sites/default/files/Termick%C3%A1%20anal%C3%BDza.pdf> (2012). Accessed 23 Mar 2016
15. Štarha, P., Trávníček, Z.: Termická analýza. Univerzita Palackého v Olomouci, Přírodovědecká fakulta, Katedra anorganické chemie. [http://agch.upol.cz/userfiles/file/pdf/Termicka\\_analyza.pdf](http://agch.upol.cz/userfiles/file/pdf/Termicka_analyza.pdf) (2011). Accessed 18 July 2018

# Visual Analysis of Ceramic Combinations with Educational Purposes for the Development of Artisan Products



H. D. Castaño and V. Suárez

**Abstract** Colombia is a country that frames a great cultural tradition with artisanal developments throughout all its regions, which allows a different approach to the use and practice of different materials when it comes to creation processes. One of the most common materials, or that can be found easily in the vast majority of regions is ceramics. And ceramics is a great world yet to be explored in terms of processes, developments and even transformation of raw materials. The main objective of this research is to analyze and evaluate the final results of the behavior of different types of clays such as red, black and gray when combined with pigments from the coloring processes, such as patinas, enamels and engobes. In this way the pedagogical process will consist of the manufacture of a series of test tubes validated in a controlled cooking process and including different percentages of pigments in combinations defined with each of the clays; In this way, a visual catalog of ceramic finishes will be obtained through which the different desired results can be observed in a methodical way when carrying out serial crafts processes by the students; result that will be a considerable input to implement practical classes, talks or workshops, to minimize expenses or losses of both products and material and additional is intended to encourage manufacturing processes of handicrafts in Colombia.

**Keywords** Ceramics · Teaching · New materials · Design

## 1 Introduction

Colombia is a country with a great and diverse variety not only of territories, fauna and flora, but also has the great wealth of possessing in its lands an enormous variety

---

H. D. Castaño (✉) · V. Suárez  
Arts and Humanities Faculty, Design Department, Instituto Tecnológico Metropolitano, ITM,  
Street 73 No. 76A - 354, Volador's Way, Medellín, Colombia  
e-mail: [hernan9611@hotmail.com](mailto:hernan9611@hotmail.com)

V. Suárez  
e-mail: [viviansuarez1a@gmail.com](mailto:viviansuarez1a@gmail.com)

© Springer Nature Switzerland AG 2019  
L. F. M. da Silva (ed.), *Materials Design and Applications II*, Advanced  
Structured Materials 98, [https://doi.org/10.1007/978-3-030-02257-0\\_9](https://doi.org/10.1007/978-3-030-02257-0_9)

of resources through which throughout its history it has been able implement them for the satisfaction of the main demands both internal and external in terms of the solution of basic needs, creation of elements, production and even export.

Faced with the great wealth and variety of raw materials existing in Colombia, there is one that has undoubtedly been applied in a great way throughout the history of national development, and is no other than ceramics [1]; not only as a source of creation of artisanal objects, but also at an industrial level, allowing the appearance of large and well-known companies that have managed to position themselves in Colombia and the world for their important and valuable developments to improve the quality of life of communities and promote the economic and social development of the same; among them stand out: ColCerámica S.A. (Corona Group), Ceramics Italy (10% of the flats market in the country), Alfagrés S.A. (national) and Euroceramica (national) [2]; all these companies being fundamental scenarios to inject income into the country's economy [3].

The Industrial Design has managed to consolidate throughout history as one of the fields of knowledge in which you can execute and develop various projects, products and experiences through which you can solve the existing needs in society [4]. A desire, a requirement or a need are the starting points from which the designer in an interdisciplinary field of work manages to think, plan and execute tangible or intangible solutions to that initial approach. And it is the Industrial Design responsible for creating new spaces, not only for the generation of objects, but to allow the improvement of processes or their optimization [5].

Understanding clearly a general context in which there should be a link between the elements presented previously: the economic and productive development of Colombia, the use of existing resources in the national territory and the applications and knowledge that Industrial Design allows for the generation of new products, processes and experiences [6]; The main objective of this research is to expose in a practical way the findings arising from the different stages necessary for the production of a ceramic product in an artisanal way [7]; with which seeks to generate processes of standardization of techniques that both in the field of education and manufacturing, will be very useful for teachers, students, craftsmen and entrepreneurs of products and ceramic pieces [8]; thus obtaining a catalog of samples in which there are evidenced finishes and different techniques that will later be replicated in specific products.

## 2 Development

The visual analysis for ceramic artisan products that was executed for educational purposes; was based on a practical and experimental development in which through interaction, observation and the result of tests (including hardness, pigment application and cooking) [9], different factors are evident that will be crucial at the time of production in series and the teaching of the different stages and techniques that are found in the framework of the manufacture of any kind of ceramic products.

In this way it is important to highlight that the whole process was within the framework of a proposed methodological development to understand and visibilize more clearly the different scenarios and moments that allow giving direct results to the initial approach, which responds to understand how to from the analysis of the formal aesthetic structure, it is possible to standardize development activities in the manufacture and subsequent surface finishes of a piece; understanding crucial stages such as molding, pigmentation technique and even cooking control [10].

The process by which the data and the partial results of the research were obtained, was based on a new work methodology, created especially for this project, in which steps or existing elements were taken from other research and creation methodologies (as the proyectual and HCD methodology) [5, 6], by means of which in real time was put in comparison studies, elements and existing developments, compared to the comparative of the own development of the raw materials and after the manufactured specimens; thus demonstrating the necessary steps to determine results on the execution of the project. In this way, the methodology used was (Fig. 1).

Once the work methodology is proposed, it is important to have the necessary inputs for the execution of the activities, on the one hand the bibliographic material or the theoretical part will have a great weight, since this will be the basis from which it can be split develop the processes; However, in an investigative activity such as this, it is not only based on following exactly what is already written, but also looking for new alternatives to obtain learning that actually nurture the analysis process; and this is how it is decided not only to work with clay and traditional liquid ceramics for the production of pieces such as gray clay, but also to perform tests to know the behavior of red and black clays and ceramic pastes liquids that arise from this raw material.

The beginning of any product or ceramic product development process will be conditioned in the first instance by the use of the base paste [11], which will be the main input to develop all types of products. Each paste will have different physical and chemical properties, which will be reflected in the characteristics of the final product; the viscosity, the thixotropy [12, 13] and even the color or raw materials with which the paste was prepared will be totally fundamental to understand the properties by which the final product will be governed (Fig. 2).

For the analysis process, it was based on the premise of handling three types of liquid ceramic pastes and different clays; the gray clay, the red and the black, and the liquid ceramic paste or “Barbotina” resulting from each of them [14]. In the market it is very common that the gray clay and the Barbotina of the same color is the most common in the manufacture of different ceramic products; however, clays of other colors provide the initial capacity to start with a much more striking color compared to gray, giving them a uniqueness; not only in the final color [11] but also in the whole process by means of which the colored liquid ceramic pastes are obtained which are not commercial in the Colombian ceramics market (Fig. 3).

Due to the delay involved in the manufacturing process of the liquid ceramic pastes, since a process of a change of state from solid to liquid of the clay is necessary (which will take into account the moisture content of the base raw material up to more than a week) [15]; in parallel the process of manufacturing a series of test





Fig. 1 Methodology of work

pieces was started using the three types of clays, in which different characteristics that the pigment will acquire in contact with each of them will be tested and that the technique and the visual properties will generate contrasts that will allow your evaluation.

**Fig. 2** Preparation of liquid ceramic pastes, mix of ceramic powders with clay and water



**Fig. 3** Fabrication of clay pieces in an artisanal way



The pieces of clay must be made one by one, since it is necessary to have a posterior control over the structure in which you work, however, to maintain the same line in the similarity of the forms, a counter mold is used that serves to cut the clay leaving the silhouette marked and the final finishes on each of the test pieces are much simpler to execute [10] (Fig. 4).

For the tests, it was decided to manufacture five specimens of each color, so it will be better to later evaluate the different techniques and pigment quantities applied to



**Fig. 4** Dry clay pieces



**Fig. 5** Burned clay pieces

each of the specimens, and a general condition of how the material should be handled and apply the additives; This is because, if only one or two specimens of each color were used, it would have a much lower degree of veracity in relation to performing more tests.

Once dry, each of the specimens should be prepared to polish the surface and work on the remaining details [16], porosities, cracks, irregularities, among others, reaching a similarity between each of the elements considerable, and any type of defect not interfere with the performance of the following tests. When all the pieces are polished, and handling a great similarity between them, the first burning process is carried out, in which the texture known as “Bizcocho” or raw pieces will be observed (Fig. 5).

As shown in the image on the left, once each piece is burned, they handle a great visual similarity to its dry state [16], however, its chemical composition when subjected to the cooking process for a period of around 5 h with a controlled temperature that reaches 1100 °C, they manage to increase the union of their internal molecules which allows the percentage of stiffness to increase, giving it a more consistent structure and that does not fracture so easily unlike the crude state where it is more prone to a break [17] (Fig. 6).

After having the pieces burned, it is time to apply the different pigments that will allow us to differentiate the finish that each of them generates compared to the



**Fig. 6** Painting process



**Fig. 7** Comparison between pieces with one and two cooking process

basic raw material, enamel (glossy finish), engobe (matt finish) and patina (oxidation effect) [15] are the three types of pigments with which the test specimens will be evaluated. These will be applied with different proportions and styles [7], but all in a brush technique, this is because the primary objective of the research is related to artisanal practices; in this way it will be possible to understand which is the best application for the final result and thus optimize resources obtaining excellent results in relation to the pigments, this speaking in applied quantities and the way in which these will be arranged on the raw pieces.

The following test pieces show the contrast between two painting techniques before and after undergoing an oven burn process; in them it can be evidenced clearly how the application factor of the surface pigment, regardless of the type, changes its texture in relation to the homogenization of the application process [18]. In both images in the top row, the application of the pigments was thick and irregular, leaving a much thicker layer of the three pigments; while in the lower row the thickness of the pigments is much lower, there they are polished and the surface is left more smooth, this using water to dilute the pigments in a few proportions (Fig. 7).



**Fig. 8** Gray and Black Barbotina's pieces in blaster molds

After the second firing, each piece acquires a surface finish much more visually pleasing. The part that remains with the raw material is observed in a lighter shade [18] while the pigmentation of each piece has some different dimensions, however, they are not very pronounced. It should be noted that in all the cooking processes in each of the three basic raw materials, there is a shadow that appears after the pigment is cooked, this shadow is reflected in relation to the color of the base paste, and is only present in the sections where the patinas were used (Fig. 8).

In relation to the pieces of Barbotina, the fundamental difference lies in two essential aspects; On the one hand, the process in which the liquid ceramic is poured into the mold to remove the pieces is almost twice as long as in the process with the gray Barbotina, in addition to obtain a considerable thickness the process can take much more. In contrast to the other differentiating element, it lies in the relation to the pigment, because the red and black slip makes the dark colors of the pigments look more vivid, but the light tones lose their appearance considerably [12].

In this way using both resources, the elaboration of test pieces and the development of pieces using plaster molds, it is possible to reach the end of the experimental process which sought to present finalized elements so that from them it is possible to start the characterization and study of the characteristics that are presented in the design process [17], some findings have been shown previously; However, educational applications will emphasize how the objects and elements acquired will be of great use for the teaching of these processes.

**Fig. 9** Initial catalog

### 3 Educational Applications

Once all the theoretical and practical process of the investigation has been executed, the resulting objects and pieces will function as the fundamental element to implement a catalog with which one can have tangible and visual references to accompany the processes of ceramic development, both in the educational field as the productive one, differentiating the existing needs between the commercial and the academic sector, both with different purposes and results, but based on a similar development process (Fig. 9).

Each of the test pieces made both in the ceramic paste and in clay are very useful to show both the behavior in the drying and cooking process [11], where the pieces of “Bizcocho” are obtained, where the texture and superficial appearance should be highlighted. Both acquire in their first stage of cooking; It will be there the first moment in which it is shown how the pigments can be reflected [18] in a second cooking process, and how the raw texture will be without any surface additive, which is often used for products such as ornamentals, ornamental elements of garden and even busts or ceramic crafts with indigenous and prehispanic styles, which are very common in the Colombian national scope throughout the different departments [19].

The catalog of parts and samples should be well-known and prolonged, because not only the application ratio of the different pigments is important, since to find characteristics such as hardness, fragility among other characteristics of the material will be of great use for subsequent applications [9]. Next, it is shown as facing a rupture test, each of the pieces is fragmented differently, and even the piece of gray clay had to undergo two impacts, because the first one that received did not do anything to him, while each of the other pieces immediately fragments [14] (Fig. 10).

As in the aesthetic component, a great focus must be made, the manufacturing process [18]; This should not be neglected, as this will be responsible for giving



**Fig. 10** Full manufacturing process: plaster molds, Barbotina's pieces, pigmentation process, cooking (left to right)

hundreds of guidelines that will govern the work to be done during the production stage, which, while it may be the most important, will be the one that opens the doors to the final finishes.

The test pieces are not the only necessary inputs in the development of the educational process; the manufactured and painted pieces with the different pigments will also help to give guidelines regarding the production of products that can be serialized with greater ease [14]; giving way to see how a product can be produced in any of the three types of clay or Barbotina, what type of pigment will stand out better and even which process would be the fastest to develop.

However, although the process was largely advanced, and there is a large amount of information captured, it is necessary to continue with the analysis of the research, adding the functional component, thus seeking the form of a globality of how the processes should be improved, facilitating the development of productions in relation to the teaching of it [20].

## 4 Conclusions

All the work developed from the conceptualization of the idea to the elaboration of the test tubes, allows to clearly visualize different results that are easily applicable in the educational processes and serial production; The most notable results are presented below:

- The existing processes within the development of any product regardless of its material, nature, function or appearance should be thought from its conception according to the existing technologies and resources within the area in which they plan to develop; in this way, its design, execution, standardization, production and

distribution will be much more successful understanding from a strategic planning analysis [21, 22].

- The different application techniques of the pigments on the ceramic pieces will have a different finish in relation to the quantity applied, to the thickness of the layer, the consistency of the pigment and even to the viscosity of the initial preparations as well as pigments and ceramic pastes to use.
- The red and black Barbotina intensify the pigments of dark tones in great quantity, in which the application of so much material is not necessary to achieve the desired color, while, in light tones, the applied layer is very thick, not the strength of color is so marked.
- The patinas generate a shade at the time of cooking against any type of raw material base; leaving a yellow color in relation to the gray clay pastes and a shadow between brown and black in the red and black pastes.
- Generating guide elements, tables, catalogs or support material is of vital importance to improve standardization processes and that, both in the educational process and in industrial manufacturing, users of the material and those who use the techniques have a point of departure through which they can be guided throughout the process.
- The ceramic paste chosen for any process or development must be analyzed from both its physical and chemical properties, as these will be responsible for conditioning the final results that the product achieves.
- Each of the stages of the ceramic development process must be well planned from the beginning, as these will be responsible for giving a successful result in the final product that you want to make.
- The creation of a new methodology of work from the blending of Munari's methodology and Human Centered Design is a space of development to a thousand of new projects, not only at the ceramic field, but also in any product development.

## References

1. Jaramillo, Y.M.: *Cerámica y ceramistas de Ráquira*. Arco, Boyacá (1974)
2. ANDI Comité Sector Cerámico: *Comité Sector Cerámico*. ANDI, Bogotá (2017)
3. Hernández Ramírez, V., Domínguez, D., Andrade Vallejo, M.A.: *Las mipymes artesanales como un medio de desarrollo para los grupos rurales en Méxic*, pp. 65–92. Universidad & Empresa, Bogotá, Colombia (2011)
4. Lofthouse, V.: *Ecodesign tools for designers: defining the requirements*. *J. Clean. Prod.* **14**, 1386–1395 (2006)
5. Munari, B.: *¿Cómo Nacen los Objetos?* Fustavo Gili, Barcelona (1983)
6. Van der Bijl-Brouwer, M., Dorst, K.: *Advancing the strategic impact of human-centred design*. *Des. Stud.* **53**, 1–23 (2017)
7. Ramírez, I.B.: *Industria cerámica clásica*. Editorial SENA, Bucaramanga (1991)
8. Rada, P.: *Técnicas de la cerámica*. Libsa, Madrid (1990)
9. Ahmed, M.A., Hamdy, D.A., El-Etreby, D.: *Finishing procedures action on mechanical*. *Fut. Dent. J.* **20** (2018)
10. Pinzón, L.B., Garzón, J.P.: *Industria Cerámica: Moldeo*. Editorial SENA, Bogotá (1993)



11. Ramírez, I.B., PlazasGarzón, J.: Pastas cerámicas. Editorial SENA, Bogotá (1993)
12. Gnanli Landroua, C.B.: A fresh look at dense clay paste: deflocculation and thixotropy mechanisms. *Colloids Surf.* 252–260 (2018)
13. Schoonheydt, R.A.: Reflections on the material science of clay minerals. *Appl. Clay Sci.* 107–112 (2016)
14. Barnes, G.: Workability of clay mixtures. *Appl. Clay Sci.* 107–112 (2018)
15. Calle, C.R.: La Cerámica. Secretaría de Educación y Cultura, Medellín (1990)
16. Kausar, A., Iqbal, M.: Dyes adsorption using clay and modified clay: a review. *J. Mol. Liq.* 395–407 (2018)
17. Schoonheydt, R.A.: Reflections on the material science of clay minerals. *Appl. Clay Sci.* 107–112 (2016)
18. Marta Sołtys, A.G.: Electrical and optical properties of glasses and glass-ceramics. *J. Non-Cryst. Solids* **12** (2018)
19. Huang, J.: Design and Development of Ceramics and Glasses, Biology and Engineering of Stem Cell Niches, pp. 315–329. London, United Kingdom (2017)
20. Costales, F.F., Olson, D.W.: Cerámica para escuelas y pequeñas industrias. Centro Regional de Ayuda Técnica, México (1964)
21. Fernández-Balbuena, G.E.: Reflexiones sobre la planeacion estrategica revista de economia y Derecho, pp. 45–56 (2007)
22. Hernández Ramírez, V., Pineda Domínguez, D., Andrade Vallejo, M.: Las mipymes artesanales como un medio de desarrollo para los grupos rurales de México, pp. 65–92. Universidad & Empresa (2011)

# Design of the Ternary Gypsum-Based Building Composite Using Simplex Optimization



M. Doleželová, J. Pokorný and A. Vimmrová

**Abstract** The main disadvantage of gypsum as a building material is the loss of its mechanical properties in a wet environment and therefore the use of pure gypsum is limited only to the interior of buildings. The resistance of gypsum materials against moisture can be improved by the addition of any pozzolanic material and an activator of the pozzolanic reaction to the gypsum. The water-resistant CSH phases are formed by the reaction and the resulting gypsum-based materials evince better behaviour in a wet environment. Several ternary materials, composed of gypsum, lime, several types of pozzolans (silica fume, ground bricks, granulated blast-furnace slag) and silica sand were studied. The best resistance against water was achieved by the material containing silica fume, but its strength was lower than the strength of the other materials. Simplex optimization was used to design a composite with better mechanical properties. Maximum compressive strength was set as the goal of the optimization with regard to the fact, that silica fume is a relatively expensive material. After several steps, an optimized material with greater strength, containing reasonable amount of silica fume was designed.

**Keywords** Gypsum-based composite · Silica fume · Mechanical properties  
Optimize · Simplex method

## 1 Introduction

Gypsum is one of the most environmentally friendly materials, firstly because it needs very low temperatures during production (under 200 °C) compared to other building binders (e.g. cement or lime—over 1000 °C) and secondly because it can be produced from a large range of secondary materials originating many in industrial processes (e.g. from flue gas desulphurization in coal-fuelled power plants or from

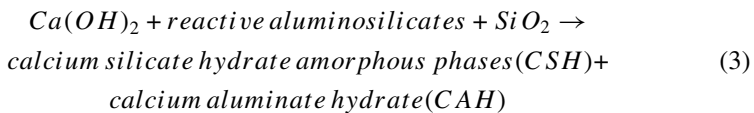
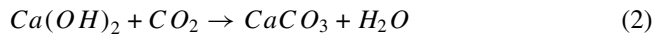
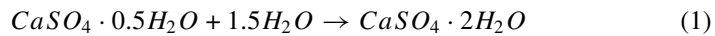
---

M. Doleželová · J. Pokorný · A. Vimmrová (✉)  
Faculty of Civil Engineering, Czech Technical University in Prague,  
166 29 Prague 6, Czech Republic  
e-mail: [vimmrova@fsv.cvut.cz](mailto:vimmrova@fsv.cvut.cz)

© Springer Nature Switzerland AG 2019  
L. F. M. da Silva (ed.), *Materials Design and Applications II*, Advanced  
Structured Materials 98, [https://doi.org/10.1007/978-3-030-02257-0\\_10](https://doi.org/10.1007/978-3-030-02257-0_10)

production of fertilizers or titanium oxide) [1–4]. Other advantages of gypsum also include its very good behaviour in fires [5, 6], good workability and aesthetics.

On the other hand, gypsum has one principal disadvantage in that it can be used only in a dry environment, because it suffers from considerable loss of its mechanical properties when wet [7]. A solution to this problem could be the use of ternary gypsum-based materials, composed of gypsum, some kind of pozzolan, containing amorphous  $\text{SiO}_2$  [8] and an activator of the pozzolanic reaction [9–12]. In these materials, gypsum first reacts with water and establishes the initial strength of the material according to Eq. (1). This is followed by two strengthening reactions, the carbonation reaction (2) and the pozzolanic reaction (3), in which pozzolan reacts with an activator and the CSH and CAH water-resistant structures are formed in the material.



Setting and hardening of gypsum starts immediately after mixing and is completed within a few hours after the production. The carbonation and pozzolanic reactions are substantially slower (several months or even years), until all the calcium hydroxide in the material is spent.

Many materials can be used as pozzolan components, e.g. blast furnace slag, metakaolin, silica fume. The activator of the pozzolanic reaction has to contain calcium hydroxide, because its presence is necessary for the pozzolanic reaction and it can also form an alkaline environment, which is essential for the reaction. From this point of view, hydrated lime or cement are the most suitable components.

Thus ternary systems contain at least three solid components and water, in addition to other additives (such as plasticizers, setting regulators or fibres). It is difficult to find the optimum composition in such multi-component systems, because all the components behave synergically. The composition of ternary systems is often formulated randomly (according to previous experiments, with testing of other binders), but in this case an optimum composition is rarely achieved. Optimization methods are very rarely used to design gypsum-based materials. Arikan and Sobolev [13] used stepwise optimization to improve some properties of gypsum-based plasters. The principle of this method lies in the search for the optimum amount of only one component. When the optimum amount of the first component is found, then the optimum amount of the second component is sought and the amount of first component stays constant, and so on. The main problem of this method is that the synergic effect between the individual components is neglected. Bose et al. [14] used the multifactorial method to design gypsum composites. This method is based on testing of all the combinations of all the components at several dosage levels. In this method, the

synergic effect is taken into account, but the number of experiments is usually very large and therefore the testing is expensive. We found that the linear optimization method, called sequential simplex optimization, can be used successfully to design gypsum-based materials [15, 16].

This paper describes the design of two ternary gypsum-based materials (paste and mortar) with silica fume. Sequential optimization was used to find the material with the best mechanical properties.

## 2 Principles of Simplex Optimization

The design of multi-component building materials and especially binders is often based on previous experience alone and a systematic design method is used rarely. This type of design is not suitable for ternary gypsum-based material, because the components act synergistically in the mixture. This fact leads efforts to use more efficient tools. Therefore, systematic design of the mixture was chosen using the SOVA 1.0 optimization freeware computer code (Luboš Svoboda, Czech Rep.) [17]. This program works on the principle of sequential optimization using the flexible simplex method. The simplex optimization method is based on finding the optimum of the function with  $m$ -variables by the creation of a geometrical shape, called a simplex, with  $m + 1$  vertices in  $m$ -dimensional space. For example, a simplex with two variables could be interpreted as a triangle and a simplex with three variables as a tetrahedron. Each vertex (e.g. mixture in this case) is evaluated according to the results of experimental measurements. The vertex with the lowest optimized value is rejected and projection is performed through the average of the remaining vertices. The shape of the simplex can be modified. Modification is based on the successful or unsuccessful projection in order to reach faster convergence towards the sought optimum. The types of convergence are depicted in Fig. 1. The scheme of the convergence process towards the sought optimum is shown in Fig. 2. Detailed information about the principles of simplex optimization can be found e.g. in [18].

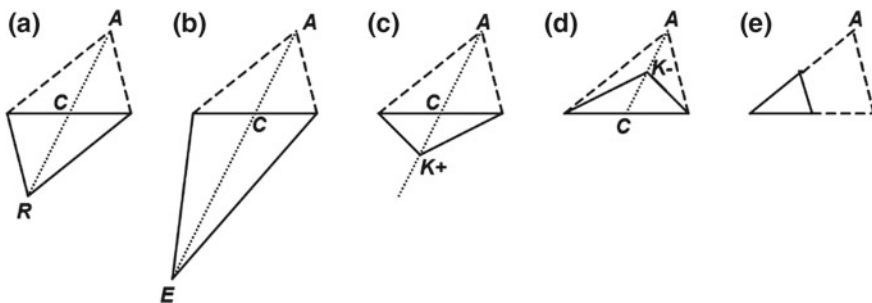


**Fig. 1** Variants of the simplex modification: **a** reflection, **b** expansion, **c** contraction, **d** reflected contraction, **e** shrinkage

**Fig. 2** The convergence process of simplex optimization (in 3-dimensional space)

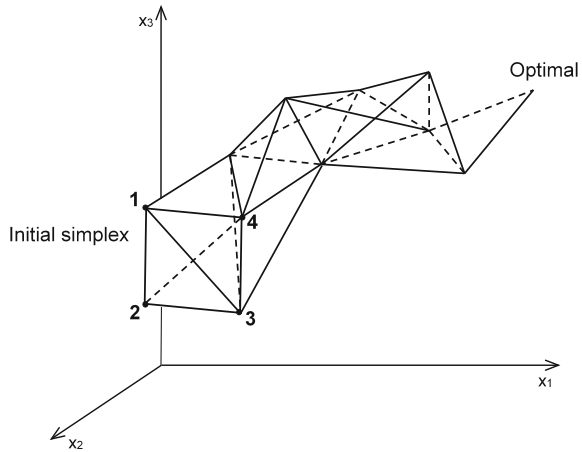


**Table 1** Initial simplex for three variables

Vertex	Representation of the variable		
	Var. 1	Var. 2	Var. 3
1	L <sub>1</sub>	L <sub>2</sub>	L <sub>3</sub>
2	U <sub>1</sub>	L <sub>2</sub>	L <sub>3</sub>
3	L <sub>1</sub>	U <sub>2</sub>	L <sub>3</sub>
4	L <sub>1</sub>	L <sub>2</sub>	U <sub>3</sub>

L<sub>i</sub>—lower limit; U<sub>i</sub>—upper limit

The optimization was carried out by the SOVA 1.0 freeware computer code. The algorithm of the method searches directly in the defined space. Each optimization goes through the following steps:

- Definition of the target criterion: minimum, maximum or the target value.
- Definition of variables: initial values of the variables for the creation of the initial simplex. Each variable is limited by lower and upper values.
- The computer code composes the initial simplex from the given upper and lower values. The number of vertices in the simplex is  $m + 1$ , where  $m$  is the number of variables. An example of the initial simplex for three variables is shown in Table 1.
- For the optimization of composite materials, each vertex corresponds to one individual composition of the mixture. These mixtures are prepared, laboratory tested and the obtained values are fed back into the computer code. The software evaluates the least favourable result, which is subsequently excluded and a new vertex is proposed on the opposite side of the original vertex, as described above. A new simplex is created this way.
- The new simplex is evaluated in the same way as the previous simplex. The worst vertex of new simplex is again excluded and a new simplex is formulated. This process is repeated until the required result value is found. The optimization can be terminated when the optimized values do not improve any more.

**Table 2** The mineralogical compositions of the gypsum and lime

Mineral name	Chemical formula	Amount [%]	
		Gypsum	Lime hydrate
Bassanite, syn	$\text{CaSO}_4 \cdot 0.5 \cdot \text{H}_2\text{O}$	95	–
Gypsum	$\text{CaSO}_4 \cdot 2 \cdot \text{H}_2\text{O}$	1	–
Anhydrite	$\text{CaSO}_4$	3	–
Quartz, syn	$\text{SiO}_2$	<1	–
Calcite	$\text{CaCO}_3$	<1	6.4
Portlandit	$\text{Ca(OH)}_2$	–	93.6

### 3 Materials and Methods

The ternary binder of all the tested materials (pastes and mortars) was always composed of gypsum, lime and silica fume. All the materials were commercially available products. The gypsum was produced by SGCP CZ a.s., Divize Rigips, Czech Republic. It is a very pure product as shown in Table 2. The mineralogical composition was determined by X-ray powder diffraction (XRD). Lime hydrate CL-90-S (producer Carmeuse CR, Czech Rep.) is used as the alkaline activator. Historically, this combination has been used more often than the combination of cement and gypsum. Silica fume was also a commercial product (producer Stachema, Czech Rep.), sold under the name Stachesil S; it contained 90% of amorphous  $\text{SiO}_2$ . The sand used in the gypsum mortars was standardized sand [19], produced by Filtrační písky Ltd., Czech Rep., with grain size to 4 mm.

The mechanical properties of the samples were tested on a set of test specimens. One set included three prisms with dimensions  $160 \times 40 \times 40$  mm [20]. The preparation process was as follows: the homogenized mixture of dry binders (gypsum, lime and silica fume) was poured into a bowl with a measured amount of water, followed by short manual mixing. Then mixture was mixed for 60 s in a standard mixer at low speed, sand was added and mixing continued at high speed for another 30 s. Then the mixture was whipped manually and mixed again mechanically at high speed for another 60 s. The mixture was then poured into the moulds and the samples were unmoulded after 1 h. The samples were stored under laboratory conditions for 6 days. The ternary systems were tested at an age of 7 days and the samples were dried at  $50^\circ\text{C}$  to a constant mass before testing.

### 4 Results and Discussion

The maximum value of the compressive strength was the optimized criterion for the studied gypsum composites. The amount of gypsum, silica fume (in % of the dry mass) and water (as the water/binder ratio) were variables which were fed into the

**Table 3** The composition of gypsum pastes

Designation	Components				Bulk density [kg m <sup>-3</sup> ]
	Gypsum [%]	Silica fume [%]	Lime [%]	Water/binder ratio	
GP1	60	6	34	0.65	1024
GP2	80	6	14	0.65	1063
GP3	60	12	28	0.65	1034
GP4	60	6	34	0.85	871
GP5	73	10	17	0.5	Refused
GP6	63	7	30	0.7	990
GP7	76	11	13	0.7	1019
GP8	83	13	4	0.7	1022
GP9	91	5	4	0.8	959
GP10	78	11	11	0.9	862

computer code for the creation of the initial simplex. The amount of lime was calculated because the sum of all the components cannot exceed 100%. This condition was not ensured in the computer code and therefore the amount of lime was not included as a variable for the optimization and it was calculated subsequently according to (4).

$$L = 100 - G - SF \quad (4)$$

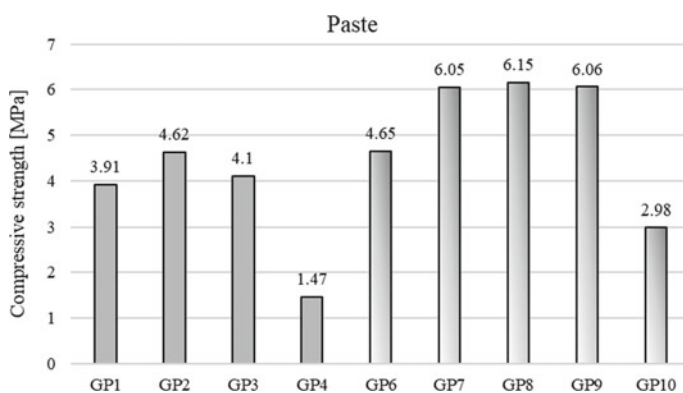
where L is the amount of lime in the mixture, G is the amount of gypsum and SF is the amount of silica fume, [% wt.].

The initial limit values for the gypsum were 60 and 80%, for the silica fume 6 and 12%. The initial values of the water/binder ratio were different for the paste and the mortar with respect to the different workability. The water/binder ratio of pastes was designed within the range 0.65–0.85. The amount of water in the gypsum mortars was greater due to its worse workability, from 1.26 to 1.33. The composition of the optimized composites is shown in Tables 3 and 4. The first four compositions of pastes/mortars (GP1–GP4/GM1–GM4) are mixtures of the initial simplex. Some designed compositions had to be excluded during the optimization. Gypsum paste GP5 was excluded because the water/binder ratio was too low and it was not possible to mix the paste properly. The problem during the optimizing of gypsum mortars was different. Mixtures GM7 and GM8 had to be excluded, because the software designed gypsum and silica fume in a sum of the amounts exceeding 100% and therefore these mixtures were not possible.

The dosage of sand in the gypsum mortars was determined according to standard ČSN EN 196-1 [9] which sets the binder/filler ratio as 1:2. The amount of filler has been maintained the same for all the mixtures to allow better comparison of the results.

**Table 4** The composition of gypsum mortars

Designation	Components					Bulk density [kg m <sup>-3</sup> ]
	Gypsum [%]	Silica fume [%]	Lime [%]	Water/binder ratio	Sand [%]	
GM1	20	2	11.3	1.26	66.7	1303
GM2	26.7	2	4.6	1.26	66.7	1329
GM3	20	4	9.3	1.26	66.7	1323
GM4	20	2	11.3	1.33	66.7	1291
GM5	24.3	0.3	8.7	1.19	66.7	1379
GM6	27.3	4.3	1.7	1.21	66.7	1381
GM7	31	5.3	-3	1.19	66.7	Refused
GM8	32.3	2.4	-1.4	1.17	66.7	Refused
GM9	23	3.7	6.6	1.24	66.7	1343

**Fig. 3** The results for the compressive strength of pastes

The compressive strength results are shown graphically in Figs. 3 and 4. The graphical representation is better suited for clarity and comparison of the results and trends. The presence of aggregates and the higher water/binder ratio lead to lower compressive strengths of gypsum mortars.

The proportions of dry binder components in the initial simplex (i.e. in the first four mixtures) are the same for mortars and pastes. The water/binder ratio and presence of filler was different. The same trend of compressive strength can be observed in the results of both initial simplexes. Mixtures GP2 and GM2 have the highest values of the compressive strength and mixtures GP4 and GM4 have the lowest compressive strength. Despite this similarity, the next step in the optimization is different for the paste and mortar.

Gypsum pastes GP7–GP9 attain an increase in the compressive strength of around 30%, compared with the best paste of the initial simplex GP2. It can be seen that the compressive strength does not directly depend on the amount of silica fume. Moreover, paste GP9 has a larger amount of water than pastes GP7–GP8 which, however,



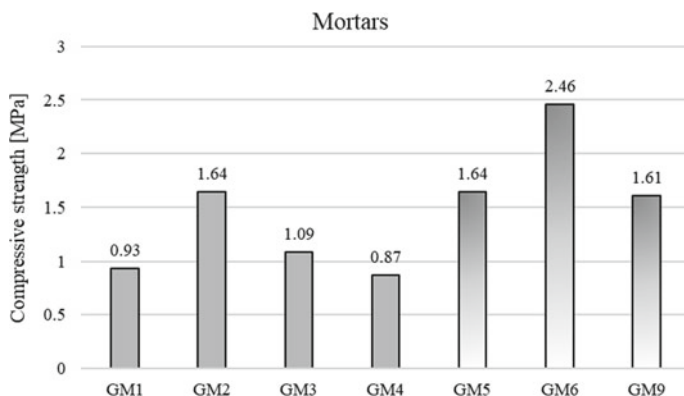


**Fig. 4** The results for the compressive strength of mortars

does not cause a loss of compressive strength in this case. The synergistic behaviour of the mixtures can be observed on these results. The designed composition of pastes with greater strength would probably not be found without using the optimization method.

The compressive strength of last designed paste GP10 is significantly lower than the strengths of the materials designed in the previous steps. Thus it was decided that the increase in the compressive strength by 30% achieved in steps 3–5 (mixtures GP7–GP9) is sufficient and the optimisation was terminated. The results of optimisation of gypsum mortars are even better. A compressive strength about 50% higher than the best materials from the initial simplex was achieved very rapidly, already in 3rd optimization step. The next step showed a decrease in the compressive strength and the optimization was also terminated because an increase of 50% (GM6) was a satisfactory result.

## 5 Conclusions

This paper describes the optimization of the compressive strengths of ternary gypsum-based pastes and mortars. The simplex optimization method was used to improve the compressive strength of all the materials. The simplex optimization method is not used very often for this type of material, because it could be time-consuming (only one composition is designed in one step). For the tested materials, the satisfactory results were achieved relatively rapidly and compositions were designed which could not have been found without optimization. Paste GP9 achieved a compressive strength about 30% greater than the best composition in the initial simplex, even though it contained a small amount of expensive silica fume (5%) and has a large water/binder ratio (0.8). In the case of ternary mortars, the material that was

already designed in the 3rd optimization step had about 50% greater compressive strength than the best material of the initial simplex.

Because all the components in the ternary material behave synergically, the achieved results would not have been obtained as rapidly by a conventional design method (e.g. by multifactorial optimization) and a substantially greater number of experiments would have to be performed.

**Acknowledgements** This research was supported by the Czech Science Foundation, Project No. 16-01438S and by the project SGS17/166/OHK1/3T/11.

## References

1. Tesárek, P., Drchalová, J., Kolísko, J., Rovnaníková, P., Černý, R.: Flue gas desulfurization gypsum: study of basic mechanical, hydric and thermal properties. *Constr. Build. Mater.* **21**(7), 1500–1509 (2007)
2. Değirmenci, N.: Utilization of phosphogypsum as raw and calcined material in manufacturing of building products. *Constr. Build. Mater.* **22**, 1857–1862 (2008)
3. Gázquez, M.J., Bolívar, J.P., García-Tenorio, R., Vaca, F.: Physicochemical characterization of raw materials and co-products from the titanium dioxide industry. *J. Hazard. Mater.* **166**, 1429–1440 (2009)
4. Kostic-Pulek, A., Marinkovic, S., Logar, V., Tomanec, R., Popov, S.: Production of calcium sulphate alpha-hemihydrate from citrogypsum in unheated sulphuric acid solution. *Ceram.-Silik.* **44**, 104–108 (2000)
5. Ryan, J.: Study of gypsum plasters exposed to fire. *J. Res. Natl. Bur. Stand. C* **66**, 373–387 (1962)
6. Lacasta, A., Haurie, L., Formosa, J., Chimenos, J.: Improvement of passive fire protection in a gypsum panel by adding inorganic fillers: experiment and theory. *Appl. Therm. Eng.* **31**, 3971–3978 (2011)
7. Karni, J., Karni, E.: Gypsum in construction: origin and properties. *Mater. Struct.* **28**(9) (1995)
8. Sabir, B., Wild, S., Bai, J.: Metakaolin and calcined clays as pozzolans for concrete: a review. *Cem. Concr. Compos.* **23**, 441–454 (2001)
9. Fraire-Luna, P., Escalante-García, J., Gorokhovskiy, A.: Composite systems fluorgypsum–blast-furnance slag–metakaolin, strength and microstructures. *Cem. Concr. Res.* **36**, 1048–1055 (2006)
10. Martínez-Aguilar, O., Castro-Borges, P., Escalante-García, J.: Hydraulic binders of Fluorgypsum-Portland cement and blast furnace slag, stability and mechanical properties. *Const. Build. Mater.* **24**, 631–639 (2010)
11. Colak, A.: The long-term durability performance of gypsum–Portland cement–natural pozzolan blends. *Cem. Concr. Res.* **32**, 109–115 (2002)
12. Dolezelova, M., Vimmrova, A.: Moisture influence on compressive strength of ternary gypsum-based binders. In: Simos, T., Tsitouras, C. (eds.) *Proceedings of the International Conference on Numerical Analysis and Applied Mathematics 2016*. American Institute of Physics, Melville (2017)
13. Arikan, M., Sobolev, K.: The optimization of a gypsum-based composite material. *Cem. Concr. Res.* **32**, 1725–1728 (2002)
14. Böse, H., Hurbanic, M., Raether, F.: Optimization of gypsum plaster composition supported by experimental design. *ConChem J.* 64–71 (1996)
15. Vimmrova, A., Koci, V., Krejsova, J., Cerny, R.: A method for optimizing lightweight-gypsum design based on sequential measurements of physical parameters. *Meas. Sci. Rev.* **16**, 160–166 (2016)

16. Vimmrova, A., Keppert, M., Michalko, O., Cerny, R.: Calcined gypsum-lime-metakaolin binders: design of optimal composition. *Cem. Concr. Compos.* **52**, 91–96 (2014)
17. Svoboda, L.: SOVA 1.0 [software] (2012). <http://people.fsv.cvut.cz/~svobodal/sova/>
18. Nelder, J.: English proofreading by a native speaker was performed prior to submission of the revised article A and Mead, R.: A simplex method for function minimization. *Comput. J.* **7**, 308–313 (1965)
19. ČSN EN 196-1 Methods of testing cement—Part 1: Determination of strength Czech Standardization Institute. Prague (1996)
20. ČSN EN 13279-2 Gypsum binders and gypsum plasters: Test methods. Czech Standardization Institute. Prague (2014)

# Study of the Influence of Sintering Temperature on Water Absorption in the Manufacture of Porcelain Cups



T. P. Duarte, J. L. Alves and P. Pereira

**Abstract** The final quality of ceramic parts is strongly related with the raw materials, which have different origins, are available in nature in different places, and present heterogeneous characteristics. The particularities of ceramic manufacturing process, like hardness and moisture of pastes, drying and firing cycles, atmospheres, etc., are a multiplicity of factors that causes variability of properties on the final parts, affecting their use in several applications. This work presents a study carried out in a ceramic company that produces products for hotelware, namely coffee plates and mugs. The objective was study the influence of the firing temperature on the porosity, measured by the water absorption capacity. Taking into account the great influence of the energy costs on the final price of the pieces, it was intended to determine the lowest sintering temperature compatible with these ceramics request. It was found that the highest porosity values (about 23%) occurred at temperatures of 750 °C. From 850 to 1050 °C, the porosity variation is not significant, ranging from 21 to 22%, so it is not necessary to use higher sintering temperatures, which significantly increases the cost of the product.

**Keywords** Porcelain · Traditional ceramics · Hotelware · Firing cycle · Porosity  
Moisture

---

T. P. Duarte (✉) · J. L. Alves · P. Pereira  
Faculty of Engineering, INEGI, University of Porto, Rua Dr. Roberto Frias,  
4200-465 Porto, Portugal  
e-mail: [tpd@fe.up.pt](mailto:tpd@fe.up.pt)

J. L. Alves  
e-mail: [falves@fe.up.pt](mailto:falves@fe.up.pt)

P. Pereira  
e-mail: [pmpereira94@gmail.com](mailto:pmpereira94@gmail.com)

## 1 Introduction

The traditional ceramic industry has, as main objective, to satisfy the needs of the consumers in the production of bricks, tiles, flooring solutions, coatings, sanitary ware and ceramic objects for utilitarian and decorative purposes. The term “ceramic” derives from the Greek word “Keramus”, the designation attributed to the product obtained from inorganic, nonmetallic, cold-formed and heat-hardened [1]. The final properties of the ceramic materials are influenced by their chemical and mineralogical composition, as well as by the chemical bonds and structure, resulting from the manufacturing process [2, 3].

The porcelain—one of traditional ceramics groups—is obtained through a mixture of refractory clays, kaolin, quartz and feldspar, that later becomes harder, translucent, vitrified and sound to the touch, firing at a maximum temperature of 1420 °C. The Venetian Marco Polo, when passed through China between 1271 and 1295, described the pieces made with porcelain paste, like objects similar to certain “porcellas” (shells), giving rise to the word porcelain. The secret of porcelain paste remained in China for hundreds of years. In the sixteenth century, Europe made several attempts to obtain this secret. It is mainly in Italy that this research becomes more active, and in 1708, the secret is discovered by the alchemist Johann Frederic Böttger and the physicist Walter von Tschirnhaus. The first hard porcelain factory appears in 1773 in Europe [4].

Porcelain is defined as a glassy or unglazed vitreous ceramic, mainly used for technical purposes [5]. The porcelains are made from triaxial ceramic pastes: clay minerals (clay and/or kaolin—50%), quartz (10%) and feldspar (40%), which are thermally treated at temperatures above 1250 °C. At the end of the production process the products obtained have low porosity (less than 0.5%), low water absorption and high glass content. They include houseware and hotelware products (dishes, cups, bowls, etc.), electrical insulators, decorative items, dental prostheses, coatings and others [6, 7].

To obtain the desired color and thin thickness, it is necessary to use raw materials of high purity and low particle size. According to the properties to be attained in the final product, namely degree of vitrification, mechanical strength, or others, appropriate formulation of the ceramic paste are demanded. It is also very important to define the final firing temperature, because is this parameter, which determines the final properties [2, 8].

Kaolin, whose chemical formula is:  $\text{Al}_2\text{O}_3 \cdot m\text{SiO}_2 \cdot n\text{H}_2\text{O}$ , where  $m$  ranges from 1 to 3 and  $n$  from 2 to 4, is defined as a rock composed of minerals of the kaolinite, and which have at least one of the following properties: high refractory and degree of whiteness greater than or equal to 76% that resists, without melting, at high temperatures [2, 5].

Feldspars are alumino-silicates with K, Na, Ca ( $\text{KAlSi}_3\text{O}_8$ ,  $\text{NaAlSi}_3\text{O}_8$ ,  $\text{CaAl}_2\text{SiO}_2\text{O}_8$ ). Its use in the ceramic industry is mainly due to its fluxing action. It allows the formation of a liquid phase at a lower temperature connecting the grains of the ceramic body to achieve the desired mechanical strength and contributes to

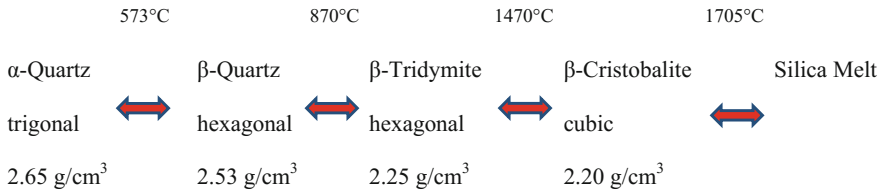


**Fig. 1** Allotropic forms of silica, transformation temperatures and densities adapted from [9]

increase the relative density. Feldspar causes considerable shrinkage in the range of 1140–1350 °C [2, 5].

Quartz is a crystalline silicon oxide (silica—SiO<sub>2</sub>), very abundant in nature. Its purity determines the type of application. It is designated as inert, because is less altered by the action of heat, than clay and feldspar. Therefore, guarantees structural strength before firing and facilitates the release of water (with less deformation) during drying. Silica has three allotropic forms: quartz is stable below 870 °C, tridymite between 870 and 1470 °C and cristobalite above this temperature, as shown in Fig. 1 [2, 5, 9]. The transition from a stable phase at low temperature to a high temperature phase, leads to volume increase (expansion), due to the fact that the various polymorphic structures have different densities. These dimensional variations can cause problems of mechanical stability in the pieces and deserve special care in the processing of ceramics based on clay [10].

The main steps for the production of porcelain products are described below.

### 1. Preparation of the ceramic paste

The milling process consists in reducing the particle size of a solid material in order to increase the free surface to rise the reaction rate and allow a more homogeneous mixing. There are various types of milling equipment. The choice is made according to the type of granulometry desired, the need to obtain greater homogenization of the components, and elimination of impurities [2, 3, 5]. For fine milling of hard raw materials (quartz and feldspar), ball milling is used.

After the milling operation, particles and products harmful to the ceramic paste are removed by sieving and desferritization, which is essential in the preparation of the porcelain paste, since one of its main characteristics is whiteness. The existence of metallic iron compounds in the slurry causes red to black stains during the firing of the slurry [11].

The plastic materials (clays and kaolins) are diluted in water to allow a homogeneous mixture. After milling the hard materials and diluting the plastics, the blends are mixed together in blenders. At this stage of the process, the ceramic paste density is controlled. For the preparation and purification of porcelain pastes, processes such as dispersion (deflocculation) and sedimentation (flocculation) are used. There are deflocculants (silicates, carbonates and sodium phosphates, for example) and flocculants (substances with an acid character) that allow to control these processes in the desired way [10, 11].

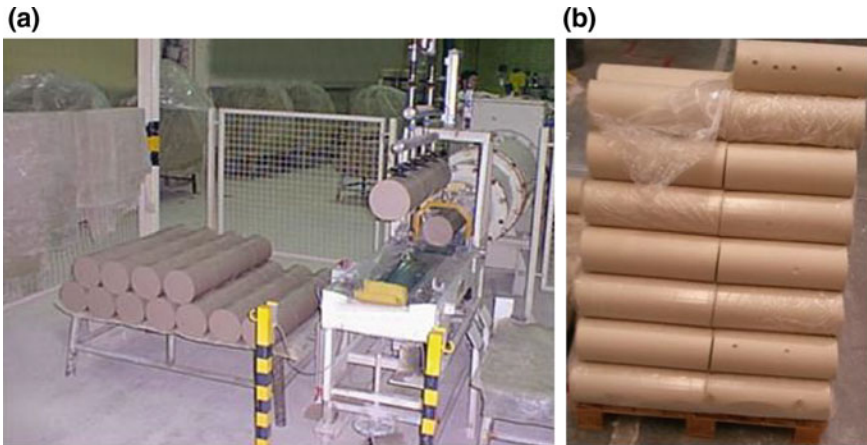


**Fig. 2** a Extrusion of the ceramic paste through the die and formation of the cylinders adapted from [12]; b a set of ceramic paste cylinders

After the excess water is withdrawn from the filter press the filter cake falls under gravity on the treadmill leading to the next stadium. It enters a worm screw, where it is destroyed, to eliminate the effects of the moisture differences. It is then extruded under vacuum, in the form of cylinders, with varying diameter and length, according to the size of the parts for which they are projected (Fig. 2). Hardness control is essential as, high hardness hamper shaping and lower hardness than that indicated for the chosen manufacturing process, gives rise to less resistant products that weakens handling in subsequent operations.

## 2. Conformation

In the manufacture of porcelain pieces for domestic use, the most efficient process is counter-molding (plastic). The plastic paste, with a water content of approximately 24wt%, is used in Roller machines, by counter-molding, producing flat and hollow pieces with an axis of symmetry [10, 13]. A slice of ceramic paste is placed over a plaster form, which has the inner (or outer) shape of the part to be obtained, and then the outer (or inner) is molded by means of a rotating metal punch, with the shape of the part. Figure 3 shows the Roller conformation.

## 3. Drying

After conformation, the pieces, with moisture contents around 22%, remain adhered to the surface of the plaster forms. If the demolding was performed, immediately after the conformation, the demolding efforts would be sufficient to deform the pieces, or else, they would deform, under the action of their own mass [14, 15]. A controlled drying process should be carried out in order to ensure the balance between the diffusion rate of the water from the interior of the piece to the surface and the evaporation ratio thereof at the surface to a value close to 20%. For this reason, in the first stage of drying, in which most of the retraction takes place, the mold (in

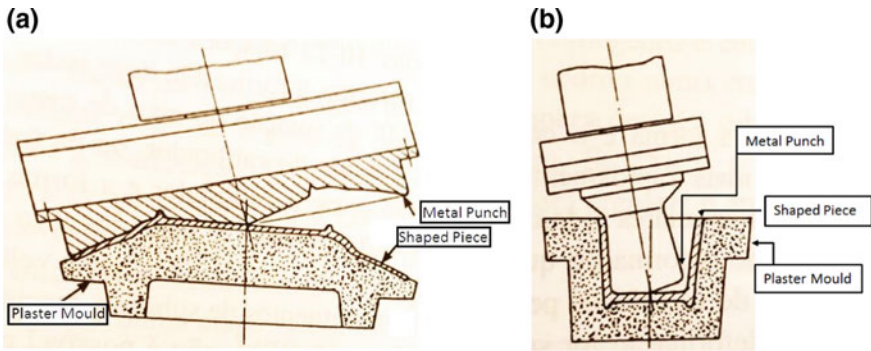


**Fig. 3** Plastic conformation by Roller: **a** external and **b** internal adapted from [14]

plaster) accompanies the part in the Roller dryer. Simultaneously with the drying of the part also the drying of the mold occurs, which allows to use it again, immediately after the demolding of the piece. The convection dryers coupled to roller machines operate with tight limits of relative moisture (40–60%) and temperature (40–60 °C) to provide easy demolding and ensure that the shaped parts acquire the necessary consistency so as not to deform in subsequent operations [14, 15].

Thereafter, a rapid drying in a first dryer is carried out to moisture contents between 12 and 16%. The parts have still poor mechanical resistance, so they must be handled carefully. Thereafter they undergo a second drying, at a temperature between 60 and 80 °C, where the moisture is reduced to 2%. The conditions of the drying air are clearly more violent than those of the previous dryer, and can reach temperatures between 90 and 120 °C and very low relative moisture. At the end of the second drying, the dried products become white, and that is why “white dryer” designation is assigned to the second dryer.

The occurrence of thermal and moisture gradients during the water elimination process leads to the appearance of mechanical stresses, which can result in product defects, deformations and cracks, reducing the parts quality. The speed at which the drying process takes place depends on external factors (temperature, relative moisture, air circulation velocity, exposed surface area and total pressure) and internal factors (physical nature, structure, moisture content, temperature and thickness of the solid) [10, 16].

In this process it is important to know the dimensional behavior of the ceramic paste as a function of temperature in order to establish a drying cycle, because when the dimensional variations end, the remaining water is easily eliminated. The clays have variable retraction curves depending their nature, dimensional distribution, degree of packaging of the particles, etc. Ceramic pastes shrink less than pure clays because they contain non-plastic materials [5, 10, 15]. In brief, the drying operation is intended to eliminate the processing water present in the shaped parts, to increase the mechanical strength of the products, in order to support the finishing operations, and to prepare them for the firing operation.



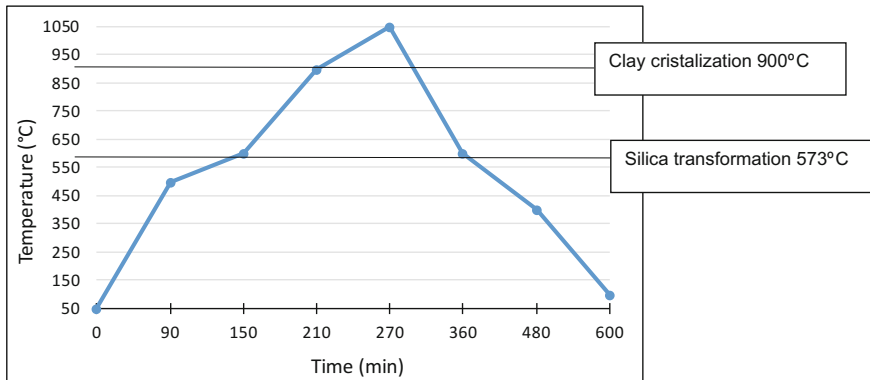


**Fig. 4** Firing cycle, with indication of starting silica transformation (573 °C) and clay crystallization (900 °C) temperatures [16–18]

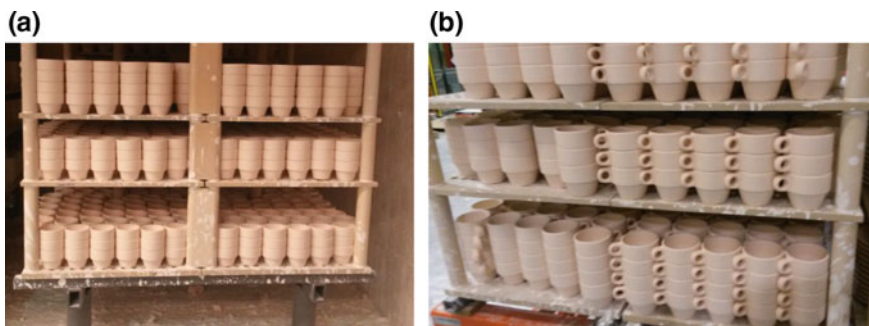


**Fig. 5** a Cup furniture before firing and b after firing (whiter)

#### 4. Firing

After drying the products are subjected to a first firing operation (Fig. 4), at temperatures ranging between 900 and 1050 °C, to consolidate the pieces [5, 13, 17]. The calculation of the firing curve is dependent on two factors: type of oven available and physical and chemical reactions desired at this stage [17, 18].

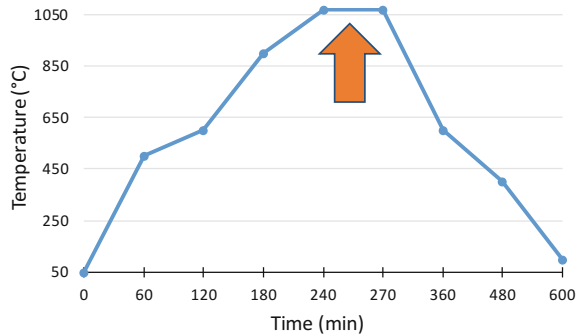
The area between 500 and 600 °C must be highlighted, both in heating and cooling, as it is the moment when the quartz transformation starts and also between 900 and 1050 °C due to clay crystallization, because they promote volumetric changes [19, 20].

This phase should allow to obtain parts with porosity around 20%, be carried out in the shortest time and at the lowest temperatures, in order to reduce the associated high energy costs. Figure 5 shows parts (cups) before and after firing.

#### 5. Glazing

Glazing consists of covering the pieces with a suspension of glaze, optionally colored or transparent. After final firing (final processing stage, described after), the glass

**Fig. 6** Glaze firing cycle for porcelain pieces for domestic use [2, 17, 18, 24]



layer gives the surface of the pieces a pleasant brightness and makes the surface smooth to the touch and easy to clean, creating an ideal support for the application of paints used in decoration.

As the main feature of porcelain relative to other ceramic materials is their whiteness, the glass used is usually transparent. This gives it even greater chemical resistance, resistance to abrasion and impermeability. The application of the glaze can be manual or automated. It is an aqueous suspension of solids (“milky”) with typical composition:  $\text{SiO}_2$ —67.7%,  $\text{Al}_2\text{O}_3$ —12.8%,  $\text{CaO}$ —6.4%, and other less important oxides [14, 21]. The optimal working density and viscosity of each glaze depends on the immersion time and the percentage and rate of water absorption of the workpiece after drying [22, 23]. High porosity values in the pieces, at this stage, consume more glaze.

## 6. Final firing

This phase of the process consists of subjecting the glazed parts to high temperature firing (it can reach 1420 °C) in a reducing atmosphere. Figure 6 shows a glaze firing cycle suitable for the production of porcelain pieces.

It should be noted that the time period up to 500 °C is lower in relation to the first firing (see Fig. 4) because the pieces have already been fired, and there are now no problems regarding the need for water removal [24]. The great difference between the firing of the glaze and the first firing lies in the period indicated in the graph (stage from 20 to 30 min). It is the glaze period maturation, in which all chemical reactions must be completed as well as allowing the removal of gaseous products [17, 18, 24].

Due to the reducing atmosphere, carbon deposition may occur on products. Thus, it is necessary to ensure the combustion of the carbon, before the vitrification of the ceramic paste begins. For this to happen, the atmosphere of the furnace should be strongly oxidizing when the temperature is between 900 and 1000 °C before the porosity is eliminated due to the formation of the liquid phase. After removal of the carbon, the high temperature firing period takes place in a reducing (or slightly oxidizing) atmosphere, depending on the color desired for the glaze [14, 25].

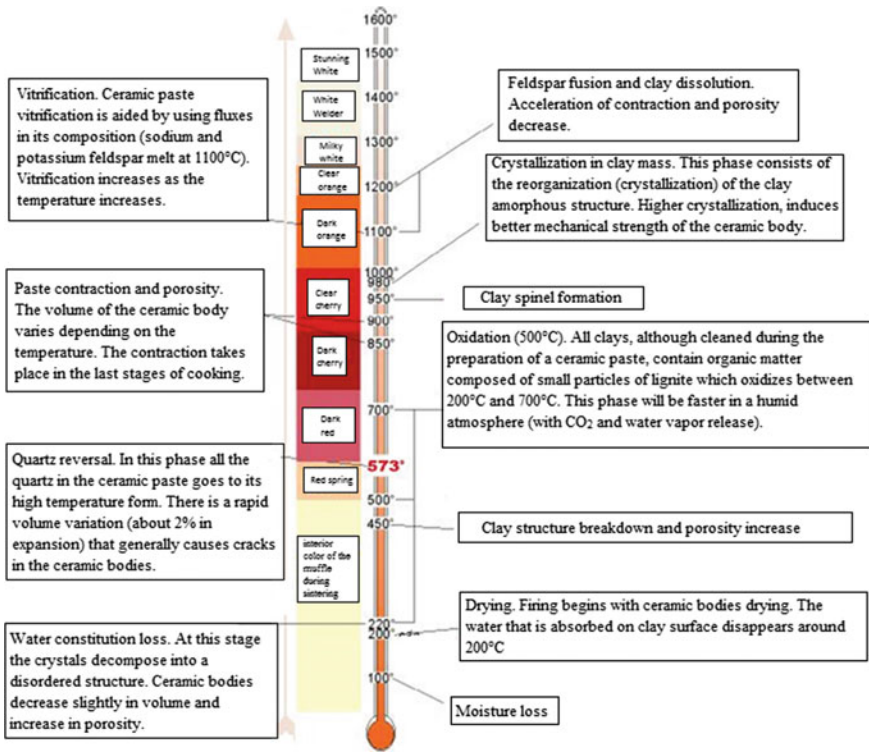


**Fig. 7** Changes occurring in a porcelain paste as a function of temperature, adapted from [19, 20, 22, 25]

The reducing atmosphere promotes the whiteness of the piece. If the firing is in an oxidizing atmosphere, the iron ( $Fe^{2+}$  and  $Fe^{3+}$ ) present in the raw materials is oxidized to trivalent iron ( $Fe^{3+}$ ) and the ceramic pieces acquire a pink coloration. To ensure that all iron is converted to  $Fe^{2+}$ , a concentration of reducing substances in the atmosphere (2–3% by volume of  $CO + H_2$ ) is required. A too much reductive atmosphere also causes a change in color paste, making it greyish due to the formation of metallic iron. Potassium feldspar reacts first with silica, resulting from the decomposition of kaolinite, and then with quartz at higher temperatures. The liquid phase begins at 985 °C and the melting potassium feldspar is complete at 1150 °C [14, 19]. After this phase the water absorption should be 0%. Figure 7 shows a summary of all changes occurring in a porcelain paste as a function of temperature.

Summing up, this paper describes hardness and moisture tests of ceramic pastes (after forming and next to first and second drying) carried out on pieces shaped by pressing, in order to analyze the variability of these characteristics in the initial stages of the manufacturing process. It was verified that the characteristics of the raw materials are quite homogeneous over time, as well as the values of moisture and porosity, in the two drying stages, after conformation. Thereafter, tests were per-

formed at various sintering temperatures between 650 and 1050 °C and the porosity was determined. Dilatometry tests were also carried out on the paste to identify the temperatures at which structural variations occur. The purpose is to determine the lowest sintering temperature compatible with these ceramics request (adequate porosity and mechanical strength to receive glaze), in order to reduce energy consumption.

## 2 Experimental Procedure

The experimental work was carried out in a ceramic company who produces porcelain pieces—cups/mugs and plates/dishes—using samples with shapes and dimensions identical to those shown in Fig. 8 and also samples of ceramic paste from different batches (see Fig. 2b).

The ceramic paste used is not produced in the company and therefore the proportions and compositions used (quantities and granulometry of clay, silica and feldspar and other components) and specific details of their production such as milling time, mixing, among others are not known or controlled. In Table 1 some relevant characteristics of the ceramic paste are indicated according to the indications of the technical data supplied by the manufacturer (Mota Pastas, Lda, Vagos, Portugal) [27]. The ceramic paste hardness is 2.6 bar. Tests were carried out to determine some characteristics of the ceramic paste in 18 cylinders (see Fig. 2) from 3 different batches.

### Hardness

The hardness of the paste is measured with the aid of a penetrometer model ST207 (Prospectors, Dural, Australia), which when pressed against the paste, indicates its hardness in bar (unit of pressure measurement). Three measurements were made in random zones in each ceramic paste cylinder belonging to different batches.

**Table 1** Characteristics of the paste used as raw material [27]

Chemical analysis	wt% (%)
SiO <sub>2</sub>	64.5
Al <sub>2</sub> O <sub>3</sub>	24.0
K <sub>2</sub> O	3.19
Na <sub>2</sub> O	0.63
MgO	0.14
CaO	0.19
Fe <sub>2</sub> O <sub>3</sub>	0.40
TiO <sub>2</sub>	0.04
Moisture	21.0–23

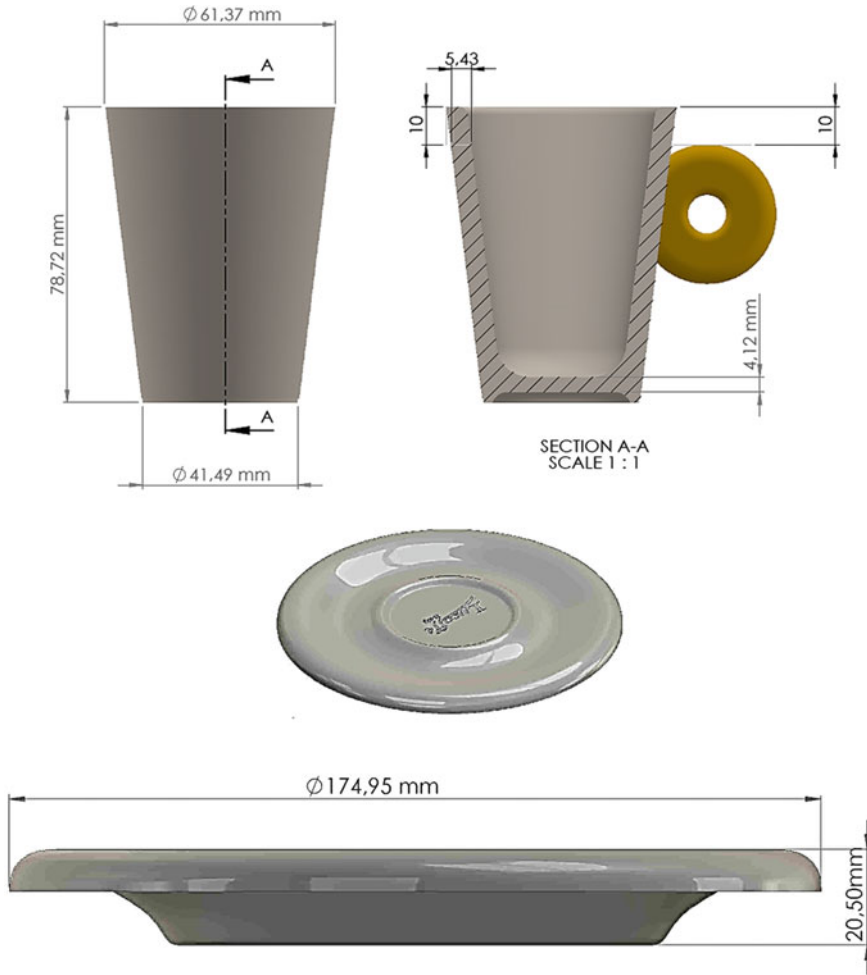


**Fig. 8** An example of cup and plate used as samples in experimental work adapted from [26]

Determination of moisture content in the ceramic paste (before forming) and in parts after forming, 1st drying and 2nd drying

To determine the moisture content, the sample is weighed (slice of ceramic paste or piece) on a precision weighing-machine model OHAUS PA214C (New Jersey, USA) (0.01 g) (P1). This sample is then placed in an oven EUROTERM (Virginia, USA) at a temperature of 100 °C for 24 h. After this time, the dried sample is taken from the oven, allowed to cool to room temperature and weighed (P2). The results presented are the average and standard deviation of 12 samples obtained in the same conditions.

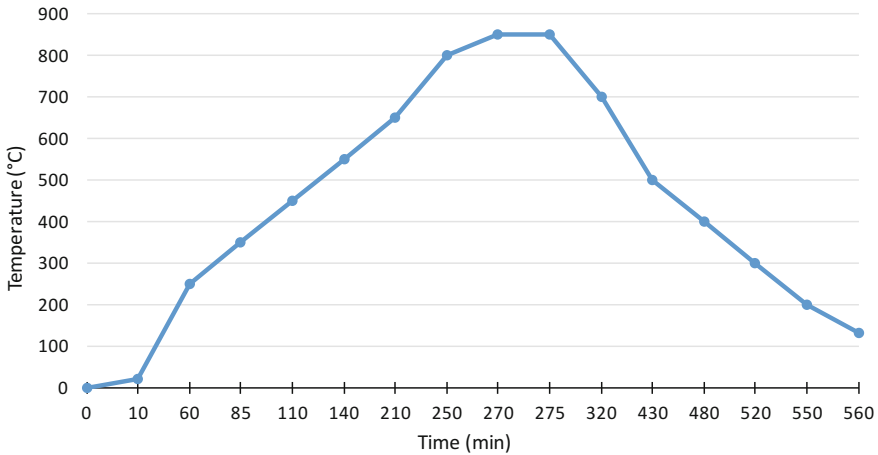


**Fig. 9** Firing cycle used in the tests

#### Determination of the influence of firing temperature on water absorption (porosity)

The water absorption by a ceramic body is influenced by the granulometric distribution of a raw material or ceramic paste, by the chemical and mineralogical composition of the clay minerals, by crystalline structure and also by the porosity after drying and firing. Water absorption indicates the level of porosity of a ceramic part. The smaller the porosity of a piece, the smaller the amount of water it absorbs [10].

Prior to this work, the percentage of water absorption (porosity) of the pieces after firing was unknown. Thus, tests were carried out to ascertain the range of porosity values of the fired pieces, as a function of temperature. The main objective of this test was to find the minimum firing temperature, to obtain glazing absorption rates of 20–21%, suitable values for this type of products. For each temperature, 12 samples were used (3 from 3 models of dishes and 3 of a cup model). These tests were carried out in a laboratory oven KLS 10/12 EUROTHERM (Virginia, USA), due to the impossibility of using the production ovens (because of their size and interruption in company production).

Samples were collected at the outlet of the 2nd dryer and firing trials were carried out at 5 different temperatures; 650, 750, 850, 950 and 1050 °C, according to the cycle shown in Fig. 9. The difference in each test was the stage temperature. In this figure it was decided to present as an example the average value of the 5 studied (850 °C).

No tests were carried out at higher temperatures to avoid the melting of some raw materials, namely feldspar (melting temperature of 1140 °C) which significantly reduces the porosity and makes difficult the subsequent glazing.

In this work these test of water absorption (WA) were carried out according to the procedure described in [28]. This procedure consists of: remove the samples to be tested (in this case plates and cups) from the firing oven at room temperature; weigh the fired samples (P1), introduce the samples into a vessel with water at room

temperature for 24 h, totally covered. After this time, remove the surface water with a damp cloth, and then weighed the samples again (P2).

#### Dilatometric analysis

Dilatometric thermal analysis is of great importance for the ceramic industry as it allows continuous recording of the volume changes that a specimen suffers when subjected to heating and cooling cycles, thus allowing the evaluation and control of the final dimensions of the products and possible occurrences of defects, such as cracks, deformations and residual stresses [29]. The thermal-dilatometric analysis allows to highlight the volume variations related to the coefficient of expansion, elimination of some constituents by the formation of volatile compounds, reactions and crystallochemical transformations, firing, and formation of the glassy phase or liquid. It also allows for kinetic studies of certain transformations, if the temperature is constantly raised and if the dilatometric recording is done as a function of time [30].

This test can be carried out on raw and/or fired specimens, supplying important indications about the mineralogical composition, volume variations and the behavior that the clay raw material has in the glue system. Generally, up to temperatures around 400 °C, a linear expansion occurs which ends when the water of constitution is eliminated [29]. This assay was performed on ceramic paste samples at a heating rate of 5 °C/min until 740 °C, due to equipment oven limit (800 °C), and cooling at a rate of 5 °C/min, model BAHR, DIL 801L (Guyancourt, France).

### **3 Results and Discussion**

#### Ceramic paste analysis—raw material

##### Hardness

The purpose of this test was to verify the values deviation between the hardness measured experimentally in the ceramic company, with the value indicated by the supplier (2.36 bar). The analysis of Fig. 10 shows the existence of deviations that are explained by the storage time before use. However, average hardness of measured and delivered values are equivalent and the standard deviation is low, which means that the technical data sheets supplied from the provider can be validated.

##### Moisture

The results obtained relative to the moisture of the ceramic paste cylinders are shown in Fig. 11. There is a slight deviation of the mean moisture measured in this work relative to the one indicated by the supplier (−0.60%). This deviation can be justified due to the excess of time spent in the warehouse, since it is received until it is used. The reduction of moisture is strongly influenced by the environment inside the factory (ambient temperature conditions always around 25 °C). However, this difference is thought to have no significant influence on the forming process since

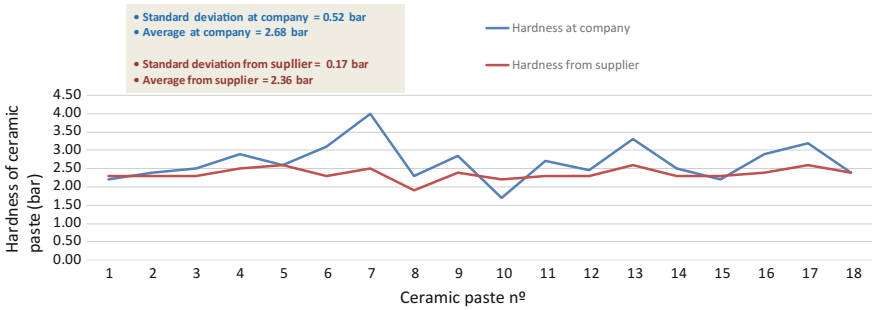


**Fig. 10** Hardness of 18 ceramic paste samples

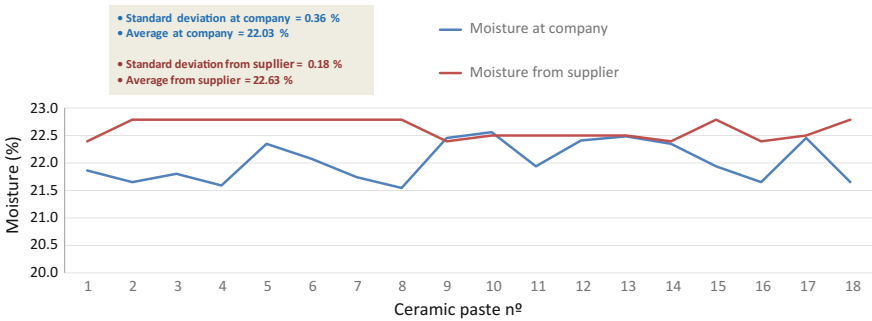


**Fig. 11** Moisture of 18 paste samples

the actual moisture content is around 22%, which is considered adequate for the forming process used and within the range indicated by the supplier.

In summary, in relation to ceramic paste, the values of hardness and moisture determined in the company in 18 cylinders and 3 measurements in each of several batches were very close to the values indicated by the supplier. Therefore, it is possible to consider that, the raw material is controlled and adapted to the type of subsequent conformation process.

Moisture after Roller conformation

Figure 12 presents the measured moisture values in cups and dishes after conformation (in Roller CERINNOV – AUTO 45(Limoges, France) cup line) but before the first drying. The values are in accordance to predicted, because they are around 20–22% (average value of 21.59% and a standard deviation of 0.70%), and are similar to those obtained in the ceramic paste (see Fig. 11) used in the conformation, which indicates that until this phase the process is controlled.



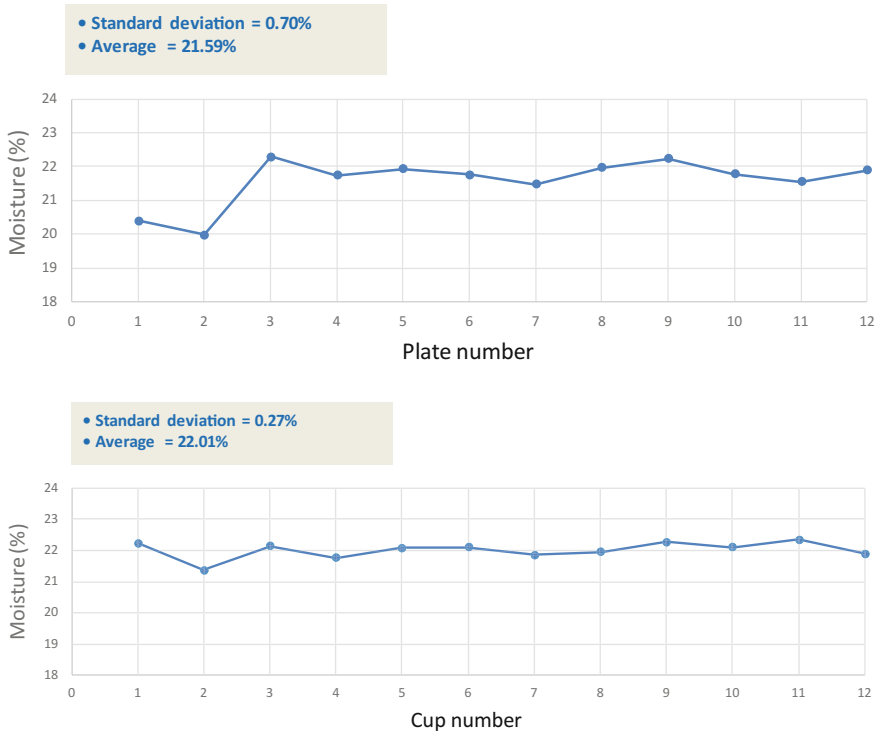


**Fig. 12** Moisture after conformation for 12 plates and 12 cups

Moisture at the exit of the 1st dryer (CERINNOV - SECHOIR DF10CP 08 08/2 PORTES (Limoges, France)) (5 to 10 min between 50 and 70 °C) after forming in the Roller

Moisture determination tests were also carried out on several pieces at the exit of the 1st dryer after demolding. The results presented in Fig. 13 show that the moisture values (average values between plates and cups of 18%) are higher than expected (between 12 and 16%), which means that this first drying does not produce the adequate results (average of 17.4% in dishes and 19.3% in cups). This effect is stronger in the cups than in the dishes and may be due to the fact that it is more difficult to uniformly dry a higher piece (cup) than a (flatter) plate. This difference may hinder the subsequent drying operation.

Moisture after 2nd dryer—white (CERINNOV - SECHOIR 34 BALANCELLES (Limoges, France)) (24 h between 45 and 50 °C)

The moisture of plates and cups determined after the second dryer is shown in Fig. 14. It is found that after this drying the moisture values are quite low (average about 0.38%) and even lower than that indicated in the literature (about 2%) which means that although the parts reach this dryer with moisture higher than indicated, at

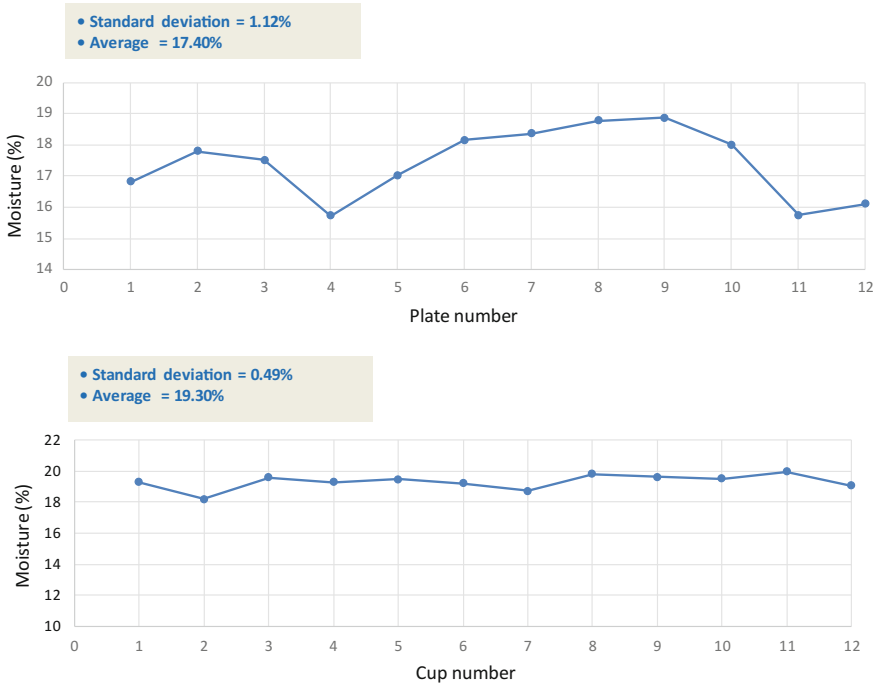


**Fig. 13** Moisture at the exit of the 1st dryer for 12 plates and 12 cups

the end of this step have lower moisture which is suitable for the next firing operation. However, very low values of moisture at the entrance of the oven can induce cracks, and consequently defects, resulting in rejection of pieces.

Water absorption/porosity with sintering temperature

In order to understand the influence of the maximum firing temperature, in water absorption/porosity of the pieces, tests were carried out at 5 different temperatures, using samples from the same batch after 1st and 2nd dryer, in order to eliminate small differences that may occur in these steps. The results obtained are shown in Fig. 15.

It can be seen that the maximum porosity is obtained for the temperature of 750 °C (22.56%). This is due to the relevant physical and chemical transformations of the clay, which makes it more porous, as already mentioned (see Fig. 7). On the other hand, from this temperature, the porosity decreases, until reaching a minimum value for 950 °C, near 21%. In a bi-firing process (as is used in the manufacture of these parts, firing before and after glazing) it is of interest that all the important transformations occurring in the firing process are carried out in this stage in order to avoid future defects in the pieces, only detected after glaze firing, since this entails costs with the processing of pieces that will be rejected. It is considered, therefore, that the temperature of 850 °C is sufficient to carry out the firing of these pieces,

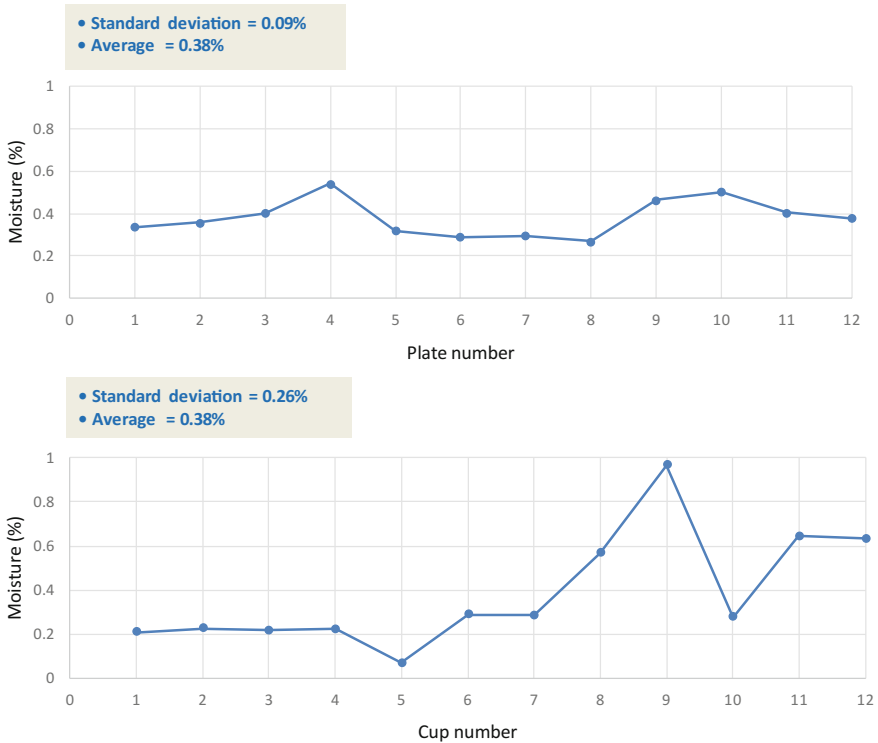


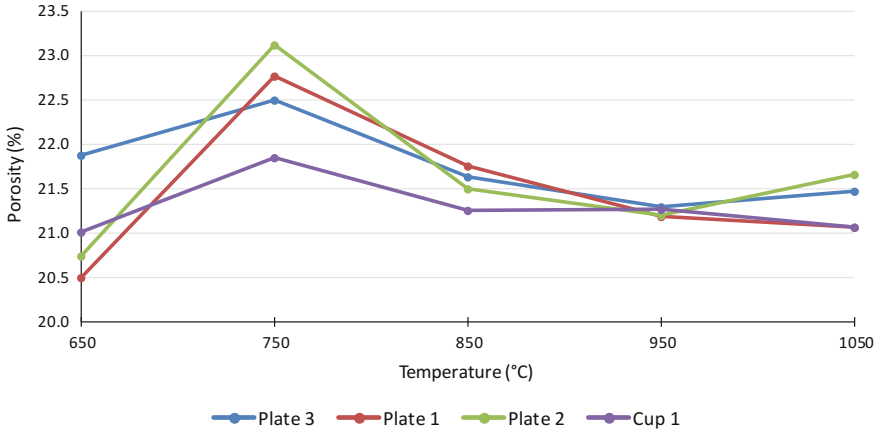
**Fig. 14** Moisture at the exit of the 2nd dryer for 12 plates and 12 cups

since it gives porosity values between 21 and 22%, suitable for glaze application. It is not defensible to use higher temperatures because they do not significantly change porosity, and causes an increase in energy cost.

To clarify this data, dilatometric analysis of the ceramic paste were used to identify the physical and chemical changes occurring with increasing temperature (Fig. 16). The dilatometric curves show a gradual increase in linear expansion, with a rapid shrinkage around 600 °C, which coincides with the beginning of the firing and vitrification processes to which the particle rearrangements of the clay minerals correspond after a rupture of their structural order and consequent amorphization. In relation to the critical temperature of 573 °C, at which the inversion of quartz occurs (changes from quartz  $\alpha$  to quartz  $\beta$ , see Fig. 1), it is possible to verify that during the heating there is no significant expansion.

With regard to shrinkage as heating begins, the volume oscillation may be associated with the release of water associated with clay minerals and the dehydration of the iron hydroxides. The dilations also occur, due to the natural response of the ceramic body to the increase in temperature.

From around 150 to 200 °C there is a progressive and considerable expansion up to 500 °C, at which transformation from quartz  $\alpha$  to quartz  $\beta$  occurs. Subsequently,



Firing Temperature (°C)	Average (%)	Standard Deviation (%)
650	21.03	0.60
750	22.56	0.53
850	21.54	0.21
950	21.24	0.05
1050	21.32	0.30

Fig. 15 Porosity variation as a function of the firing temperature

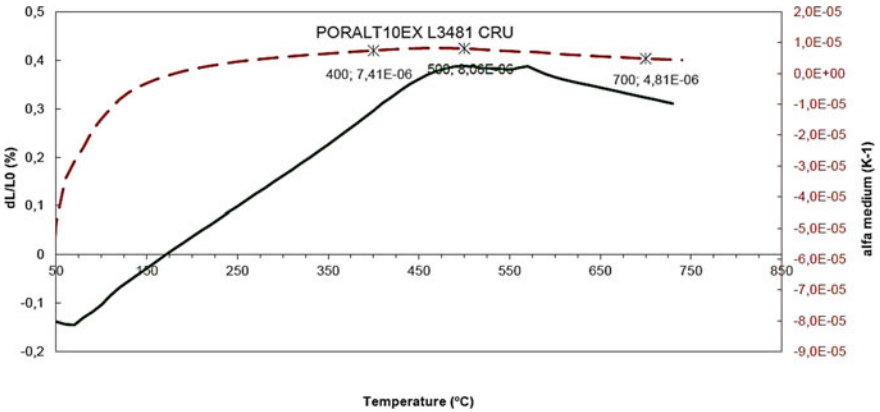


Fig. 16 Dilatometric test performed on ceramic paste until 740 °C

a slight stabilization between 500 and 600 °C is observed. This stabilization level is related to a strongly illitic composition of the raw materials and to the difficulty of releasing the strongly bound structural water. After stabilization, a slight retraction of the ceramic body occurs up to 750 °C.

## 4 Conclusions

The manufacture of porcelain parts depends on numerous variables from the choice of raw material, forming process, drying and firing cycles, which determines the final properties of the products. In this work, some relevant parameters of the ceramic paste used in the conformation of plates and cups were studied and tests were carried out on the various stages of the manufacturing process to determine the final porosity before glazing as a function of temperature.

### Tests carried out on the ceramic paste (raw material)

The hardness and moisture determination, revealed small deviations between the experimental value and the one indicated by the supplier, however they are still adequate for the conformation process. It must be kept in mind that the ceramic paste, sometimes, remains stored for a few days until its use which changes the hardness and moisture, and this case these values should be controlled to confirm that they are still suitable for forming.

### Tests on parts—moisture

After the shaping operation, it was concluded that moisture values are as expected, since the ceramic paste enters the conformation with moisture percentages around 22%, and less than the heat provided by the forming head, which is very residual, the parts (plates and cups) keep the same levels of moisture. It is verified that after passing through the 1st dryer, the plates lose approximately 4.2% moisture and the cups only 2.7%. After drying in the second dryer the percentage of moisture is reduced to 0.38% for both cups and dishes (less than 2% suitable for the pieces before they are fired). These values may be too low and cause cracks and fissures to appear during firing.

### Ratio between firing temperature and water absorption/porosity of cooked parts

The temperature of 850 °C produces parts with suitable porosity for subsequent glazing and therefore it is not necessary to use higher temperatures.

**Acknowledgements** The author(s) disclosed receipt of the following financial support for the research, authorship, and/or publication of this article: Project NORTE-01-0145-FEDER-000022 SciTech Science and Technology for Competitive and Sustainable Industries, cofinanced by Programa Operacional Regional do Norte (NORTE2020), through Fundo Europeu de Desenvolvimento Regional (FEDER).

## References

1. Powel, H.: *The Pottery Handbook Of Clay, Glaze and Colour*. Blandford Press (1967)
2. Hlavac, J.: *The Technology of Glass and Ceramics—An Introduction*. Elsevier (1983)
3. Kingery, W.D., et al.: *Introduction to Ceramics*. Wiley (1975)
4. *Enciclopédia Luso-Brasileira de Cultura*. Edição Século XXI. Verbo (1963)
5. Schneider, S.J.: *Engineered Materials Handbook—Ceramics and Glass*, vol. 04. ASM International (1991)

6. Motta, J.F.M., et al.: As Matérias-Primas Cerâmicas. Parte I: O Perfil das Principais Indústrias Cerâmicas e seus Produtos. *Cerâmica Industrial* **6**(2), 28–39 (2001)
7. Echeverrigaray, S.G., et al.: Low-valued raw materials challenge the common eligibility criteria for triaxial ceramics. *Ceram. Int.* **42**(9), 10671–10681 (2016)
8. Güngör, F., Ay, N.: The effect of particle size of body components on the processing parameters of semi transparent porcelain. *Ceram. Int.* **44**(9), 10611–10620 (2018)
9. [http://www.quartzpage.de/gen\\_mod.html](http://www.quartzpage.de/gen_mod.html)
10. Rodrigues, C.M.V.: *Optimização da Barbotina para Enchimento de Alta Pressão de Artigos de Porcelana*. Master Thesis, Universidade de Aveiro (2009) (in Portuguese)
11. Oliveira, C.S.: *Controlo estatístico - Indústria Cerâmica*. Master Thesis, Departamento de Química Universidade de Coimbra (2012) (in Portuguese)
12. [http://www.springwise.pt/uploadedfiles/ProductsFiles\\_219\\_tvD0Q.jpg](http://www.springwise.pt/uploadedfiles/ProductsFiles_219_tvD0Q.jpg)
13. Schindler, K., et al.: Wet-pressing of handles in table porcelain manufacturing. In: *Refereed Reports IX Conference & Exhibition of the European Ceramic Society*, J. Eur. Ceram. Soc. **27**(2), 1889–1892 (2007)
14. Fonseca, A.T.: *Tecnologia do processamento Cerâmico*. Universidade Aberta (2000) (in Portuguese)
15. Neklyudova, T.L., Zakharov, A.: Effect of the molding method on the structure of porcelain articles. *Glass Ceram.* **70**(7/8), 260–264 (2013)
16. Norton, F.H.: *Ceramica fina, tecnología Y aplicaciones*. Edições ómega S.A. (1988) (in Spanish)
17. Barsoum, M.W.: *Fundamentals of Ceramics*. McGraw-Hill Company, Inc. (1997)
18. German, R.M.: *Sintering and Practice*. Wiley (1996)
19. Bailey, M.: Changes in clay during firing. *Ceram. Rev.* **259**, 64–67 (2013)
20. Laita, E., Bauluz, B.: Mineral and textural transformations in aluminium-rich clays during ceramic firing. *Appl. Clay Sci.* **152**, 284–294 (2018)
21. Technical data sheet, Glaze VDAT 10T
22. Martín-Márquez, J., et al.: Effect of firing temperature on sintering of porcelain stoneware tiles. *Ceram. Int.* **34**(8), 1867–1873 (2008)
23. Oliveira, J.O., Labrincha, J.A.: *Esmaltes e Engobes para Monoporosa*. *Cerâmica Industrial* **7**(2) (2002) (in Portuguese)
24. Anusavice, K.J., Lee, R.B.: Effect of firing temperature and water exposure on crack propagation in unglazed porcelain. *J. Dent. Res.* **68**(6), 1075–1081 (1989)
25. Loginov, V.M., et al.: Influence of porcelain production conditions on its whiteness. *Glass Ceram.* (English translation of *Steklo i Keramika*) **46**(1–2), 10–12 (1989)
26. Pereira, P.: *Análise e melhoria do processo de fabrico de louça de hotelaria*, Master Thesis, FEUP, UPorto (2018) (in Portuguese)
27. [www.mota-sc.com](http://www.mota-sc.com), Setembro (2010)
28. CENCAL – Centro de Formação Profissional para a Indústria Cerâmica. *Procedimentos de Controlo de Processo*. Serviços Técnicos (2008) (in Portuguese)
29. Alves, T.F.L.P.: *Formulação de Pastas Cerâmicas a partir de Matérias-Primas Argilosas dos Concelhos de Vila Viçosa e Redondo para a Produção de Olaria Tradicional*. Tese de Mestrado, Departamento de Geociências Universidade de Évora (2015) (in Portuguese)
30. Gomes, C.F.: *Argilas – o que são e para que servem*. Fundação Calouste Gulbenkian (1988)

# **Part IV**

## **Composites**

# Design and Characterization of Porous Collagen/Gelatin/Hydroxyethyl Cellulose Matrices Containing Microspheres Based on $\kappa$ -Carrageenan



J. Kozłowska, K. Pauter, J. Skopinska-Wisniewska and A. Sionkowska

**Abstract** Polymeric microspheres have a wide range of medical and cosmetic applications and synthesis of these microparticles is the subject of numerous studies. The strategy of incorporating polymer microspheres into three-dimensional matrices to construct controlled-release materials have been attracting increased attention in recent years. The aim of this study was to obtain new materials by means of incorporating polymer microparticles (containing *Calendula officinalis* flower extract) in the three-dimensional polymer matrix with a porous structure. The microspheres were produced from  $\kappa$ -carrageenan,  $\kappa$ -carrageenan with addition of locust bean gum or sorbitol by extrusion and 2-phase emulsion methods. In the next step, microspheres were incorporated into a collagen/gelatin/hydroxyethyl cellulose matrix and materials were cross-linked using EDC/NHS mixture. The mechanical properties (Young's modulus) of the obtained materials were characterized. The porous polymeric matrices combined with  $\kappa$ -carrageenan microparticles may become the basis for a new cosmetic or dermatological formulation. The size of the microparticles, their composition and quantity have a significant influence on their mechanical properties.

**Keywords** Microspheres · Microencapsulation ·  $\kappa$ -carrageenan  
*Calendula officinalis* flower extract · Polymeric matrices

## 1 Introduction

Microencapsulation is a relatively new and dynamically developing technique. Microencapsulation technology can be defined as the incorporation process, i.e. closure of an active substance using thin polymer coatings, resulting in small particles referred to as microcapsules or microspheres [1, 2]. The incorporated active sub-

---

J. Kozłowska (✉) · K. Pauter · J. Skopinska-Wisniewska · A. Sionkowska  
Faculty of Chemistry, Department of Chemistry of Biomaterials and Cosmetics, Nicolaus Copernicus University in Torun, Gagarina 7, 87-100 Torun, Poland  
e-mail: [justynak@chem.umk.pl](mailto:justynak@chem.umk.pl)

© Springer Nature Switzerland AG 2019  
L. F. M. da Silva (ed.), *Materials Design and Applications II*, Advanced Structured Materials 98, [https://doi.org/10.1007/978-3-030-02257-0\\_12](https://doi.org/10.1007/978-3-030-02257-0_12)



stance is called the core material and the material that surrounds the encapsulated component is named a coating, shell or wall material [3].

Microencapsulation is mainly used in areas where particular attention is paid to the stability, efficiency and bioactivity of the obtained materials [4]. This technique is used, among others things, in the pharmaceutical, medical, food and cosmetics industries. The quality of the obtained microparticles is influenced by many factors, including: appropriate choice of wall material (shell), type of the core, as well as microencapsulation methods [5]. The synthesis and characteristics of polymer microparticles are the subject of numerous studies [6–9].

The pot marigold flower extract (*Calendula officinalis* flower extract) can be used as the internal phase of the microparticles. It is a one-year-old herbaceous plant with large orange-yellow flowers. The phytopharmacological studies of marigold flower extract confirm its anti-inflammatory and antiviral activity. In addition, marigold extract contains salicylic acid with a bactericidal and fungicidal properties [10, 11].

The shells based on natural polymers are relatively popular [12–14]. Carrageenan is often used in the encapsulation technique [15–17]. This polysaccharide is obtained by the extraction of some red marine algae (Rhodophyceae). Due to a number of interesting features such as: biocompatibility, biodegradability, high water absorption capacity, as well as good mechanical properties, this polymer has found wide application in various fields, including: medicine, tissue engineering, cosmetics industry, biotechnology, horticulture, as well as agriculture [18–20].

The aim of this paper is to obtain and characterize the mechanical properties of composite materials for potential cosmetic or dermatological applications. The materials were prepared by incorporating polymer microparticles (containing plant extract) in the three-dimensional polymer matrix with a porous structure. The microspheres were produced from carrageenan and carrageenan with addition of locust bean gum or sorbitol through the emulsion and extrusion method. In the next step, microspheres were incorporated into a collagen/gelatin/hydroxyethyl cellulose matrix. As an active compound used in pharmacy and cosmetics, pot marigold (*Calendula officinalis*) flower extract was loaded into the microspheres.

## 2 Materials and Methods

### 2.1 Microencapsulation Procedure

Carrageenan-based microspheres were prepared by extrusion and water-in-oil emulsion described by Muthukumarasamy et al. with modifications [21].  $\kappa$ -carrageenan, locust bean gum and sorbitol (Sigma-Aldrich Co., Poznań, Poland) were used as wall materials for microencapsulation of 0.1% *Calendula officinalis* flower extract (Provit S.A., Barcelona, Spain). 1.5% (w/v) carrageenan and 1.5% (w/v) carrageenan plus 0.1% (w/v) locust bean gum (LBG) or 1.5% (w/v) carrageenan plus 20% (w/v) sor-

bitol were used for microencapsulation by both extrusion and a 2-phase (water/oil) emulsion system.

$\kappa$ -carrageenan-based wall materials were maintained at 40 °C to prevent solidification. Extrusion was performed by expression of the wall material/*Calendula officinalis* flower extract mixture through a syringe needle ( $\varnothing = 0.6$  mm) dropwise into 0.5 M CaCl<sub>2</sub>. Microspheres were held at 25 °C for 30 min to ensure complete solidification and then they were separated by filtration through Whatman nr 4 filter paper.

The (phase separation) method involved adding 1 part of wall material (with added extract) to 5 parts of paraffin oil (mineral oil) (v/v) (P. P. H. Stanlab, Lublin, Poland) containing 0.02% tween 80 (Sigma Aldrich, Poznan, Poland.). The mixture was warmed to 40 °C and stirred at 800 rpm for 5 min using a mixer (IKA®, model T25 digital ULTRA—TURRAX) to form a uniform water-in-oil emulsion. The dispersed polymer was allowed to cool to 25 °C to form microspheres. Then 0.5 M CaCl<sub>2</sub> was added at the sides of the beaker until the emulsion was completely broken. The beads formed were collected by vacuum filtration through Whatman nr 4 filter paper.

## 2.2 *Production of Collagen/Gelatin/Hydroxyethyl Cellulose Matrices Incorporating $\kappa$ -Carrageenan-Based Microcapsules*

Collagen (col) type I was obtained in our laboratory from fish scales of *Esox lucius* [22]. Gelatin type A (gel), hydroxyethyl cellulose (hec), carbodiimide (EDC), N-hydroxysuccinimide (NHS) were purchased from Sigma-Aldrich (Poznań, Poland).

To prepare microsphere-loaded matrices, 0.15 or 1.5 of microbeads were mixed with 15 ml collagen suspension (0.5% w/v), 15 ml aqueous gelatin type A solution (0.5% w/v), and hydroxyethyl cellulose (0.15 g), and magnetically stirred for 30 min. The weight ratio of collagen and gelatin to microspheres was 1:1 or 1:10. Then, the mixtures were frozen (−20 °C) and lyophilized (−55 °C, 5 Pa, 24 h). After lyophilisation, matrices were cross-linked using a cross-linking mixture. The chemical modification of the samples was carried out in 96% ethanol in the presence of 50 mM EDC and 25 mM NHS at room temperature for 4 h. After this time, the matrices were washed with 0.1 M Na<sub>2</sub>HPO<sub>4</sub> (washing was done for 2 h, changing the solution after 1 h). To remove the residue of the cross-linking mixture, the samples were washed 4 times with distilled water (washing performed for 2 h, changing the water every 30 min). The cross-linked matrices were frozen (−20 °C) and lyophilized (5 Pa, −55 °C, 48 h). A matrix without microspheres was used as a control sample.

### 2.3 Mechanical Properties

Cylindrical samples with a diameter of ~16 mm and a height of ~21 mm were produced for mechanical testing by placing each of col/gel/hec and  $\kappa$ -carrageenan-based microsphere mixtures into polystyrene cylindrical containers, freezing and freeze drying. All the testing was carried out using a mechanical testing machine (Z.05, Zwick/Roell, Germany) at room temperature. Dry samples, as well as samples soaked in PBS buffer at pH 5.7 were used for the analysis. Prior to the measurements, the samples were carefully measured (diameter and height). Next, the samples were placed between the compression plates of a computer-controlled testing machine and they were pressed with the cross-head speed set at 2 mm min<sup>-1</sup> to 10% deformation of the material. The results were recorded using the testXpert II computer program. The compressive modulus (Young's modulus,  $E_c$ ) was calculated from the slope of the stress-strain curve in the linear region (strain from 0.05 to 0.25%). The presented values are the average values calculated from five measurements for each type of matrix.

## 3 Results

Porous collagen/gelatin/hydroxyethyl cellulose-based composites were fabricated by using freeze-drying method. The microspheres obtained by extrusion method have significantly larger sizes than the microspheres obtained by emulsion method (Table 1).

Stress-strain curves for all the samples were similar and they were linearly shaped to 10% deformation of the material (results not shown). The measurement of the compressive modulus was carried out for dry col/gel/hec-based matrices. The results summarized in Tables 2 and 3 are the average of five measurements for each type of sample.

It can be observed that the incorporation of microspheres obtained by extrusion into col/gel/hec matrices has a significant effect on the mechanical properties of the studied materials. The Young's modulus of the control sample was ~5.23 kPa and after

**Table 1** The size of obtained microparticles (swollen and dry)

Type of microsphere	Size of microspheres [ $\mu\text{m}$ ]			
	Extrusion method		Emulsion method	
	Swollen	Dry	Swollen	Dry
Carrageenan	962 $\pm$ 13	730 $\pm$ 9	262 $\pm$ 12	187 $\pm$ 11
Carrageenan/locust bean gum	1042 $\pm$ 5	923 $\pm$ 7	398 $\pm$ 9	213 $\pm$ 4
Carrageenan/sorbitol	1165 $\pm$ 8	1080 $\pm$ 7	417 $\pm$ 8	332 $\pm$ 7

**Table 2** Compressive modulus of matrices with incorporated microspheres prepared by extrusion

Matrices with incorporated microspheres (the type of microspheres)	$E_c \pm SD$ [kPa]	
	1:1	1:10
Control sample	$5.23 \pm 0.94$	$5.23 \pm 0.94$
Carrageenan	$6.72 \pm 0.67$	$8.73 \pm 0.59$
Carrageenan/locust bean gum	$6.00 \pm 0.93$	$7.03 \pm 1.10$
Carrageenan/sorbitol	$5.70 \pm 1.31$	$6.71 \pm 1.06$

**Table 3** Compressive modulus of matrices with incorporated microspheres prepared by emulsification method

Matrices with incorporated microspheres (the type of microspheres)	$E_c \pm SD$ [kPa]	
	1:1	1:10
Control sample	$5.23 \pm 0.94$	$5.23 \pm 0.94$
Carrageenan	$5.38 \pm 0.99$	$5.25 \pm 0.61$
Carrageenan/ locust bean gum	$5.48 \pm 0.23$	$5.61 \pm 0.80$
Carrageenan/sorbitol	$5.48 \pm 0.41$	$5.99 \pm 0.97$

an addition of microparticles to the matrix, the values of Young's modulus were much higher. The highest value of the compression module was observed for the matrix containing carrageenan microspheres, whereas a carrageenan/sorbitol microsphere-loaded matrix had lower stiffness. The values of Young's modulus were higher for matrices with a higher content of microparticles.

However, in the case of matrices containing microparticles obtained by emulsion method, we have observed that the incorporation of microspheres into polymeric matrices does not have a significant effect on the mechanical properties of these materials. With the increase of the quantity of microspheres in this matrix, the stiffness of the material was slightly higher.

## 4 Conclusions

Carrageenan-based microspheres with spherical shape were synthesized by different methods with particle sizes ranging  $\sim 187$ – $1080 \mu\text{m}$  (after lyophilisation). Porous three-dimensional collagen/gelatin/hydroxyethyl cellulose matrices containing different amounts of microspheres were fabricated and characterized. The size of the microspheres depends primarily on the method of their obtaining. Microspheres obtained by extrusion were much larger than those obtained by emulsion tech-

nique. Moreover, the size of the incorporated particles also affects the stiffness of the obtained materials. After adding the larger microparticles to the matrix the values of Young's modulus were increased. In addition, the composition of the wall material plays an important role. Thus, during the designing of three-dimensional polymeric materials containing incorporated microparticles, we can influence their mechanical parameters by adjusting the size of the used microparticles, their composition and quantity.

**Acknowledgements** Financial support from National Science Centre (NCN, Poland) Grant no. UMO-2016/21/D/ST8/01705 is gratefully acknowledged.

## References

1. Wang, Q., Li, J., Xu, T., Lu, X., Zhi, W., Weng, J.: Porous hydroxyapatite scaffolds containing dual microspheres based on poly(lactide-co-glycolide) and chitosan for bone regeneration. *Mater. Lett.* **188**, 387–391 (2017)
2. Mao, S., Guo, C., Shi, Y., Li, L.C.: Recent advances in polymeric microspheres for parenteral drug delivery—Part 2. *Expert Opin. Drug Deliv.* **9**, 1209–1223 (2012)
3. Hossain, K.M.Z., Patel, U., Ahmed, I.: Development of microspheres for biomedical applications: a review. *Prog. Biomater.* **4**, 1–19 (2015)
4. Jyothi, N.V., Prasanna, P.M., Sakarkar, S.N., Prabha, K.S., Ramaiah, P.S., Srawan, G.Y.: Microencapsulation techniques, factors influencing encapsulation efficiency. *J. Microencapsul.* **27**, 187–197 (2010)
5. Das, S.K., David, S.R.N., Rajabalaya, R., Mukhopadhyay, H.K., Halder, T., Palanisamy, M., Khanam, J.: Microencapsulation techniques and its practice. *Int. J. Pharm. Pharm. Sci.* **6**, 1–23 (2011)
6. Devi, N., Sarmah, M., Khatun, B., Maji, T.: Encapsulation of active ingredients in polysaccharide-protein complex coacervates. *Adv. Colloid Interface Sci.* **239**, 136–145 (2017)
7. Midha, K., Nagpal, M., Arora, S.: Microspheres: a recent update. *Int. J. Recent. Sci. Res.* **8**, 5859–5867 (2015)
8. Kozłowska, J., Stachowiak, N., Sionkowska, A.: Collagen/gelatin/hydroxyethyl cellulose composites containing microspheres based on collagen and gelatin: design and evaluation. *Polymers* **10**, 1–16 (2018)
9. Freiberg, S., Zhu, X.X.: Polymer microspheres for controlled drug release. *Int. J. Pharm.* **282**, 1–18 (2004)
10. Jan, N., Andrabi, K.I., John, R.: *Calendula officinalis*—an important medicinal plant with potential biological properties. *Proc. Indian Natl. Sci. Acad.* **83**, 769–787 (2017)
11. Basch, E., Bent, S., Foppa, I., Haskmi, S., Kroll, D., Marigold (*Calendula officinalis* L.): An evidence-based systematic review by the natural standard research collaboration. *J. Herb. Pharmacother.* **6**, 135–159 (2006)
12. Singh, M.N., Hemant, K.S.Y., Ram, M., Shivakumar, H.G.: Microencapsulation: A promising technique for controlled drug delivery. *Res. Pharm. Sci.* **5**, 65–67 (2010)
13. Gasperini, L., Mano, J.F., Reis, R.L.: Natural polymers for the microencapsulation of cells. *J. R. Soc. Interface* **11**(20140817), 1–19 (2014)
14. Rodrigues, F.J., Omura, M.H., Cedran, M.F., Dekker, R.F.H., Barbosa-Dekker, A.M., Garcia, S.: Effect of natural polymers on the survival of *Lactobacillus casei* encapsulated in alginate microspheres. *J. Microencapsul.* **34**, 431–439 (2017)
15. Gbassi, G.K., Vandamme, T.: Probiotic encapsulation technology: From microencapsulation to release into gut. *Pharmaceutics* **4**, 149–163 (2012)

16. Suzuki, S., Lim, J.K.: microencapsulation with carrageenan-locust bean gum mixture in a multiphase emulsification technique for sustained drug release. *J. Microencapsul.* **11**, 197–203 (1994)
17. Scremin, F.R., Veiga, R.S., Silva-Buzanello, R.A., Becker-Algeri, T.A., Corso, M.P., Torquato, A.S., Bittencourt, P.R.S., Flores, E.L.M., Canan, C.: Synthesis and characterization of protein microcapsules for eugenol storage. *J. Therm. Anal. Calorim.* **131**, 653–660 (2018)
18. Shori, A.B.: Microencapsulation improved probiotics survival during gastric transit. *HAYATI J. Biosci* **24**, 1–5 (2017)
19. Stenner, R., Matubayasi, N., Shimizu, S.: Gelation of carrageenan: effects of sugars and polyols. *Food Hydrocoll.* **54**, 284–292 (2016)
20. Necas, J., Bartosikova, L.: Carrageenan: a revive. *Vet. Med.* **58**, 187–205 (2013)
21. Muthukumarasamy, P., Allan-Wojtas, P., Holley, R.A.: Stability of *Lactobacillus reuteri* in different types of microcapsules. *J. Food Sci.* **71**, M20–M24 (2006)
22. Kozłowska, J., Sionkowska, A., Skopińska-Wiśniewska, J., Piechowicz, K.: Northern pike (*Esox lucius*) collagen: extraction, characterization and potential application. *Int. J. Biol. Macromol.* **81**, 220–227 (2015)

# Effects of Fiber Treatment on the Properties of Epoxy Curaua-Reinforced Composites



F. C. Amorim, J. F. B. Souza and J. M. L. Reis

**Abstract** Natural fiber research is getting attention worldwide due to its sustainability and ecofriendly nature. It combines low density and interesting properties. Curaua fiber is an abundant natural fiber, which has low cost and several applications. The mechanical properties have a strong dependence on the interface adhesion between the fiber and the polymer matrix. In this work, surface modifications induced by sodium hydroxide (NaOH) on Curaua fibers were studied in order to investigate NaOH as a chemical agent in fiber reinforced epoxy polymer composites. Raw fibers were treated with 1%, 3% and 5 wt% sodium hydroxide solution for different periods of time (24, 72 and 168 h) at room temperature. Specimens of treated Curaua/Epoxy composites were tested and compared in tensile and in flexion to observe the mechanical properties. DMA analyses were performed to evaluate the composites physical properties due to temperature variation. Results showed that fibers treated with 5% of sodium hydroxide for 72 h produced improved superficial roughness increasing mechanical properties. The results also showed an increase in the viscoelastic stiffness of the epoxy matrix by the incorporation of Curaua fibers.

**Keywords** Natural fibers · NaOH treatment · Mechanical properties

## 1 Introduction

The studies of natural fibers as reinforcement of polymeric composite structures have been developing in the past few years. The lignocellulosic fibers are a type of green material that has been used considering some advantages over synthetic fibers,

---

F. C. Amorim · J. F. B. Souza · J. M. L. Reis (✉)

Laboratory of Theoretical and Applied Mechanics, Graduate Program in Mechanical Engineering, Universidade Federal Fluminense, Rua Passo Da Pátria 156, Niterói, RJ 24210-240, Brazil  
e-mail: [jreis@id.uff.br](mailto:jreis@id.uff.br)

F. C. Amorim

Department of Mechanical Engineering, Federal Center for Technological Education of Rio de Janeiro, CEFET-RJ, UnED Itaguaí, Itaguaí, RJ, Brazil

© Springer Nature Switzerland AG 2019

L. F. M. da Silva (ed.), *Materials Design and Applications II*, Advanced Structured Materials 98, [https://doi.org/10.1007/978-3-030-02257-0\\_13](https://doi.org/10.1007/978-3-030-02257-0_13)

such as: low cost, low specific mass, considerable specific strength, low energy consumption, renewable and biodegradability resource [1–3].

Curaua fiber (*Ananas erectifolius*) is a Brazilian fiber developed in the Amazon region (Pará state). Given the competitive industrial market, the research for new materials is more frequent. Considering the fact that the natural fibers can meet great mechanical and chemical properties with low cost and weight, they have been used in place of synthetic fibers as glass and carbon.

Lignocellulosic fibers gain attention in many industrial areas such as automotive, aerospace and construction. Especially the automobile sector constantly seeks to reduce the weight and the emissions of carbon dioxide through the manufacture of its interior components based on natural fibers [4].

Natural fiber polymer composites are materials composed of two phases: polymeric matrix and fibers. Polymeric matrix (thermosets or thermoplastics) protects the fibers against the environmental or chemical factors. The fibers with superior mechanical strength can support the load. An important mechanical aspect of composites is the load transfer by the matrix to the fibers.

In order to achieve a good performance of composite material, the correct adhesion between fiber and matrix is required. The drop in interfacial mechanical properties between composite parts commonly decreases the fibers ability as reinforcing component. Some characteristics of the natural fibers, are related to the composition (cellulose, hemicellulose, lignin and waxes) and the elevated capacity of moisture absorption, which contribute to the weak adhesion between the polymeric matrix and fibers. The properties of natural fibers have a strong dependency of its chemical composition [5–7].

A great challenge of composite reinforced with natural fibers is the bonding process between fiber and matrix. With a view to improving the adhesion between the composite phases, surface treatments are needed, in order to remove the residues such as waxes and other non-cellulosic substances that promote poor adhesion between hydrophobic epoxy resin and hydrophilic fibers [8, 9].

The treatment with NaOH solution contributes to remove the residues at the interface region of fibers, improving the mechanical properties of the composite.

In this study the mechanical properties, tensile and flexural properties of Curaua/Epoxy composites with Curaua fibers treated with a different %wt NaOH solution are investigated and also its viscoelastic behavior from very low temperatures,  $-50\text{ }^{\circ}\text{C}$ , to elevated ones,  $180\text{ }^{\circ}\text{C}$ . Viscoelastic behavior was evaluated by Dynamic Mechanical analysis and also the glass transition temperature.



## 2 Materials and Methods

### 2.1 Surface Treatment with NaOH

The Curaua fibers were treated with different NaOH concentrations (1%, 3% and 5 wt%) and immersion time (24, 72 and 168 h) at room temperature. These parameters were combined forming a  $3 \times 3$  result matrix. Thereafter, the Curaua fibers were washed in running water for 30 min (post-treatment), dried in an electric oven at 80 °C for 24 h and the fibers were reprocessed. Figure 1 shows the NaOH fiber treatment and it is possible to see that 5 wt% NaOH solution removes more residues than others concentrations at the same immersion period.

### 2.2 Materials

To produce the Curaua/Epoxy composite, the natural treated fibers and polymeric resin were mixed with 50% of fiber content, placed in the 200 mm  $\times$  200 mm  $\times$  4 mm steel frame mold and cured for 7 days at room temperature before testing. The composite material was post-cured for 8 h at 80 °C in order to speed up the curing process and improve mechanical properties of composite. Subsequently, the flexural and tensile samples were produced according to standards.

The polymeric epoxy resin used in this study was provided by Epoxyfiber®. Based on diglycidyl ether of bisphenol A and an aliphatic amine hardener. The



**Fig. 1** Fiber treatment

**Table 1** Properties of epoxy resin at room temperature

Property	Epoxy
Viscosity at 25 °C $\mu$ (mPa s)	12,000–13,000
Density $\rho$ (g/cm <sup>3</sup> )	1.16
Heat distortion temperature HDT (°C)	100
Modulus of elasticity E (GPa)	5.0
Flexural strength (MPa) (ASTM D790)	60
Tensile strength (MPa) (ASTM D638)	73
Maximum elongation (%)	4

**Fig. 2** Curaua fibers

epoxy resin has low viscosity and the mix ratio to hardener of 4:1. Resin properties by the manufactures are shown in Table 1.

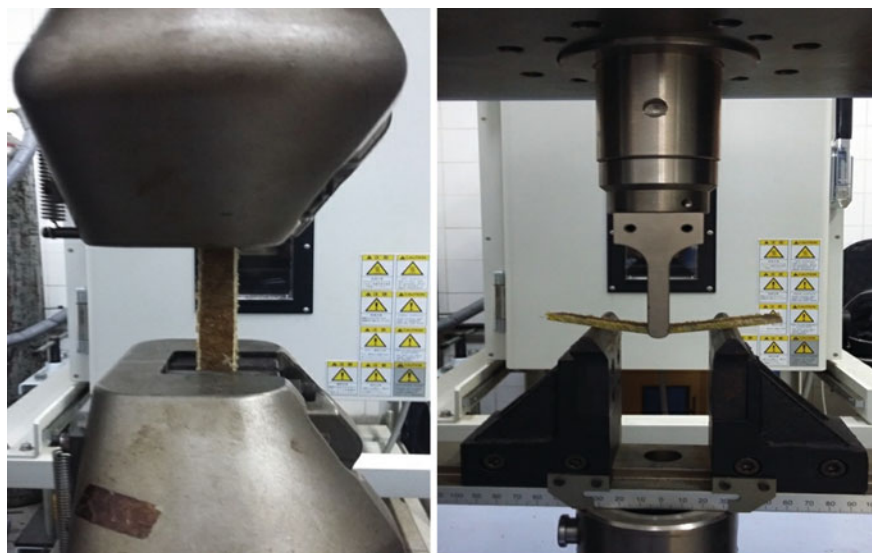
Curaua fiber (*Ananas erectifolius*) from Pará state is a type of lignocellulosic fiber. The fiber has a diameter of 50  $\mu$ m and a length of 6 mm and the aspect ratio (L/D) is 120. The Curaua fibers are shown in Fig. 2. The mechanical properties of Curaua fiber are presented in Table 2.

### 2.3 Methods

Mechanical tensile and flexural tests for different weight % NaOH treated Curaua fibers were performed by Shimadzu®AG-X universal testing machine according to ASTM D3039/D3039 M-14 [11] and ASTM D790-10 [12], respectively. The tensile tests were performed with a cross-head speed of 2 mm/min and the three-point

**Table 2** Properties of Curaua fiber [10]

Property	Curaua
Density $\rho$ (g/cm <sup>3</sup> )	1.4
Modulus of elasticity E (GPa)	11.8
Tensile strength (MPa) (ASTM D638)	500–1150
Maximum elongation (%)	3.7–4.3
Fiber diameter ( $\mu\text{m}$ )	50
Fiber length (mm)	6

**Fig. 3** Tensile and flexural test set-up

bending with a speed of 1.5 mm/min. Four specimens were tested for each type of mechanical testing. Figure 3 shows the tensile and three-point bending set-up for Curaua/Epoxy tests.

The dynamic mechanical analysis—DMA was used for measuring the temperature influence in elastic properties of all formulations of natural fiber composite. Tests were performed with three-point bending configuration and the span of the supports was 40 mm, according to ASTM D7028 [13]. The samples were scanned from  $-50$  to  $180$  °C with a heating rate of  $2$  °C/min at different frequencies: 0.01, 0.1, 1, 10 and 100 Hz.

**Table 3** Tensile properties of Curaua/Epoxy composite

	Maximum tensile strength (MPa)			Young's modulus (GPa)		
	24 h	72 h	168 h	24 h	72 h	168 h
1%	26.90 ± 1.64	28.00 ± 2.59	24.66 ± 2.43	2.86 ± 0.07	2.50 ± 0.11	2.49 ± 0.13
3%	26.99 ± 3.41	28.67 ± 3.82	27.37 ± 1.63	2.87 ± 0.23	2.71 ± 0.26	2.70 ± 0.12
5%	29.21 ± 2.28	30.21 ± 4.28	27.94 ± 0.82	2.89 ± 0.20	2.73 ± 0.13	2.74 ± 0.04

**Table 4** Flexural properties of Curaua/Epoxy composite

	Maximum flexural strength (MPa)			Flexural modulus (GPa)		
	24 h	72 h	168 h	24 h	72 h	168 h
1%	60.24 ± 4.55	61.62 ± 5.36	57.12 ± 4.05	4.76 ± 0.47	5.03 ± 0.28	4.66 ± 0.38
3%	60.41 ± 2.53	62.97 ± 3.21	59.09 ± 2.54	4.84 ± 0.36	5.03 ± 0.35	4.73 ± 0.41
5%	61.99 ± 6.16	63.30 ± 4.55	59.41 ± 4.14	5.29 ± 0.47	5.74 ± 0.57	4.03 ± 0.44

### 3 Results and Discussion

#### 3.1 Tensile and Flexural Experiments

The tensile and three-point bending test results of composite with Curaua fiber (50% fiber content) treated with different NaOH concentration (1%, 3% and 5 wt%) and immersion time (24, 72 and 168 h) are presented in Tables 3 and 4.

From Tables 3 and 4 it is visible that the tensile and flexural maximum strength and stiffness are dependent of NaOH concentration and immersion time. As NaOH wt% content increase the tensile and flexural modulus increase and tensile and flexural stiffness also increase. Although the immersion time improves the strength and stiffness of composite, there is an optimal time (72 h) where the properties reach their best values, after this period of time occurs the degradation of the Curaua fibers and thus the mechanical properties decrease.

Figure 4 shows the tensile stress versus strain curves for Curaua/Epoxy composite with 50% of fiber treated with 1, 3 and 5 wt% of NaOH treatment at a different immersion time (24, 72, 168 h).

The plots presented in Fig. 4 show a hard dependence on surface treatment and immersion time in NaOH solution. Both modulus of elasticity and maximum strength are treatment-dependent.

Figure 5 displays the three-point bending stress vs. strain curves for Curaua/Epoxy composite with 50% of fiber treated with 1, 3 and 5 wt% of NaOH treatment at a different immersion time (24, 72, 168 h).

The curves showed in Fig. 5 present the strong influence of chemical treatment with NaOH solution at different immersion period (24, 72, 168 h). Overall, composites reinforced with Curaua fibers immersed for 72 h in a 5% wt% aqueous solution are stiffer and high strength, tensile and flexural, compared to untreated Curaua fiber composites [14].

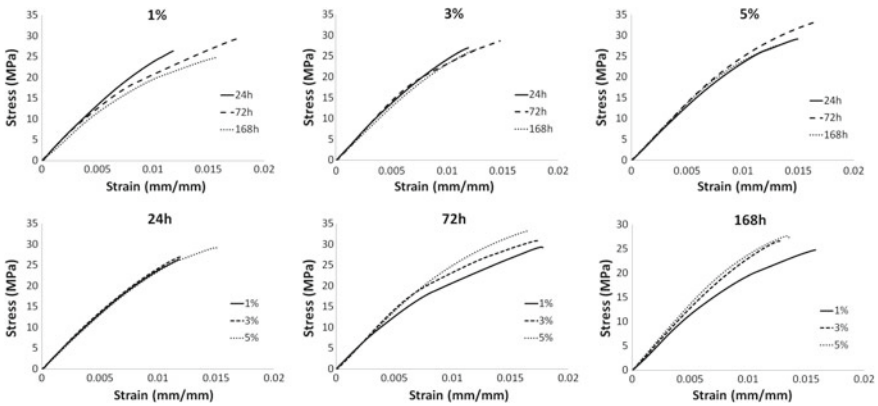


Fig. 4 Typical tensile stress versus strain curves of treated Curaua/Epoxy composite

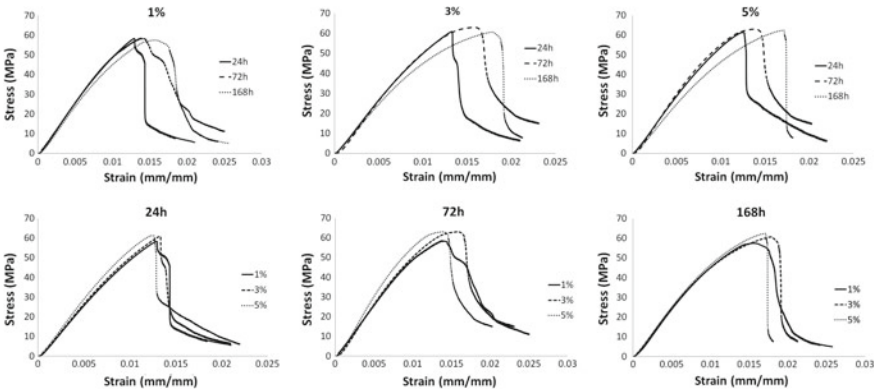


Fig. 5 Typical flexural stress versus strain curves of treated Curaua/Epoxy composite

### 3.2 Thermal Analysis—DMA

The DMA results of 1 Hz for 5 wt% of NaOH solution at different immersion time (24, 72 and 168 h) analysis are presented in Fig. 6. The specimens were tested under  $-50$  to  $180$  °C.

According to Fig. 6 it can be seen a typical  $E'$  dependence on temperature for crystalline material, with the first drop due to the glass transition. High crystallinity is due to high  $E'$  value. Table 5 shows the storage modulus ( $E'$ ), glass transition temperature ( $T_g$ ) and loss modulus ( $E''$ ) of Curaua/Epoxy composite with chemical treatment of 1, 3 and 5 wt% NaOH at different immersion periods (24, 72 and 168 h).

The increase in NaOH wt% up to 5% and immersion period for 72 h improve the storage modulus ( $E'$ ) and unaltered the glass transition temperature ( $T_g$ ). Higher loss modulus is also observed for the composites reinforced with Curaua fibers immersed

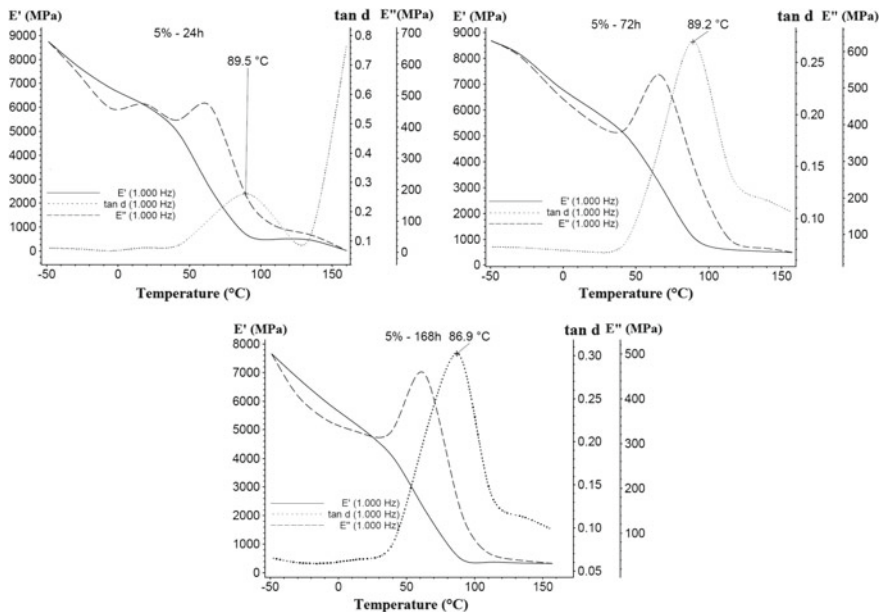


**Fig. 6** DMA results of treated Curaua/Epoxy composite with 5 wt% NaOH treatment

**Table 5** DMA test results of Curaua fiber composites

	Storage modulus $E'$ (GPa)			Glass temperature $T_g$ (°C)			Loss modulus $E''$ (GPa)		
	24 h	72 h	168 h	24 h	72 h	168 h	24 h	72 h	168 h
1%	4.65	5.46	3.91	83.4	89.0	85.3	1.18	1.60	0.98
3%	4.85	6.41	4.12	91.4	70.5	70.7	1.44	1.55	1.03
5%	5.59	6.83	4.31	89.5	89.2	86.9	1.47	1.84	1.30

in 5% of NaOH for 72 h. Loss modulus ( $E''$ ) or dynamic loss modulus, is related to the predisposition of the material to dissipate energy applied to it [15], a viscous response of the materials. The dynamic loss modulus is often associated with “internal friction” and is sensitive to different kinds of molecular motions, transitions, relaxation processes, morphology and other structural heterogeneities. Therefore, better surface treatment leads to increase fiber/matrix bonding resulting in better mechanical properties.

Figure 7 shows the viscoelastic behavior of composite material when it exhibits a dependency on test frequency; the elastic character is more evident at higher frequencies.

According to Fig. 7 it can be seen the viscoelastic response of Curaua/Epoxy composites with 5 wt% NaOH treatment for every immersion period. After all expo-

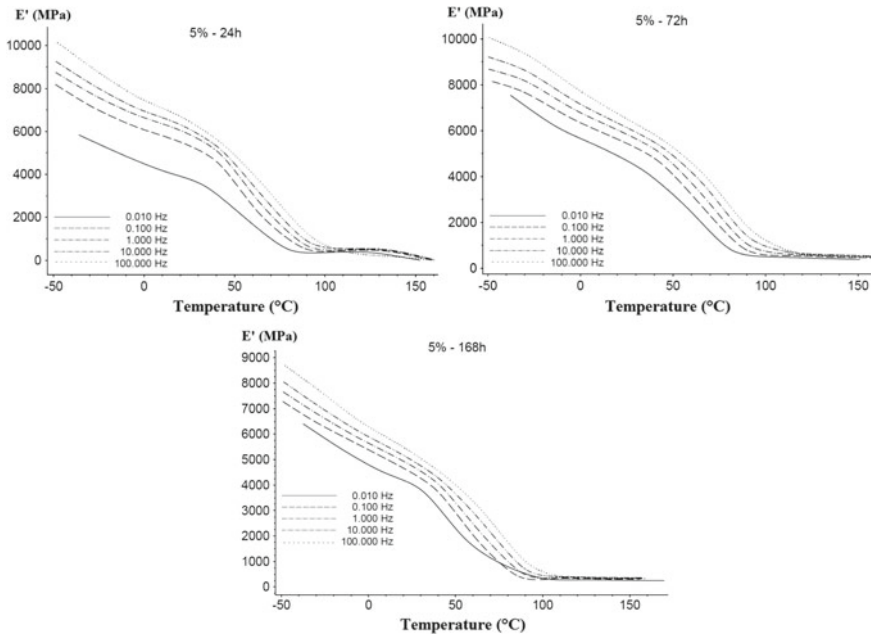


Fig. 7 Storage modulus ( $E'$ ) for different frequencies composite with 5 wt% NaOH treatment

sure periods, it can be observed that high frequencies led to higher storage modulus, which are related to the composite stiffness.

#### 4 Conclusions

In this work, a new composite material based on natural fiber was developed. The influence of fiber treatment with NaOH solution in Curaua/Epoxy composites was analyzed. The increase in NaOH content in a chemical solution and the increase in a period of immersion improve the tensile and flexural properties until the optimal time of the 72 h, after this time the degradation process of the fibers is more intense. The best NaOH concentration was 5 wt% since it removed all residues of the fibers and exhibited the good mechanical properties.

The DMA analysis shows that the DMA properties have a strong relation to the chemical treatment with NaOH and the immersion time. Extreme temperatures  $-50$  to  $180$   $^{\circ}\text{C}$  were used to measure stiffness and phase change of the composite. The resultant composite material exhibited the viscoelastic behavior when shows dependence on test rate. The elastic characteristics related to storage modulus ( $E'$ ) are more evident at higher frequencies.

Increase in fiber treatment NaOH concentration increase stiffness, tensile and flexural strength.

The results of the mechanical tests presented a good agreement between traditional and DMA flexural tests.

**Acknowledgements** The author would like to thank the Research Directorate of the Southern Office of Aerospace Research and Development (SOARD), Air Force Office of Scientific Research (AFOSR) for supporting the work presented here.

## References

1. Milanese, A.C., Cioffi, M.O.H., Voorwald, H.J.C.: Mechanical behavior of natural fiber composites. *Procedia Eng.* **10**, 2022–2027 (2011)
2. Saba, N., Tahir, P.M., Jawaid, M.: A review on potentiality of nano filler/natural fiber filled polymer hybrid composites. *Polymer* **6**, 2247–2273 (2014)
3. Malkapuram, R., Kumar, V., Yuvraj, S.N.: Recent development in natural fibre reinforced polypropylene composites. *J. Reinf. Plast. Compos.* **28**, 1169–1189 (2008)
4. Sain, M., Panthapulakkal, S.: Green fibre thermoplastic composites. In: *Polymer Composites and the Environment*. Woodhead Publishing, p. 181–206 (2014). ISBN 978-1-85573-739-6
5. Spinacé, M.A.S., Fermoseli, K.K.G., De Paoli, M.A.: Recycled polypropylene reinforced with curaua fibers by extrusion. *J. Appl. Polym. Sci.* **112**(6), 3686–3694 (2009)
6. Almeida Júnior, J.H.S., Amico, S.C., Botelho, E.C., Amado, F.D.R.: Hybridization effect on the mechanical properties of curaua/glass fiber composites. *Compos. Part B* **55**, 492–497 (2013)
7. Thiré, R.M.S.M., Cardoso, P.H.M., Bastian, F.L.: Curaua fibers/epoxy laminates with improved mechanical properties: effects of fiber treatment conditions. *Macromol. Symp.* **344**(1), 63–70 (2014)
8. Ku, H., Wang, H., Pattarachaiyakoop, N., Trada, M.: A review on the tensile properties of natural fiber reinforced polymer composites. *Compos. Part B* **42**(4), 856–873 (2011)
9. Ferreira, S.F., Pepe, M., Martinelli, E., Silva, F.A., Filho, R.D.T.: Influence of natural fibers characteristics on the interface mechanics with cement based matrices. *Compos. Part B* **140**, 183–196 (2018)
10. Faruk, O., Bledzki, A.K., Fink, H.P., Sain, M.: Biocomposites reinforced with natural fibers: 2000–2010. *Prog. Polym. Sci.* **37**, 1552–1596 (2012)
11. ASTM D3039/D3039 M-14. Standard Test method for Tensile Properties of Polymer Matrix Composite Materials (2014)
12. ASTM D790-10. Standard Test Methods for Flexural Properties of Unreinforced and Reinforced Plastics and Electrical Insulating Material (2010)
13. ASTM D7028-07. Standard Test Method for Glass Transition Temperature (DMA T<sub>g</sub>) of Polymer Matrix Composites by Dynamic Mechanical Analysis (DMA) (2007)
14. Amorim, F.C., Souza, J.F.B., Reis, J.M.L. The quasi-static and dynamic mechanical behavior of epoxy matrix composites reinforced with Curaua fibers. *Mat. Res.* **21** Epub (2018). ISSN 1980-5373
15. Jawaid, M., Abdul Khalil, H.P.S., Hassan, A., Dungani, R., Hadiyane, A.: Effect of jute fibre loading on tensile and dynamic mechanical properties of oil palm epoxy composites. *Compos. Part B Eng.* **45**(1), 619–624 (2013)



# **Part V**

## **Design**

# The Effect of the Position of Compression Screw in Plate-Screws Method Used in Fracture Treatment on Fatigue Strength of Joint



R. Cagri Kutlubay, Tezcan Sekercioglu and A. Cagdas Yorukoglu

**Abstract** A number of combination studies on the use of plate-screws, which has become a traditional method in fracture treatment, have been conducted to obtain a more rigid joint. These studies in the literature were reviewed and it was seen that the effect of the position of the compression screw, used with the aim of making the fracture line come closer to each other during fracture fixation, on the fatigue strength of the joint hasn't been investigated. Within the scope of this study, a screw combination study by including Limited Contact Dynamic Compression Plate (LC-DCP) plates that possess combined hole properties was carried out. Three different combinations were created during the study. In these combinations, the unlocked screw that was located on the part where the force was applied and that was used for compression was placed in different holes and fatigue strengths of the joints were investigated under dynamic bending force. As a result of the study, it was observed that as the compression screw moved away from the fracture line, fatigue strength of the joint consisting of plate, screw and bone decreased. In addition, it was found that all the joints in the 3rd combination got damaged as a result of the fracture of the bone.

**Keywords** Anatomic plate · Plate screw  
Limited contact dynamic compression plate (LCP) · Fatigue · Biomechanics

---

R. Cagri Kutlubay  
Technology Faculty, Department of Biomedical Engineering, Pamukkale University,  
Denizli, Turkey

T. Sekercioglu (✉)  
Engineering Faculty, Department of Mechanical Engineering, Pamukkale University,  
Denizli, Turkey  
e-mail: [tsekerci@pau.edu.tr](mailto:tsekerci@pau.edu.tr)

A. Cagdas Yorukoglu  
Faculty of Medicine, Department of Orthopaedics and Traumatology, Pamukkale University,  
Denizli, Turkey

## 1 Introduction

Bone is the most important part that provides support in our body. Although the bones have a durable structure, they can be broken because of various forces it is exposed to. The broken bones are treated by internal and external methods. One of the internal fixation methods used in fracture treatment is the plate-screw method. As a result of the treatment, the strength of the joint formed by the plate-screw method is influenced by many factors like the number of screws, the screw type, the screw position, the fracture type, the plate type, the plate length, etc. It is aimed to make the patients healthier in their healing process by conducting many studies on these factors theoretically, experimentally and in computer environment.

Törnkvist et al. investigated the relationship between the screw fixation strength and the number of screws and screw distance. The related groups were compared among themselves and it was found that the wider located screw groups were stronger in the four point and beam bending tests and that the screwing strength was independent of the screwing system and was dependent on the number of screws used [1]. Field et al. investigated the effects of decreasing the number of screws on the tensile strength of the bone surface and structure in plate-bone applications and they concluded that the reduction of 40% of the total number of screws in a plate-bone application does not have a significant damage to the structural strength [2]. ElMaraghy et al. investigated the effect of the number of cortical screws on the fixation strength of the diaphyseal fractures with the plate, and they found out that with the increase in number of screws a gradual increase in torsion and bending strength occurred [3]. Sanders et al. looked into the biomechanical effects of screw number and plate length, and they revealed that all long plates used the experiments having minimum screws are stronger than the plates including 6-hole plates with 6 screws [4].

Stoffel et al. investigated how to control stability in locked internal fixators by means of the LCP plate biomechanical test and it was seen that working length is the most important factor affecting axial and torsional rigidity. More than 3 screws that were located on both sides of the fracture line increased the axial strength in a small amount. When the number of screws was increased to 4, there was a significant increase in the torsional rigidity [5]. Stoffel et al. investigated the hypothesis that the oblique screws at the plate ends increased the fixation strength and found out that the oblique screw at the end of the plate increased the fixation strength in all tests. It has been found out that in the torsional load, the fixation strength actually depends on the number of screws [6]. Bekler et al. investigated the contribution of the use of locking plate and angled screws in osteoporotic bone to the durability of stabilization and the average pull-out strength was found to be the highest in the group where the screws were inserted 15° divergently [7]. Freeman et al. conducted a study on how many locked screws should be attached to fix hybrid plates in osteoporotic bones. It was found that when 4 or more screws are used, at least 3 of these should be locked screws [8].

Hak et al. studied the adequacy of 2 locked screws for each piece in locking plate fixation used in osteoporotic arm bone shaft fractures and the addition of a third screw in the locked plate did not contribute to mechanical stability in the axial load, bending and twisting [9]. Grawe et al. compared the use of three unlocked screws against two locked screws in fracture fixation and compared unlocked constructions and fewer cycles were seen for damage in locked structures used in normal density bones in eccentric axial loading [10]. Lee et al. investigated that the adequate number and optimal position of the screws used on the plate would be in order to ensure the fixation stability of the LCP used in the femur fractures. As a result of the finite element analyses and biomechanical tests performed, it was seen that 6 locked screws are required for fixation stability [11]. Overturf et al. biomechanically compared unicortical screws attached to opposite cortex with bicortical locked screws, and no significant difference was found between them in the experiments [12].

As a result of the literature review, it is seen that it has generally been investigated how to make the joint more rigid and stable with fewer screws. In these studies, the screws have generally been reduced symmetrically or non-symmetrically on both sides of the fracture line and various mechanical tests or analysis by finite elements method were carried out. In addition, investigations have been carried out on the effects of angles of the screws, screwing shapes and different distance of the screws in fracture line.

In the literature review, no study has been found on how the distance to the fracture line of the unlocked screw, which is used for compression with the same number and properties screw joints, affects the fatigue strength of the existing joint. In the scope of the study, it was tried to give an idea on how a more rigid and stable fixation can be obtained with the same number of screws having the same quality. Also, the effects of the compression screw's distance to the fracture line explained on the fatigue strength of joint.

## 2 Material and Experimental Procedure

For the study to be conducted, a test rig which is shown in Fig. 1 and works with the pneumatic system was used. The test period is calculated by means of the system used in the test rig and so is the number of strokes applied to the sample by means of the optical sensor attached to the board. The force-applied to the sample can be measured by the load sensor attached to the force measurement system used in the test rig. The force measurement system was used to calibrate the instrument on all samples prior to the start of the experiment. Thanks to the pneumatic conditioner on the system, the pressure and the number of strokes depending on it can be adjusted.

As shown in Fig. 2, three different combinations were identified to prepare the test samples. The identified combinations were named according to the presence of the compression screw at three different locations in the force application area. In combination 1, the compression screw was placed in the 3rd hole, which is the furthest one to the fracture line in the force application area. In combination 2,

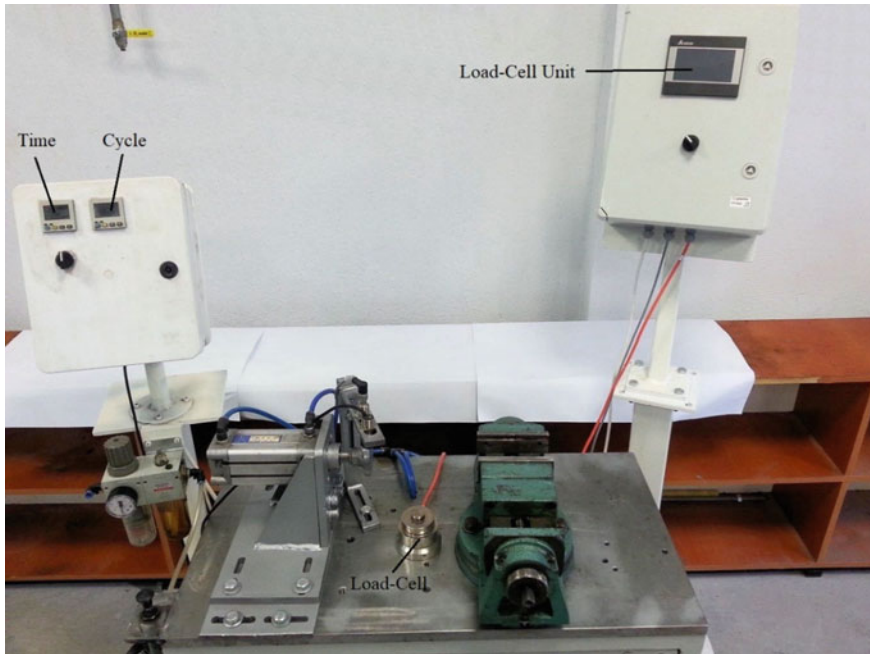


**Fig. 1** Test rig

the compression screw was placed in the 2nd hole in the force application area. In combination 3, the compression screw was placed in the 1st hole, which is the closest one to the fracture line in the force-applied part. A total of 15 samples were divided into three groups, including 5 samples in each group. One sample from each group was used for controlling purposes. The remaining samples were tested.

The sheep bones which were one-year-old on average, obtained from the butchers, were removed of all the soft tissues after the required length and diameter measurements had been made. Once the bones had been cleaned, they were stored in deep freezes at  $-20^{\circ}\text{C}$  to avoid decay in the outer environment. After the sample to be prepared for the experiment had been removed from the deep freeze, measurements were taken for plate settlement and the place to be cut was marked. After the measurement, the plate was bended by means of the plate bender, in such a manner that the bend of the plate would be slightly more than the shape of the bone. Oblique fracture model was formed by cutting from the marked spots in bones with the help of handsaw. After creating the oblique fracture model, fracture parts were put together and the plate was placed on the bone. 7-hole LC-DCP plates which were made of titanium and featured with combi hole, with the size of  $100\text{ mm} \times 14\text{ mm} \times 3.8\text{ mm}$ , were used during the preparation of the samples.

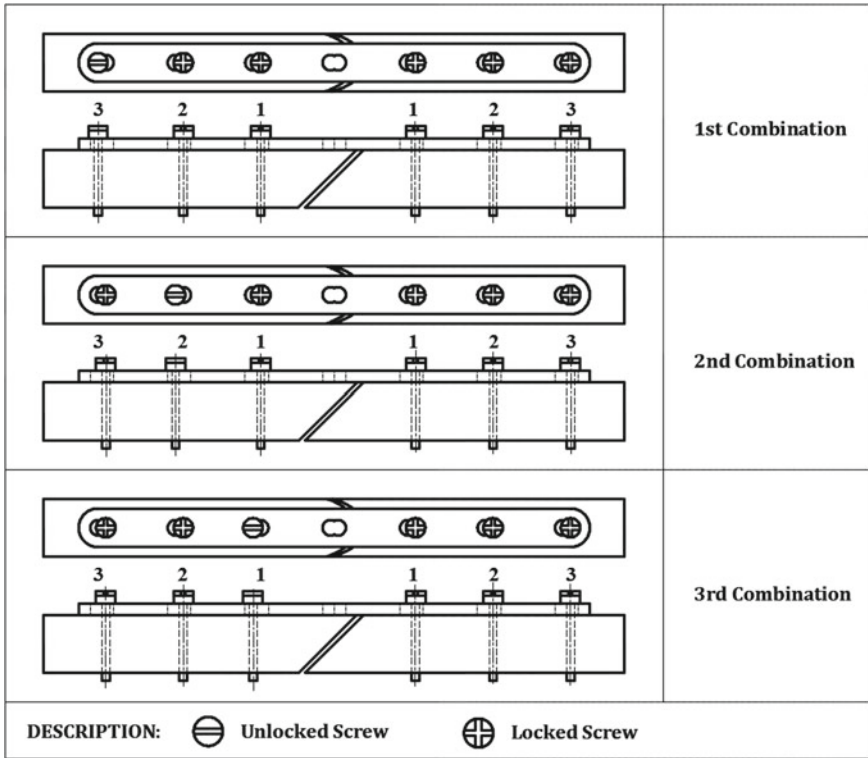
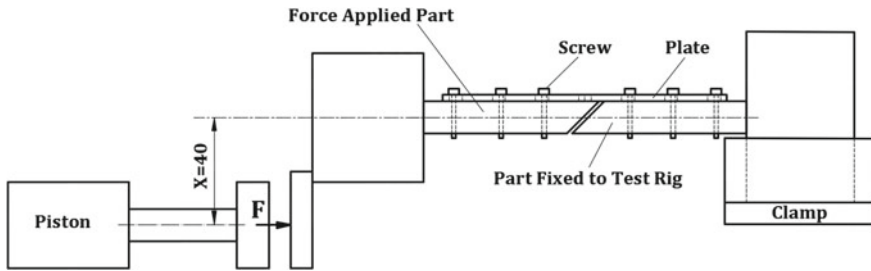


Fig. 2 Combinations

The bones were drilled with drill bits with a diameter of 2.7 mm and a drill guide was used during the drilling of the holes to which the locked screws would be attached. Locked and unlocked screws with a diameter of 3.5 mm were used to fix the plate to the bone. In the process of plate fixation, the AO principle was applied for the compression method. After the plate was inserted, one locked screw was inserted into the one side of the bone which was to be fixed to the test rig and it was tightened with a torque screwdriver. Then, according to the combinations prepared to place the compression screw in the force-applied part of the bone, 1 unlocked screw was inserted after drilling the relevant place and compression was applied to the fracture line by tightening with a torque screwdriver. After inserting the compression screw, the other remaining 4 holes were drilled leaving the hole in the centre of the plate empty, and locked screws were inserted in all of them. All screws were attached to form a double cortex and tightened with a torque screwdriver by applying 2 Nm of torque. Thus, the placement of 3 screws on both sides of the fracture line was completed (Fig. 3).



**Fig. 3** Test specimen



**Fig. 4** Schematic view of the test rig

In order to attach the prepared sample to the test rig, a fixation procedure to metal moulds with the acrylic dental prosthesis was used. The large side of the bone (the part fixed to the experimental setup) was fixed to the metal moulds which were prepared with a size of  $80\text{ mm} \times 80\text{ mm} \times 60\text{ mm}$ , and the small side of it (the part that force was applied to) was fixed to the ones which were prepared with a size of  $60\text{ mm} \times 60\text{ mm} \times 45\text{ mm}$ .

After the calibration of the test rig whose schematic view was shown in Fig. 4 was performed, the sample was attached to the clamp as shown in Fig. 5. At the beginning of the experiments, the calibration procedures were performed in a manner that the piston would apply a force of  $82 \pm 3\text{ kg}$  to the sample and would make 400 cycles to the test sample per minute. Also, the axis of the piston stroke was lowered 40 mm down from the axis of the bone in order to generate the eccentric compression force. At the time of conducting the tests, the test rig was stopped at every 5000 cycle, and screw and joint controls were made and recorded.

### 3 Result and Discussion

During the experimental study, it was decided to terminate the tests in the following cases.

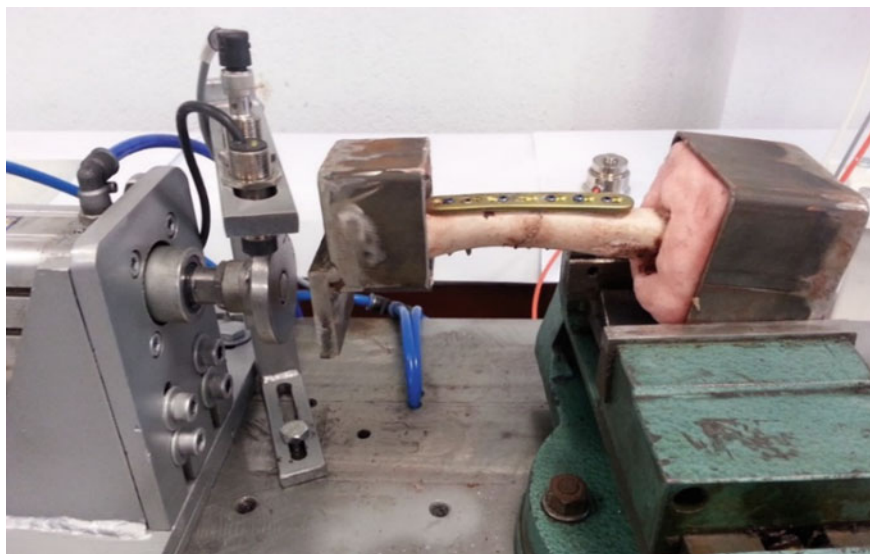


**Fig. 5** Connecting the specimens to the test rig



**Fig. 6** Failed specimens

- loosening of the bone-plate joint,
- a screw which is at least 2 mm out of plate surface,
- plate fracture,
- bone fracture.

Some of the samples that were damaged as a result of the experiments are shown in Fig. 6.



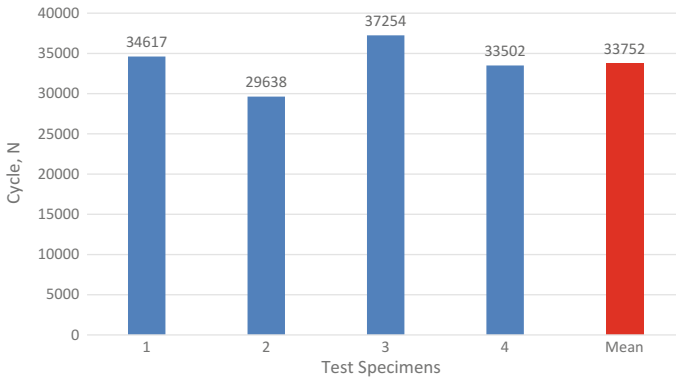


**Fig. 7** First combination

### ***3.1 Damages Occurring in the Joints According to Combinations***

#### **3.1.1 Combination 1**

The experiment of combination 1.1 (first combination-first sample) was terminated at 34,617 cycles. The upper part of the locked and unlocked screws located at the force-applied part moved out more than 2 mm from the plate surface. Therefore, at the force-applied part, more than 2 mm of gap occurred on the surface between the bone and the plate, and the joint was loosened. Additional fracture wasn't observed in the bone.

The experiment of combination 1.2 was terminated at 29,638 cycles. The upper part of the locked screws placed at the part which was fixed to the test rig loosened more than 2 mm from the upper surface of the plate. Thus, more than 2 mm gap between the plate and the bone occurred. In addition, more than 2 mm of loosening, was observed in the locked screw in the bone at the force-applied part. A bone fracture was observed at the force-applied part.

The experiment of combination 1.3 was terminated at 37,254 cycles. The upper part of the screws on both sides loosened more than 2 mm from the plate surface. Between the bone and the plate, occurred more than 2 mm gap at the force-applied part. In addition, due to the movement on the lateral surfaces, the bone axis slipped. Additional fracture wasn't observed in the bone.

The experiment of combination 1.4 was terminated at 33,502 cycles. At the part on which the fixed to the test rig, all locked screws loosened more than 2 mm and at the force-applied part, only the locked screw in the second hole loosened more than 2 mm. Also, more than 2 mm gap between the bone and the plate occurred. Additional fracture wasn't observed in the bone. Figure 7 shows the experimental results of the combination 1.

### 3.1.2 Combination 2

The experiment of combination 2.1 was terminated at 39,842 cycles. In the part fixed to the test rig, in locked screws and in the force-applied part, the locked screw in the first hole was loosened 2 mm from the upper surface of the plate. More than 2 mm gap between the bone fragment and the plate occurred in the part fixed to the test rig. Additional fracture wasn't observed in the bone.

The experiment of combination 2.2 was terminated at 42,970 cycles. As a result of the experiment, it was observed that the upper surfaces of the screws moved out from the upper surfaces of the plate. At the force-applied part, the locked screws at the third and first holes moved out more than 2 mm and 1.5 mm respectively. At the part fixed to the test rig, the locked screws at the first and second holes moved out about 2 mm. The deviation from the screw vertical axis where was detected. It was observed that the actual motion that caused the joint to be damaged stemmed from the movement of the lateral surfaces. Additional fracture wasn't observed in the bone.

The experiment of combination 2.3 was terminated at 37,083 cycle. The upper part of the locked screws in the part fixed to the test rig loosened more than 2 mm. Thus, between the bone and the plate occurred more than 2 mm gap at the part fixed to the test rig. Additional fracture wasn't observed in the bone.

The experiment of combination 2.4 was terminated at 34,915 cycles. More than 2 mm gap between the bone fragment and the plate occurred at the part fixed to the test rig. At the part fixed to the test rig, the upper part of the screws was moved out from the upper surface of the plate. The locked screws in holes 1 and 3, moved out from the plate and no separation was observed in the screw in the second hole. The locked screw in the second hole was eluded from the screw thread in the bone part. In the force-applied part, the upper surface of the screw moved out from the upper surface of the plate by about 1 mm in the first hole and more than 2 mm in the third hole. Additional fracture wasn't observed in the bone. Figure 8 shows the results of combination 2.

### 3.1.3 Combination 3

The experiment of combination 3.1 was terminated at 60,600 cycles. As a result of the experiment, a fracture occurred in the opposite cortex of the locked screw closest to the fracture line and the screw loosened. In addition, additional fractures were observed under the other 2 locked screws at the part fixed to the test rig.

The experiment of combination 3.2 was terminated at 55,364 cycles. As a result of the experiment, in the part where the force was applied, a fracture occurred in the bone around the unlocked screw nearest to the fracture line and the screw loosened.

The experiment of combination 3.3 was terminated at 25,214 cycles. As a result of the experiment, at the part fixed to the test rig, additional fracture occurred in the opposite cortex of the locked screw closest to the fracture line and the screw loosened. The experiment of combination 3.3 was concluded earlier compared to the

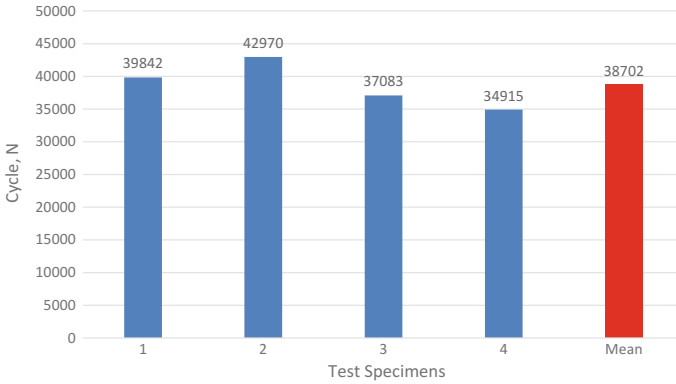


**Fig. 8** Second combination

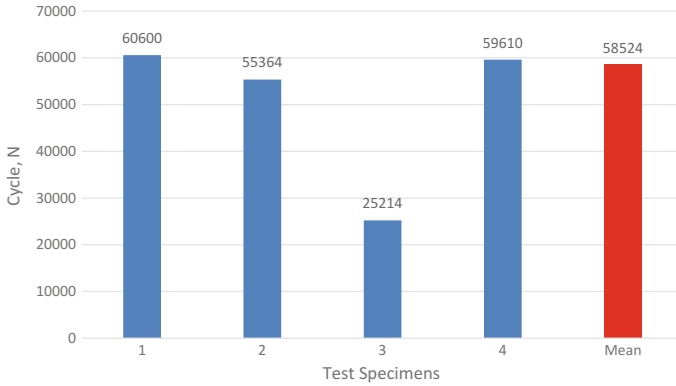


**Fig. 9** Third combination

other experiments in the combination 3 and it was not evaluated so that it wouldn't affect the average obtained negatively.

The experiment of combination 3.4 was terminated at 59,610 cycles. As a result of the experiment, in the part where the force was applied, a very little additional fracture occurred under the unlocked screw nearest to the fracture line and the screw loosened. Figure 9 shows the experimental results of the combination 3.

### **3.2 Comparison of the Measured Values Obtained at Each Combination**

When the test results are examined, it is shown in Fig. 10 that the compression screw's moving away from the fracture line leads to earlier loosening in the plate-screw joints. Moreover, it was observed that the movement in the fracture line started

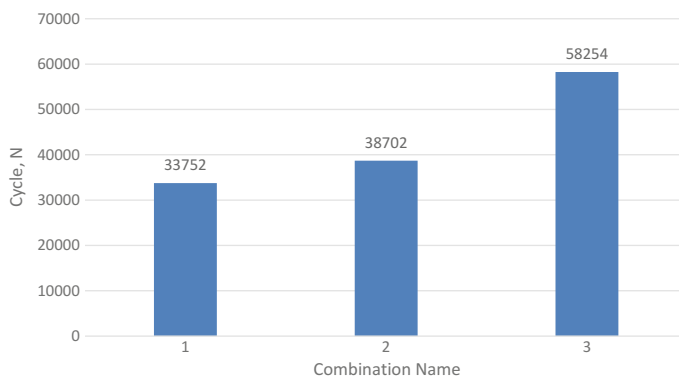


**Fig. 10** Comparison of combinations

early as a result of the fact that the compression screw was moved away from the fracture line.

According to design rules, the force must be transferred in the shortest way. In the case that the compression screw, which enables the bone pieces to connect to each other, is screwed nearest to the fracture line, we move the force in the shortest way to obtain a more rigid joint.

## 4 Conclusions

As the unlocked screw used for compression is moved away from the fracture line, the strength of the construction consisting of plates, screws and bones decreases. During the experiments carried out, the damages occurring in the 1st and 2nd combination experiment groups mostly resulted in the dissolution of the screws and thus the loosening of the joints. When the results obtained in the 3rd combination experiments are examined, no loosening of the joints occurred due to dynamic loading in the joints, and in all experiments, joints got damaged as a consequence of the fracture of the bone. During the experiments performed, in the combination 1 and combination 2 samples, the fracture line began to move earlier compared to the combination 3 samples, and screw dissolution was observed due to dynamic loading without bone damage.

Making the compression screw closer to the fracture line strengthened the joint by approximately 73% according to the average of the results of the combination 1 experiment and by approximately 50% according to the results the average of the combination 2 experiment results. The average of the combination 2 experiment results was 15% higher than the average of the combination 1 experiment results.

As a result, in fixation processes in which plate-screws are used, the compression screw should be screwed as close as possible to the fracture line. It has been observed

that the position of compression screw, which enables the fracture surfaces to connect closer to the fracture line increases the rigidity of the joint. In this way, a more rigid joint is obtained with the screws used in the same number and feature.

**Acknowledgements** This study was performed in the framework of The Scientific Projects Unit of Pamukkale University, Project No: 2016-FEBE-038

## References

1. Törnkvist, H., Hearn, T.C., Schatzker, J.: The strength of plate fixation in relation to the number and spacing of bone screw. *J. Orthop. Trauma* **10**, 204–208 (1996)
2. Field, J.R., Törnkvist, H., Hearn, T.C., Summer-Smith, G., Woodside, T.D.: The influence of screw omission on construction stiffness and bone surface strain in the application of bone plates to cadaveric bone. *Int. J. Care Injured* **30**, 591–598 (1999)
3. ElMaraghy, A.W., ElMaraghy, M.W., Nousiainen, M., Richards, R.R., Schemitsch, E.H.: Influence of the number of cortices on the stiffness of plate fixation of diaphyseal fractures. *J. Orthop. Trauma* **15**, 186–191 (2001)
4. Sanders, R., Haidukewych, G.J., Milne, T., Dennis, J., Latta, L.L.: Minimal versus maximal plate fixation techniques of the ulna: the biomechanical effect of number of screws and plate length. *J. Orthop. Trauma* **16**, 166–171 (2002)
5. Stoffel, K., Dieter, U., Stachowiak, G., Gächter, A., Kuster, M.S.: Biomechanical testing of the LCP-how can stability in locked internal fixators be controlled. *Int. J. Care Injured* **34**, B11–B19 (2003)
6. Stoffel, K., Stachowiak, G., Forster, T., Gächter, A., Kuster, M.: Oblique screws at the plate ends increase the fixation strength in synthetic bone test medium. *J. Orthop. Trauma* **18**, 611–616 (2004)
7. Bekler, H., Bulut, G., Usta, M., Gökçe, A., Okyar, F., Beyzadeoğlu, T.: Osteoporotik kemikte kilitli plak ve açılı vida kullanımının stabilizasyonun dayanıklılığına katkısı: Deneysel çalışma. *Acta Orthop. Traumatol.* **42**, 125–129 (2008)
8. Freeman, A.L., Tornetta, P., Schmidt, A., Bechtold, J., Ricci, W., Fleming, M.: How much do locked screw add to the fixation of “hybrid” plate construct in osteoporotic bone? *J. Orthop. Trauma* **24**, 163–169 (2010)
9. Hak, D.J., Althausen, P., Hazelwood, S.J.: Locked plate fixation of osteoporotic humeral shaft fractures: are two locking screw per segment enough? *J. Orthop. Trauma* **24**, 207–211 (2010)
10. Grawe, B., Le, T., Williamson, S., Archdeacon, A., Zardiackas, L.: Fracture fixation with two locking screws versus three non-locking screws, a biomechanical comparison in a normal and an osteoporotic bone model. *Bone Joint Res.* **1**, 118–124 (2012)
11. Lee, C.H., Shih, K.S., Hsu, C.C., Cho, T.: Simulation-based particle swarm optimization and mechanical validation of screw position and number for the fixation stability of a femoral locking compression plate. *Med. Eng. Phys.* **36**, 57–64 (2014)
12. Overturf, S.J., Morris, R.P., Gugala, Z., Lindsey, R.W.: Biomechanical comparison unicortical far-cortex-abutting locking screw-plate fixation for comminuted radial shaft fractures. *J. Hand Surg. Am.* **39**, 1907–1913 (2014)

# Life Cycle Cost Assessment and the Optimum Design of Timber Roofs for Sustainable Construction



Kamil Krzywiński and Łukasz Sadowski

**Abstract** This paper describes the optimum design and life cycle cost (LCC) assessment of timber roofs for sustainable construction. For this purpose, collar beam roof construction in a typical single-family house was analyzed. Special focus was placed on the impact of the patch cross-section position for different rafter spacing. The calculations were performed for four roof angles (15°, 30°, 45°, 60°). The main goal was to find the optimum LCC for each angle. It was found that smaller rafter spacing generates a higher assembly cost and takes more time to construct. On the other hand, the wood cost for these elements is lower. The implications of LCC were evaluated to find out which patch and rafter cross-section, as well as rafter spacing for each roof angle is the most economical solution.

**Keywords** Life cycle cost · Collar beam roof · Patch · Rafter · Optimum design Sustainable construction

## Nomenclature

### Latin Upper Case Letters

$A$	Cross-sectional area (m <sup>2</sup> ),
$E_{mean}$	Mean value of modulus of elasticity (GPa),
$E_{mean,fin}$	Final mean value of modulus of elasticity (GPa),
$F$	Force (kN),
$F_d$	Design force (kN),
$F_{x,Ed}$	Design value of a force in capacity in x-direction (kN),
$F_{y,Ed}$	Design value of a force in capacity in y-direction (kN),
$H$	Overall rise of collar beam (m),

---

K. Krzywiński · Ł. Sadowski (✉)

Wrocław University of Science and Technology, Wybrzeże Wyspiańskiego 27, 50-370 Wrocław, Poland

e-mail: [lukasz.sadowski@pwr.edu.pl](mailto:lukasz.sadowski@pwr.edu.pl)

© Springer Nature Switzerland AG 2019

L. F. M. da Silva (ed.), *Materials Design and Applications II*, Advanced Structured Materials 98, [https://doi.org/10.1007/978-3-030-02257-0\\_15](https://doi.org/10.1007/978-3-030-02257-0_15)

$I_y$	First moment of area about the strong axis ( $m^4$ ),
$I_z$	Second moment of area about the weak axis ( $m^4$ ),
$L$	Length (m),
$M_d$	Design moment (kNm),
$M_y$	Moment of y axis (kNm),
$M_z$	Moment of z axis (kNm),
$N$	Axial force (kN),
$N_c$	Compression force (kN),
$P$	Human force (kN),
$V$	Volume ( $m^3$ ),
$V_t$	Shear force (kN),
$W_y$	Section modulus about axis y ( $m^3$ ).

## Latin Lower Case Letters

$a$	Distance (m),
$b$	Width (m),
$f_{c,0,d}$	Design compressive strength along the grain (MPa),
$f_{c,w,d}$	Design compressive strength of web (MPa),
$f_{m,k}$	Characteristic bending strength (MPa),
$f_{m,y,d}$	Design bending strength about principal y-axis (MPa),
$f_{m,z,d}$	Design bending strength about principal z-axis (MPa),
$g$	Weight load (kN/m),
$h$	Height of element; house height (m),
$k_{crit}$	Factor used for lateral buckling (–),
$k_m$	Factor considering re-distribution of bending stresses in a cross-section (–),
$k_{mod}$	Modification factor for duration of load and moisture content (–),
$m$	Mass per unit area ( $kg/m^2$ ),
$q_p$	Peak velocity pressure ( $kN/m^2$ ),
$s$	Snow load (kN/m),
$s_k$	Characteristic value of snow on the ground at the relevant site ( $kN/m^2$ ),
$u_{fin}$	Final deformation (mm),
$u_{inst}$	Instantaneous deformation,
$l_{eff}$	Rafter spacing distance (m),
$w$	Wind load (kN/m).

## Greek Lower Case Letters

$\alpha$	Angle between the direction of the load and the loaded edge; Angle between horizontal axis and rafter ( $^\circ$ ),
----------	---

$\gamma_M$	Partial factor for material properties, also accounting for model uncertainties and dimensional variations (–),
$\sigma_{c,0,d}$	Design compressive stress along the grain (MPa),
$\sigma_{m,y,d}$	Design bending stress about the principal y-axis (MPa),
$\sigma_{m,z,d}$	Design bending stress about the principal z-axis (MPa),
$\tau_d$	Design shear stress (MPa).

## 1 Introduction

The construction of traditional sloped roofs is mainly made from wood elements. The construction of this kind of elements needs about two times less embodied energy [26]. These elements include rafter, patch and counter battens (see Fig. 1). The main constructional element of these kinds of roofs is a rafter [23, 27]. A patch usually has to be constructed on the rafter in order to enable the installation of roof tiles (e.g. made of ceramic or cement) [19]. The patches participation in the cost of a roof construction stands at about 15–25%. Thus, one of the pillars of sustainable construction is the optimum economic design of structural parts of traditional buildings [1, 22]. This may reduce the total weight and cost of the roof. Recent standards focus on the optimum design of rafters. However, they do not allow for the optimum design of patches.

Cabeza et al. [3] observed that most life cycle assessment is carried out on low energy buildings and highlighted that there are only a very few studies on traditional buildings. It is proper to note that this kind of buildings are mostly found in our cities. Techniques of manufacture are on a high level nowadays. It is due to promoting the use of more advanced techniques and eco-innovation [2]. Building materials have better quality than in past. Production of building materials, their transport and construction of the building accounts for 2.2% of primary energy consumption [14]. It has impact on global primary energy demand. What's more Mora [18] pointed out that it is necessary to distinguish between the sustainability of the construction activity and the sustainability of works constructed. Therefore, roof construction should be designed in a more clever way. It may give the possibility to build it without breaks. It can reduce impact on environment [4] and it is beneficial for life cycle cost results [21].

Islam et al. [12] calculated that for 8 alternative roofing the most attractive is the flat one. It imposes thought that more flat roofs need fewer working hours for constructing and give opportunity to save money. Rafter spacing mostly allows to reduce wood consumption. In combination with rational design of rafter cross-section, it is possible to reduce big part of roof construction costs. Timber roofs expected life amounts more than 100 years [17]. Therefore, roof costs have impact on a few generations which will live in designed house. Time between every next generation was taken to consider for the life cycle cost.

Considering the above, the article focuses on the selection of patch when modeling a roof structure and rafter spacing. Patch dimensions are usually ignored in the



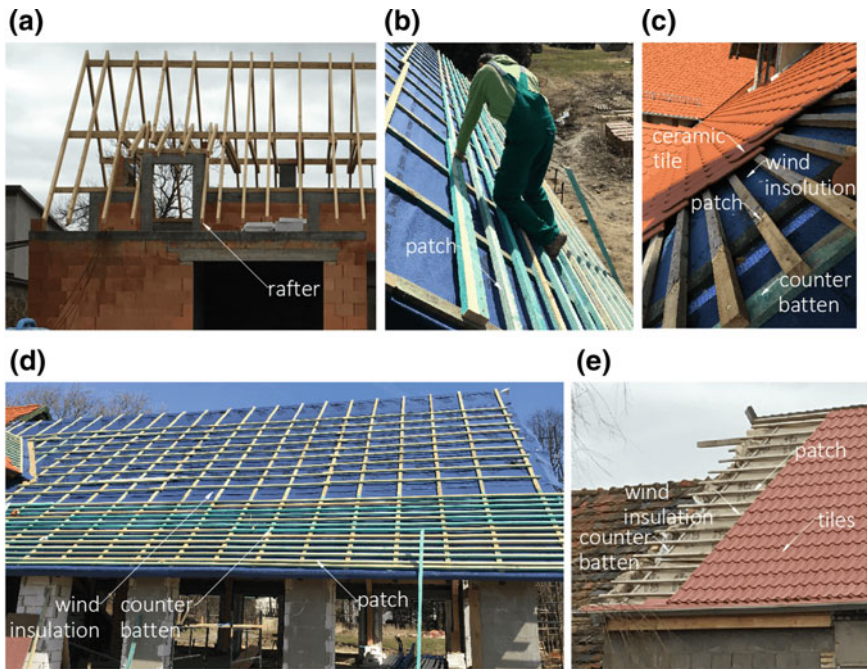


**Fig. 1** The example of the construction of traditional sloped roofs where the following can be perceived: **a** rafter spacing, **b** force from a standing carpenter on a patch, **c** loads from roof covering, **d** patch participation in roof construction, **e** roof covering and patch spacing

design. The decision about its dimensions is made by carpenters. This issue needs a considered approach at the beginning of the design process. There is a need to deliver a reliable method of the optimum design of wooden patch roofs in the simplest possible way to solve this problem. In economic terms, there is a need to analyze the price of wood and the cost of execution in order to achieve the most efficient construction. It is possible to understand the impact of different stages during the construction phase using life cycle cost analysis.

## 2 Basic Informations

### 2.1 Permanent Assumptions

Figure 2 presents the static scheme of a patch with two position variants. Human force  $P$  and own weight with coverage  $g$  was taken for the calculations. The location of  $P$  force was constant in order to analyze deflection and the bending moment.

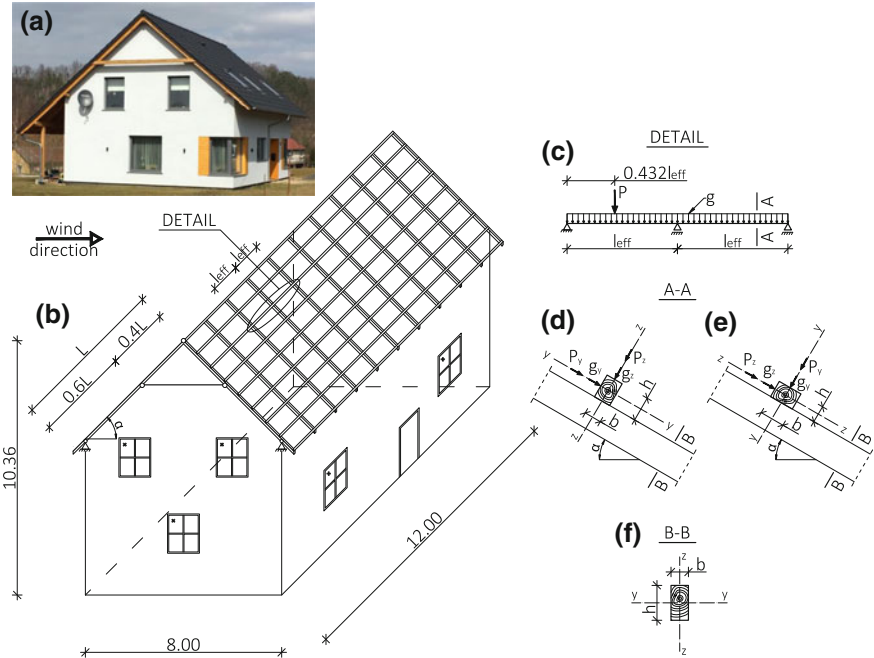


**Fig. 2** Single family house: **a** exemplanary view, **b** dimensions with roof construction, **c** scheme of the patch with loads; patch cross-section: **d** stronger y-y axis, **e** lower z-z axis; **f** rafter cross-section

To further analyze selected dimensions of the patch  $b$  and  $h$  are from 3.8 to 6.3 cm at constant intervals (Table 1).

Rafter spacing is calculated from 60 to 120 cm at 5 cm intervals.

The analyzed house is located in the 1st snow [5] and wind [6] zone (Table 2).

## 2.2 Variables

In Poland the roof angle depends on local loads from snow or wind and also the roof angles of houses from the neighborhood. It is mostly imposed from above by the local spatial development plan. Four types of roof scheme were taken for the calculations (Fig. 3).

Every type of scheme has the same collar beam roof construction but because of various roof angles there are different leading loads. Snow load has more influence on flat roofs. When  $\alpha \geq 60^\circ$  snow is not considered in the calculations. On the other hand, wind load has a higher value for steeper roofs. The weight of a roof is slightly growing with an increasing roof angle, which is due to the bigger dimensions of elements.

**Table 1** Dimensions for Fig. 2c and rafter length dependent on roof angle

$\alpha = 15^\circ$	$b$ [cm]	5.0	6.0	7.0	7.0	7.0	7.0	7.0	7.0	7.0	7.0	8.0	–	4.66
	$h$ [cm]	13.0	13.0	12.0	13.0	14.0	15.0	16.0	17.0	18.0	19.0	20.0	–	
	$A$ [cm <sup>2</sup> ]	65.0	78.0	84.0	91.0	98.0	105.0	112.0	120.0	128.0	135.0	144.0	–	
$\alpha = 30^\circ$	$b$ [cm]	6.0	6.0	6.0	7.0	7.0	7.0	8.0	8.0	9.0	9.0	9.0	9.0	5.20
	$h$ [cm]	13.0	14.0	15.0	14.0	15.0	16.0	17.0	18.0	19.0	20.0	21.0	–	
	$A$ [cm <sup>2</sup> ]	78.0	84.0	90.0	98.0	105.0	112.0	120.0	128.0	135.0	144.0	153.0	–	
$\alpha = 45^\circ$	$b$ [cm]	7.0	8.0	8.0	8.0	9.0	9.0	9.0	9.0	9.0	9.0	9.0	9.0	6.36
	$h$ [cm]	14.0	14.0	15.0	16.0	16.0	17.0	17.0	18.0	18.0	19.0	19.0	–	
	$A$ [cm <sup>2</sup> ]	98.0	112.0	120.0	128.0	135.0	144.0	153.0	162.0	171.0	180.0	189.0	–	
$\alpha = 60^\circ$	$b$ [cm]	9.0	9.0	10.0	10.0	10.0	10.0	10.0	10.0	10.0	10.0	10.0	–	9.00
	$h$ [cm]	16.0	17.0	17.0	18.0	18.0	19.0	19.0	20.0	20.0	21.0	21.0	–	
	$A$ [cm <sup>2</sup> ]	144.0	153.0	170.0	180.0	190.0	200.0	210.0	220.0	230.0	240.0	250.0	–	

**Table 2** Other permanent assumptions

Description	Load	Unit	Cost	
Roof covering—ceramic tile—11 tiles/m <sup>2</sup> (one tile weight)	0.40	kN	—	—
Heat insulation—mineral wool	0.40	kN/m <sup>3</sup>	—	—
Wood class—C24	4.20	kN/m <sup>3</sup>	380	€/m <sup>3</sup>
Roof construction execution (per 1 m <sup>2</sup> roof area)	—	—	7.15	€/m <sup>2</sup>
Characteristic value of snow on the ground $s_k$	0.70	kN/m <sup>2</sup>	—	—
Peak velocity pressure $q_p(z)$	0.58	kN/m <sup>2</sup>	—	—

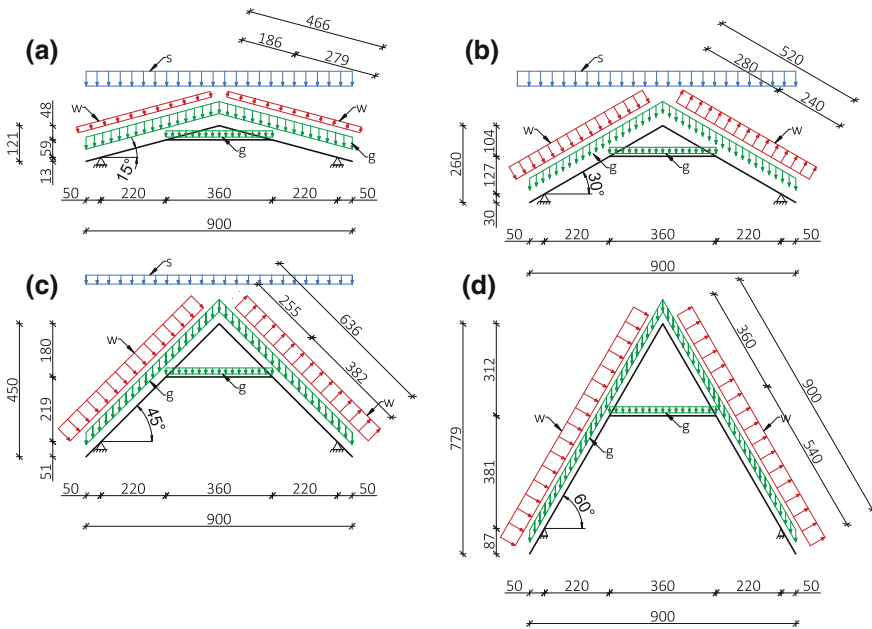


**Fig. 3** Different types of roof angle and loads: **a**  $\alpha = 15^\circ$ , **b**  $\alpha = 30^\circ$ , **c**  $\alpha = 45^\circ$ , **d**  $\alpha = 60^\circ$

### 2.3 Calculations

Calculations of collar beam roof are started from patch. The snow and wind load does not have an essential influence on the patch. Therefore only the load of its own weight and the human point load are taken into account in the static scheme. The main loads on the collar beam construction come from snow, wind and the roof weight with covering.

There are various factors that have an impact on the total cost of a construction. Different patch and rafter dimensions, rafter spacing, and roof gradient were used to calculate wood volume consumptions. A combination of execution and wood costs enables an optimum roof construction to be designed. The LCC approach shows future costs with current value and gives an opportunity for deeper analysis.

## 3 Structural Analysis

### 3.1 Loads

Only own the weight of the patch, coverage and the force from a human [5] was used to analyze the cross-section. Loads from snow and wind do not have an influence on its dimensions. This is because of the frequent patch spacing and small area of stress.

Calculations for ULS and SLS were done in MS Excel.

For different patch dimensions, the adequate own weight was taken.

The rafter was calculated with loads for  $l_{eff} = 1.00$  m. Other calculations for ULS were done in MS Excel. SLS was analyzed using Robot Structural Analysis.

The snow load [6] in the table below is for 1st zone for roof angle  $\alpha = 15^\circ$ .

The wind load [7] is equal to peak velocity pressure for the 1st zone. A different factor  $c_{pe,10}$  was analyzed for every wind area (D, E, F, G, H, I), dependent on the roof angle.

### 3.2 Ultimate Limit State—ULS

The design values of loads were taken from Table 3 for the ULS calculation for the static scheme from Fig. 2.

According to [8, 20] the design bending stress about the principal y- and z-axis is:

$$\sigma_{m,i,d} = \frac{M_i}{W_i} \quad (1)$$

**Table 3** Loads for patch and rafter analysis

Patch			
Load	Characteristic value	Load factor $\gamma_M$ [-]	Design value
$g^*$	0.187 (kN/m)	1.35	0.252 (kN/m)
$P$	1.000 (kN)	1.50	1.500 (kN)
Rafter			
Load	Characteristic value (kN/m)	Load factor $\gamma_M$ [-]	Design value (kN/m)
$g$	0.770	1.35	1.040
$s$	0.560	1.50	0.840
$w$	0.580	1.50	0.870
Total $\Sigma$	1.910	–	2.750

$g^*$ —own weight for patch  $5 \times 5$  cm and coverage

where:  $i = \{y; z\}$ ,  $M$  is the bending moment and  $W$  is section modulus, for rafter calculations  $\sigma_{m,z,d} = 0$ .

According to [6, 24] the design compressive stress along the grain is:

$$\sigma_{c,0,d} = \frac{N}{A} \quad (2)$$

where:  $N$  is the axial force and  $A$  is the cross-sectional area

According to [6, 16] the design bending strength about the grain and principal axis is calculated for wood class C24:

$$f_{c,0,d} = \frac{k_{mod} \cdot f_{c,0,k}}{\gamma_M} \quad (3)$$

$$f_{m,i,d} = \frac{k_{mod} \cdot f_{m,i,k}}{\gamma_M} \quad (4)$$

where:  $i = \{y; z\}$ ,  $k_{mod}$  is the modification factor for the duration of the load and moisture content ( $k_{mod} = 1.1$  for 2nd service class and short-term load-duration class),  $\gamma_M$  is the partial factor for the material properties ( $\gamma_M = 1.3$  for solid timber), for wood class C24  $f_{c,0,k} = 21$  MPa and  $f_{m,y,k} = 24$  MPa.

Patch ULS check:

$$\begin{cases} k_m \cdot \frac{\sigma_{m,y,d}}{f_{m,y,d}} + \frac{\sigma_{m,z,d}}{f_{m,z,d}} \leq 1.00 \\ \frac{\sigma_{m,y,d}}{f_{m,y,d}} + k_m \cdot \frac{\sigma_{m,z,d}}{f_{m,z,d}} \leq 1.00 \end{cases} \quad (5)$$

Rafter ULS check:

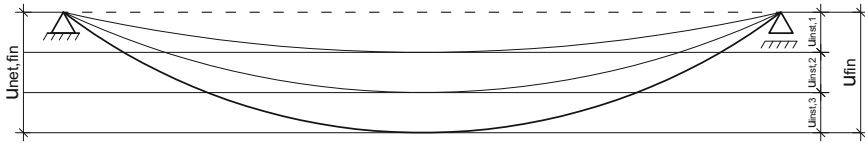


Fig. 4 Definitions of vertical deflections

$$\begin{cases} \left( \frac{\sigma_{c,0,d}}{f_{c,0,d}} \right)^2 + k_m \cdot \frac{\sigma_{m,y,d}}{f_{m,y,d}} + \frac{\sigma_{m,z,d}}{f_{m,z,d}} \leq 1.00 \\ \left( \frac{\sigma_{c,0,d}}{f_{c,0,d}} \right)^2 + \frac{\sigma_{m,y,d}}{f_{m,y,d}} + k_m \cdot \frac{\sigma_{m,z,d}}{f_{m,z,d}} \leq 1.00 \end{cases} \quad (6)$$

where:  $k_m$  is the factor considering the re-distribution of bending stresses in a cross-section ( $k_m = 0.7$  for a rectangle cross-section).

### 3.3 Serviceability Limit State—SLS

The characteristic values of loads were taken from Table 3 for the SLS calculation for the static scheme from Fig. 2.

The Fig. 4 presents the form of different long-term deformations and also the additional part of the deflection due to the variable actions to get the final deformation.

Final critical deformation for timber roof boarding can be defined as follows:

$$u_{net,fin} = \frac{l_{eff}}{x} \quad (7)$$

where:  $x = \{150; 300\}$  ( $x = 150$  for timber roof boarding and  $x = 300$  for timber roof boarding).

Instantaneous deformation  $u_{inst}$  was taken from individual loads (own weight, local force).

Final deformation:

$$u_{fin,(y,z)} = u_{inst} \cdot (1 + k_{def}) \quad (8)$$

$$u_{fin} = \sqrt{u_{fin,y}^2 + u_{fin,z}^2} \quad (9)$$

Patch and rafter SLS check:

$$u_{fin} \leq u_{net,fin} \quad (10)$$

### 4 Life Cycle Cost (LCC) Modeling Approach [9, 11, 13]

Present cost is the equal sum of the construction and disposal costs, which were taken for further analysis in order to get the LCC results. There is a growing interest in building designs with a low economic and environmental impact. LCC is an estimate of the total cost throughout the lifetime of a building. In this article, LCC was calculated for 20 years because it is approximately the time for every next family generation where different changes may occur. Future costs are discounted to their present value using a suitable rate over their lifetime [10] and were calculated using present cost and average inflation [25] from the last 15 years (2003–2017) of  $f = 1.02\%$ . It was assumed that the disposal value is equal to 60% of the roof execution costs according to:

$$FC = PC \cdot (1 + f)^n \tag{11}$$

where:  $FC$  is the future cost,  $PC$  is the present cost,  $f$  is the inflation rate and  $n$  is the number of years.

Future costs were discounted using Eq. (12) to present the value of a suitable discount rate [15]. Because of future risk, the discount rate exceeds the inflation rate. Thus, in this study, the discount rate was changed from 3 to 6% at 1% intervals.

$$DPV = \frac{FC}{(1 + d)^n} \tag{12}$$

where:  $DPV$  is the discounted present value and  $d$  is the discount rate.

### 5 Results

For the purposes of this section, the following expressions shall be fulfilled:

$$\begin{cases} k_m \cdot \frac{\sigma_{m,y,d}}{f_{m,y,d}} + \frac{\sigma_{m,z,d}}{f_{m,z,d}} \leq 1.00 \\ \frac{\sigma_{m,y,d}}{f_{m,y,d}} + k_m \cdot \frac{\sigma_{m,z,d}}{f_{m,z,d}} \leq 1.00 \end{cases} \tag{13}$$

Figure 5 presents the ratio of external stress to ultimate limit state for different angles.

Which axis is lower or stronger depends on roof angle. Figure 5 shows that, for lower axes, the ratio  $\sigma/f$  is more linear than for stronger axes. For smaller patch cross-sections changing the axis gives the possibility to design roof constructions with bigger rafter spacing. The patch volume comparison for y-y and z-z axis is presented in Fig. 6.



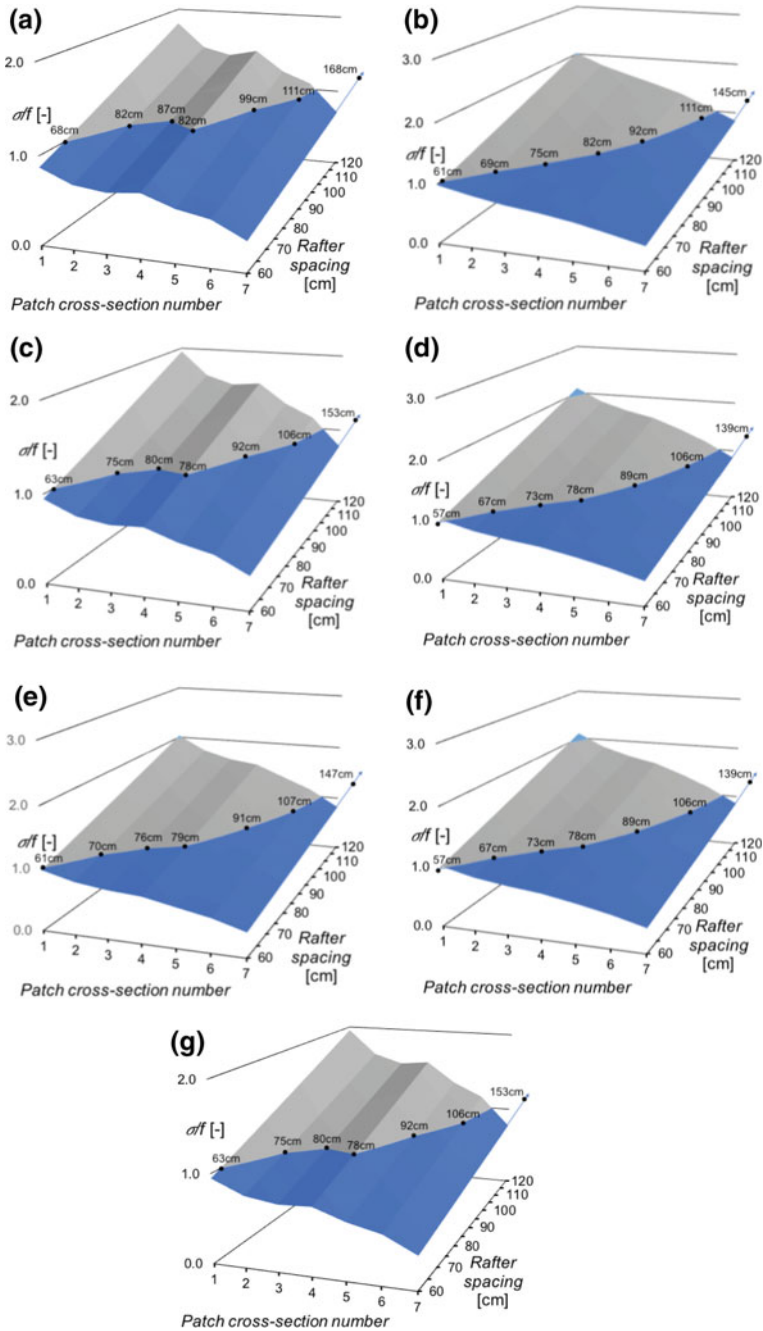


**Fig. 5** Ratio of external stress to ultimate limit state:  $\alpha = 15^\circ$ : **a** y-y axis, **b** z-z axis;  $\alpha = 30^\circ$ : **c** y-y axis, **d** z-z axis;  $\alpha = 45^\circ$ : **e** y-y and z-z axis;  $\alpha = 60^\circ$ : **f** y-y axis, **g** z-z axis

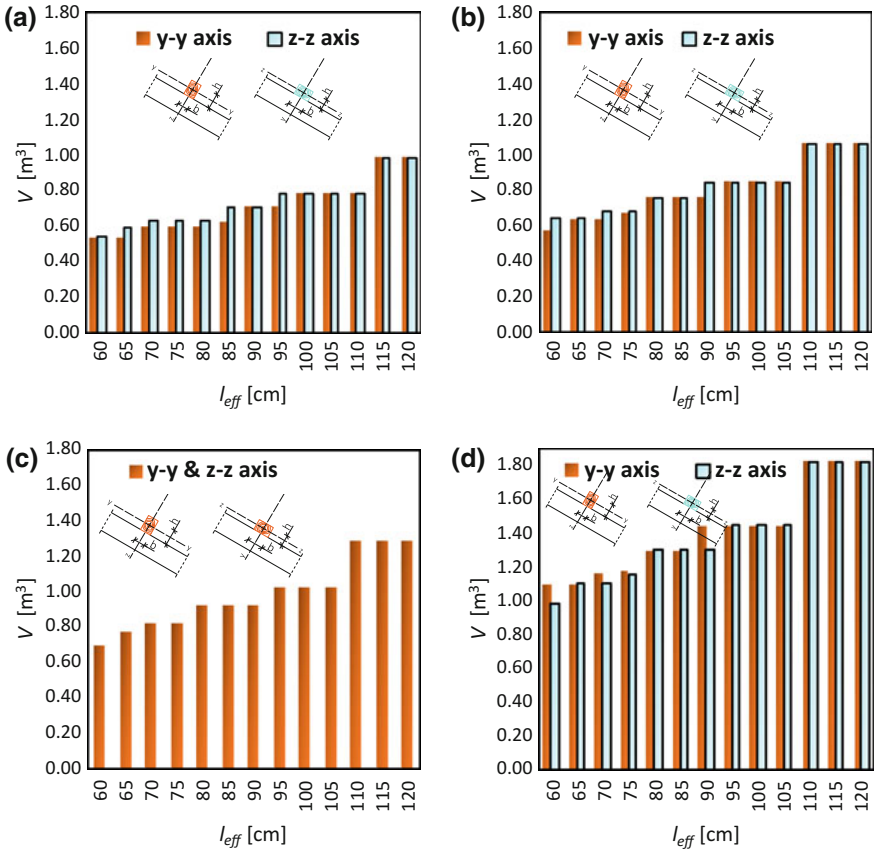


**Fig. 6** Patch volume comparison for y-y and z-z axis: **a**  $\alpha = 15^\circ$ ; **b**  $\alpha = 30^\circ$ ; **c**  $\alpha = 45^\circ$ ; **d**  $\alpha = 60^\circ$

From Fig. 6 it is easy to perceive, that for some rafter spacing there is a possibility to decrease the wood volume. With a steeper roof angle there is a need to give more patches, and therefore the volume is growing. Figure 7 presents the analysis of the participation of patch volume in a roof construction for different rafter spacing (y-y axis). A patch with the y-y axis will be taken for further analysis.

It can be seen from Fig. 7, that patch participation is more important for bigger rafter spacing and has the most influence on flat roofs.

House length and width does not depend on the roof angle. Thus, for every analyzed roof the number of rafter elements is the same (see Fig. 8). Figure 9 presents the wood volume for a whole roof construction for different rafter spacing. On the other side, Fig. 10 shows the collar beam roof execution cost for different rafter spacing.

Figure 9 shows that there is anomaly for  $l_{eff} = 110$  cm, where the wood volume is the smallest.

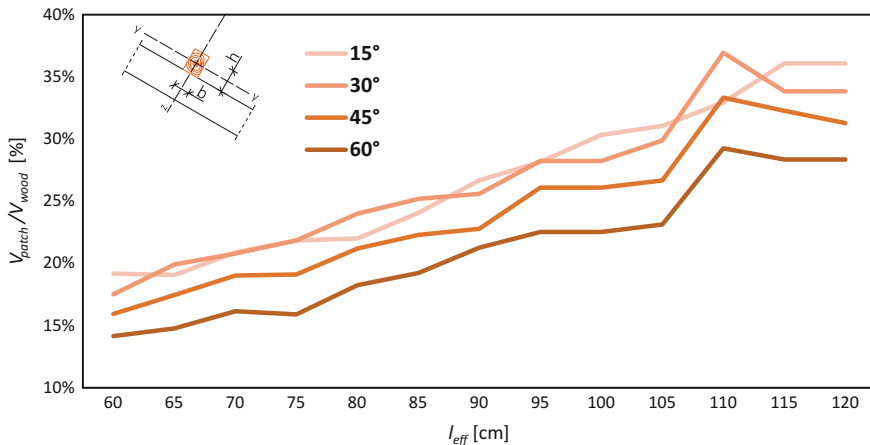


Fig. 7 Participation of patch volume in a roof construction for different rafter spacing (y-y axis)

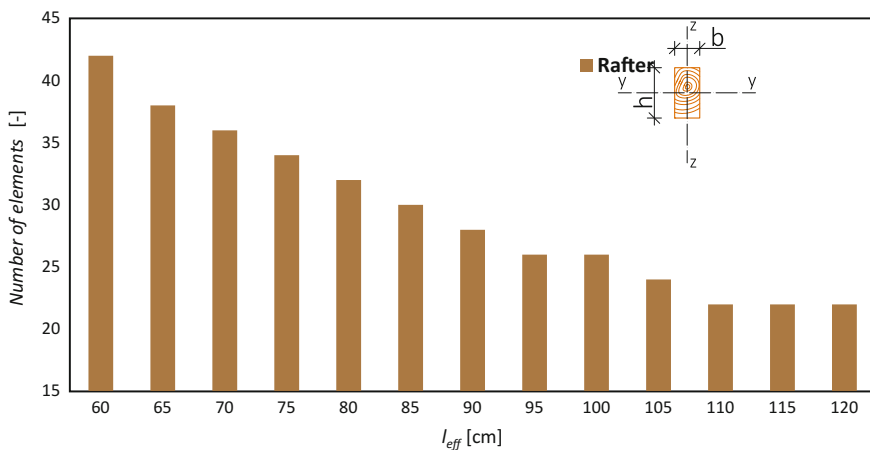


Fig. 8 Number of rafters for different rafter spacing

As it can be seen from Fig. 10 a bigger number of rafters corresponds to a bigger cost of execution. A steeper roof angle increases the roof area and makes execution more expensive. Thus, Fig. 11 presents the total cost of collar beam roof construction for different rafter spacing.

It is visible from Fig. 11, that in global analysis it can be seen that the best rafter spacing is  $l_{eff} = 110$  cm with a patch cross-section of  $b \times h \rightarrow 5 \times 5$  cm. The difference between the lowest and highest price is bigger for steeper roofs. Figure 12 presents the Pareto chart for every roof construction element and execution.

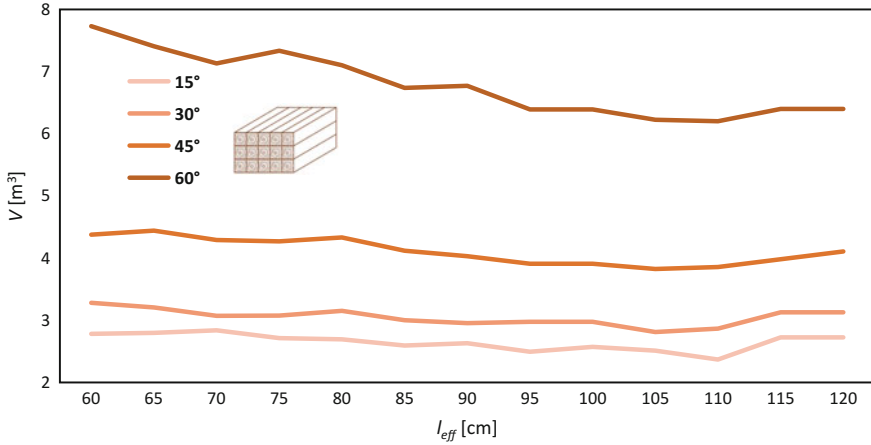


Fig. 9 Wood volume for a whole roof construction for different rafter spacing

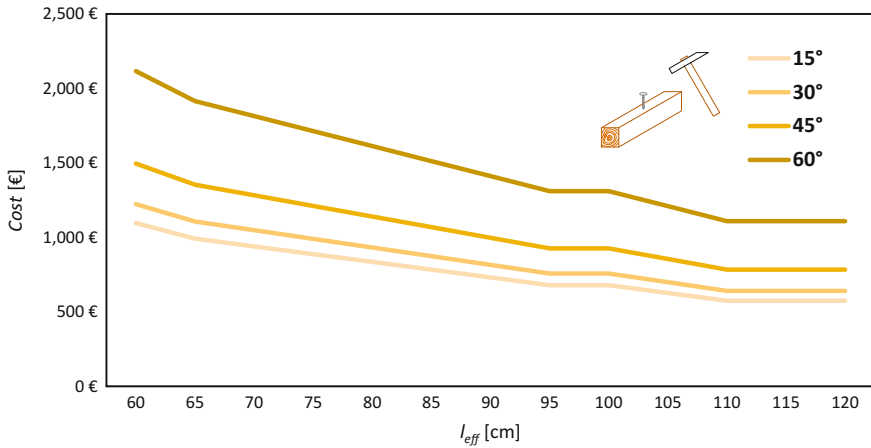


Fig. 10 Collar beam roof execution cost for different rafter spacing

It can be concluded from Fig. 12, that the execution and rafter costs are the biggest. The patch costs are also relevant. For smaller roof angles, the cost of execution has the most impact on the total cost, but for  $\alpha = 60^\circ$  the rafter cost is the biggest.

Next, the LCC analysis was carried out in order to obtain the best results of the total cost for every roof angle (Fig. 13).

It can be seen from Fig. 13, that costs are growing with an increasing roof angle. The construction value is approximately halved after the first twenty years of a construction's lifetime. The value lost is greater for a roof with  $\alpha = 60^\circ$  than for  $\alpha = 15^\circ$ .

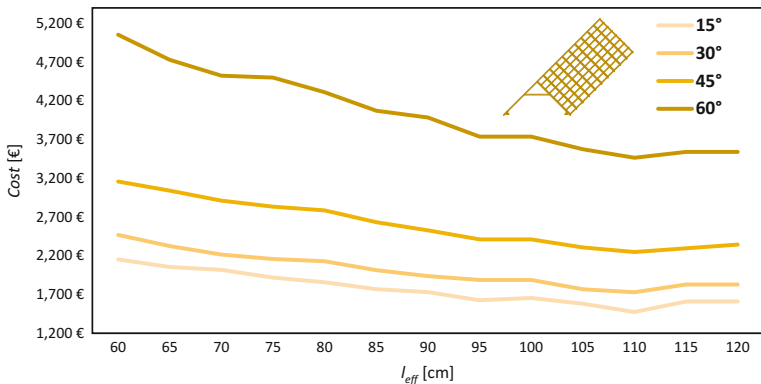


Fig. 11 Total cost of collar beam roof construction for different rafter spacing

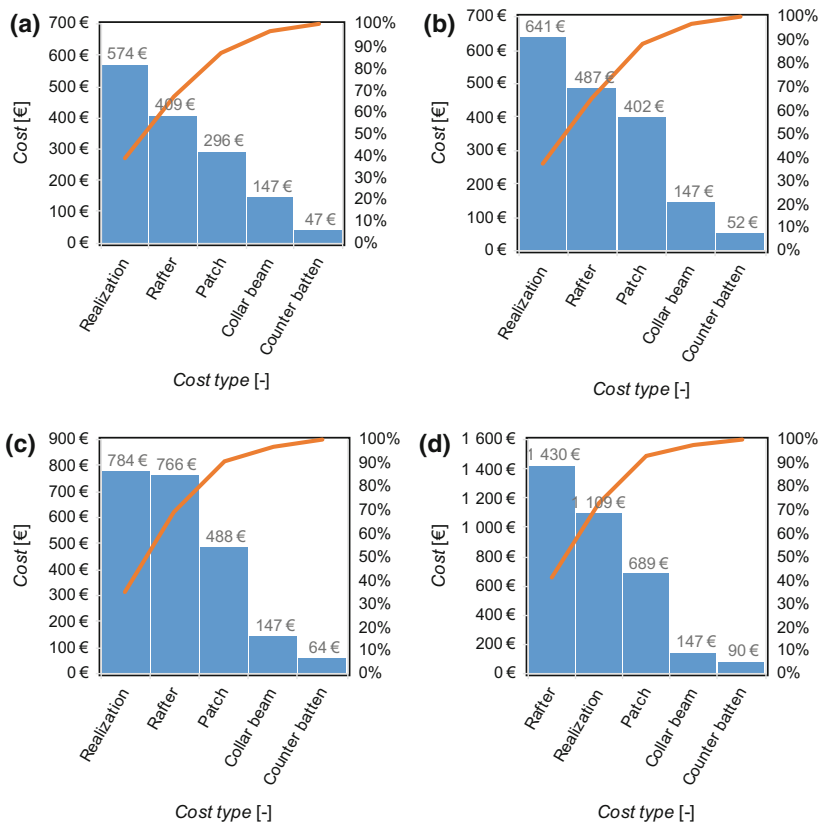


Fig. 12 Pareto chart for every roof construction element and execution

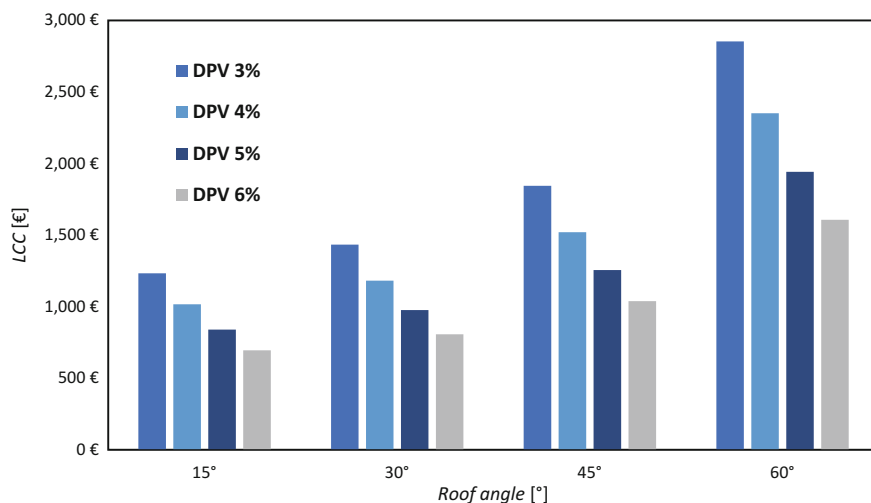


Fig. 13 Life cycle cost for the next twenty years

## 6 Conclusions

This paper presents the optimum design and life cycle cost (LCC) assessment of timber roofs for sustainable construction. For this purpose, collar beam roof construction in a typical single-family house was analyzed. It was found that smaller rafter spacing generates a higher assembly cost and takes more time to construct. The implications of LCC were evaluated to find out that:

- a rafter spacing of  $l_{eff} = 110$  cm gives the best result for every calculated roof angle. It gives the lowest cost of building. In Poland it is popular to design  $l_{eff} = 60 \div 80$  cm and, only due to insulation, have a rafter  $h$  dimension of about 20 cm. Roof constructions are redesigned, which generates unnecessary costs,
- the participation of patch volume in roof construction for  $l_{eff} = 110$  cm is between 29 and 37%. It is therefore important to take into account patch dimensions. To reduce costs engineers should design roofs with a rafter spacing of  $l_{eff} = 100 \div 120$  cm or consciously choose patch dimensions that are dependent on rafter spacing. Rafter cost is only bigger than execution cost for  $\alpha = 60^\circ$ , which is because of rafter length,
- for bigger roof angles it is more important to focus on rafter dimensions and rafter spacing.

Life cycle cost after taking into account the discount rate, shows that the value lost is lower for flatter roofs. Moreover, it is cheaper to build a roof construction that has a lower wood volume request.

## References

1. Barthelemy, J.F., Haftka, R.T.: Approximation concepts for optimum structural design—a review. *Struct. Multidiscip. Optim.* **5**(3), 129–144 (1993)
2. Bribián, I.Z., Capilla, A.V., Usón, A.A.: Life cycle assessment of building materials: Comparative analysis of energy and environmental impacts and evaluation of the eco-efficiency improvement potential. *Build. Environ.* **46**(5), 1133–1140 (2011)
3. Cabeza, L.F., Rincón, L., Vilarinho, V., Pérez, G., Castell, A.: Life cycle assessment (LCA) and life cycle energy analysis (LCEA) of buildings and the building sector: a review. *Renew. Sustain. Energy Rev.* **29**, 394–416 (2014)
4. Chau, C.K., Leung, T.M., Ng, W.Y.: A review on life cycle assessment, life cycle energy assessment and life cycle carbon emissions assessment on buildings. *Appl. Energy* **143**, 395–413 (2015)
5. EN 1991-1-1:2002. Eurocode 1 Actions on Structures. Part 1–1: General Actions—Densities, Self-Weight, Imposed Loads for Buildings, European Standard
6. EN 1991-1-3:2003. Eurocode 1 Actions on Structures. Part 1–3: General Actions—Snow Loads, European Standard
7. EN 1991-1-4:2005+A1:2010. Eurocode 1 Actions on Structures. Part 1–4: General Actions—Wind Actions, European Standard
8. EN 1995-1-1:2004+A1:2008. Eurocode 5: Design of Timber Structures. Part 1–1: General—Common Rules and Rules for Buildings, European Standard
9. Ewins, R.: A review of computational optimisation methods applied to sustainable building design. *Renew. Sustain. Energy Rev.* **22**, 230–245 (2013)
10. Gluch, P., Baumann, H.: The life cycle costing (LCC) approach: a conceptual discussion of its usefulness for environmental decision-making. *Build. Environ.* **39**(5), 571–580 (2004)
11. Islam, H., Jollands, M., Setunge, S., Ahmed, I., Haque, N.: Life cycle assessment and life cycle cost implications of wall assemblages designs. *Energy Build.* **84**, 33–45 (2014)
12. Islam, H., Jollands, M., Setunge, S., Haqu, N., Bhuiyan, M.A.: Life cycle assessment and life cycle cost implications for roofing and floor designs in residential buildings. *Energy Build.* **104**, 250–263 (2015)
13. ISO, B.: 15686-5: 2017. Buildings and constructed assets. Service life planning. Life-cycle costing. BSI (2017)
14. Khasreen, M.M., Banfill, P.F., Menzies, G.F.: Life-cycle assessment and the environmental impact of buildings: a review. *Sustainability* **1**(3), 674–701 (2009)
15. Langston, C.: Life-cost approach to building evaluation, 2nd edn. University of New South Wales Press, NSW, Australia (2013)
16. McKenzie, W.M., Zhang, B.: Design of Structural Timber: To Eurocode 5, 2nd edn. Macmillan International Higher Education, Basingstoke, New York (2007)
17. Mithraratne, N., Vale, B.: Life cycle analysis model for New Zealand houses. *Build. Environ.* **39**(4), 483–492 (2004)
18. Noone, M.J., Woellner, W.C.: Roofing tile, roof and method of assembling. US Patent 6,178,703, Jan 30 2001 (1993)
19. Mora, E.P.: Life cycle, sustainability and the transcendent quality of building materials. *Build. Environ.* **42**(3), 1329–1334 (2007)
20. Porteous, J., Kermani, A.: Structural Timber Design to Eurocode 5, pp. 104–115. Blackwell, London (2007)
21. Singh, A., Berghor, G., Joshi, S., Syal, M.: Review of life-cycle assessment applications in building construction. *J. Archit. Eng.* **17**(1), 15–23 (2010)
22. Sonmez, F.O.: Optimum design of composite structures: A literature survey (1969-2009). *J. Reinf. Plast. Compos.* **36**(1), 3–39 (2017)
23. Southerland, R., Canition, J.: Rafter assembly and fixtures. US Patent 4,335,555, 22 June 1982 (1980)
24. Stalnaker, J., Harris, E.: Structural Design in Wood. Springer Science & Business Media, Dordrecht (1997)

25. Statistics Poland—Główny Urząd Statystyczny, Warsaw. <http://stat.gov.pl> (2018). Accessed 5 May 2018
26. Worth, Z., Boyle, C., McDowall, R.: Combined life-cycle cost assessment of roof construction. *Proc. Inst. Civil Eng.—Eng. Sustain.* **160**(4), 189–198 (2007)
27. Wrightman, R.: Roof construction. US Patent 7,581,358, 1 Sept 2009 (2004)



# Analysis and Conceptual Development of a New Packaging Material—Air Pack



J. Silva and J. L. Alves

**Abstract** The packaging industry, besides motivation, usability and appealing to the customer, considers the protection of products a necessity and obligation for its success, contemplating all the necessary steps to reach the desired goal. The current paper presents the research and development work, conducted in the scope of the Master Program in Product and Industrial Design of University of Porto (MDIP), in partnership with Bosch Security Systems. The main objective was the study and development of a new material—Air Pack—for the packaging industry. Firstly, several studies of the material were carried out in order to characterize its operation and benefits, more focused on the industry but with big impact in the research field. Two solutions were developed for the company products, taking into account their complexity, shape and implementation on the manufacturing process. Principles such as consumer usability, the nature of packaging, technical protection aspects and methods of transport were well established in both projects. The new material allowed the company and the university to cooperate with each other, granting the student space to understand the business world but also indispensable research. Finally, the material is a good improvement for the packaging industry, where mechanical properties are sometimes better compared to materials such as EPS. The two solutions developed showed that the material can be shaped for a specific product. This material offers a more cost competitive approach to packaging materials and a significant reduction in volume and storage space occupation.

**Keywords** Packaging · Sustainability · Air pack · Design

---

J. Silva (✉)

Faculdade de Engenharia, Universidade do Porto, Rua Dr. Roberto Frias, Porto 4200-465, Portugal  
e-mail: [joao.393@hotmail.com](mailto:joao.393@hotmail.com)

J. Silva · J. L. Alves

Product and Industrial Design, University of Porto, 4200-465 Porto, PT, Portugal

J. L. Alves

INEGI, FEUP, Rua Dr. Roberto Frias, 4200-465 Porto, PT, Portugal

© Springer Nature Switzerland AG 2019

L. F. M. da Silva (ed.), *Materials Design and Applications II*, Advanced Structured Materials 98, [https://doi.org/10.1007/978-3-030-02257-0\\_16](https://doi.org/10.1007/978-3-030-02257-0_16)

203

## 1 Introduction and Framework

The objective of this study performed within MDIP [1], was the evaluation of a new packaging material, where several considerations such as transportation, mechanical properties, 3D modelling, material specification and sustainability were taken into consideration.

Bosch Security Systems (Ovar, Portugal), being an international company and having such an impact on global economy, view this research as an important opportunity for reducing several issues currently existing in the distribution and production systems. It is considered that an important change around sustainability is vital, and with the new law to reduce the production of plastic [2], a new approach must be established.

Beyond the study and characterization of the new material, two case studies were developed and industrialized. The solutions developed tried to, as far as possible, fulfil the mechanical and physical constraints imposed by the company and reduce the cost of packaging material. Finally, both cases allowed improvements on the production system of the company, the complete protection of the product and User Experience.

## 2 State of the Art

### 2.1 Packaging Materials

Nowadays, companies are concerned with more sustainable solutions for their goods. Examples of applications of eco-friendly packaging can be found everywhere, however cases of success, at an industrial level, for high cost and fragile products are almost inexistent [3, 4].

The following work focuses the research conducted on protective packaging, and mostly on materials already used by the company. This type of packaging protects the product from the external impacts supported during transportation and storage. The main requirements for these materials are the reduction of impact and vibration, the immobilization inside the boxes and finally the occupation of empty space during transportation. The average cost of packaging on the total product cost should be less than 3% of the total price of the product [5]. A review of all the current packaging materials is presented on Fig. 1 [5].

The packaging materials were separated into 5 primary groups.

- Filling material which is normally used as a helper on occupation of empty space inside boxes, characterized by peanut foams;
- Blisters, present on general materials, are very important, especially for high volumes and high production cycles;
- Inflatable materials, where the Air Pack is integrated, have an important ratio volume/mass compared to other materials;

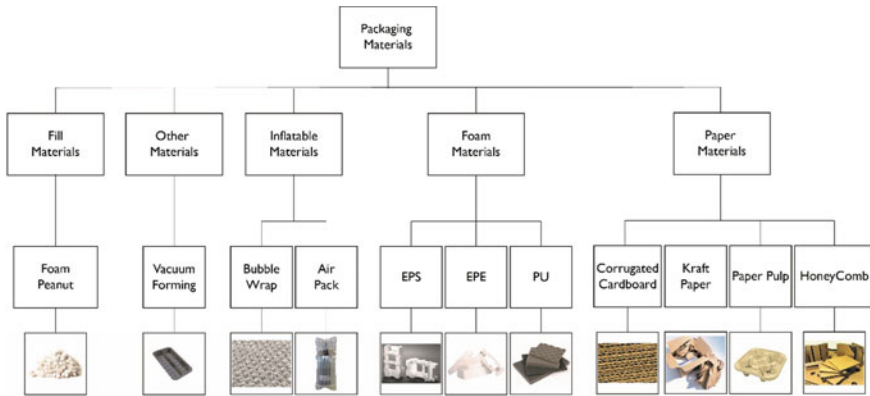


Fig. 1 Main packaging materials currently employed on the company [5]

- Foam materials, one of the most common materials, are applied for heavier and sensible products, because of the high deformation that can be obtained;
- Paper materials, another common material, are currently used in almost every box for transportation.

## 2.2 Air Pack

The Air Pack is considered an inflatable material because it uses compressed air as a mechanism of protection. This product is an extruded polymer composed of polyamides with adequate mechanical resistance, and low-density polyethylene which provides ductility and resilience [6, 7]. This film can be composed up to 9 layers of co extruded material with different thickness [8], conferring it a range of properties tailored for different applications.

Although the Air Pack product is an inflatable material, in contrary to the bubble wrap, it does not need an industrial equipment to be inflated [9, 10]. After the films are produced, they are joined and heat sealed together forming separate chambers. Later they are inflated with air and form a protective barrier between the product and the exterior. The air inside the chambers can be compressed because an anti-return valve is placed at the top of each chamber, which prevents the air to leave after being injected inside, as illustrated in Fig. 2.

While this filler material is recent in the packaging industry, it has already been implemented in some range of products such as wine industry. Currently, the applications are almost endless, except for products with sharp hedges and very complex shapes. The low density and volume of the material confers it a different approach to electronics products and it can easily replace foam materials.

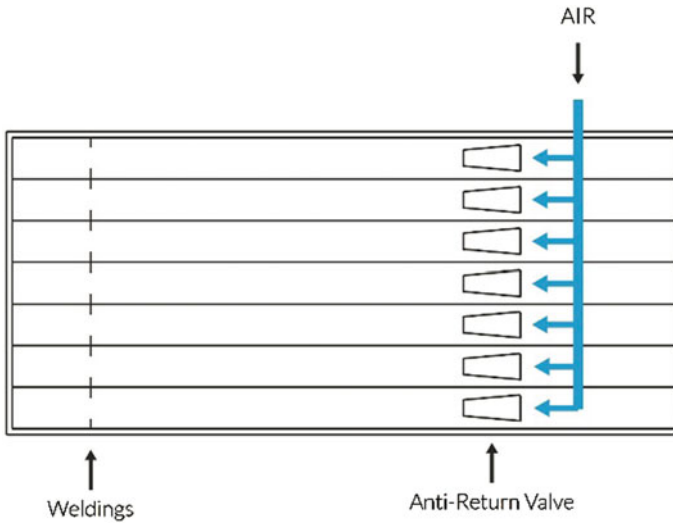


Fig. 2 Scheme of air path during inflation [5]

### 2.3 Packaging Tests

The principal purpose of packaging materials is preventing damage on the products until they reach the final customer, so, for that, there are a set of packaging tests necessary to consider and perform, in order to guarantee the quality of developments [11].

Product fragility is a term used to characterize the ability of a product to sustain high levels of accelerations. Electronics devices are very delicate and can be damaged during their handling and transportation [12–14]. In the standard ASTM D3332 [15], it is described a methodology to define an area of acceleration damage where the product must not be located. For the company these values and areas are used to understand what are the necessary stages that must be reached during the evaluation tests.

Based on international standards, such as ISTA 2 Series [16] and ASTM D6198 [17], the company built its own standard for the tests to be performed. The principal evaluation tests for the packaging are the following: 1. Atmospheric conditioning, to submit the products to various levels of relative humidity and temperature; 2. Compressions tests, to verify the stacking ability of the boxes during storage. The compression load that must be reached is based on the weight and volume of the boxes; 3. Vibration test, simulates all the possible ways of transportation. Although there are standards values to perform the tests, the best way is to evaluate their route during distribution cycles; 4. Impact test, validates box drops during transportation. The evaluation methodology is composed of drops in all boxes sides at a height based on the weight of the product.

## 3 Experimental Work

### 3.1 Material Study

The first part of the experimental work was the characterization of the material. The following evaluations were done with material already inflated. No specific evaluation was done to the quantities of each raw material present on the film. The supplier stated that the average distribution is 80% LDPE (low density polyethylene) and 20% Nylon. The evaluations performed were based on the typical distribution systems of the company and the possible external effects during transportation.

The material was measured before and after inflation so that the implications of requesting samples and correctly define tolerances for the material drawings were understood.

The material was tested through evaluations of height, based on the standard ASTM D6653 [18], checking the implications of different pressure variations [19]. Three tests were done on a vacuum chamber, with  $\pm 0.001$  bar, intended to simulate a transport at different altitudes considering the atmospheric pressure variation; a truck (3658 m) with an atmospheric pressure of 0.64 bar, a commercial pressurized airplane (2438 m) with a atmospheric pressure of 0.75 bar and a non-pressurized airplane (4877 m) with 0.55 bar of atmospheric pressure.

The influence of relative humidity and temperature has a significant impact on the material [19]. Based on various locations of the distribution centres and production facilities of the company, a total of 8 evaluations were defined. The range of temperature was comprised between 45 and  $-15$  °C and the range of relative humidity was between 98 and 10%. The tests had different durations ranging from 72 to 100 h.

The static compression the manufactured product would produce on the packaging material was another important aspect. For this purpose, a total of 36 tests were done varying the diameter of the chambers from 30 to 60 mm and the inflation pressure inside each chamber from 0.5 to 1.5 bar, to analyse the air pack dimensional changes before and after inflation.

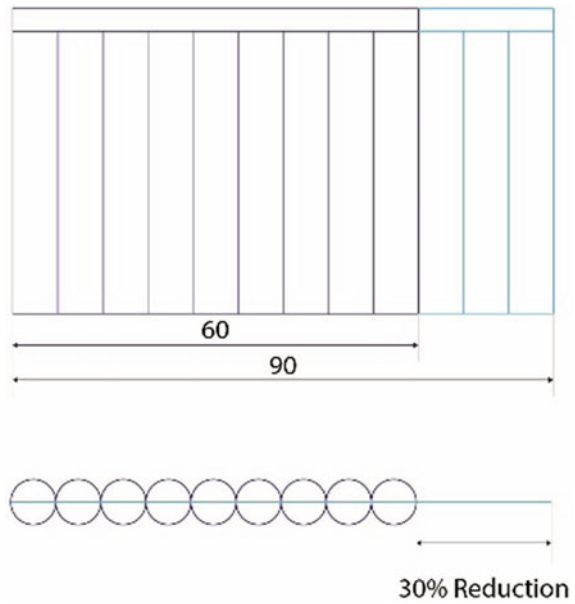
## 4 Results

The results presented are a summary of the set of evaluations and some refinements of the data.

The material has a reduction of 30% of its length after inflation, as shown on Fig. 3. The width of the material doesn't suffer any considerable change. The diameter of the chamber is not the same after inflation as initially specified, there is an average reduction of 40% between the two dimensions.

After testing the material for different altitudes, it was concluded that it is able to sustain all the outside pressures imposed, with the previously specified internal pressurized air. For the typology of transportations analysed, the material will not have

**Fig. 3** Illustration of the material sizes reduction after inflation [5]



any limitations. The maximum altitude was 6500 m, where 0.35 bar of atmospheric pressure was considered, and, in that period, only the higher diameter chambers started to deform and burst (Fig. 4).

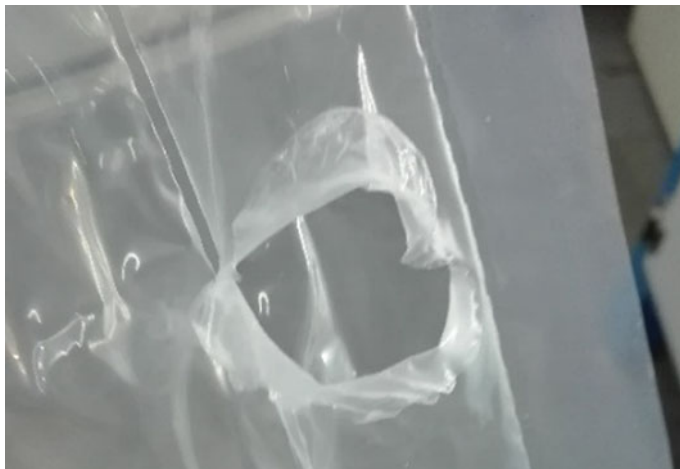


**Fig. 4** Test to simulate the altitude pressure in internal pressurized chambers, showing burst of some chambers with 60 mm diameter

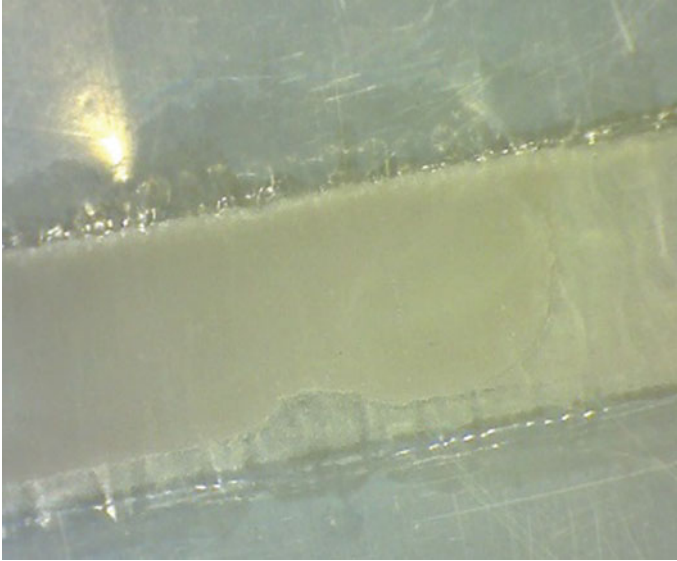


**Fig. 5** Results from temperature and humidity tests, showing some residual water droplets inside sealed areas

No severe limitations or impossibilities occurred during the tests varying the temperature and relative humidity in inflated and deflated air pack. One important aspect that was noticed after the tests was the appearance of water droplets on the sealed areas (Fig. 5). Although this only appear on high humidity tests, near 98%, it can damage the integrity of the material, although no chamber burst or deformations has been registered.

For the compression tests the samples were cut with three chambers, helping on standardization and verification. The material can support static forces, applied by a flat plate, up to 5.000 N. The maximum internal pressure obtained in the tests was 15 bar, based on the initial pressurized air. Although the promising results, it is beneficial not to use this material in such heavy products and with high internal pressure.

## 5 Case Studies

The main objectives to study during these developments were the improvement on User Experience for the costumer, reduction of costs and volumes in packaging material, decrease and enhance the production cycles and better protection of products.

The developments were initially proposed for two cameras, discussed here as cameras A and B. They vary in size, complexity, shape and weight.

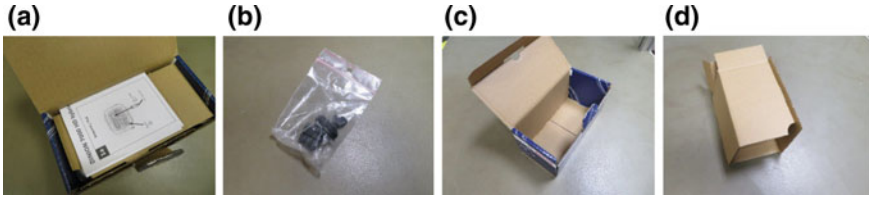


**Fig. 6** Illustration of existent solution for camera A. **a** Installation guide; **b** accessories bag; **c** product box **d** cardboard inlay

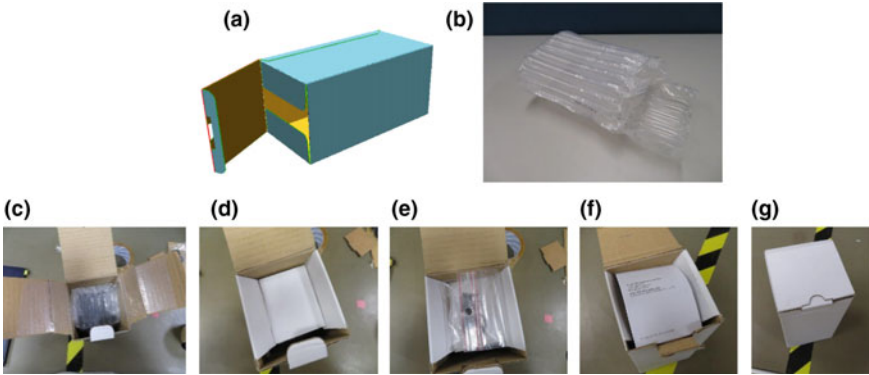


**Fig. 7** Final solution for the box and air pack. **a** New product box; **b** new Air pack inlay; **c-g** assembly sequence of the new solution for camera

Although the cameras are already in production, these developments will improve the goals above but also another special feature for each one.

Camera A is characterized by its small format, normally used in building surveillance. In this case the solution would have to allow the installer to do the pre-configuration of all the cameras before they go for installation.

Camera B has more complexity in terms of shape and volume. The development needed to consider the possibility of a camera to be shipped with and without a set of 2 more accessories.

Currently, camera A uses 5 materials in order to be safely transported. Corrugated cardboard is used on the product protection and for the outside box (FEFCO 0470). The camera is placed inside a polyethylene bag before being placed on the cardboard inlay. Finally, there is a set of accessories placed in a zip bag and a manual which is placed at the top of the assembly (Fig. 6).

On the new solution, air pack was used as a mean to protect the product. The outside box was change to an automatic folding instead of manual folding, improving the production cycle. On the new solution the box is open on top allowing for the desired pre-configuration of the camera without the need to remove it from the package. Figure 7 shows the sequence of assembly steps, the solution for the new box and for the air pack material.



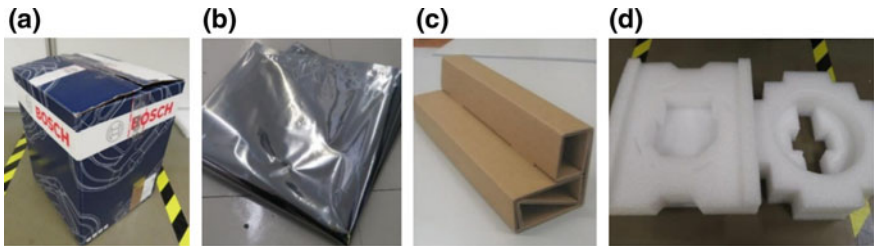


**Fig. 8** Illustration of the existent solution for camera B. **a** Product box; **b** ESD shield bag; **c** cardboard corner inlay; **d** expanded polyethylene foam inlay

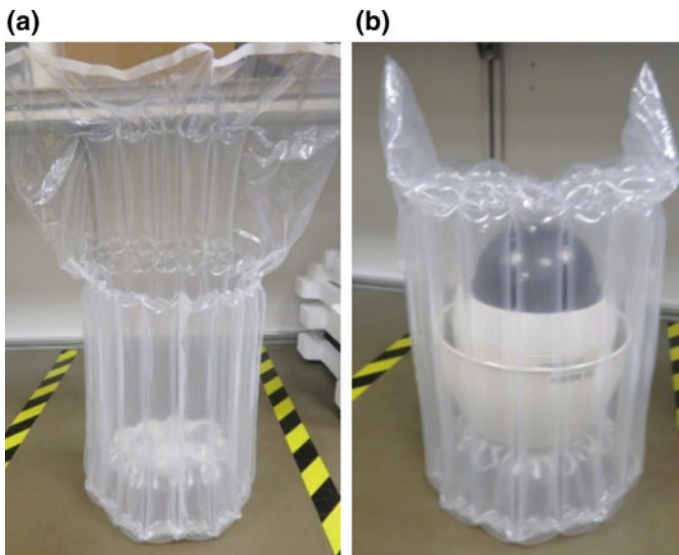


**Fig. 9** Air pack solution for camera B. **a** New air pack inlay; **b** camera B inside inlay

Camera B, because of having higher complexity and fragility uses a more intricate assembly sequence and more costly materials. The outside box is made of corrugated cardboard (FEFCO 0201). The camera is placed inside a shield zip bag, preventing electric discharges and humidity. The shock protection is obtained by two EPE foam inlays placed on the top and bottom of the box and 4 corrugated cardboard corners (Fig. 8).

For the new development and since it can be transported with and without accessories, the solution was divided in two portions that help on assembly and transportation. The first development consists on the protection of the camera itself. It is made of a circular air pack bag, closed on the bottom and open on top (Fig. 9), allowing an easy separation of camera and accessories. The following solution, because of its shape, will also remove the zip bag and create a complete separation between the exterior and the camera.



**Fig. 10** Air pack solution for accessories of camera B. **a** New accessories air pack inlay; **b**, **c** accessories inside new inlay

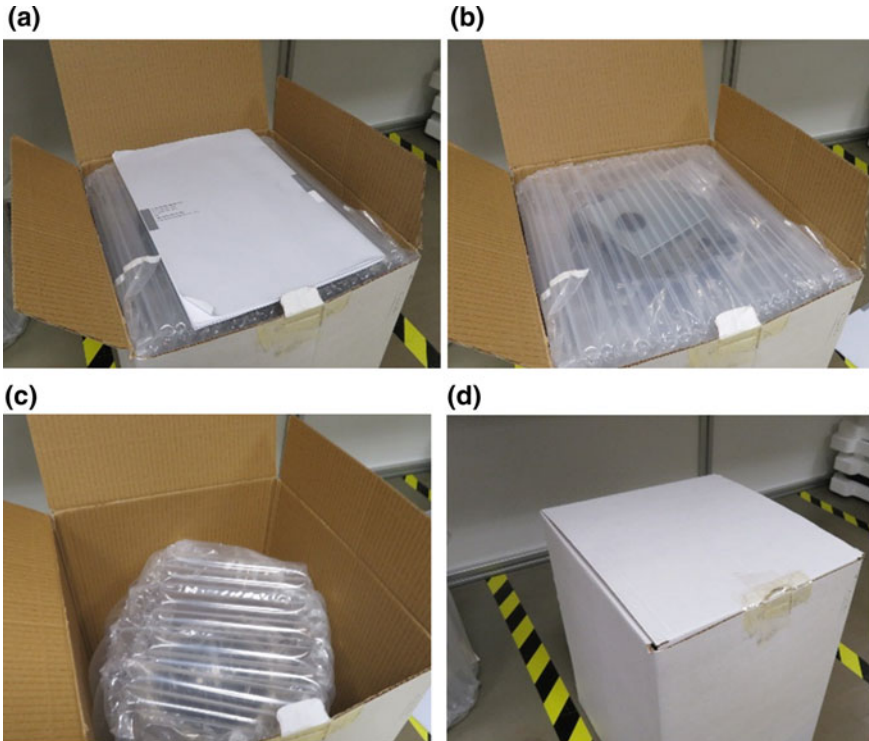


**Fig. 11** a–d Assembly sequence of the new solution for camera B

Secondly, the development for the accessories was also a custom-made solution were the design consists of a rectangular shaped bag. Inside were placed both accessories separated by a plastic film not inflated, which prevents any scratch on the parts (Fig. 10). Depending on the camera model to be shipped, the accessories bag will be empty or with the necessary accessories.

The final new sequence of assembly is shown on the Fig. 11.

## 5.1 Cost Reduction

One important aspect analysed during both developments was the material savings obtained by the two new solutions. Currently, because the company uses all the materials described above, the total cost of material for both solutions in a year of production is around 189.000€. The new solutions presented above will produce a total cost around 89.000€, which allow for a reduction in 100.000€ on packaging material for the two cameras. Besides the monetary savings the new material could produce savings in warehouse up to 300%.

## 6 Conclusions

This paper presents two solutions that were implemented for packaging of two electronic surveillance cameras. The new solution discarded the polystyrene foam that is a material that has been forbidden due to its impact on environment.

The solutions developed allow for a confirmation that various shapes and forms can be developed which confers a big versatility to packaging various products.

The mechanical and physical properties found after the experimental work position the air pack as an equivalent and substitute to EPS and EPE. It was shown that the material was able to support all the requests in terms of humidity and temperature. A more extended research must be done on impact and compression, although the results gathered are a good indicator for the packaging industry of electronic products.

Besides all the considerations referred, the material has three important characteristics that will help define him in the future; a more competitive price and volume per product compared to EPS and EPE; a better User experience for the costumer but also for the production cycles and production workers; and finally the low waste creation and better sustainability.

## References

1. Gomes, A., Rangel, B., Carneiro, V., Lino, J.: "Learning by Doing" Integrated Project Design in a Master Program on Product and Industrial Design", Contributions to Higher Engineering Education (2018)
2. A European Strategy for Plastics in a Circular Economy. European Commission (2018)
3. Racounter.: Future of packaging 2016 report, London, October 2016
4. Racounter.: Future of packaging 2015 report, London, September 2015
5. Silva, J.: Análise e desenvolvimento conceptual de um novo material para embalagem, Master Thesis, MDIP, UPorto, Portugal, October 2017
6. "PA—Polyamide." PA Polyamide Nylon—TECAMID | Ensinger
7. Lazonby, J.: "Polyamides." The Essential Chemical Industry online (2017)
8. Corporation, D.: "What is Coextruded Multi-layer Film?" What is Coextruded Multi-layer Film? | DIC Corporation

9. Systems, A.: “Air Packaging | Inflatable Packaging | Bottle Packaging | Packing Systems.” | Airpack Systems
10. Sales, S.: “Column Air Packaging.” | Sealer Sales Column Air Packaging
11. Schueneman, H.H.: Cushion Material Testing. Westpak, Inc. (1993)
12. Schueneman, H.H.: Fragility Assessment: An In-Depth Look at a Now Familiar Process. Westpak, Inc
13. Newton, R.E.: Fragility assessment theory and test procedure (1968)
14. Schueneman, H.H.: Product Shock Fragility Testing: Acquisition and use of Critical Velocity Change Data. Westpak, Inc. (1993)
15. ASTM D3332-99 (2016), Standard Test Methods for Mechanical-Shock Fragility of Products, Using Shock Machines, ASTM International, West Conshohocken, PA, (2016)
16. ISTA 2 SERIES Partial Simulation Performance Tests, ISTA International Safe Transit Association (2011)
17. ASTM D6198-18, Standard Guide for Transport Packaging Design, ASTM International, West Conshohocken, PA (2018)
18. ASTM D6653/ D6653 M-13, Standard Test Methods for Determining the Effects of High Altitude on Packaging Systems by Vacuum Method, ASTM International, West Conshohocken, PA (2013). [www.astm.org](http://www.astm.org)
19. Singh, S.P., Singh, J., Stallings, J., Burgess, G., Saha, K.: Measurement and analysis of temperature and pressure in high altitude air shipments. *Packag. Technol. Sci.*, **23**, 35–46 (2010). <https://doi.org/10.1002/pts.877>

# The Toy as a Factor of Better Children's Integration in Hospitalization Context



T. Freitas, B. Rangel and J. Lino Alves

**Abstract** Nowadays, about 121.000 pediatric hospitalizations occur every year in Portuguese hospitals. Hospital admission is a process in which individuals are imposed to change their routines and daily habits and be integrated in a completely new environment. For children, this process is worse than for adults and it leads to undesirable feelings, such as fear and anxiety, which can result in a traumatic experience that negatively affects the recovering process. This paper presents the research work that has been conducted in the scope of the Master Program in Product and Industrial Design of University of Porto, seeking to understand how Design, along with the strategies already used to reduce the negative impact caused by hospitalizations in children's life, can be used to create a toy that promotes moments of abstraction from the environment in which children are inserted in, as well as moments of play combined with learning and physical, cognitive and social development. Based on the analysis of data collected, a building toy was developed, “*Boneco Cubo*”, composed by different parts that can be attached to each other in different ways and that intends to contribute to a better integration in the hospital environment while simultaneously stimulating the children's development. It also intends to be an ally to healthcare professionals as an instrument of children development evaluation.

**Keywords** Toys in hospitals · Hospitalization · Child · Design

---

T. Freitas (✉) · B. Rangel · J. L. Alves  
Product and Industrial Design, University of Porto, Porto, Portugal  
e-mail: [teresa.m.v.freitas@gmail.com](mailto:teresa.m.v.freitas@gmail.com)

B. Rangel  
e-mail: [brangel@fe.up.pt](mailto:brangel@fe.up.pt)

J. L. Alves  
e-mail: [falves@fe.up.pt](mailto:falves@fe.up.pt)

T. Freitas  
Design Studio, Faculty of Engineering, University of Porto, Rua Dr. Roberto Frias, Porto  
4200-465, Portugal

J. L. Alves  
INEGI, Faculty of Engineering, University of Porto, Porto, Portugal

© Springer Nature Switzerland AG 2019  
L. F. M. da Silva (ed.), *Materials Design and Applications II*, Advanced  
Structured Materials 98, [https://doi.org/10.1007/978-3-030-02257-0\\_17](https://doi.org/10.1007/978-3-030-02257-0_17)

## 1 Introduction

In Portugal, accordingly to *Instituto Nacional de Estatística*—INE,<sup>1</sup> there are about 121.000 pediatric admissions every year, affecting children from 0 to 18 years old [1–3]. Besides not being in their comfort zone and being forced to leave their daily routines, the child is also faced with other factors that may have a negative and traumatic impact on his development when submitted to an admission in hospital. Factors such as various hospital procedures; examinations and treatments; environment and unknown people; negative feelings like pain, fear and anxiety; distance from family and friends and others may contribute to a negative experience in their life and influence their development and recovery [4].

The significance of hospital experience varies in type and degree and depends on the diversity of causes that are involved, from disease-related aspects to the psychological characteristics of children themselves. Reflecting on these meanings, becomes important with regard to pediatric management and guidance and may have a determining influence on the development of the hospitalized child [5]. Both the environment and the creation of recreational spaces, activities and projects influence the child's well-being and, if they follow certain norms, can make hospital experience less traumatic and reduce the effects of hospitalization on children to a minimum [6–8].

Piaget, during his researches, considered playing a typical children behavior, which allowed them to have moments of pleasure and happiness [9]. It is through play that children learn, experience, discover and develop their capacities, both physical and cognitive ones. It is also playing that provides moments of relaxation and abstraction from the hospital context and it can be a great ally to the accomplishment of therapies. In addition, it is through play that they also express their feelings, frustrations, anxieties, criticisms and interests, which means it can contribute to a better diagnosis [10, 11].

Concluding, incorporating activities, projects and play spaces, as well as the toy, into the daily life of the hospitalized children, will be very important and can positively help the recovery process, as they provide the continuity of growth and development [11, 12].

## 2 Methodology

Qualitative approach was used to collect relevant information about hospitalized children's needs, behaviors, problems, preferences and wishes. With this in mind, data for research was collected from two pediatric centers located in the Northern region of Portugal, one with specialty and another of general clinic. Data has been

---

<sup>1</sup>National statistical institute of Portugal (INE) is an organization charged with the overall coordination of statistical services. It provides statistics on demography, economy and society of all regions of Portugal.

collected from three distinct sources: (1) direct analysis by observing children behavior in the context of hospitalization; (2) surveys answered by multidisciplinary teams from pediatric centers, parents, family and friends; (3) validation tests applied to the proposed solution with all research participants.

### 3 Data Collected

Data collection was made in two distinct phases: state of the art—research by exploring what has already been studied by other authors; and on-site data collection.

#### 3.1 Secondary Research and Visual Research

##### *Strategies and Spaces*

Some strategies have been adopted in order to improve children's conditions inside hospitals. It was verified that both the environment and the creation of play spaces positively influence the well-being of children; and that if they follow certain standards, they may make hospital experience less traumatic, thus minimizing the negative effects of internment on children [11].

Hospitals are already trying to improve the conditions in pediatric internment to minimize, as much as possible, the negative impact of hospital admission and procedures, providing more tranquility and less disturbance in hospitalized children [5].

Making the hospital environment as close as possible to the external reality can interfere with the children's emotional state and thus influence their recovery in a positive way. A decoration adapted to the children's age groups, as is the example of the Morag Myerscough bedroom decoration project of the Sheffield Children's Hospital pediatric service [13] or others Pediatric centers in Portugal (Fig. 1), combined with playful and pedagogical activities, for example the visits of the Red Nose Operation Clown Doctors [14], make children closer to their reality and distract them from hospital procedures. This is also achieved by including ludic-pedagogical



**Fig. 1** Pediatrics service inner decoration in Northern of Portugal



**Fig. 2** Activity’s rooms of pediatrics service in Northern of Portugal



**Fig. 3** Activity’s rooms of pediatrics service in Northern of Portugal

rooms in pediatric services. These rooms are spaces where children can play, read, draw, socialize, in a more playful context (Figs. 2 and 3).

**Toys**

All toys develop specific abilities in children, stimulating cognitive and motor development. For this reason, toys are considered a great ally to the development of children.

Some toys were already designed for hospital context. From those toys, one can point out: (1) ELO—teddy bear which was developed for children with cancer who have to spend much of their time in isolation, away from their family and friends [15]



**Fig. 4** Little bear ELO By Amaral Carvalho Hospital, Brasil. Illustration based on Ref. [15]



**Fig. 5** Kompis robot By Linus Sundblad. Illustration based on Ref. [16]

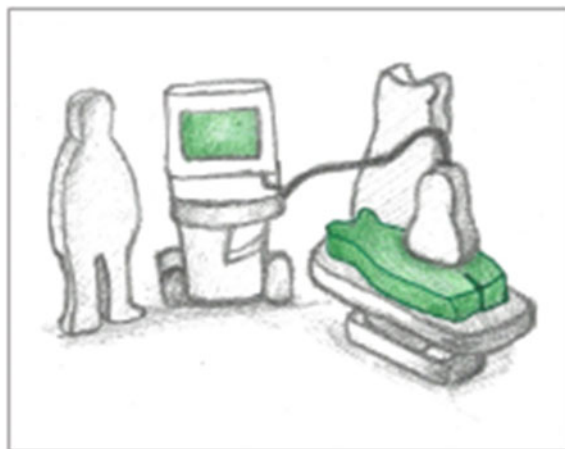


**Fig. 6** Novel hospital toys By Hikaru Imamura. Illustration based on Ref. [17]

(Fig. 4); (2) Kompis—which was designed with the purpose of acting as a companion for children in the hospital and as a platform for communication between children and their friends/parents [16] (Fig. 5); (3) Novel Hospital Toys—allowed children to better accept and understand some medical exams [17] (Fig. 6).

With the analysis of all toys that already exist in healthcare, it is easier to understand this particular market and perceive how helpful toys can be for children.

**Materials and Manufacturing Processes**

Materials and its choice are truly important in any design project as it is from it one can apply multiple specification to the product—from textures and colors to resistance and density. When talking about a toy for hospitalized children, it is even more important as several requirements need to be taken into account:

- Resistant to impact;
- Easy to clean;
- Resistant to chemical cleaning products;
- Low density (lightweight);
- Flexible and touch-friendly;
- Low cost.

After some research, it was easily noticed that toys are mainly made of plastic. There are also some toys made of wood, fabric and cardboard. These materials cannot be applied to hospital context as they do not fulfill the majority of requirements imposed, due to the characteristics each material presents. These properties can be analyzed in more detail in Table 1.

By using CES EduPack database (Granta Design, Cambridge, UK) [18], an analysis on materials characteristics was conducted. From this study, it was concluded that polymers are the family of materials that fit the most for clinical toys. Polymers are usually cheap and its main characteristics are: low density, high resistance to shock, high resistance to fret and flexibility. An interesting characteristic of this type of material is that it allows several distinct visual aspects (transparency, opacity,

**Table 1** Materials properties, from database of CES EduPack 2017 (Granta Design, Cambridge, UK) [18]

Material's properties							
Materials	Density	Resistance	Accumulation of external agents	Disinfectable	Resistance to aqueous solutions	Resistance to ethanol	Resistance to sterilization
Polymers	Low	Very resistant	No	Yes	Yes	Yes	Mostly yes
Paper	Low	Damage very easily	Yes	No	No	No	No
Card	Low		Yes	No	No	No	No
Wood	Average/high	Resistant	Depends on insulation	Depends on insulation	Depends on insulation	Depends on insulation	No
Fabrics	Low	Low resistance	Yes	No	No	No	Yes

etc.) with a wide range of colors [19]. However, there are many polymers and it is important to select the ones that most fit the requirements.

After some research, it was found that the most common polymers for manufacture of toys are: Acrylonitrile butadiene styrene (ABS), Polypropylene (PP), Polyethylene (PE), Polycarbonate (PC) and Polyvinyl chloride (PVC), (Table 2).

According to Table 2, all polymers are resistant to the chemicals, that are used to disinfect toys on hospitals. The most ductile materials are PP and PE, the latter being of low or high density, changing both mechanical and physical characteristics. A very important factor is the melting point of each polymer due to the possibility of being submitted to the sterilization for decontamination in the hospital context. PC is the material with the highest melting point however, it is an expensive material, quite rigid and is not resistant to chemicals.

Based on CES database [18], it has been found that the most common processes associated with the polymers are injection molding and extrusion. The raw material of the polymers is in the form of pellets which, prior to their shaping, may be added a colored pigment to subsequently the object be in the desired color.

### ***3.2 Primary Research—Direct Analysis and Surveys***

In Design there is a concern to create human-centered products. Based on this, it is important that future users and other elements are part of the development process by participation in data collection sessions and by testing the product as it is incrementally developed.

In order to achieve the aforementioned, a field research was implemented in the pediatric services of two hospitals in the north of Portugal—one of specialty and another one of general practice. This research was carried out over a period of five months between April and September 2017. The methods used to collect data were: direct observation and questionnaires.

As research participants, everyone that is involved in daily routines of hospitalized children was considered, such as parents, friends, family and hospital assistants: nurses, doctors, etc.; and the child himself.

#### ***Surveys***

Two different approaches were adopted for the questionnaires, depending on the participants of the research. In relation to the sample of the multidisciplinary technical team, it was decided to approach the heads of each team in order to serve as liaison element in the delivery and collection of the questionnaires. Regarding the sample of parents and relatives, it was decided to address each family or group of relatives in person, explaining the context of the project and ask for collaboration in filling in the questionnaires. As results, one hundred and seventy questionnaires were filled out and taken into account.

The statistical analysis of the data obtained in the questionnaires was done by using SPSS Statistics 24 software (IBM, New York, USA) [20]. The statistical anal-

**Table 2** Comparison of polymers characteristics, from database of CES EduPack 2017 (Granta Design, Cambridge, UK) [18]

Polymers characteristics									
Polymer	Type	Density kg/m <sup>3</sup>	Price EUR/kg	Fracture toughness MPa. m <sup>0.5</sup>	Melting point °C	Hardness	Resistance		
ABS	Thermoplastic	1.01e3–1.21e3	2.15–2.54	1.19–4.29	~175	Rigid	Aqueous solutions	Ethanol	Acetone
PP	Thermoplastic	890–910	1.52–1.58	3–4.5	150–175	Rigid/flexible	Excellent	Unacceptable	Unacceptable
PE	Thermoplastic	939–960	1.44–1.48	1.44–1.72	125–132	Rigid/flexible	Excellent	Excellent	Excellent
PC	Thermoplastic	1.14e3–1.21e3	3.04–3.26	2.1–4.6	225–250	Rigid	Excellent	Excellent	Unacceptable
PVC	Thermoplastic	1.3e31.58e3	1.25–1.43	1.46–5.12	180	Rigid	Excellent	Excellent	Limited usage
Rubber	Elastomer	930–940	2.06–2.69	0.15–0.25	–	Flexible	Excellent	Excellent	Excellent
Silicone	Elastomer	1.3e3–1.8e3	2.84–5.3	0.03–0.5	–	Flexible	Excellent	Excellent	Limited usage

ysis methods used were frequency analysis and fashion analysis. In general, all the questions in the questionnaire contribute significantly to the design development, however it is possible to highlight some of them in particular that will help to define the characteristics of the toy.

The behaviors, reactions and needs of hospitalized children aged 2–5 years helped to understand how children react to the hospital context and how the toy could help to overcome some negative aspects. Research participants answered that the most frequent behaviors and reactions in this age group would be: Fear of the environment and procedures (16.1% specialty, 20.6% overall); Distrust (9.4%—specialty, 11.3%—general); Cry (9.4%—specialty, 13.5%—general); Separation anxiety (13.8%—general); and as necessities, the main ones were: play activities, with 26.7%—specialty and 28.9%—general, and the company with 21.4%—specialty and 25.2%—general.

When parents were asked if children brought their toys to the hospital and the reason they bring them, 82.9% of the specialty sub-sample and 76.9% of the general reported that their child brought at least one toy to accompany them during hospitalization. Of those children who brought toys, they used them more to play alone (42.9%—specialty, 30.2%—general) and as a sleeping companion (26.8%—specialty, 31.7%—general).

In relation to what they brought, the toys were quite varied, from stuffed animals, construction toys, puzzles, carts and even the video games found on smartphones and tablets. About the most used toys, participants said the most used ones are: video games, puzzles, construction toys, dolls and reading stories. They also pointed out that the most recommended toys for children to share are: games, such as puzzles, memory games, association games, construction games and crafts. Regarding the opinion of the respondents on the most relevant characteristics that the toy should follow, the majority of answers considered to be important: the colors; the materials; be funny; and be educational. The attendants also mentioned that it is must be easily disinfected as it is a toy for the hospital context.

### **Results**

The most important thing in the creation of a toy for the hospital context is to understand what characteristics it should contain in order to better adapt to the context and the specific target audience. By analyzing the results retrieved from data collected in the surveys and direct observation, it was possible to conclude that the toy should obey the characteristics described in Table 3.

## **4 Experimental Work**

As a result of the entire research process, a toy was developed for children between the ages of 2 and 5 who are subject to hospital admission. With this toy it is intended to facilitate children integration into the new environment and to reduce the negative impact of hospitalization. The main goals of this product are: (1) minimize the

**Table 3** Characteristics of a toy for hospital context

Characteristics of a toy for hospital context	
Material	Resistant to shock and external aggression; resistant to hygienic chemicals; low density; flexible and pleasant to the touch
Colors	Adapted to each child or context. Do not contain too many colors, to not have too much information
Shapes	Simple, easy to understand, geometric
Price	Low
Type of toy	Recreational and/or therapeutic. Of construction, puzzles or characters
Resistant to high temperatures	Sterilization chamber
Hygiene standards	Resistant to hygiene products; easily disinfectable
Safety rules	Do not contain small parts; operating instructions, indication of all contraindications, age range
Easy to storage	Lack of space in the rooms, of activities of the pediatrics services
Dimensions	Suitable for the 2-5 years age group
Adaptability to several contexts	Rooms of internment and isolation and rooms of activities. Adaptable to various clinical pathologies
Possibilities	Sharing games between children. Personal toy
Integration element	Help integrate the child into the hospital

impact of hospital admission; (2) stimulate the development of bonds among children, parents and health technician; (3) promote moments of fun inside the hospital environment, and (4) stimulate children, both at physical, cognitive and social levels, allowing them to continue their development.

#### **4.1 Concepts**

From the previous research, it was found out that the toy should (1) be of education character; (2) provide companionship to children, as they miss their parents; (3) include handwork; (4) be a construction toy to improve children development as a person (Fig. 7).

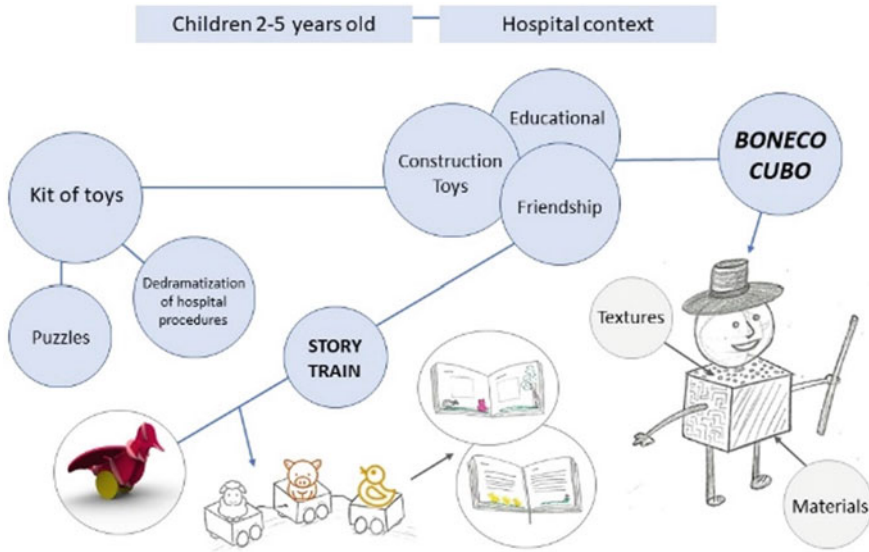
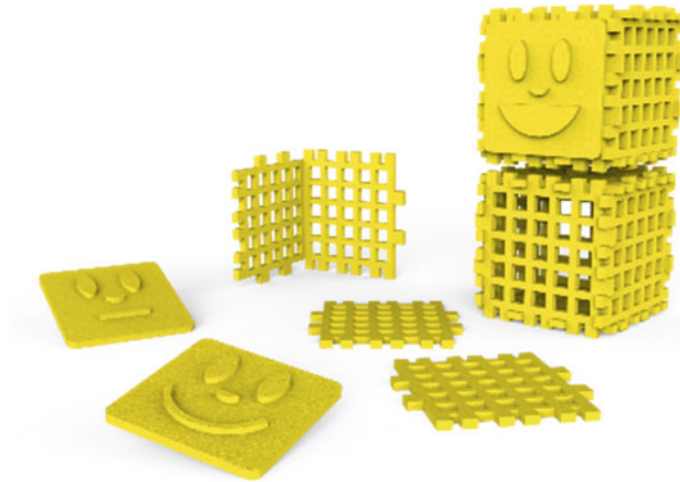


Fig. 7 Concept chart

### 4.2 Product Proposal

“Boneco Cubo” (Fig. 8) is a toy directed to children from 2 to 5 years old, submitted to a hospital admission or clinical interventions. This toy was developed according to all information retrieved on state-of-the-art analysis and onsite research and tries to fulfill all requirements imposed for being a toy for hospital environment. It aims to: (1) minimize the impact of hospital admission, (2) stimulate children integration with other children, parents and healthcare professionals, (3) promote moments of relax and fun in the hospital context. It also intends to facilitate the integration of children inside the hospital environment and follow the children during the entire process of hospital admission. Simultaneously, it helps to decrease negative impact that admission may cause, and it is intended that the toy also stimulates children development either at the physical, cognitive or social level. It is a toy of construction, in the form of a Kit, composed by several pieces that give the possibility to fit and to make multiple constructions. It is presented in the form of two cubes that represent the body and head of a doll, giving it a friendly character. This toy, in the form of a doll, aims to be a companion for children in hospital, not only to provide moments of fun, but also to face the fear of certain hospital procedures. Like all construction games, develops children’s motor, social and emotional abilities. With the textures and with the construction approach, it develops fine motor skills, eye-hand coordination, logical thinking, imagination and creativity. With different facial expressions, it is possible to work the children’s emotions and facilitate contact with professional health technicians, because about 70% of communication at these ages



**Fig. 8** “Boneco Cubo” on its final state



**Fig. 9** Diversity of fittings

is non-verbal.<sup>2</sup> The modular approach gives the possibility of several fittings (Fig. 9), allowing to make three-dimensional constructions or even flat. It was designed with a flexible and impact resistant material and resistant to hygienic chemicals.

### 4.3 Features

The “*Boneco Cubo*” has several facets and can be an ally not only to the hospital context but also to children’s daily life. It is a toy of integration of children in the internment by its friendly character. It can also serve as an instrument for evaluating the child’s development and to allow an easier communication between child and healthcare professional, thus having a therapeutic feature. This toy can be easily adapted to the Pediatric Pain Scale (Fig. 10), using the different facial expressions and colors. In the research it has been found that children transpose their feelings and personality into their toys and thus, adapting this scale, it will facilitate communication between health workers and children.

<sup>2</sup>Information obtained by a doctor of Pediatrics Service during a field research.





Fig. 10 Illustration based on Pediatric Pain Scale of Ref. [21]

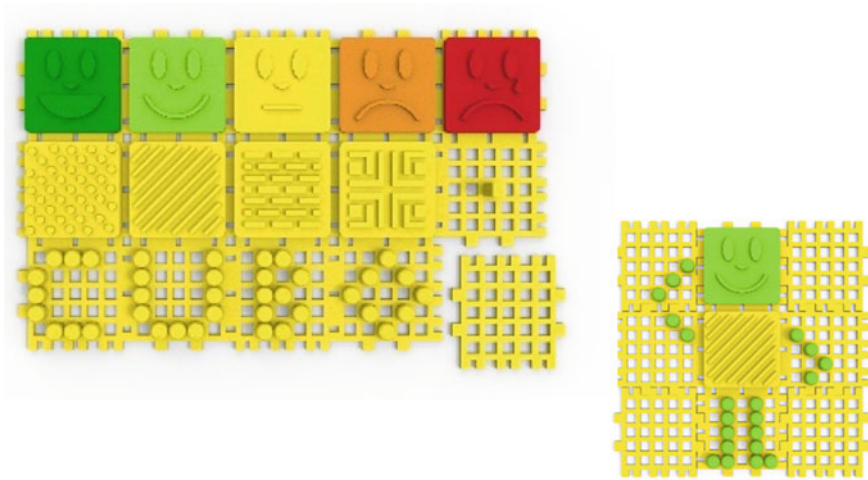


Fig. 11 “Boneco Cubo”—planification

Under the flat shape, the development of the child can be evaluated using pieces with textures. In this flat form (Fig. 11), it will give the possibility to learn how to plan the cube and to explore the toy. Through pins that fit the frame, suitable for children from 4 years of age, it is possible to draw multiple shapes, letters and numbers. While the child is having fun to assemble and disassemble the doll, it enters into a learning process, thus providing the continuity of its development. In the future, it will also be possible to use the alphabet and numbering.

#### 4.4 Materials

Based on the information studied about the materials that are most suitable for the manufacture of toys for the hospital context, the material chosen was Low Density Polyethylene (LDPE). This polymer has the following advantages:

- Flexible;
- Low density (0,939–0,960 g/cm<sup>3</sup>), which gives the possibility of floating in water;
- Excellent resistance to aqueous solutions, as well as to ethanol and acetone—used for the disinfection of toys;
- Cheap compared to other polymers;
- Non toxic;
- Very ductile and tough.

In relation to the high temperature resistance of the sterilization chamber, the melting point of this material is between 125 and 132 °C and the temperature at which begins to deform is between 90 and 110 °C, so it is recommended to regulate the temperature of the sterilization to below 90 °C. This is not a problem as during the onsite research, it was found out that most toys are only disinfected with hygienic chemicals such as ethanol [18]. As it is a construction toy, no mechanical connections were used. For the manufacturing process, the Injection Molding process is forecast, as it is a fast, and capable of producing a significant quantity of parts per hour. Not only due to the speed of production, it is the most indicated process according to the design of the toy.

In order to calculate the final production cost of each part it is necessary to add the cost of the material to the cost of the mold and divide by the number of parts to be manufactured. For a better understanding, a cost estimation is presented:

- Material: 1.44 – 1.48€/kg;
- Mold: €2.940 – €29.400 (since the molds are small and of little complexity, the estimation will be €3000 per mold (several parts can be manufactured on the same mold));
- Number of molds: x2 (€6.000);
- Number of pieces: 100.000;
- Weight per kit of 20 pieces:  $\approx \leftarrow 100$  g;
- Weight per piece:  $\approx \leftarrow 5$  g;
- Weight for 10 kits (200 pieces): 1 kg (€1,48);
- Material cost for 100.000 pieces: €740;
- Production cost of each piece:  $6.000 + 740 = 6740/100.000 \approx \leftarrow \leftarrow 0,0674$ ;
- Production cost of each kit:  $0.0674 \times 20 \approx \leftarrow \leftarrow 1,348$ .

This value is only a rough estimation and it may vary according to the quantity produced to amortize the price of the mold. In this estimation, some other costs were not considered such as: packaging costs, labor costs, fixed costs (electricity, maintenance, etc.). These costs would increase the price per kit.

## 5 Tests and Final Results

### 5.1 Prototyping

In order to proceed with product’s usability tests, a real-scale functional prototype was made in the 3D printing laboratory of FEUP, in a low-cost 3D printer. The Fused Deposition Modelling (FDM) is the most popular Additive Manufacturing process consisting in extruding a filament of melted material, normally plastic, and depositing it, layer by layer, on the machine’s platform, in order to create the model [22, 23].

To start the prototyping process, all parts of the toy were modeled in 3D, using SolidWorks 2016–17 student edition (Dassault Systèmes SolidWorks Corporation, Waltham, USA) and exported into STL files. After that, these files were converted into a gcode file by the machine’s software, which is all the required information for starting the printing process, such as temperature, positioning, trajectories, etc. [24]. The pieces were made on a 3D printer Hello Bee Prusa (BEE Very Creative, Aveiro, Portugal), with the materials—PLA (rigid material), TPU and FLEX (flexible materials) (Fig. 12). The printing of each piece took, on average, 50 min.

First step was to print a total of 6 base pieces, corresponding to the construction of a cube in PLA, to realize the volumetric and the fittings of the pieces. It was found that the material did not comply with the required properties because it was too rigid, and it was not possible to test the flexibility strand. It was also concluded that, being a rigid material, it could hurt the children and it was complicated to fit and undo the pieces all together (Fig. 13).

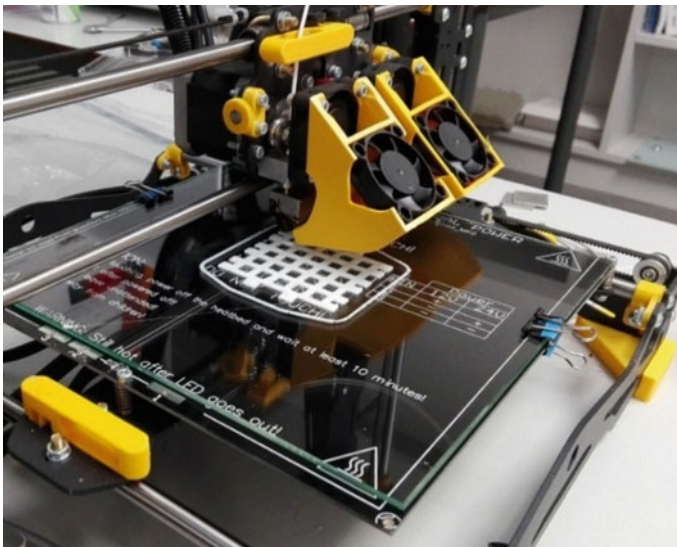
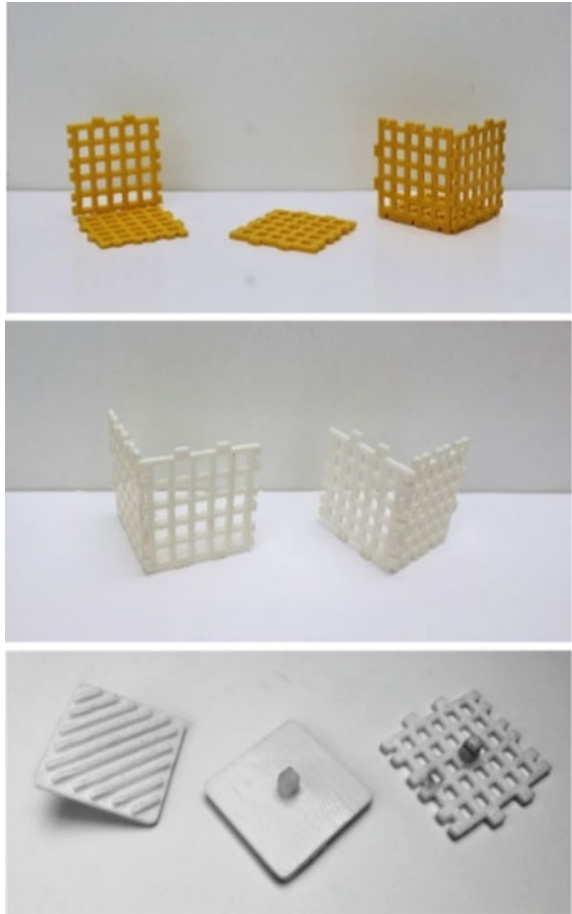


Fig. 12 3D printer Hello Bee Prusa

**Fig. 13** Printed tests



The second step was to print the same parts on a flexible filament (TPU) to test the fittings and flexibility. It was verified that the fittings were not very consistent, which forced to increase their size and to make a new printing. With this change, it was verified that the fittings already worked, and the parts were very close to the real one (Fig. 13). In this way, 3D printing of the functional prototype was carried out with 20 pieces (Fig. 14). The fittings of the faces and textures were printed on transparent PLA and then glued to these pieces.



**Fig. 14** Final printing pieces

## ***5.2 Usability Tests and Results***

After the functional prototype was printed, the product validation tests were carried out in three different phases: (1) presenting the results to the multidisciplinary teams of each pediatric service, testing the product and applying a customer satisfaction questionnaire; (2) tests of product usability with the children and their parents, testing the toy and applying the same questionnaire; (3) application of the toy in speech therapy and psychology sessions. The objective of these tests was to share the results obtained in the field research and to make an evaluation of the toy as an opportunity to collect suggestions for improvements and future work. In addition, the toy was presented in the CMIN SUMMIT'17 UP event, Portugal, in a poster format, as a mean of dissemination to the medical community.

Regarding the usability tests in the pediatric services, it was possible to prove that the children are not all the same and that they can reach the stages of development at different periods. An example of that was a 7-year-old child, participating in the study, who had the same difficulty in fitting the pieces as a 4-year-old, and yet another child of the same age was able to immediately understand how the fittings work. This development depends on the stimuli to which children are exposed. Children who were not stimulated to play with puzzles or with construction games, will present greater difficulties in this type of games. Children between the ages of 2 and 12 years also participated in these usability tests (Fig. 15). Although 7, 9 and 12-year-old children do not belong to the target age, the toy was also accepted by them, and it



**Fig. 15** Usability testes

could easily be extended to more age groups. It was also verified that children with 3 and 4 years of age showed some difficulty in making the association of fittings of the parts, because in these ages, they are accustomed to using toys with association of images or equal fittings, however, this association was also observed in some adults. In addition to the already described features of the toy, some children explored and added a new functionality to the toy, allied to plastic expression, using the facial expressions as stamps (Fig. 15). It was the general opinion of health professionals that the fact that the toy could be combined with the Pain Scale, as a pain assessment tool, becomes an added value for the product. Moreover, the fact that it can be used in occupational therapies and speech therapies as an instrument for the evaluation of fine motor skills at developmental scales, was also mentioned as an advantage and an important factor.

## 6 Conclusions

The toy is an important instrument for children in hospital admission that significantly helps the recovering process, and consequently, reduces the negative impact of hospitalization. However, it was also found that there is a lack of products for this purpose, which led to the creation of a toy that seeks to mitigate the needs of these hospitalized children. Based on the analysis of data collected, a “*Boneco Cubo*” was developed, a building toy, composed of different parts that can be attached to each other in different ways and that intends to contribute to a better integration in the hospital environment while simultaneously stimulating the children development. It can also be an ally to healthcare professionals as an instrument of children development evaluation. By using 3D printing, a functional prototype was built which was useful to test the result with the target audience. From these tests, several new ways of using the toy came up: first, due to children imagination; second, due to healthcare professionals’ suggestions to use the toy as a therapy tool. This study contributed not only to a deeper understanding of hospital admission and to the real needs of the children in this environment, but also to create awareness that design can also serve as a tool to improve people’s life, acting as an ally in diverse areas. By directly interacting with the target audience, all aspects of hospital admission were better understood which allowed to find a better solution that meets all the needs

which are imposed by this reality. Usability tests allowed to get some suggestions for improvement and to find out parents and healthcare professionals' reactions to the toy. Due to the positive results, these tests allowed to validate the created product and to open an opportunity for the industrialization of the product manufactured by injection molding of a thermoplastic.

**Acknowledgements** To the Hospital Centers participating in this research, especially the multi-disciplinary teams, parents and children who got involved in this study.

**Funding** The author(s) disclosed receipt of the following financial support for the research, authorship, and/or publication of this article: Project NORTE-01-0145-FEDER-000022 SciTech Science and Technology for Competitive and Sustainable Industries, co financed by *Programa Operacional Regional do Norte (NORTE2020)*, through *Fundo Europeu de Desenvolvimento Regional (FEDER)*.

**Declaration of Conflicting Interests** The author(s) declared no potential conflicts of interest with respect to the research, authorship, and/or publication of this article.

## References

1. INE Web page. (cited January 2017): Health statistics 2013. Lisboa: Statistics Portugal (2015). Portuguese version. [https://www.ine.pt/xportal/xmain?xpid=INE&xpgid=ine\\_publicacoes&PUBLICACOESpub\\_boui=138737&PUBLICACOESmodo=2&xlang=pt](https://www.ine.pt/xportal/xmain?xpid=INE&xpgid=ine_publicacoes&PUBLICACOESpub_boui=138737&PUBLICACOESmodo=2&xlang=pt)
2. INE Web page. (cited January 2017): Health statistics 2014. Lisboa: Statistics Portugal (2016). Portuguese version. [https://www.ine.pt/xportal/xmain?xpid=INE&xpgid=ine\\_publicacoes&PUBLICACOESpub\\_boui=257402707&PUBLICACOESstema=00&PUBLICACOESmodo=2](https://www.ine.pt/xportal/xmain?xpid=INE&xpgid=ine_publicacoes&PUBLICACOESpub_boui=257402707&PUBLICACOESstema=00&PUBLICACOESmodo=2)
3. INE Web page. (cited January 2017): Health statistics 2015. Lisboa: Statistics Portugal (2017). Portuguese version. [https://www.ine.pt/xportal/xmain?xpid=INE&xpgid=ine\\_publicacoes&PUBLICACOESpub\\_boui=257779974&PUBLICACOESstema=00&PUBLICACOESmodo=2](https://www.ine.pt/xportal/xmain?xpid=INE&xpgid=ine_publicacoes&PUBLICACOESpub_boui=257779974&PUBLICACOESstema=00&PUBLICACOESmodo=2)
4. Redondeiro, M.: O quotidiano hospitalar da criança: constrangimentos e possibilidades de desenvolvimento, Master thesis in Sociology of hildhood Universidade do Minho, Braga, Portugal (2003). <http://hdl.handle.net/1822/7992>
5. Blom, G.E.: The reactions of hospitalized children to illness. *Pediatrics* **22**(3), 590–600 (1958)
6. Engenheiro, O., Geadas, C., Lobo, C., Azougado, C., Figueiredo, J., Simpson, C.: Benefits of play therapy in hospitalized children: an integrative review of the literature. *RIASE—Ibero-Am. J. Health Aging* **2**(1), 454–464 (2016)
7. Nicola, G.H.M.B., Gomes, G., Costenaro, R., Nietzsche, E., Ilha, S.: Ludic care for hospitalized children: perspective of family caregivers and nursing staff. *Res. J.: Cuidado é Fundam.* Online **6**(2), 703–715 (2014). <https://doi.org/10.9789/2175-5361.2014v6n2p703>
8. Rocha, P., Caleffi, C., Anders, J., Souza, A., Burciaga, V., Serapião, L.: Contribution of structured therapeutic play in a nursing care model for hospitalised children. *Rev. Gaúcha de Enferm* **37**(2), 1–8 (2016). Online version Portuguese/English. <http://dx.doi.org/10.1590/1983-1447.2016.02.58131>
9. McLeod, S.: Jean Piaget. *Simply psychology* (2009)
10. Kishimoto, T.: *Brincar e suas teorias*. Cengage Learn. Editor. (1998)
11. Sousa, L., Vitta, A., Lima, J., Vitta, F.: The act of playing within the hospital context in the vision of the accompanying persons of the hospitalised children. *J. Hum. Growth Dev.* **25**(1), 41–49 (2015). <https://doi.org/10.7322/jhgd.96766>

12. Dias, J., Silva, A.P., Freire, R., Andrade, A.: Experience of children with cancer and the importance of recreational activities during hospitalization. *REME—Rev. Min. Enferm.* **17**(3), 614–619 (2013). <https://doi.org/10.5935/1415-2762.20130045>
13. DesignBoom Web page. (cited April 2017). Sheffield children’s hospital bedrooms by Morag Myerscough. <https://www.designboom.com/art/morag-myerscough-sheffield-childrens-hospital-bedrooms-02-02-2017/>
14. Clown doctor, “Operação Nariz Vermelho” Web page. (cited April 2017). <https://www.narizvermelho.pt/>
15. Little bear ELO. (cited April 2017). <https://www.youtube.com/43.44.watch?v=cEZ4Ob1RL08>
16. Kompis the hospital robot. (cited April 2017). <http://www.belowtheclouds.com/en/2010/12/21/sjukhusroboten-kompis/>
17. Novel Hospital Toys. (cited April 2017). <http://www.hikaruimamura.com/NOVEL-HOSPITAL-TOYS>
18. Granta Design Ces Edupack Web page. <http://www.grantadesign.com/education/edupack/index.htm>
19. Young, R. J., Lovell, P. A.: *Introduction to polymers*. CRC press (2011)
20. IBM Web page. IBM ibm spss statistics 24 software. <https://www.ibm.com/products/spss-statistics>
21. Lundeberg, S., Lundeberg, T.: Pain in infants and children—Physiological background and clinical aspects. *Acupunct. Relat. Therapies* **1**(4), 46–49 (2013). ISSN 2211-7660. <https://doi.org/10.1016/j.arthe.2013.05.002>
22. Santana, L., Alves, J.L., Netto, A.D.C.S.: A study of parametric calibration for low cost 3D printing: seeking improvement in dimensional quality. *Mater. Des.* **135**, 159–172 (2017)
23. Ferreira, I.A., Alves, J.L.: Low-cost 3D food printing. *Ciência & Tecnologia dos Materiais* **29**(1), 265–269 (2017)
24. Ferreira, D., Duarte, T., Alves, J.L., Ferreira, I.: Development of low-cost customized hand prostheses by additive manufacturing. *Plast. Rubber Compos.* **47**(1), 25–34 (2018)



# Evaluation of Sustainability in the Development of Food Packaging



V. L. Suárez, G. Barrera and R. M. Naveiro

**Abstract** In recent years, sustainable development has frequently appeared in technical and non-technical publications, particularly in regards to the pressing issues of high level of consumption and constant increase of waste in production processes. This has brought serious consequences in the environmental degradation, mainly due to the faster discarding of products, especially packaging. The process of packaging development must comply with the requirements of environmental preservation. This paper aims at evaluates packaging sustainability, company packages, two of them fulfilling for environmental requirements development by the National Institute of Technology (INT) in Rio de Janeiro, Brazil, and other two are not considered environmental constraints in the design. The evaluation was developed using a checklist approach, a qualitative evaluation instrument that defines the level of attendance of sustainability requirements. Some of the criteria used were: sustainable materials, reuse, reuse during harvest, post-harvest, transportation, exhibition and placement at the point of sale and reduce costs for the producer and the final vendor. Finally, the checklist approach served to define: what is the best package of sustainable behavior? and can be used in other similar studies.

**Keywords** Food packaging · Sustainability · Sustainable packaging

---

V. L. Suárez (✉) · G. Barrera

Arts and Humanities Faculty, Design Department, Metropolitan Technological Institute,  
ITM, Street 73 N° 76A – 354, Volador's Way, Medellín, Colombia  
e-mail: [viviansuarez@itm.edu.co](mailto:viviansuarez@itm.edu.co)

G. Barrera

e-mail: [giovannibarrera@itm.edu.co](mailto:giovannibarrera@itm.edu.co)

R. M. Naveiro

Arts and Humanities Faculty, Design Department, Technology Center,  
Federal University of Rio de Janeiro, UFRJ, Horácio Macedo Street,  
Block G, Rio de Janeiro, Brazil  
e-mail: [ricardo.naveiro@poli.ufrj.br](mailto:ricardo.naveiro@poli.ufrj.br)

© Springer Nature Switzerland AG 2019

L. F. M. da Silva (ed.), *Materials Design and Applications II*, Advanced  
Structured Materials 98, [https://doi.org/10.1007/978-3-030-02257-0\\_18](https://doi.org/10.1007/978-3-030-02257-0_18)

235

## 1 Introduction

According to data released by the Food and Agriculture Organization of the United Nations (FAO), annually wastes worldwide are 1.3 billion tons of food (one-third of the total production) destined for human consumption. In Brazil, 30–40% of fruits and vegetables do not reach the consumer due to losses during harvest and transport of the product. Packaging and misuse are the main factors for these losses, according to the Brazilian Company of Agro-fishery Research—EMBRAPA.

As long as the consumption of food and non-perishable goods grows, the packaging industry will grow as well, according to data from the Brazilian Packaging Association [1]. The gross value of packaging production reaches R\$47.2 billion in 2012, almost 3% higher than the R\$45.9 billion generated in 2013. Plastics represent the largest part in the gross value of production corresponding to 39.05% of total, followed by cellulose packaging with 36.51% (corrugated paper with 20.21%, paperboard, and cardboard with 10.31% and paper with 5.99%), metallic with 16.7%, and glass with 5.07%. The increasing volume of plastic packaging discarded after use, has immense environmental consequences, making society push for changes in consumer behavior [1].

Reducing the volume of materials, mainly plastic, is increasingly understood to be determinant on the behavioral changes in companies, it is a great challenge which aims to environmental improvements. Search for materials, methodologies and manufacturing process of packaging are necessary to achieve the goal of sustainable development.

There are two relevant problems to solve. The first is to reduce the loss of food after harvest, and the second is reduce the volume of discarded packaging; both problems can be solved with the development of sustainable packaging that helps to reduce the waste.

In this paper, an analysis is provided as the sustainability criteria are applied in the food packaging industry. A comparative analysis is carried between packaging developed with sustainable methodologies that are not on the market and another packaging without sustainability criteria that are already on the market, evaluating qualitatively the benefits of inclusion of sustainability in its three pillars: environmental, economical, and social.

Finally, this analysis presents an example of checklist sustainability criteria, adapted from the guidelines for the design of sustainable packing [2], that aims to for future evaluations and development of sustainable packaging.

## 2 Sustainable Packaging

### 2.1 Sustainable Development

Sustainable development implies not exceeding the limits of the biosphere, using natural resources efficiently and from an environmental standpoint (environmental), granting the same level of satisfaction to future generations, generating equality in the distribution of resources (social) and enabling economically viable solutions (economic), reaching these three aspects known as the pillars of sustainability [3].

The National Council for Advance Manufacturing, defines the process of sustainable production as the creation of manufactured products that use processes that are non-polluting, that conserve energy and natural resources, and that are economically viable and safe for workers, communities, and consumers [4].

In this way, the constant market demand for products that reduce environmental impact reinforces companies' social responsibility, leading them to apply concepts of sustainable development to their strategies. The inefficiency of industrial processes, in addition to causing scarcity of natural resources, generates an elevated number of toxic wastes that contaminate the air, water, and most of all, human health [5].

According to Bhamra and Lofthouse [6], the main benefits that companies obtain after applying sustainable design as a strategy, are the following:

- Reduction of the environmental impact of their products/processes;
- Optimization of the consumption of raw materials and energy use;
- Improvement of waste management and of pollution prevention systems;
- Encouragement of good design and innovation;
- Cost cutting;
- Satisfaction of users' needs, exceeding current expectations of price, performance, and quality;
- The increase in the possibility of the commercialization of the product;
- Improvement of the company's image.

### 2.2 Environmental Problems with Packaging

Packaging is the main link connecting the consumer, the product, and the brand, given that it is through the packaging that the consumer identifies, chooses, and uses the product [7].

According to Moura and Banzato [8], is considered packaging—something that contains, protects, and stores its contents—exists naturally, like the peels that protect fruit or the cocoon that protects the butterfly. Such examples perform the basic functions of packaging and, for this reason; humans began to adopt models from nature in order to supplement our own needs. Vessels made of clay, shells, scales,

hollow pieces of wood, animal skins, and leaves were used to contain and transport essential products.

According to the Brazilian Packaging Association, the clearest perception of value in packaging design include the protection of a product, practicality, convenience, ease of use, comfort, and security.

Every day it becomes harder to imagine daily life without these types of products, but we must be conscience of the problems caused by packaging, mainly in reference to the excess of solid waste generated. After performing its last duty, transporting the product securely to the consumer's home, packaging turns into, in the current system, a bothersome object. However, these days discard ability is a luxury that the planet can no longer handle; there are many environmental problems caused by the excess of packaging waste, among them: urban solid waste, water pollution, air pollution, forest destruction, depletion of raw materials, energy consumption, social problems, and climatic changes [9].

In this way, it is necessary that we re-think the development of products and packaging, which has already been happening, aiming for sustainable solutions in their totality (environmental, economic and social). Considering that the design methodology offers support for the systematic and controlled development of the project, it is necessary to understand how sustainable criteria are being applied to packaging design.

### ***2.3 Fruit and Vegetable Packaging***

The Agrifood sector includes fruit and vegetables. According to Oliveira and Aquino [10] the fruit is a product coming from fruiting, destined to be consumed "in nature"; vegetables are generally the green part, utilized as a food in their natural state; now, vegetables are the fruit or the seed of different plant species, mainly leguminous ones, used as food.

As far as the design of packaging, the process passes through multiple stages before finishing, including the study of materials, regulations, and laws, function and purpose, as well as other factors like the life cycle of the products.

The following functions were identified as part of the life cycle of packaging products:

- Packaging for storage and producer distribution at the distribution center;
- Packaging for storage and distribution for the supply warehouse at points of sale;
- Packaging for exposition at the point of sale;
- Packaging for storage utilized for the transportation of the product from the point of sale to the residence of the consumer.

As the packaging increases its functions, its development, and environmental contributions improve. On the other hand, the more a perishable product is displaced from one packaging to another during the different transportation processes, the more food will be lost.

As far as materials employed in the commercialization of fruit and vegetable packaging a large presence are made from expanded polystyrene (EPS—Isopor), polypropylene (PP), PET, and cardboard in a variety models has been established [7].

In spite of the predominance of polymer-based packaging that is the focus of the argument of the possibility of recycling, some types of packaging offer another approach. These packaging's are biodegradable, principally those made from tapioca starch and bioplastics, or those produced from recycled materials.

## ***2.4 Criteria for the Development of Sustainable Packaging***





The construction of the literature review of concepts related to sustainability, its tenets, and the possibilities of intervention of design in this field, along with the analysis of concepts and main criteria necessary to orient the design of packaging based on research already done in the field and according to Pereira and Silva [2], make it possible to conclude that packaging is considered sustainable when it complies with the following conditions:

1. designs systems that extend the life of the product;
2. optimizes the use of resources;
3. minimizes and values the waste/by-products;
4. aims for biocompatibility;
5. designs to optimize transport;
6. reduces toxicity;
7. increases equity and integrates actors in the system;
8. promotes responsible consumption;
9. fortifies and promotes local resources;
10. maintains economic viability in the development of the product.

Given that developing sustainable packaging means integrating these conditions into the design of a product along with the inclusion of sustainable strategies such as cleaner production, the development of cradle to cradle, the eco-design and the analysis of the life cycle (ALC), it is possible to orient the work of the designer in the making of decisions with the goal of minimizing, most of all, the environmental impact in the development of the packaging.



Table 1 present the previous ten parameters where each one was expanded into a group of questions. This table was organized into ten sections deployed in other questions, totaling 72 questions. In the analysis presented in item 4.2, the questions that are considered the most important for the case studied are used.

**Table 1** Check list of sustainability criteria for the development of packaging

Questions	Case 1. Fruits in general		Case 2. Strawberries	
	INT	Current market	INT	Current market
Design systems that extend the life of the product				
	Does the packaging have the possibility of being maintained, repaired, and substituted?	Yes	Sometimes	No
	Can the packaging be reused?	Yes	Sometimes	Yes
	Was the packaging made with modular and changeable parts?	Yes	No	No
	Is the packaging made with the intention of being reutilized by retailers?	Yes	Sometimes	No
Optimize the use of resources	Will the consumer receive an incentive to return the packaging?	No	No	No
	Does the packaging use the minimum number of materials and/or additives necessary?	Yes	No	Yes
	Does the packaging reduce and eliminate unnecessary materials, parts or special finishes?	Yes	No	Yes

(continued)

**Table 1** (continued)

Questions	Case 1. Fruits in general		Case 2. Strawberries	
	INT	Current market	INT	Current market
				
Thinking about the group of materials used from the raw material up until the transportation, is the quantity optimized?	Yes	No	Yes	No
Are local partnerships looked for to recycle production waste?	Yes	Yes	Yes	Sometimes
Is the packaging designed using materials with recycled, recyclable and compostable content?	Yes	No	No	No
Does the packaging facilitate the separation of its parts so that they can be recycled?	Yes	No	Yes	Yes
Does the packaging reduce the different kinds of materials used as much as possible?	Yes	No	Yes	No
Are there agreements established that strive for the use of local and renewable resources in the design of the packaging?	Yes	Sometimes	Yes	Sometimes

(continued)

**Table 1** (continued)

Questions	Case 1. Fruits in general		Case 2. Strawberries	
	INT	Current market	INT	Current market
				
Is the base material and all other components of the packaging biodegradable, and do not result in a chemical composition when being composted?	Yes	Sometimes	No	No
Is the transport packaging eliminated through the redesign of the primary packaging, or vice versa?	Yes	No	No	No
Is the primary packaging designed modularly in relation to the secondary packaging or to distribution?	Yes	Yes	Yes	Yes
Is the transport packaging recyclable or returnable?	Yes	Sometimes	Yes	Sometimes
Did the packaging contribute to diminish product loss during transport?	Yes	No	Yes	No
Is the packaging designed with the aim of eliminating pallets?	Yes	No	Yes	No
Are additives or other materials that contain heavy metals avoided in the packaging?	Yes	Yes	Yes	Yes

(continued)



**Table 1** (continued)

Questions	Case 1. Fruits in general		Case 2. Strawberries	
	INT	Current market	INT	Current market
Increase equity and integrate system actors				
	Yes	Sometimes	Yes	Yes
	Is the Exchange of knowledge between the participants in the system promoted and facilitated?		Yes	Yes
	Are the suppliers and sub-suppliers involved in the design and decision processes?	No	Yes	No
	Is the packaging accessible to low-income people?	No	Sometimes	Yes
Promotion of responsible consumption	Yes	No	Yes	No
	Does is promote co-design systems, where different actors participate in the development of the packaging?		Yes	No
	Is information was given to educate clients about responsible and sustainable behavior?	No	Yes	No
Strengthen and promote local resources	Yes	No	Yes	No
	Is the client/final user is involved in the production, implementation, and/or customization of the packaging?		Yes	No
Can the development of the packaging adapt and promote systems of use from local resources?	Yes	Yes	Yes	Yes

(continued)

**Table 1** (continued)

Questions	Case 1. Fruits in general		Case 2. Strawberries	
	INT	Current market	INT	Current market
				
Are the territory, attributes, and origin of the products identified on the packaging?	No	No	No	No
In terms of production costs, were accessible materials and processes used in the development of the packaging?	Yes	Yes	Yes	No
Was production processes simplified, avoiding special finishes, complex geometric structures and multiple components for assemblage in the development of the packaging?	Yes	No	No	No

Maintain economic viability

### 3 Case Study

The experimental method used was a study of multiple cases, given that a case study, for Yin [11], studies a contemporary phenomenon in its real-life context, especially when the boundaries between the phenomenon and the context are not clearly defined.

According to the goal of this research, which is to identify the importance of including sustainability criteria in the development of packaging, this investigation aims to answer the following question: How was the packaging design developed?

#### 3.1 Data Collection

The search for and collection of data was performed directly by visiting the business where the packaging is designed, during each visit, a questionnaire was filled out by interviewing the designers responsible for the development of the packaging. The interviews were also recorded as an additional source for the results.

After the collection of data, the verification list was filled out. This list is used in order to check the sustainability level of each packaging product, evaluating both comparatively and qualitatively.

## 4 Comparative Evaluation of Packaging Products

### 4.1 Description of Case Studies

Were studied two cases: the first being packaging for a variety of fruits (persimmon, mango, and papaya) and the second specifically for strawberries, as the following description explains:

Case 1: Packaging for a variety of fruits from the INT (Fig. 1).

The National Institute of Technology (INT) developed a packaging system for mangoes, persimmons, and papayas, made up of two parts: a moveable and returnable base, and a tray appropriate for the product that will be conditioned according to the caliber and commercialization needs of each format. This packaging system has already development 40 patents for inventions were taken out, both for pieces as well as for product development methodologies (Figs. 2 and 3).

Typical packaging for fruit on the market is a corrugated paper box which is developed by different companies in Brazil. The biggest advantage of this type of packaging is its resistance. It can be used for greens and vegetable as well as for fruit.

Case 2: Packaging for strawberries from the INT (Fig. 4).

Recoverable packaging developed by the INT and perfectly detailed, made with PET, maintains the conditions necessary for strawberries to stay in healthy conditions for



**Fig. 1** Recoverable packaging from the INT—the modular configuration for transport and display of 3 floors



**Fig. 2** Recoverable packaging from the INT—from left to right the first image shows the folded base, the second image shows the process of opening the base, the third image shows the tray to be installed on the base and the last located fruits on the tray



**Fig. 3** Typical packaging for fruit on the market, the image on the left shows the stacking system of the carton packaging and on the right the distribution of primary and secondary packaging is shown

over 30% longer than normal; it has specific perforations for ventilation and its design is focused on pallet transport (Fig. 5).



**Fig. 4** Strawberry packaging from INT—the image to the left shows the prototype in 3D modeling with lam accommodation of the fruit and the image to the right shows the package stacked



**Fig. 5** Packaging of the current market for strawberries, the two images show the display in gondolas of the primary and secondary packaging

Typical market packaging for strawberries.

Traditional packaging for strawberries made of two parts: a PET tray and a polystyrene layer that covers the fruit; the fruit is exhibited and exposed to the touch of users.

#### **4.2 Evaluation of Sustainability Criteria**

After the data was collected, the following table was completed in order to validate whether or not the packaging products that were developed take into account sustainable criteria, and whether those that comply are actually sustainable.

As noted on the theoretical reference Boylston [9] affirms that for a package to become sustainable it should bring environmental, social and economic benefits,

both attribute to the process of package development, and for who will make use and dispose of the product, in other words, during the all life cycle.

Most important requirement to design a packaging for fruits is to maintain the best conditions for preserving food, this research shows fruit such as persimmon, papaya, and mango (case 1) and strawberry (case 2); for the case study 1 the packaging of INT for the formal and structural development and for the terms of trays PET to adjust to the shape of each fruit, creates an internal atmosphere more favorable for the preservation of fruits. This means that from harvesting, storage, and transport, through fairs and supermarkets, the fruit is to remain protected, until it reaches the table of the final consumer, the food stays fresher, nutritious and tasty, besides reduce significantly the waste load for damage during transportation; different from the cardboard box that the conditions of moisture absorption of the material are difficult to keep in structurally adequate for reuse because of the wet and dirty conditions of the fruit, these unavoidable conditions weaken the walls of the cardboard packaging, making them less adequate for reuse.

As for mounting and versatility the packaging of the INT (case 1) was designed with modular parts (structure and trays) to facilitate the maintenance and replacement of parts and was also designed with interchangeable trays one for each type of fruit, being able to adapt to every shape and size of the fruit; so that the packaging is versatile and practical. Though the manufacturing process for the sheets of cardboard is simple to assembly, the box uses adhesives and glues that worsen the conditions, and after its use cannot be recycled. The packaging of the INT does not use adhesives or additives in its manufacturing process, obtaining a material with better conditions to be reused or recycled. Furthermore, the packaging of INT generates an assembly time, significantly lower to the cardboard packaging. Cardboard packaging has to be folded, glued and also it occupies a larger physical space in storage than the INT (Fig. 3). It is clear that the INT packaging includes more sustainability criteria that the cardboard current market.

As seen in case 2 INT could design a PET packaging with a special structure for stacking developed for the display of strawberries, allowing the final consumer can to see all the packaged strawberries, which reduces the need for handling, reduce losses and eliminate the practice of misleading consumers. The packaging has also been structurally designed with strategically placed holes to improve the ventilation conditions and preservation of fruit compared to common market packaging that lacks a strong structure that can maintain strawberries in these conditions.

Regarding the conditions of transport and export the packaging of the INT was designed with the elimination of pallets, unlike traditional packaging that needs an additional secondary packaging for stacking and conditioning on pallets.

Finally, in regards to materials the common packing used two different materials (PET for the support and polystyrene to cover the strawberries) for a single-piece package, compared with the packing of INT that can add support and cover in one piece of PET making the process of recycling and reuse easier with the common packaging. This packaging can be reused to contain strawberries because the polystyrene that covers the strawberries will be discarded after consumption. As a result, the packaging of INT meets the more sustainability criteria than the common package.

## 5 Conclusions

The study of the packaging used for perishable agricultural products allowed for the identification of a greater valorization of the packaging when it is developed with the inclusion of sustainability criteria.

In the first case study, the result of the interviews and the application of the verification list shows that the INT packaging has additional benefits that the typical packaging on the market does not have because design decisions were included at the beginning of the packaging that considered the whole life cycle and understood the needs of the process of harvest, transport, and sale. This created packaging that, while not low-cost, brings greater benefits like the protection of product during the transport cycle, which lowers food loss from 60 to 10%. The typical packaging is not adapted to the holistic process; the environmental benefits are lesser in comparison with the packaging from INT, although corrugated cardboard might be a better alternative than recycled plastic (INT) as a production material.

The participatory process of the INT shows that the inclusion of suggestions made by producers and possible packaging clients brings significant contributions, for example, an increased interest of the client in buying these foods, which does not happen with the typical packaging used.

And finally, for the INT packaging, the investment in technology during the product development brings as a consequence that more than four national and three international companies are interested in acquiring technology for manufacturing that is the process that is missing in order for the product to go on to the market, in comparison with the typical packaging the investment in technology is lower and there is no interest in technology transfer to other companies.

For the second case study, one of the most significant contributions of INT packing is to increase the useful life of refrigerated strawberries and without any chemical used, reach 15 days, as existing packages allow reaching a maximum of 10 days; furthermore, another contribution is the reduction of materials, and that it meets all the requirements of content protection, of maintaining the nutritional and sensory qualities of the strawberry, of adjusting to transport be it individually or collective, to transport, of adjusting to the exposition, particularly at points of sale in comparison with typical packaging, that has more materials and that, although it may be planned to be transported in good conditions, the process of assembling the packaging means the cost is higher.

Even though there has been some application in food packaging, this continues to be a fertile field for the intervention of sustainable design.

**Acknowledgements** The authors are thankful for the support provided by CNPq, CAPES, Metropolitan Institute of Technology—ITM and Mr. Luiz Carlos do Carmo Motta of the Institute National of Technology for their support.

## References

1. ABRE—Brazilian Packaging Association. Market Data—2013. <http://www.abre.org.br/setor/dados-of-mercado/> (2016). Accessed 10 Sept 2016
2. Pereira, P., da Silva, R.P.P.: Identificação e Sistematização de Diretrizes para o Design de Embalagens Sustentáveis. *Design & Tecnologia Review*, 5th edn. (2013)
3. Sachs, I.: *Desenvolvimento: Incluído, sustentável, sustentado*. Garamond, Rio de Janeiro (2008)
4. NAFCAM. National Council for Advanced Manufacturing. <http://www.nacfam.org> (2017). Accessed 13 July 2017
5. Almeida, F.: *Os desafios da Sustentabilidade: uma ruptura urgente*. Elsevier, Rio de Janeiro (2007)
6. Bhamra, T., Lofthouse, V.: *Design for sustainability. A Practical Approach*, pp. 28–29, 1st edn. Gower, England (2007)
7. Grazziotin., L., Vieira, G.: Organização de referências na concepção de embalagens sustentáveis de produtos hortifrutícolas. In: 9th Brazilian Congress on Research and Development in design. 13 to 16 Oct 2010 at the University Anhembi Morumbi (2010)
8. Moura, R., Banzato, J. M.: *Embalagem, utilização e containerização*. IMAM, São Paulo (1997)
9. Boylston, S.: *Design Sustainable Packaging*, 1st edn. Laurance King, London (2009)
10. Oliveira, D., Aquino, A.M.: *Guia para Comprovação da Segurança de Alimentos e Ingredientes*, Agência Nacional de Vigilância Sanitária – ANVISA (2013)
11. YIN, R.K.: *Estudo de caso - Planejamento e métodos*, 4th edn, 248 pp. Bookman (2010)



**Part VI**  
**Power Generation**

# Experimental Investigations of a MR Clutch for a Centrifugal Pump



A. I. Bosioc, T. Ardelean, R. Szakal, S. Muntean, I. Borbath and L. Vékás

**Abstract** A magneto-rheological clutch was designed and built in order to modify the speed of an axial rotor mounted in front of a centrifugal pump. The main goal by modifying the speed of the axial rotor is to increase the operating regimes with less cavitation and to uniform the flow at the inlet of the pump impeller. The magneto-rheological clutch is tested separately on a preliminary test rig, in order to analyse in detail, the working parameters (generated torque, the interior and exterior temperature). Also, the test rig serves testing different MR fluids available on the market as well as several MR fluids developed and characterized in our laboratory. The preliminary test rig consists in one fixed (2500 rpm) and one variable speed electric motors (2000–2500 rpm), a torque transducer (0–20 Nm), the magneto-rheological clutch, temperature sensors as well as a control and acquisition system. The aim of this study is to provide a first experimental evaluation of the magneto-rheological clutch designed and built for a special application. First, the paper presents the problem and our solution using the MRC. Second, we focus on the magneto-rheological clutch and the test rig; the magnetic and mechanical design of the clutch is presented, while for the test rig the operating conditions will be described. The third part analyses the

---

A. I. Bosioc (✉) · T. Ardelean · R. Szakal · S. Muntean  
University Politehnica Timișoara, Bv. Mihai Viteazu, No. 1, 300222 Timișoara, Romania  
e-mail: [alin.bosioc@upt.ro](mailto:alin.bosioc@upt.ro)

T. Ardelean  
e-mail: [timotei.ardelean@yahoo.com](mailto:timotei.ardelean@yahoo.com)

R. Szakal  
e-mail: [raul.szakal@student.upt.ro](mailto:raul.szakal@student.upt.ro)

S. Muntean  
e-mail: [seby@acad.tim.tm.edu.ro](mailto:seby@acad.tim.tm.edu.ro)

S. Muntean · L. Vékás  
Romanian Academy - Timișoara Branch, Bv. Mihai Viteazu, No. 24, 300224 Timișoara, Romania  
e-mail: [vekas.ladislau@gmail.com](mailto:vekas.ladislau@gmail.com)

I. Borbath  
SC. Roseal S.A., Odorheiu Secuiesc, Str. Nicolae Balcescu, No. 5A, 535600 Odorheiu Secuiesc, Romania  
e-mail: [borbathistvan@roseal.eu](mailto:borbathistvan@roseal.eu)

results: the generated torque and power at different speeds, the interior and exterior temperature. The last section draws the conclusions.

**Keywords** MR clutch · Mechanical–magnetic design · Experimental investigation

## 1 Introduction

Magnetic fluids have been developed at the beginning of the 1948, when Rabinow [1] developed a clutch device. According with Rabinow, the advantages of using this kind of clutch with magnetic fluids are: the amount of electrical power necessary to control is small and time response is also small. Since then the magneto rheological fluids have been implemented in many applications [2]. Several important applications can be found in: sealing's [3–5], sensors [6, 7], dampers [8–11] and brakes [12–14]. The seal applications can be found in gas industry or in micro pumps (used in chemical analyses, biological sensing and drug delivery) to reduce the volumetric losses through the clearance between the tips of gears and the housing. In case of sensors, the magneto rheological fluids are used in aerodynamic measurements for low pressure values or for the micro level motion control applications. The damping devices using magneto rheological fluids can be found in automotive domain and even for rotors and its frame in order to reduce the excessive vibrations of rotating machines. A controllable damping device will allow to obtain their optimum performance in a wide range of operating speeds.

Magneto-rheological clutches (MR clutch) are one important research direction concerning these smart materials. Some of the advantages are convenient low-power control (through electrically generated magnetic field) and very strong torque to good weight ratio [15, 16]. The latter recommends them for applications where small devices able to generate high value of torque are needed [17]. The electrical control possibility (the magnetic field can easily be electrically generated and controlled) is one advantage [18, 19]. Another advantage of MR clutches consist on variable torque transmission using a hybrid MR clutch with a permanent magnet and a coil for generating supplementary magnetic field. Accordingly, high torque transmissions can be obtained, [15, 16, 20] with negligible power consumption reduced size and absence of axial loads compared with conventional electromagnetic clutches.

The paper presents the design details and testing results of a MR clutch. The main challenge in designing the MR clutch is the requirement of the application. The device is used for speed control of an axial rotor mounted in front of a centrifugal pump [21, 22]. The numerical investigations has shown that slowing down the speed of the axial rotor, the minimum pressure is increased (the cavitation behaviour is improved) and the flow field non-uniformity is diminished at the pump inlet. The second section of the paper describes the MR clutch with the mechanical design. The third section shows experimental setup, the control system and the data acquisition program. Fourth section presents the experimental result and the conclusions are drawn in the last section.

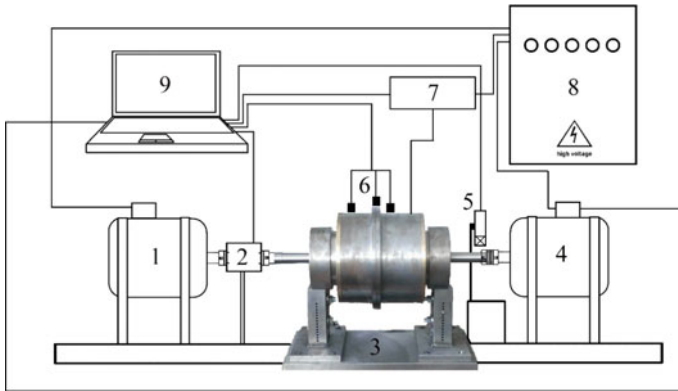


**Fig. 1** Test rig for MR clutch applications, image from laboratory (up) and sketch of the test rig with main components (down)

## 2 Experimental Test Rig and MR Clutch

A MR clutch was designed, built and installed in Laboratory of Hydraulic Machinery from Politehnica University Timisoara in order to slow down the speed of an axial rotor mounted in front of a centrifugal pump [21]. A test rig was designed, developed and built to analyse in detail the behaviour at variable speeds [23] in order to test independently the performances of the MR clutch. Also, the test rig serves for testing different MR fluids available on the market as well as several MR fluids developed and characterized in our laboratory. The method for slow down the speed of axial rotor, was chosen taking into account the mechanical properties of the MR clutch (easy to control, small dimensions, adjustable parameters). The test rig presented in Fig. 1 consists in a variable speed drive motor, a torque sensor, the MR clutch, temperature and speed sensors and the control system and the data acquisition program.

According with Fig. 1, the main characteristics and technical data for the preliminary MR clutch test rig are presented below in Table 1.

The control system sets the speed of the variable electrical motor and the data acquisition system records the following data: (i) the torque, (ii) the motor speed, (iii) the voltage and current from the coil of the clutch, (iv) the interior and exterior clutch temperature, respectively. The temperature is acquired on the external surface of the clutch while the inside point is located close to MR fluid with  $\pm 1.5$  °C accuracy. Note that this investigation was performed in air.

The designed and built MR clutch, presented in Fig. 2, is a bell shaped MR clutch, with an important advantage: it encapsulates two clutches by doubling the friction surface. The MR clutch has a drive shaft connected at the fixed speed electric motor and an output shaft connected at the variable speed electric motor, (Fig. 2, up). It was designed in order to ensure the magnetic flux where the MR fluid is mounted (Fig. 2, middle). Accordingly, the MR clutch was designed with two types of materials: magnetic and non-magnetic. The driving part (constant speed) is the shaft and disc

**Table 1** Main characteristics of the MR clutch test rig

	Component	Main characteristics
1	High speed electrical motor	2500 rpm, 3 kW (fixed speed)
2	Torque sensor	0–9000 rpm, $\pm 20$ Nm
3	MR clutch	Fixed speed (drive shaft): 2500 rpm Variable speed (output shaft): 2500–2000 rpm
4	Variable speed electrical motor	2500–2000 rpm, 3 kW (variable speed)
5	Optical speed sensor	0–10,000 rpm, $\pm 0.5\%$ accuracy
6	Temperature sensors	2 temperature sensors: close to MR fluid (0–200 °C), on external surface (0–100 °C)
7	DC source	0–32 V, 0–10 A, programmable DC source
8	Control/acquisition system	<ul style="list-style-type: none"> <li>• 10 Hz acquisition frequency</li> <li>• Maintain a constant speed independently by torque variation</li> </ul>

(bell shape) at a constant speed of 2500 rpm (red colour). The magnetic circuit is mounted on the fixed part and the variable speed part is built using two pieces: the coil and the magnetic casing, respectively. The clutch radius was increased as much as possible to increase the torque of the MR clutch. The diameter of the clutch was limited at 0.25 m due to the geometrical constraints associated to the pump setup, where the MR clutch will be installed. The magnetic design of the coil ensures a radial magnetic field, in order to use the entire surface of contact where MR fluid is inserted. The entire magnetic circuit is built using magnetized iron.

A special attention has been paid to the magnetic circuit during design stage of the MR clutch. The coil is responsible for generating the magnetic flux density. It was designed a coil using a copper wire of  $\varnothing$  0.35 mm, with 2000 turns, with a maximum current intensity of 1 A. The generated magnetic flux by the coil was directed through magnetic materials in the area where MR fluid is inserted on the clutch. At the end, the final geometrical configuration of the clutch was numerically analysed from magnetic point of view using the FEMM 4.2 programme available on <http://www.femm.info/wiki/download>, property of Aladdin Enterprises, Menlo Park, California, U.S.A. The results show that the magnetic flux density is directed on the magnetic casing of the clutch, with a maximum value of 1T close to the coil and lower values along to the magnetic circuit, see Fig. 3. The 2D axial-symmetric plots of magnetic flux density along to the length where MR fluid is inserted shows a constant flux of 0.35 mT at maximum current intensity of 1 A. This result supports our choices performed at the design stage confirms the final geometrical configuration as well as the materials selected are appropriate.

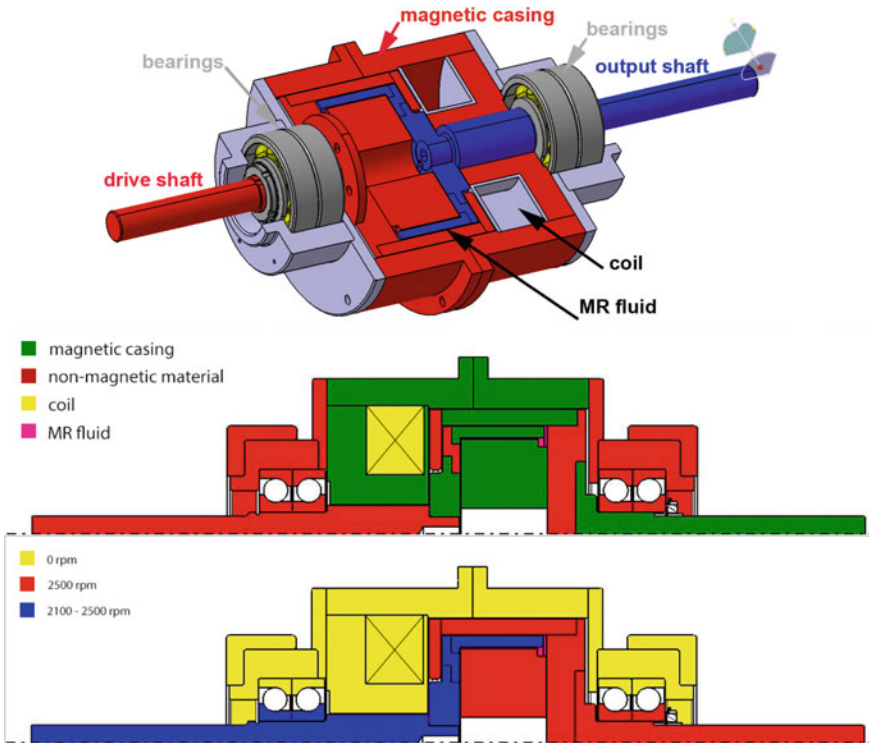


**Fig. 2** Sketch of the tested MR clutch considering the magnetic properties of the materials (middle) and the speed of each component of the device (down)

**Table 2** Main properties of the MR fluid used for clutch application

MR fluid	336 AG
Operating temperature	-40 °C ÷ 150 °C
Density (kg/m <sup>3</sup> )	3450
Viscosity (Pa s)	Between 0.05 and 0.2 according with shear rate measurements
Specific heat	0.65 J/g °C
Thermal conductivity	0.2 w/m °C

### 3 MR Fluid and the Experimental Setup

The MR fluid used in the experiments is MRF 336 AG produced by the Lord Corporation. The MR fluid has two main components: silicone oil as carrier fluid together with iron micro particles. The main properties are presented in Table 2.

It was chosen using this type of MR fluid due to high operating temperature (stable up to 150 °C) and quite good behaviour in applications [23].

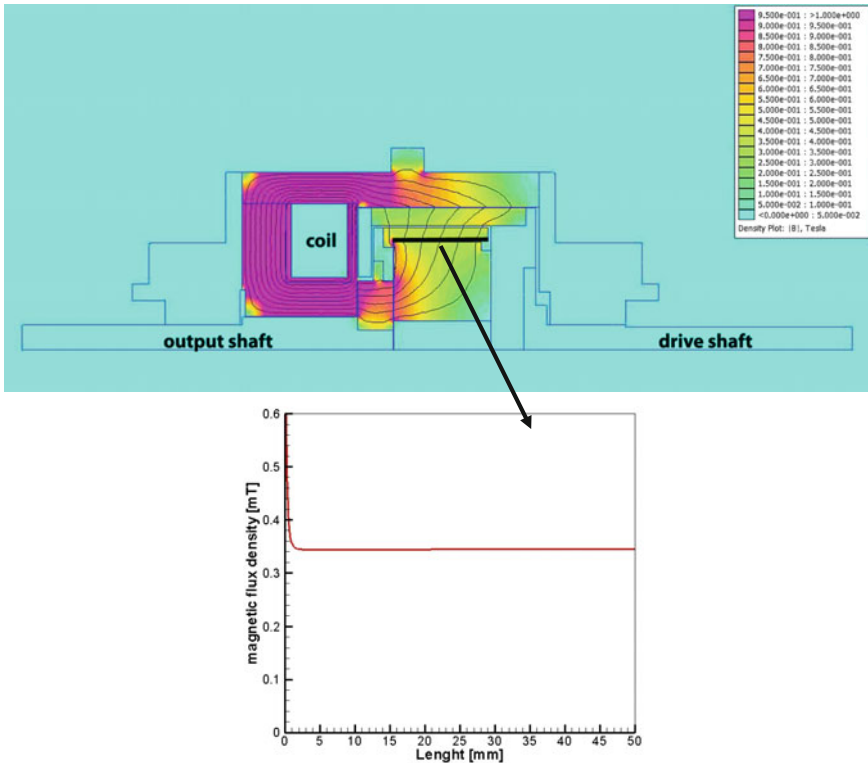


**Fig. 3** Magnetic flux density through designed MR clutch (up) and 2D axial-symmetric plot in the length of the clutch, where MR fluid is inserted (down)

**Table 3** The control and acquisition system characteristics

Used platform	Control parameters	Acquired parameters
SCADA	Variable speed for electric motor	Torque—for variable and fixed speed motor
	Fixed speed for electric motor	Speed—for variable and fixed speed motor
	Variable voltage (applied at the coil clutch)	Temperature—on two points (close to the MR fluid and at the exterior wall of the clutch)
	Maximum torque (for safety precautions)	Power, voltage and current—applied at the coil

The control system allows us to setup the speed of the variable motor with a smooth start. Parallel the program allows monitoring the torque and the speed in real time. At the end of each measurement the acquired data can be saved in different formats (Table 3).

**Table 4** Investigated regimes

Regime	Fixed speed motor (drive shaft) (rpm)	Variable speed motor (output shaft) (rpm)	DC source voltage
$\Delta n$ 50	2500	2450	0 ... 30 V, step size 1 V
$\Delta n$ 100	2500	2400	0 ... 30 V, step size 1 V
$\Delta n$ 150	2500	2350	0 ... 30 V, step size 1 V
$\Delta n$ 200	2500	2300	0 ... 30 V, step size 1 V
$\Delta n$ 250	2500	2250	0 ... 30 V, step size 1 V
$\Delta n$ 300	2500	2200	0 ... 30 V, step size 1 V
$\Delta n$ 350	2500	2150	0 ... 30 V, step size 1 V
$\Delta n$ 400	2500	2100	0 ... 30 V, step size 1 V
$\Delta n$ 450	2500	2050	0 ... 30 V, step size 1 V
$\Delta n$ 500	2500	2000	0 ... 30 V, step size 1 V

The measurements have been performed in air at environmental temperature of 22 °C. The setup for each measurement consists in a constant speed for high speed electrical motor of 2500 rpm while the variable speed of the second (driven) electrical motor varies between 2450 and 2000 rpm with a step size decrement of 50 rpm. At each regime the coil voltage was modified between 0 and 30 V with a step size increment of 1 V. The measurement were performed considering a time period of 10 s with a frequency of acquisition of 10 Hz for each step size of 1 V. Accordingly, 100 samples is registered for each step from 0 to 30 V. All investigated regimes are presented in Table 4.

## 4 Results

Firstly, the experimental investigations were focussed on measuring the torque generated by each electric motor at each regime. The torque for variable speed motor was determined/estimated using the frequency converter. The torque for fixed speed motor is recorded using torque sensor. Before measurements, for the torque sensor calibration curve was obtained and integrated in the data acquisition system.

From the first evaluation, a small torque value of 1.5 Nm is observed for the variable speed motor at regimes with lower  $\Delta n = 50$  rpm and it rises up to a value of 1.8 Nm for the highest  $\Delta n = 500$  rpm, Fig. 4. Note that the torque value measured at 0 V is only due to viscosity of the MR fluid. The torque starts to increase once the voltage is applied on the coil, reaching a difference of 1.9 Nm for the lowest speed variation  $\Delta n$  of 50 rpm and 1.5 Nm for the highest speed variation  $\Delta n$  of 500 rpm, respectively.

The torque difference measured for the fixed speed motor is significant when the applied voltage at the coil varies from 0 to 30 V. The reference torque value



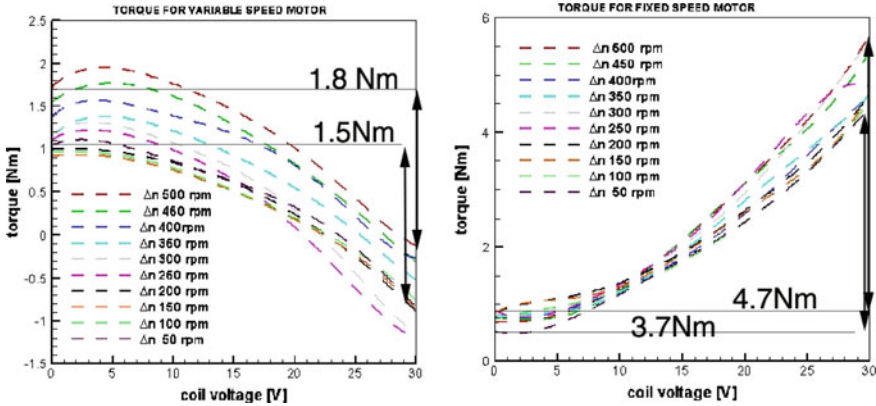


**Fig. 4** Measured torque for variable speed motor (left) and fixed speed motor (right) at 10 investigated regimes by modifying the applied voltage at the coil

considered for the torque difference corresponds to 0 V applied voltage at the coil. The torque difference is around 3.7 Nm at the lowest speed variation  $\Delta n$  of 50 rpm while the torque difference is approximately 4.7 Nm for the highest speed variation  $\Delta n$  of 500 rpm for the fixed speed motor, Fig. 4 right.

The torque difference measured for each electric motor (variable speed and fixed speed) is cumulated in a total torque. The total torque determined on each regime is plotted in Fig. 5. The total torque is represented for three coil voltages of 10, 20 and 30 V. One can be observed that the maximum torque value around 5.8 Nm is yielded at maximum applied voltage of 30 V. The clutch covers a maximum torque value measured with 33% larger than our requirements considered by the design specifications. The torque requirement has been determined from 3D numerical simulations performed on the pump system with axial rotor at variable speeds [22].

A last analysis consists in measuring the external and internal temperature for the MR clutch, see Fig. 6. The measurements have been performed in air with no cooling system. The acquired external temperature is recorded on the clutch exterior wall, while the internal temperature is registered at 1 mm close to MR fluid. The temperature is measured in order to observe the maximum temperature generated by the clutch which can modify the magnetic properties of the MR fluid. The recorded temperature corresponds to a complete measurement regime by varying the voltage between 0 and 30 V in a time interval of around 10 min.

According with the variation of the temperature, see Fig. 6, the maximum temperature is acquired registered for the maximum speed difference as it is expected. The maximum temperature is approximately 42 °C close to the MR fluid. The temperature is small, due to high volume of the clutch and good dissipation of the heat inside the clutch. Even so, the maximum temperature does not reach the threshold temperature given by the producer for this type of MR fluid (150 °C).

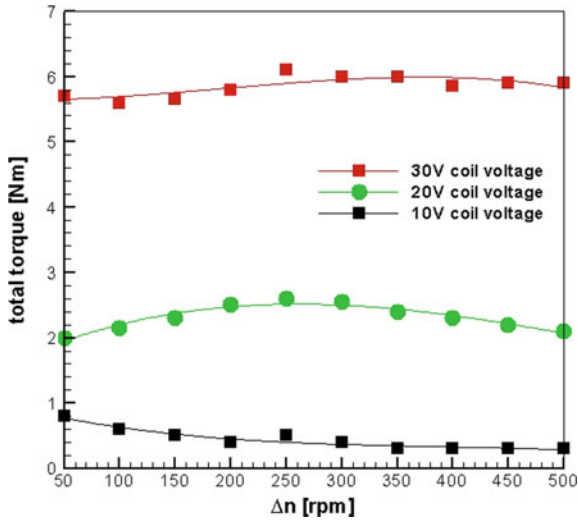


Fig. 5 Total torque generated by the MR clutch at three voltage values applied to the coil

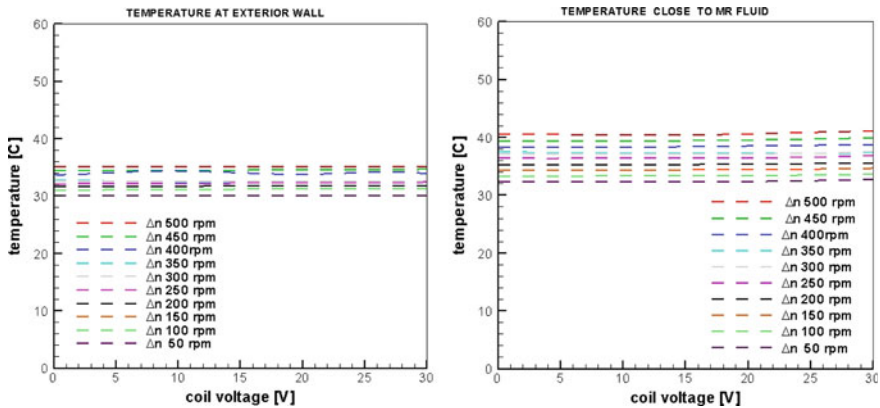


Fig. 6 Temperature variation for each regime, measured at the exterior wall of the clutch and close to MR fluid

### 5 Conclusions

The paper focuses on experimental investigation of a new MR clutch. The MR clutch will be used for speed control of an axial rotor mounted in front of the pump impeller. The main purpose of the axial rotor installed in front of the pump impeller is to improve the cavitation behaviour of the pump increasing the minimum pressure on the impeller blades when the speed of the axial rotor is slow down with 15% with respect to the speed of the pump impeller [22].

The design of the MR clutch was performed taking into consideration the geometrical constraints of the pump system. A challenge issue during the design stage was the design and analysis of the magnetic field of the MR clutch. The magnetic design of the MR clutch was performed in order to direct the magnetic flux density in the area where MR fluid is inserted in the device. According with numerical results, the maximum value of magnetic flux density is around 0.35 mT at the maximum current intensity of 1 A applied at the coil of the MR clutch in the gap where MR fluid is available in the clutch.

The MR clutch was tested on a test rig. The test rig serves for experimental investigation of different MR brakes and MR clutches required for our applications. Different MR fluids available on the market as well as several MR fluids developed and characterised by our laboratory are tested on this test rig.

The experimental results have been performed on two directions: the torque measurements and temperature measurements. The total torque representing the torque cumulated from both sides of the MR clutch. The total torque measured on our test rig shows a value around 5.8 Nm being with 33% larger than the value selected at the design. The external and internal temperature measured on the MR clutch help us to observe the maximum temperature generated by the clutch, which can modify the magnetic properties of the MR fluid. During the measurements, the maximum temperature is registered at the maximum speed difference ( $\Delta n = 500$  rpm) inside the MR clutch close to MR fluid and even so not exceeds the threshold temperature of the MR fluid. As a result, the MR clutch designed, built and tested for speed control of the axial rotor accomplishes the initial requirements for torque and temperature operation.

Further investigations are planned, concerning the experimental evaluation of the MR clutch for longer time periods, in order to compare its operation with real operating conditions.

**Acknowledgements** This work was supported by a grant of the Romanian Ministry of Research and Innovation, CNCS—UEFISCDI, project number PN-II-RU-TE-2014-4-1089 and mobility grant project number PN-III-P1-1.1-MC-2018-0423, within PNCDI III.

## References

1. Rabinow, J.: The magnetic fluid clutch. *AIEE Trans.* **67**, 1308–1315 (1948)
2. Olabi, A.G., Grunwald, A.: Design and application of magneto-rheological fluid. *Mater. Des.* **28**, 2658–2664 (2007)
3. Moskowitz, R.: Dynamic sealing with magnetic fluids. *ASLE Trans.* **18**(2), 135–143 (1975)
4. Bica, D., Balanean, F., Borbath, I., Boros, T.F., Galffy, D., Vekas, L.: Process for preparing composite magnetic fluids for magneto-fluidic rotary seals, for high pressures. Romania, Patent RO122725-B1 (1999)
5. Liang, Y., Alvarado, J., Iagnemma, K., Hosoi, A.E.: Dynamic sealing using magneto-rheological fluids. *Appl. Phys.* 1802.07912 (2018)

6. Popa, N.C., Rousseau, J.J., Siblino, A., Chatelon, J.P., Jamon, D., Royer, F., Robert, S., Choueikani, F.: Gas distribution control system using magnetic fluid sensors. *Rom. Rep. Phys.* **337–349**(58) (2006)
7. Kaluvan, S., Thirumavalavan, V., Kim, S., Choi, S.-B.: A new magneto-rheological fluid actuator with application to active motion control. *Sens. Actuators A* **239**, 166–173 (2016)
8. Liță, M., Popa, N.C., Velescu, C., Vékás, L.: Investigation of a magnetorheological fluid damper. *IEEE Trans. Magn.* **40**(2), 469–472 (2004)
9. Kazakov, Y.B., Morozov, N.A., Nesterov, S.A.: Development of models of the magnetorheological fluid damper. *J. Magn. Magn. Mater.* **431**, 269–272 (2017)
10. Sireteanu, T., Ghita, G., Stancioiu, D.: *Fluide și amortizoare magneto-reologice*. Ed. Bren, Bucuresti, Romania (2005)
11. Ferfecki, P., Zapomel, J., Kozanek, J.: Analysis of the vibration attenuation of rotors supported by magnetorheological squeeze film dampers as a multiphysical finite element problem. *Adv. Eng. Softw.* **104**, 1–11 (2017)
12. Karakoc, K., Park, E., Suleman, A.: Design considerations for an automotive magnetorheological brake. *Mechatronics* **18**, 434–447 (2008)
13. Nguyen, Q.H., Choi, S.B.: Selection of magnetorheological brake types via optimal design considering maximum torque and constrained volume. *Smart Mater. Struct.* **21**, 015012 (2012)
14. Li, W.H., Du, H.: Design and experimental evaluation of a magnetorheological brake. *Int. J. Adv. Manuf. Technol.* **21**, 508–515 (2033)
15. Bose, H., Gerlach, T., Ehrlich, J.: Magnetorheological torque transmission devices with permanent magnets. *J. Phys.: Conf. Ser.* **412**, 012050 (2013)
16. Bucchi, F., Forte, P., Frendo, F., Musolini, A., Rizzo, R.: A fail-safe magnetorheological clutch excited by permanent magnets for the disengagement of automotive auxiliaries. *J. Intell. Mater. Syst. Struct.* **25**(16), 2102–2114 (2014)
17. Rizzo, R., Musolino, A., Bucchi, F., Forte, P., Fredo, F.: A multi gap magnetorheological clutch with permanent magnet. *Smart Mater. Struct.* 075012 (2015)
18. Bucchi, F., Forte, P., Frendo, F.: Geometry optimisation of a magnetorheological clutch operated by coils. *J. Mater. Des. Appl.* **231**(1–2), 100–112 (2017)
19. Kielan, P., Kowol, P., Pilch, Z.: Conception of the electronic controlled magnetorheological clutch. *Electr. Rev.* **87**(3), 93–95 (2011)
20. Torocsik, D.: Some design issues of multi-plate magnetorheological clutches. *Hung. J. Ind. Chem.* **39**(1), 41–44 (2011)
21. Muntean, S., Susan-Resiga, R.F., Bosioc, A.I., Constantin, S., Maxim, D., Tanasa, C., Vekas, L., Borbath, I., Anton, L.E.: Equipment to reduce the cavitation effects and to uniform the flow at pumps inlet. Patent application RO131578-A3 (2016)
22. Bosioc, A.I., Constantin, S., Muntean, S., Anton, L.E.: Numerical assessment of the flow field induced by an axial rotor with variable speed in a pump impeller. In: 19th International Seminar on Hydropower Plants, Vienna, Austria, in *Wasserkraftlangen TU Wien*, pp. 423–433. ISBN 978-3-9504338-07 (2016)
23. Bosioc, A.I., Beja, E., Muntean, S., Borbáth, I., Vekas, L.: Experimental investigations of MR fluids in air and water used for brakes and clutches. *Mater. Des. Appl.* 197–207 (2017). ISBN 978-3-319-50783-5

# Experimental Investigations of a Magneto-Rheological Brake Embedded in a Swirl Generator Apparatus



R. A. Szakal, A. I. Bosioc, S. Muntean, D. Susan-Resiga and L. Vékás

**Abstract** A magneto-rheological brake (MRB) is designed and embedded in a swirl generator apparatus in order to control the runner speed. Several swirling flow configurations are obtained slowing down the runner speed. The main challenge for MRB is associated with its operation under water conditions. As a result, two magneto-rheological fluids (a conventional one and one based on ferrofluid) are selected together with an appropriate sealing solution to avoid expelling the solid particles. Firstly, a commercial magneto-rheological fluid (MRF 336AG) manufactured by Lord Co. is tested in MRB. Secondly, a nano-micro composite magneto-rheological fluid, with 35% volume fraction of the micron-size iron particles (SMR 35%Fe), designed and manufactured by Magnetic Fluids Laboratory from Romanian Academy—Timisoara Branch was selected for experimental investigations. The mechanical solution designed for MRB is presented. The magneto-rheological properties determined for both MRFs are compared. Challenging investigations were performed at several runner speeds with MRB under water conditions. A relative speed variation behaviour associated with the runner rotation has been identified due to rupture and rebuild of large chain-like agglomerates in the MRF. This relative speed variation is

---

R. A. Szakal · A. I. Bosioc · S. Muntean (✉)  
Polytechnica University Timisoara, Bv. Mihai Viteazu, No. 1, 300222 Timișoara, Romania  
e-mail: [seby@acad-tim.tm.edu.ro](mailto:seby@acad-tim.tm.edu.ro)

R. A. Szakal  
e-mail: [raul.szakal@student.upt.ro](mailto:raul.szakal@student.upt.ro)

A. I. Bosioc  
e-mail: [alin.bosioc@upt.ro](mailto:alin.bosioc@upt.ro)

S. Muntean · D. Susan-Resiga · L. Vékás  
Romanian Academy - Timisoara Branch, Bv. Mihai Viteazu, No. 24, 300222 Timișoara, Romania  
e-mail: [daniela.resiga@gmail.com](mailto:daniela.resiga@gmail.com)

L. Vékás  
e-mail: [vekas.ladislau@gmail.com](mailto:vekas.ladislau@gmail.com)

D. Susan-Resiga  
West University of Timisoara, Bd. Vasile Parvan No. 4, 300223 Timișoara, Romania

directly correlated with the braking level of MRB. The conclusions are drawn in the last section together with the future work.

**Keywords** Magneto-rheological fluids properties · Magneto-rheological brake Swirl generator apparatus · Speed control

## 1 Introduction

Nowadays, the magneto-rheological devices are widely used in application such as magneto-rheological dampers [1–7], brakes [7–10], clutches [11, 12], valves [13] and rotating seals [14, 15]. The first magneto-rheological device was a magneto-rheological brake (MRB) [8]. MRBs are the most commercially used devices after MR damper. Such devices slow down the angular speed of a rotating shaft immersed in the magneto-rheological fluid (MRF). Generally, MRB consists of rotor, stator, coil, and MRF. The shape and size of rotor depend on the MRB type. Lord Corporation has developed and manufactured MRBs which are known as controllable rotary resistance device [1, 2]. The MRBs require low power consumption ensuring a smooth operation. MRB mainly works in shear mode while its performances depend on several parameters such as: (i) clearance gap, (ii) working speed, (iii) magnetic field strength and (iv) effective area, respectively. Usually, MRB is controlled by modifying the magnetic field strength in the effective area. Therefore, clearance gap and working speed are important parts of the design constraint.

MRFs conventionally consist of micron-sized iron particles dispersed in various types of carrier fluid [15–23]. MRFs are very popular because of its behaviours and easy making being mainly produced by Lord Co [16]. MRFs belong to an important part of smart materials domain whose rheological properties change rapidly with the application of magnetic field. Under the action of external magnetic field, the MRF changes its behaviour in a few milliseconds and transforms into a semi-solid state (due to intense particle chaining) from the initial liquid state [17]. It can be controlled by varying the magnetic field involving low power consumption. These changes are very significant and reversible. But conventional MRFs have some disadvantages: they manifest reduced kinetic stability and poor re-dispersion properties.

The paper presents our investigations performed on the swirl generator equipped with MRB working under water conditions. The second section describes the swirl generator test rig together with a detailed view of the swirl apparatus and the MRB embedded on it. The magneto-rheological properties of two MRFs are presented in third section in order to assess their behaviour under magnetic field. MRF 336AG manufactured by Lord Corporation is one fluid selected in our investigation. The second fluid is a nano-micro magneto-rheological fluid designed and manufactured by Magnetic Liquid Laboratory from Romanian Academy—Timisoara Branch. The composite fluid is a nano-micro MRF with a magnetic liquid as carrier and 35% volume fraction of the micron-size iron particles. The nano-micro MRF has an improved kinetic stability, which is attributed to the formation of a nano particle cloud around

each micron size Fe particle [18–23]. They also have a low abrasive effect according to Ahmadian and Norris [4]. Next section provides the experimental data acquired at several runner speeds with MRB using both MRFs. The speed deviation is measured for several runner values in order to assess its behaviour during the brake stage. The conclusions are drawn in the last section together with the future work.

## 2 Experimental Test Rig

An experimental test rig equipped with a swirl generator was developed at Politehnica University Timișoara, Fig. 1a. A swirl generator consists of the guide vanes (blue in Fig. 1b) and the rotating blades (green in Fig. 1b), designed to deliver a swirling flow configuration with stagnant region [24, 25]. Therefore, the rotating blades (called runner) spin freely at runaway speed in order to balance the flow energy from the hub towards the shroud. A technical solution using a magneto-rheological control technique is applied considering a MRB to slow down the speed of the runner in order to control the swirling flow configuration and its associated self-induced instabilities [10]. The MRB device was designed, manufactured and implemented on the swirling flow test rig by Bosioc et al. [26] to assess its performances. The swirling flow configurations and its associated unsteady effects are controlled changing the speed of the runner using MRB. The main challenge in designing the MRB is the fact that entire swirl apparatus needs to work under water. As a result, a magneto-rheological fluid (MRF) with good immiscible properties [27] has to be selected and a proper sealing solution needs to be implemented in order to protect MRB against water leakages. An important advantage of this solution is that the MRB is operating in water avoiding any cooling system.

The main advantage of applying a magneto-rheological braking to the swirling generator is due to the compact solution of the MRB and its properties for easy control. However, the main challenge is to avoid the interaction between the water flowing in the hydraulic passage of the test rig and the MRFs inside the brake. For this purpose, a series of bearings and seals made of graphite Teflon were mounted above and below of the runner.

The main component of the brake device is represented by the MRF installed between the fixed part and the rotating part, respectively. In our case, the fixed part is given by the magnetic housing whilst the rotating part is linked by the runner. A coil is mounted inside of the housing in order to generate the magnetic field. A sealing plate is used to isolate the coil from the MRFs. The housing has been specially designed to drive the magnetic field perpendicular on the gap where MR fluid is available. MRB embedded in the swirl generator apparatus is presented in Fig. 2.

The runner's blade has 5 mm thickness in the middle area and a cylindrical magnet ( $D \times H = \varnothing 3 \text{ mm} \times 8 \text{ mm}$ ) of neodymium-iron-boron (NdFeB) is installed on each tip blade [28]. A magnetic sensor was installed on the wall of the test section to measure the runner's speed, Fig. 2. Its sensing distance is up to 60 mm at a maximum frequency of 1 kHz. The MM12-60APS-ZCK sensor manufactured by Sick (SICK

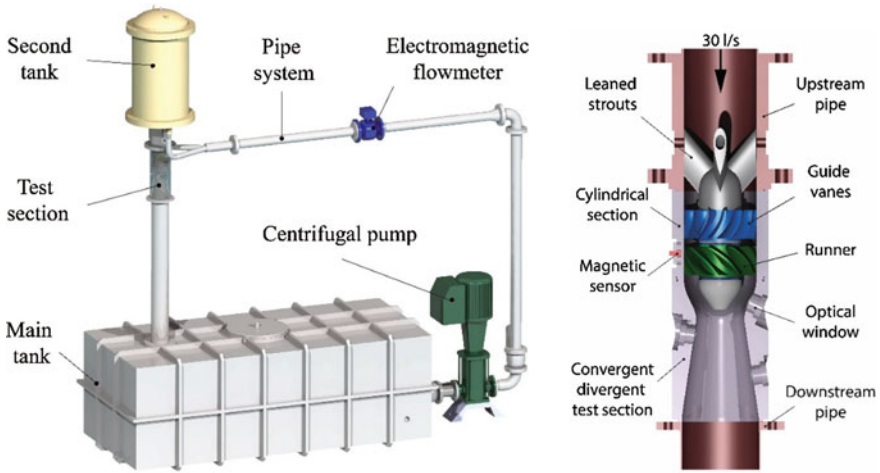


**Fig. 1** Experimental test rig for investigation of the decelerated swirling flow (left) and a detailed view of the test section (right)

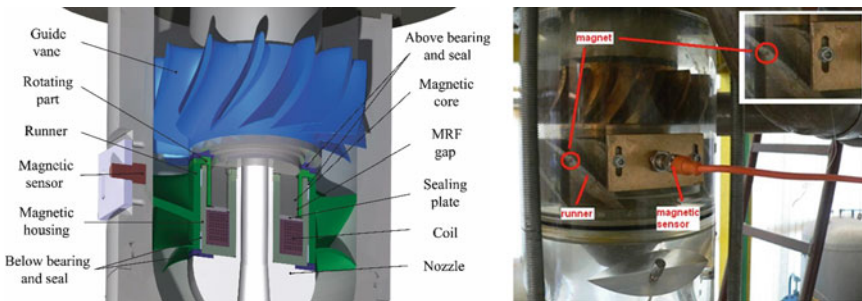


**Fig. 2** MRB embedded in swirl generator apparatus (left) and magnetic sensor installed on the wall of the test section (right), [10]

AG, Waldkirch, Germany) is installed to capture the magnetic flux generated by each magnet. A sensor’s assembling mechanism allowing distance adjustment is designed, Fig. 2. Each blade passing in front of the sensor generates a rectangular pulse. The runner’s rotation generates a train of pulses (ten of them corresponding to one complete rotation of the runner).

Laser Doppler Velocimetry (LDV) system is used to register the experimental data. The LDV system is an optical technique in order to measure the velocity field inside the convergent-divergent test section. A series of the analog and digital signals are acquired in the same time (e.g. four pressure signals on the walls, two velocity components along to survey axis and the pulses delivered by the magnetic sensor corresponding to the speed of the runner). Accordingly, the pulses delivered by the magnetic sensor are processed to examine the speed variation of the runner.



**Table 1** Type of the MRFs and their proprieties

MR fluid	Technical data	Manufacturer
MRF 336AG	Carrier liquid: silicone oil Particles: micrometer size Fe $\eta_B = 0.354 \text{ Pa s at } 20^\circ$	Lord Corporation
SMR 35%Fe	Carrier liquid: mineral oil based ferrofluid Particles: nanometer range $\text{Fe}_3\text{O}_4$ and micrometer size Fe $\eta_B = 11.78 \text{ Pa s at } 20^\circ$	Magnetic Fluids Laboratory from Romanian Academy—Timisoara Branch

### 3 Magneto-Rheological Fluids

Two MRFs have been selected to control the MRB. The first MRF is a commercial fluid MRF 336AG delivered by Lord Corporation while the second one is a nano-micro magneto-rheological fluid with 35% volume fraction of the micron-size iron particles dispersed in ferrofluid carrier, designed and manufactured by Magnetic Fluids Laboratory from Romanian Academy—Timisoara Branch labelled SMR 35%Fe [29]. The proprieties of both MRFs are given in Table 1.

The magneto-rheological measurements were performed using a PHYSICA MCR 300 Rheometer delivered by Anton Paar and supplied with a magneto-rheological cell MRD/TI-SN18581. All components are manufactured using nonmagnetic materials to prevent the occurrence of the radial magnetic forces acting on the shaft of the measuring system [30]. A gap of 0.2 mm thickness was selected between the parallel plates of MR cell. Each plate have 20 mm diameter and according with this dimension a very small volume of sample is required ( $V = 0.063 \text{ ml}$ ). The temperature of  $20^\circ\text{C}$  was considered for each test. MRF was mixed before to start any type of measurement in order to ensure the probe homogeneity. The samples were placed in a vacuum generator to remove the air bubbles occurred during the mixing process. The applied magnetic field was generated with the coil inside the cell, perpendicular to the sample layer. For each investigated MRF were measured the viscosity curves  $\eta(\dot{\gamma})$  at several density values of the magnetic field from 0 to 566 mT. The magnetic flux density corresponding to various electrical current values applied to the coil of the magneto-rheological cell was measured with a FW Bell Hall probe inserted under the bottom plate of the cell. The rotational test was performed for shear rate between 0.01 and  $1000 \text{ s}^{-1}$ . Firstly, the viscosity curves (shear viscosity versus shear rate  $\eta(\dot{\gamma})$ ) for both MRFs (MRF 336AG and SMR 35%Fe) are presented in Fig. 3. This type of curve describes the behaviour of each MRF at different magnetic flux densities. One observe that the shear viscosity increasing with the magnetic flux density, Fig. 3. It is happened due to agglomeration of the particles induced by the magnetic field. These agglomerations are progressively destroyed with the shear intensification as a result the behaviour of fluids is strongly shear-thinning. Magneto-viscous effect is more pronounced for composite sample.

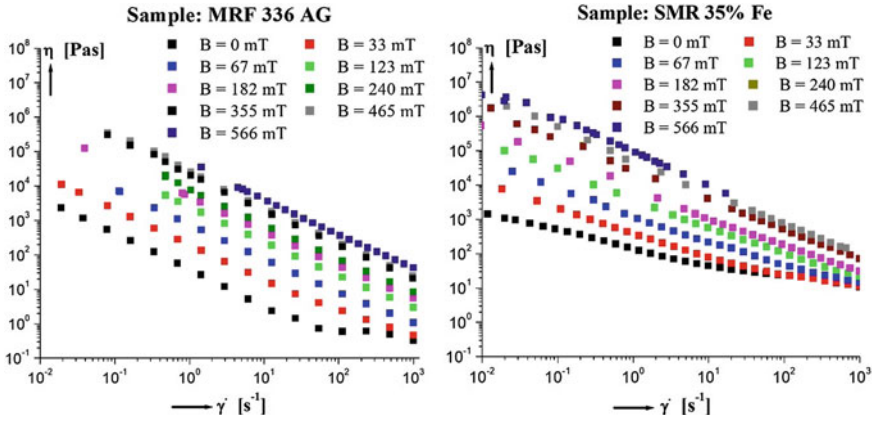


**Fig. 3** Viscosity curves  $\eta(\dot{\gamma})$  measured for both MRFs: MRF 336AG (left) and SMR 35%Fe (right)

This first evaluation helps us to understand how the MR fluid samples acts in the presence of an exterior magnetic field. In order to compare both fluids in terms of braking performances, it was also necessary to determine the static yield stress test. A pre-shearing step was applied before to start the strain sweep mode test with a shear rate of  $\dot{\gamma} = 100 \text{ s}^{-1}$  during 60 s then a magnetic field with a strength corresponding to the planned test during 30 s. The sample is replaced after each test due to exceeding the MRF shear stress threshold.

The dependence of the shear stress ( $\tau$ ), on the shear strain ( $\gamma$ ) determined using the strain sweep mode test for all the magnetic flux density values ( $B = 33, 67, 123, 182, 240, 355, 465, 566 \text{ mT}$ ) is plotted in Fig. 4 for both MRFs. The static yield stress represents the maximum of the  $\tau = \tau(\gamma)$  curve when the sample is subjected to a logarithmic increase in shear strain  $\gamma$  [31]. At great values of the Fe volume fraction and of the deformation, the shear stress becomes increasingly unstable. These oscillations of the shear stress seem to be related to the rupture and rebuild of large chain-like agglomerates in concentrated samples under the influence of applied field [19]. The static yield stress  $\tau_y$  are selected together with the magnetic flux density for both probes for plotting the  $\tau_y = \tau_y(B)$  curves.

The static yield stress dependence of the magnetic flux density for both MRFs are comparatively presented in Fig. 5. We observe the saturation of this dependence at high values of the magnetic flux density ( $B$ ), for both samples, probably when the average chain length approaches the gap size of the measuring geometry (gap-spanning structure) [32]. It can be seen that the SMR 35%Fe reaches higher values than MRF 336AG as follows: 5 times larger at 100 mT, 2.5 times larger from 100 to 200 mT and around 2 times on the plateau of saturation zone for values over 350 mT. It means that SMR 35%Fe accepts higher magnetic fluxes than MRF 336AG being an advantage in our application.

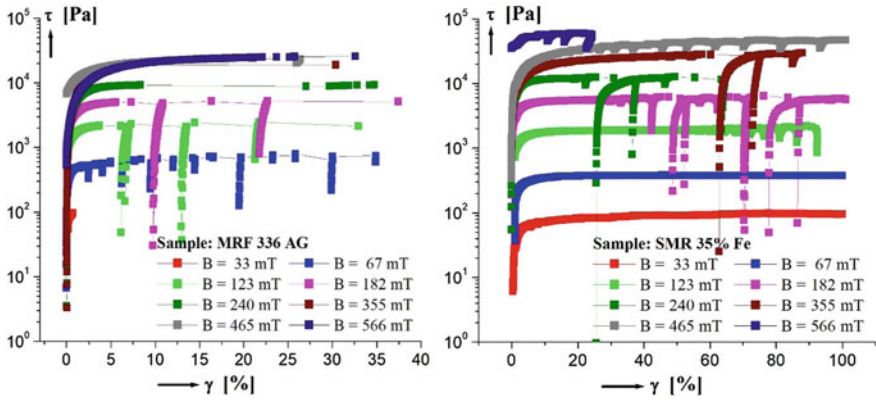
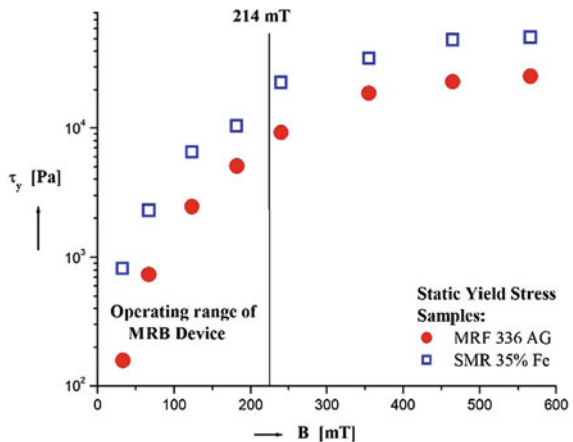


Fig. 4 Strain sweep mode test for both MRFs: MRF 336 AG (left) and SMR 35% Fe (right)

Fig. 5 Influence of the magnetic flux density on the static yield stress for both MRFs: MRF 336 AG (red dots) and SMR 35% Fe (blue squares)



### 4 Experimental Investigations of MRB Device

MRB device has been investigated both mounted in the swirling flow apparatus and separately on it. The investigations of the magnetic field induced by the coil in the gap of the MRB device have been performed using the same FW Bell Hall probe mentioned in the previous section. A meridian section through MRB device allows us to observe the probe inserted in the gap, Fig. 6. The magnetic yoke was designed that the magnetic field to perpendicularly cross the gap filled with MRF.

Two types of tests were performed on the MRB not embedded in the swirl generator apparatus, see Table 2. To carry out the first test, each MRF was filled in the device, then the coil was plugged into electrical voltage from 0 to 32 V (with step of 1 V) and a maximum electrical current of 5A. The power consumed by the coil was monitored through the DC source. The density of the magnetic flux for each

**Fig. 6** MRB device meridian section

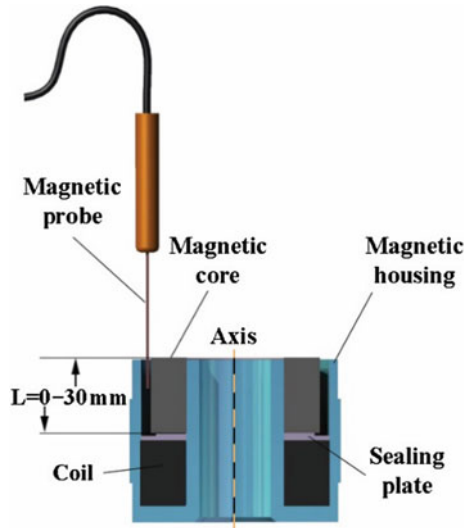


**Table 2** MRB device tests

Measuring probe position (mm)	Tension (V)	Fluid
L = 18	0...32	SMR 35%Fe MRF 336AG
L = 0...36	10 and 30	SMR 35%Fe MRF 336AG

value of the applied voltage was measured at a probe position of  $L = 18$  mm. The data obtained during the first test are presented as the magnetic flux density versus the power consumed by the coil in Fig. 7 (left).

The results show that the magnetic flux density reaches a maximum of 214 mT when SMR 35%Fe is available inside of the MRB device. This value is higher with 12% with respect to the MRF 336AG. The maximum electrical power ( $P_{eMAX}$ ) consumption on the coil is 37.7 W at 32 V. One can observe on Fig. 5 that the maximum values of the magnetic flux density in MRB device are far away to the maximum saturation thresholds for both MRFs allowing us larger braking levels if it is required.

The second test is performed to measure the magnetic flux density along to the length of the gap for two applied voltage values of 10 and 30 V. The position near to the coil corresponds to the length of 0 while the length of 30 mm is associated to the upper side of the MRB device. The magnetic flux density measured along to the length of the gap is comparatively given in Fig. 7 (right) for both MRFs: SMR 35%Fe (blue squares) and MRF 336AG (red circles). It can be seen that a constant value of the magnetic flux density is measured along to half of the length. Contrary, a deviation of the magnetic flux density was measured at the extremities of the gap

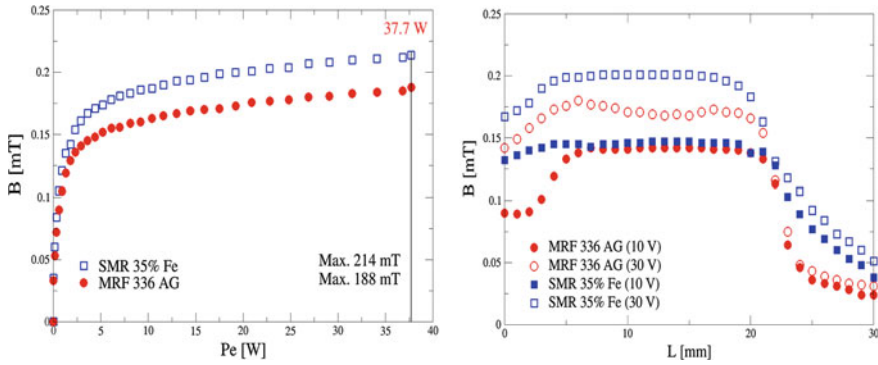


**Fig. 7** Magnetic flux density  $B$  [mT] is measured with respect to: the electric power consumption at one single probe position of  $L = 18$  mm (left) and along the length of the gap for two values of the applied voltage of 10 and 30 V (right)

(from 0 to 4 mm as well as from 20 to 30 mm). Clearly, SMR 35%Fe provides higher value of the magnetic flux density as well as it is covering a larger length along to the gap than the MRF 336AG.

Next, the runner speed behaviour is examined when the speed is slow down with MRB. The data was collected using the magnetic sensor installed on the test section wall at the runner level. Five operating regimes with different runner speeds have been selected for each MRF: 585, 684, 729, 740 and 791 rpm for MRF 336AG and 650, 789, 827, 870 and 898 rpm for SMR 35%Fe, respectively.

From each signal acquired is identified the following values: the maximum ( $n_{MAX}$ ), the minimum ( $n_{min}$ ) and the average values  $\bar{n}$  of the runner speed, Fig. 8. Next, the absolute amplitude of variation ( $A_{av}$ ) is determined according to Eq. (1) and the relative amplitude of variation ( $A_{rv}$ ) is defined with Eq. (2), respectively. The relative amplitude deviation of the runner speed is taken to quantify the MRB behaviour. Ten complete rotations are plotted for two regimes (one regime for each MRF) to evidence the speed deviation.

$$A_{av} = (n_{MAX} - n_{min}) \text{ [rpm]} \tag{1}$$

$$A_{rv} = \frac{A_{av}}{\bar{n}} * 100 \text{ [%]} \tag{2}$$

Two regimes (one runner speed associated to each MRF) are selected in order to examine the runner behaviour. The runner speed value of 726 rpm is selected for MRF 336AG while the regime with speed value of 792 rpm is considered for SMR 35% Fe. These two regimes are comparatively examined due to both producing the same braking level of 80% with respect to the runaway speed value associated to each MRF.

The minimum/maximum runner speed values of 709/748 rpm were identified on the pulse signal acquired at the regime with the average value of 726 rpm for

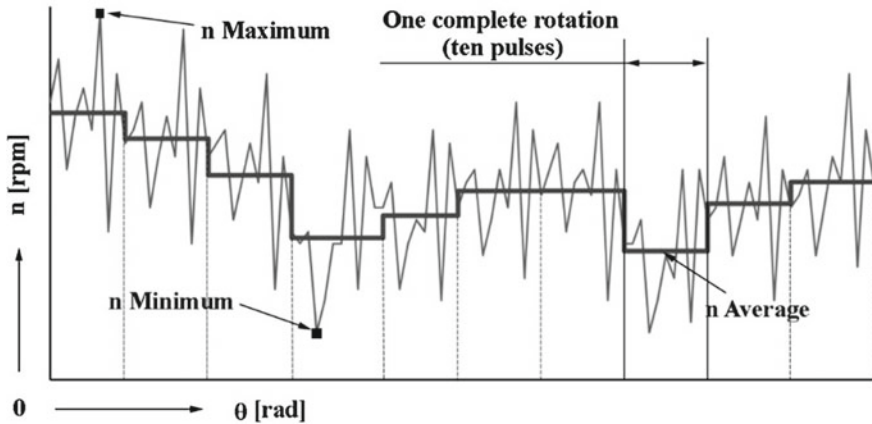


**Fig. 8** Pulse signal acquired (grey line) and average value on each complete rotation of the runner (solid thick line)

MRF 336AG, Fig. 9. The minimum/maximum runner speed values of 698/858 rpm were determined on the regime with average value of 792 rpm for SMR 35%Fe. The average speed for each rotation (black solid line) shows us the evolution of the runner speed in accordance with its magneto-rheological brake. Also, the relative speed variation value of 3.96% is obtained for MRF 336AG while a value of 8.43% is yielded for SMR 35%Fe. It can be noted that the runner speed operation is smoother when the braking is performed with MRF 336AG than SMR 35%Fe.

The pulse signals acquired for both samples (MRF 336AG—up, SMR 35%Fe—down) in terms of the angular position of the runner are presented in Fig. 9. Each signal represents the speed acquired during runner operation. The black solid line corresponds to the average value of runner on one complete rotation (6.28 radians).

A comparative analysis of the data obtained for both MRFs clearly shows that the values corresponding to MRF 336AG is more scattered, Fig. 10. This statement is supported by  $R^2 = 0.5433$  value corresponding to the linear regression function  $A_{rv} = -0.0345n + 31.27$  (red solid line in Fig. 10) yielded on data of MRF 336AG. This value associated to data of MRF 336AG is smaller than  $R^2 = 0.8954$  value corresponding to the linear regression function  $A_{rv} = -0.0354n + 35.841$  (blue solid line in Fig. 10) applied on data of SMR 35%Fe supporting the above assertion about more scattered data of MRF 336AG.

One can observe in Fig. 10 that both linear regressions associated to MRFs are parallel (almost the same slope value). This means that the difference between both data sets is the runaway speed. The runaway speed associated to the experimental investigations performed with MRF 336AG is around 906 rpm while its value around 1012 rpm corresponds to SMR 35%Fe. This difference between the two runaway speeds comes from the mechanical friction of the runner produced by pre-stressing level of the nozzle, Fig. 2.

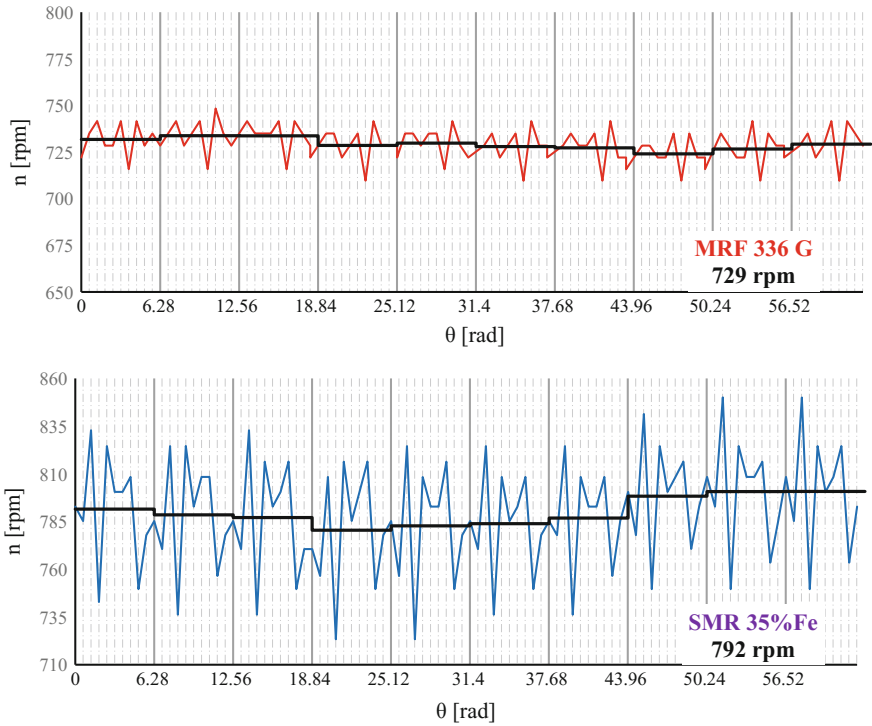


**Fig. 9** Pulse signals acquired for MRF 336 AG (up)/SMR 35% Fe (down) and average value on each complete rotation of the runner (solid black line)

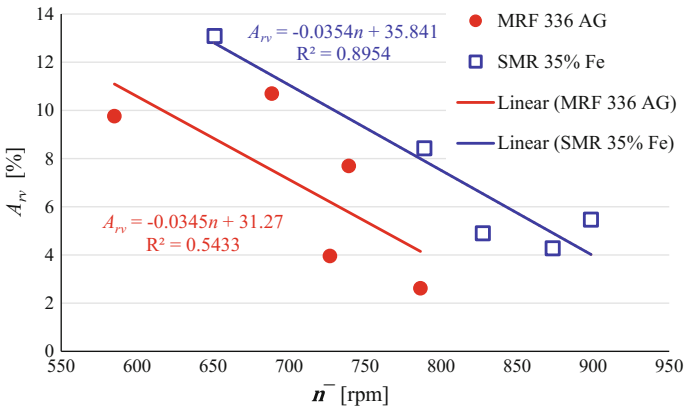


**Fig. 10** Relative amplitude variation of the speed runner versus the average speed of the runner

It is important to underline that the SMR 35%Fe provides a higher braking level than MRF 336AG confirming the conclusion already drawn above based on magneto-rheological investigations presented in Sect. 3. Also, the relative amplitude variation values of the speed runner associated to the SMR 35% Fe are larger than obtained with MRF 336AG. This meaning that the behaviour associated with the runner rotation presents a variation of the speed in operation. The runner speed variation is directly correlated with the braking level of MRB. This behaviour is linked with the rupture and rebuild of large chain-like agglomerates in the MRF. As a result, this behaviour is up to 2 times more significant for SMR 35%Fe than MRF 336AG.

It was observed during the experimental investigation that SMR 35% Fe behaves better under water conditions than MRF 336AG. The period of time that the working MRF is washed out from the MRB for investigations with SMR 35% Fe is up to 5 times greater than with MRF 336AG. This is caused by the carrier liquid which is mineral oil based ferrofluid for SMR 35%Fe and silicone oil for MRF 336AG. As a result, SMR 35% Fe is selected based on these results for further investigations to control the runner speed to mitigate the self-induced unsteady phenomena in swirling flows.

## 5 Conclusions

This paper is focused on experimental investigations of a MRB embedded in a swirl generator apparatus. The runner speed of the swirl generator apparatus was controlled with a MRB device using two MRFs. The main challenge for MRB is associated with its operation under water conditions. As a result, two magneto-rheological fluids are selected as following: (1) a commercial conventional magneto-rheological fluid (MRF 336AG) manufactured by Lord Co. (2) a nano-micro composite with 35% volume fraction of micron-size iron particles in a ferrofluid carrier, designed and manufactured by Magnetic Fluids Laboratory from Romanian Academy—Timisoara Branch. The experimental investigations were performed to determine the magneto-rheological properties of the two MRFs, as well the behaviour of the MRB. The magneto-rheological measurements were done considering the viscosity curves (shear viscosity versus shear rate  $\eta(\dot{\gamma})$ ) and the strain sweep tests at several values of the magnetic flux density from 0 to 566 mT. As a result, the influence of the magnetic flux density on the static yield stress was determined for each MRF. It was observed that the saturation of this dependence is reached for high values of B. Also, the measurements with MRB device embedded in swirling flow apparatus revealing an oscillation behaviour that is related to the rupture and rebuild of large chain-like agglomerates in concentrated samples under the influence of applied field. SMR 35%Fe shows a higher value of saturation with respect to MRF 336AG.

The mechanical solution designed for MRB is presented together with an appropriate sealing solution to avoid expelling the solid particles. The magnetic field is measured in the gap of the MRB using both MRFs. The magnetic flux density measured along to the length of the gap shows a constant value on a half length. This is



an important result for design stage. Challenging investigations were performed at several runner speeds with MRB under water conditions. A relative speed variation behaviour associated with the runner rotation has been identified due to rupture and rebuild of large chain-like agglomerates in the MRF. The runner speed analysis shows that relative amplitude variation of the controlled runner with SMR35%Fe is two times larger than in the case of MRF 336AG. This relative speed variation is directly correlated with the braking level of MRB. SMR 35%Fe provides a higher braking level than MRF 336AG confirming the conclusion yielded on magneto-rheological investigations. Also, it was observed during the experimental investigation that SMR 35% Fe behaves better under water conditions than MRF 336AG. This is caused by the carrier liquid which is transformer oil for SMR 35%Fe and silicone oil for MRF 336AG. As a result, SMR 35%Fe is selected based on these results for further investigations to control the runner speed in order to mitigate the self-induced unsteady phenomena in swirling flows.

**Acknowledgements** The authors affiliated with the Romanian Academy—Timisoara Branch have been supported by two research programs of the Center for Fundamental and Advanced Technical Research: “Unsteady Hydrodynamics of Helical Vortex Flows” of Hydrodynamics and Cavitation Laboratory and “Magnetically controllable fluids and complex flows. Engineering and biomedical applications” of Magnetic Liquid Laboratory.

## References

1. Carlson, J.D., Catanzarite, D.M., St. Clair, K.A.: Commercial magneto-rheological fluid devices. *Int. J. Mod. Phys. B* **10**(23&24), 2857–2865 (1996)
2. Jolly, M., Bender, J., Carlson, J.: Properties and applications of commercial magnetorheological fluids. *J. Intell. Mater. Syst. Struct.* **10**(1), 5–13 (1999)
3. Lita, M., Popa, N., Velescu, C., Vekas, L.: Investigations of a magnetorheological fluid damper. *IEEE Trans. Magn.* **40**(2), 469–472 (2004)
4. Ahmadian, M., Norris, J.: Experimental analysis of magnetorheological dampers when subjected to impact and shock loading. *Commun. Nonlinear Sci. Numer. Simul.* **13**(9), 1978–1985 (2008)
5. Olabi, A.G., Grunwald, A.: Design and application of magnetorheological fluid. *Mater. Des.* **28**(10), 2658–2664 (2007)
6. Milecki, A., Hauke, M.: Application of magnetorheological fluid in industrial shock absorbers. *Mech. Syst. Signal Pr.*, 1–14 (2011)
7. Wang, J., Meng, G.: Magnetorheological fluid devices: principles, characteristics and applications in mechanical engineering. *Proc. Inst. Mech. Eng. L J. Mater. Des. Appl.* **215**(3), 165–174 (2001)
8. Carlson, J.D.: Magneto-rheological brake with integrated flywheel. US Patent 6186,290 (2001)
9. Sukhwani, V.K., Hirani, H.: Design, development, and performance evaluation of high-speed magnetorheological brakes. *Proc. Inst. Mech. Eng. L J. Mater. Des. Appl.* **222**(1), 73–82 (2008)
10. Muntean, S., Bosioc, A.I., Szakal, R.A., Borbath, I., Vekas, L., Susan-Resiga, R.F.: Hydrodynamic investigation in a swirl generator using a magneto-rheological brake. In: da Silva (ed.) MDA2016: topics in power generation. 1st International Conference on Materials Design and Applications, Porto, July 2016. *Advanced Structured Materials*, vol. 65, pp. 209–218. Springer, Heidelberg (2016)

11. Rabinow, J.: The Magnetic Fluid Clutch. *AIEE Trans.* **67**(2), 1308–1315 (1948)
12. Bucchi, F., Forte, P., Frendo, F.: Geometrical optimization of a magnetorheological clutch operated by coils. *Proc. Inst. Mech. Eng. L J. Mater. Des. Appl.* **231**(1–2), 100–112 (2016)
13. Grunwald, A., Olabi, A.: Design of magneto-rheological (MR) valve. *Sens. Actuat. A Phys.* **148**(1), 211–223 (2008)
14. Borbáth, T., Bica, D., Potencz, I., Borbáth, I., Boros, T., Vékás, L.: Leakage-free rotating seal systems with magnetic nanofluids and magnetic composite fluids designed for various applications. *Int. J. Fluid Mach. Syst.* **4**(1), 67–75 (2011)
15. Borbáth, T., Bica, D., Potencz, I., Vekas, L., Borbáth, I., Boros, T.: Magnetic nanofluids and magnetic composite fluids in rotating seal systems. *IOP Conf. Series Earth Env. Sci.* **12**(1), 012105 (2010)
16. Carlson, J.D.: What makes a good MR fluid? *J. Intell. Mater. Syst. Struct.* **13**(7), 431–435 (2002)
17. Vekas, L.: Ferrofluids magnetorheol. fluids. *Adv. Sci. Tech.* **54**, 127–136 (2008)
18. Bossis, G., Volkova, O., Lacis, S., Meunier, A.: Magnetorheology: fluids, structures and rheology. In: Odenbach, S. (ed.) *Ferrofluids: Magnetically Controllable Fluids and their Applications*. Lecture Notes in Physics, vol. 594, pp. 202–230 (2002)
19. de Vicente, J., Klingenberg, D.J., Hidalgo-Álvarez, R.: Magnetorheological fluids: a review. *Soft Matter* **7**, 3701–3710 (2011)
20. López-López, M.T., de Vicente, J., Bossis, G., González-Caballero, F., Durán, J.D.G.: Preparation of stable magnetorheological fluids based on extremely bimodal iron–magnetite suspensions. *J. Mater. Res.* **20**(4), 874–881 (2005)
21. López-López, M.T., Kuzhir, P., Lacis, S., Bossis, G., González-Caballero, F., Durán, J.D.G.: Magnetorheology for suspensions of solid particles dispersed in ferrofluids. *J. Phys. Condens. Matter* **18**(38), S2803–S2813 (2006)
22. Magnet, C., Kuzhir, P., Bossis, G., Meunier, A., Nave1, S., Zubarev, A., Lomenech, C., Bash-tovoi, V.: Behaviour of nanoparticle clouds around a magnetized microsphere under magnetic and flow fields. *Phys. Rev. E* **89**(3), 032310 (2014)
23. Iglesias, G.R., Fernández Ruiz-Morón, L., Durán, J.D.G., Delgado, A.V.: Dynamic and wear study of an extremely bidisperse magnetorheological fluid. *Smart Mater. Struct.* **24**(12), 127001 (2015)
24. Susan-Resiga, R.F., Muntean, S., Tănasă, C., Bosioc, A.I.: Hydrodynamic design and analysis of a swirling flow generator. In: Paper Presented at the 4th German-Romanian Workshop in Turbomachinery, University of Stuttgart, Stuttgart, Germany (2008)
25. Susan-Resiga, R.F., Muntean, S., Stuparu, A., Bosioc, A.I., Tănasă, C., Ighişan, C.: A variational model for swirling flow states with stagnant region. *Eur. J. Mech. B Fluids* **55**, 104–115 (2016)
26. Bosioc, A.I., Muntean, S., Tănasă, C., Susan-Resiga, R.F., Vékás, L.: Unsteady pressure measurements of decelerated swirling flow in a discharge cone at lower runner speeds. In: Désy, N. (ed.) *IAHR 2014: Topics in Unsteady and Transient Phenomena*. 27th IAHR Symposium on Hydraulic Machinery and Systems, Montreal, September 2014. IOP Conference Series: Earth and Environmental Science, vol. 22, pp. 032008 (2014)
27. Bosioc, A.I., Beja, T.E., Muntean, S., Borbáth, I., Vékás, L.: Experimental investigations of MR fluids in air and water used for brakes and clutches. In: da Silva (ed.) *MDA2016: Topics in Power Generation*. 1st International Conference on Materials Design and Applications, Porto, July 2016. *Advanced Structured Materials*, vol. 65, pp. 197–207. Springer, Heidelberg (2017)
28. Muntean, S., Bosioc, A.I., Stanciu, R., Tănasă, C., Susan-Resiga, R.: 3D numerical analysis of a swirling flow generator. In: Gajic, A., Benisek, M., Nedeljkovic, M. (eds.) *IAHRWG2011: In Swirling Flow*. Proceedings of the 4th IAHR International Meeting of the Workgroup on Cavitation and Dynamic Problems in Hydraulic Machinery and Systems, Belgrade, October 2011. University of Belgrade, Faculty of Mechanical Engineering, pp. 115–123 (2011)
29. Susan-Resiga, D., Vekas, L.: Yield stress and flow behaviour of concentrated ferrofluid-based magnetorheological fluids: the influence of composition. *Rheol. Acta* **53**(8), 645–653 (2014)

30. Laun, H.M., Schmidt, G., Gabriel, C., Kieburg, C.: Reliable plate–plate MRF magnetorheometry based on validated radial magnetic flux density profile simulations. *Rheol. Acta* **47**(9), 1049–1059 (2008)
31. Yang, Y., Li, L., Chen, G.: Static yield stress of ferrofluid-based magnetorheological fluids. *Rheol. Acta* **48**, 457–466 (2009)
32. de Gans, B.J., Duin, N.J., van den Ende, D., Mellema, J.: The influence of particle size on the magnetorheological properties of an inverse ferrofluid. *J. Chem. Phys.* **113**, 2032–2042 (2000)

**Part VII**  
**Additive Manufacturing**

# Orientation of the Digital Model for SLA 3D Printing and Its Influence on the Accuracy of the Manufactured Physical Objects for Micro- and Nano Technologies



E. H. Yankov  and M. P. Nikolova

**Abstract** In modern mechanical engineering, there is increased need to find solutions for fast manufacturing of real prototypes. One of these is the fast-growing up-to-date CAD/CAM/CAE system enabling to create digital prototypes. Using CAD systems the conceptual design is analyzed and tested before producing the real prototype. This reduces the compliance costs for manufacturing of the physical models and tooling as well as the production time of the prototype is lessened several times. With the development of technology, and especially in medicine, it is necessary to produce prototypes that can be obtained relatively quickly and meet the requirements of accuracy. Rapid prototyping technologies have such capabilities that they can reproduce digital models with their manufacturer's precision. To determine the accuracy of printing, a SLA system is used. To determine the accuracy of printing, a SLA system is used. One of the peculiarities of making a detail by this method is the appearance of distortions in the initial stage of construction at large rectilinear plots. In order to determine the minimum printing deviations, a strategy for printing prototype models at a different slope of  $0^{\circ}$ – $90^{\circ}$  was used. Patterns are made with coordinate networks, enabling post-print deviations to be evaluated by matching the digital model. The present study will be useful in developing prototype models for micro and nanotechnology in mechanical engineering and medicine, providing a solution for their optimal location with minimal deviations.

**Keywords** Micro model · SLA 3D printing · Photopolymer · Material for casting CAD system

---

E. H. Yankov (✉) · M. P. Nikolova

Department of Material Science and Technology, University of Ruse, 7017 Ruse, Bulgaria  
e-mail: [eyankov@uni-ruse.bg](mailto:eyankov@uni-ruse.bg)

© Springer Nature Switzerland AG 2019

L. F. M. da Silva (ed.), *Materials Design and Applications II*, Advanced Structured Materials 98, [https://doi.org/10.1007/978-3-030-02257-0\\_21](https://doi.org/10.1007/978-3-030-02257-0_21)

## 1 Introduction

The wide application of the 3D printers in the areas of machinery, jewelry, medicine [1–6] expands over recent years and give rise to widespread studies concerning the possibility of receiving precise printed parts. By the development of technologies, the 3D printing machines are becoming increasingly smaller and more compact. The printing precision improves and reaches levels around  $6\ \mu\text{m}$  allowing to obtain precise parts. It emerges that the problems with printing reach further. Additional factors that influence the 3D printing precision are the thermodynamic processes depending on the heating and cooling rates. These processes create internal stresses in the 3D printed materials that trigger local mini-deformations and these mini-deformations accumulate during the building-up of the model and turn into macro-deformations [7, 8].

The present study aims at assessing the influence of the position of the model in the working area in order to decrease the micro-deformations during the SLA 3D printing.

## 2 Experimental Procedures

For the purpose of this study was constructed numerical model with dimensions  $30 \times 30\ \text{mm}$  and a thickness of  $3\ \text{mm}$ . The model contained  $15 \times 15$  in number micro-squares with dimensions of  $500 \times 500\ \mu\text{m}$  and depth of  $500\ \mu\text{m}$  with a separating interval of  $1000\ \mu\text{m}$  (Fig. 1a). The models were stored in \*.OBJ format suitable for the 3D printing.

The “PreForm” software was used for the pre-operation for printing where the digital model was multiplied six times and tilted at  $0^\circ$ ,  $30^\circ$ ,  $45^\circ$ ,  $60^\circ$ ,  $75^\circ$  and  $90^\circ$  with respect to X-axis of the working table (Fig. 1b). The models were printed by SLA 3D printer Formlabs 2.0 (Fig. 2a).

The physical models were printed from Castable Resin photopolymer and a precision of  $25\ \mu\text{m}$  was used. The measurement of the coordinates of the micro-squares after the 3D printing was carried out by a “Carl Zeiss”—Jena, Germany optical microscope at  $6.3\times$  magnification (Fig. 2b). For that purpose, 5MP digital camera with S-EYE software was adapted to the microscope (Fig. 3a). The coordinates’ measurements of the physical models were tabulated and compared with those of the digitals models. The assessment of the deviations was done by using the coordinate grid method (Fig. 3b) [9–11].

The relative “distortions” in different directions ( $\varepsilon_x$  and  $\varepsilon_y$ ) were measured by the equations:

$$\varepsilon_x = \frac{\Delta X}{X_i} = \frac{X_{i,j} - X_i}{X_i}, \varepsilon_y = \frac{\Delta Y}{Y_i} = \frac{Y_{i,j} - Y_i}{Y_i}, \quad (1)$$

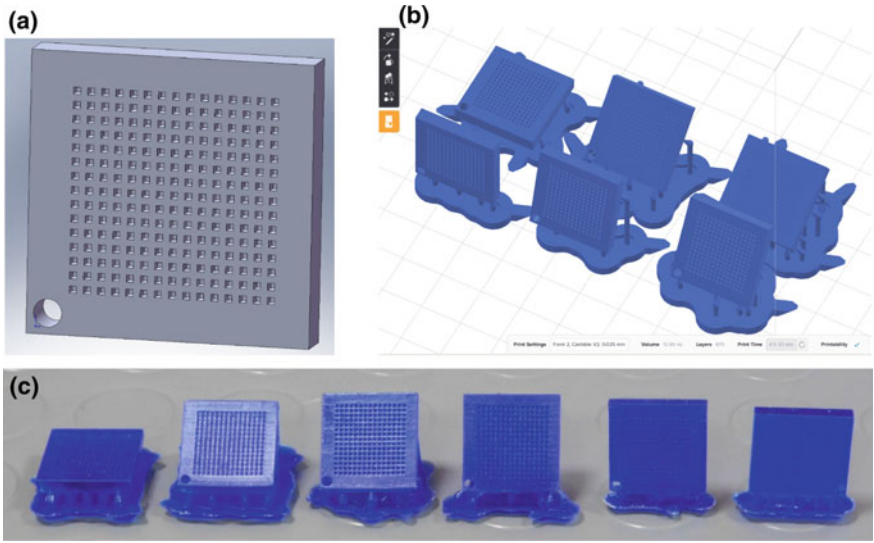


**Fig. 1** Prototype models: **a** 3D CAD model, **b** positioning of the models in the operating space; **c** physical 3D printed models

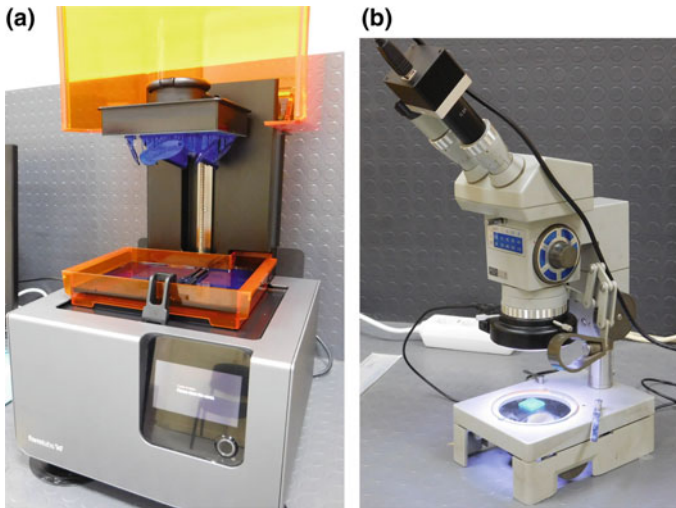


**Fig. 2** General view of **a** 3D printer Formlabs 2, **b** Carl Zeiss (Jena) optical microscope

where  $X_i$  and  $Y_i$  are the coordinates of the each micro-square center in the digital model,  $X_{i,j}$  and  $Y_{i,j}$  are the coordinates of the each micro-square center in the physical 3D model.

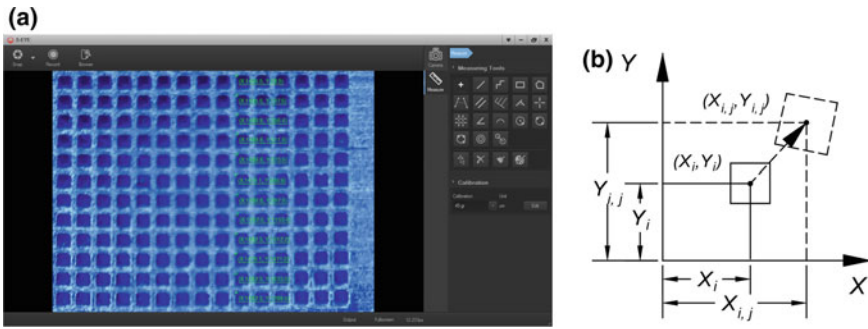


**Fig. 3** The setting of the deviations by **a** measuring the physical model, **b** calculating the relative distortions

Based on the calculated relative “distortions” in  $X$  and  $Y$  directions, colored graphics of the deviations were plotted indicating the relative shift of each square against the reference digital model.

### 3 Experimental Results

After mathematical processing of the results colored cards of the micro-squares’ deviation in  $X$  and  $Y$  directions of the 3D printed models build in all tilt angles ( $0^\circ$ ,  $30^\circ$ ,  $45^\circ$ ,  $60^\circ$ ,  $75^\circ$  and  $90^\circ$ ) are obtained (Figs. 4 and 5). For the  $0^\circ$  tilt model (horizontally positioned) the distribution of the deviations in the  $X$  direction is uneven (Fig. 4a). In the first vertical pillar near to the marked angle the material highly shifts in positive direction that means an increase in size while in the second vertical pillar the highest shrinking of the material is measured. In the middle of the model, a strong shrinkage is also found while in the other areas these effects are insignificant. As the tilt angles of the models increase from  $30^\circ$  up to  $90^\circ$ , the highest is the shrinkage in the first vertical pillar for all of them (Fig. 4b–f).

This area is located near to the supporting props which fact influences the results obtained. As the number of the printed layers increases, the deviations decrease for all of the tilt samples. When reaching the last layers of the  $30^\circ$ ,  $60^\circ$  and  $75^\circ$  tilt samples the deviations have positive values (meaning extension) while those of the  $45^\circ$  and  $90^\circ$  tilted specimens retain a slight shrinkage that is comparable to the accuracy of the 3D printer.

In  $Y$  direction shrinkage is found in the first row of all of the printed models (Fig. 5). When the height of the model increases, the deviations gain positive values meaning an extension of the model. The shrinkage is also related to the near located supporting props. The models printed at  $0^\circ$ ,  $30^\circ$  and  $60^\circ$  tilt angle show a large number of deflected cells values, while those of the  $45^\circ$ ,  $75^\circ$ , and  $90^\circ$  tilt specimens are less influenced. With the increase in the 3D printed layers, the deviations rise



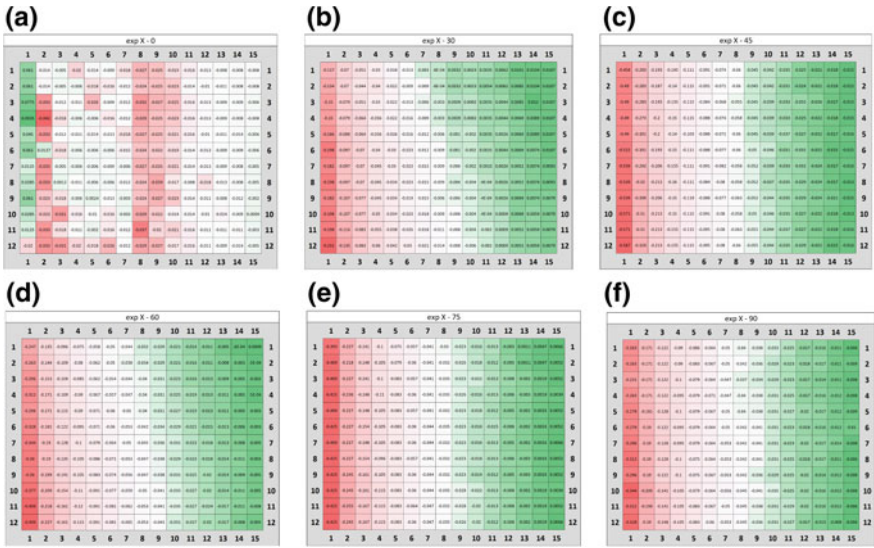


**Fig. 4** Colored cards of the deviations with respect to X direction: **a** 0°, **b** 30°, **c** 45°, **d** 60°, **e** 75°, **f** 90°

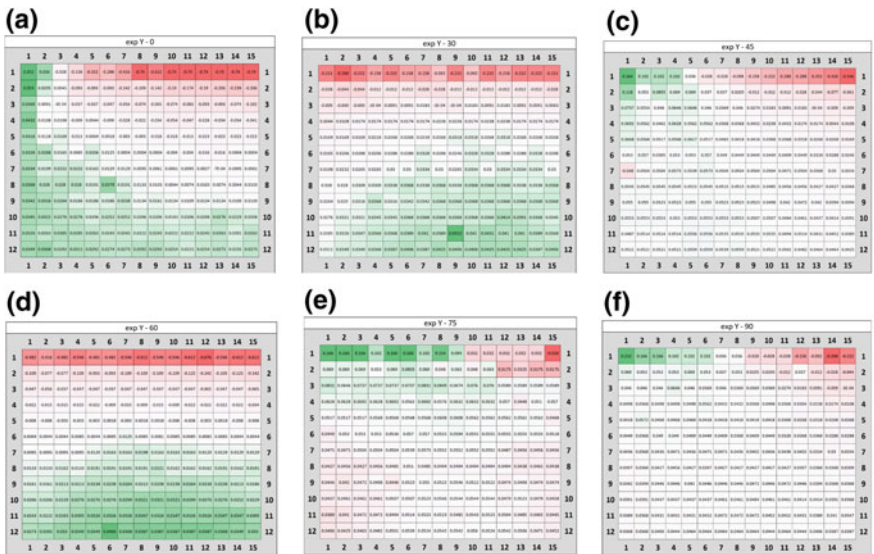


**Fig. 5** Colored cards of the deviations with respect to Y direction: **a** 0°, **b** 30°, **c** 45°, **d** 60°, **e** 75°, **f** 90°

up. This effect was found out also in X direction because of the systematic error when building the layers. The error is comparable with the printer precision and accumulates in each subsequent layer which influences the size of the squares.

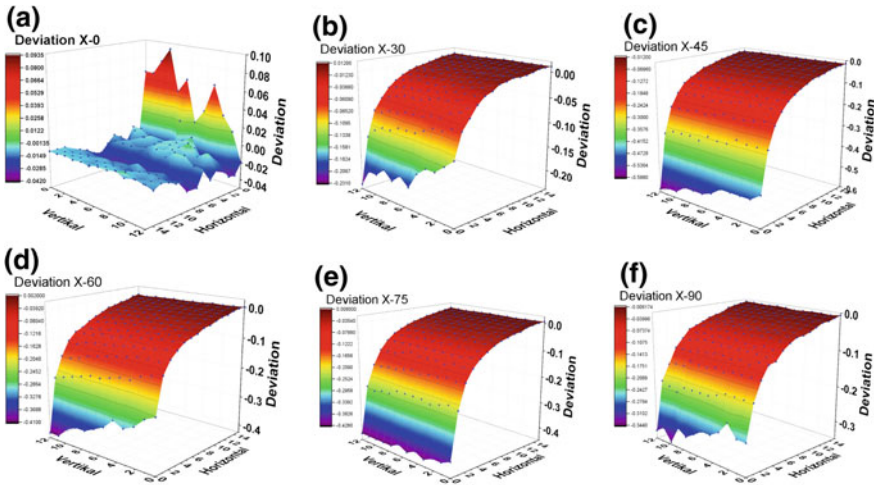


**Fig. 6** Deviations of the relative distortions after printing with respect to X: **a** 0°, **b** 30°, **c** 45°, **d** 60°, **e** 75°, **f** 90°

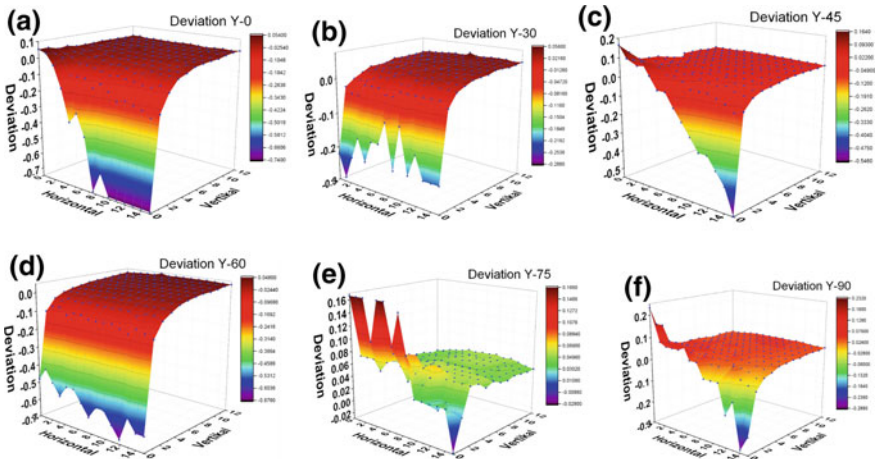


**Fig. 7** Deviations of the relative distortions after printing with respect to Y: **a** 0°, **b** 30°, **c** 45°, **d** 60°, **e** 75°, **f** 90°

Figures 6 and 7 represent the deviations limits during printing for all of the examined tilt angles in both X and Y directions. The red color indicates maximum values of deviations while the violet marks the minimum values.

The deviations in the distortions in the X direction for the 0° tilt sample are the smallest (varying from -0.042 up to 0.0935) (Fig. 6a). This fact is attributed to the relatively low number of layers in height which directly correlates with the low number of accumulated systematic errors during printing. When increasing the

printing angle from  $30^\circ$  to  $45^\circ$  the deviations reach maximum values (from  $-0.588$  to  $-0.012$ ). For the  $90^\circ$  tilt sample the deviations gradually decline down to values from  $-0.344$  to  $-0.006174$  which values are higher than those of the  $0^\circ$  and  $30^\circ$  tilt samples. In  $Y$  direction (Fig. 7) the deviations in sizes have higher values than those in the  $X$  direction with the exception of the model printed at  $75^\circ$  tilt angle (Fig. 7e) where the values are lower. The higher deviations in the distortions in the  $Y$  direction are detected for the  $45^\circ$ ,  $60^\circ$  and especially for the  $0^\circ$  angle of printing where they are the highest (from  $-0.74$  up to  $0.054$ ). The  $30^\circ$  printed sample demonstrates the low deviations in the distortions while for the  $75^\circ$  tilted one the variations are the smallest (from  $0.02$  up to  $0.16$ ). The reason for the higher deviations in the distortions in the  $Y$  direction is due to both systematic error and layer-by-layer building up of the model in the moving  $Z$  axis.

The  $Z$ -axis coincides with the step of the building of each layer and its systematic error of relocation accumulates errors in the sizes of the 3D printed model. Besides, during the layer-by-layer printing, the photopolymerized film unsticks from the silicone of the bath which triggers micro-tensile stresses in the build model. These micro-tensile stresses cause an increase in size in the  $Y$  direction and a decrease in the  $X$  direction. This effect explains most of the negative deformations values in the  $X$  direction and the positive one in the  $Y$  direction.

In order to find an optimum option for the angle of printing, a comparative analysis of the positive and negative distortions in  $X$  and  $Y$  directions against the printing angle is done (Fig. 8). The minimum ( $\varepsilon_X(-)$ ,  $\varepsilon_Y(-)$ ) and maximum ( $\varepsilon_X(+)$ ,  $\varepsilon_Y(+)$ ) values of the deviations in the distortion in  $X$  and  $Y$  directions are used. As seen, the lowest range of the deviations is observed for the  $0^\circ$  printing angle while the deviation range is the highest for the model printed at  $45^\circ$  tilt angle. In  $Y$  direction the range of the minimum and maximum values is the smallest for the  $75^\circ$  printing angle and the highest for the  $0^\circ$ .

A comparative analysis of both negative values and both positive values in  $X$  and  $Y$  direction is also done. The sum of both values is taken into account. The analysis of the negative values in  $X$  and  $Y$  directions discloses that the range for the  $30^\circ$  angle of printing is the lowest and those for the  $45^\circ$  is the highest. The analysis of the positive deviations in the distortions shows that the values for the  $60^\circ$  angle of printing are the lowest and these for the  $90^\circ$  tilt angle are the highest.

For the selection of the optimum option for the angle of printing the complex analysis of the positive and negative deviations in the distortions in  $X$  and  $Y$  directions were taken into account. This complex analysis indicates that the deviations in the distortions when printing the model at  $30^\circ$  tilt angle are the smallest.

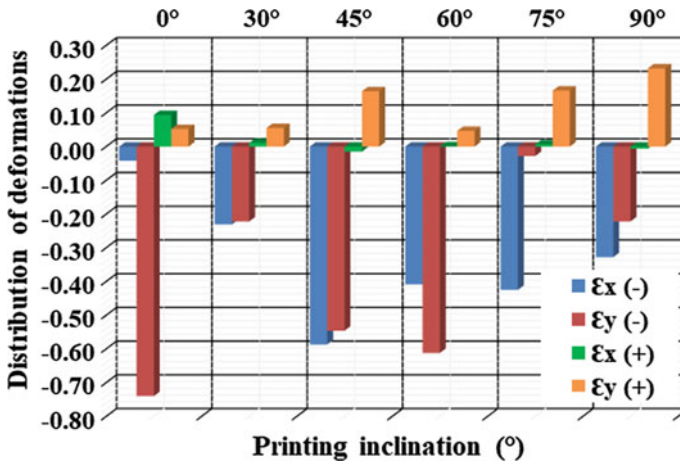


**Fig. 8** Comparative diagram of the relative distortions at upper and lower limit with respect to X and Y direction

## 4 Conclusions

In this research establishes the reasons for deviations occurred after 3D printing, and a decision to reduce them as follows:

1. The deviation because of the shrinking of the model in X and Y directions is found in the initially printed layers due to the position of the supporting props while an expansion of the layers is accumulated as a systematic error with a further layer-by-layer building.
2. The deviations in the relative distortions with respect to X-axis are less than those in Y direction with the exception of the model printed at 75°. The reason for the increased distortions is the coincidence of the Y direction with the moving Z axis. The latter axis is a factor in determining the thickness of the layers. Additionally, the unsticking of the photopolymerized layers happens in Z direction that triggers micro-tensile strains to occur in the build-up model and enlarges the sizes in Y direction while decreasing those in the X direction.
3. The maximum distortion deviations with respect to X-axis are found to occur at a tilted angle of 45°, while those in Y direction peak at a tilted angle of 0°. The maximum distortion deviations with respect to Y axis are detected at a tilted angle of 0°, while those in Y direction maximize at a tilted angle of printing equal to 75°.
4. An optimum option with fewer distortion deviations with respect to X and Y axis are established for the 30° tilted model where the deviations amount  $-0.243$  and  $0.344$ , respectively.
5. The largest distortion deviations are found in the 45° and 60° tilted models both in X and Y directions.

**Acknowledgements** The study was supported by contract of University of Ruse “Angel Kanchev”, № BG05M2OP001-2.009-0011-C01, “Support for the development of human resources for research and innovation” at the University of Ruse “Angel Kanchev”. The project is funded with support from the Operational Program “Science and Education for Smart Growth 2014–2020” financed by the European Social Fund of the European Union.

## References

1. William II, S.L., Bin, Z., John, Z., Angela, D.: 43rd Proceedings of the North American Manufacturing Research, Institution of SME (Procedia Manufacturing), vol. 1, pp. 393–403 (2015). <https://doi.org/10.1016/j.promfg.2015.09.047>
2. Ivan, G., Emil, S., Ľuboš, K., Volodymyr, K.: Surface finish techniques for FDM parts. Mater. Sci. Forum **818**, 45–48 (2015). <https://doi.org/10.4028/www.scientific.net/MSF.818.45>
3. Ivan, G., Ildiko, M., Tomasz, J., Tor-Swiatek, A.: Proceedings of 8th International Engineering Symposium at Bánki, Paper 32 (2016). Print: ISBN: 978-615-5460-95-1
4. Gajdoš, I., Kaščák, Ľ., Spišák, E., Slotá, J.: Eng. Mater. **635**, 169–173 (2015). <https://doi.org/10.4028/www.scientific.net/KEM.635.169>
5. Yu, H.Y., Ma, D.D., Wu, B.L.: Nan Fang Yi Ke Da Xue Xue Bao. J. South. Med. Univ. **37**, 668–672 (2017)
6. Kuss, M.A., Harms, R., Wu, S., Wang, Y., Untrauer, J.B., Carlson, M.A., Duan, B.: RSC Adv. **7**, 29312–29320 (2017)
7. Sames, W.J., List, F.A., Pannala, S., Dehoff, R.R., Babu, S.S.: The metallurgy and processing science of metal additive manufacturing. Int. Mater. Rev. 1743–2804 (2016). <http://dx.doi.org/10.1080/09506608.2015.1116649>
8. Emil, Y., Maria, N., Vania, Z.: Modern methods for measuring temperature, stresses, and strains in the field of micro- and nanotechnologies. In: Science Conference of Ruse University, Bulgaria, pp. 66–76 (2017). ISBN: 1311-3321
9. Nikolai, F., Valentin, G., Ecaterin, M.: Proceedings of Avangard Technologies and Machine Building Materials, VMEI Gabrovo, pp. 187–191 (1992)
10. Boris, T., Valentin, G., Nikolai, F., Ecaterin, M.: Proceedings of 9th Machine Tool Conference, University Politehnica of Bucharest, pp. 264–269 (1994)
11. Valentin, G.: Testing and Processing of Contemporary Materials. Ljubljana-Ruse-Gliwice, pp. 125–136 (1997)

**Part VIII**  
**Machining**

# Effect of Additives on the Machinability of Glass Fiber Reinforced Polymer



Jean-François Chatelain, C. M. Ouellet-Plamondon, B. Lasseur  
and H. Kuate-Togue

**Abstract** Glass fiber reinforced polymers (GFRP) are composite materials widely used in all fields of applications. Once cured to near net shape, GFRP parts often need several finishing operations such as trimming, milling or drilling in order to meet final dimensions and accommodate fastening hardware. The cutting temperature is crucial when dealing with such finishing operations for synthetic composite materials. Cutting temperatures higher than the glass transition temperature ( $T_g$ ) of the resin matrix are highly undesirable: they cause degradation of the matrix around the cut edges, which can severely affect the mechanical performance of the entire component. This research aims to study the effect of adding different particles to the epoxy matrix of glass fiber reinforced polymers (GFRP) on the cutting temperature and surface finish for the trimming operation of this material. Five plaques were made, each with a different epoxy mixture: no additive, wetting agent (WA), WA and clay, WA and wax, WA and clay and wax. From the results, it can be concluded that wax particles significantly decrease the cutting temperature for the trimming process. The maximum recorded temperature was found to be 30% lower than for the reference plaque having no additive. Regarding the surface roughness, the wax particles also seem to have a positive effect, with the  $R_a$  value decreasing by a value of up to 32% versus the reference material. The synergy between the clay and the wax particles added to epoxy is promising for improving GFRP machining.

**Keywords** Glass fiber reinforced polymer (GFRP) · Trimming  
Cutting temperature · Cutting force · Surface finish · Clay nanoparticles  
Wax particles · Wetting agent

---

J.-F. Chatelain (✉) · B. Lasseur · H. Kuate-Togue  
Mechanical Engineering Department, École de Technologie Supérieure de Montréal,  
1100 Notre Dame Street, West, Montreal, QC H3C 1K3, Canada  
e-mail: [jean-francois.chatelain@etsmtl.ca](mailto:jean-francois.chatelain@etsmtl.ca)

C. M. Ouellet-Plamondon  
Construction Engineering Department, École de Technologie Supérieure de Montréal,  
1100 Notre Dame Street, West, Montreal, QC H3C 1K3, Canada

© Springer Nature Switzerland AG 2019  
L. F. M. da Silva (ed.), *Materials Design and Applications II*, Advanced  
Structured Materials 98, [https://doi.org/10.1007/978-3-030-02257-0\\_22](https://doi.org/10.1007/978-3-030-02257-0_22)

## 1 Introduction

Composite materials are largely used for applications requiring a low weight-to-strength ratio, such as in the automotive, aerospace, wind energy domains, etc. Despite the fact that the materials are produced to near net shape, machining operations, like trimming, drilling or milling are required to satisfy final dimensions and specified tolerances. The machining of synthetic composites is different and more complicated than the machining of conventional metals and their alloys due to the abrasive nature and anisotropy of the latter. Defects such as delamination, fiber pull-out, uncut fibers, matrix cracking and burning may appear on machined surfaces [1, 2]. The occurrence and magnitude of these defects depend on many factors, with the cutting parameters and machining configuration affecting the quality of cut most directly [2, 3]. In the case of Carbon Fiber Reinforced Polymer (CFRP) machining, a high cutting speed coupled with a low feed rate generally constitutes the best combination to favor the surface roughness and integrity of the material [4–6]. Another factor significantly affecting the surface finish is the orientation of the fiber with respect to the cutting feed direction. Pecat et al. [7] found that  $-45^\circ$  and  $90^\circ$  fiber angles led to severe damage in the form of cracks, while their micrographs showed best trimmed surfaces for  $0^\circ$  and  $+45^\circ$  orientations. Chatelain et al. [8] also obtained similar results for the trimming of quasi-isotropic aerospace CFRP laminates. They demonstrated that a typical roughness profile “signature” was related to each ply orientation ( $0^\circ$ ,  $+45^\circ$ ,  $90^\circ$  and  $-45^\circ$ ). The worst longitudinal roughness was found for the plies oriented at  $-45^\circ$ . Other researches also confirmed this orientation to be the worst one with respect to the surface finish [9–12]. The cutting parameters also influence thermal damage and tool wear. The cutting temperature decreases with a feed rate decrease and a cutting speed increase. The same phenomenon is observed for tool wear [13–15]. This is due to the contact time of the teeth with the material, which is reduced while the chip size increases for these conditions [14, 15]. Finally, it was found that the cutting temperature increases as the tool wear increases [1, 13, 16].

The type of fiber involved is also a source of temperature increase and tool wear. Synthetic fibers such as glass and carbon are so abrasive that machining such materials is known to be difficult. They cause rapid tool wear, which increases the cutting temperature [1, 9, 17, 18]. Establishing a contrast with metallic materials, Hamedanianpour [9] demonstrated that a tool wear increase leads to a better surface finish (lower roughness average values) due to the softening/spreading of the epoxy matrix on the trimmed surfaces. In addition to being abrasive, composites also have low thermal conductivity, due to resin properties. The heat generated through the cutting mechanism is thus concentrated at the cutting zone, and does not properly propagate to the workpiece. The cutting temperature is problematic when it exceeds the glass transition temperature ( $T_g$ ) of the resin. Over this critical temperature, the matrix degrades and leads to drops in mechanical performances of the material [16, 19].

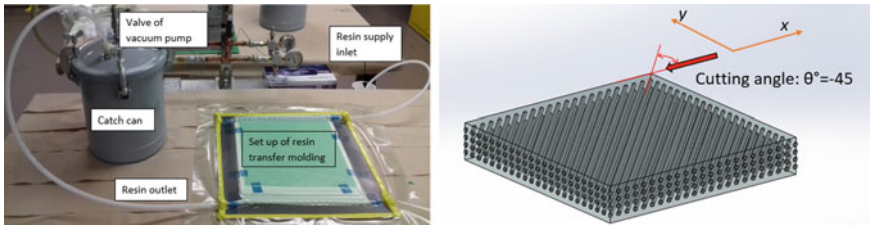


The innovative approach we propose to address this problem consists in adding nanoparticle additives to the matrix in order to improve its temperature tenure during the cutting process. In conducting a literature survey, we did not find any study regarding this specific aspect. All research works in fields examining additives within composite materials focus on the effect of these additives and their concentration on the resulting mechanical properties of the material. In particular, with respect to the clay nanoparticles as additives to the epoxy matrices of composites, the literature reveals two important trends: the mechanical performances may be improved [20–26], but the weight ratio of clay leading to the best performances is critical, and found to be between 1.5 and 2 wt% [20–22, 27]. Lin et al. [24] studied the effect of Cloisite 15A clay microparticles on the flexural modulus and strength for 1, 3 and 5 wt% content of GFRP/epoxy. They found a significant increase of the modulus as the % content increases, but a very slight decrease of the flexural strength. Chowdury et al. [25] had similar results in their study regarding the modulus, but a dissimilarity regarding the flexural strength. Their clay type was different, as was as their fiber type. It consisted of a montmorillonite Nanomer I-28E nanoclay which was added to the epoxy of CFRP composite (1, 2 and 3 wt% concentrations). The flexural modulus of the material was increased by a value of 5.71%, 14.29% and 8.57%, respectively for the 1 wt%, 3 wt% and 5 wt% concentrations. The Flexural strength was also increased by a value of 15.68, 25.16 and 17.97% with respect to the same concentrations, versus the previous study. Zhou et al. [21] found similar results. In their study, the clay type was a K-10 grade montmorillonite, while the material consisted of carbon fibers and epoxy. For a 2 wt% concentration, the flexural strength and ultimate strength were respectively improved by a value of 13.5 and 7.9%, while no significant change resulted for the flexural modulus. Regarding the tensile strength and ultimate deformation, the authors found an increase of 11% and 4.1%, respectively, as compared to the epoxy without additive. Withers et al. [22] found similar beneficial effects using Cloisite 30B clay added to the epoxy of a glass fiber composite material. For the 2 wt% concentration tested, they found a 10.6% increase of the tensile modulus, a 10.5% increase of the ultimate deformation and an 11.7% increase of the tensile strength. Finally, regarding the shear strength, Quaresimin et al. [20] compared two different clay particles (RXG7000 and Cloisite 30B) added to a glass fiber epoxy composite under 1, 3 and 5 wt% concentrations. The shear strength was slightly improved for the Cloisite 30B (3 wt%) as compared to the epoxy without additive, but decreased slightly for the 1 wt% content. Kong et al. [26] also tested two types of clay (nanoclay and montmorillonite) to verify their impact on the shear strength of glass fiber reinforced diallyl phthalate composite. The tested concentration of 2.5 wt% showed a respective increase of 7.64 and 14.80% in shear strength with the nanoclay and the montmorillonite additives as compared to the matrix without any additive. Regarding SEM images used to analyze the fracture zones of the composites modified using additives, it would appears that the resin adherence to the fibers was also improved using clay particles as additives [20–22].

The objective of this work is to compare the machinability, in terms of cutting forces and temperature, as well as surface finish, of five different glass fiber reinforced polymer (GFRP) materials, carried out using mixtures of additives to the

**Table 1** Characteristics of the materials

Material	Name	Company	Density (g/cm <sup>3</sup> )	Surface density	Resin viscosity
Fiber	E-glass	TEXONIC	1.239	200 g/m <sup>2</sup>	–
Resin	Marine 820	ADTECH	1.106	–	1.2 Pa s

**Fig. 1** Vacuum infusion process and fibers' orientation

epoxy matrix. The additives studied were organophilic phyllosilicate garmite 1958 (BYK) clay nanoparticles, Ceraflour #996 (BYK) micronized polytetrafluoroethylene (PTFE) modified polyethylene wax particles, and W-972 wetting agent (BYK), which is a high density copolymer specially developed to better disperse clay and wax particles, as well as stabilize and homogenize the system. The originality of this work is to consider both the effect of PTFE and clay particles on machinability. A total of five plaques were made through the resin infusion process, using the following epoxy mixtures: plain epoxy (no additive); 1 wt% wetting agent (WA); 1 wt% WA and 1.5 wt% clay; 1 wt% WA and 2 wt% wax; 1 wt% WA, 1 wt% clay and 1 wt% wax.

## 2 Experimental Methodology

### 2.1 Materials

The material utilized in this study consists of a composite laminate made of epoxy resin reinforced with glass fibers. The characteristics of the components are presented in Table 1. A total of 16 plies were stacked to form 4.7 mm thick plaques, using the vacuum infusion process. The fiber orientation with respect to the cutting direction was  $-45^\circ$ , with this angle having been proven to represent the worst case surface finish, as mentioned above (Fig. 1). This orientation is therefore considered to be the best to use to compare the effects of the additives on the machining quality of GFRP.

**Table 2** Characteristics of the additives

Additives	Characteristics and supplier
Wetting agent (WA)	BYK-W 972, BYK
Clay particles (C)	$\text{Ø}_{\text{max}} = 58 \text{ }\mu\text{m}$ , Garamite-1958, BYK
Wax particles (W)	$\text{Ø}_{\text{max}} = 11 \text{ }\mu\text{m}$ , Ceraflour 996, BYK

### Additives:

The literature review clearly demonstrates that the addition of nanoclay particles to composite matrices has a significant effect on the resulting mechanical properties. However, no study was found covering the effect of such additives on the machinability of composites. Also, we did not find any study examining the effect of wax nanoparticles or of the wetting agent on the machinability of composites. In the present study, the additives listed in Table 2 were tested to understand their effect on cutting forces, cutting temperature and surface quality.

According to the literature and the technical documentation from the suppliers, the proposed additives should provide the following effects/benefits:

- The wetting agent (WA), which is an antistatic, should better disperse, homogenize and stabilize the additive particles in the mixture with the epoxy resin. In the case of one mixture studied, where no additive particles are added to the epoxy, the WA is supposed to enable a better cohesion of the glass fibers with the matrix. The WA is a block copolymer with high molecular weight.
- The clay particles have a storage stability and sag resistance. As gathered from the literature review, adding these particles to the matrix of composite materials mostly improves the mechanical performances of the latter. It should be recalled though that no research was found which looked at the effect of this additive on the machining process and the resulting quality of cut. A laser diffraction volume distribution analysis performed on this material indicates a size lower than  $28 \text{ }\mu\text{m}$  for 50% of content (D50) and  $58 \text{ }\mu\text{m}$  for 90% of content (D90).
- Wax particles, which have a low transition temperature  $288.15 \text{ K}$  ( $115 \text{ }^\circ\text{C}$ ) and a low viscosity, should melt at the cutting surface during high temperature machining. They are expected to act as a lubricant during trimming, thus reducing the cutting temperature. The laser diffraction volume distribution analysis performed on this material indicates a size lower than  $6 \text{ }\mu\text{m}$  for 50% of content (D50) and  $11 \text{ }\mu\text{m}$  for 90% of content (D90).

### Epoxy mixtures tested in the machining experiments

Five plaques were manufactured, each having a different type of epoxy mixture as matrix. Table 3 summarizes the components and concentrations of the five mixtures: epoxy E, epoxy/wetting agent E/WA, epoxy/wetting-agent/clay E/WA/C, epoxy/wetting-agent/wax E/WA/W and epoxy/wetting-agent/clay/wax E/WA/C/W.

The protocol utilized to prepare the mixtures referenced the studies by Quaresimin et al. [20], Zhou et al. [21] and by Withers et al. [22]. First, it consisted in

**Table 3** Type of mixtures for the experiments

Additive/name	E (wt%)	E/WA (wt%)	E/WA/C (wt%)	E/WA/W (wt%)	E/WA/C/W (wt%)
Epoxy	100	99	97.5	97	97
Wax	0	0	0	2	1
Wetting agent	0	1	1	1	1
Nanoclay	0	0	1.5	0	1

adding the additives with the epoxy in a Silverson L5 M-A (Fig. 2) mixer to mix the components for 1 h, at a rotational speed of 3500 RPM. During the operation, the recipient with mixture was placed in a bath of cold water and ice cubes to reduce the heating temperature of the solution due to its high viscosity. Particularly in the case of clay particles, previous works recommend proceeding with a sonication operation to ensure that all particles are adequately exfoliated into nanoparticles [28]. The process was 30 min long using a Qsonica Q700 instrument (Fig. 2), and after it was complete, the mixture was placed under a vacuum autoclave at room temperature to eliminate all residual bubbles produced during the previous operations. Figure 3 shows the difference in transparency of the E/WA/C mixture before and after the sonicating process. Finally, the hardener was added to the mixture and degassed to prepare it for vacuum infusion.

It is interesting to note the effect of the clay and wax concentrations on the mixture viscosity. In the case of the E/WA/C/W plaque, many experiments were performed to obtain a mixture concentration that allowed a proper infusion process. For example, it was difficult to mix 1.5 wt% of clay and 2 wt% of wax without seeing a damaging effect due to high viscosity. In these contexts, the heat due to the mixing and sonicating processes was too high to successfully complete the infusion process before the epoxy hardening. We found that respective rates of 1 wt% of wax and 1 wt% of clay were appropriate concentrations to adequately manufacture these plaques (Table 3).

## 2.2 Machining Setup

In this study, a 9.50 mm diameter CVD diamond-coated carbide tool was used to trim the GFRP plaques in test coupons 330 mm in length and 13 mm in width (Fig. 4). The specifications of the cutting tool are detailed in Table 4. The plaques were clamped on a 3-axis Kistler 9255B dynamometer table to record the cutting forces during the trimming process (Fig. 4). As shown in Fig. 5, the machining mode was up-milling using dry condition. After each pass of the tool, the plate was turned to ensure a symmetrical temperature profile for each side of the specimen. The tool was installed in a holder equipped with a telemetry transmitter device Type M-320, manufactured by Michigan Scientific Corporation (Fig. 6), whose role is to transmit the cutting tool temperature during rotation. It was designed to send the

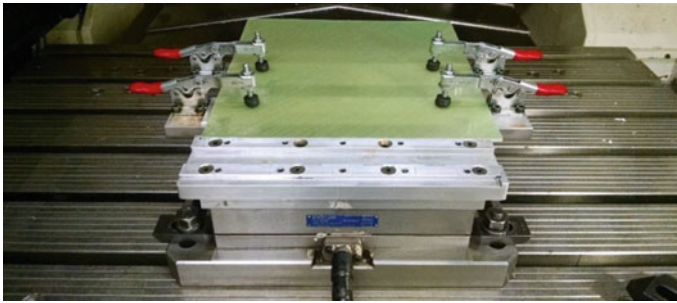


Fig. 2 Mixing (left) and sonicating operations (right)



Fig. 3 E/WA/C mixture before (left) and after (right) the sonicating process

signals to a receiver unit and data acquisition system without contact with the spindle under a maximum rotational speed of 10,000 RPM. This spindle speed enabled us to perform our experiments at a 300 m/min cutting speed, according to the cutting tool diameter selected. Following Hamedanianpour's study [9], the feed rate was set to 1140 mm/min (0.0190 mm/tooth) to minimize the cutting forces. To measure the cutting temperature using the telemetry transmitter device M-320, two thermocouples located 180° apart were fixed at the cutting edge of the tool close to the cutting area.

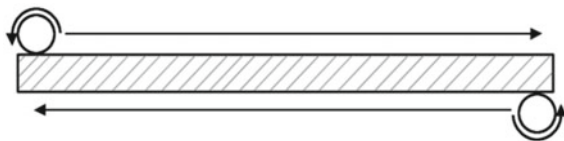


**Fig. 4** Machining setup

**Table 4** Cutting tool specifications

Material	Tungsten carbide
Coating	Diamond
Coating process	Chemical vapor deposition (CVD)
Diameter	9.50 mm (3/8")
Helix angle	10°
Number of flutes	6
Rake angle	8°
Relief angle	10°
Cutting edge radius	15 μm

**Fig. 5** Trimming of test coupons



The hot junctions of the K-type thermocouples were bonded to the cutting edges with OMEGABOND® 400 # OB-400 cement, which is an excellent thermal conductor. To maintain the hot junctions in place during machining, the cement was covered with epoxy resin. Mullier et al. [16] demonstrated that a distance of 1.7 mm from the cutting zone was sufficient to avoid removal of the thermocouple due to the combined effect of chip flow and temperature variation (Fig. 6). The machining center utilized was a Huron K2X10 equipped with a vacuum system for dust collection.

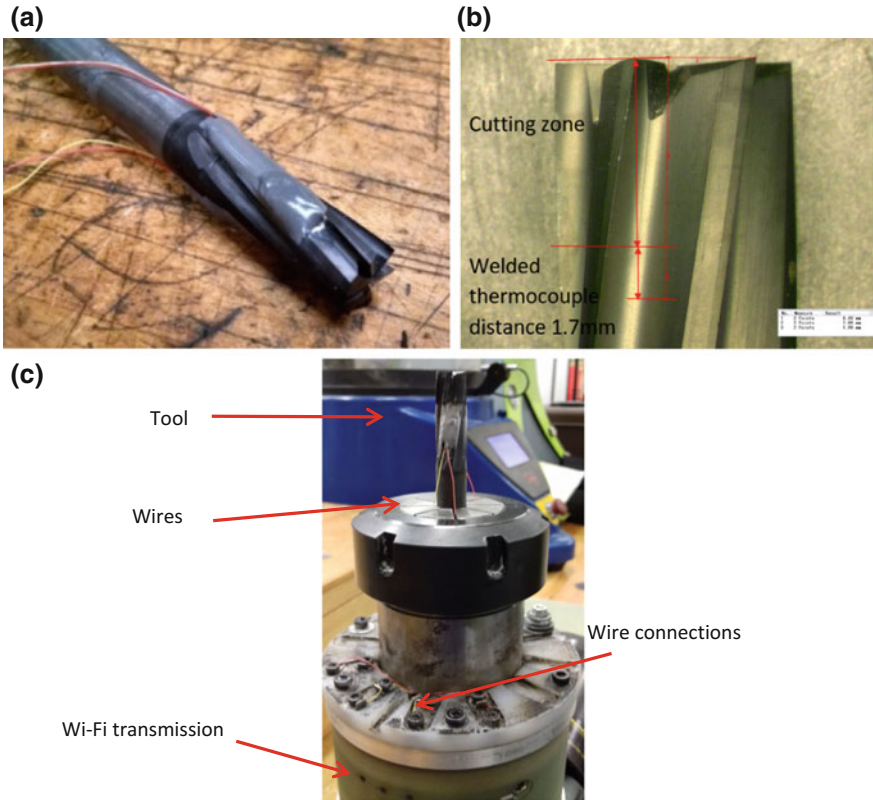


**Fig. 6** Cutting tool with thermocouples (a), cutting zone (b), and Wi-fi transmission of signals (c)

### 2.3 Surface Analysis and Roughness Measurement System

The roughness measurement is intended to show how the additive in the epoxy influences the surface finish of the trimmed coupons. These measurements were carried out using a SurfTest SJ-400 profilometer (Mitutoyo) equipped with a 2  $\mu\text{m}$  radius diamond tip with a 90° angle (Fig. 7). The surface profile was analyzed using the SURFPAK-SJ acquisition software. For each test coupon, 10 measurements were performed at the same locations for each specimen. The measured zones were spaced 40 mm apart from each other and the tool entrance and exit zones were avoided since they correspond to unstable machining conditions. In accordance with the ISO 3274 standard, the cut-off and measurement length were set from a preliminary measurement test. The measurement parameters are specified in Table 5.

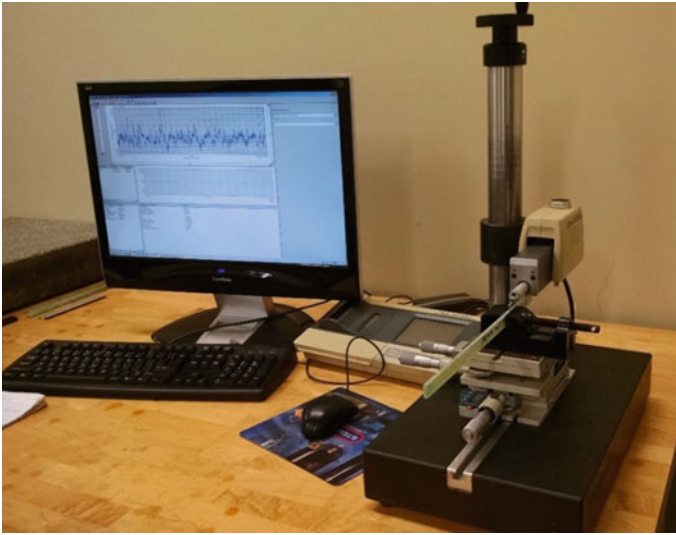


**Fig. 7** Surface roughness measurement setup

**Table 5** Surface roughness measurement parameters

Pre-travel	0.2 mm
Post-travel	0.2 mm
Evaluation length ( $L_m$ )	12.5 mm
Sampling length ( $L_e$ )	0.8 mm
Cut-off length ( $L_c$ )	0.8 mm
Number of samples	10
Number of sampling points	12,000
Parameter	Ra ( $\mu\text{m}$ )

### 3 Results

#### 3.1 Influence of the Additives on the Cutting Forces

In their study, Rao et al. [23] explain that high frequency variations of the cutting forces during composite material machining are the result of repeated fractures of the fibers and matrix of the material. In that context, they analyzed their cutting force components in terms of the average of the maximal values recorded during machining. In this paper, we present our results using that approach. The force components of interest in our study are the feed forces, which are the ones in the direction of the cutting tool trajectory, and the thrust forces, which are situated along the axial direction of the cutting tool. These components were recorded midway along the 300 mm trajectory, over a 20 mm distance. The force components were



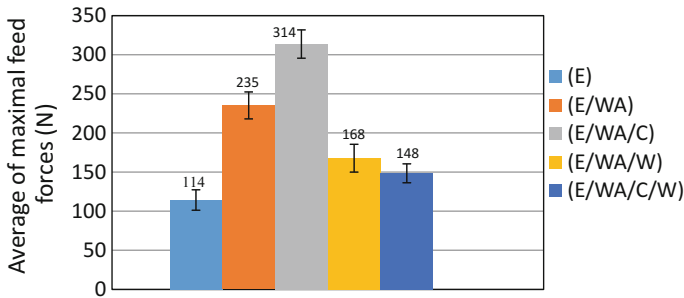


**Fig. 8** Feed force average for each plaque

thus averaged over a 140–160 mm feed distance, which represents a corresponding interval of cutting time  $t = 11.74$  s to  $t = 12.79$  s.

### Feed force analysis

As shown in Fig. 8, the lowest feed forces are found for the reference plaque E, which contains no additive, while the highest forces are found for the plaque with the wetting agent and clay additives E/WA/C (175% higher than the reference plaque E). There is also an increase in feed forces for the E/WA plaque as compared to the reference E (106% increase). It appears that for all mixtures, except for the E, the wax nanoparticles contribute to lowering the feed force components. Still, these components are higher than for the reference E, which is surprising, particularly for the E/WA/W plaque, where the wax acted as a lubricant during the cutting mechanism, but the wetting agent added the cutting resistance.

### Thrust force analysis

According to Fig. 9, the thrust forces are respectively 16%, 10% and 24% lower than the reference “E” for the E/WA, E/WA/W and E/WA/C/W plaques. The highest thrust force is found for the E/WA/C with a value 34% higher than for the E reference plaque. Considering the standard deviations, the results are significant. However, for all other results, the thrust force components are less significant.

## 3.2 Influence of the Additives on the Cutting Temperature

Figure 10 presents the average difference in the cutting temperature reached over the 300 mm trimming distance of a modified plaque as compared to the reference plaque E. The difference is calculated for all 15 points plotted on the curves of Fig. 11 (cutting temperature vs. cutting distance). The average of the temperature differences for the E/WA/C/W plaque reaches a value of  $-20.8\%$ , representing a significant decrease in cutting temperature, as compared to the reference plaque E. This result shows the synergy between the clay and wax particles. Similarly, the E/WA/W plaque reaches

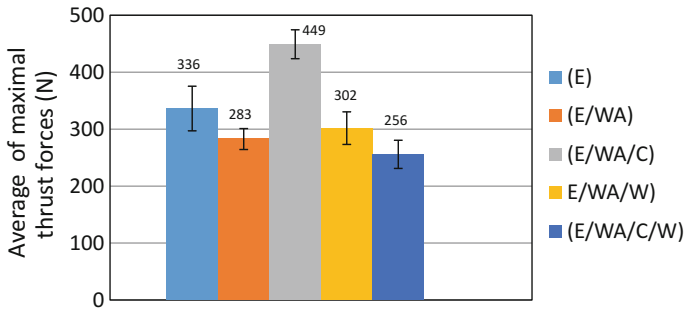


**Fig. 9** Thrust force average for each plaque

a value of  $-13.5\%$ , which is still a significant temperature decrease, considering the standard deviation. The cutting temperature of the E/WA/C is the highest, being  $9.6\%$  higher as compared to the reference plaque.

Although the E/WA/C/W plaque performs better than the E/WA/W plaque over a 300 mm cutting distance ( $-20.8\%$  versus  $-13.5\%$ ), the latter mixture performs better in terms of maximum temperature reached, which is just below  $200\text{ }^{\circ}\text{C}$  (Fig. 10). This is observed in Fig. 11, which presents the evolution of the cutting temperature over a 300 mm distance for all epoxy mixtures. Effectively, both curves cross at a 280 mm cutting distance, where the E/WA/W curve stabilizes (plateaus), while the E/WA/C/W curve still shows an increase in temperature as a function of the cutting distance.

### 3.3 Influence of the Additives on the Surface Roughness

The results show a significant effect of the additives on the surface roughness average measured on the test coupons. As illustrated in Fig. 12, without a combination with the other additives, the wetting agent has a harmful effect on the resulting surface roughness. It increases the roughness value by up to  $53\%$  as compared to the reference epoxy E. For all other mixtures for which wax are added to an E/WA mixture, the surface roughness is improved. Regarding the addition of clay to the E/WA mixture, a slight improvement is observed; however, when wax particles are added, a significant reduction in the surface roughness is observed. In fact, for the wax and wetting agent mixture, E/WA/W, the surface roughness was reduced by a value of  $31.9\%$  as compared to the reference epoxy E and by a value of  $28.9\%$  for the combination of wax, clay and wetting agent E/WA/C/W.

Scanning Electron Microscopy (SEM) images confirm the effect of the additives on the surface finish of the trimmed coupons. As shown in Fig. 13, for the reference epoxy, the tooth passages on the surface can be seen. As well, some uncut fibers and holes representing pull-out fibers (tiny holes) can be seen. The same types of

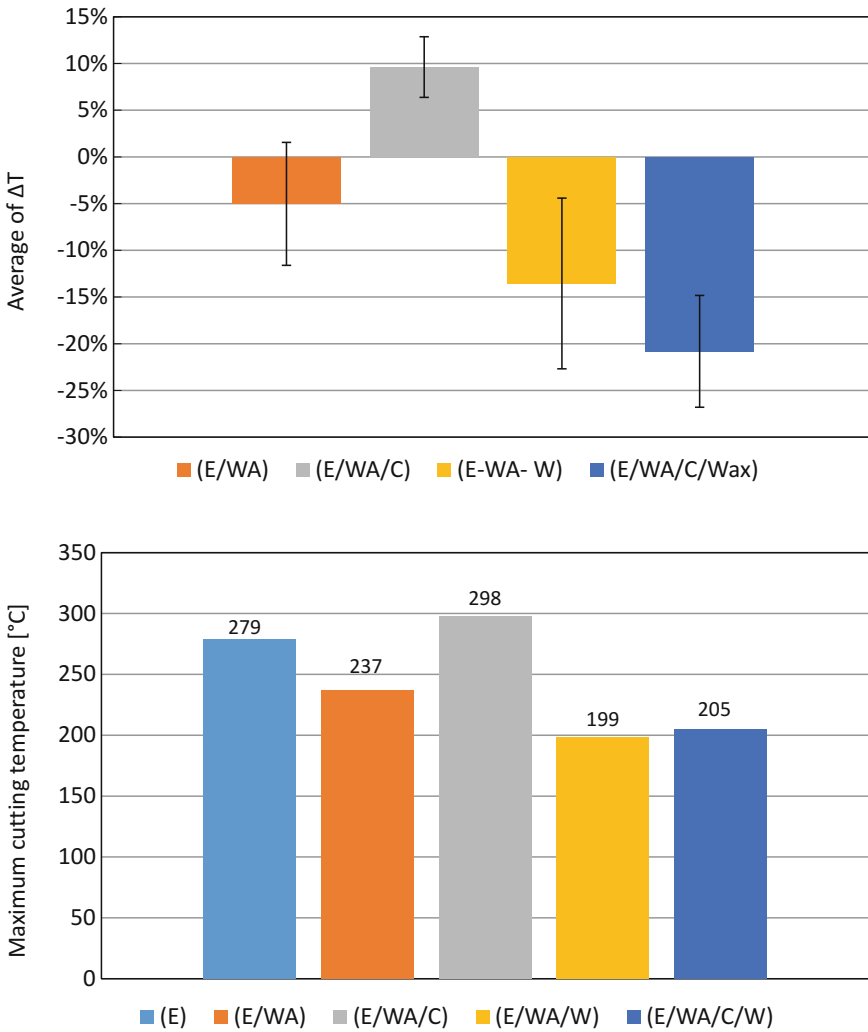


**Fig. 10** Maximum cutting temperature (bottom) and average of temperature differences versus reference (top)

default are perceptible in the case of the E/WA/C trimmed surface. However, the latter surface looks cleaner and less rough than the former. This explains the slight decrease in surface roughness for this mixture.

With respect to the coupons manufactured using the wetting agent alone without any particle added, the trimmed coupon is significantly less smooth and rougher than all the other surfaces shown in Fig. 13. Some uncut fibers are visible and seem bonded and rest down on the surface after the cutting tool passage.

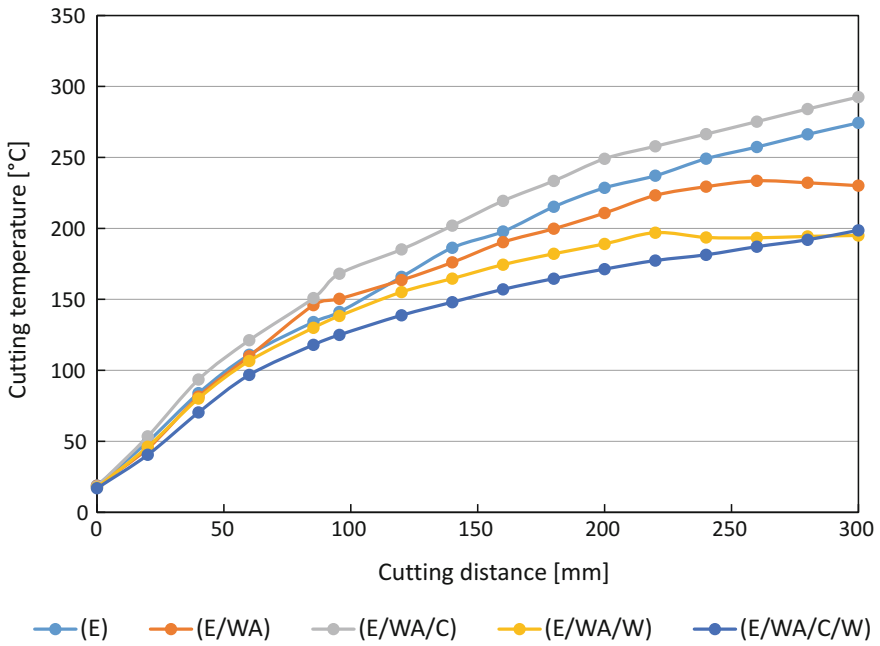


Fig. 11 Machining temperature of GFRP with additives

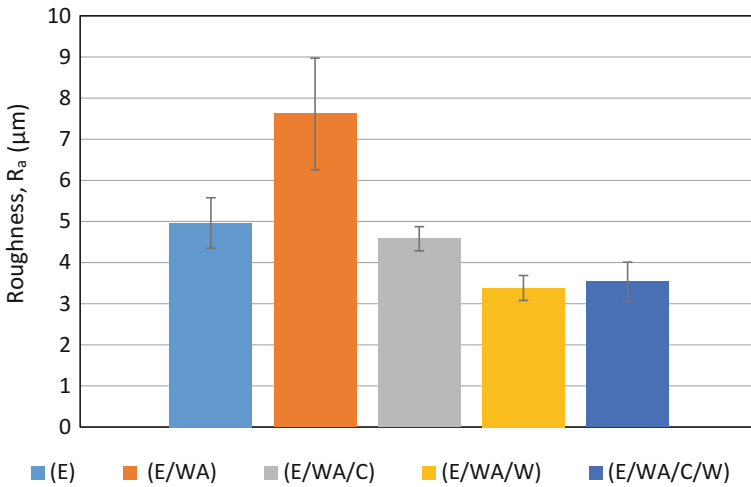
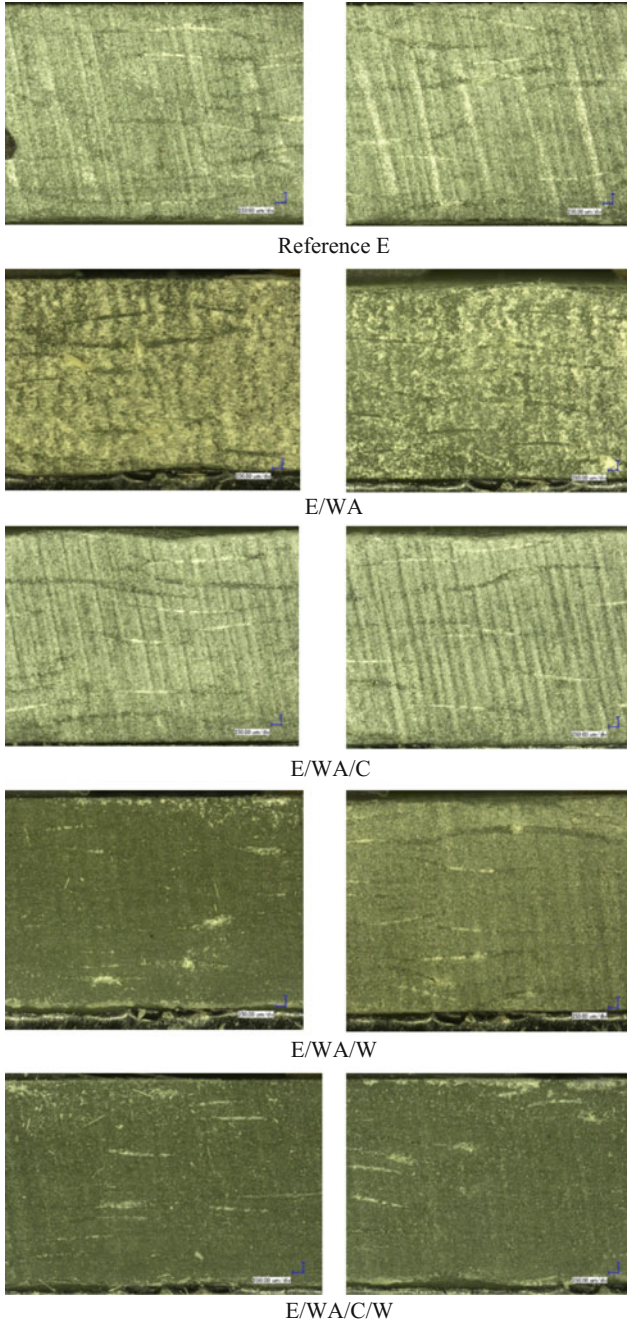


Fig. 12 Machining temperature of GFRP with additives



**Fig. 13** SEM images of trimmed coupons (Magnification: 250  $\mu\text{m}/\text{div}.$ )

The best results are shown on the micrography related to the addition of wax in the epoxy matrix. Both E/WA/W and E/WA/C/W trimmed coupons look similar. Adding wax into the mixture results in a much cleaner cut surface. No tooth passage is perceptible and very few defects are observed, as compared to the other test coupons. This is in agreement with the surface roughness  $R_a$  improvement.

## 4 Conclusion

The main objective of this study was to determine the effect of additives within the epoxy matrix of Glass Fiber Reinforced Polymer on its machinability. A total of five different types of epoxy mixtures were produced following a rigorous protocol for manufacturing GFRP plaques, which were then trimmed to analyze the cutting forces and temperatures during machining. The resulting surface finish of the trimmed coupons was also measured to evaluate the effect of the additives. Regarding the wetting agent, the expected benefits were not observed when it was used alone, but rather, only in the presence of wax. This product was supposed to stabilize and improve the fiber/resin bonding in the presence of additives.

The hypothesis that wax particles could lower the cutting temperatures due to their intrinsic lubricating effect is validated. Both epoxy mixtures with wax particles that were examined resulted in a significant cutting temperature decrease as compared to all others. In fact, the maximum recorded temperature during the cutting process of the E/W was 80 °C lower than for the E reference plaque. This represents almost a 30% drop in the cutting temperature. The wax particles significantly improved the surface finish of the trimmed coupons. Both the SEM images and the  $R_a$  values demonstrated fewer defects and better surface roughness. The surface roughness, cutting forces and cutting temperature were similar for the E/WA/C/W and the E/WA/W plaques. This may suggest that the clay effect is likely annihilated due to the presence of the wax particles. In other words, the effect of the wax particles seems to predominate over the clay particle effect. One reason for this could be that the wetting agent is not the right one for this type of clay, and as a result, more investigation is needed to find the right wetting agent or to remove the wetting agent used. The surface finish and defects shown with SEM are very similar to those with the reference E.

Finally, although both E/WA/C/W and E/WA/W plaques showed similar results, the cutting temperature during most of the 300 mm trajectory remained lower for the former. This is interesting and raises the hypothesis that there may be a possible beneficial interacting effect when using both additives within the epoxy matrix of the GFRP composite.

**Acknowledgements** This research was supported by the National Research Council of Canada. We thank our colleagues, Claude-Daniel Legault, Éric Marcoux and Nabil Mazeghrane, who provided technical assistance that greatly assisted us in this research.

## References

1. Teti, R.: Machining of composite materials. *CIRP Ann. Manuf. Technol.* **51**, 611–634 (2002)
2. Sheikh-Ahmad, J., Urban, N., Cheraghi, H.: Machining damage in edge trimming of CFRP. *Mater. Manuf. Process.* **27**(7), 802–808 (2012)
3. Haiyan, W., Xuda, Q., Hao, L., Chengzu, R.: Analysis of cutting forces in helical milling of carbon fiber-reinforced plastics. Part B *J. Eng. Manuf.* **227**, 62–74 (2013)
4. Rajasekaran, T., Vinayagam, B.K., Palanikumar, K., Prakash, S.: Influence of machining parameters on surface roughness and material removal rate in machining carbon fiber reinforced polymer material. *Front. Automob. Mech. Eng. (FAME)* **1**, 75–80 (2010)
5. Bhatnagar, N., Ramakrishnan, N., Naik, N.K., Komanduri, R.: On the machining of fiber reinforced plastic (FRP) composite laminate. *Int. J. Mach. Tools Manuf.* **35**, 701–716 (1994)
6. Davim, J.P.: *Machining Composite Materials*. Wiley, London, England (2010)
7. Pecat, O., Rentsch, R., Brinksmeier, E.: Influence of milling process parameters on the surface integrity of CFRP. *Procedia CIRP* **1**, 466–470 (2012)
8. Chatelain, J.-F., Zaghbani, I., Monier, J.: Effect of ply orientation on roughness for the trimming process of CFRP laminates. *Int. J. Ind. Manuf. Eng.* **6**, 1516–1522 (2012)
9. Hamedanianpour, H., Chatelain, J.-F.: Effect of tool wear on quality of carbon fiber reinforced polymer laminate during edge trimming. *Appl. Mech. Mater.* **325–326**, 34–39 (2013)
10. Ghafarizadeh, B., Lebrun, G., Chatelain, J.-F.: Experimental investigation to study cutting temperature and surface quality during milling of unidirectional carbon fiber reinforced plastic. *J. Compos. Mater.* **50**(8), 1059–1071 (2016)
11. El-Hofy, M.H., Soo, S.L., Aspinwall, D.K., Sim, W., Pearson, D., Harden, P.: Factors affecting workpiece surface integrity in slotting of CFRP. *Procedia Eng.* **19**, 94–99 (2011)
12. Sharid, A.A.: *Effect of Edge Trimming on Surface Quality and Tensile Strength of CFRP Composites*. The Petroleum Institute, ProQuest Dissertations Publishing: Sas Al Nakhl, Abu Dhabi, UAE (2012)
13. Sakamoto, S., Iwasa, H.: Effect of cutting revolution speed on cutting temperature in helical milling of CFRP composite laminates. *Key Eng. Mater.* **523–524**, 58–63 (2012)
14. Valavan, U.: *Tool life prediction based on cutting forces and surface temperature in edge trimming of multidirectional CFRP composites*. Ph.D. Thesis, Wichita State University, Wichita, KS, USA (2007)
15. Yashiro, T., Ogawa, T., Sasahara, H.: Temperature measurement of cutting tool and machined surface layer in milling of CFRP. *Int. J. Mach. Tools Manuf.* **70**, 63–69 (2013)
16. Mullier, G., Chatelain, J.-F.: Influence of thermal damage on the mechanical strength of trimmed CFRP. *Int. J. Mech. Aersp. Ind. Mechatron. Manuf. Eng.* **9**(8), 1509–1516 (2015)
17. Sheikh-Ahmad, J.Y.: *Machining of Polymer Composites*. Springer, Boston, MA, USA (2009). ISBN 978-0-387-68619-6.2009
18. Inoue, T., Hagino, M., Matsui, M., Gu, L.: Cutting characteristics of CFRP materials with end milling. *Key Eng. Mater.* **407**(408), 710–713 (2009)
19. Hawileh, R.A., Abu-Obeidah, A., Abdalla, J.A., Al-Tamimi, A.: Temperature effect on the mechanical properties of carbon, glass and carbon-glass FRP laminates. *Constr. Build. Mater.* **75**, 342–348 (2015)
20. Quaresimin, M., Salviato, M., Zappalorto, M.: Fracture and interlaminar properties of clay-modified epoxies and their glass reinforced laminates. *Eng. Fract. Mech.* **2012**(81), 80–93 (2012)
21. Zhou, Y., Hosur, M., Jeelani, S., Mallick, P.K.: Fabrication and characterization of carbon fiber reinforced clay/epoxy composite. *J. Mater. Sci.* **47**(12), 5002–5012 (2012)
22. Withers, G.J., Yu, Y., Khabashesku, V.N., Cercone, L., Hadjiev, V.G., Souza, J.M., Davis, D.C.: Improved mechanical properties of an epoxy glass–fiber composite reinforced with surface organomodified nanoclays. *Compos. B Eng.* **2015**(72), 175–182 (2015)
23. Rao, G.V.G., Mahajan, P., Bhatnagar, N.: Micro-mechanical modeling of machining of FRP composites—cutting force analysis. *Compos. Sci. Technol.* **67**, 579–593 (2006)

24. Lin, L.-Y., Lee, J.-H., Hong, C.-E., Yoo, G.-H., Advani, S.G.: Preparation and characterization of layered silicate/glass fiber/epoxy hybrid nanocomposites via vacuum-assisted resin transfer molding (VARTM). *Compos. Sci. Technol.* **66**, 2116–2125 (2006)
25. Chowdhury, F.H., Hosur, M.V., Jeelani, S.: Studies on the flexural and thermomechanical properties of woven carbon/nanoclay-epoxy laminates. *Mater. Sci. Eng.* **2006**(421), 298–306 (2006)
26. Kong, Z.X., Wang, J.H.: Interlaminar shear strength of glass fiber reinforced dially phthalate laminates enhanced with nanoclay. *Adv. Mater. Res.* **79**(82), 1779–1782 (2009)
27. Gurusideswar, S., Velmurugan, R.: Strain rate sensitivity of glass/epoxy composites with nanofillers. *Mater. Des.* **2014**(60), 468–478 (2014)
28. Kuate-Togue, H., Chatelain J.-F., Ouellet-Plamondon, C.: Effect of additives on cutting temperature of glass fibers reinforced polymers. In: *Proceedings of the Canadian Society for Mechanical Engineering International Congress 2018, May, Toronto, Canada*



# Influence of Surface Topography of HSS Edges Produced by Different Methods on Their Technological and Functional Properties



Maciej Jan Kupczyk and Jędrzej Komolka

**Abstract** The determination of the applicability range of conventional high-speed steel and sintered high-speed steel is only seemingly simple and obvious. According to the literature, the properties of cutting edges made of both kinds of steel depend mainly on the distribution of carbide phases in the steel. However, earlier research of the present authors indicates that the topography of the surface of cutting edges is at least equally important in determining the functional properties of the edges. Different surface topography in the case of conventional high-speed steel edges and sintered high-speed steel edges leads to different durability of edges in dry friction conditions and in the presence of the lubricant, at different cutting speeds. Contrary to expectations, the sintered high-speed steel edges do not always display better properties than the cutting edges made of conventional high-speed steel. Therefore it is necessary to determine the applicability ranges of both kinds of steel. In article selected fragments of investigations of technological and functional properties of cutting edges made of conventional and sintered high speed steel with similar chemical composition are presented. Investigations of technological and functional properties have comparative character and concern among other things estimation of chemical composition, hardness, structure and durability during toughening steel machining.

**Keywords** Conventional and sintered high-speed steels • Durability  
Coefficient of friction • The volume of oil surface

---

M. J. Kupczyk (✉) · J. Komolka  
Poznan University of Technology, ul. Piotrowo 3, 60-965 Poznan, Poland  
e-mail: [maciej.kupczyk@put.poznan.pl](mailto:maciej.kupczyk@put.poznan.pl)

J. Komolka  
e-mail: [jędrzej.komolka@gmail.com](mailto:jędrzej.komolka@gmail.com)

© Springer Nature Switzerland AG 2019  
L. F. M. da Silva (ed.), *Materials Design and Applications II*, Advanced  
Structured Materials 98, [https://doi.org/10.1007/978-3-030-02257-0\\_23](https://doi.org/10.1007/978-3-030-02257-0_23)

## 1 Introduction—Aim and Scope of the Study

Conventional high-speed steels are still widely used for the manufacturing of cutting tools applied at moderate cutting speeds [1, 12–14]. This is despite the dynamic development of other materials used to produce cutting edges. The main advantages of high-speed steels are their considerable resistance to bending and torsion as compared to other tool materials, as well as the relatively low cost of production. Literature studies [2, 5–7, 20] indicate that because the functional characteristics of cutting edges made of conventional high-speed steels can no longer be improved, sintered high-speed steel is gradually replacing conventional steel in these tools. However, the cost of manufacturing sintered high-speed steel tools is still high and only mass production of these tools is cost-effective [5, 12, 14, 20]. The advantage of powder metallurgy over classical metallurgy lies in the fact that powder metallurgy gives one more freedom in deciding the chemical composition of the final product, combining components which potentially dissolve in one another, which have different melting points, and which have different chemical bonds [3–11, 16–21].

The determination of the applicability range of conventional high-speed steel and sintered high-speed steel is only seemingly simple and obvious. According to the literature [5, 17, 20, 21], the properties of cutting edges made of both kinds of steel depend mainly on the distribution of carbide phases in the steel. However, earlier research of the present authors [12–14] indicates that the topography of the surface of cutting edges is at least equally important in determining the functional properties of the edges. Different surface topography in the case of conventional high-speed steel edges and sintered high-speed steel edges leads to different durability of edges in dry friction conditions and in the presence of the lubricant, at different cutting speeds. Contrary to expectations, the sintered high-speed steel edges do not always display better properties than the cutting edges made of conventional high-speed steel. Therefore it is necessary to determine the applicability ranges of both kinds of steel.

## 2 Materials Used in the Study

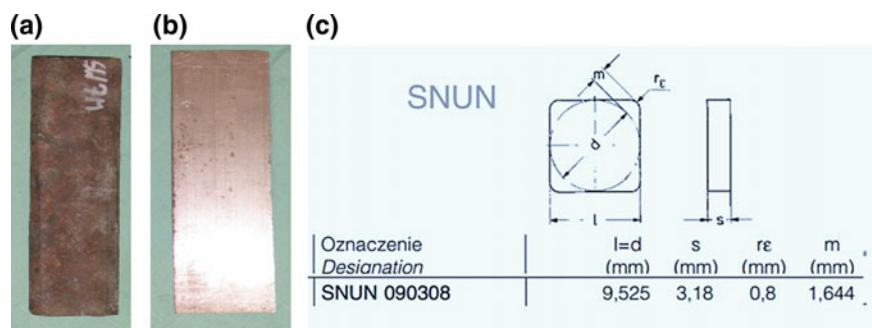
### 2.1 Cutting Edges

To produce multi-blade cutting inserts, two kinds of high-speed steel of similar chemical composition were used:

- (1) conventional HS6-5-2 high-speed steel:
  - in the forged form,
  - in the rolled form;
- (2) sintered PM6-5-2 high-speed steel.

**Table 1** Approximate chemical analysis of both conventional (HS6-5-2) and sintered (PM6-5-2) steels

Item	Chemical composition (%)					
	C	W	Mo	V	Cr	Mn
Conventional steel HS6-5-2	Standards: EN—HS6-5-2, PN—SW7 M, DIN—1.3343, AISI—M2					
	0.8–0.84	5.9–6.7	4.7–5.2	1.7–2.0	4.2	0.4
Sintered steel PM6-5-2	0.87–1.0	6.0–6.4	5.0	1.9–2.0	4.2–4.5	0.3

**Fig. 1** Images of **a** row semi-finished product, **b** semi-finished product after rough grinding, **c** form and dimensions of cutting inserts used in the study

The selection is justified by the fact that these kinds of steel are most commonly used.

Table 1 shows the approximate chemical composition of conventional and sintered high-speed steels according to different standards (EN, PN, DIN, AISI) and data from [15].

The cutting inserts made of conventional high-speed steel were obtained from metallurgical products in the form of billets, while cutting inserts made of sintered high-speed steel were obtained from commercial semi-finished flat bars. On delivery, both types of steel used in the study were in the softened state. Figure 1a shows the semi-finished products to be used for the cutting inserts.

To achieve the required thickness, billets made of conventional high-speed steel and flat bars made of sintered high-speed steel were ground on a flat-surface grinding machine. Next, cutting inserts of the SNUN type were obtained from the so-prepared semi-finished products, with the use of the Agiecut Classic 2 wire electro-erosion machine (produced by AGIE SA—Losone, Switzerland). The obtained cutting inserts were of rectangular shape with the tool included angle of  $90^\circ$  and dimensions:  $l = 9.525 \pm 0.08$  mm,  $m = 1.644 \pm 0.13$  mm (Fig. 1c). Cutting inserts of this geometry are recommended for machining toughening steels, creep-resisting steel, stainless steels,

alloy steels and soft steels with low carbon content [13]. The insert edges after cutting were finish-ground, and then polished. Efforts were made to obtain a similar surface roughness of cutting inserts made of conventional and sintered high-speed steel (the average value of Ra equals 0.1 mm) in order to make correct inferences later. After the polishing process, the inserts were degreased.

The required properties of HS6-5-2 and PM6-5-2 steels were achieved after heat-treatment quenching and tempering (Fig. 2). In order to obtain hardness of approx. 65 HRC, the austenization temperature was set at 1150 °C and the tempering temperature was 560 °C. These temperatures allow the temporary heating of the edge during the machining process to 600 °C without the risk of substantial softening of the edge material. At properly selected tempering temperature, the secondary hardening process takes place. Cutting edges prepared in this way retain working ability at elevated temperatures, close to the temperature of the tempering of the cutting edge [1, 4–7, 12–15, 20].

Due to low heat conductivity, the material was heated gradually. The entire process was carried out in vacuum due to the risk of decarburisation and oxidation. Figure 1 shows the run of heat treatment. The above process was conducted in a SECO/WARWICK type 6.0VPT-4022/241QHV vacuum furnace (produced by ECM Technologies—Grenoble, France), with a high vacuum system.

## 2.2 Processed Material

The workpiece used in the study was in the shape of shafts with diameter of  $\phi$  110 mm and a length of 350 mm, made of 36HNM toughening steel with the hardness of 30 HRC. This steel grade is used for components requiring high reliability, durability and ductility. The yield strength of this material is 880 MPa, and the tensile strength is 1030 MPa. Table 2 shows the chemical composition of the 36HNM steel according to EN, PN, DIN and AISI standards.

**Table 2** Approximate chemical analysis of the 36HNM steel (according to PN-EN ISO 4597)

Equivalents (according to standards)							
PN	DIN	EN		AISI			
36HNM	1.6511	36CrNiMo4		6342			
Chemical composition (%)							
C	Si	Mn	Cr	Mo	Ni	S	P
0.32–0.40	0.17–0.37	0.5–0.8	0.9–1.2	0.15–0.25	0.9–1.2	Max: 0.035	Max: 0.035



Fig. 2 Run of heat treatment of cutting edges in SECO/WARWICK 6.0VPT-4022/241QHV vacuum furnace [13]. a The red line—temperature, b the green line—pressure

### 3 Study of Functional Characteristics

The tests of wear and durability of cutting edges were performed in the process of turning of 36HNM toughening steel quenching and tempering to hardness of  $26 \pm 2$  HRC.

The cutting inserts were clamped in a hR 110.16-220 holder. The geometry of the cutting edge in the holder is as follows:

- tool orthogonal clearance  $\alpha_0 = 6^\circ$ ,
- tool orthogonal rake angle  $\gamma_0 = -6^\circ$ ,
- tool cutting edge angle  $Kr = 75^\circ$ ,
- tool cutting edge inclination  $\lambda_s = -6^\circ$ ,
- tool included angle  $\varepsilon_r = 90^\circ$ .

The following conditions were assumed for the processing:

- workpiece—36HNM steel,
- cutting speed— $v_{c1} = 33.75$ ;  $v_{c2} = 42.9$ ;  $v_{c3} = 59.86$  [m/min],
- feed— $f = 0.2$  [mm/rev],
- cutting depth— $a_p = 0.75$  [mm],
- “dry” cutting or cutting with lubricating the cutting tool.

In the process of turning, the semi-synthetic emulsion S455N Statoil Toolway, produced in Norway, was used as the cutting-tool lubricant.

The durability of the cutting edge is usually defined as the time period of machining until the accepted value of the blunting indicator is achieved. Taking into account the wear curves obtained in the course of the preliminary investigations, as well as data from other publications and standards: PN-83/M-58350; PN-ISO 3685, the value of the indicator of the wedge blunting was assumed to be the band width of the corner wear  $VB_c = 1.6$  mm. The  $VB_c$  value is measured using the Brinell magnifier.

The present investigations concerned cutting inserts made of high-speed steel obtained in the following way:

- conventionally (HS6-5-2),
- utilizing powder metallurgy (PM6-5-2).

Before handing over the inserts for study, the surfaces of the rake face, flank face and cutting edge were examined. All the inserts were free from defects such as chipping, dents or cracks.

Figures 3, 4 and 5 show the wear curves for cutting edges made of both types of high-speed steels—without and with cutting-tool lubrication.

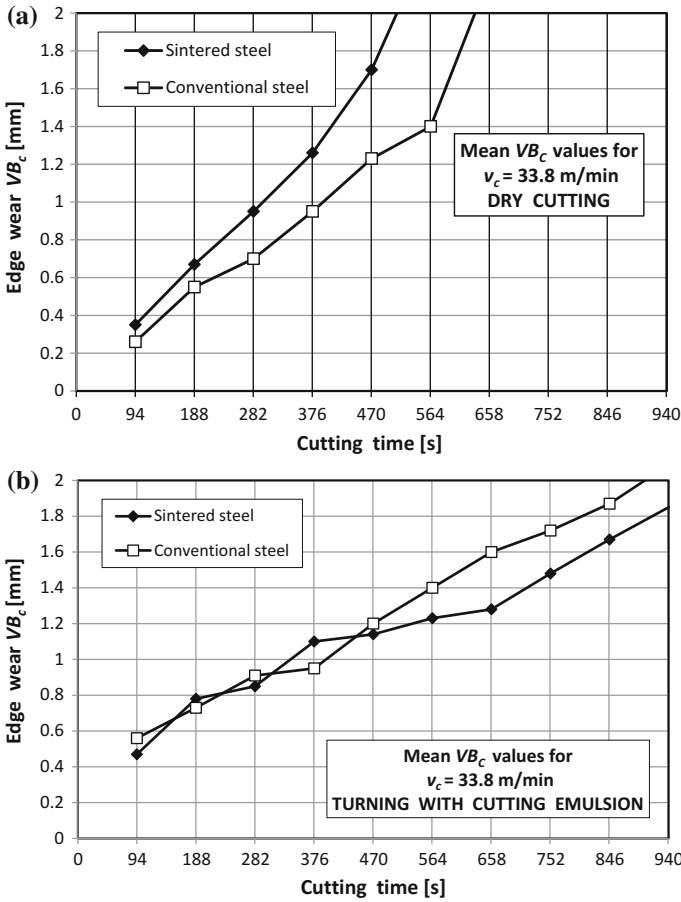


**Fig. 3** Wear curves for cutting edges made of HS6-5-2 conventional steel and PM6-5-2 sintered steel during machining 36HNM steel: **a** without, **b** with cutting tool lubricant (emulsion) for  $v_{c1} = 33.8$  m/min

Based on the obtained wear curves, tool life for cutting edges was determined at the value  $VB_c = 1.6$  mm. The results of the durability of tools made of conventional and sintered steel when turning 36HNM steel with and without cutting-tool lubricating are presented in Fig. 6.

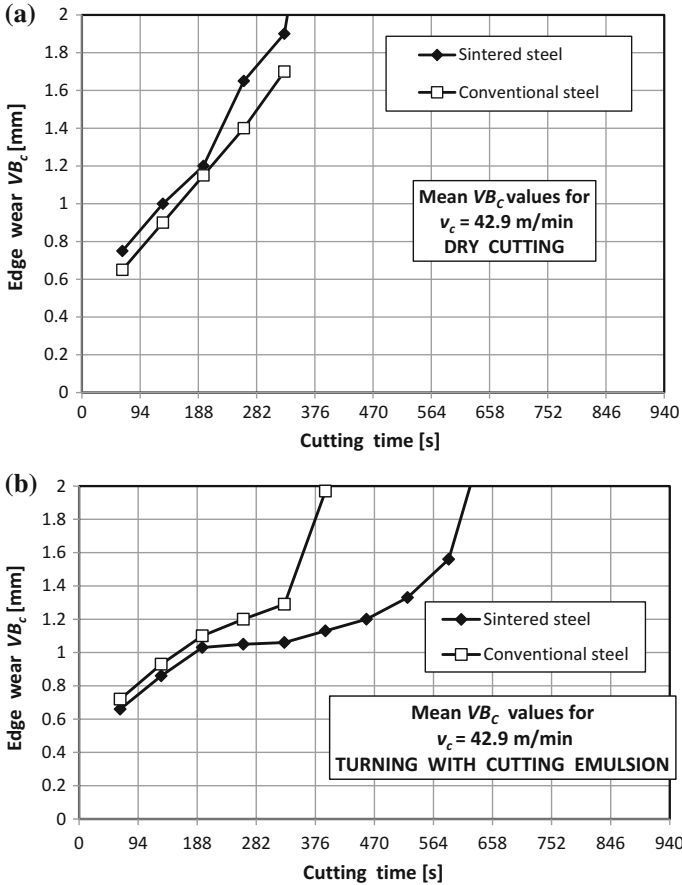


**Fig. 4** Wear curves for cutting edges made of HS6-5-2 conventional steel and PM6-5-2 sintered steel during machining 36HNM steel: **a** without, **b** with cutting tool lubricant (emulsion) for  $v_{c2} = 42.9$  m/min

### 4 Verification Studies

Verification tests were aimed at finding the causes of different behavior of the inserts made of conventional and sintered high-speed steel during turning 36HNM toughening steel.

In the Vickers hardness test, a PICODENTOR HM500 hardness tester manufactured by Fischer (Sindelfingen, Germany) was used. Hardness was measured by applying penetrator load of 30 kg for 20 s in accordance with the appropriate standard. One of the conditions for obtaining accurate hardness measurements was to treat the surface of the tested material so that its roughness was at least 10 times less



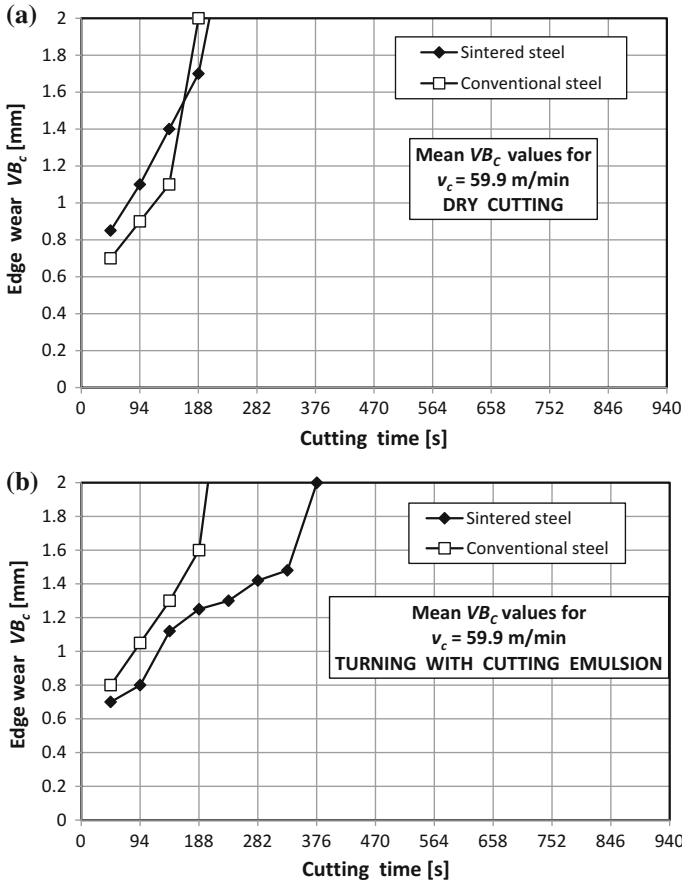


**Fig. 5** Wear curves for cutting edges made of HS6-5-2 conventional steel and PM6-5-2 sintered steel during machining 36HNM steel: **a** without, **b** with cutting tool lubricant (emulsion) c, e) for  $v_{c2} = 59.9$  m/min

than the depth of penetration. To this end, the insert surface was polished. After the polishing process, the inserts were degreased.

For the Vickers hardness test, 5 indentations were performed for each insert, bearing in mind that the spacing should be equal to at least 3 times the diameter of the impression. As evidenced by the measurement, the hardness of sintered steel cutting edges is about 5% higher than the hardness of conventional steel, amounting to 1030.5 HV30 on average for sintered steel, and 982.3 HV30 for conventional steel, which conforms to the data obtained by Sandvick [15].

The real chemical composition of cutting edges was established by means of the X-ray fluorescence spectrometer—XDV-SDD Fischerscope X-ray (produced by FISCHERSCOPE—Sindelfingen, Germany) [13]. Selected results of these tests are presented in Fig. 7.

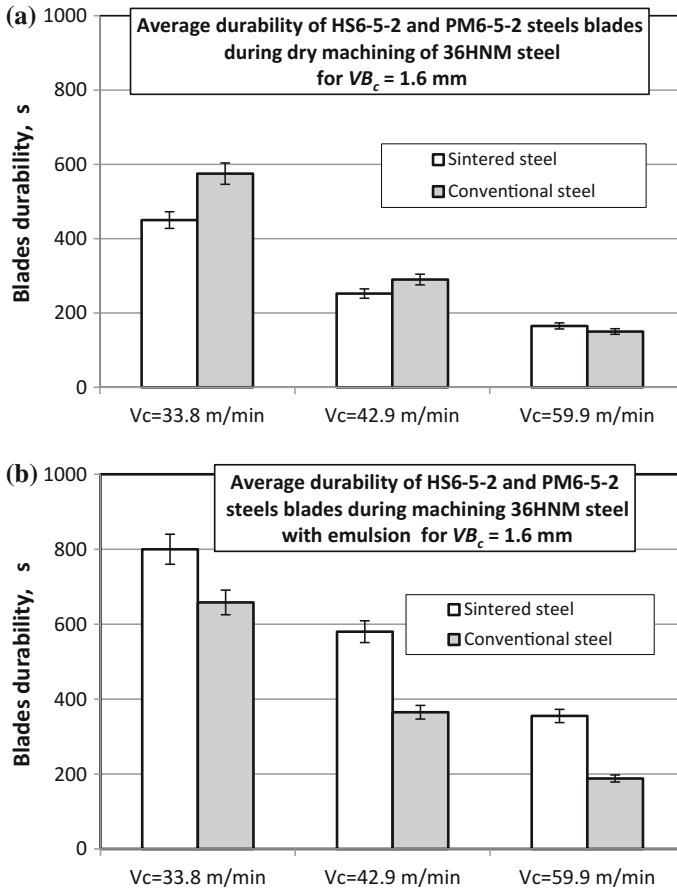


**Fig. 6** Mean tool life of edges made of conventional and sintered HSS steels during machining of 36HNM steel **a** without cutting-tool lubricant, **b** with cutting-tool lubricant

Eight measurements of chemical composition were carried out for conventional and sintered high-speed steel. The average values of alloy elements content did not vary significantly from the values given in Table 1. This fact was confirmed by means of calculations of significance of differences between the assumed values and measured values for significance level  $\alpha = 0.05$  and the number of degrees of freedom 7.

Using a Tescan Vega 5135 scanning microscope (produced by TESCAN Brno, s.r.o.—Brno, Czech Republic) [14], a series of photographs of the surface of conventional and sintered high-speed steel edges were taken (Fig. 8).

The microscope images confirmed a more even distribution of carbides in the matrix in the case of sintered steel, compared to conventional hot-rolled and forged steels.

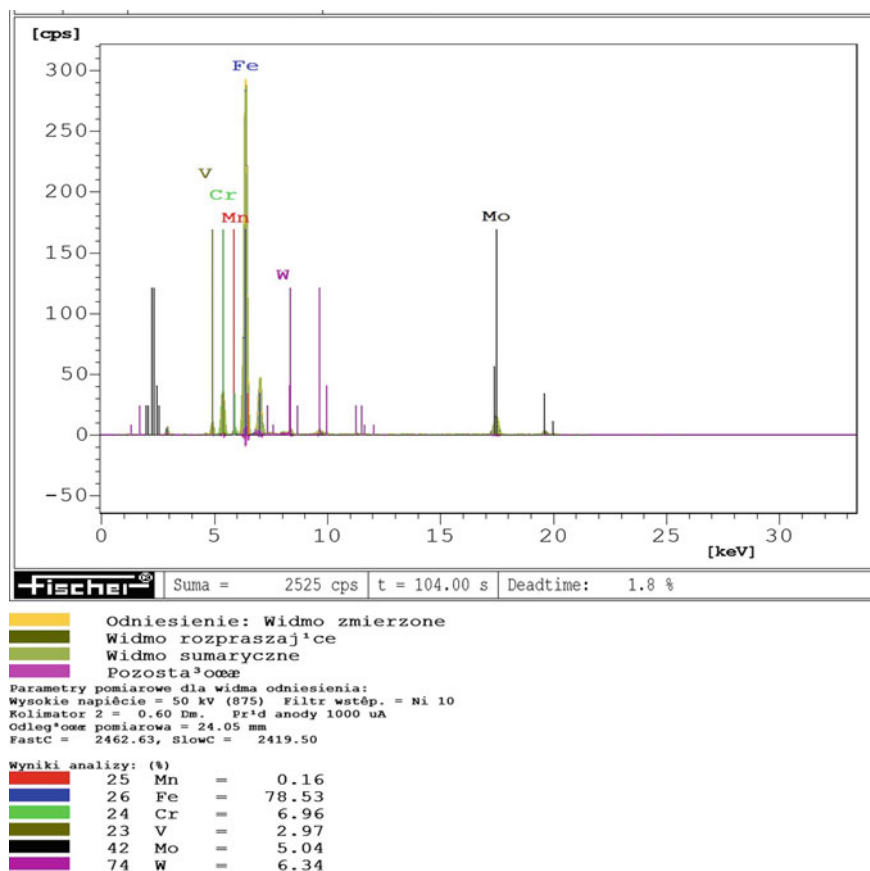
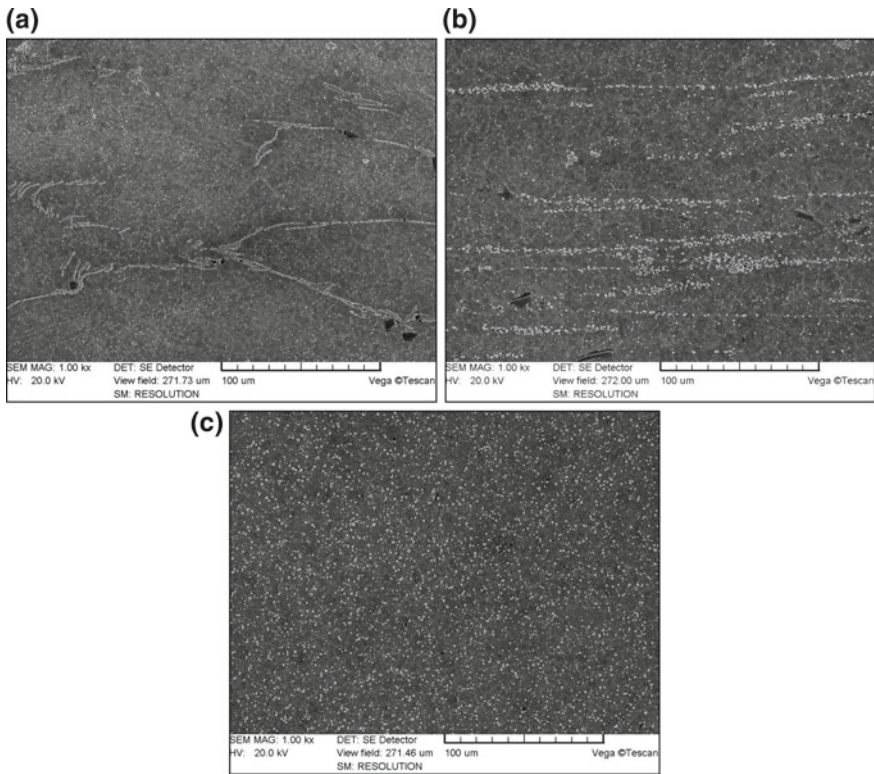


Fig. 7 Selected images of chemical microanalysis of edges made of the PM6-5-2 sintered steel

With regard to the conventional high-speed steel, the BS images show that the carbides are not evenly distributed and still form local band clusters, which is typical for high-speed steels subjected to rolling, stretch forging, or stretch forging with indirect upsetting.

Using the metallographic microscope Neophot 32 (produced by Carl Zeiss—Jena, Germany) [13], a series of photos of the edges made of conventional and sintered high-speed steel were taken (Fig. 9).

Images from the microscope showed a significant difference in surface morphology of the conventional and sintered high-speed steel. The surface of sintered steel was formed from grains with sharp edges, while the surface of conventional hot-rolled and conventional forged steel did not have this topography (the grains were “fused” to form a more continuous surface), despite the fact that both surfaces had a similar roughness of  $R_a = 0.1 \mu\text{m}$  (Fig. 10).



**Fig. 8** The SE images of high speed steel edges made of: **a** conventional hot-rolled steel, **b** conventional forged steel, **c** sintered steel

On the basis of the topography, it was found that the surfaces of the cutting inserts made of conventional and sintered high-speed steel were characterized by the same values of the surface roughness parameter ( $R_a = 0.1 \mu\text{m}$ ) [13].

In Fig. 11 are presented selected data of surface topography and Abbott-Firestone curve for cutting edges made of conventional hot-rolled steel, conventional forged steel and sintered steel.

On the basis of the measured surface topography parameters, the oil volume of the surface of the cutting edges made of the conventional forged, the conventional hot-rolled and sintered high-speed steel was determined. The value of oil volume of a surface is calculated from [13]:

$$V_o = R_{vk}(100 - M_{r2})/200,$$

where:

$V_o$  the oil volume of the surface,  
 $R_{vk}$  surface valley,

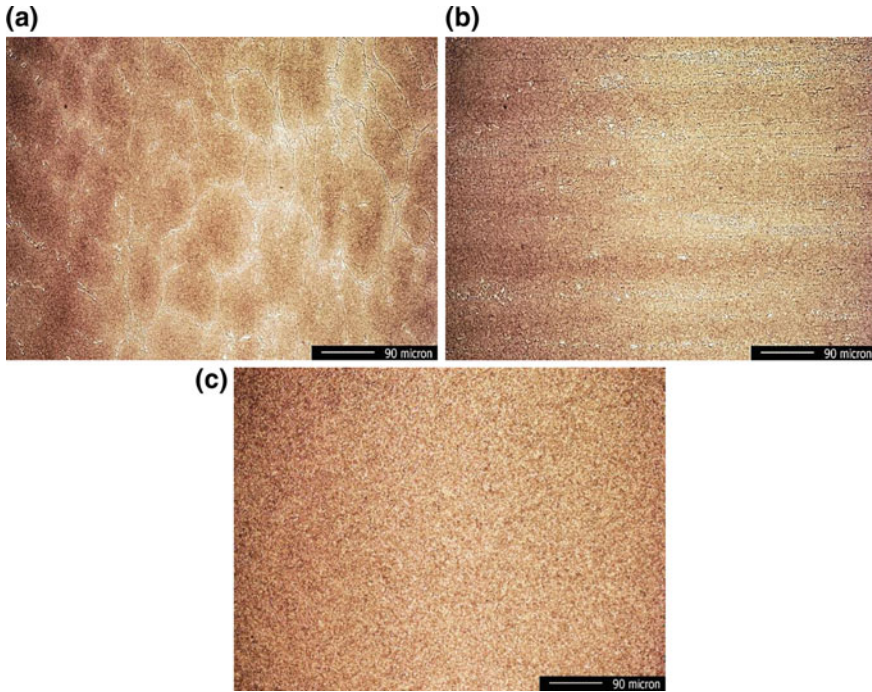


**Fig. 9** The secondary electron images of surface topography of high speed steel edges made of: **a** conventional hot-rolled steel, **b** conventional forged steel, **c** sintered steel

$M_{r2}$  the fracture (part) of material for the lower limit of the core roughness profile.

The  $R_{vk}$  parameter describes the surface valley. It is a measure of the ability of the operating surface of the edge to retain the grease in the existing cavities. The  $M_{r2}$  parameter specifies the value of the fracture of material for the lower limit of the core roughness profile, while  $M_{r1}$ , is the value of the fracture of material for the upper limit of the core roughness profile. The parameters described above give information about the irregularities of surface, which largely determines the behavior of the edges in the machining process.

Figure 12 shows the results of average oil volume of the cutting edges made of high-speed steel: (1) sintered, (2) conventional forged and (3) conventional hot-rolled.

Based on the obtained results, it was found that despite almost identical roughness of the surface of cutting inserts made of conventional (forged and hot-rolled steels) and sintered high-speed steel,  $R_a = 0.1 \mu\text{m}$ , the cutting inserts differ considerably in terms of oil volume of the surface.

The oil volume of the surface of the sintered high-speed steel is twice as big as the respective volume for conventional forged high-speed steel, and almost three times bigger than the respective value of the conventional hot-rolled high-speed steel.

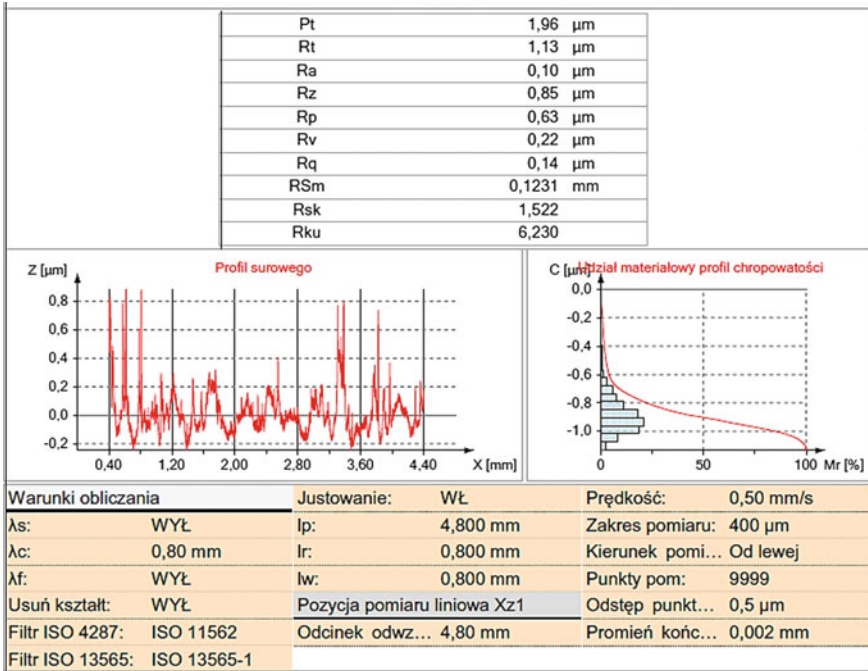


**Fig. 10** Exemplary set of the results of surface roughness measurements for used inserts made of high speed steel

In order to fully interpret the test of functional characteristics of cutting edges obtained during turning the 36HNM steel, further tests were conducted, concerning the coefficient of dry friction and friction coefficient in the presence of cutting tool lubrication.

During tribological tests, the following conditions were assumed:

Material of friction pair	<ul style="list-style-type: none"> <li>• Sample—made of the HS6-5-2 conventional steel and the PM6-5-2 sintered steel</li> </ul>
Material of counter-sample	• 36HNM
Peripheral speed of counter-sample	• 27.6 (m/min)
Load $F$ (N)	• 300/400/500/600 (N)
Time $t$ (s)	<ul style="list-style-type: none"> <li>• 1200 (s) for dry friction</li> <li>• 2400 (s) for friction with cutting-tool lubricant</li> </ul>
Friction	<ul style="list-style-type: none"> <li>• Dry</li> <li>• In the presence of cutting-tool lubricant</li> </ul>

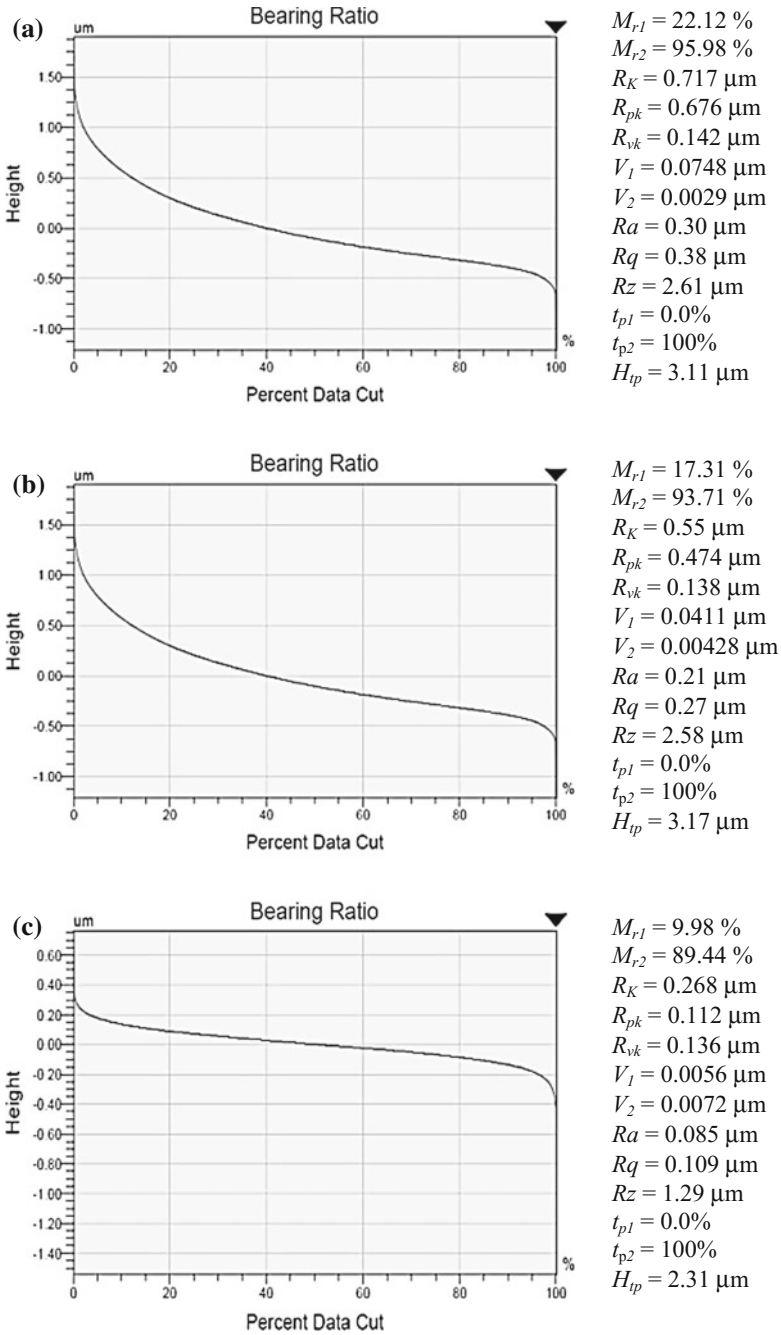


**Fig. 11** Data of surface topography and abbott-firestone curve for cutting edges made of: **a** conventional hot-rolled steel, **b** conventional forged steel, **c** sintered steel

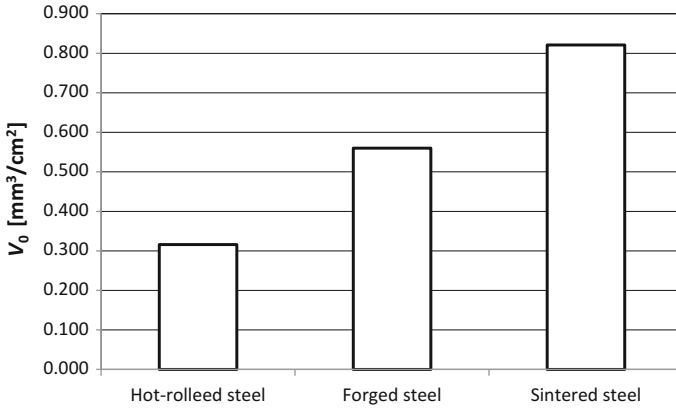


**Fig. 12** Average oil values for surfaces of the cutting edges made of high speed steel: (1) sintered, (2) conventional forged and (3) conventional hot-rolled

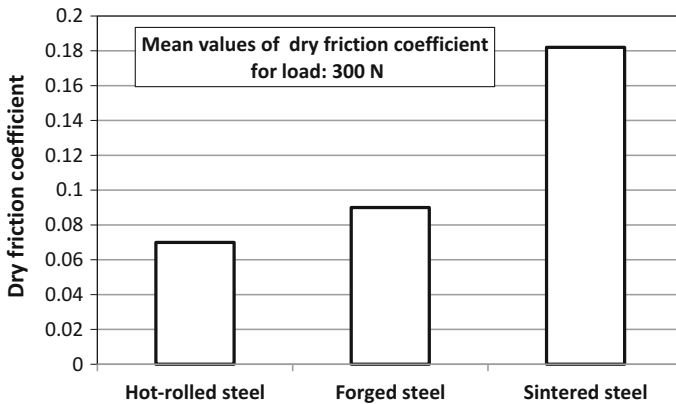


**Fig. 13** The results of the coefficient of dry friction

Figure 13 shows the results of the coefficient of dry friction.

The results of the tribological tests confirmed results of durability tests conducted during “dry” cutting. The tribological results also confirmed the conclusions drawn from the observations of microscopic images. Sintered material has grains with sharp edges and conventional steel has grains “fused” into whole grains.

Figure 14 summarizes the results of the friction coefficient in the presence of cutting-tool lubricant for different values of loading.



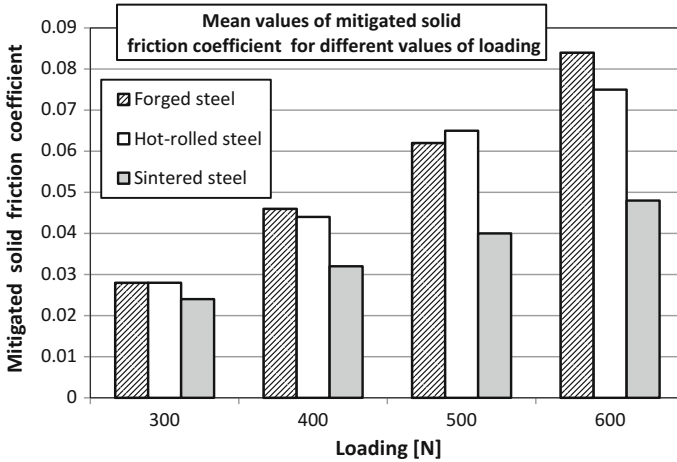


Fig. 14 The results of the friction coefficient in the presence of cutting-tool lubricant

## 5 Conclusions

As evidenced in the performed tests, cutting edges made of sintered steel exhibit slightly better technological characteristics (i.e. higher mean hardness, more uniform distribution of carbides—no adverse banding resulting from the processes of forging or rolling conventional high-speed steel).

The cutting edges made of sintered high-speed steel during the machining in the presence of cutting-tool lubricant have a significantly longer tool-life than edges made of conventional high-speed steel because of larger oil volume which influences on the value of the friction coefficient of the edge against the workpiece material (counter-sample).

In the “dry” processing conditions (no cutting-tool lubrication) cutting edges made of conventional high-speed steel particularly for the lowest cutting speed applied ( $v_c = 33.8$  m/min) exhibit higher durability than sintered steel edges, due to favorable surface topography (no grains with sharp edges and thus a lower value of dry friction coefficient).

**Acknowledgements** The work was performed from financial resources of a research project No. 02/22/DSPB/1433 DS. The authors thank Prof. E. Feldshtein, Dr. R. Majchrowski and Dr. M. Jenek for access to the station to frictional investigations, profile measurement gauge and SEM.

## References

1. Adamczyk J., Dobrzanski, L.A., Hajduczek, E.: Works Inst. Metall. Iron, **33–34**, 49 (1978)
2. Almond, E.A., Al-Yasir, L.B.H., Jagger, F.L.: Comparison of strength and toughness of wrought and directly sintered T6 high speed steel. Powder Metall. **22**, 109 (1979)
3. Arnhold, V., Duda, D., Wahling, R.: Schneidwerkzeuge aus pulvermetallurgischen Schnellarbeitsstählen. Powder Metall. Int. **21**(2), 67 (1989)
4. Bryjak, E.: Plastic forming and properties of high-speed steel produced by ASEASTORA. Metall. News **7–8**, 225 (1973)
5. Dobrzanski, A.: Bases of the Theory about Materials and the Metallurgy. WNT, Warsaw (2002)
6. Dobrzanski, L.A., Hajduczek, E.: Proceedings of VI International Symposium on Composite Metallic Materials, p. 339. CSRR, Stara Lesna (1986)
7. Dobrzanski, A., Hajduczek, E., Marciniak, J., Nowosielski, R.: The Metallurgy and the Heat Treatment of Tool Materials. WNT Publishing House, Warsaw (1990)
8. Kolker, W.: Mehr Fertigungssicherheit durch Werkzeuge aus pulvermetallurgischen Schnellstahl. Werkstatt Betr. **127**, 356 (1994)
9. König, U., Fabry, J.: Schneidstoffe – stand und Tendenzen Metall. **H7**, 709 (1983)
10. König, U., Bong, A.: Standfest Maschinenmarkt **18**, 36 (1987)
11. Krupp-Widia: Technische Information. Werkzeugtechnik. Moderne Maschinen erfordern modern Schneidstoffe, Essen, HVT 78.021
12. Kupczyk, M.J.: Manufacturing and Using of Cutting Tools with Wear-Resistant Coatings. Poznan University of Technology Publishers, Poznan (2009)
13. Kupczyk, M.J., Komolka, M., Jenek, M.: Comparative investigations of cutting edges properties made of high-speed steel manufactured by conventional methods and in powder metallurgy process. In: Monography: Machining—Investigations and Development, Red, pp. 153–162, Jan Burek. Publishing House of Rzeszow University of Technology (2017)
14. Kupczyk, M.J.: Surface Engineering—Cutting Tools. Poznan University of Technology Publishers, Poznan (2015)
15. Materials produced by Sandvik Company (catalogue)
16. Mesquita, H.A., Barbosa, C.A.: Evaluation of as-hipped PM high speed steel for production of large-diameter cutting tools. Mater. Sci. Forum **416–418**, 235–240 (2003)
17. Mesquita, R.A., Barbosa, C.A.: High-speed steels produced by conventional casting, spray forming and powder metallurgy. Mater. Sci. Forum **496–499**, 244–250 (2005)
18. Pieczonka, T., Cias, A., Konstanty, J.: Sintered high-speed steel. Metall. Metall. News **2**, 54 (1994)
19. Weck, M., König, U., Bong, O.: HSS-Wende Schneideplatten – Vorteil durch Pulvermetallurgie, Industrie Anzeiger, 55/56, 36 (1988)
20. Wysiecki, M.: Modern Tool Materials. WNT Publisher House, Warsaw (1997)
21. Zhang, G., et al.: Microstructure evolution and mechanical properties of T15, high speed steel prepared by twin-atomizer spray forming and thermo-mechanical processing. Mater. Sci. Eng. A **558**, 566–571 (2012)

# Comparative Investigations of Durability of Cutting Edges Made of Nanocrystalline Cemented Carbides with Different Growth Inhibitors



Maciej Jan Kupczyk, Jędrzej Komolka and Piotr Siwak

**Abstract** This article presents the investigations of durability of the cutting tools (insert cutting edges) made of the nanocrystalline sintered carbides. Cutting insert edges were sintered using the Pulse Plasma Sintering (PPS) method elaborated at the Department of Materials Science Warsaw University of Technology. This article contains the results of comparative investigations of durability of the cutting edges made of WC-5wt% Co nanocrystalline cemented carbides with the TaC-NbC or Cr<sub>3</sub>C<sub>2</sub> growth inhibitor and without it sintered by the PPS method, and cutting edges made of a standard cemented carbides of the same chemical composition (obtained by the Hot Pressing (HP) method) during turning the EN-36CrNiMo4 (PN-36HNM) toughening steel. The nanocrystalline cemented carbides have much higher hardness and smaller average grain size than standard carbides with the same chemical composition. For these reasons, cutting inserts made of the nanocrystalline cemented carbides particularly with TaC-NbC inhibitor have significantly greater hardness and from here greater resistance to wear and greater durability during machining the toughening steel.

**Keywords** Durability · Cutting edges · Nanocrystalline cemented carbides

---

M. J. Kupczyk (✉) · J. Komolka · P. Siwak  
Poznan University of Technology, Ul. Piotrowo 3, 60-965 Poznań, PL, Poland  
e-mail: [maciej.kupczyk@put.poznan.pl](mailto:maciej.kupczyk@put.poznan.pl)

J. Komolka  
e-mail: [jędrzej.komolka@gmail.com](mailto:jędrzej.komolka@gmail.com)

P. Siwak  
e-mail: [piotr.siwak@put.poznan.pl](mailto:piotr.siwak@put.poznan.pl)

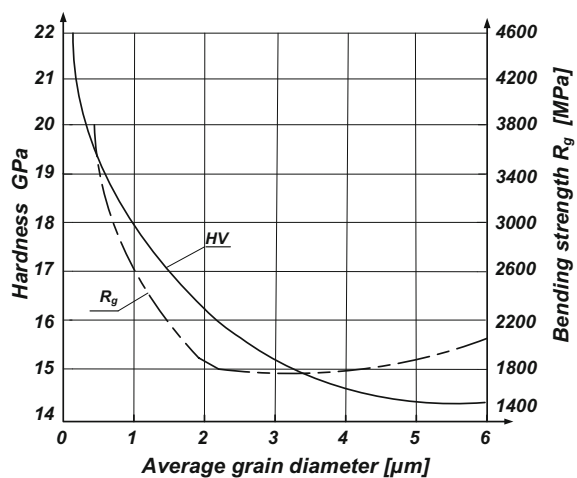
© Springer Nature Switzerland AG 2019  
L. F. M. da Silva (ed.), *Materials Design and Applications II*, Advanced Structured Materials 98, [https://doi.org/10.1007/978-3-030-02257-0\\_24](https://doi.org/10.1007/978-3-030-02257-0_24)

## 1 Introduction

Cemented carbides cutting edges are widely used in a different methods of machining, such as milling, drilling and turning [3]. In typical, conventional powder metallurgy processes, cutting edges made of WC-Co cemented carbides are most often produced by sintering with participation of a liquid cobalt phase [16, 18]. The presence of liquid Co phase during the WC-Co sintering causes the growth of the tungsten carbide grains. The growth of the WC grains is due to the high-rate diffusion of tungsten carbide into the liquid cobalt phase. This phenomenon has very important influence on the hardness, bending strength and fracture toughness of cemented carbides. Taking into account the literature data [8–10, 12–14, 16, 18] it can be stated that a decrease in the tungsten carbide grain size in the WC-Co cemented carbides increases such mechanical properties as hardness, bending strength, fracture toughness. The influence of the WC average grain diameter on the hardness and bending strength of the WC-Co cemented carbides is shown in Fig. 1.

However one should underline, that in the newest sintering methods [4–8, 15, 16, 20], the sintering process is carried out at lower temperature than in the conventional methods. A characteristic feature of the SPS (Spark Plasma Sintering), FAST (Field Assisted Sintering), PEDC (Pulse Electro-Discharge Consolidation) and PAS (Plasma Assisted Sintering) methods is a current pulse for heating the powders during sintering. In methods like Spark Plasma Sintering, Field Assisted Sintering and Plasma Assisted Sintering, the sintering process is very short. Spark discharges are ignited in the pores between powder particles during a current pulse. The discharges formed in the pores remove absorbed gases and oxides from the surface of powder particles, thereby facilitating the formation of active contact between them. Such as SPS, PAS and FAST methods in PPS method (applied during this investigations) the spark discharges during a current pulse are ignited in the pores (Fig. 2).

**Fig. 1** Influence of the WC average grain diameter on the bending strength and hardness of the WC-Co cemented carbides (elaborated on the basis of [9, 10, 18])



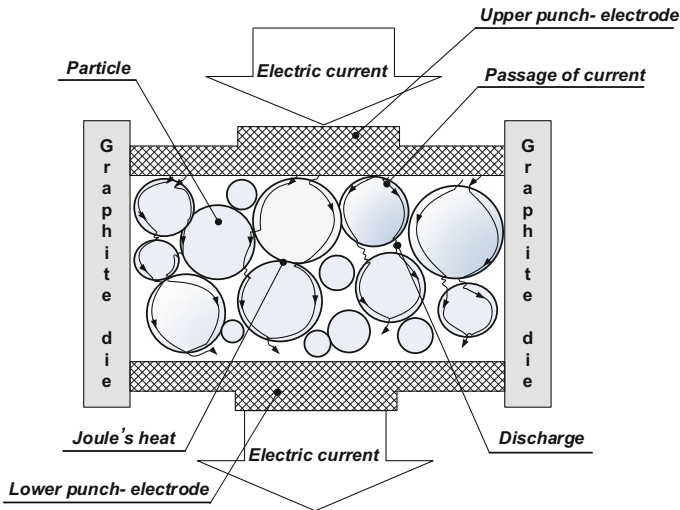


**Fig. 2** Phenomena occurring in pulse plasma sintering process [8–10, 16]

The present investigation was concerned with sintering the WC-5wt% Co, the WC-5wt% Co+2.5wt% (TaC-NbC) and WC-5wt% Co+0.9wt% Cr<sub>3</sub>C<sub>2</sub> nanocrystalline powders using a new PPS (Pulse Plasma Sintering) method [8–10]. Based on preliminary researches [8] it was stated, that, from point of view of hardness, 0.9% content of the Cr<sub>3</sub>C<sub>2</sub> and 2.5% of TaC-NbC of growth inhibitors is most advantageous.

The article presents the investigations of influence of growth inhibitors on durability of the cutting tools (insert cutting edges) made of the nanocrystalline sintered carbides. Cutting insert edges were sintered using the Pulse Plasma Sintering method elaborated at the Department of Materials Science Warsaw University of Technology [8, 11, 13, 17, 19].

## 2 Materials and Methods

This paper presents results of comparative investigations of durability of the cutting edges made of the WC-5wt% Co, the WC-5wt% Co+0.6wt% Cr<sub>3</sub>C<sub>2</sub> and the WC-5wt% Co+2.5wt% (TaC-NbC) nanocrystalline cemented carbides sintered by the Pulse Plasma Sintering method, and additionally the edges made of the standard cemented carbides of the same chemical composition (i.e., cemented carbides type the H20 (the WC-5wt% Co) and cemented carbides type the H20S (WC-5wt% Co+2.5 wt% (TaC-NbC)), sintered by the Hot Pressing method. Durability of the cutting edges was determined during turning the PN-36HNM (i.e., EN-36CrNiMo4, DIN-1.6511, AISI-6342) toughening steel.

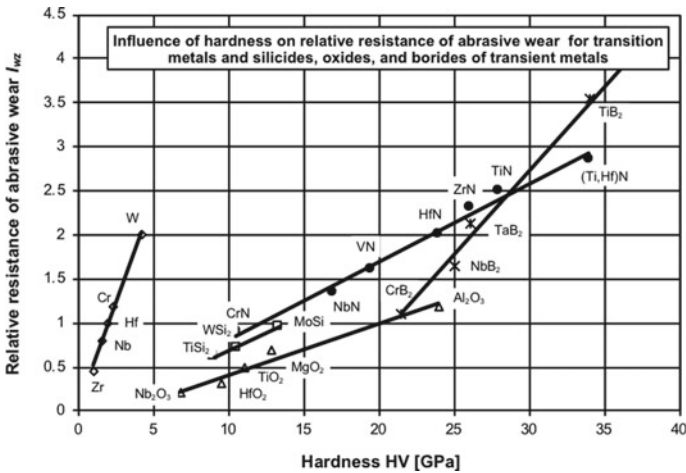


**Fig. 3** Influence of hardness on relative resistance of abrasive wear for transition metals and selected compounds [10, 18]

On the basis of own investigations [8, 10], the nanocrystalline cemented carbides are significantly harder than the standard cemented carbides. Addition of 2.5% of the TaC-NbC growth inhibitor to the WC-Co nanocrystalline cemented carbides additionally increases the hardness of the cutting edges from about 19 GPa to about 23 GPa, but addition of 0.9% of the Cr<sub>3</sub>C<sub>2</sub> growth inhibitor to the WC-Co nanocrystalline cemented carbides additionally increases the hardness of the cutting edges to about 22 GPa through the limitation of the growth of the WC grains during the sintering process of cemented carbides.

Study conducted by the present author [8–10] as well as literature data [1–3, 12, 13, 16, 18] show that it is well-known fact that an abrasive wear resistance increases with the increase in hardness. Many experiments have shown linear dependence between hardness and abrasive wear for different materials (metals, silicides, oxides and borides of transition metals) [10, 18] (Fig. 3).

The nanocrystalline WC-5wt% Co powder of the purity of 99.9% with the TaC-NbC or Cr<sub>3</sub>C<sub>2</sub> addition and without it was consolidated in our investigations by the Pulse Plasma Sintering (PPS) method. Both WC and Co powder grains before sintering were from 40 to 80 nm in diameter. The WC-Co powder was delivered by the Inframat Co., USA.

In the Pulse Plasma Sintering apparatus, the WC-Co powder is placed between two graphite punches in the graphite die (Fig. 4). A capacitor battery is the energy source which delivers high-current electric pulses [8, 16].

Figure 5 presents the pressure and the temperature variation during the Pulse Plasma Sintering process.

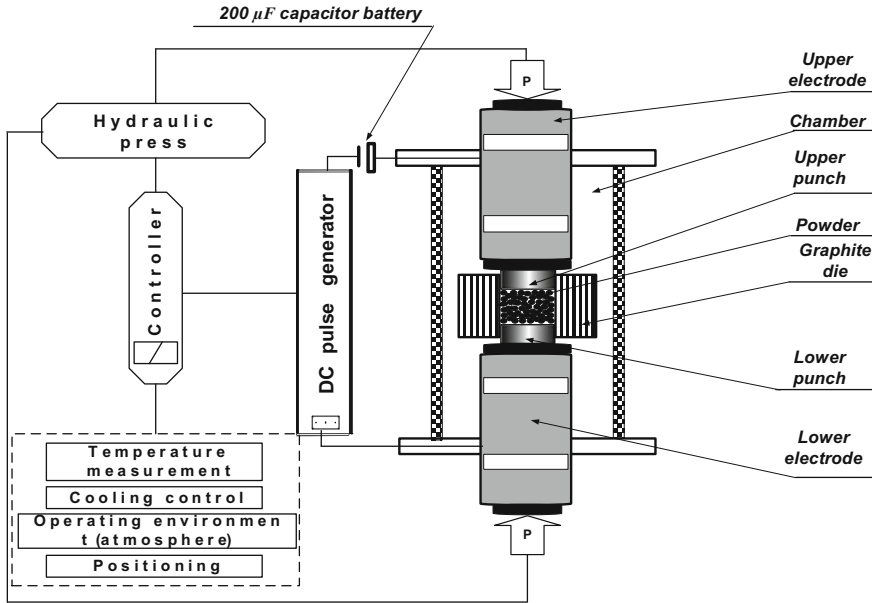


Fig. 4 Scheme of the pulse plasma sintering (PPS) facility (elaborated on the basis of [8, 10, 16])

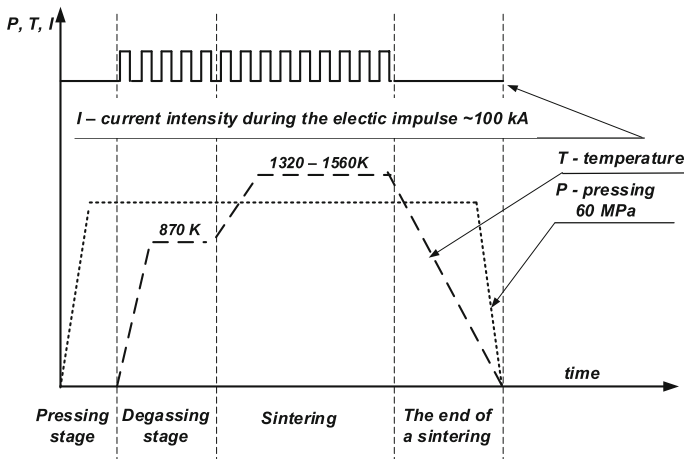


Fig. 5 The temperature and the pressure variation during the pulse plasma sintering process (elaborated on the basis of [8])

The run of the pulse plasma sintering process was as follows. Prior to the sintering the air from chamber was pumped out to a pressure of 0.05 Pa. In the first stage, the samples were heated for 60 s under a load of 60 MPa at a temperature of 870 K. In this stage of the PPS process the frequency of pulse repetition was  $1 \text{ s}^{-1}$ , discharge

energy was 2.5 kJ and voltage was 5 kV. During this process, the gases and the organic compounds absorbed on the powder surface were evaporated. In the second stage, the sample was heated up to the required sintering temperature in a vacuum of 0.05 Pa and under a load of 60 MPa for 500 s. In this stage of the PPS process frequency of pulse repetition was  $1 \text{ s}^{-1}$ , while discharge energy was 6.4 kJ and voltage was 8 kV [8].

Insert cutting edges ( $9.5 \times 9.5 \times 3.15 \text{ mm}$ ) made of nanocrystalline cemented carbides without and with TaC-NbC or  $\text{Cr}_3\text{C}_2$  growth inhibitor were sintered at temperature of 1520 K for 500 s. Based on preliminary researches [8] it was stated, that, from point of view of hardness, 1520 K is most advantageous sintering temperature. The temperature of the graphite die surface was measured during the sintering using a pyrometer equipped with an infrared sensor scaled from 770 to 2270 K with an error of  $\pm 1\%$ . The temperature of the sample during sintering was determined with a NiCr-NiAl thermocouple [8].

The microstructure of cutting edges was observed using SEM images formed in both the secondary electrons (SE) and the backscattered electrons (BSE) contrasts.

The hardness of the sample was measured using the Vickers hardness tester. The hardness was determined under a load of 294 N (HV30).

The tool life investigations of cutting edges concerned durability of edges during turning the PN-36HNM toughening steel hardened and tempered to  $32 \pm 2 \text{ HRC}$ .

On the basis of wear curves the tool life values for edges during turning the 36HNM toughening steel were estimated for the accepted value of the indicator of the edge blunting (mean band width of the corner wear  $VB_c = 0.9 \text{ mm}$ ).

The following conditions of machining during investigations of tool wear and life were applied:

- feed  $f = 0.2 \text{ mm/rev}$ ,
- cutting speed  $v_c = 120 \text{ m/min}$ ,
- depth of cut  $a_p = 1 \text{ mm}$ .

The insert cutting edges were clamped in the hR 110.16–220 holder. The cutting edge after clamped in the holder has the following geometry:

- tool orthogonal clearance  $\alpha_0 = 6^\circ$ ,
- tool orthogonal rake angle  $\gamma_0 = -6^\circ$ ,
- tool cutting edge inclination  $\lambda_s = -6^\circ$ ,
- tool cutting edge angle  $K_r = 75^\circ$ ,
- tool included angle  $\varepsilon_r = 90^\circ$ .

Insert cutting edges made of the standard cemented carbides (type: the H20 (WC-5wt% Co) and the H20S (WC-5wt% Co+TaC-NbC) were produced by Baildonit.



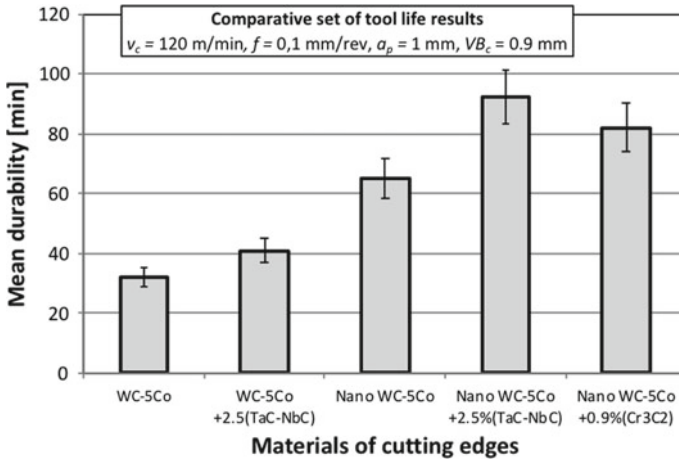


**Fig. 6** Tool life of cutting edges made of the standard H20 (WC-5% Co), H20S (WC-5% Co+2.5 wt.% (TaC-NbC)) and the nanocrystalline cemented carbides without and with growth inhibitors during machining the 36HMN toughening steel

### 3 Results

On the basis of the wear curves were determine the tool life of the cutting edges for an indicator of the edge blunting  $VB_c = 0.9$  mm. Figure 6 presents a graphical interpretation of the tool life of cutting edges made of the standard H20 (WC-5% Co), H20S (WC-5% Co+2.5wt% (TaC-NbC)) and the nanocrystalline cemented carbides (NanoWC-5% Co, NanoWC-5% Co+2.5wt% (TaC-NbC) and NanoWC-5% Co+0.9%Cr<sub>3</sub>C<sub>2</sub>) during machining the 36HNM toughening steel.

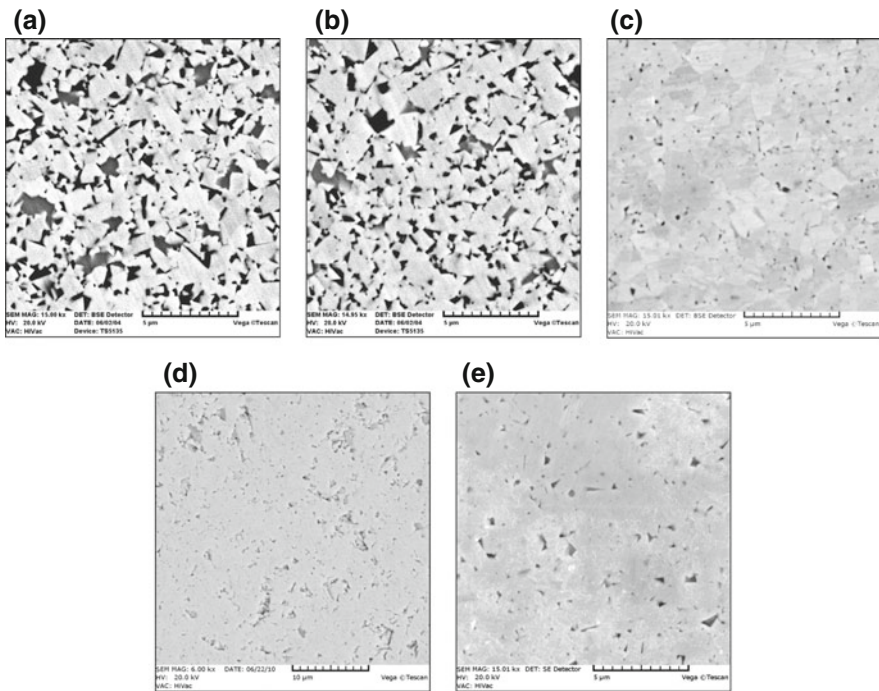
In Table 1 are compared the grain size, hardness, and durability during turning the 36HNM toughening steel of the nanocrystalline cemented carbides sintered by the PPS method with the properties of the standard cemented carbides of a similar chemical composition sintered by the HP method. The durability of the cemented carbides sintered by the Pulse Plasma Sintering method particularly with 2.5wt% of the TaC-NbC or 0.9% Cr<sub>3</sub>C<sub>2</sub> growth inhibitor exceed the values of standard cemented carbides obtained by the Hot Pressing method.

Figure 6 and Table 1 includes the obtained values of the tool life of the cutting edges made of nanocrystalline cemented carbides produced at a temperature of 1520 K.

It follows from Fig. 6 and Table 1 that the values of the durability (mean tool life) of the nanocrystalline cemented carbides sintered by the PPS method considerably exceed the respective values of the standard cemented carbides obtained by the HP method.

**Table 1** Tool life results obtained during turning the 36HNM steel for the indicator of edge blunting  $VB_c = 0.9$  mm of the cutting edges made of nanocrystalline and standard cemented carbides

Variant	Sintering method	Material of cutting edges	Grain size after sintering [7, 8] (nm)	Hardness (GPa)	Mean durability (min)
(1)	HP	WC-5 wt.% Co	2000–3000	15.5	32.2
(2)	HP	WC-5 wt.% Co + 2.5 wt.% (TaC-NbC)	1500–2000	16.5	41.0
(3)	PPS	WC-5 wt.% Co	150–300	19.1	65.0
(4)	PPS	WC-5 wt.% Co + 2.5 wt.% (TaC-NbC)	80–150	23.1	92.3
(5)	PPS	WC-5 wt.% Co + 0.9 wt.% Cr <sub>3</sub> C <sub>2</sub>	80–120	21.8	82.1



**Fig. 7** Selected BSE images of microsections of: **a** the standard H20 (WC-5% Co), **b** the standard H20S (WC-5% Co + 2.5 wt.% (TaC-NbC)), **c** NanoWC-5% Co, **d** NanoWC-5% Co + 2.5 wt.% (TaC-NbC), **e** NanoWC-5% Co + 0.9%Cr<sub>3</sub>C<sub>2</sub>

## 4 Conclusions

The tool life of the cutting edges made of the nanocrystalline cemented carbides with the TaC-NbC growth inhibitor sintered by the Pulse Plasma Sintering method is about 3 times higher than the durability of the cutting edges made of standard cemented carbides during turning the 36HMN toughening steel for  $VB_c = 0.9$  mm.

The nanocrystalline cemented carbides with the TaC-NbC growth inhibitor sintered at 1520 K under a pressure of 60 MPa for 500 s have the best exploitation properties (durability—92.3 min.), (better than nanocrystalline cemented carbides with  $Cr_3C_2$  growth inhibitor) due to high hardness (23.1 GPa) and the small size of the WC crystallites (80–120 nm).

Figure 7 shows differences in the structure between the standard cemented carbides (H20 and H20S) and the nanocrystalline cemented carbides without and with growth inhibitor. Measurements of grain size in cemented carbides were carried out using SEM—Vega TS 5135 (magnification: 20 000–500 000 times; resolution: 4 nm) and the Atomic Force Microscope (AFM-2D and 3D: Quesant Q-Scope 250).

**Acknowledgements** The authors acknowledge the financial support of the Ministry of Science and Higher Education (Polish State Committee for Scientific Research, contract No. N N503 147734). The work was also performed from financial resources of a research project No. 02/22/DSPB/1433 DS. The authors thank Prof. A. Michalski and Dr. M. Rosinski from Warsaw University of Technology and Dr. K. Jozwiak from Poznan University of Technology for preparation of the samples and for access to apparatus.

## References

1. Allen, C., Sheen, M., Williams, J., Pugsley, V.A.: The wear ultrafine WC-Co hard metals. *Wear* **250**, 604–610 (2001)
2. Feldshtein, E.E.: Selected methods of experimental researches of surface layer. ZGU Publisher, Zielona Gora (2017). ISBN 978-83-7842-270-9
3. Feldshtein, E.: Selected problems of machining. ZGU Publisher, Zielona Gora (2013). ISBN 978-83-7842-104-7
4. Groza, J.R., Zavaliangos, A.: Nanostructured bulk solids by field activated sintering. *Adv. Mater. Sci.* **5**, 24–33 (2003)
5. Kim, H.C., Jeong, I.K., Shon, I.J., Ko, I.Y., Doh, J.M.: Fabrication of WC-8 wt.% Co hard materials by two rapid sintering processes. *Int. J. Refract. Met. Hard Mater.* **25**, 336–340 (2007)
6. Kim, H.C., Shon, I.J., Yoon, J.K., Doh, J.M.: Consolidation of ultrafine WC and WC-Co hard metals by pulsed current activated sintering and its mechanical properties. *Int. J. Refract. Met. Hard Mater.* **25**, 46–52 (2007)
7. Kim, H.C., Oh, D.Y., Shon, I.J.: Sintering of nanophase WC-15 vol.% Co hard metals by rapid sintering process. *Int. J. Refract. Met. Hard Mater.* **22**, 197–203 (2004)
8. Kupczyk, M.J., Michalski, A., Zurek, J., Jozwiak, K., Rosinski, M., Siwak, P.: Report on Research Project of the Ministry of Science and Higher Education, contract No. N N503 147734, Poznan (2010) (unpublished)
9. Kupczyk, M.J.: Surface engineering—cutting tools. Publishing house of the Poznan University of Technology, Poznan (2015). ISBN 978-83-7775-396-5

10. Kupczyk, M.J.: Manufacturing and using of cutting tools with wear-resistant coatings. Poznan University of Technology Publishers, Poznan (2009). ISBN 978-83-7143-864-6
11. Michalski, A.: Physical and chemical principles of coating obtained from vapour. WUT Publisher, Warsaw (2000). ISBN 83-7207-171-3; ISBN 83-7207-202-7
12. Milman, Y.V., Luyckx, S., Northorp, I.T.: Influence of temperature, grain size and cobalt content on hardness of WC-Co alloys. *Int. J. Refract. Met. Hard Mater.* **17**, 39–44 (1999)
13. Olszyna, A.R.: Superhard ceramics. WUT Publisher, Warsaw (2001). ISBN 83-7207-312-0
14. Richter, V., Ruthendorf, M.V.: On hardness of ultrafine nanocrystalline hard metals. *Int. J. Refract. Met. Hard Mater* **17**, 141–152 (1999)
15. Risbud, S.H., Shan, ChH: Fast consolidation of ceramics powders. *Mater. Sci. Eng.* **A204**, 146–155 (1995)
16. Siemiaszko, D.: Structure and properties of the WC-Co composites made of tungsten, carbon and kobalt powders sintered by high-electric current pulses. Doctor's thesis; Warsaw University of Technology, Warsaw (2006)
17. Sokolowska, A.: Unconventional means of materials synthesis. PWN Publisher, Warsaw (1991). ISBN 83-01-10848-7
18. Wysięcki, M.: Modern tool materials. WNT Publisher, Warsaw (1997). ISBN 83-204-2114-4
19. Zdunek, K.: Pulse plasma in surface engineering. WUT Publisher, Warsaw (2004). ISBN 83-7207-476-3
20. Zhu, L.H., Huang, Q.W., Zhao, H.F.: Preparation of nanocrystalline WC-10Co-0.8VC by spark plasma sintering. *Int. J. Refract. Met. Hard Mater.* **22**, 1631–1633 (2003)

# Evaluation of Machining Defects in a Composite Laminate by Combining Non-destructive and Tensile Testing



Louis-Alexandre Généreux, Gilbert Lebrun, Martin Viens  
and Jean-François Chatelain

**Abstract** Although composite structures can be molded to nearly final shape, they generally require different finishing operations, such as drilling and trimming, to meet dimensional tolerances and enable assembly. Conventional drilling and trimming methods tend to induce internal damage to the composite, mainly in the form of edge delamination, matrix thermal degradation, fiber fracture or fiber pullout. As the damage mechanisms and progression are not yet fully understood, it is crucial that the appropriate tools be used to verify the structural integrity of composite parts. NDT techniques allow observing the extent of damage in composites; however they have limited resolution for shallow edge defects. On the other hand, well-designed tensile tests, made from coupons taken over extra materials intentionally left around a part, are sensitive to the reduction of mechanical properties of trimmed composite samples due to, among others, thermal degradation and smearing of the matrix. In that respect, the main objective of this work is to evaluate the possibility to detect and quantify small edge machining damage using the ultrasonic testing (UT) method and combine this approach with mechanical testing to determine the influence of machining on the quality of trimmed parts. Indeed, a combination of mechanical testing and NDT techniques could provide an interesting avenue to appropriately certify the quality of a machined composite part. A non-destructive testing (NDT) method and tensile mechanical testing will thus be used to characterize the extent and the influence of damage induced by the trimming operation of quasi-isotropic carbon/epoxy composites. First, the resolution and the precision of ultrasonic testing (UT) are evaluated with composite samples comprising internal (artificial) defects. Next, this method is used to evaluate machined samples prepared by using high performance machining tools for composites. It is shown that the UT technique is able to detect the very small edge defects induced by trimming. Then, mechanical testing of narrow tensile coupons is performed to compare impact of milling, abrasive

---

L.-A. Généreux · M. Viens (✉) · J.-F. Chatelain  
Department of Mechanical Engineering, École de technologie supérieure, Montreal, Canada  
e-mail: [martin.viens@etsmtl.ca](mailto:martin.viens@etsmtl.ca)

G. Lebrun  
Department of Mechanical Engineering, Université du Québec à Trois-Rivières (UQTR),  
Trois-Rivières, Canada

© Springer Nature Switzerland AG 2019  
L. F. M. da Silva (ed.), *Materials Design and Applications II*, Advanced  
Structured Materials 98, [https://doi.org/10.1007/978-3-030-02257-0\\_25](https://doi.org/10.1007/978-3-030-02257-0_25)

cutting and sanding on the quality of trimmed surfaces. Results suggest that some type of damage could efficiently be quantified when coupons of reduced width is used to magnify the influence of defects on the measured strength.

**Keywords** Polymer matrix composites (PMCs) · Machining  
Non-destructive testing · Mechanical testing

## 1 Introduction

### 1.1 Ultrasonic Testing

Ultrasonic testing is a dominant technique in the inspection of composite structures. This technique consists in the transmission of high-frequency acoustic waves in a material. The waves are generated by a piezoelectric transducer that converts an oscillating electrical signal into high-frequency vibrations, and propagates into the tested sample by displacement of the material particles [1]. When ultrasonic waves encounter a variation in the acoustic impedance of the medium, part of the energy is reflected, while the remaining part is transmitted. This feature allows two modes of inspection: in transmission with a transmitter and a receiver positioned on either side of the part, and in reflection, where the same transducer acts both as a transmitter and a receiver [2]. In transmission mode, defects will appear as high attenuation zones (a defect will obstruct the propagation of the waves through the material) [2], while in reflection mode, defects will appear as high intensity zones (a defect will reflect energy) [3]. Delaminations, disbonds, porosities and voids are easily detected with this method, and foreign materials may also be detected, provided the acoustic impedance is significantly different from the composite material [1, 4].

### 1.2 Machining Damage in Composite Materials

For the sake of convenience, conventional machining processes are generally used for composites, but their machining strongly differs from isotropic materials due to the inhomogeneous nature of composites. The cutting edges of the tool encounter the strong and brittle fibers successively, as well as the weak and more ductile matrix [5]. The machining of metals is characterized by shearing and plastic deformation, while in composites; rupture is intermittent and uncontrolled because of the brittle behavior of fibers [5]. The mechanisms of chip formation for laminated composites depend on the orientation of fibers with respect to the cutting edge of the tool. The worst case occurs when fibers are at  $-45^\circ$  relative to the cutting direction. In this case, the fracture of fibers occurs by bending, which also causes the propagation of cracks along the fiber/matrix interface [6–9]. Thermal degradation of the matrix, surface

ply delamination, uncut fibers and fiber pullout have also been observed [10–14]. The machining quality in composites refers not only to surface roughness, but also to the extent of damage [5]. Because some forms of damage, especially interlaminar and intralaminar cracks, are not visible on the machined surface, the use of the UT method to assess the quality of machined composites is proposed in this work. Very little work has been done in this domain. Some authors have used ultrasound or infrared thermography techniques, but only in evaluating damage caused by drilling operations [15, 16].

Other authors have also studied the effect of machining operations on the mechanical properties of composites. Howarth and Strong tested the tensile specimens of different widths obtained by two methods of cutting, waterjet and laser beam cutting [17]. The objective was to evaluate the effect of the damage (damaged zone produced by the cutting operations) on the tensile strength and modulus. Unfortunately, no trend can be drawn from their results. The authors explain this by experimental errors and the small number of tested samples. Ghidossi, El Mansori and Pierron investigate the influence of cutting parameters on the damage level and the ultimate tensile stress of off-axis glass/epoxy unidirectional coupons obtained by side milling. Their results show that the tensile failure stress of the specimens is significantly influenced by the machining parameters used to prepare them [18]. The effect of machining has also been studied with four-point flexure tests by Arola, Ramulu and Colligan [19]. They compared the flexural strength and modulus of quasi-isotropic graphite/epoxy samples prepared by abrasive diamond saw, waterjet cutting and orthogonal machining with a polycrystalline diamond tool. Very few differences were observed on the flexural stiffness and no significant variations were observed on the ultimate strength [6, 19, 20]. However, the same experiments performed on a graphite/bismaleimide laminate show a significantly reduced bending strength for the samples machined by orthogonal cutting compared to the abrasive diamond saw [21]. The machined surfaces seem also to influence the performance of laminates under dynamic three-point bend tests [6, 22, 23]. According to the works of Arola and Williams, an increase in the surface roughness obtained from different waterjet cutting conditions reduces the stiffness during a four-point flexural cyclic loading test [24].

### ***1.3 Objective of Current Work***

In this work, an attempt is made to combine the UT technique, used to detect edge defects obtained under trimming, with tensile test results made with coupons of increasingly smaller width. The objective is to validate the hypothesis that, by combining these two inspection methods, it is possible to develop a procedure that will ultimately provide a mean to certify the quality of a machined composite part. First of all, in the next section, the UT technique is described and evaluated for its capacity to detect very small edge defects, such as those induced in trimming composite parts. This evaluation is carried out using real machined coupons and two types of artificial defects, located along the side of composite plates. The tensile tests are performed

next by measuring the tensile strength and modulus of small width coupons. Coupons with increasingly smaller widths are proposed to increase the influence of the edge defects on the reduction of material's elastic modulus and strength. Indeed, with smaller widths, defect size represents a larger portion of the coupon's cross-section.

## 2 Evaluation of Ultrasonic Testing Resolution

### 2.1 Testing Setup

The ultrasonic system used was a TecScan® (Boucherville, Quebec, Canada) 5-axis industrial immersion scanner. The sample was placed in the immersion tank filled with water and serving as a coupling medium for the ultrasounds. All samples had a rough and a smooth surface, a characteristic inherent to the vacuum bagging molding method (vacuum bag on one side and tool surface on the other side for molding in an autoclave). Scans were performed on the samples with the ultrasonic beam normal to the smooth surface to avoid the scattering of waves by the surface roughness. The transducer used was a single element, focalized on a point on the surface of the samples. Reflection mode (pulse echo) was used. The UT technique was evaluated using two sets of tests. In the first set (described in the next section), samples were prepared with artificial defects of two different types, i.e., machined circular notches and square Teflon tapes inserted at mid-thickness. This was done to determine the ability to detect defects confined to the machined edge of a part. Next, the technique was evaluated on samples machined using combinations of cutting tools and machining parameters producing realistic machining damages. In all cases, quasi-isotropic carbon-epoxy laminates with a fiber volume content of 64% were used. The laminates were obtained by hand layup and cured in an autoclave following aeronautic standards. The experimental details for the two sets of tests are presented in the following paragraphs.

### 2.2 Artificial Defects Manufacturing

Two plates made of 24 plies were used for the tests with artificial defects. Each plate had a quasi-isotropic stacking sequence and a thickness of 3.58 mm. The first plate had eight semi-circular notches, all located at mid-thickness on the edges of an approximately 107 mm × 198 mm plate. Notches depth ranges from 0.79 to 7.62 mm, as shown in Fig. 1a. The notches were machined on a CNC machine using a 0.64 mm thick abrasive disc 24 mm in diameter. For the second plate, artificial defects were produced using eight Teflon® films inserted at mid-thickness of the plate during the layup process. The Teflon tape used was 12.7 mm wide by 0.127 mm thick and the penetration length inside the plate ranged from 1.59 to 10.22 mm, as shown in Fig. 1b.



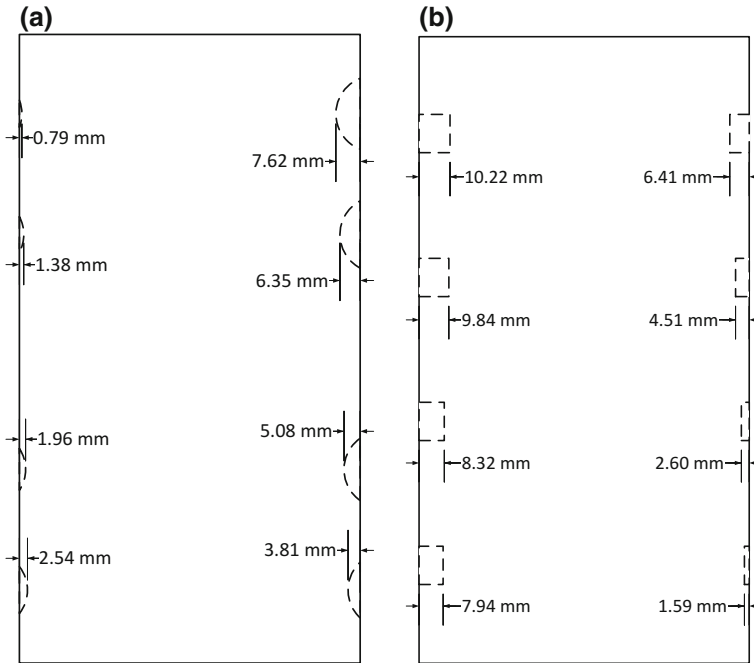


**Fig. 1** **a** Sample with machined notches and **b** sample with Teflon inserts

In this case, the plate was about 109 mm wide by 196 mm long. For the ultrasonic testing and for all samples with artificial defects, a transducer with a center frequency of 7.5 MHz and a focal length of 44.5 mm was used (corresponding to a 0.46 mm focal spot diameter in water). The scan was done with a step increment of 0.38 mm in both scan and index directions.

### 2.3 Samples Machined with Cutting Tools

For the tests with machined coupons, a 4.62 mm thick, 32-ply quasi-isotropic laminate was used. As detailed in Zaghbani et al. [25], a 300 mm × 300 mm laminate was firmly maintained on a milling jig using 49 screws (Fig. 2). The trimming operation was then performed in order to cut 49 square test coupons, each fixed in its center with one of the screws. To change the machining parameters from coupon to coupon, large engagement holes were pre-drilled at the intersection corner of each coupon. The individual square coupons were machined using two cutting tools and a set of machining parameters summarized in Tables 1 and 2. The machining direction for tool C1 was at 90° with respect to the fibers orientation within the first two plies of the laminate, while for tool C2, it was at 0°. For the top and left sides of the coupons,

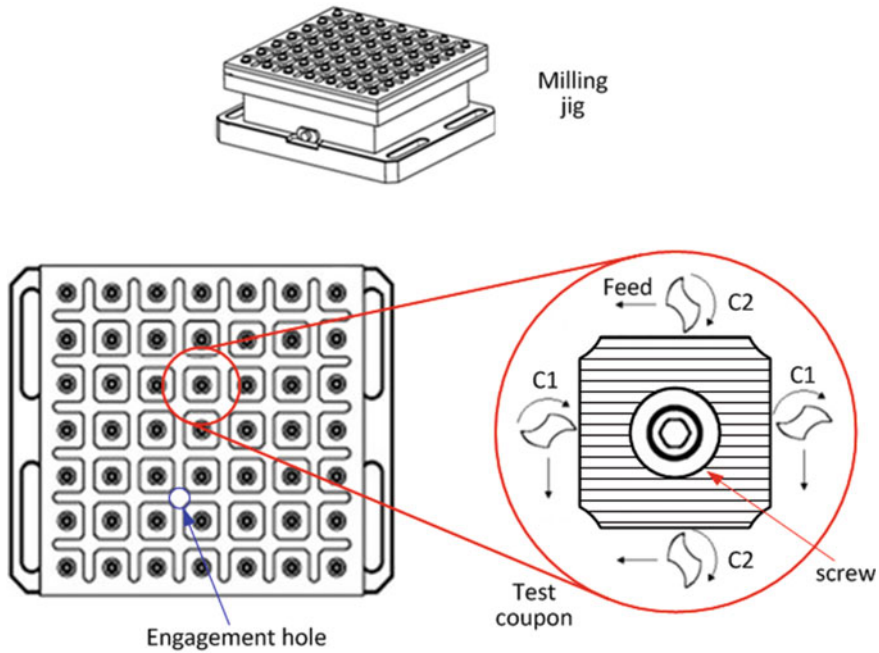


Fig. 2 Set-up for the trimming experiments (adapted from [25])

Table 1 Cutting tools characteristics

Tool	Material	Number of flutes	Rake (°)	Relief (°)	Helix (°)	Diameter (mm)
C1	CVD coated carbide	6	≈10°	≈15°	≈10°	9.525
C2	Polycrystalline diamond (PCD)	2	≈10°	≈20°	≈0°	9.525

these directions correspond to the up-milling mode, which has been identified as producing trimmed surfaces with higher quality as compared with down-milling cutting mode (bottom and right sides of the coupons). Among all machined coupons, 17 were selected for the non-destructive inspections. Selection has been made according to the resulting quality and stability of the machining process, considering both tools (Table 1) and cutting parameters (Table 2). In this case, a 10 MHz transducer with a 25.4 mm focal length was used (corresponding to a 0.20 mm focal spot diameter in water). The scan was done with a step increment of 0.08 mm in both scan and index directions. A slightly better resolution could thus be expected from these inspections as compared with the one used for the two samples with artificial defects. Data analysis was performed with an in-house program developed under Matlab® (MathWorks, Natick, MA, USA).

**Table 2** Cutting parameters

Cutting speed (m/min)	200, 300, 400, 500, 650, and 800
Feed rate (mm/rev)	0.10, 0.20, 0.25, 0.36, 0.41, and 0.51

### 2.4 Ultrasonic Results: Samples with Artificial Defects

Figure 3 shows the images obtained by ultrasonic testing for the two samples with artificial defects. In both cases, the defects are clearly visible. The brighter strips visible at the bottom of the sample with circular notches and at the top of the sample with Teflon inserts are due to a decrease in the thickness of the plate, a phenomenon that occurs when molding with vacuum bags. The three circles visible around the sample with notches are screw heads that serve to position the samples during the inspection. To assess the sensitivity of the technique, the depth of the defects from the edge of the plate is measured and compared with the design values. First, all signals are corrected to compensate for the attenuation of the waves in the material. This is known as Time Corrected Gain (TCG). This allows the echoes from flaws that are far underneath the plate surface to be displayed with the same magnitude as if they were closer to the surface. After that, a damage threshold is applied to separate the noise from the signals representative of defects. When the maximum absolute amplitude value of the A-Scan signal, as it appears between the surface and the backwall echoes, exceeds this threshold, the corresponding pixel on the C-scan is marked as a defect (white pixels in Fig. 4b). The value of this damage threshold was chosen to be half of the maximum amplitude value obtained from a defective area on the sample. With this approach, we obtain a binary image that can clearly discriminate the defect areas from the healthy zones. The dimension of defects is then known as Full Width at Half Maximum (FWHM). Figure 4 shows the result for the sample with circular notches. The two vertical lines on the A-Scan are the gate limits and the horizontal ones are the damage threshold. The gate is placed between the top surface echo and the backwall echo to display the signals from the internal structure through the complete thickness of the samples. The measured dimensions of defects are presented in Table 3. It is found that the dimensions of the defects measured for the sample with machined notches are very close to design values. The error is always less or equal to 0.25 mm, so smaller than the pixel size (0.38 mm). It would probably be possible to obtain even better results with smaller inspection steps. For the sample with Teflon inserts, the errors are slightly higher. However, this is most likely due to the manual positioning of the film during molding which leads to deviations from drawing specifications. As observed in Fig. 3b, the insertions are even not exactly straight.

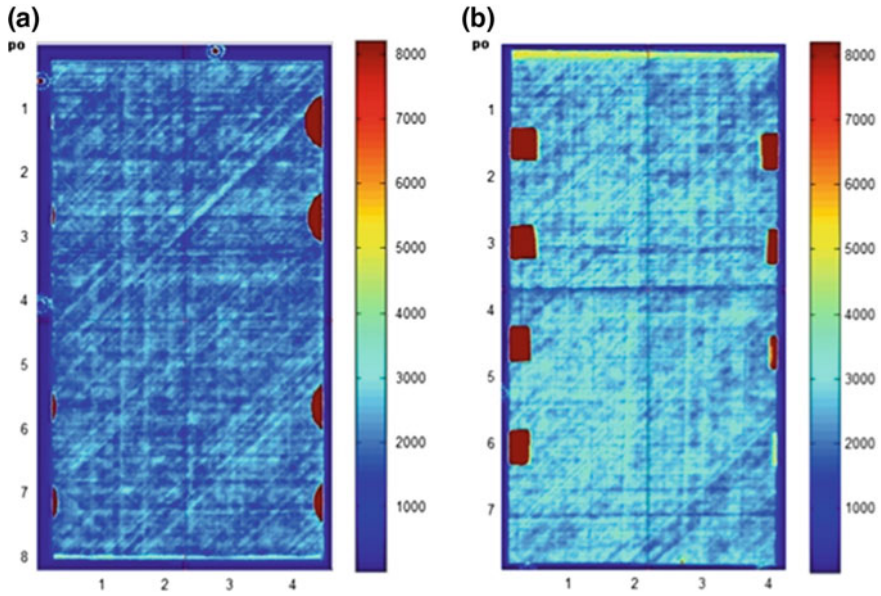


**Fig. 3** C-Scan images of **a** sample with notches and **b** sample with Teflon inserts

**Table 3** Measured dimensions of artificial defect versus design values

	Design depth (mm)	Measured depth (mm)	Error (pixel)
Machined notches	7.62	7.62	0.00
	6.35	6.48	0.34
	5.08	5.33	0.66
	3.81	3.81	0.00
	2.54	2.67	0.34
	1.96	1.91	0.13
	1.38	1.52	0.37
	0.80	0.76	0.08
Teflon inserts	10.22	11.05	2.18
	9.84	10.67	2.18
	8.32	8.76	1.16
	7.94	8.38	1.16
	6.41	7.24	2.18
	4.51	4.95	1.16
	2.60	3.05	1.18
	1.59	1.52	0.18

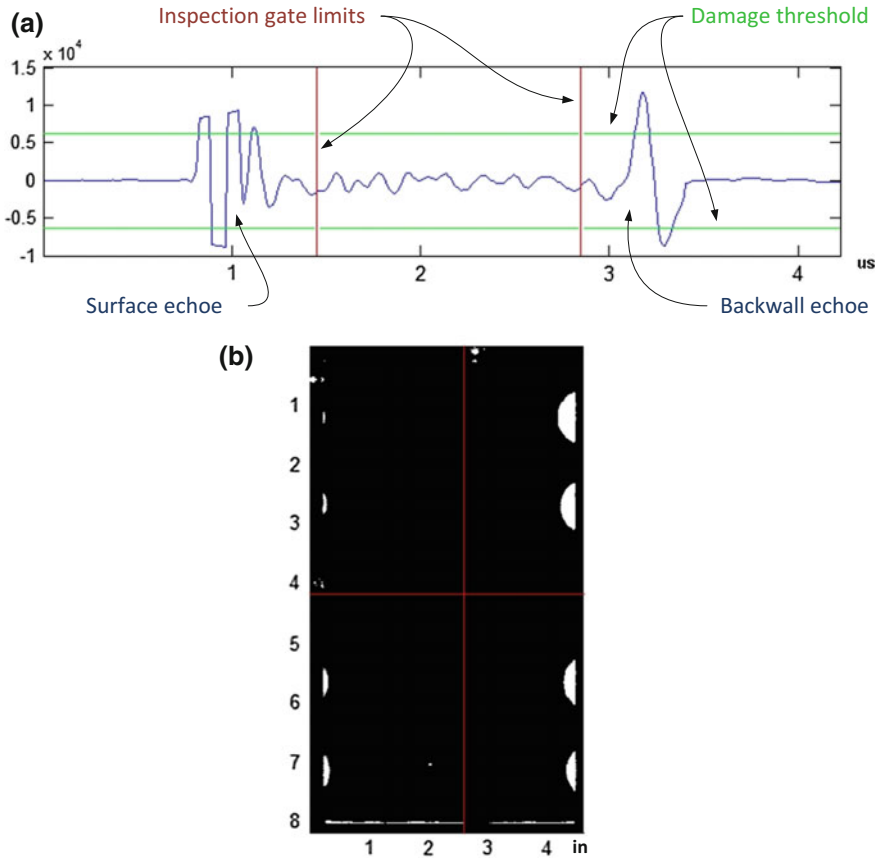


Fig. 4 Defect evaluation on sample with machined notches. **a** A-Scan and **b** binary C-Scan

### 2.5 Ultrasonic Results: Machined Samples

Figure 5 shows ultrasonic C-scan results on one typical sample. The dark red region observed in the center of the sample is due to a delamination caused by the drilling of the fastening hole in which a screw was inserted during edge trimming (Fig. 2). Other delaminations are frequently observed in the corners of most samples because of the drilling of the engagement holes. The extent of these damages is probably attributable to the use of inappropriate tool or cutting conditions. The dark bands extending along the trimmed edges of the samples are of greater interest. They most likely correspond to machining damages. Figure 6a shows a closer view on a raw C-scan image while Fig. 6b shows the same edge after image processing with a damage threshold (Fig. 4). From this binary image, the extent of damages is quantitatively assessed. Two measures are proposed: the maximum depth of damages and the damage coverage along the length of the machined edge. The first measure

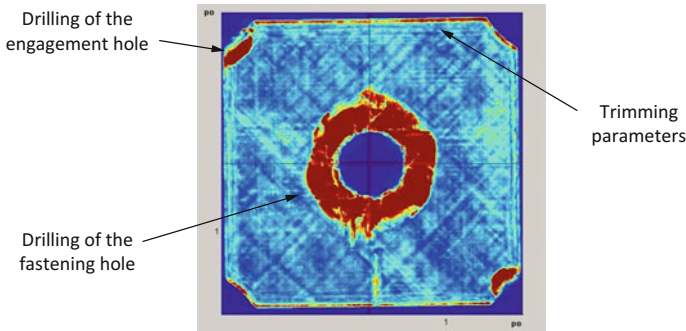


Fig. 5 Ultrasonic C-scan of a typical machined sample

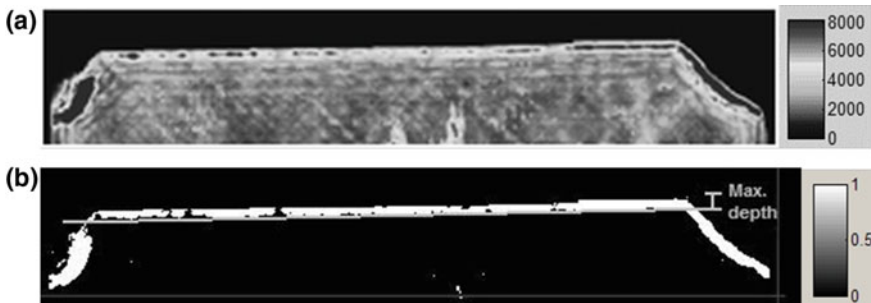


Fig. 6 Evaluation of machining damage. Sample machined with C1 at 650 m/min, 0.10 mm/rev

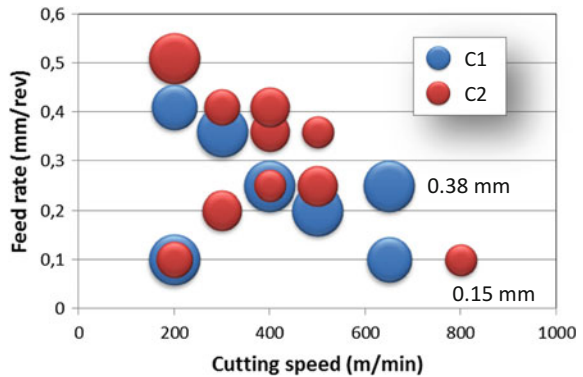
corresponds to the greatest depth of damage found along the edge, while the second measure refers to the occurrence of damages, deeper than half of the maximum value, along the same edge. This second measure is expressed in percentage of the total machined edge length.

Table 4 shows the results for all the machining conditions evaluated, with the third and fourth columns corresponding to the maximum defect depth and the damage coverage, respectively. The two measures are also plotted with respect to machining parameters in Figs. 7 and 8, respectively. It is difficult to come up with a conclusion on the influence of machining parameters on the extent of induced damages. There is no clear relationship between them. However, the maximum depth of damage seems to be smaller for tool C2 than for tool C1. This could be partly explained by the fact that, as mentioned previously, for C2, the fibers in the first plies are at 0° with respect to the cutting direction while they are at 90° for C1 (see Fig. 2). It has to be noted that, due to the lack of support from adjacent plies, the first plies of a composite are more likely to delaminate, hence their importance in the current analysis. Looking at the work done by Ramulu [6], it is easily understood that a 0° orientation will favor

**Table 4** Extent of damage measured by ultrasounds for 17 test coupons

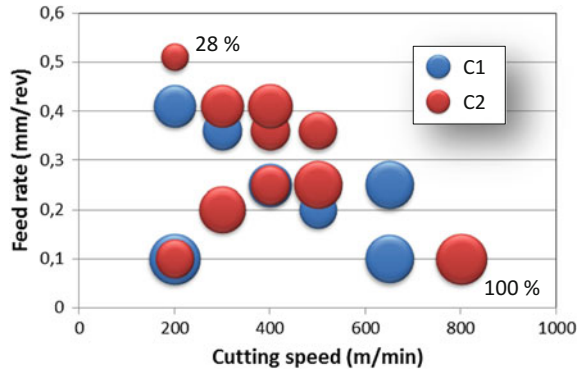
Tool	Cutting speed (m/min)	Feed rate (mm/rev)	Maximum depth (mm)	Coverage (%)
C1	200	0.10	0.38	100
		0.41	0.30	69
	300	0.36	0.38	58
	400	0.25	0.38	71
	500	0.20	0.38	53
		0.10	0.30	92
		0.25	0.38	87
C2	200	0.10	0.19	57
		0.51	0.38	28
	300	0.20	0.23	82
		0.41	0.19	72
		0.25	0.15	60
	400	0.36	0.23	60
		0.41	0.23	76
		0.25	0.23	88
	500	0.36	0.15	56
		0.10	0.15	100

**Fig. 7** Maximum delamination depth for various machining conditions



smooth and continuous chip formation while, for 90° orientation, delamination are likely to occur between fibers. Nonetheless, even if the extent of damage is small and confined to the edge of the samples, it seems that the ultrasonic testing method is able to efficiently detect these damages, reflecting the usefulness of the method in evaluating the machining quality in composite laminates.

**Fig. 8** Damage coverage along the machined length for various machining conditions



### 3 Tensile Testing

#### 3.1 Experimental Details

Tensile tests were performed following ASTM D3039/D3039 M-00 standard. The tensile specimens were obtained from the same carbon/epoxy laminates used for the UT testing with artificial defects. After fabrication, the quality of the laminated plates was verified by the UT method. 254 mm long tensile coupons were prepared in three widths: 19.05; 12.7 and 6.35 mm. By reducing the width, the influence of cutting defects on the measured strength and modulus was expected to increase thus increasing sensitivity to induced damages. Each specimen width was obtained by three cutting methods, namely, by abrasive diamond saw, abrasive diamond saw followed by dry sanding, and finally by milling in a full slotting operation. The abrasive diamond saw is a cutting method commonly used as a reference method in the literature. Here, a tile saw with an abrasive diamond blade of 178 mm in diameter was used. The rotation speed of the blade was 3450 rpm, and the material feed was controlled manually. Water was used to cool the blade and for dust extraction. The second cutting method used the same abrasive saw, except that the sides of the samples were sanded after cutting to remove any defect produced during cutting. The sanding was done on a CNC milling machine with a specially designed fixture (Fig. 9). Sanding bands with grit #240 were used with a spindle speed of 12,000 rpm and a feed rate of 0.03 mm/rev to obtain an excellent finish. These samples served as a reference for the other two methods.

Finally, the last cutting method for the preparation of the tensile coupons represents the industrial case of composite trimming by CNC machines. The composite laminates are clamped between a base and an aluminum plate with a series of bolts in order to prevent the vibration of the tensile coupons during machining (Fig. 10). Engagement holes were predrilled in the composite to allow the engagement of the cutting tool. Each side of the tensile specimens was machined in up-milling mode and in a single step (full slotting operation), such that the engagement of the tool



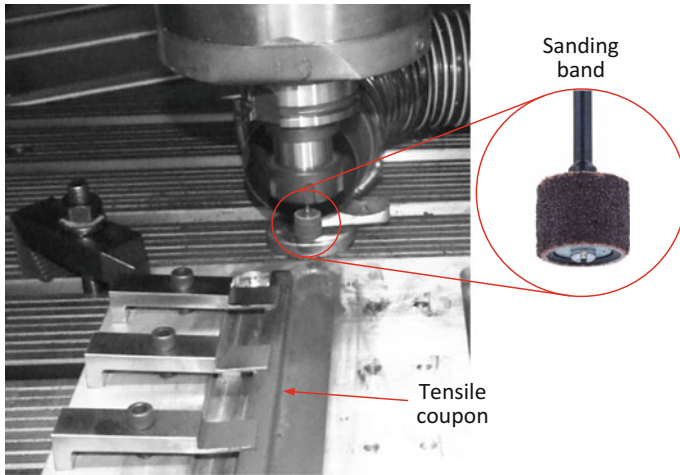


**Fig. 9** Set-up used for the sanding of tensile coupons

corresponded to the full thickness of the plate and the full diameter of the tool. The selected cutting tool was specially designed for the machining of carbon/epoxy composites. It was a tungsten carbide tool with a chemical vapor deposition (CVD) diamond coating (similar to C1 tool). The tool has 8 flutes and is 6 mm in diameter. Machining parameters were selected to provide the best trimmed surfaces quality, and new tools were frequently introduced in the cutting process to avoid the effect of tool wear on the quality of the cut. The machining of the tensile coupons was done at a cutting speed of 190 m/min and a feed rate of 0.32 mm/rev.

After cutting, aluminum tabs were bonded at the ends of each sample to promote failure in the gage section, as specified in ASTM D3039. Each coupon was then inspected by ultrasound, using the same approach as for the machined specimens presented in the previous section. However, considering the time required to measure the defects with the UT method, only a small part of the tensile coupon was scanned, namely, a 7 mm by 25.4 mm zone located along the edge. This was considered enough to obtain representative values of the defect sizes for each coupon. A specimen representative of each cutting method was also retained for scanning electron microscope observations. Finally, samples were tested up to failure on an Instron® (Norwood, MA, USA) LM-I150/I equipped with mechanical wedge grips. A 50.8 mm mechanical extensometer was used for elongation measurements. Specimens were tested with a constant displacement speed of 1.27 mm/min with the elongation recorded at a frequency of 25 samples/second. A total of 62 coupons have been tested (3 cutting methods  $\times$  3 coupon widths  $\times$  6 to 8 coupons per conditions).

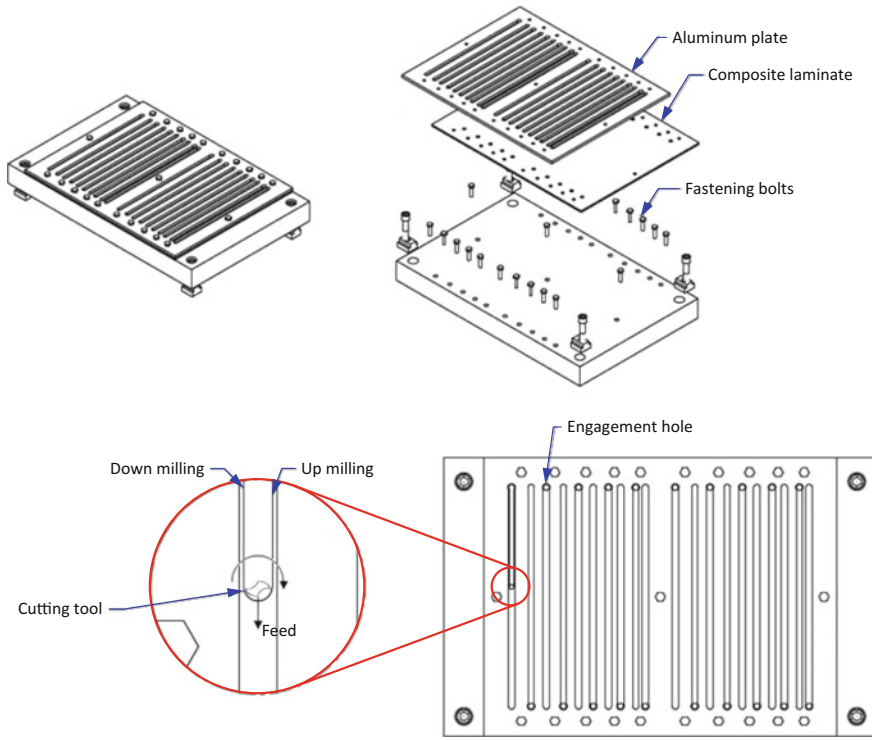


**Fig. 10** Set-up used for the trimming of tensile coupons

### 3.2 *Ultrasonic Inspection*

Ultrasonic inspections of the tensile coupons did not reveal any damages for the samples obtained by milling. However, it has to be noted that, in this case, the first ply is oriented at  $0^\circ$  with respect to the feed direction of the cutting tool thus reducing the probability to induced damages in the laminate. Results are slightly different for the samples obtained by abrasive cutting. In this case, shallow delaminations are suspected along the edge of the coupon for the surface plies. Such a result could be explained by the fact that, by using a sawing blade, one component of the cutting forces is normal to the laminate plane, thereby promoting the delamination at the exit of the blade. However, for all coupons produced with this method (18 coupons), an average maximum delamination depth of only 0.155 mm (2 pixels) with a standard deviation of 0.054 mm has been found. Delaminations, if there are any, are thus at the sensitivity limit of the ultrasonic inspection method.

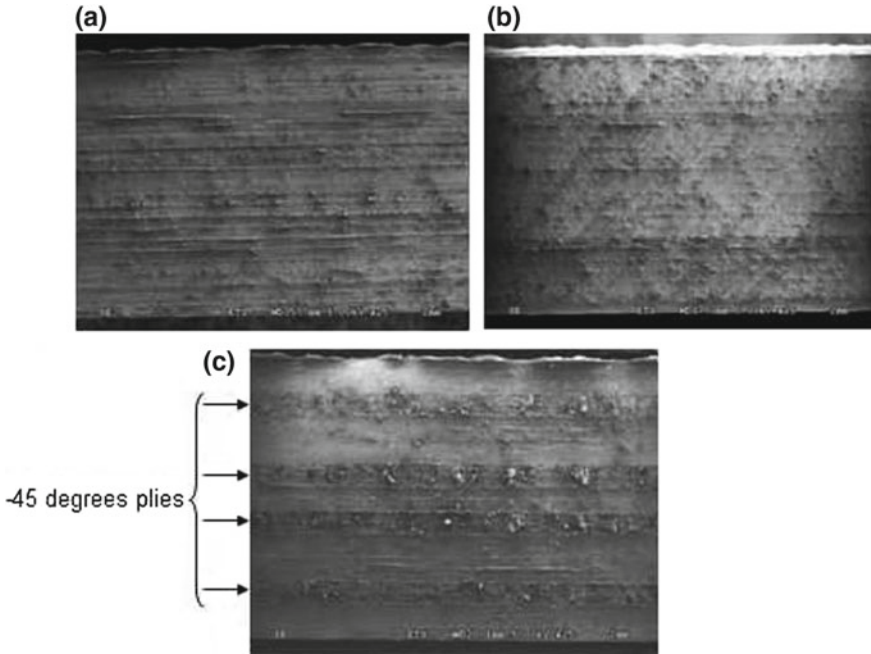
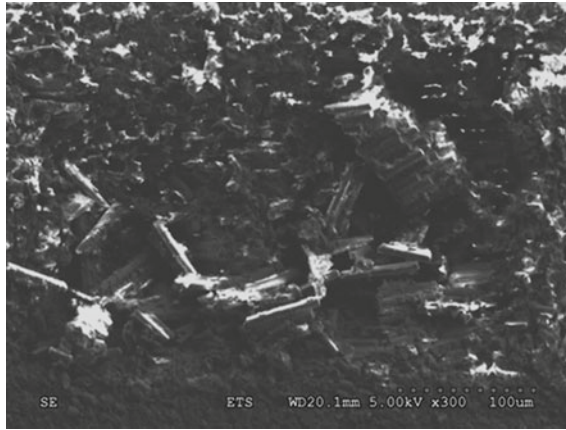


**Fig. 11** Surfaces obtained by **a** sanding **b** abrasive cutting and **c** milling

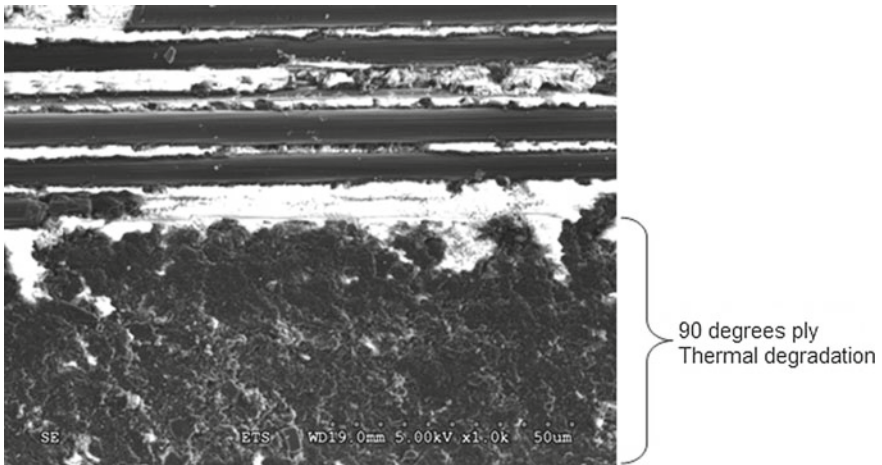
### 3.3 Scanning Electron Microscope Observations

Figure 11 shows 25X magnification photographs of the cut surfaces obtained with each preparation method. Sanding obviously gives the most uniform surface of the three methods (Fig. 11a). The surface obtained by the abrasive diamond saw has no major damage either, but the roughness is slightly higher (Fig. 11b). We observe streaks caused by the diamond grains that are coarser than the grains of the sanding bands. We also note that the direction of the material removal is not the same as compared to sanding and milling operations. In these cases, material removal occurs in parallel with the machined surface, while for the abrasive cutting, material removal is through the thickness of the plate. In addition, in Fig. 11c (sample obtained by milling), we can clearly distinguish the damaged plies oriented at  $-45^\circ$ . Figure 12 shows a 300X magnification of one of these plies; the fibers are clearly torn in bundles, giving a very rough surface.

The numerous fiber fractures shown suggest significant bending during the chip formation. This bending may have led to crack propagation along the fiber/matrix interface, followed by the fracture of fibers by bending. The surfaces obtained by milling also exhibit matrix smearing (due to thermal degradation), mainly in the 90



**Fig. 12** Sample obtained by milling, damage observed on  $-45^\circ$  ply, 300X magnification



**Fig. 13** Sample obtained by sanding, thermal damage on  $90^\circ$  ply, 1000X magnification

and  $+45^\circ$  plies. Thermal degradation of the matrix is also present on samples obtained by sanding (Fig. 13). The high rotational speeds and low feed rates, combined with dry cutting conditions, are favorable to heat generation, which may exceed the glass transition temperature of the matrix so as to produce smearing and cause thermal damage. Thermal damages are less significant on samples obtained by abrasive diamond saw, but are still present. The use of water to cool the blade and remove dust helps to prevent this type of damage.

### 3.4 Tensile Test Results

Tables 5, 6 and 7 summarize the measured mechanical properties for tested specimens. The average strength was calculated from coupons that failed far enough from the bonded tabs (distance larger than the width of the sample) to ensure that the failure was not influenced by the grips. Consequently, the number of measures left for this calculations is also given in the tables. For the modulus of elasticity, all tests were considered because this value is not affected by the fracture location. Figures 14 and 15 show the variation of the average strength and the modulus of elasticity as a function of the samples width. Considering the standard deviations obtained, the observed differences for coupons of both 19.05 mm and 12.7 mm in width are not significant enough to clearly show the influence of cutting methods on the measured properties. However, even if the results are based on a limited number of tests, when the specimen width is reduced to 6.35 mm, there seems to be a trend toward a classification of the results in terms of efficiency of the preparation method (milling, sawing or sanding). This is particularly true for the strength in Fig. 14. This could be attributed to the larger influence of the defects over the test results when smaller specimens are used (the defects induced along the coupon edge during preparation being proportionally larger with respect to the cross-section of the specimen). Globally, Fig. 14 suggests that the samples obtained by milling have the highest tensile properties, while samples obtained by sanding exhibit the lowest ones. This is quite surprising considering that Fig. 11 suggests a more uniform surface for the sanded coupon, which should normally produce a greater tensile strength. It is possible that the thermal degradation of the matrix induced by dry sanding has more influence on the composite strength, by deteriorating the matrix deeper in the specimen as compared with the defects induced by the other cutting methods. More evaluations will be needed to clarify these aspects. Nonetheless, it appears that combining mechanical testing with NDT techniques, by using appropriate tensile specimens of tailored widths, could be useful for evaluating different cutting methods for critical composite parts. This is supported by the results of Fig. 15 for the modulus of elasticity. A modulus drop is observed for all preparation methods when going from 12.7 mm to 6.35 mm, without evident classification regarding their influence however. Again, because the defects cover a higher proportion of the specimen cross-section for thin coupons, they could alter the composite over a relatively larger portion of the specimen to reduce the overall stiffness. The interlaminar stresses that develop at the edge of a quasi-isotropic tensile specimen (see [26, 27]) are another aspect to consider in this case. For thin coupons and in the presence of edge defects, these stresses are spread over a larger portion of the specimen cross-section, and could affect the

**Table 5** Mechanical properties for sanded samples

Sanding	Width	19.05 mm	12.7 mm	6.35 mm
Strength (MPa)	Mean	535.76	553.07	512.50
	Standard deviation	40.34	3.45	9.54
	Number of measures	3	2	2
Modulus of elasticity (GPa)	Mean	35.42	35.39	33.72
	Standard deviation	1.00	1.41	1.13
	Number of measures	6	6	8

**Table 6** Mechanical properties for abrasive diamond saw cutting

Abrasive saw	Width	19.05 mm	12.7 mm	6.35 mm
Strength (MPa)	Mean	575.68	564.32	541.37
	Standard deviation	13.44	10.40	4.93
	Number of measures	2	5	3
Modulus of elasticity (GPa)	Mean	36.09	36.05	33.35
	Standard deviation	0.88	1.41	1.50
	Number of measures	6	6	7

global stiffness by interacting with the defects. Globally, these results suggest that where the thermal degradation and very small defects are not detected by the NDT techniques because the cracks are too small, or simply absent, considering the matrix smearing, their effects could be evaluated by using appropriate tensile tests in support of the NDT results. Combining NDT evaluations with well-designed destructive tests (made from coupons taken over extra materials intentionally left around a part), is an interesting avenue to qualify the machining quality of critical composite parts. As shown in the present work, because NDT methods cannot detect all the defects in a part, especially the small trimming defects located along side edges, it is important to look at alternatives to efficiently quantify these defects.

**Table 7** Mechanical properties for samples obtained by milling

Milling	Width	19.05 mm	12.7 mm	6.35 mm
Strength (MPa)	Mean	569.57	562.83	563.88
	Standard deviation	23.98	15.66	14.66
	Number of measures	5	7	4
Modulus of elasticity (GPa)	Mean	36.44	36.25	34.09
	Standard deviation	1.37	1.13	1.00
	Number of measures	8	8	7

**Fig. 14** Variation of the average strength as a function of the samples width

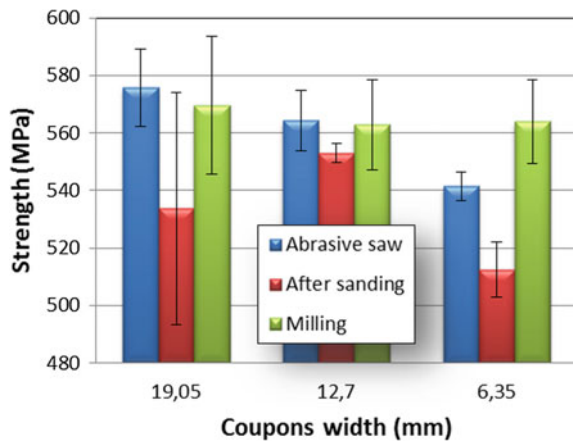
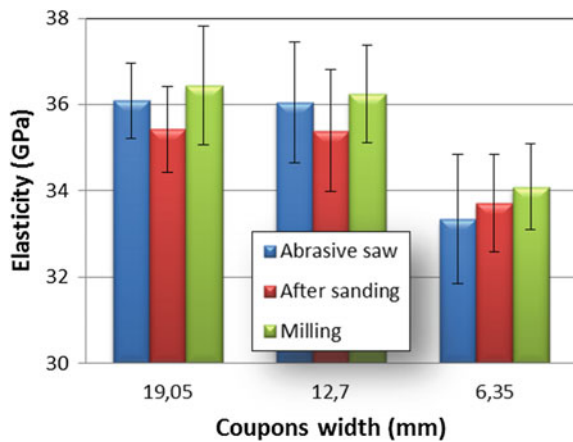


**Fig. 15** Variation of the modulus of elasticity as a function of the samples width



## 4 Conclusions

In this work, the extent of damage induced by the trimming operation in carbon/epoxy composites was assessed using the ultrasonic testing method and mechanical testing. Globally, the following conclusions can be drawn:

1. It appears that the ultrasonic technique is able to detect and quantify the extent of damage, as shallow as a fraction of a millimeter, caused by the milling operation of a part.
2. The machining damages detected by UT seem to appear mainly as delaminations at the surface of the laminate due to the absence of support from adjacent plies. The extent of damage appears to be related to the orientation of the fibers with respect to the cutting direction. However, it was not possible to reach a conclusion on the effect of the machining parameters on the extent of damage; no clear trend was observed for the tested machining parameters.
3. Scanning electron microscope observations revealed that the milling operation creates craters and microcracks in  $-45^\circ$  plies and thermal degradation of the matrix in  $45$  and  $90^\circ$  plies.
4. Globally, the coupons obtained by dry sanding showed lower strength and modulus than those obtained by milling and sawing. Even if the surface was smoother for sanded specimens, matrix smearing and thermal degradation was observed under microscope, so it is possible that such matrix damages affect the mechanical properties more than the roughness observed in the other types of specimens.

In future works, more tests will be needed to clarify the effect of the width of tensile specimens on its mechanical properties. Smaller widths should be tested and numerical models could be prepared to evaluate how the coupon geometry could be optimized to develop an efficient test in support to NDT tests for the evaluation of edge defects in composite parts.

**Acknowledgements** Thanks to the Natural Sciences and Engineering Research Council of Canada (NSERC), NanoQuébec and MITACS for their financial support. This work was also funded by the Consortium for Research and Innovation in Aerospace in Québec (CRIAQ) and its partners, the Natural Sciences and Engineering Research Council of Canada (NSERC), MITACS, Bombardier Aerospace, Avior Integrated Products, Delastek and AV&R Vision & Robotics.

## References

1. Fahr, A.: Ultrasonic C-scan inspection of composite materials. *Eng. J. Q. Univ.* **5**, 201–222 (1992)
2. Baker, A., Dutton, S., Kelly, D.: *Composite Materials for Aircraft Structures*, 2nd edn, pp. 403–433. American Institute of Aeronautics and Astronautics, Reston, VA (2004)
3. Scarponi, C., Briotti, G.: Ultrasonic detection of delaminations on composite materials. *J. Reinf. Plast. Compos.* **16**, 768–790 (1997)
4. Adams, R.D., Cawley, P.: A review of defect types and nondestructive testing techniques for composites and bonded joints. *NDT Int.* **21**, 208–222 (1988)



5. Ahmad, J.: *Machining of Polymer Composites*. Springer, Boston, MA (2009)
6. Ramulu, M.: Machining and surface integrity of fibre-reinforced plastic composites. *Sadhana Acad. Proc. Eng. Sci.* **22**, 449–472 (1997)
7. Wang, D.H., Ramulu, M., Arola, D.: Orthogonal cutting mechanisms of graphite/epoxy composite. Part I: unidirectional laminate. *Int. J. Mach. Tools. Manuf.* **35**, 1623–1638 (1995)
8. Wang, D.H., Ramulu, M., Arola, D.: Orthogonal cutting mechanisms of graphite/epoxy composite. Part II: multi-directional laminate. *Int. J. Mach. Tools. Manuf.* **35**, 1639–1648 (1995)
9. Bhatnagar, N., Nayak, D., Singh, I., Chouhan, H., Mahajan, P.: Determination of machining-induced damage characteristics of fiber reinforced plastic composite laminates. *Mater. Manuf. Processes* **19**, 1009–1023 (2004)
10. Colligan, K., Ramulu, M.: Delamination in surface plies of graphite/epoxy caused by edge trimming process. In: Srivatsan, T.S., Chandrashekhar, S. (eds.) *Processing and Manufacturing of Composite Materials*. ASME Prod. Eng. Div. **49**, 113–126 (1991)
11. Guegan, P., Lemaitre, F., Hamann, J.: Contribution à l'usinage des matériaux composites. *Iframer* **1080**, 470–479 (1992)
12. Sadat, A.B.: Delamination and other types of damage of graphite/epoxy composite caused by machining. *ASME Appl. Mech. Div.* **208**, 41–52 (1995)
13. Sendekyj, G.P.: Effects of defects in composite structures. In: Noor, A.K., Shuart, M.J., Starnes Jr., J.H., Williams, J.G. (eds.) *Failure Analysis and Mechanisms of Failure of Fibrous Composite Structures*. NASA Conf. Pub. **2278**, 305–312 (1983)
14. Ghidossi, P., El Mansori, M., Pierron, F.: Edge machining effects on the failure of polymer matrix composite coupons. *Compos. A Appl. Sci. Manuf.* **35**, 989–999 (2004)
15. Avdelidis, N.P., Almond, D.P., Dobbinson, A., Hawtin, B.C., Ibarra-Castaneda, C., Maldague, X.: Aircraft composites assessment by means of transient thermal NDT. *Prog. Aerosp. Sci.* **40**, 143–162 (2004)
16. Tsao, C.C., Hocheng, H.: Taguchi analysis of delamination associated with various drill bits in drilling of composite material. *Int. J. Mach. Tools Manuf.* **44**, 1085–1090 (2004)
17. Howarth, S.G., Strong, A.B.: Edge effects with waterjet and laser beam cutting of advanced composite materials. In: Janicki, G., Bailey, V., Schjelderup, H. (eds.) *Advanced Materials—The Challenge for the Next Decade*. Natl. SAMPE Symp. Exhib. Proc. **35**, 1684–1697 (1990)
18. Ghidossi, P., Mansori, M.E., Pierron, F.: Influence of specimen preparation by machining on the failure of polymer matrix off-axis tensile coupons. *Compos. Sci. Technol.* **66**, 1857–1872 (2006)
19. Ramulu, M., Arola, D., Colligan, K.: Preliminary investigation of machining effects on the surface integrity of fiber reinforced plastics. In: Faghri, A., Yaghoubi, M.A. (eds.) *Proceedings of the 2nd Biennial European Joint Conference on Engineering Systems Design and Analysis*. ASME Petro. Div. **64**, 93–101 (1994)
20. Arola, D., Ramulu, M.: Machining-induced surface texture effects on the flexural properties of a graphite/epoxy laminate. *Composites* **25**, 822–834 (1994)
21. Arola, D., Ramulu, M.: Net-shape machining and the process-dependent failure of fiber-reinforced plastics under static loads. *J. Compos. Technol. Res.* **20**, 210–220 (1998)
22. Arola, D., Ramulu, M.: Net shape manufacturing and the performance of polymer composites under dynamic loads. *Exp. Mech.* **37**, 379–385 (1997)
23. Arola, D., Ramulu, M.: An examination of the effects from surface texture on the strength of fiber reinforced plastics. *J. Compos. Mater.* **33**, 102–123 (1999)
24. Arola, D., Williams, C.L.: Surface texture, fatigue, and the reduction in stiffness of fiber reinforced plastics. *J. Eng. Mater. Technol.* **124**, 160–166 (2002)
25. Zaghbani, I., Chatelain, J.F., Songmene, V., Bérubé, S., Atarsia, A.: A comprehensive analysis of cutting forces during routing of multilayer carbon fiber-reinforced polymer laminates. *J. Compos. Mater.* **46**, 1955–1971 (2012)

26. O'Higgins, R.M., McCarthy, M.A., McCarthy, C.T.: Comparison of open hole tension characteristics of high strength glass and carbon fibre-reinforced composite materials. *Compos. Sci. Technol.* **68**, 2770–2778 (2008)
27. Aymerich, F., Fould, M.S.: Response of notched carbon/PEEK and carbon/epoxy laminates subjected to tension fatigue loading. *Fatigue Fract. Eng. Mater. Struct.* **23**, 675–683 (2000)

# The Effect of Machining on Surface Integrity of Gamma Titanium Aluminides Using Different Cemented Carbide Tools



S. D. Castellanos, J. Lino Alves, R. Neto and A. Cavaleiro

**Abstract** Gamma titanium aluminides are a new generation of light materials that compete with nickel or cobalt superalloys, when it comes to the manufacture of very high resistance requirement components such as low and high-pressure compressor blades, in the case of aeronautical applications. Machining is a process used to manufacture such components. However, in available literature, the specific information regarding machining performance of gamma titanium aluminides is scarce. The present research focused on the comparative study of the performance of coated tungsten carbide (WC-Co) inserts with round geometry in face milling operation of a gamma titanium aluminide alloy (Ti-48Al-2Nb-0.7Cr-0.3Si). Six different cutting-inserts in a combination of three different compositions of WC-Co substrates and two edge-geometries (XL and XM) recommended for conventional titanium alloys were tested. Milling experiments were carried out for different cutting speed, depth of cut and chip thickness. The results are discussed in terms of the correlation between cutting parameters with cutting force, surface roughness and work-hardening. The study showed that chip thickness, significantly affected the machined surface integrity in related with the tool insert geometry. Insert type C-XL showed better performance for cutting speed to 45 m/min, while inserts types A-XL and B-XM showed better behavior for cutting speed to 70 m/min.

**Keywords** Machinability · Gamma titanium aluminides · Surface integrity  
Coated tungsten carbide tools

---

S. D. Castellanos (✉) · J. Lino Alves · R. Neto · A. Cavaleiro  
Faculdade de Engenharia da Universidade do Porto, INEGI, Rua Dr. Roberto Frias, 4200-465  
Porto, Portugal  
e-mail: [sdcastellanos@espe.edu.ec](mailto:sdcastellanos@espe.edu.ec)

S. D. Castellanos  
Universidad de las Fuerzas Armadas - ESPE, Av. General Rumiñahui, P.O. Box 171-5-231B,  
Sangolquí, Ecuador

© Springer Nature Switzerland AG 2019  
L. F. M. da Silva (ed.), *Materials Design and Applications II*, Advanced  
Structured Materials 98, [https://doi.org/10.1007/978-3-030-02257-0\\_26](https://doi.org/10.1007/978-3-030-02257-0_26)

## 1 Introduction

Machining of titanium aluminide-based alloys is considered by several authors [1–5] as a challenge. This is due to their mechanical properties (ductility, specific strength, low thermal conductivity and mechanical resistance at elevated temperatures) which leads to an unusual response pattern to the cutting process causing surface and sub-surface defects. The main drawbacks on the workpiece surface (feed marks, smearing, tearing surface, surface cracks, lay patterns) are mainly due to the uncertain selection of machining parameters (cutting parameters, tool material, tool geometry, cutting environment) [6–9]. Several authors [8, 10–14] agree that the lack of studies on the machining performance of titanium aluminides-based alloys (cutting parameters, optimization of tool geometry and material) is still one of the main factors limiting the growth of their industrial application.

Cutting tools and cutting parameters are the most important factor affecting the machining operation. The machining of titanium aluminides induced thermal and mechanical effects on the cutting tool that can affect its working life [15–17]. The combination of high cutting force and high temperature in the cutting area during the machining of these materials causes the tool edges to plastically deform or break by chipping. Also, it has been shown that from the perspective of surface integrity and productivity in the machining of titanium aluminides it is more difficult to optimize the performance of cutting tools [18, 19].

In the machining of titanium aluminides, cemented tungsten carbide tools are the most studied by researchers. Several types of tool wear mechanisms were reported during the cutting process [13, 20–22]. However, coated or uncoated WC cutting tools are the primary choice for machining titanium aluminides, carbide tools use single or multi layers coating of Aluminum Oxide ( $Al_2O_3$ ), Titanium Nitride (TiN), Titanium Carbide (TiC), Titanium Carbo-Nitride (TiCN) or Titanium Aluminum Nitride (TiAlN) in order to protect the tool from wear and improve tool performance.

There are several defects that affect the quality of surface integrity in titanium aluminides, the main ones being cracks, lamellar deformation, work-hardening, smearing between other. These types of defects have been observed by different researchers [3, 18, 23–25] and are affected by the characteristics of the cutting tool and the cutting parameters. Surfaces cracking showed proportional to the flank wear on the cutting tool and influenced by the low ductility of these alloys [5]. Low thermal conductivity leads to increase temperatures on the cutting edge and promote the flank wear on the tool's cutting edge.

On the other hand, several studies on the integrity of the machined surface have been carried out using cemented tungsten carbide (WC) tools with and without coating [15, 18, 19, 22, 25, 26]. Based on these investigations it is observed that surfaces produced with WC tools show a greater tendency to surface cracking compared to the use of other tools such as polycrystalline cubic boron nitride (PCBN), polycrystalline diamond (PCD) and cubic boron nitride (CBN) [1].

The main disadvantages of the microstructure by the machining process in titanium aluminides is the plastic lamellar deformation. This behavior is indicative of

the ability of this material to keep the mechanical strength at high temperatures and low ductility [1, 27]. Researchers such as Mantle, Aspinwall and their research teams [5, 19, 23, 24] have studied these effects and demonstrated that several factors such as cutting parameters (cutting speed, feed rate and cutting depth), tool parameters (geometry, material, coating, wear) and part parameters (material composition, grain size) influence the tendency of plastic lamellar deformation in these materials.

On the other hand, in the machining of titanium aluminides reduction in tool wear decrease the depth of surface alterations (from 30 to 10  $\mu\text{m}$ ) [3]. This indicates that the cutting conditions are important factors and that high temperatures and tool wear are also important factors for lamellar plastic deformation.

The work-hardening tendency is strongly influenced by the low deformation capacity of titanium aluminides alloys. This surface hardness can increase up to 65% of its initial hardness (bulk material), with a depth of up to 50  $\mu\text{m}$  after the first cutting pass [24]. Based on the results analysed in most of the conducted research [15, 24, 28, 29], it is possible to conclude that there is no evidence hardened layers greater than 250  $\mu\text{m}$ , and peak values reached at a maximum depth of 50  $\mu\text{m}$  and it is observed that the thermal softening effect is less than the work-hardening effect in these alloys. It is for this that the effect of the surface hardening is improving by the cutting tool.

Machinability of titanium aluminides can be researched from multiple approaches and cutting forces values are one of the main data that provide comprehensive information about the machining process, thus contributing to better understanding of the machinability of these alloys. It has been reported by some publications [21, 30] that the cutting forces in machining titanium aluminide-based alloys are considerably higher than in other titanium-based alloys such as Ti-6Al-4V ( $F_a = +200\%$ ,  $F_r = +200\%$ , and  $F_t = +130\%$ ) or Ti-6Al-2Zr-1Mo-1V ( $F_a = +200\%$ ,  $F_r = 190\%$  and  $F_t = 180\%$ ). The experimental results show that the energy used for machining titanium aluminides based alloys is approximate ~5 times higher than that of conventional titanium alloys [11, 16, 31].

For the improvement of the surface integrity of workpieces, an analysis of the material cutting process is the starting point for an adequate study of cutting tools and cutting parameters to obtain the expected results.

In order to study the machinability of gamma titanium aluminide alloys, the aims of this paper were to investigate the performance of six coated cemented carbide tools with round geometry under a range of cutting parameters (cutting speed, depth of cut and chip thickness) for face milling operations. Milling experiments are presented and discussed in terms of cutting forces, work-hardening, and roughness.

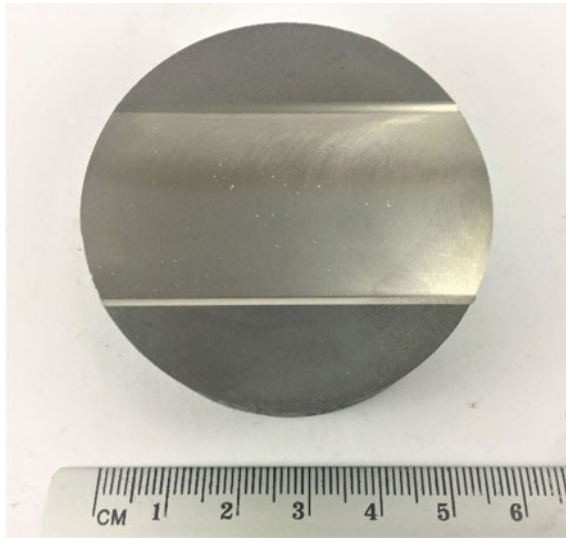


**Fig. 1** Cutted EDM and machined sample

## 2 Experimental Procedure

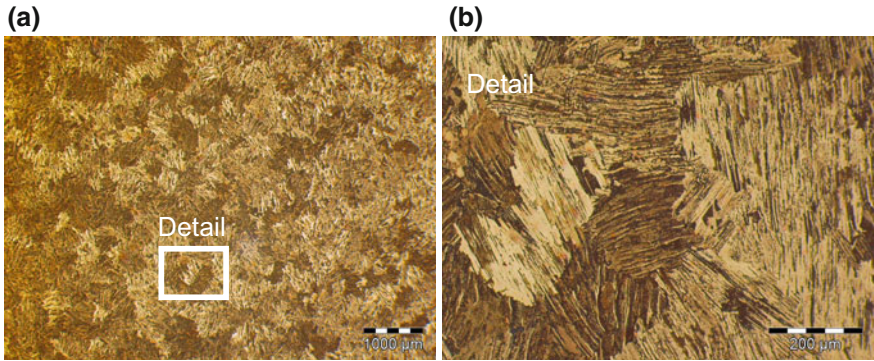
### 2.1 Workpiece Material

The material used in this work is a  $\gamma$ -titanium aluminide (Ti-48Al-2Nb-0.7Cr-0.3Si at.%) produced by GfE Metalle und Materialien GmbH (Nuremberg, Germany) via VAR skull melting. Samples were cut out of a 55 mm diameter bar using a (machine name) electrical discharge wire machine (EDWN). Also, axial and radial specimens of the machined samples were cut to perform the metallographic analysis. The machined and non-machined sample is illustrated in Fig. 1.

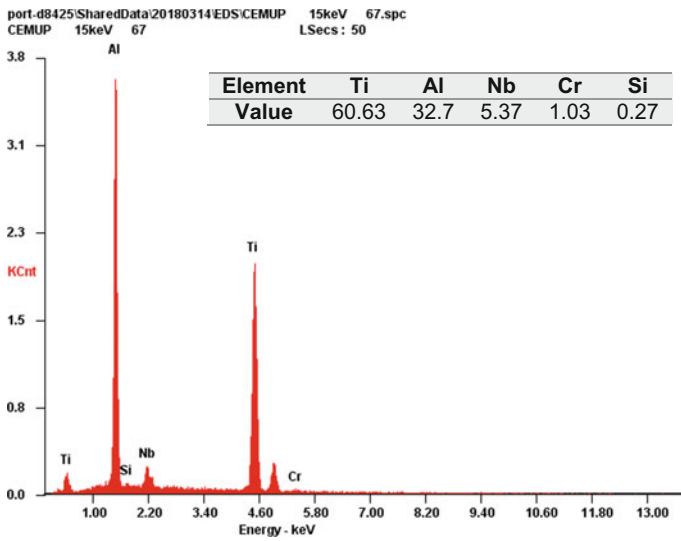
The metallographic test samples were hot mounted in bakelite in a Struers Prontopress-2 mounting press, ground and polished in a semiautomatic polishing machine at 150 rpm (Struers Planopol-3). The process began with sandpaper numbers 80, 320, 600, 1000 and 1200, and polished in a cloth with 0.01  $\mu\text{m}$  alumina and a solution of hydrogen peroxide ( $\text{H}_2\text{O}_2$ ). Polished samples were chemically etched with Kroll reagent (1 ml of hydrofluoric acid, 3 ml of nitric acid and 500 ml of water).

The microstructural analysis was performed using an optical microscope Zeiss Axiophot. Characteristic images taken at 150X and 23X (Fig. 2) reveals a near gamma lamellar microstructure consisting of  $\gamma$  (TiAl) and  $\alpha_2$  ( $\text{Ti}_3\text{Al}$ )- $\gamma$  (TiAl) phases with a different orientation of lamellae. No significant alterations of the microstructure were detected both in the axial than in the radial direction of the samples.

The chemical composition of the alloy is listed in Fig. 3, while the main properties at room temperature are reported in Table 1. Furthermore, a tensile test was performed



**Fig. 2** Microstructure of  $\gamma$ -titanium aluminide (Ti-48Al-2Nb-2Cr-0.3Si at.%)

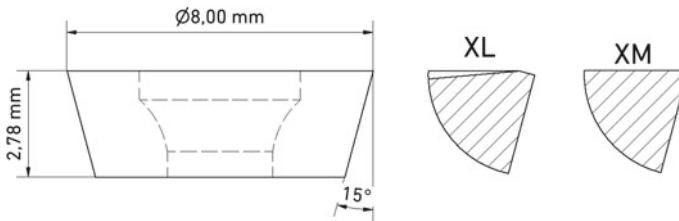


**Fig. 3** Chemical composition of workpiece material (wt%)

in accordance with the EN 10002-1 standard, by means of a MTS 810 testing machine and the elongation was measured with a mechanical extensometer MTS 634.25F-24. Specimens of 3 mm in thickness were cut out from a material bar. The tests were conducted at a test speed of 0.25 mm/min until a tensile failure occurred. Workpiece hardness was measured before machining test, by a Wolpert Dia Testor 2Rc universal hardness tester, according to HV40 test condition, the hardness showed an average hardness of 275 HV40 (with a standard deviation of 5 HV40).

**Table 1** Mechanical properties of tested titanium aluminide [32]

Mechanical properties	Value
Density ( $\text{g/cm}^3$ )	3.95
Hardness (HV10)	285
Young Modulus at RT (GPa)	155
Young Modulus at 800 °C (GPa)	102
Ultimate tensile strength (MPa)	530
0, 2 Yield strength (MPa)	464
Melting temperature (°C)	1605

**Fig. 4** Cutting insert and edge geometries

## 2.2 Cutting Tool Material

In order to investigate the influence of the cutting tool on the workpiece surface on  $\gamma$ -TiAl, comparative trials were carried out with a fine grain (grain size  $< 1 \mu\text{m}$ ) carbide insert. Tool selection was based on the previous researches [24, 29, 33, 34] and the recommendations of the tool manufacturers for titanium alloys. An indexable milling cutter for face milling operation with double positive geometry and  $\varnothing 35 \text{ mm}$  for round cutting inserts were used in this study. Round cutting inserts with  $\varnothing 8 \text{ mm}$  of two different cutting-edge geometries (Fig. 4) and three substrate cemented carbide compositions are analyzed in the present study. Carbide insert characteristics are shown in Table 2.

## 2.3 Machining Tests

Machining tests were performed on a five-axis CNC milling machine DeckelMaho Mori Seiki DMU 60 eVo, with a Heidenhain iTNC530 controller with a maximum spindle speed of 18.000 RPM, drive power of 25 HP and 50 m/min of maximum feed rate. The experimental trial uses finishing cutting parameters and high-pressure coolant (HPC) lubrication conditions with 6% emulsion of AVILUB METACOOOL BFH oil miscible in water supplied at a 70 bar of pressure through spindle coolant



**Table 2** Cutting insert specifications (Tool geometry and materials)

Designation	A-XL	A-XM	B-XL	B-XM	C-XL	C-XM
<i>Substrate characteristics</i>						
Hardness (HV)	~1900	~1900	~1650	~1650	~1550	~1550
Coating	PVD (Ti, Al) N <sub>2</sub>					
<i>Geometry characteristics</i>						
Rake angle	5°	0°	5°	0°	5°	0°
Rake land angle	15°	0°	15°	0°	15°	0°
Clearance angle	15°					

**Table 3** Cutting parameters for the experimental work

Taguchi orthogonal array L4			
Test	Cutting speed (m/min)	Axial depth (mm)	Hex (mm)
Trial 1	70	0.3	0.03
Trial 2	70	0.5	0.04
Trial 3	45	0.3	0.04
Trial 4	45	0.5	0.03

supply. These cutting conditions were chosen according to previous research studies and recommendations of the tool’s manufacturers [3, 9, 11, 16, 19, 35, 36].

Taguchi’ DOE approach was adopted to reduce the number of trials. The experimentation was based on Taguchi’s L4 orthogonal array and was performed by each cutting insert type. Test matrix with three factors and two levels of cutting parameters with four trials by cutting inserts are being considered. Three repetitions of each experimental trial have been performed, and the tests were executed following a random order. The specific cutting parameters and orthogonal array are given in Table 3. The radial depth of cut was kept constant (full engagement arc). Collected data were statistically evaluated using the analysis of means which was performed using Minitab software.

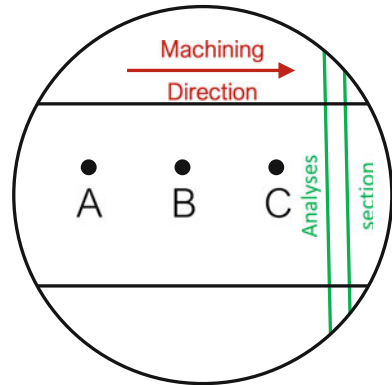
### 2.4 Cutting Force and Surface Integrity Testing

Cutting force tests were carried out by a four-component piezo-electric dynamometer Kistler 9272 mounted on the worktable and connected to a charge amplifier Kistler 5070A. The amplified cutting forces signal was acquired in a computer with an Advantech USB 4750A data acquisition card capable of the testing rate at 800 Hz. Figure 5 shows the machining setup of the experiment.



**Fig. 5** Experimental setup

**Fig. 6** Machining workpiece cutting section used for the analysis



The surface roughness was measured by A 3D digital MICROSCOPE Bruker Nplex, with a standard lens of 10X, with an optical resolution of  $0.9 \mu\text{m}$ . Sampling surface area of measuring was  $250 \mu\text{m} \times 250 \mu\text{m}$ . Three zones 130 mm from each other along the milling direction on the surface were selected to obtain the roughness average (Points A, B, and C in Fig. 6). Surface hardness was measured by the same hardness tester used to measure the bulk material, according to HV40 test condition. Indentations were performed next to roughness measurement area. Surface hardness values showed an average of these three points.

### 3 Results and Discussions

The results and discussion are focused on the workpiece surface integrity on the finishing procedures when milling Ti-48Al-2Nb-2Cr-0.3Si with six different cutting tools. The results obtained by each insert are cutting forces, work-hardening, roughness and surface defects.

### 3.1 Cutting Forces and Surface Integrity Analysis

The discussion in this study is focused on the effect of cutting parameters (Cutting speed, depth of cut and chip thickness) in the cutting forces and the surface integrity when milling titanium aluminides. The test was performed on a workpiece with no surface discontinuities to avoid the correlation of the cutting forces with the depth of cut variation. Moreover, these tests have been carried out by full engagement operation in order to obtain a complete cutting force waves and continuous cutting-edge contact for analysis purposes. In all trials, a full new insert was used.

The tests are conducted using a single cutting insert to avoid the effect of runout. The feed rate per revolution to reflect the single insert cutting was adapted in the NC program. Also, toolpath trajectory to prevent higher cutting forces at the cutting entrance tool wear and vibration have been programmed. The comparative analysis of the cutting forces was conducted at a zone on 40 mm from the start cutting point (Fig. 7). The results indicate that in general terms the Fz force (axial force) is the dominant force component, being approximate ~1.5 and ~1.7 times that of the Fx and Fy, respectively. since the variation between Fz, Fx and Fy follow the similar trend in all the tests. The discussion about cutting forces was focused on resultant cutting force (Fr).

#### 3.1.1 Influence of the Cutting Speed

Cutting speed is the main cutting parameter. Considering the low ductility and brittle nature of titanium aluminides, was expectable that the cutting inserts with neutral XM geometry would produce higher cutting forces than the XL geometry. However,

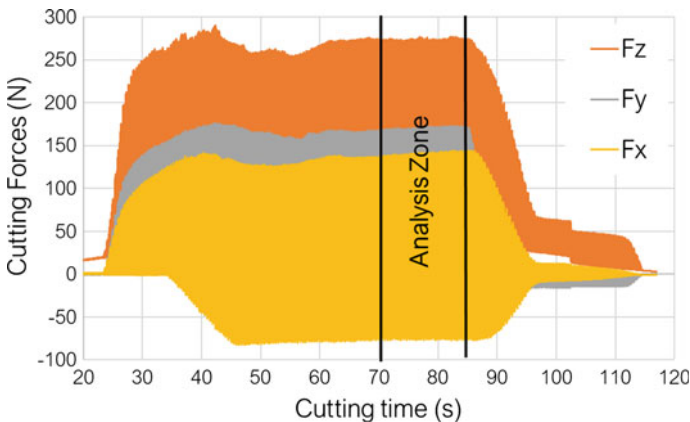


**Fig. 7** Cutting forces profile on machining of RNT 650 at  $V_c = 70$  m/min,  $a_p = 0.5$  mm and  $hex = 0.04$  mm with A-XL cutting insert

**Table 4** Increase of the cutting forces according to the depth of cut variation

Cutting inserts	Hardness of cutting insert (HV40)	Cutting forces with Vc = 45 m/min	Cutting forces with Vc = 70 m/min	Cutting force variation	
		(N)	(N)	(N)	(%)
A-XL	1900	355.00	354.00	-1.00	0.3
A-XM	1900	381.00	392.00	11.00	2.9
B-XL	1650	364.00	409.00	45.00	12.4
B-XM	1650	351.00	350.00	-1.00	0.3
C-XL	1550	318.00	564.00	246.00	77.4
C-XM	1550	384.00	845.00	461.00	120.1

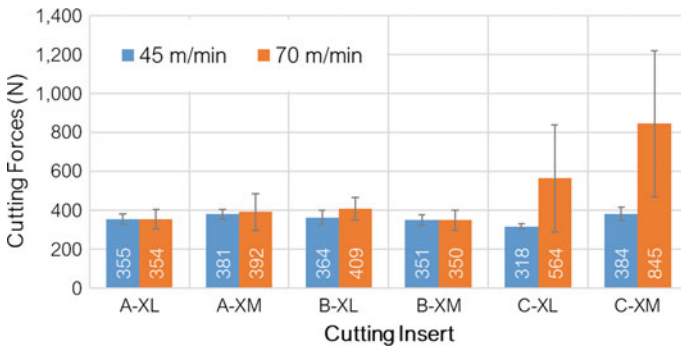


**Fig. 8** Effect of the cutting speed in the resultant cutting force

a non-significant difference was found between both geometries mainly for A and B insert types (Table 4).

The effect of variation of the cutting speed on the cutting forces for each individual insert is shown in Fig. 8. As can be seen for cutting inserts B, cutting forces for XL geometry are 6.3% higher than XM, while that with A inserts, the cutting forces were 1.6% lower for the XL geometry. This behavior is attributed to the combination of the substrate properties (composition, hardness) and the cutting-edge geometries. Also, C cutting inserts show a similar performance to A insert. This allows us to determine a tendency of the XL geometry to present lower cutting forces. For B cutting inserts, it is not possible to define a similar trend than for A and C inserts.

The considerable difference showed for C cutting inserts at cutting speed of 70 m/min was caused by early wear under this cutting condition. It has been demonstrated that for C-XM insert use of cutting speed of 70 m/min was catastrophic regardless of the depth of cut or chip thickness selected. However, for C-XL insert, wear was only observed after 40 s of cutting using cutting conditions of Vc = 70 m/min, ap of 0.5 mm and hex = 0.04 mm, (Fig. 9).

On the other hand, cutting speed of 45 m/min regardless of the depth of cut or chip thickness was the best performance for all the inserts in terms of cutting forces.

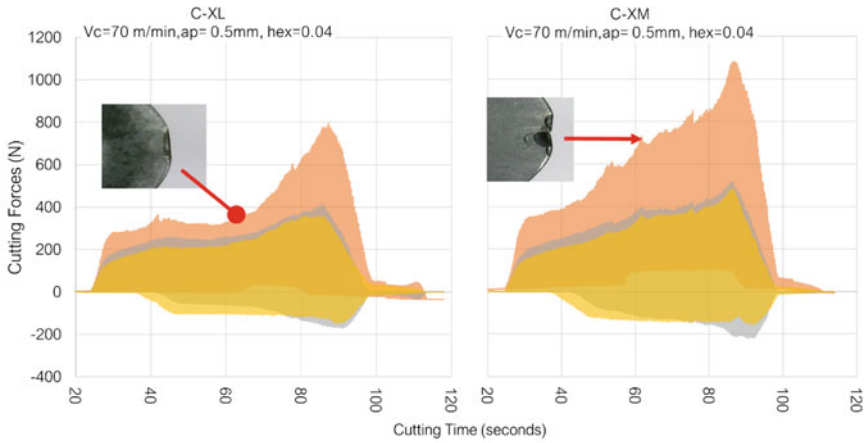


**Fig. 9** Cutting forces profiles for cutting insert C-XL and C-XM

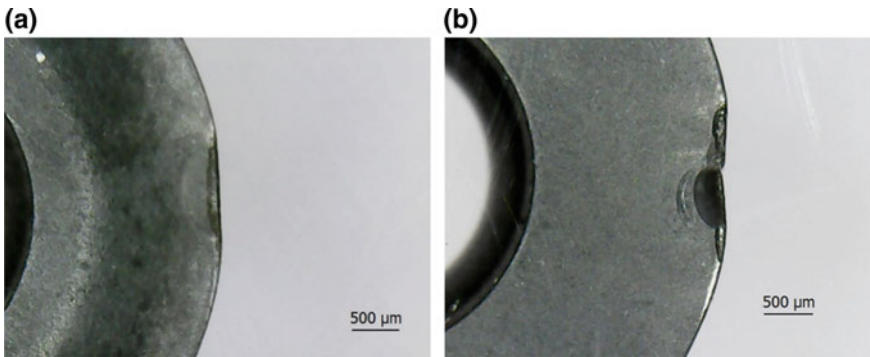


**Fig. 10** Cutting inserts. **a** C-XL geometry and **b** C-XM geometry

On the other hand, wear on the cutting edge of C cutting inserts demonstrate the characteristic abrasive wear caused when machining titanium aluminides [13]. Cutting forces profile for C-XM cutting insert has a constant growth (Fig. 9) indicates the progressive tool wear, which leading the cutting-edge fracture (Fig. 10b). While for XL geometry at  $V_c = 70$  m/min,  $a_p = 0.5$  and hex 0.04 mm the flank wear after 35 s was of  $50 \mu\text{m}$  (Fig. 10a). On A and B cutting inserts with both geometries, no significant wear (less than  $10 \mu\text{m}$ ) was observed.

In terms of surface integrity, all machined surface showed a hardened layer in response to the chip cutting process, demonstrating work hardening tendency. Figure 11 shows the hardness increment according to the cutting forces. A hardness increment between 29 to 39 HV40 are present for cutting forces from 300 to 400 N. Likewise, it can be observed that work hardening is sensitive to the variation of cutting forces.

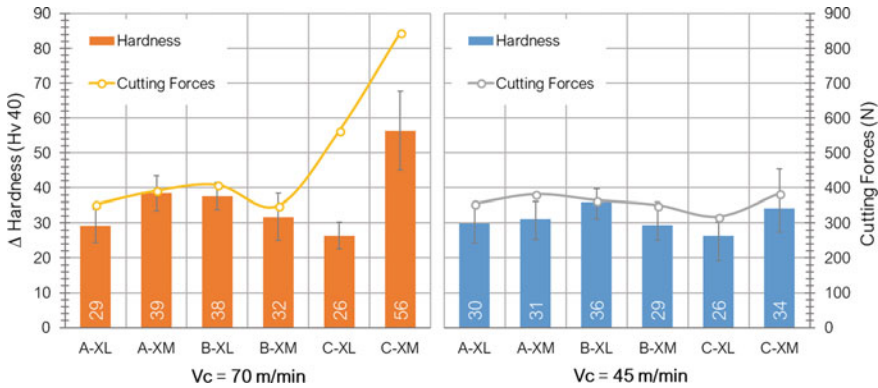


**Fig. 11** Surface hardness increment according to cutting forces and cutting speed on TiAl alloy

Where the sensitivity of the material by the fracture of the cutting edge of the C-XM insert is highlighted, which causes a greater increase in surface hardness. This is probably due to the greater deformation that would occur in the cutting area caused by the notches on the cutting edge. However, an unexpected result was caused by the C-XL insert, which showed a lower increase in hardness, even in the presence of cutting-edge wear. This behavior could be indicated by the decrease in the depth of cut caused by the cutting-edge wear that affects the depth of the surface work hardening.

With regard to the geometries, there are no significant differences that allow us to conclude an effect of these geometries for work hardening in this range of cutting conditions.

For surface roughness, the results are presented in Fig. 12. A decrease of ~17.5% in the surface roughness was observed when the cutting speed increase 55%. All surface roughness values measured for the experimental trials were less than 0.450  $\mu\text{m}$ , including those obtained with worn inserts (C-XL and C-XM) at cutting speed of 70 m/min. Demonstrating surface roughness values suitable for applications with demanding surface specifications [1].

Use of round geometry (nose radius 4 mm) shows that it has advantages for machined surface of titanium aluminides thanks to the larger contact area. With reference to the effect of both cutting speed and nose radius, it is important to note that the values obtained by cutting inserts A-XL and B-XM are similar to those obtained by authors such as [3, 22, 30], which reports average roughness values of 0.250  $\mu\text{m}$  at cutting speeds of 120 m/min in milling and turning operations for some cases also with cryogenic cooling conditions. Considering the performance of these two inserts, it would be expected that at cutting speeds higher than 70 m/min lower roughness values could be obtained.

On the other hand, XL and XM cutting edge geometries improve surface roughness by 20% and 15% respectively, when cutting speed increases from 40 m/min to

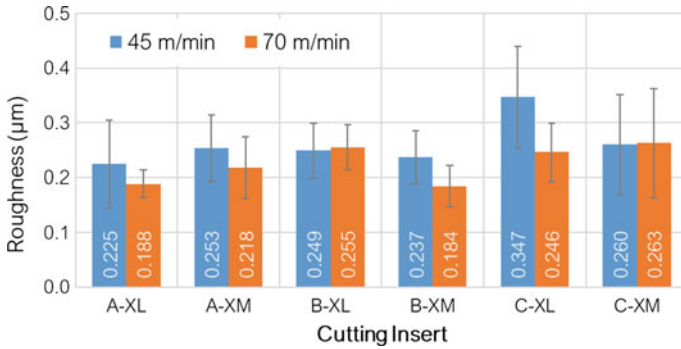


Fig. 12 Effect of cutting speed in surface roughness (in feed directions)

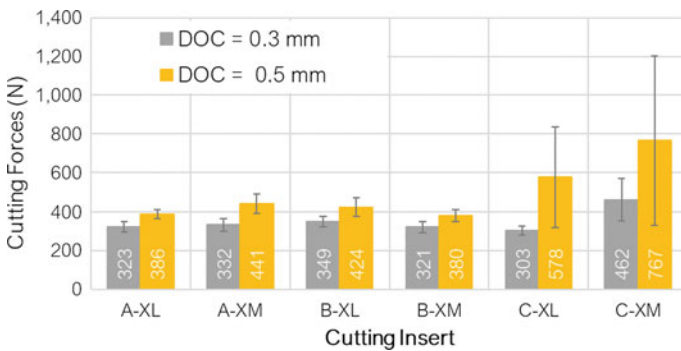


Fig. 13 Effect of depth of cut in the resultant cutting forces

70 m/min. Based on this difference, it can be concluded that cutting inserts with XL geometry provide slightly better performance than XM.

### 3.1.2 Influence of the Depth of Cut

The depth of cut is usually the most influential factor for machining of any material. This is due to the effect it has on the removal rate of material. For cutters with round cutting inserts, the variation of the cutting depth has a different performance than straight-edged inserts. This is due to the orientation of the cutting forces. A deeper depth of cut for these inserts increases the angle of entry ( $K_r$ ), orienting the cutting forces towards the spindle and improving the stability of the cutting process. In addition, the cutting depth in this round geometry varies the effective cutting diameter ( $D_{cap}$ ) that modifies the material removal rate. Figure 13 shows the results for depth of cut.

The data obtained indicate an expected reaction, where the greater cutting depth increases the cutting forces. For this case, as well as in the analysis of cutting speeds,

**Table 5** Increase of the cutting forces according to the depth of cut variation

Cutting inserts	Hardness of cutting insert (HV40)	Cutting forces with DOC 0.3 mm	Cutting forces with DOC 0.5 mm	Cutting force increase	
		(N)	(N)	(N)	(%)
AXL	1900	322.62	386.46	63.83	19.8
AXM	1900	332.36	440.94	108.58	32.7
BXL	1650	348.73	424.35	75.63	21.7
BXM	1650	320.52	379.93	59.41	18.5
CXL	1550	303.48	578.41	274.93	90.6
CXM	1550	461.78	766.61	304.84	66.0

the inserts with substrates A and C indicate lower cutting forces with XL geometry. Whereas for XM geometry the B substrate caused the lowest resultant cutting force. Table 5 shows the increases in cutting force in response to the increase in the depth of cut (60%).

As can be appreciated, the C cutting inserts were more sensitive to this variation as a result of their hardness (1550 HV). However, an increase of 100 HV and 350 HV in hardness for the B and A cutting insert respectively, substantially improved the performance of the cutting tools. This response of the material to the hardness of the inserts suggests that the connection between the cutting-edge geometry and the material has a strong influence on cutting forces [37]. As can be seen from the behavior of the A-XL and B-XM inserts.

Nevertheless, the higher hardness of the A cutting inserts does not exhibit the best performance of the experimentation. It was the A-XL and B-XM inserts that showed the best performance in this range of cutting conditions.

With regard to the work hardening of the surface, a deeper cutting depth generally results in a thinner hardened layer of the machined surface. This behavior is observed in Fig. 14. In terms of hardness variation, all inserts have a homogeneous performance with a maximum variation of 5 HV. However, for the tendency to surface hardening, the C-XL cutting insert has the lowest value but not too far from the other cutting tools. This indicates that the depth of cut for finishing operations with toroidal geometry tools would not have a significant impact on the hardening tendency of TiAl. In addition, the use of a low DOC, contrary to expectations, leads to a higher surface hardening effect and probably a thicker hardening layer. This concept will be analyzed in greater detail in future studies with varying cutting conditions and insert diameters.

With reference to surface roughness, Fig. 15 shows the results obtained. As expected the variation in depth of cut does not cause any noticeable response in surface roughness. The variations observed between cutting depths for each insert are very slight, with exception of A-XL insert which reduces roughness by 25% at a depth of 0.5 mm.



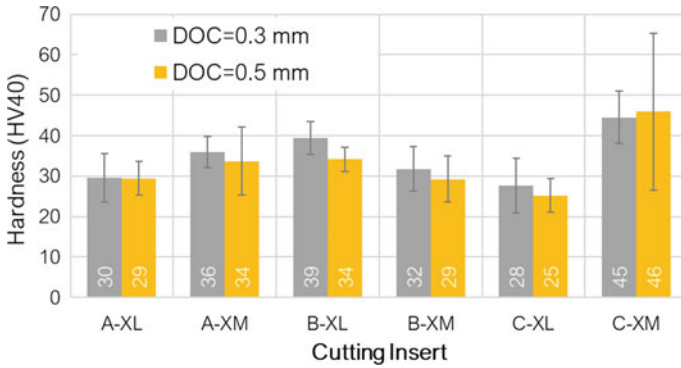


**Fig. 14** Surface hardness increment according to cutting forces for DOC of 0.3 and 0.5 on TiAl alloy

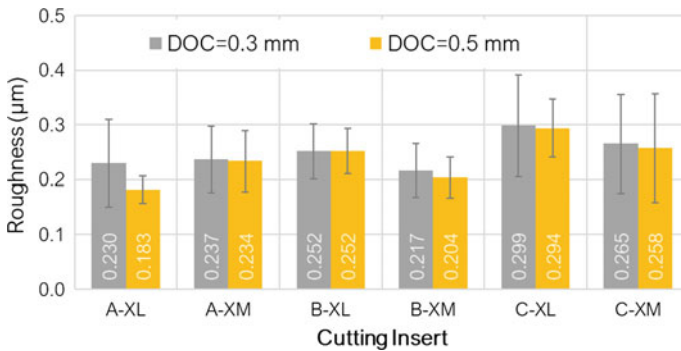


**Fig. 15** Effect of depth of cut in surface roughness (in feed directions)

### 3.1.3 Influence of the Chip Thickness

As for the cutting forces, it is normal for them to increase in proportion to the amount of cutting material. Therefore, depth of cut and feed rate are the parameters that most affect this variation.

On the other hand, the feed rate of the cutting tool is strongly related to the geometry and thickness of the chip that is formed in the cutting process. In the case of inserts with round geometry, the chip thickness ( $h_c$ ) varies according to the cutting depth and the angle entered, which allows increasing the feed rate. Consequently, this variable was selected as the reason for the study instead of the advance.

The effect of chip thickness on cutting forces was higher to presented at the depth of cut. A considerable increase in cutting forces occurred with an increase of only 0.01 mm in chip thickness demonstrating more sensitivity to this variable. As shown in Fig. 16, cutting insert BXM presents the best combination of variation and magnitude of cutting forces. In addition, the cutting forces caused by XL geometry

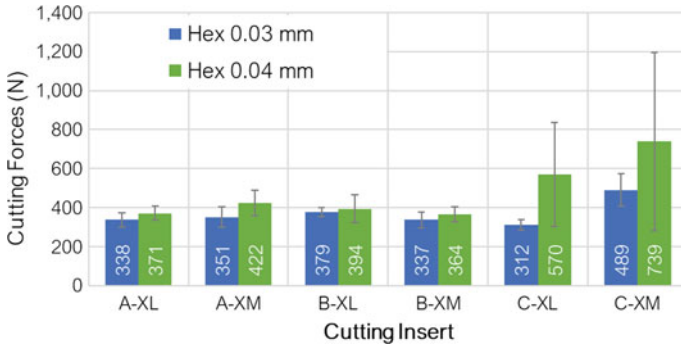


**Fig. 16** Chip thickness effect in the resultant cutting forces

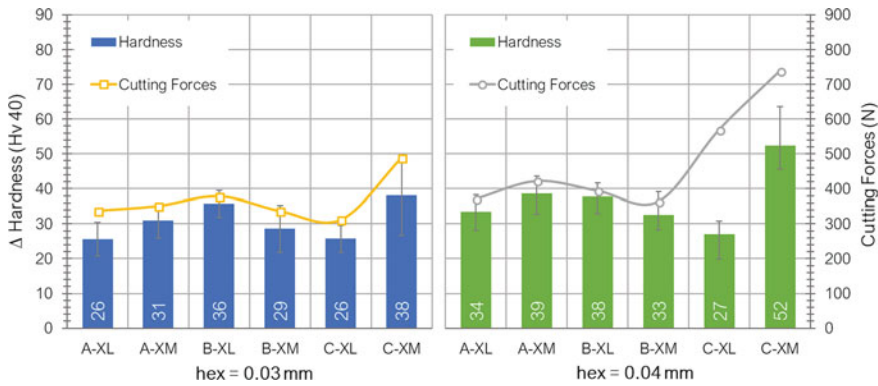


**Fig. 17** Surface hardness increment according to cutting forces and chip thickness on TiAl alloy

cutting inserts tend to vary less than those of XM geometry due to chip thickness variation.

For work hardening, a homogeneous variation between the cutting forces and the increase of the surface hardness is achieved, especially with a chip thickness of 0.03 mm. Variation in hardening has the opposite behavior to that of the depth of cut, in this case, a greater amount of material removed (hex = 0.04) promotes growth in surface hardness (Fig. 17).

As expected, chip thickness is the main factor affecting surface roughness. As shown in Fig. 18 the results obtained in terms of arithmetic mean roughness Ra for each tested cutting inserts. The A and B cutting inserts with both geometries cause roughness values that do not exceed 350 m, while for C inserts the values reach ~450 m. With regard to the performance of the C-XL geometry, this indicates that initial wear of the cutting edge does not strongly affect the surface finish due to the increased radius of the cutting edge. With the C-XM insert, the breakage of the cutting edge affects the surface roughness to a greater extent. This is also compatible

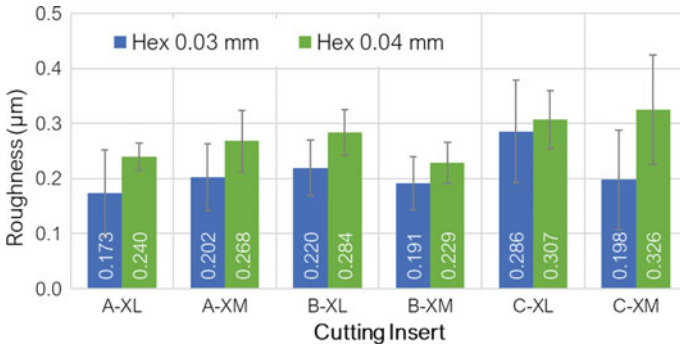


**Fig. 18** Effect of chip thickness in surface roughness (in feed directions)

**Table 6** Increase of the surface roughness according to the chip thickness variation

Cutting inserts	Hardness of cutting insert (HV40)	Roughness with hex 0.03 mm	Roughness with hex 0.04 mm	Roughness increase	
		(µm)	(µm)	(µm)	(%)
AXL	1900	0.173	0.240	0.067	38.7
AXM	1900	0.202	0.268	0.066	32.7
BXL	1650	0.220	0.284	0.064	29.1
BXM	1650	0.191	0.229	0.038	19.9
CXL	1550	0.286	0.307	0.021	7.3
CXM	1550	0.198	0.326	0.128	64.6

with the results obtained by [18]. However, the roughness values of the C-XL insert are higher than those of the other inserts.

The results in terms of roughness variation listed in Table 6 highlight that a 0.01 mm difference in chip thickness causes a 20–60% increase in surface roughness for almost all cutting inserts. An exception was the C-XL insert which varies by 7% for the reasons explained above. In terms of geometries, there is a slight tendency of XL geometry to affect roughness in response to the increase in chip thickness. As a result, the surface roughness is more affected by the 0.01 mm variation in chip thickness than by the 25 m/min cutting speed or the 2 mm cutting depth.

### 3.1.4 Surface Defects

As has been previously commented, the machining of titanium aluminide alloys leads to an unusual response pattern to the cutting process causing surface and sub-surface defects such as feed marks, smearing, surface cavities and cracks [1, 6–9, 33]. The surface integrity defects confirmed are strongly linked to cutting speed, feed rate, depth of cut, tool geometry, rake angle, nose radius among other. Optical and SEM

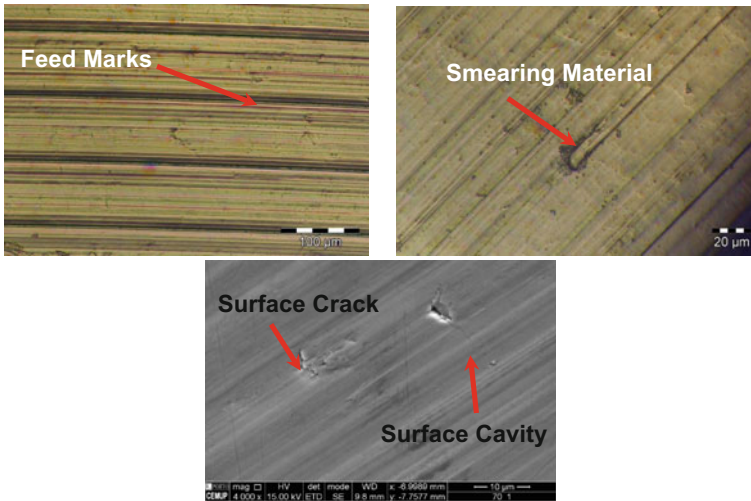


**Fig. 19** Surface defect feed marks, smearing, surface cracks and cavities on machined surfaces

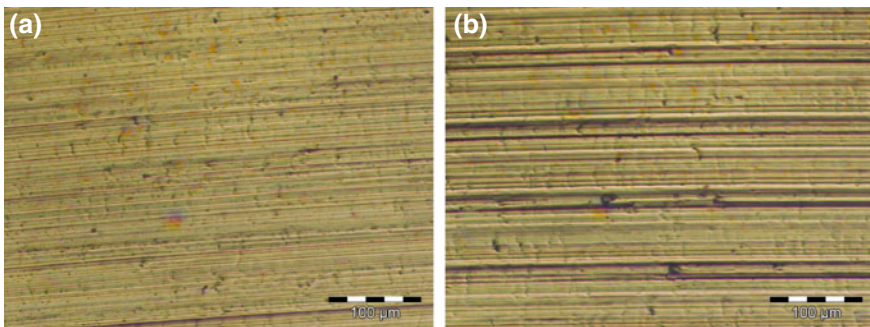


**Fig. 20** Machined surfaces with C-XL cutting insert at  $V_c = 70$  m/min. **a**  $DOC = 0.5$  mm and  $hex = 0.04$  mm, **b**  $DOC = 0.3$  mm and  $hex = 0.03$  mm

observation on the machined surfaces around the hardness and roughness analyzed area was conducted. The surface observation of the machined samples showed several defects that confirmed the results presented in the surface integrity analyses (Fig. 19).

All specimens showed some defect. Considering the analyzed range of machining parameters for all inserts, the combination of cutting speed of 70 m/min, depth of cut of 0.5 mm and chip thickness of 0.04 mm, exhibited a tendency to cause feed marks, surface cracks, and material smearing. In contrast to this trend, the surfaces machined with the same cutting speed but with the depth of cut of 0.3 and a chip thickness of 0.03 showed a lower number of defects. This behavior would demonstrate that the effect of cutting speed on the surface defect formation is less than the material removal rate (Fig. 20).

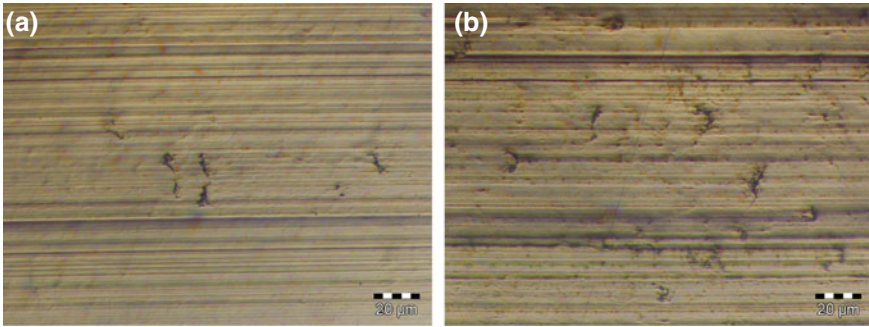


**Fig. 21** Machined surfaces at  $V_c = 70$  m/min,  $DOC = 0.3$  mm and  $hex = 0.03$  mm with **a** worn cutting insert C-XL and **b** broken cutting-edge C-XM

It was also evident that the fracture of the cutting edge of the C-XM insert generated the worst quality surface. On the other hand, the C-XL insert has a more homogeneous and smooth surface. Caused by cutting edge wear of the insert (Fig. 21).

Regarding the performance of the cutting inserts in relation to surface defects. The A-XL cutting insert showed the best overall quality of the machined surfaces with all combinations of cutting parameters, followed by the B-XM. In contrast, the

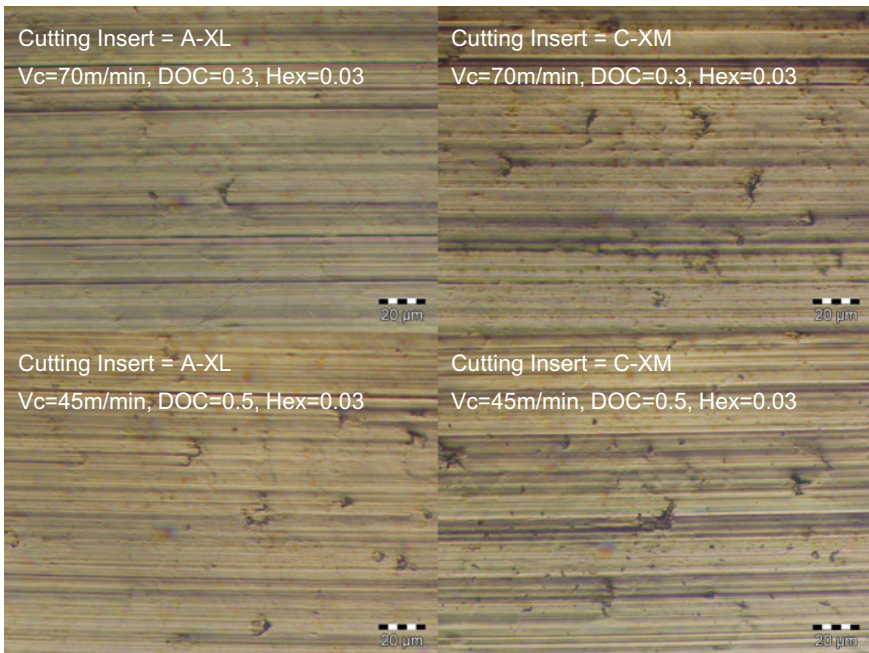


**Fig. 22** Machined surface obtained with of A-XL and C-XM at different cutting parameters

surfaces that showed the greatest number of defects were those obtained with the C-XM insert. In Fig. 22 it is possible to compare the surfaces obtained with the A-XL and C-XM inserts. The performance of these inserts confirms the previous analysis of cutting forces, surfaces roughness and work-hardening tendency.

## 4 Conclusions

The results of milling experiments conducted on a gamma TiAl alloy for finishing cutting conditions show that for cutting forces increase of the cutting speed has a slight effect, while the depth of cut and mainly chip thickness caused a stronger impact. This trend was identified without considering the effect of cutting-edge wear.

The surface roughness  $R_a$  shows an expected dependence on cutting speed and chip thickness mainly. It was found that wear on the cutting edge improves surface roughness due to the increased contact area.

For surface hardness tendency chip thickness was revealed as the most influential parameter. An unusual trend occurred with the depth of cut. The surface work hardening tendency diminished when the depth of cut was increased from 0.3 to 0.5 mm. This improvement is probably due to the thermal softening caused by the higher DOC. Cutting speed does not cause significant differences in the explored range.

In terms of surface defects, it was not possible to obtain defect-free surfaces, but at cutting speeds of 70 m/min there is a tendency to exhibit fewer defects. This leads to the conclusion that the surface integrity can be improved by increasing cutting speed. All cutting inserts showed surfaces with higher or fewer defects according to the cutting parameters used in these trials. Consequently, a diminished the surface defects would be possible. A suitable combination of cutting parameters and cutting-edge geometry must be selected for improved milling on  $\gamma$ -TiAl.

Summarizing, chip thickness had the greatest effect on the surface integrity variables analyzed in this research, at least in the range studied. In terms of performance, the 1010 EPL and S30T cutting inserts were the ones that provided the best surface integrity and demonstrated the potential for increased productivity.

**Acknowledgements** Authors acknowledge the funding of Project NORTE-01-0145-FEDER-000022—SciTech, co-financed by NORTE2020, through FEDER. Authors also acknowledge Sandvik Coromant which offered the cutting inserts.

## References

1. Aspinwall, D.K., Dewes, R.C., Mantle, A.L.: The machining of  $\gamma$ -TiAl intermetallic alloys. *CIRP Ann. Manuf. Technol.* **54**, 99–104 (2005)
2. Beranoagirre, A., López de Lacalle, L.N.: Optimising the milling of titanium aluminide alloys. *Int. J. Mechatron. Manuf. Syst.* **3**, 425 (2010)

3. Klocke, F., Settineri, L., Lung, D., Priarone, P.C., Arft, M.: High performance cutting of gamma titanium aluminides: Influence of lubricoolant strategy on tool wear and surface integrity. *Wear* **302**, 1136–1144 (2013)
4. Priarone, P.C., Rizzuti, S., Rotella, G., Settineri, L.: Technological and environmental aspects in milling of  $\gamma$ -TiAl. *Adv. Mater. Res.* **223**, 340–349 (2011)
5. Mantle, A.L., Aspinwall, D.K.: Surface integrity and fatigue life of turned gamma titanium aluminide. *J. Mater. Process. Technol.* **72**, 413–420 (1997)
6. Ginting, A., Nouari, M.: Surface integrity of dry machined titanium alloys. *Int. J. Mach. Tools Manuf.* **49**, 325–332 (2009)
7. Lindemann, J., Glavatskikh, M., Leyens, C.: Surface effects on the mechanical properties of gamma titanium aluminides. *Mater. Sci. Forum* **706**, 1071–1076 (2012)
8. Beranoagire, A., López de Lacalle, L.N.N.: Grinding of gamma TiAl intermetallic alloys. In: *Procedia Engineering*, pp. 489–498 (2013)
9. Radkowski, G., Sep, J.: Surface quality of a milled gamma titanium aluminide for aeronautical applications. *Manag. Prod. Eng. Rev.* **5**, 60–65 (2014)
10. Clemens, H., Mayer, S.: Design, processing, microstructure, properties, and applications of advanced intermetallic TiAl alloys. *Adv. Eng. Mater.* **15**, 191–215 (2013)
11. Beranoagire, A., Olvera, D., López De Lacalle, L.N.: Milling of gamma titanium-aluminum alloys. *Int. J. Adv. Manuf. Technol.* **62**, 83–88 (2012)
12. Zitoune, R., Krishnaraj, V., Davim, J.P.: *Machining of Titanium Alloys and Composites for Aerospace Applications* (2013)
13. Priarone, P.C., Klocke, F., Faga, M.G., Lung, D., Settineri, L.: Tool life and surface integrity when turning titanium aluminides with PCD tools under conventional wet cutting and cryogenic cooling. *Int. J. Adv. Manuf. Technol.* **85**, 807–816 (2016)
14. Uhlmann, E., Frommeyer, G., Herter, S., Knippscheer, S., Lischka, J.M.: Studies on the conventional machining of TiAl based Alloys. In: *Ti-2003 Science and Technology 10th World Conference on Titanium*, pp. 2239–2300 (2003)
15. Aspinwall, D.K., Mantle, A.L., Chan, W.K., Hood, R., Soo, S.L.: Cutting temperatures when ball nose end milling  $\gamma$ -TiAl intermetallic alloys. *CIRP Ann. Manuf. Technol.* **62**, 75–78 (2013)
16. Hood, R., Aspinwall, D.K., Sage, C., Voice, W.: High speed ball nose end milling of  $\gamma$ -TiAl alloys. *Intermetallics* **32**, 284–291 (2013)
17. Uhlmann, E., Herter, S., Gerstenberger, R., Roeder, M.: Quasi-static chip formation of intermetallic titanium aluminides. *Prod. Eng.* **3**, 261–270 (2009)
18. Priarone, P.C., Rizzuti, S., Settineri, L., Vergnano, G.: Effects of cutting angle, edge preparation, and nano-structured coating on milling performance of a gamma titanium aluminide. *J. Mater. Process. Technol.* **212**, 2619–2628 (2012)
19. Hood, R., Aspinwall, D.K., Soo, S.L., Mantle, A.L., Novovic, D.: Workpiece surface integrity when slot milling Gamma TiAl intermetallic alloy. *CIRP Ann. Manuf. Technol.* **63**, 53–56 (2014)
20. Zhang, H., Wise, M.L.H., Aspinwall, D.K.: The machining of TiAl-based intermetallics. In: Kochhar, A.K. (ed.) *Proceedings of the Thirtieth International MATADOR Conference*, p. 739. Palgrave, London (1993)
21. Sharman, A.R.C., Aspinwall, D.K., Dewes, R.C., Bowen, P.: Workpiece surface integrity considerations when finish turning gamma titanium aluminide. *Wear* **249**, 473–481 (2001)
22. Settineri, L., Priarone, P.C., Arft, M., Lung, D., Stoyanov, T.: An evaluative approach to correlate machinability, microstructures, and material properties of gamma titanium aluminides. *CIRP Ann. Manuf. Technol.* **63**, 57–60 (2014)
23. Bentley, S.A., Mantle, A.L., Aspinwall, D.K.: Effect of machining on the fatigue strength of a gamma titanium aluminide intermetallic alloy. *Intermetallics* **7**, 967–969 (1999)
24. Mantle, A.L., Aspinwall, D.K.: Surface integrity of a high speed milled gamma titanium aluminide. *J. Mater. Process. Technol.* **118**, 143–150 (2001)
25. Novovic, D., Dewes, R.C., Aspinwall, D.K., Voice, W., Bowen, P.: The effect of machined topography and integrity on fatigue life. *Int. J. Mach. Tools Manuf.* **44**, 125–134 (2004)

26. Mathew, N.T., Vijayaraghavan, L.: Environmentally friendly drilling of intermetallic titanium aluminide at different aspect ratio. *J. Clean. Prod.* **141**, 439–452 (2017)
27. Appel, F., Paul, J.D.H., Oehring, M.: *Gamma Titanium Aluminide Alloys: Science and Technology*. Wiley-VCH Verlag GmbH & Co. KGaA, Weinheim, Germany (2011)
28. Priarone, P.C., Rizzuti, S., Rotella, G., Settineri, L.: Tool wear and surface quality in milling of a gamma-TiAl intermetallic. *Int. J. Adv. Manuf. Technol.* **61**, 25–33 (2012)
29. Vargas Pérez, R.G.: Wear mechanisms of WC inserts in face milling of gamma titanium aluminides. *Wear* **259**, 1160–1167 (2005)
30. Ge, Y.F., Fu, Y.C., Xu, J.H.: Experimental study on high speed milling of  $\gamma$ -TiAl alloy. *Key Eng. Mater.* **339**, 6–10 (2007)
31. Kolahdouz, S., Hadi, M., Arezoo, B., Zamani, S.: Investigation of surface integrity in high speed milling of gamma titanium aluminide under dry and minimum quantity lubricant conditions. *Procedia CIRP* **26**, 367–372 (2015)
32. Gfe Metalle und Materialien GmbH: *Advanced Materials  $\gamma$ -TiAl RNT650 Ingots*. 9315 (2010)
33. Weinert, K., Bergmann, S., Kempmann, C.: Machining sequence to manufacture a  $\gamma$ -TiAl-conrod for application in combustion engines. *Adv. Eng. Mater.* **8**, 41–47 (2006)
34. Tebaldo, V., Faga, M.G.: Influence of the heat treatment on the microstructure and machinability of titanium aluminides produced by electron beam melting. *J. Mater. Process. Technol.* **244**, 289–303 (2017)
35. Klocke, F., Lung, D., Arft, M., Priarone, P.C., Settineri, L.: On high-speed turning of a third-generation gamma titanium aluminide. *Int. J. Adv. Manuf. Technol.* **65**, 155–163 (2013)
36. Sun, S., Brandt, M., Dargusch, M.S.: Characteristics of cutting forces and chip formation in machining of titanium alloys. *Int. J. Mach. Tools Manuf.* **49**, 561–568 (2009)
37. Mantle, A.L., Aspinwall, D.K.: Cutting force evaluation when high speed end milling a gamma titanium aluminide intermetallic alloy. In: Morris, D.G., Moris, S.N., Caron, P. (eds.) *Intermetallics and Superalloys*, pp. 209–215. Wiley-VCH, Weinheim (2000)



**Part IX**  
**Fracture Mechanics**

# Analysis of the Semi-circular Bend (SCB) Specimen: Finite Element Method Determination of T-stress, $K_I$ and $K_{II}$



E. Shahabi and P. M. S. T. de Castro

**Abstract** The semi-circular specimen under three-point bending loading (SCB specimen) may be used for determining mode I and mixed-mode (I and II) fracture toughness for brittle materials; this subject is covered in several references. This paper presents T-stress and stress intensity factor for SCB specimen in mode I and mixed-mode (I and II), exploring direct uses of finite element method to calculate those parameters. The commercial FE software ABAQUS was used to model the SCB specimen. Several cases including different crack lengths for investigating mode I, various crack angles for mixed-mode (I and II) and T-stress are presented. Since SCB specimen is loaded in bending, a comparison of the SCB and SE (B) specimen (ASTM E399-08 standard) was performed for mode I, discussing dimensions and amount of material involved. Finally, the result obtained from the presented finite element model are compared with results from the literature.

**Keywords** T-stress · Stress intensity factor · Finite element method · Mode I Mixed-mode

## 1 Introduction

The manner in which a crack propagates through a material gives insight into the mode of fracture. With a ductile fracture, a crack moves slowly and is accompanied by a large amount of plastic deformation around the crack tip. A ductile crack will usually not propagate unless an increased stress is applied and may cease propagating when loading is removed. In a ductile material, a crack may progress to a region of the material where stresses are slightly lower and stop due to the blunting effect of plastic deformations at the crack tip. On the other hand, with brittle fracture, cracks

---

E. Shahabi (✉) · P. M. S. T. de Castro  
FEUP, Faculty of Engineering, University of Porto, Porto, Portugal  
e-mail: [shahabi@fe.up.pt](mailto:shahabi@fe.up.pt)

P. M. S. T. de Castro  
e-mail: [ptcastro@fe.up.pt](mailto:ptcastro@fe.up.pt)

© Springer Nature Switzerland AG 2019  
L. F. M. da Silva (ed.), *Materials Design and Applications II*, Advanced Structured Materials 98, [https://doi.org/10.1007/978-3-030-02257-0\\_27](https://doi.org/10.1007/978-3-030-02257-0_27)

spread very rapidly with little or no plastic deformation. The cracks that propagate in a brittle material will continue to grow once initiated.

Crack propagation is also categorized by the crack characteristics at the microscopic level. A crack that passes through the grains of the material is a phenomenon known as transgranular fracture. A crack that propagates along the grain boundaries is termed an intergranular fracture. Typically, the bonds between material grains are stronger at room temperature than the material itself, so transgranular fracture is more likely to occur. When temperatures increase enough to weaken the grain bonds, intergranular fracture is the more common fracture mode.

There are three basic modes of deformation in classical fracture mechanics. In mode I or opening mode, the crack faces are displaced in a direction normal to the crack plane without any sliding. In mode II or shear mode, the crack faces slide normal to the crack front without any opening. In mode III or out-of-plane shear mode, the crack faces slide parallel to the crack front.

The simulation of crack propagation has been attracting the attention of researchers. It is impossible to predict the crack propagation path without having the knowledge of the angle of crack initiation, a problem that needs to be studied in mixed mode. Several criteria have been proposed for predicting crack initiation angles.

## ***1.1 SCB Specimen***

The semi-circular (SC) and SCB geometries are ideal testing configurations due to minimal preparation required for each test [1]. The SC geometry is ideal for field testing purposes as it is easily fabricated from cores removed from the testing material. It is important when field-testing to conduct a set of small-scale tests to correlate fracture properties with the large-scale tests. The SCB became the basis of the small-scale field testing, prompting the detailed analysis presented in this work. The SCB test configuration has been advocated as a possible standard test method for rocks [2]. For the case of mode I loading (the edge crack being normal to the base), the SCB has been studied by Chong and Kuruppu and more recently by Lim et al. [2]. In the work by Chong and Kuruppu [3], limited numerical results are presented; Lim et al. [2] provide solutions over a wider range of crack lengths and spans and correlate the accuracy of the earlier solution. The latter paper bridges solutions by curve fitting. Although these papers provide a means of calculating the fracture toughness from experimental data, apparently no rigorous SIF results exist; moreover, there has been no information provided concerning the associated crack opening displacements.

An essential component for furthering the understanding of rock fracture is the availability of suitable experimental techniques for mixed-mode rock fracture toughness testing. Several techniques now exist [4]. In a review by Lim et al. [2], it was proposed that only two experimental techniques are presently suitable. The first is the semi-circular specimen under three-point bend (SCB) developed by Chong and

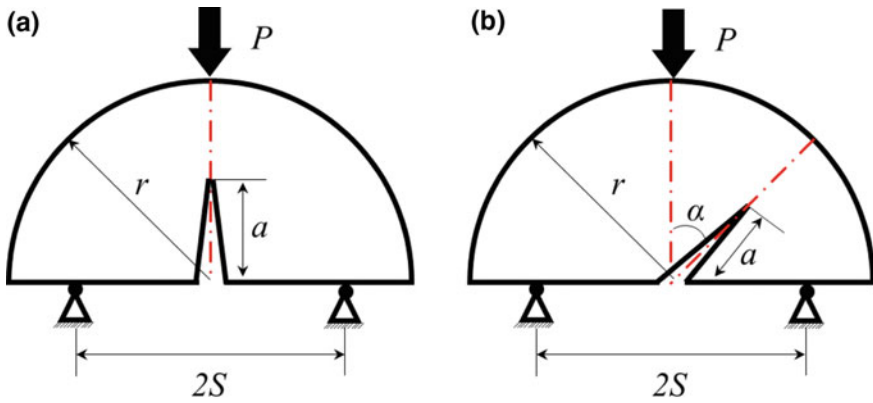


**Fig. 1** Semi-circular bend (SCB) specimen: **a** under pure mode I loading, **b** under mixed-mode loading

Kuruppu [3]. The second is the central cracked Brazilian disc under diametral compression (CCBD) advocated by Sun et al. [5]. The SCB approach is to be preferred as it is more cost-effective, reliable and versatile. However, the latter is more appropriate when fatigue pre-cracking is a necessary requirement. This study will concentrate on the SCB specimen as depicted in Fig. 1. In the original work of Chong and Kuruppu [3] and Chong et al. [6] the variation in stress intensity factor (SIF) was determined numerically using the finite element method for mode I and mixed-mode loading respectively. However, only very limited ranges of crack lengths and spans were examined. This study focuses on mode-I, mode-II, mixed mode I-II and seeks to address this through the use of the finite element method.

Figure 1 shows a schematic diagram of the semi-circular bend (SCB) specimen which has been widely used by several researchers in the past to investigate mixed-mode fracture in brittle materials [7–10]. The SCB specimen containing an angled crack of length  $a$  is a semicircular disc of radius  $r$  and subjected to three-point bending. The specimen is loaded by the vertical load  $P$  and is placed on two bottom supports separated by a distance  $2S$ . Different combinations of mode I and mode II in the SCB specimen are obtained by producing specimens with varying crack angles. When the crack inclination angle  $\alpha = 0$  the specimen is subjected to pure mode I. By increasing the angle  $\alpha$ , the stress intensity factor (SIF) of mode II is increased, while for mode I it gives an opposite result.

### 1.2 SE Specimen

The SE specimen is a common specimen for measurement of fracture toughness standardized by the American Society for Testing and Materials (ASTM E399-08)

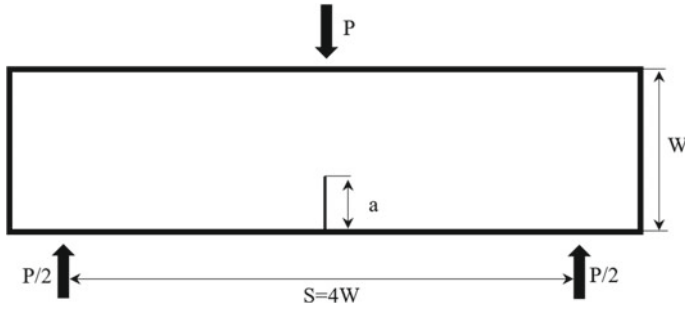


Fig. 2 Illustration of SE specimen,  $B = w/2$  is thickness

[11], consisting of a rectangular beam with a single edge notch under three-point bending load, Fig. 2.

The single edge notched beam in three-point bend (SENB) specimen was developed and standardized [11] for measuring the fracture toughness of metals.

## 2 Computation of Stress Intensity Factors

The in-plane linear elastic stresses around the tip of a crack can be described as symmetric and antisymmetric fields, called mode I and mode II respectively. The stresses for each of the fields can be written as an eigen series expansion [12]. Near the tip of the crack, where the higher order terms of the series expansion are negligible, stresses, for mode I and mode II, are [12]

$$\begin{aligned}
 \sigma_{xx} &= \frac{K_I}{\sqrt{2\pi r}} \cos \frac{1}{2}\theta \left[ 1 - \sin \frac{1}{2}\theta \sin \frac{1}{2}(3\theta) \right] + T + O(r^{1/2}) \\
 \sigma_{yy} &= \frac{K_I}{\sqrt{2\pi r}} \cos \frac{1}{2}\theta \left[ 1 - \sin \frac{1}{2}\theta \sin \frac{1}{2}(3\theta) \right] + O(r^{1/2}) \\
 \tau_{xy} &= \frac{K_I}{\sqrt{2\pi r}} \cos \frac{1}{2}\theta \sin \frac{1}{2}\theta \cos \frac{1}{2}(3\theta) + O(r^{1/2})
 \end{aligned} \tag{1}$$

$$\begin{aligned}
 \sigma_{xx} &= \frac{K_{II}}{\sqrt{2\pi r}} \sin \frac{1}{2}\theta \left[ 2 + \cos \frac{1}{2}\theta \cos \frac{1}{2}(3\theta) \right] + O(r^{1/2}) \\
 \sigma_{yy} &= \frac{K_{II}}{\sqrt{2\pi r}} \sin \frac{1}{2}\theta \cos \frac{1}{2}\theta \cos \frac{1}{2}(3\theta) + O(r^{1/2}) \\
 \tau_{xy} &= \frac{K_{II}}{\sqrt{2\pi r}} \cos \frac{1}{2}\theta \left[ 1 - \sin \frac{1}{2}\theta \sin \frac{1}{2}(3\theta) \right] + O(r^{1/2})
 \end{aligned} \tag{2}$$

where  $\sigma$  and  $\tau$  are normal and shear stress,  $K_I$  and  $K_{II}$  are the mode I and mode II stress intensity factors (SIF) and  $r$ ,  $\theta$ ,  $x$  and  $y$  are co-ordinates in conventional polar and Cartesian systems with the crack tip at the origin.

Practical structures are not only subjected to tension but also experience shear and torsion loading leading to a mixed-mode interaction. Correspondingly, the stress state ahead of a crack is frequently based on mixed-mode I/II type of interactions, which designate the amplitude of the crack tip stresses because of skew-symmetric loading. Many modern components, from microchips to ships and large wind turbine blades are made of materials arranged in layers. Mixed mode cracking is commonly observed in such structures, since they often have weak planes. For Mixed mode I–II,  $K_{eff}$  can be defined as

$$K_{eff} = \sqrt{K_I^2 + K_{II}^2} \quad (3)$$

Four computation techniques for evaluating SIF are now mentioned.

## 2.1 Displacement Correlation Technique (DCT)

The SIF is computed [13] using:

$$\begin{aligned} K_I^{DCT} &= \frac{G}{k+1} \sqrt{\left(\frac{2\pi}{L_Q}\right) \{4(v'_B - v'_D) + (v'_C - v'_E)\}} \\ K_{II}^{DCT} &= \frac{G}{k+1} \sqrt{\left(\frac{2\pi}{L_Q}\right) \{4(u'_B - u'_D) + (u'_C - u'_E)\}} \end{aligned} \quad (4)$$

where  $G$  is shear modulus,  $k$  is  $(3 - \nu)/(1 + \nu)$  for plane stress and is  $3 - 4\nu$  for plane strain and axisymmetry.  $\nu$  is Poisson's ratio and  $L_Q$  is length of quarter-point element (QPE) along crack face.  $u'$  and  $v'$  are local displacement along and normal to crack axis.

## 2.2 Quarter-Point Displacement Technique (QPDT)

The SIF is given [14] by:

$$\begin{aligned} K_I^{QPDT} &= \frac{2G}{k+1} \sqrt{\left(\frac{2\pi}{L_Q}\right) \{v'_B - v'_D\}} \\ K_{II}^{QPDT} &= \frac{2G}{k+1} \sqrt{\left(\frac{2\pi}{L_Q}\right) \{u'_B - u'_D\}} \end{aligned} \quad (5)$$

### 2.3 Displacement Extrapolation Technique (DET)

Chan et al. [15] who estimated the SIF by extrapolating the nodal displacements along the crack face first employed this technique. The expression is given as:

$$\begin{aligned}
 K_I^{\text{DET}} &= \lim_{r^{*i} \rightarrow 0} K_I^{*i}; K_{II}^{\text{DET}} = \lim_{r^{*i} \rightarrow 0} K_{II}^{*i} \\
 K_I^{*i} &= \frac{G}{k+1} \sqrt{\left(\frac{2\pi}{r^{*i}}\right) \{v'(r^{*i})\}} \\
 K_{II}^{*i} &= \frac{G}{k+1} \sqrt{\left(\frac{2\pi}{r^{*i}}\right) \{u'(r^{*i})\}}
 \end{aligned} \tag{6}$$

where  $r^{*i}$  distance between the  $i$ th node and the crack tip.

A “best fit” straight line is fitted through the nodal  $K^{*i}$  and its intercept with the ordinate at  $r = 0$  is  $K^{\text{DET}}$ . A detailed description of obtaining a “best” fit through the use of linear regression can be found in Lim et al. [14].

### 2.4 Limited Displacement Extrapolation Technique (LDET)

A variant to the DET was proposed by Lim et al. [14], whereby a restriction is applied to the possible combinations of  $K^{*i}$ . Only the first three nodal  $K^{*i}$  values associated with an element immediately adjacent to the crack tip element are to be curve fitted. Mathematically, it is expressed as:

$$K_I^{\text{LDET}} = \lim_{r^{*i} \rightarrow 0} F(K^{*2}, K^{*3}, K^{*4}) \tag{7}$$

where  $F$  = a “best” fitted line through  $K^{*2}$ ,  $K^{*3}$ ,  $K^{*4}$  and  $i$  ranges from 2 to 4.

Only one linear regression analysis is required in this approach, thereby considerably reducing the computational effort relative to the DET.

## 3 Calculation of Crack Parameters for the SCB Specimen

### 3.1 Mode I

Various finite element models of the SCB specimen are analyzed using the commercial general-purpose finite element package Abaqus [16] for calculating  $K_I$  and  $K_{II}$ . Figures 3 and 4 depict the geometry of SCB specimen, applied force and boundary condition. A typical mesh pattern generated for simulating the SCB specimen is

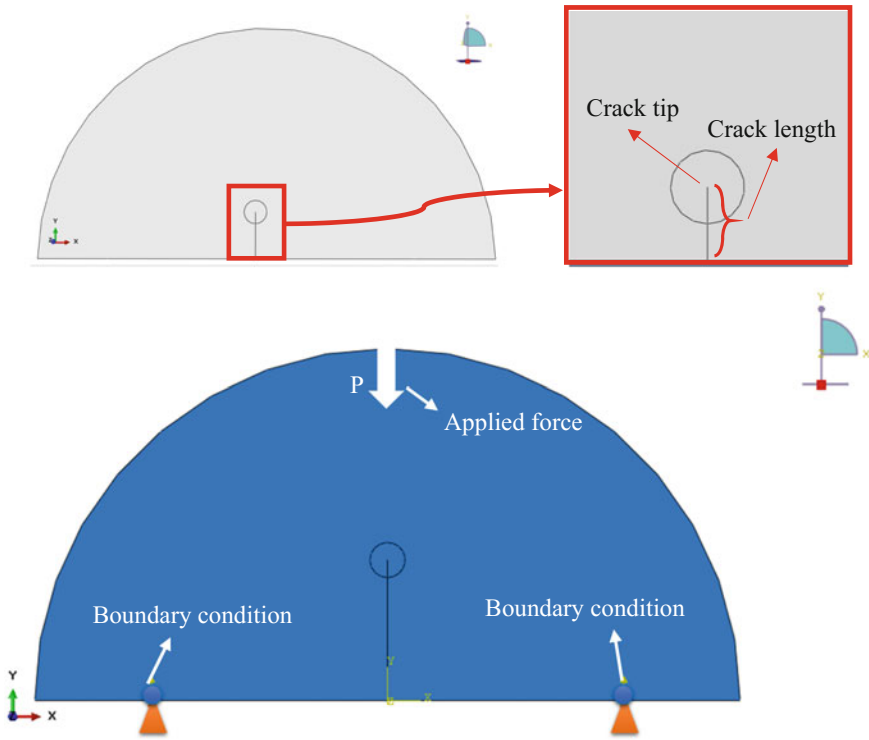


Fig. 3 SCB specimen subjected to three-point bending

shown in Fig. 4. In this model, the following parameters are applied:  $r=100$  mm,  $P=100$  N,  $t=1$  (under plane stress conditions),  $2S=80$  mm, elastic modulus  $E=72$  GPa and Poisson’s ratio  $\nu=0.3$ . A total number of 35,568 plane stress quadratic elements are used in these simulations.

In addition, a numerical convergence study was performed for the SCB test technique with the normalized crack length  $a/r=0.5$ , the normalized span  $s/r=0.8$  and the crack inclination angle  $\alpha=0$ . Four mesh densities were examined, as depicted in Fig. 5. As in the preceding section, an outer mesh and an inner mesh were defined whereby for a given mesh density, the outer mesh remained unchanged while all mesh variations occurred within the inner mesh. For each mesh density, the number of element layers within the inner mesh was progressively increased. A mesh sensitivity analysis is performed to ensure optimum mesh size for proper convergence and accurate numerical results.

The results of the analyses are given in Fig. 6 in terms of the mode I normalized stress intensity factor  $Y_I$ , which is defined as:

$$Y_I = \frac{K_I}{\sigma_0 \sqrt{\pi a}}$$



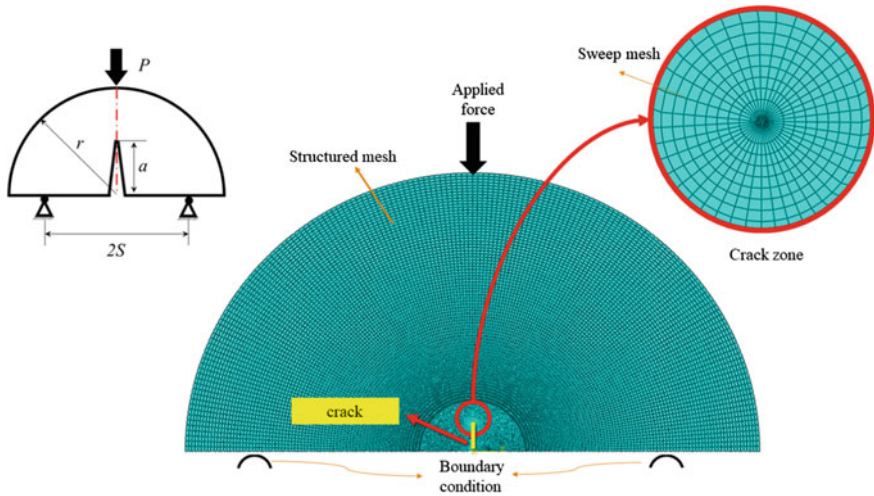


Fig. 4 Finite element model of SCB specimen for Mode I

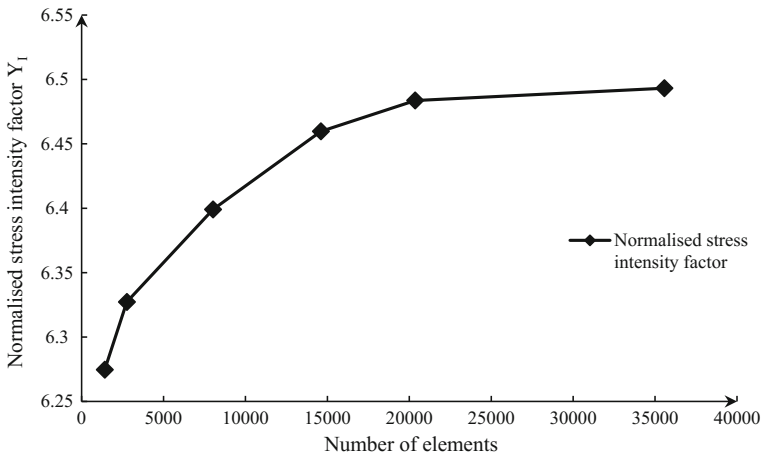


Fig. 5 Convergence in  $Y_I$ , with increasing number of elements

where:

$K_I$  is the mode I stress intensity factor  $\sigma_0 = P/2rt$ .

$t$  is specimen thickness.

$P$  is applied load.

Figure 6 shows the numerical results obtained for the mode I loading with  $s/r = 0.5, 0.61, 0.67$  and  $0.8$  [2, 17]. In Fig. 5 is shown the comparison between proposed Abaqus model and strain energy, elliptical displacement theory which are presented

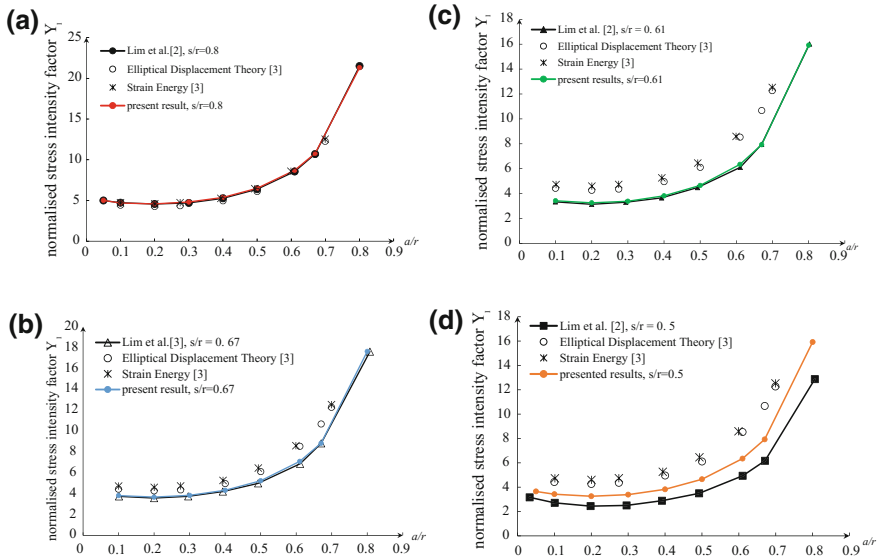


**Fig. 6** Computed normalized mode I stress intensity factor  $Y_I$ , for  $\alpha = 0$  and **a**  $s/r = 0.8$ , **b**  $s/r = 0.67$ , **c**  $s/r = 0.61$  and **d**  $s/r = 0.5$

by Chong and Kuruppu [3, 18] and the finite element model which is presented by Lim and Johnston [19], Webb and Widjaja [20] for different  $s/r$  ratios.

Figure 7 shows the proposed Abaqus finite element models and results obtained for the mode I with various  $a/r$  ratio.  $s/r = 0.67$  and  $a/r = 0.4$ .

### 3.2 Mixed Mode I/II

A similar comparison was made for the mixed-mode loading with  $a/r = 0.5$  and  $s/r = 0.67$ .

In this model, the following parameters are applied:  $r = 100$  mm,  $P = 100$  N,  $t = 1$  (under plane stress conditions),  $2S = 67$  mm, elastic modulus  $E = 72$  GPa and Poisson’s ratio  $\nu = 0.3$ , crack length  $a = 50$  mm. The finite element was performed with different crack angles like  $= 0^\circ, 10^\circ, 15^\circ, 20^\circ, 30^\circ, 45^\circ, 50^\circ, 60^\circ, 70^\circ, 75^\circ$ . In Fig. 8, the mesh pattern generated for simulating mixed mode I/II is shown.

Although similar trends are discernible, Fig. 9 shows definite differences between the proposed Abaqus model results and those of Chong and Kuruppu [21], and close similarity with the finite element model which is presented by Lim and Johnston [19]. Figure 10 shows the finite element model of SCB specimen for mixed mode and deformation results. Finite element models and results for various crack angles are shown in Fig. 11.

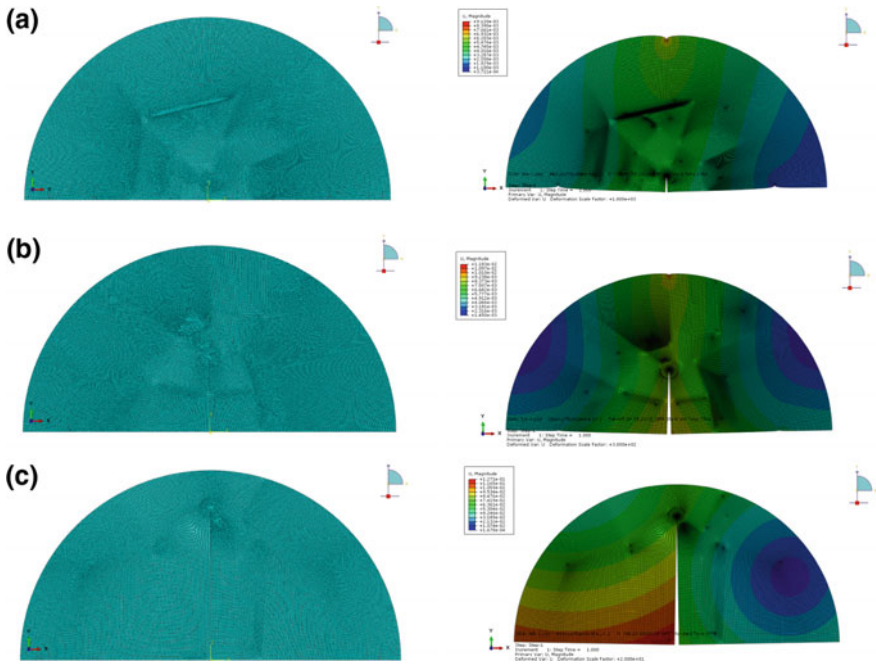


**Fig. 7** a Proposed Abaqus finite element model and deformation results obtained for the mode I loading with  $a/r=0.1$  and  $s/r=0.67$ , b  $a/r=0.4$  and  $s/r=0.67$ , c  $a/r=0.8$  and  $s/r=0.67$

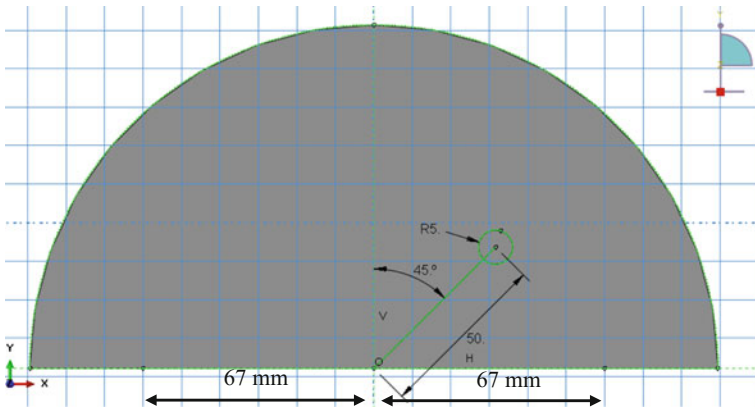


**Fig. 8** Geometry of SCB specimen for mixed mode I/II

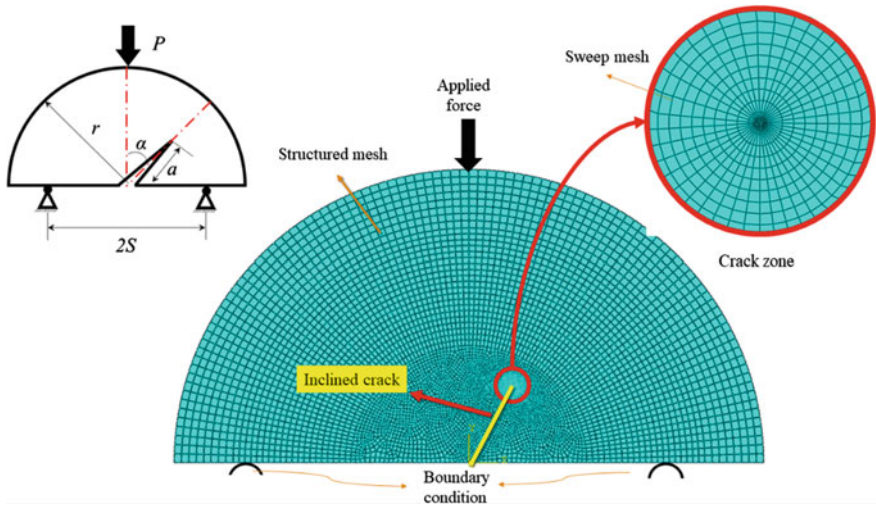


Fig. 9 Finite element mesh used for simulating SCB specimen (mode I-II)

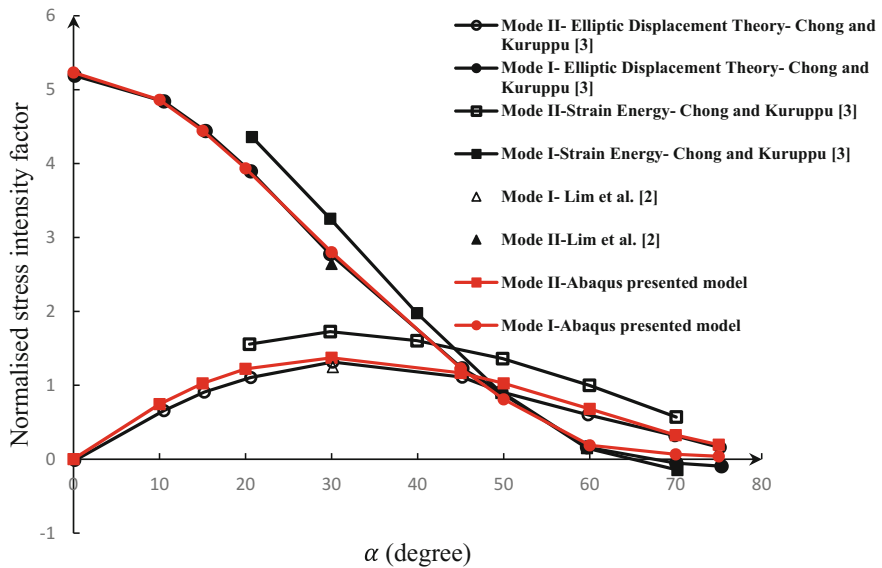
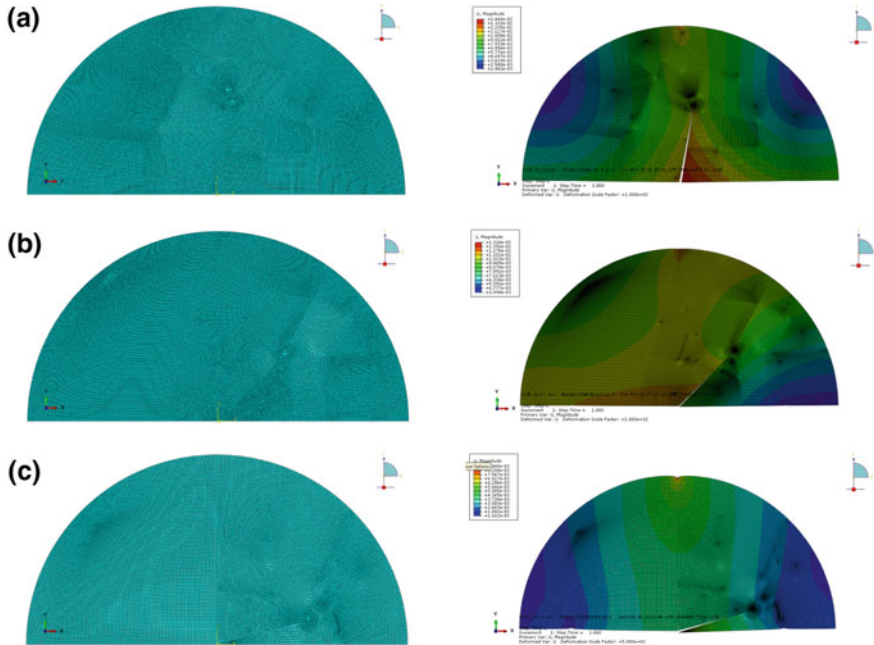


Fig. 10 Comparison of computed normalized mixed-mode stress intensity factor Y for  $a/r=0.5$  and  $s/r=0.67$



**Fig. 11** a Proposed Abaqus finite element model and results obtained for the mixed mode loading with  $s/r=0.67$ ,  $a/r=0.5$  and  $= 10^\circ$  b  $s/r=0.67$ ,  $a/r=0.5$  and  $= 45^\circ$  c  $s/r=0.67$ ,  $a/r=0.5$  and  $= 75^\circ$

#### 4 Calculation of Crack Parameters for the SE Specimen

In fracture mechanics, the SE specimen is better known and more commonly used than the SCB specimen. Therefore a comparison between both specimens should be performed. In Fig. 12, the concept of comparison between both SCB and SE specimens is illustrated. This comparison was made based on crack length and uncracked ligament.

Similar to SCB specimen the FE model for SE specimen was prepared. All the procedures to define the mesh types and mesh convergence were also carried for the SE specimen. In Fig. 13, the FE model of SE specimen for mode I is presented.

The differences between the SIF obtained for SE and for SCB specimens are depicted in Fig. 14. It can be noticed that there is a significant difference in SIF, for the same load and crack length, between these two specimens. In comparison with SIF obtained for the SE specimen, the SIF for SCB is less dependent on crack length (for example, between  $a/r=0.1$  and  $a/r=0.67$ ,  $K_I$  increases 6.25 times in the case of SE specimen, and just 5.8 times in the case of SCB obtained from SE specimen, the SIF more or less is constant.

In addition, the same results and trends are obtained in  $T$  stress. Since very long cracks are unpractical for laboratory use  $a/r=0.8$  was eliminated (Fig. 15).

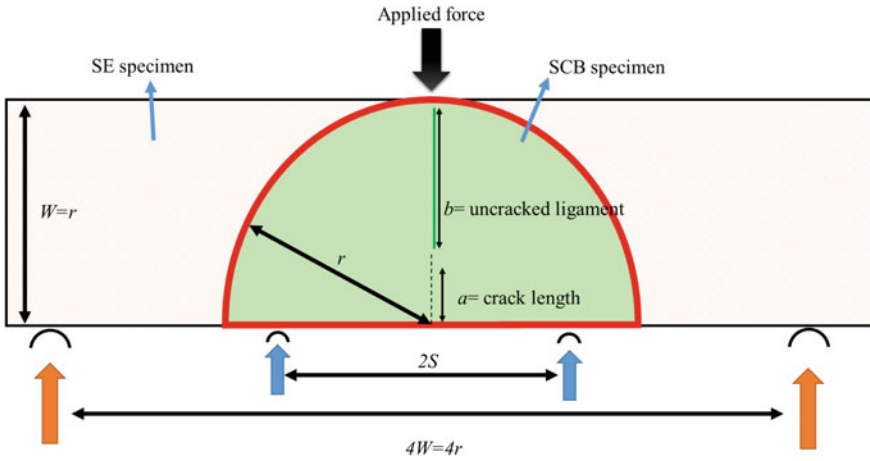


Fig. 12 Dimensional comparison between SE and SCB specimen

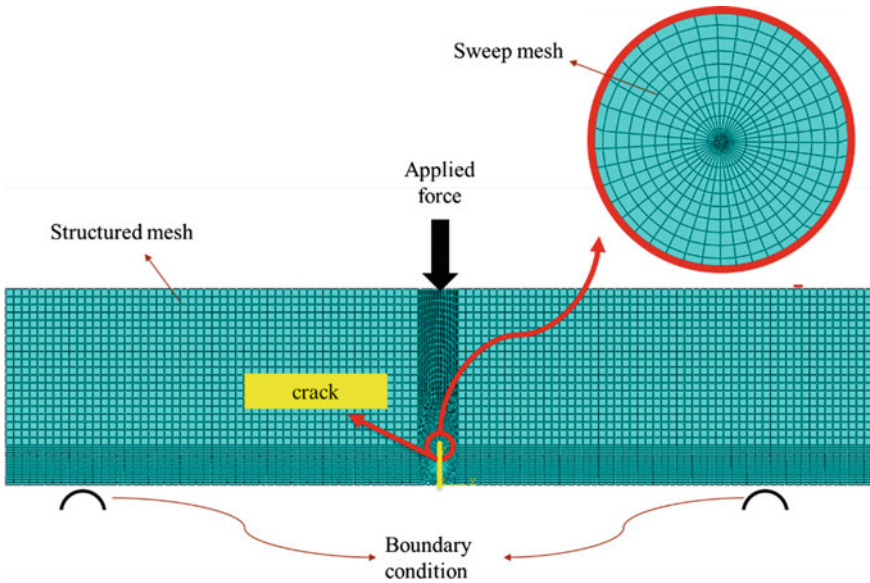
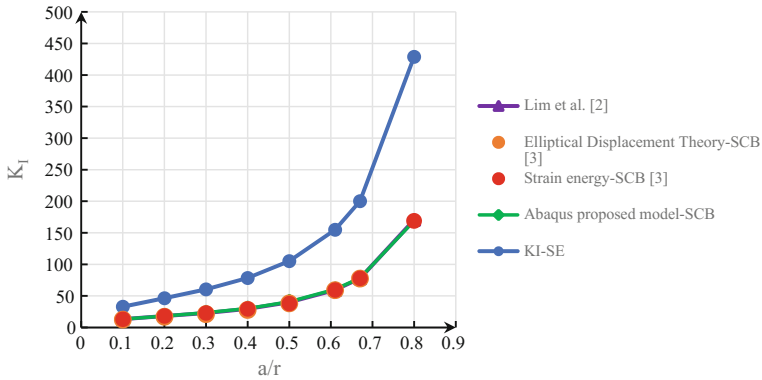
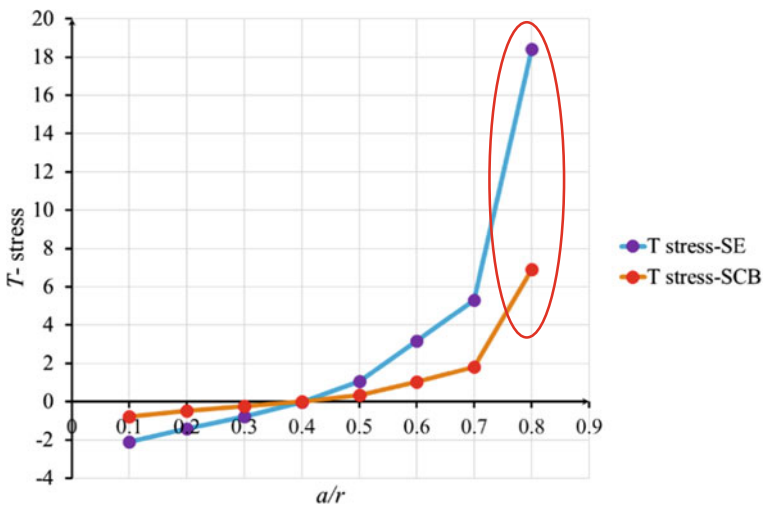


Fig. 13 Finite element mesh used for simulating SCB specimen (mode I-II)

It can be noticed that  $T$  stress for the SE is clearly more dependent on crack length than in the case of SCB specimen. For crack lengths  $a/r$  above 0.4,  $T$  stress in the SE specimen is much higher than in the SCB specimen.  $T$  stress in the SCB specimen is weakly dependent on crack length, while  $T$  stress in SE specimen has a significant dependency [22, 23].



**Fig. 14** Comparison of computed mode I stress intensity ( $K_I$ ) in SE specimen and SCB specimen for  $s/r=0.8$  and  $W=r=100$  mm



**Fig. 15** Comparison of computed T stress in SE specimen and SCB specimen for  $s/r=0.8$  and  $W=r=100$  mm

## 5 Conclusions

In this study, a finite element analysis of the SCB specimen, for mode I and mixed mode I-II situations, is presented. The  $K_I$  and  $K_{II}$  results are validated through comparison with Lim and Chong and Kurupu (elliptic dis. theory and strain energy). It was observed that in mode I, except for  $a/r=0.5$  a good agreement between the proposed Abaqus model and Lim et al. [19] results is found. In mode I, increasing the crack length the stress intensity factor increases sharply. Increasing the ratio  $s/r$

(support span length divided by radius) the difference between proposed Abaqus model and the Chong and Kuruppu [18, 21] increases.

For mixed mode, there is a good agreement between proposed Abaqus model and Lim et al. [2, 19]. In mixed mode the normalized stress intensity factor  $Y_I$ , decreases sharply when the crack angle is increased. For mode II, the normalized stress intensity factor  $Y_{II}$  as a function of crack angle firstly increases and then decreases. The analyses demonstrated that the SCB specimen enables the entire range of mixed-mode I and II to be created.

The comparison is performed for specimens with identical uncracked ligament. The SE specimen presents a wider range of  $K_I$  values than the SCB specimen. The SCB specimen presents a lower dependence of  $T$  stress as a function of crack length. In SE specimens an effect of increasing fracture toughness with decreasing crack length has been identified by several researchers and this is attributed to a  $T$  stress depending. The implication of the present work is that measurements of fracture toughness using SCB specimens are less likely to present effects related to crack length than the SE specimens.

## References

1. Adamson, R.M., Dempsey, J.P., Mulmule, S.V.: Fracture analysis of semi-circular and semi-circular-bend geometries. *Int. J. Fract.* **77**(3), 213–222 (1996)
2. Lim, I.L., Johnston, I.W., Choi, S.K.: Stress intensity factors for semi-circular specimens under three-point bending. *Eng. Fract. Mech.* **44**, 363–382 (1993)
3. Chong, K.R., Kuruppu, M.D.: New specimen for fracture toughness determination of rock and other materials. *Int. J. Fract.* 13–25 (1984)
4. Whittaker, B.N., Singh, R.N., Sun, G.X.: *Rock Fracture Mechanics-Concepts Design and Applications*. Elsevier, Amsterdam (1992)
5. Sun, G.X., Whittaker, B.N., Singh, R.N.: Use of the Brazilian disk test for determining the mixed-mode I-II fracture toughness envelope of rock. In: *Proceedings of International Conference on Mechanics of Jointed and Faulted Rocks, Austria*, pp. 447–454 (1990)
6. Chong, K.P., Kuruppu, M.D., Kuszmaul, J.S.: Fracture toughness determination of rocks with core-based specimens SEM/RILEM. *International Conference on Fracture of Concrete and Rock, Texas*, pp. 13–25 (1987)
7. Ayatollahi, M.R., Aliha, M.R.M., Hassani, M.M.: Mixed mode brittle fracture in PMMA-an experimental study using SCB specimens. *Mater. Sci. Eng. A* **417**(1–2), 348–356 (2006)
8. Aliha, M.R.M., Ayatollahi, M.R., Akbaridoost, J.: Typical upper bound-lower bound mixed mode fracture resistance envelopes for rock material. *Rock Mech. Rock Eng.* **45**(1), 65–74 (2012)
9. Aliha, M.R.M., Ayatollahi, M.R., Smith, D.J., Pavier, M.J.: Geometry and size effects on fracture trajectory in a limestone rock under mixed mode loading. *Eng. Fract. Mech.* **77**(11), 2200–2212 (2010)
10. Xie, Yousheng, Cao, Ping, Jin, Jin, Wang, Min: Mixed mode fracture analysis of semi-circular bend (SCB) specimen: a numerical study based on extended finite element method. *Comput. Geotech.* **82**, 157–172 (2017)
11. “Standard Test Method for Measurement of Fracture Toughness,” *ASTM E 1820, ASTM International, West Conshohocken, PA* (2015)
12. Williams, M.L.: On the stress distribution at the base of a stationary crack. *J. Appl. Mech.* **24**, 109–114 (1957)



13. Yehia, N.A.B., Shephard, M.S.: On the effect of quarter-point element size on fracture criteria. *Int. J. Numer. Meth. Eng.* **21**, 1911–1924 (1985)
14. Lim, I.L., Johnston, I.W., Choi, S.K.: Comparison between various displacement-based stress intensity factor computation techniques. *Int. J. Fract.* **58**, 193–210 (1992)
15. Chan, S.K., Tuba, I.S., Wilson, W.K.: On the finite element method in linear fracture mechanics. *Eng. Fract. Mech.* **2**(1), 1–17 (1970)
16. Abaqus, User's Manual 6.14, Pawtucket, RI, USA: Pawtucket, RI, USA (2016)
17. Davenport, J.C.W., Smith, D.J.: A study of superimposed fracture modes I, II and III on PMMA. *Fatigue Fract. Eng. Mater. Struct.* **16**, 1125 (1993)
18. Chong, K.P., Kuruppu, M.D.: New method to determine the fracture toughness of rocks and oil shale. In: SME-AIME Fall Meeting Denver, Colorado, vol. 278, pp. 1853–1857 (1984)
19. Lim, I.L., Johnston, W.: Stress intensity factors for semi-circular specimens under three-point bending. *Eng. Fract. Mech.* **44**(3), 363–382 (1993)
20. Webb, J.E., Widjaja, S.: R-curve behavior in porous cordierite honeycombs. *Ceram. Eng. Sci. Proc.* **7**(29), 339–348 (2009)
21. Chong, K.P., Kuruppu, M.D.: A new specimen for mixed-mode fracture investigation of geomaterials. *Eng. Fract. Mech.* **30**, 701–712 (1988)
22. Quintana-Alonso, I., Mai, S.P., Fleck, N.A., Oakes, D.C.H., Twigg, M.V.: The fracture toughness of a cordierite square lattice. *Acta Mater.* **58**, 201–207 (2010)
23. Huang, J.S., Chiang, M.S.: Effects of microstructure, specimen and loading geometries on  $K_{Ic}$  of brittle honeycombs. *Eng. Fract. Mech.* **54**(6), 813–821 (1996)

# Analysis of Mode II and Mixed Mode I-II in Fracture and Fatigue: A Numerical and Experimental Study



J. Baganha Marques, S. M. O. Tavares and P. M. S. T. de Castro

**Abstract** The aim of this work is to analyse fatigue crack propagation under pure mode II and mixed mode I-II loading conditions. Bidimensional numerical simulations were carried out using models created with the software *Abaqus Standard*, making use of the conventional finite element method to calculate the stress intensity factors and of the extended finite element method to predict the crack propagation path. The experimental tests were performed on single edge notch specimens, under asymmetrical four-point bending. By varying the position of supports and loads relatively to the crack several situations of mixed mode loading I-II and pure mode II were achieved. The equivalent stress intensity factor for mixed mode I-II and pure mode II was calculated using the finite element method and the software *Abaqus Standard*. The  $da/dN = f(\Delta K_{eq})$ , where  $a$  is the crack length,  $N$  is the number of cycles, and  $\Delta K_{eq}$  is the range of the equivalent stress intensity factor, was obtained and compared with the mode I Paris law equation for the given material, NASGRO material database and other authors' results. The initial fatigue crack growth (FCG) propagation angles were found to be well described by the minimum strain energy density criterion. Regarding the FCG rates, mixed mode results differ from mode I. Several factors like pre-existing flaws in the material, accumulation of experimental and/or post-processing errors and roughness-induced crack closure may have played a part in the differences obtained between the experimental material curve based on  $K_{eq}$  and the NASGRO and Paris law equations based upon  $K_I$ . It is however noted that other authors also found some difference in the  $da/dN$  versus  $\Delta K_{eq}$  or versus  $\Delta K_I$  relationships. Finally, as regards cracks paths, xFEM predictions and experiments showed a variable degree of agreement: very good in some cases, and only approximate in others.

---

J. B. Marques · S. M. O. Tavares (✉) · P. M. S. T. de Castro  
Faculdade de Engenharia da Universidade do Porto, Porto, Portugal  
e-mail: [sergio.tavares@fe.up.pt](mailto:sergio.tavares@fe.up.pt)

P. M. S. T. de Castro  
e-mail: [ptcastro@fe.up.pt](mailto:ptcastro@fe.up.pt)

**Keywords** Fracture mechanics · Fatigue · Mixed mode loading I-II · Mode II loading · Extended finite element method

## 1 Introduction

The behaviour of mechanical structures when subjected to cyclic loading is a very important factor when it comes to design, therefore the mechanical and fatigue properties of used materials must be well understood, including pure mode II and mixed mode I-II loading. In this work a characterization of the Aluminium alloy AA6082-T6 was carried out experimentally using four-point bending specimens and numerically using the finite element method.

In a cracked body there are three basic modes of loading that can be applied to the crack region: mode I, mode II and mode III loading (Fig. 1). In mode I loading, also called opening mode, the principal load is normal to the crack surface and the displacements of the crack surface are perpendicular to the crack plane. In mode II loading, or shear mode, one face tends to slide with respect to the other due to in-plane shear loading. The displacements occur in the crack plane and normal to the leading edge of the crack. Mode III, or tear mode, is caused by out-of-plane shear. The displacements of the crack surface take place in the crack plane parallel to the leading edge of the crack, [1, 2].

The stress intensity factor (SIF) is usually given a subscript to denote the mode of loading, i.e.,  $K_I$ ,  $K_{II}$ ,  $K_{III}$  [1]. The whole linear elastic stress field at the crack tip is known when the stress intensity factor is known [2]. In another words, the SIFs reflect the redistribution of stresses in a body due to the introduction of a crack [3].

Standardized test specimens for mode II and mixed mode I-II still do not exist, as opposed to mode I loading. However, various specimens have been suggested for this purpose. The optimal mixed mode specimen, designed for fracture and fatigue tests should meet some criteria according to [4], namely:

- Full range of mixed mode I-II combinations;

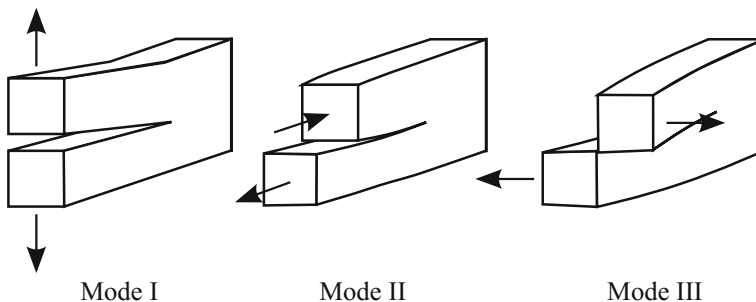


**Fig. 1** Three modes of loading that can be applied to a crack

- Compactness of the specimen;
- Simple manufacturing process;
- Ability to create fatigue pre-cracks under mode I loading;
- Clamping and loading conditions must be easy to achieve;
- Simple test procedure and evaluation;
- Realizability of a state of plane strain;
- Small minimum dimensions to give small fracture loads.

In the following work the Single Edge Notch Bend (SENB) specimen was used in an asymmetrical four-point bend set up.

Compared with mode I FCG, there is a limited amount of data of FCG in mixed mode situations. Some of it is obtained using CTS specimen, eg. Borrego et al. [5]. The CTS specimen pre-crack is loaded under mixed mode situation, but the crack quickly turns to the direction perpendicular to the principal stress, leaving limited possibility for actual mixed mode FCG characterization. It does not surprise that using CTS specimens Borrego et al. [5] found  $da/dN$  versus  $\Delta K_{eq}$  very similar to the  $da/dN$  versus  $\Delta K_I$  data for the material tested (AlMgSi1-T6 aluminium alloy); nevertheless, slightly lower  $da/dN$  values were recorded for the mixed mode tests. A greater decrease in  $da/dN$  for mixed mode tests was observed by Qian and Fatemi on tests of SAE 1045 hot rolled and normalized steel using 4 point bend specimens [6]. In the present work, FCG tests using 4 point bend specimens of Al alloy 6082 are presented, attempting to characterize  $da/dN$  for a range of values of  $K_I/K_{II}$  found along the crack path.

## 2 Tested Material AA6082-T6

All specimens tested were made from the Aluminium alloy AA6082-T6, with the mechanical properties presented in the Table 1.

As for the fatigue properties, the stress intensity factor threshold ( $\Delta K_{th}$ ) was obtained using NASGRO empirical equations and material database, resulting in  $\Delta K_{th} = 113.34 \text{ MPa mm}^{0.5} = 3.58 \text{ MPa m}^{0.5}$ .

**Table 1** Mechanical properties of the Aluminium alloy AA6082-T6

Al 6082-T6	
Young modulus (E)/GPa	69
Yield strength ( $\sigma_{Yield}$ )/MPa	<260
Ultimate strength ( $\sigma_U$ )/MPa	310
Poisson ratio	0.33

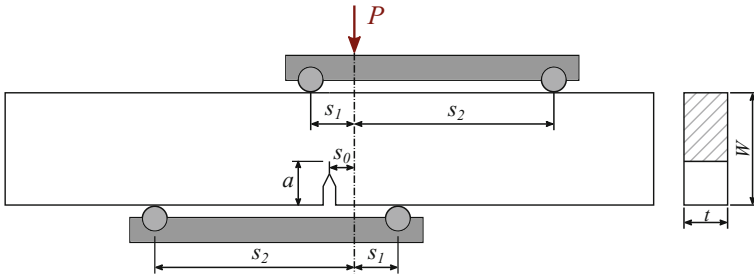


Fig. 2 Four-point bend specimen under asymmetric loading (I-II mixed mode fracture)

### 3 Mixed Mode Fracture with Four-Point Bending Test

The asymmetrical four-point bending set up allows the study of fracture behaviors of a specimen under pure mode II and mixed mode I-II.

Using an asymmetric loading, Fig. 2, mode II and mixed mode stress intensity factor ratios  $K_I/K_{II}$  can be obtained by varying the distance of the applied load  $P$  to the pre-crack plane ( $S_0$ ). Using the set up shown in Fig. 2 in order to obtain pure mode II the distance between the load  $P$  and the pre-crack plane has to be 0 ( $S_0 = 0$ ). This corresponds to a null bending moment along the crack plane.

For mixed mode analysis, varying the value of  $S_0$  will make the mode I component increase, leading to various combinations of shear force and bending moment at the crack plane. According to [7], the stress intensity factors for mixed mode loading I-II can be given by,

$$K_I = \frac{6(S_0 - c_0) * Q}{W^2 t} \sqrt{\pi a} F_I \left( \frac{a}{W} \right) \tag{1}$$

$$K_{II} = \frac{\eta * Q}{W^{0.5} t} \frac{\left(\frac{a}{W}\right)^{1.5}}{\left(1 - \frac{a}{W}\right)^{0.5}} F_{II} \left( \frac{a}{W} \right) \tag{2}$$

where,

$$F_I \left( \frac{a}{W} \right) = \sqrt{\frac{2W}{\pi a} \tan \frac{\pi a}{2W}} \frac{0.923 + 0.199 \left(1 - \sin \frac{\pi a}{2W}\right)^4}{\cos \frac{\pi a}{2W}} \tag{3}$$

or,

$$F_I \left( \frac{a}{W} \right) = 1.121 \left( \frac{a}{W} \right) + 3.740 \left( \frac{a}{W} \right)^2 + 3.873 \left( \frac{a}{W} \right)^3 - 19.05 \left( \frac{a}{W} \right)^4 + 22.55 \left( \frac{a}{W} \right)^5 \tag{4}$$

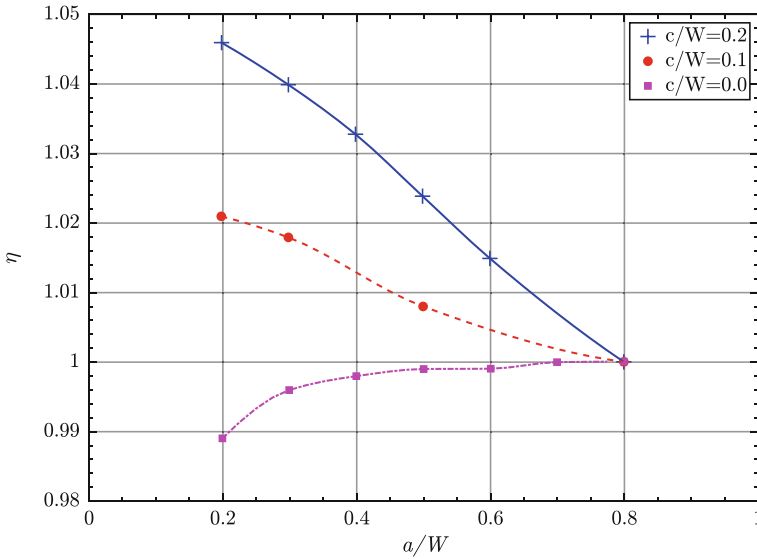


Fig. 3 Correction factor for mode II intensity factor, (adapted from [7])

$$F_{II}\left(\frac{a}{W}\right) = 7.264 - 9.37\left(\frac{a}{W}\right) + 2.74\left(\frac{a}{W}\right)^2 + 1.87\left(\frac{a}{W}\right)^3 - 1.04\left(\frac{a}{W}\right)^4 \quad (5)$$

where  $Q$  is the shear force at the crack tip and  $Q = \frac{S_2 - S_1}{S_2 + S_1} P$  being  $P$  the applied load. The width, thickness and crack length are given by  $W$ ,  $t$  and  $a$  respectively. The relative distance of the applied load location to the pre-crack plane is given by  $\eta = S_0/W$ .  $F_I$  and  $F_{II}$  are the geometry factors which are functions of relative crack length  $a/W$ .

According to [7]  $c_0$  and  $\eta$  (Fig. 3) are correction factors that are functions of  $(a/W)$ ,  $(c/W)$ ,  $(s_1/W)$  and  $(s_2/W)$ . Equations 4 and 5 are only valid for  $0 \leq (a/W) \leq 0.7$  and  $0 \leq (a/W) \leq 1$ , respectively.

Figures 4 and 5 show the relation of the SIF ratio ( $K_I/K_{II}$ ) as well as  $\beta = \text{atan}(K_I/K_{II})$  with the load distance to the pre-crack plane ( $S_0$ ) for  $s_1 = 85$  mm,  $s_2 = 15$  mm,  $P = 36,000$  N,  $a = 14$  mm,  $W = 35$  mm,  $t = 20$  mm.

## 4 Experimental Procedure

In order to prepare the specimens to determinate the crack path under mode II and mixed mode I-II conditions, a fatigue pre-crack was created using a three-point bending set up (mode I loading), ensuring that the plastic region at the crack tip of

**Table 2** Pre-crack dimensions

Specimen	Pre-crack [mm]	Crack deviation
1	3.965	-8.5°
2	3.115	-
3	3.805	-3.5°
4	4.175	-6°
5	4	-6.5°
6	3.905	3.5°
7	3.85	2°

the specimen (Fig. 6) is very small. To fulfill that requirement the recommendations of the document BS DD 19:1972 and the standards ASTM E399, ISO 12108-2002 were followed.

The pre-crack dimensions (mean value) obtained in all specimens are presented in Table 2.

All the specimens were polished using abrasive paper and alumina, concentrating in the surrounding zone where the pre-crack was located was submitted to this process, being that is the region of interest for the current work. The specimens were first polished by hand using a 1200P SiC abrasive paper, followed by a 800P SiC paper and finalized with an alumina abrasive (1.0 μm). It should be noted that the abrasive paper polishing movement was made at ±45° relative to the tip of the notch.

Surface polishing was made in an attempt to facilitate the visualization of the pre-crack and crack tip, making it easier to measure and track crack growth using a camera in the subsequent four-point bend tests.

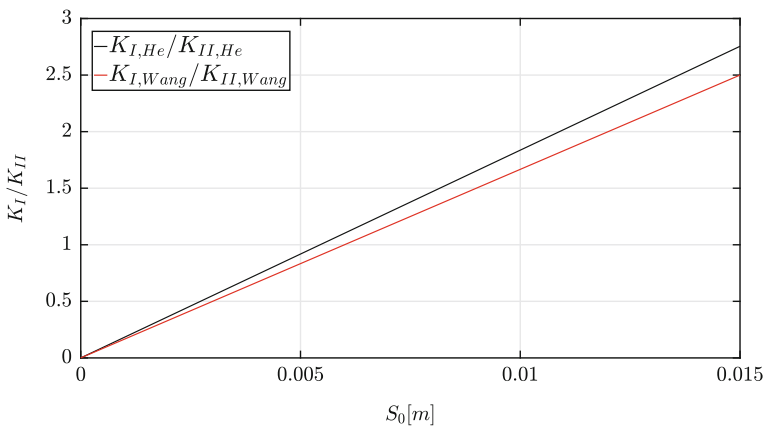


**Fig. 4** Adimensional SIFs versus load distance from crack plane

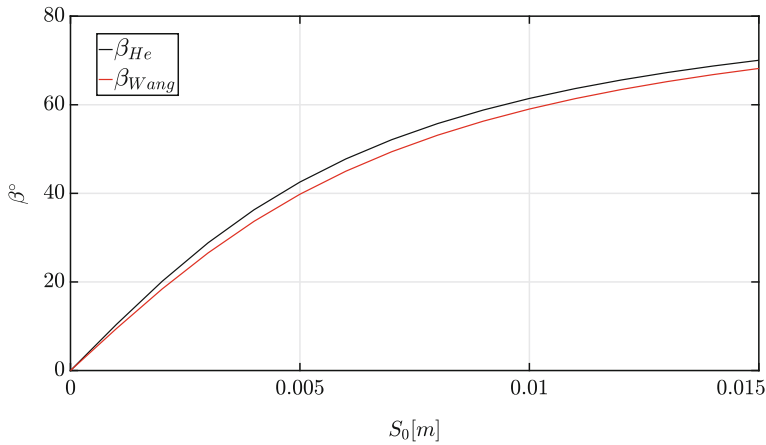


Fig. 5  $\beta$  versus load distance from crack plane

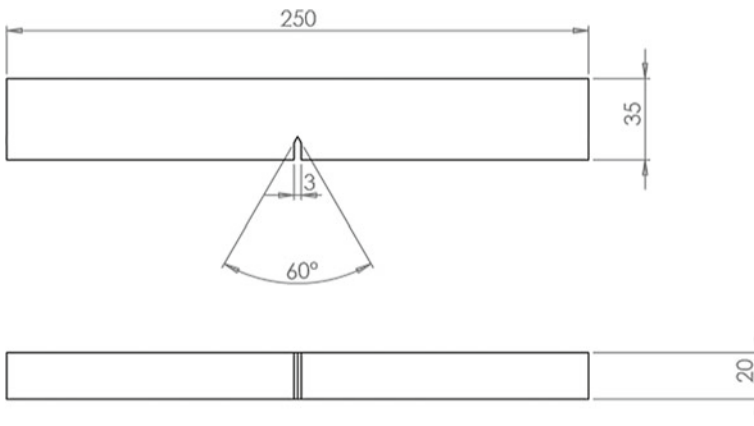


Fig. 6 Single edge notch specimen (mm)

Supported in preliminary tests (Gicquel [8]), the initial chosen equivalent SIF for mode II loading was  $K_{eq,Irwin} = 12.7 \text{ MPa}\sqrt{\text{m}}$ , where  $K_{eq,Irwin} = \sqrt{K_I^2 + K_{II}^2}$ . The specimen would be under the calculated load until it showed signs of crack propagation, if at the end of a considerable number of cycles no changes were verified the load  $P$  would be increased by roughly 10% and the whole process would be repeated until crack growth occurred. In order to verify if there was any noticeable crack growth, during the fatigue test, at the end of a certain number of cycles, the crack would be examined under a microscope that was set up on one face of the specimen, as seen in Fig. 7.

The methodology described for the pure Mode II loading experiment is the same for all the other experiments. Table 3 presents the specimens tested alongside with the





**Fig. 7** Experimental set up

**Table 3** Tested specimens

Specimen nr	$\frac{K_I}{K_{II}}$	$S_1$ [mm]	$S_2$ [mm]	$S_0$ [mm]	Frequency [Hz]
1	0	95	5	0	2
4	0.23	95	5	1	2
3	1.10	85	15	4	8
5	2.79	85	15	10	8

distances used in the each set up for different situations of mode mixcity, considering the dimensions represented in (Fig. 8).

It should be noted that:

- The  $R$  value was 0.1 throughout all the tests
- Specimens 1 and 4 width were reduced from 35 to 28 mm
- Specimens 3 and 5 width were reduced from 35 to 25 mm
- Specimen 1 was intended to be under pure mode II ( $K_I = 0$ )
- Specimen 4 was under pure mode II with compression
- Specimens 3 and 5 were under mixed mode I-II.

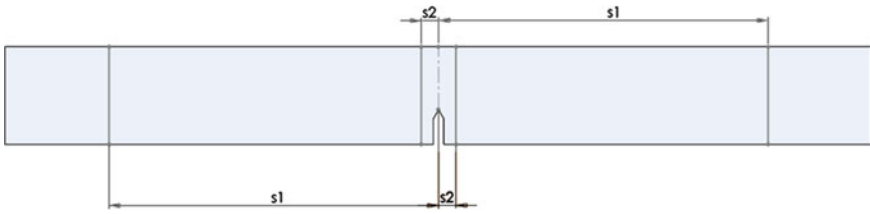


**Fig. 8** Single edge notch specimen

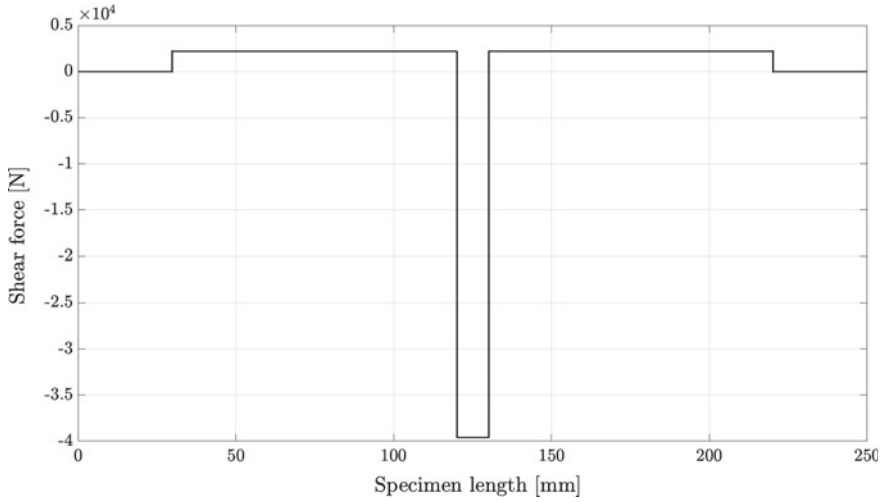


**Fig. 9** Shear force diagram for the experimental pure mode II loading

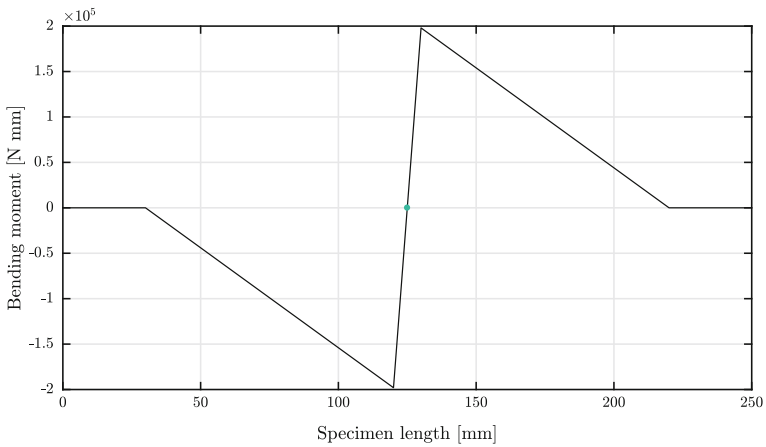


**Fig. 10** Bending moment diagram for the experimental pure mode II loading

**Table 4** Data for the fatigue tests for specimen 1 under pure mode II loading

Width (mm)	$P$ [N]	$K_{eq}$ [MPa $\sqrt{m}$ ]	$\Delta K_{eq}$ [MPa $\sqrt{m}$ ]	No. of cycles	Obs.
35	40060.1	12.7	11.4	90,000	No growth
28	36000.0	16.6	14.9	85,000	No growth
28	40000.0	18.4	16.6	52,500	No growth
28	44000.0	20.3	18.2	56,475	Growth

**Table 5** Data for the fatigue test for specimen 4 under mixed mode I-II loading ( $\beta = 13^\circ$ )

Width (mm)	$P$ [N]	$K_{eq}$ [MPa $\sqrt{m}$ ]	$\Delta K_{eq}$ [MPa $\sqrt{m}$ ]	No. of cycles	Obs.
28	37000.0	17.8	16.0	68,697	No growth
28	41000.0	19.7	17.8	59,613	No growth
28	43000.0	20.7	18.6	191,001	No growth
28	44000.0	21.2	19.1	21,825	No growth
28	46000.0	22.1	19.9	24,256	Growth

**Table 6** Data for the fatigue test for specimen 3 under mixed mode I-II loading ( $\beta = 48^\circ$ )

Width (mm)	$P$ [N]	$K_{eq}$ [MPa $\sqrt{m}$ ]	$\Delta K_{eq}$ [MPa $\sqrt{m}$ ]	No. of cycles	Obs.
25.0	21000.0	13.3	12	13968.0	Growth

**Table 7** Data for the fatigue tests for specimen 5 under mixed mode I-II loading ( $\beta = 70^\circ$ )

Width (mm)	$P$ [N]	$K_{eq}$ [MPa $\sqrt{m}$ ]	$\Delta K_{eq}$ [MPa $\sqrt{m}$ ]	No. of cycles	Obs.
25	15600.0	20.0	18.0	36,596	No growth
25	18200.0	23.4	21.0	36,199	No growth
25	20800.0	26.7	24.1	357,999	No growth
25	23000.0	29.5	26.6	241,287	No growth

Using solid mechanics the shear force and bending moment throughout the specimen was calculated for each case. In Figs. 9 and 10 the shear force and bending moment diagrams are presented for pure mode II loading.

The data obtain from the fatigue tests for all specimens is presented in Tables 4, 5, 6 and 7.

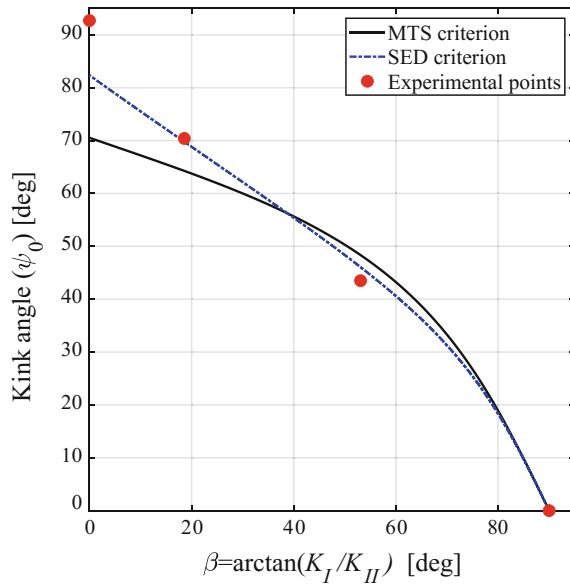
It should be noted that;

- The kink angle, corresponding to the direction of propagation from the initial mode I pre-crack measured on both sides of each specimen, and the average is given as function of  $\text{atan}(K_I/K_{II})$  in Table 8,

**Table 8** Mode mixicity and kink angle

Cases	$K_I/K_{II}$	$\beta$	$\psi_0$
Specimen 1	0.336	18.57°	70.4°
Specimen 4	0	92.7°	92.7°
Specimen 3	1.331	43.5°	43.5°
Mode I (pre-crack)	–	90°	0°

**Fig. 11** Kink angle  $\psi_0$  versus  $\beta$



- Specimen 1 was intended to be pure mode II but due to some inclination of the pre-crack that was not completely achieved, and instead a mixed mode test resulted.
- Specimen 4 was tested under conditions of pure mode II combined with compression of the crack faces, (although it was initially intended for  $K_I/K_{II} = 0.23$ ).

In Fig. 11 the experimental points were plotted alongside the MTS [9] and SED [10] criteria.

## 5 Numerical Models: Crack Propagation Path

In order to determine the crack path the extended finite element method (xFEM), available in *Abaqus Standard*, was used. This method allows the modelling of crack and crack growth without remeshing, since it is a fully mesh independent technique. Otherwise to study the evolution of the crack and crack path propagation one would have to redo and remesh the crack increment by increment, a very tedious and time

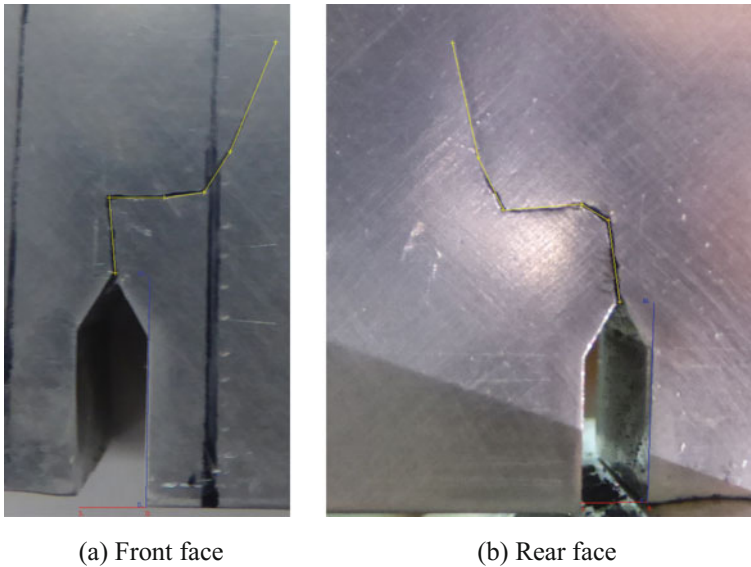


**Fig. 12** Crack path obtained with image digitizer

consuming process. Throughout the experimental procedure, several pictures were taken of each side of the specimens. Using an image digitizer, Fig. 12, it was possible to trace the crack path of each side, obtain an average and compare it to path obtained using the xFEM feature available in the software *Abaqus Standard* [11].

The figures were obtained for specimen 1, and this methodology was followed for all specimens.

For specimen 1, the model represented in Fig. 13a used a coarse mesh on the crack domain with elements with 2 mm length (seed size 2), the rest of the mesh is structured and the elements have 3 mm length (seed size 3). In order to compare the mesh influence in xFEM a finer mesh was used with elements with 1 mm length (seed size 1) in the crack region, Fig. 13b.

The numerical results obtained were then compared to the experimental crack path, presented in Fig. 14.

## 6 Equivalent Stress Intensity Factor Determination

Most of the data available for materials, including the one used in this work, is obtained for pure mode I loading, which can lead to imprecise results of life prediction for an component, since in actual practice mixed mode situations are usually found.

Using the data obtained in the experimental results, that being the number of cycles ( $N$ ) and photographs taken along the tests, together with numerical results

provided by finite element models, a comparison between the NASGRO material curve, Paris law equation and material curves obtained by other authors was made.

By post processing of the images acquired the crack path geometry can be recreated in a finite element model and through that model the stress intensity factors can be determined for each crack tip. Given that for each photograph the number of cycles was recorded, it is possible to determine the crack growth  $\Delta a$  associated with the increase in number of cycles  $\Delta N$ .

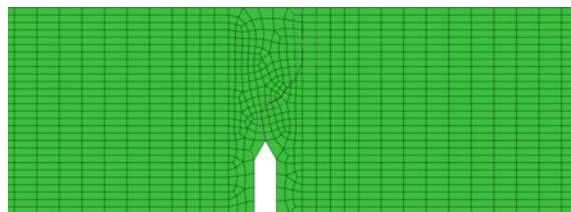
From all the photographs taken a few were selected based on quality and crack growth. The situations for specimens 4 and 5 were not modelled. The cases modelled were for pure mode II and mixed mode loading with  $K_I/K_{II} = 1.10$ .

Starting with specimen 1, tested under pure mode II loading, the higher quality pictures are presented in Fig. 15. The tool used to process the images was a plot digitizer in which, by hand, the crack path was traced allowing the acquisition of its coordinates  $x$  and  $y$ . The graph of the coordinates acquired for this specimen is presented in Fig. 16.

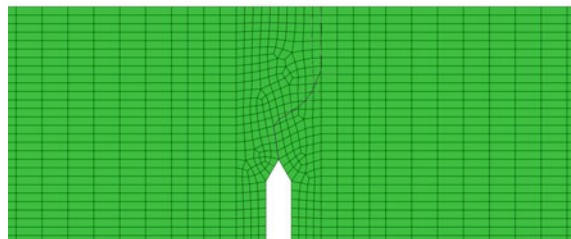
An approximation of the crack geometry was created on a bidimensional finite element model using the software *Abaqus Standard* and for each crack tip three values (before, at and after the crack) of SIFs were obtained using the J integral and VCCT techniques, being that the mean value of all 3 SIFs was used through. Crack length for each increment is obtained by using the norm of the  $x$  and  $y$  coordinates ( $\sqrt{x^2 + y^2}$ ) between each crack tip. Figure 17 show the model at the instance photograph 4 was taken. The crack was modelled from the end until the beginning (starting in the last photo and finishing on the first).

In order to calculate the SIFs using the two techniques a square partition was created at the crack tip (Fig. 18).

**Fig. 13** Crack path obtained with xFEM for specimen 1



(a) coarse mesh

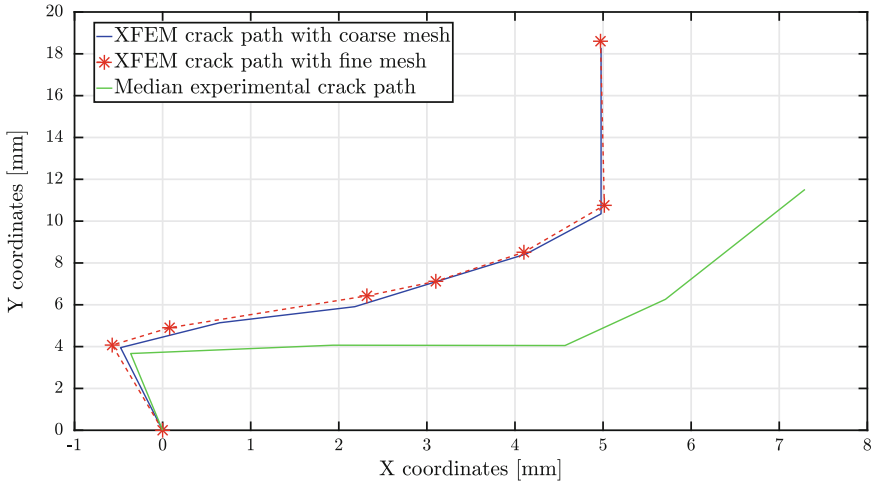


(b) fine mesh

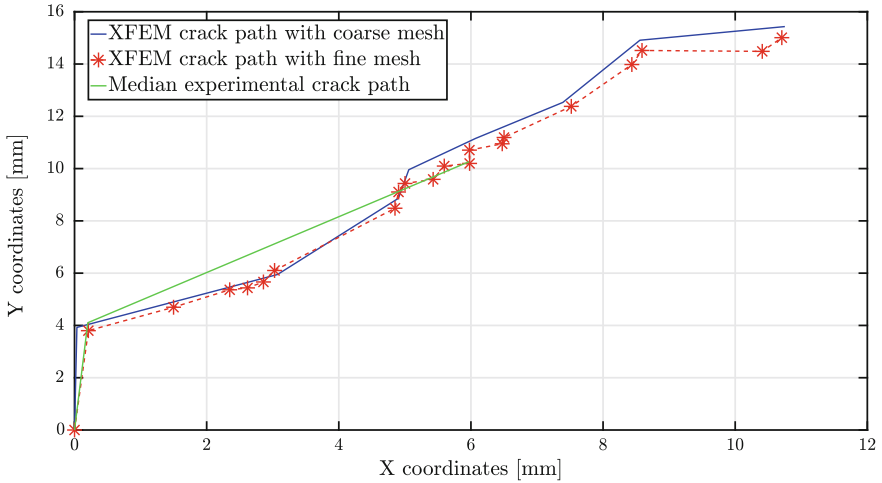
Figures 19 and 20 show the square partition with the J integral contours used (10) and the free body cut and coordinate system used in the VCCT, respectively.

For the J-integral technique the mode I and mode II SIFs were obtained for three points: a point before the crack, at the crack and after the crack being that the median value of all three was used to describe the respective stress intensity factors.

The stress intensity factors obtained by the J-integral and VCCT for specimen 1 are shown in Table 9.

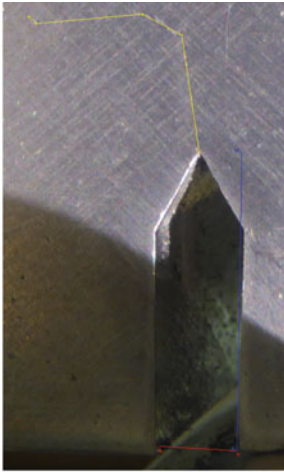


(a) Specimen 1

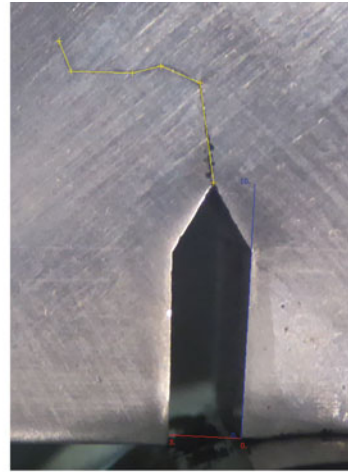


(b) Specimen 3

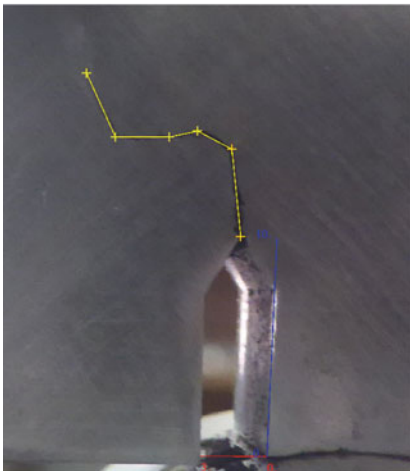
**Fig. 14** Comparison between crack path obtained with xFEM for fine mesh, coarse mesh and experimental crack path



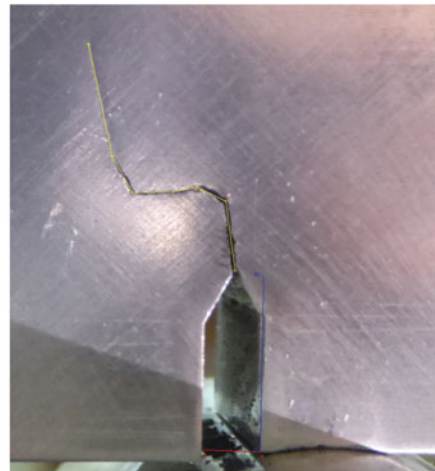
(a) Photo 1 - specimen 1



(b) Photo 2 - specimen 1



(c) Photo 3 - specimen 1



(d) Photo 4 - specimen 1

**Fig. 15** Pictures of specimen 1

Since the values from each method are very similar the following calculations will be done using the VCCT values. Through the created finite element model, crack growth between pictures ( $\Delta a$ ) was measured and presented in Table 10 alongside with the corresponding equivalent SIFs ( $K_{eq, Irwin}$ ) and number of cycles  $\Delta N$ .

The exact same methodology was used for specimen 3, obtaining Fig. 21.

The crack coordinates are negative because this specimen was measured in a different position than the previous one.



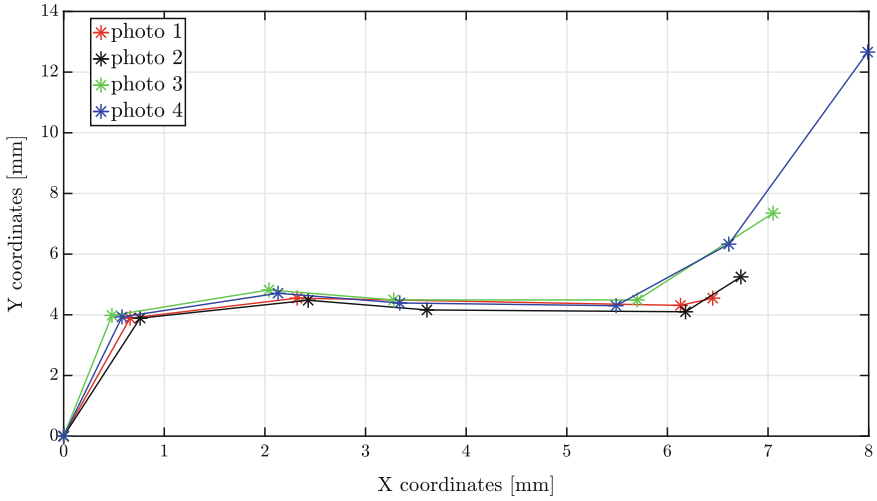


Fig. 16 Plot of the coordinates obtained from image post processing—specimen 1

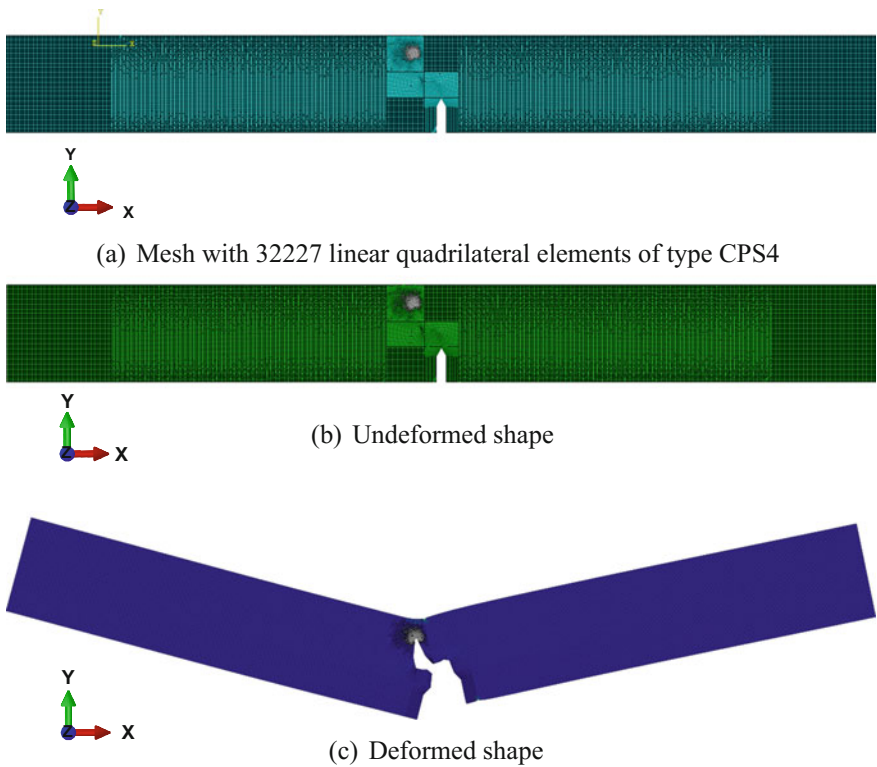


Fig. 17 Photo 4—specimen 1

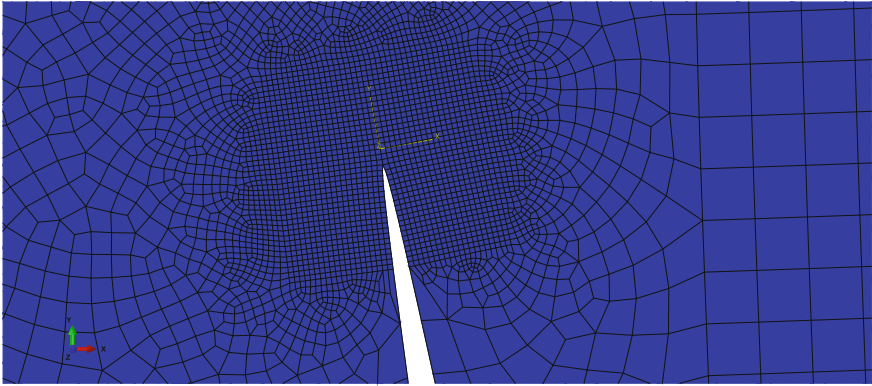


Fig. 18 Partition at crack tip specimen 1—photo 4

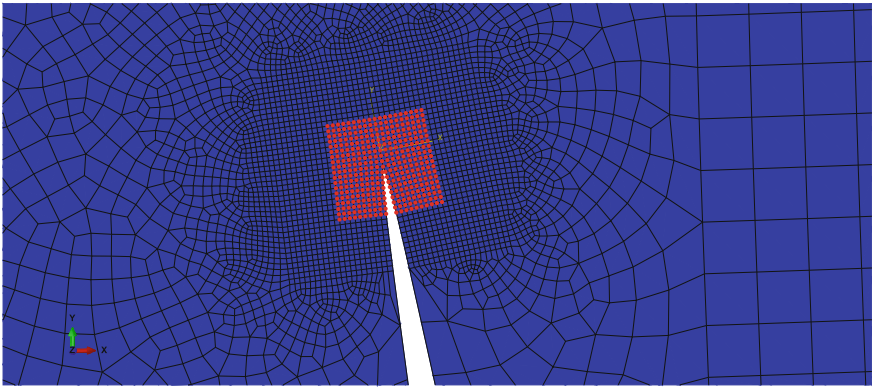


Fig. 19 Square partition and mesh contours used for the J integral

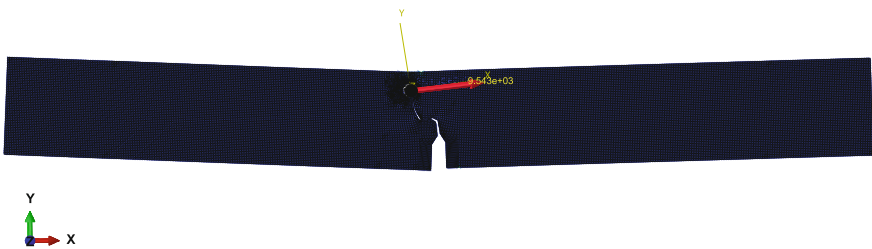


Fig. 20 Free body cut and coordinate system used for the VCCT

**Table 9** Mode I and mode II equivalent SIFs for specimen 1

	VCCT				J integral	
	$K_I$	$K_{II}$	$K_{eq, Irwin}$		$K_{eq, Irwin}$	
		[MPa√mm]	[MPa√mm]	MPa√m	MPa√mm	MPa√m
Pre-crack	172.3	512.9	541.1	17.1	533.1	16.9
Photo 1	738.6	9.6	738.7	23.4	737.3	23.3
Photo 2	834.6	51.0	836.1	26.4	827.0	26.2
Photo 3	1076.0	83.7	1079.2	34.1	1056.8	33.4
Photo 4	3091.5	176.2	3096.5	97.9	3138.1	99.2

**Table 10** Values of the equivalent SIFs and the correspondent  $\frac{\Delta a}{\Delta N}$  for specimen 1

	$\Delta a$ [mm]	$\Delta N$ cycle	$\frac{\Delta a}{\Delta N}$ [mm · cycle <sup>-1</sup> ]	$\Delta K_{eq, Irwin}$	
				[MPa√mm]	[MPa√m]
Pre-crack to photo 1	5.9	39,689	1.5E-04	487	15.4
Photo 1 to photo 2	0.9	14,400	5.9E-05	664.8	21.0
Photo 2 to photo 3	1.9	1858	1.0E-03	752.5	23.8
Photo 3 to photo 4	5.4	528	1.0E-02	971.3	30.7

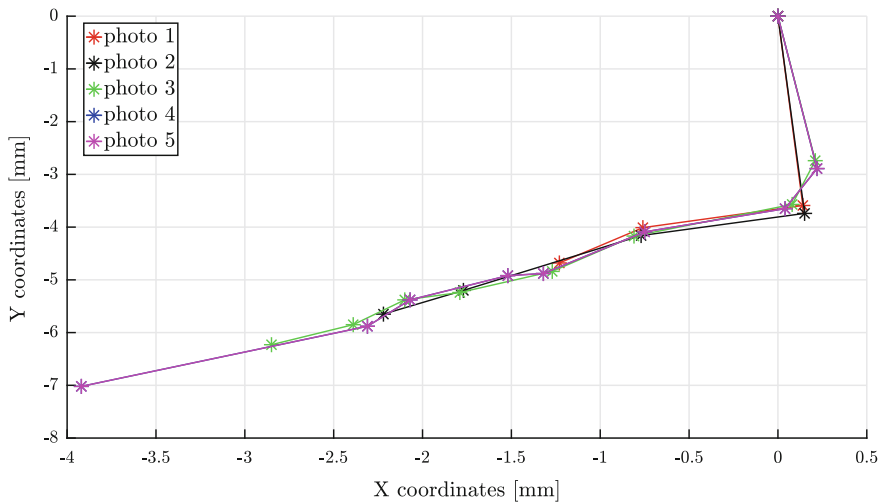


**Fig. 21** Plot of the coordinates obtained from image post processing—specimen 3

**Table 11** Mode I and Mode II equivalent SIFs for specimen 3

	VCCT				J integral	
	$K_I$	$K_{II}$	$K_{eq, Irwin}$		$K_{eq, Irwin}$	
		[MPa√mm]	[MPa√mm]	[MPa√m]	MPa√mm	MPa√m
Pre-crack	344.7	258.9	431.2	13.6	431	13.6
Photo 1	574.9	100.5	583.6	18.5	583.4	18.4
Photo 2	840.0	50.6	841.5	26.6	830.0	26.3
Photo 3	919.4	183.5	937.5	29.6	946.4	29.9
Photo 4	1169.8	132.3	1177.2	37.2	1177.7	37.2
Photo 5	1704.9	404.0	1752.1	55.4	1751.4	55.4

**Table 12** Values of the equivalent SIFs and the correspondent  $\frac{\Delta a}{\Delta N}$  for specimen 3

	$\Delta a [mm]$	$\Delta N$ cycle	$\frac{\Delta a}{\Delta N}$ [mm · cycle <sup>-1</sup> ]	$\Delta K_{eq, Irwin}$	
				[MPa√mm]	[MPa√m]
Pre-crack to photo 1	0.97	10,000	9.7E-05	388.0	12.3
Photo 1 to photo 2	2.1	1500	1.4E-03	525.2	16.6
Photo 2 to photo 3	0.9	2122	4.1E-04	757.4	24.0
Photo 3 to photo 4	1.3	218	6.0E-03	843.8	26.7
Photo 4 to photo 5	2.4	128	1.9E-02	1059.5	33.5

Using the information gathered in Tables 10, 11 and 12 the points of the values of  $da/dN$  as function of  $\Delta K_{eq, Irwin}$  were plotted in the NASGRO material fitting curve ( $R = 0.1$ ) [12], along with the Paris law fitting curve which, according to [13] is as follows,

$$\frac{da}{dN} = 85.409 \cdot 10^{-15} \Delta K^{3.7554} \tag{6}$$

A non-linear regression was also done using the obtained data, being that the second point from specimen 1 was not included in it due to being an outlier relatively to the rest of the data (Fig. 22).

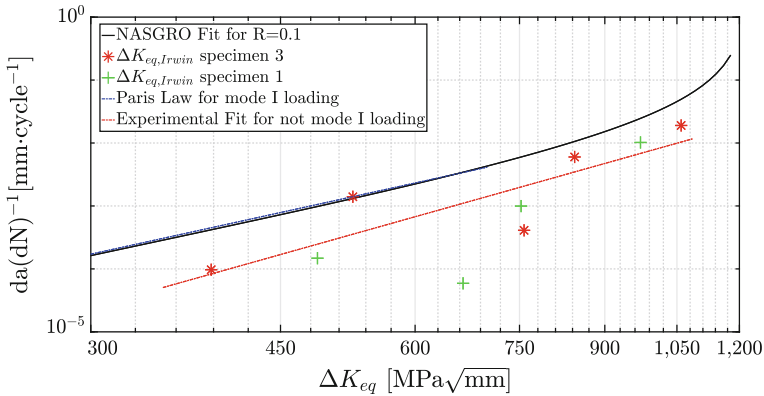


**Fig. 22** Comparison between NASGRO material fitting curve, Paris law and points obtained from the experimental procedures post processing

## 7 Conclusions

The main conclusions that were taken from this work relatively to the experimental and numerical procedures are,

- The asymmetrical four-point bending set up used is extremely sensitive to the distances between the supports and loads, so precise and adequate instrumentation should be used while assembling the test in order to achieve accurate results.
- The observation and record of the experimental fatigue tests should be done thoroughly, using a high quality camera allowing good quality footage of crack growth and facilitating image post-processing.
- The results obtained from the finite element models created throughout this work showed good agreement with analytical predictions, when such were possible, demonstrating that the finite element method is an excellent tool to estimate the stress field at the crack tip.
- The crack paths obtained using the extended finite element method showed a variable degree of agreement with the paths obtained experimentally, which doesn't mean the numerical model results are wrong, it is more likely that the data input on the model was not the most accurate.
- The fatigue crack growth behaviour results, expressed as a function of  $\Delta K_{eq}$ , for mixed mode I-II and mode II loading were different from the mode I data from the NASGRO database and Paris law equation for the studied material. That may be due to the accumulation of experimental and/or post-processing errors (cycle and crack growth recording, manual image processing), roughness-induced crack closure and thus friction between crack surfaces. Nevertheless, several authors also found differences in the  $da/dN$  versus  $\Delta K_{eq}$  for various mode mixicities when compared to the  $da/dN$  versus  $\Delta K_I$ .
- The asymmetrical four-point bending set up seems to provide a simple way of testing material fatigue properties for mixed mode and mode II loading.

## References

1. Anderson, T.: Fracture Mechanics, 3rd edn. Taylor & Francis Group, LLC (2005)
2. Broek, D.: Elementary Engineering Fracture Mechanics, Fourth revised edn. Martinus Nijhoff Publishers (1986)
3. de Moura Branco, C.: Mecnica dos Materiais, 5th edn. Fundao Calouste Gulbenkian (2011)
4. Richard, H.: Specimens for investigating biaxial fracture and fatigue processes. In: Biaxial and Multiaxial Fatigue, pp. 217–229. Mechanical Engineering Publications (1989)
5. Borrego, L., Antunes, F., Costa, J., Ferreira, J.: Mixed-mode fatigue crack growth behaviour in aluminium alloy. *Int. J. Fatigue* **28**(5–6), 618–626 (2006)
6. Qian, J., Fatemi, A.: Fatigue crack growth under mixed-mode I and II loading. *Fatigue Fract. Eng. Mat. Struct.* **19**(10), 1277–1284 (1996)
7. He, M., Hutchinson, J.: Asymmetric four-point crack specimen. *J. Appl. Mech.* **67**(1), 207–209 (2000)
8. Gicquel, L.: Cracked beam subjected to asymmetric four-point bending. Technical report, Faculdade de Engenharia da Universidade do Porto (July 2017)
9. Erdogan, F., Sih, G.C.: On the crack extension in plates under plane loading and transverse shear. *J. Basic Eng.* **85**(4), 519–525 (1963)
10. Sih, G.C.: *Mechanics of Fracture Initiation and Propagation*. Springer Science+Business Media (1991)
11. Dassault Systèmes: Abaqus documentation. Dassault Systèmes Simulia Corporation (2017)
12. NASGRO.: Fracture Mechanics and Fatigue Crack Growth Analysis Software, Version 4.02. Southwest Research Institute (SwRI), September (2002)
13. Ferreira, M.A.C.: Mixed mode crack propagation: numerical and experimental study. Master thesis, Faculdade de Engenharia da Universidade do Porto (2017)

# **Part X**

## **Joining**

# The Friction Weldability of AA6063 Tube to AA6082 Tube Plates Using an External Tool



E. Korkmaz, A. Gülsöz and C. Meran

**Abstract** Aluminum and its alloys are frequently used in industry due to their low density as well as their high strength and corrosion resistance. Although the most common welding methods for aluminum are TIG, MIG, and plasma, due to the high temperatures during welding, the metallurgical precipitates formed in the heat affected zone disrupt the interior and affect the mechanical properties negatively. Friction welding of tube to tube plate using an external tool (FWTPET) which is a fairly new method has been developed to overcome this shortcoming and tube to tube plate welding has started to be made with this method. In this study, aluminum alloy AA6063 tubes were successfully joined to AA6082 plate by FWTPET. The welding groove on the plate, the gap between the tube and the plate, and the tube projection length were studied experimentally. The effects of all parameters on shear strength, micro hardness, and the formation of internal structure of the weld zone were investigated, as a result the optimum welding parameters are founded.

**Keywords** Friction welding · Aluminium welding · FWTPET  
Tube to tube plate welding

## 1 Introduction

Friction welding of tube to tube plate using an external tool (FWTPET) is a new solid state welding method [1–3] first time applied in 2006 [4–8]. This method can be used for joining tube to tube plate of similar or dissimilar materials [9–11]. FWTPET may be used in many sectors like manufacturing industries, automotive, aerospace industries [12, 13]. FWTPET provides quality joints compared to the conventional welding methods such as fusion welding [14–16]. FWTPET produces high-quality

---

E. Korkmaz · A. Gülsöz · C. Meran (✉)  
Engineering Faculty, Department of Mechanical Engineering, Pamukkale University,  
Denizli 20020, Turkey  
e-mail: [cmeran@pau.edu.tr](mailto:cmeran@pau.edu.tr)

© Springer Nature Switzerland AG 2019  
L. F. M. da Silva (ed.), *Materials Design and Applications II*, Advanced  
Structured Materials 98, [https://doi.org/10.1007/978-3-030-02257-0\\_29](https://doi.org/10.1007/978-3-030-02257-0_29)



leakproof joints. Unlike traditional welding methods, FWTPET is an energy efficient, environmentally friendly method [1].

During the production of heat exchangers, economizers and central heating boilers considerable amount of time spent for the plate welds of the tubes. The aim of this study is to determine suitable welding parameters of tubes to tube plates by using the FWTPET method, and reduce the welding time and costs compared to traditional welding [17–19].

Friction welding has many advantages. One of them is to weld non-weldable alloys. Another important feature of the friction welding process is that the welded material is not melted and recast [5, 20]. The FWTPET which is a mixture of friction stir welding [21] and friction welding [19] methods. There is a tool of shoulders and pins similar to the friction stir welding. This tool is in contact with the tube surface, and a friction-induced softening is provided. Unlike the friction stir welding, the pin does not mix with to softened metal, and the travelling is not given to pin over the tool or workpiece [22].

There are many parameters that influence the quality of welding in the FWTPET [23]. Some important parameters are tool rotational speed, the vertical load of the tool, the clearance between the tube and the pin, the clearance between the tube and the plate, tube projections, the time of the contact, the diameter of the tool shoulder, the diameter of the pin and the welding temperature [19].

In addition to these parameters in this study, the effect of the welding groove on welding quality, which has not been tried in the literature before, is investigated. In order to increase the volume of the softened metal between the tube and the plate, the welding groove is provided on the plates.

## 2 Materials and Methods

Aluminium alloys, EN AW-6082-T6 as plate material, and EN AW-6063-T5 as tube materials were used for the experiments. The chemical composition of plate, tube, and tool materials were given in Table 1.

The plates were prepared in dimensions of  $5 \times 50 \times 70$  mm, and tubes in the dimensions of  $\text{Ø}20 \times 2$  mm. The tubes were cut at 32 mm with tube projections of 3 mm, Fig. 1. One of the most important parameters affecting the quality of welding in FWTPET was vertical load [22]. Keeping the vertical load values constant was very important to be able to perform every welding operation under the same conditions. The vertical load values during welding was different when the tool was in contact with the tube and plate. It was difficult to keep the same vertical load value under control for each welding operation.

That's why a test setup was manufactured. The vertical load during each test could be kept under control using this special test setup. The general view of test setup and its components were shown in Fig. 2.

**Table 1** The chemical composition of plate, tube, and used tool materials (%)

	C	Fe	Si	P	S	Cu	Mn	Mg	Zn	Cr	Al
EN AW-6082-T6 (Plate)	-	0.5	0.7-1.3	-	-	0.1	0.4-1.0	0.6-1.2	0.2	0.15	Bal.
EN AW-6063-T5 (Tube)	-	0.35	0.2-0.6	-	-	0.1	0.1	0.45-0.9	0.1	0.1	Bal.
X210Cr12 (Tool)	1.90-2.20	Bal.	0.10-0.60	0.030	0.030	-	0.20-0.60	-	-	11.00-13.00	-

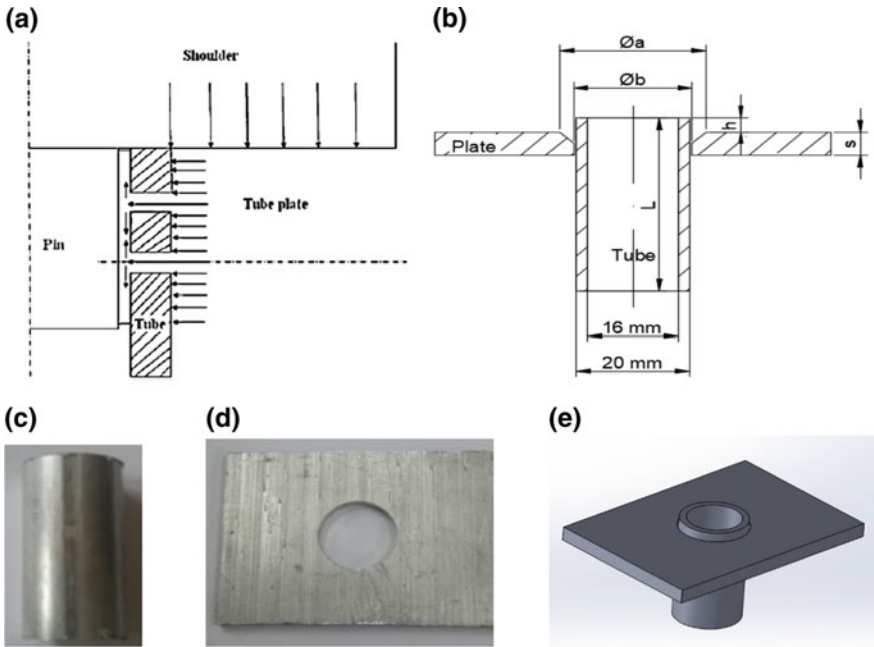


**Fig. 1** The principle of FWTPET (a) [6], dimensions (b), tube (c), plate (d), and assembling (e) used welding

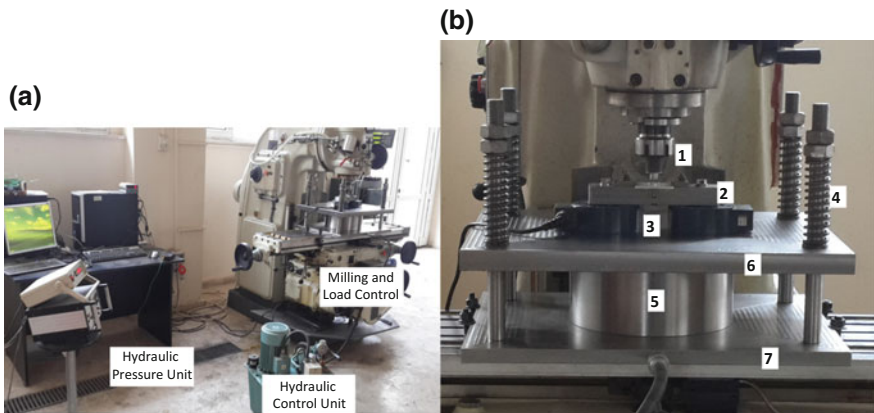


**Fig. 2** The view of the test setup, a general, b detail view of fixing system (1: Tool, 2: Sample holder, 3: Load cell, 4: Counter-force spring, 5: Hydraulic cylinder, 6: Moving table, 7: Fixed table)

The upper table which was connected with the workpiece could move upwards using a load control unit. Thanks to the hydraulic pressure adjustment unit, the vertical force in each welding operation could be kept at about the same value [22].

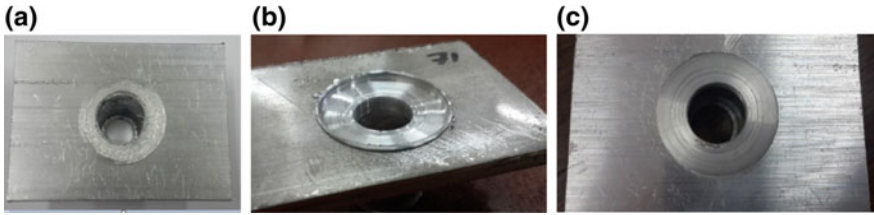


**Fig. 3** Insufficient softening during welding (a), the rotating tool is sinking on the plate (b), proper welding (c)

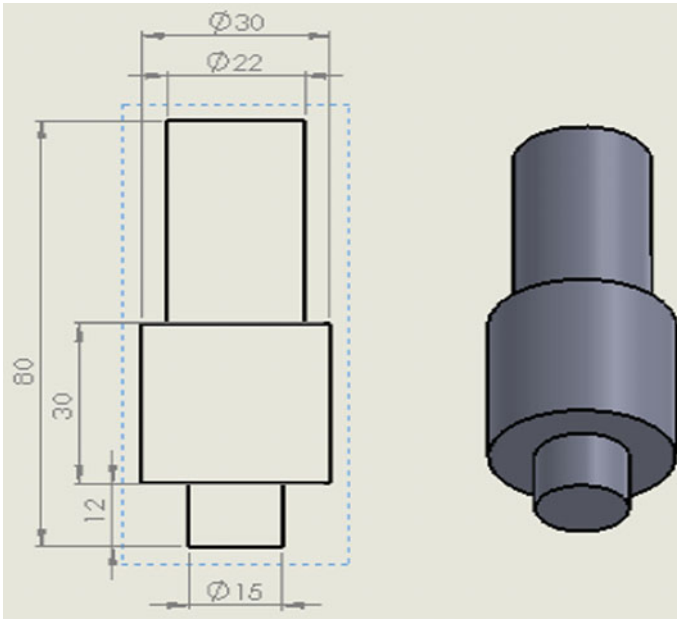


**Fig. 4** The dimension of tool (X210Cr12) used for FWTPET

It was observed that if the value of load applied from rotating tool to the workpiece was less than 200 kg, where the tool shoulder was in contact with the plate, sufficient softening was not achieved as in Fig. 3a. The rotating tool was over sinking on the plate when the vertical force was too high. This was not desirable because it would cause the notch effect, Fig. 3b. A fairly well-welded was obtained when the vertical load kept about 300 kg, Fig. 3c.

Although the geometry of tool pin, and shoulder were important welding parameter, both of them were kept constant in this study. The tool pin diameter was smaller than the tube inner diameter, causing part of the softened metal volume to flow into the tube instead of the gap between the tube and the plate. The hardened cold work tool steel was used for all weldings shown in Fig. 4.

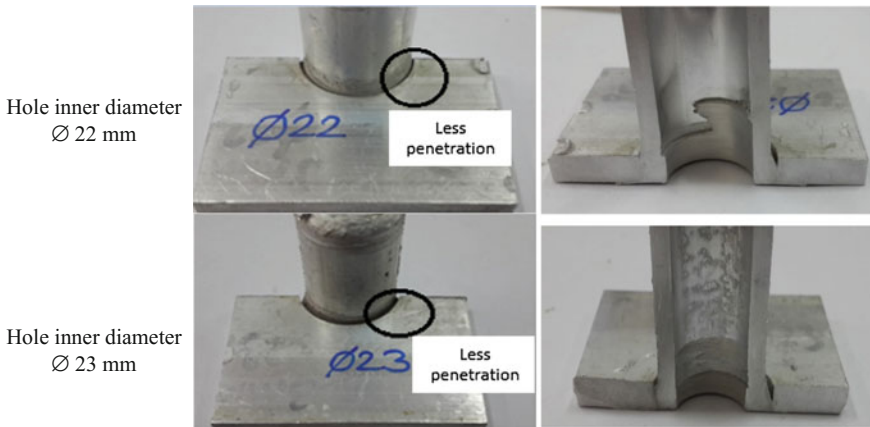


**Fig. 5** Cross-sectional view of the welded sample with a hole diameter of 22 and 23 mm

The compression tests were carried out to find out the shear strength of welded joints. An apparatus had been fabricated to fix up the samples during the compression tests. Other important parameters of FWTPET were tool rotational speed and temperature. FWTPET was a solid state welding method, there was no need for complete melting during welding of materials. During welding, the temperature must reach about 0.6–0.7 times of the melting temperature of welded metals [22]. The temperature could be measured by thermocouples and infrared thermometer during welding.

The tool rotational speed and the vertical force directly affected the softening temperature of welded metals. Insufficient heat input occurred when welding was carried out at low rotational speeds. This is affected by the contact time between the tool and the workpiece during welding. The optimum tool rotational speed on the shear strength were obtained at 1180 rpm [22].

The effect of welding quality on the void space between the tube and the plate was observed during the tests. During FWTPET, the softened metal flowed the gap between the tube and the plate to fill. The tube projections affected the softened metal volume. The minimum volume of softened metal should be calculated according to tube projection, the hole diameter on the plate, gap between the tube and the plate [19].

After theoretically and practically calculation it was observed that the entire volume of the softened metal did not fill the gap between the plate and the tube. Some of the softened metal was swept from the outside, while some of the softened metal flowed into the interior of the tube. When the diameter of the hole drilled on the plate ( $\text{Ø}b$ ) was 22 and 23 mm, the tube projection ( $h$ ) was chosen to be 3 mm the selected metal did not fill the gap between the plate and the tube, Fig. 5.

Cross-sectional views of the samples that the hole diameters drilled on the plate were 22 and 23 mm were given in Fig. 5. In this study, 20 and 21 mm holes were drilled on the plate and compared. The effect of open welding groove on the plate were also examined. While some of the softened metal filled the gap between the

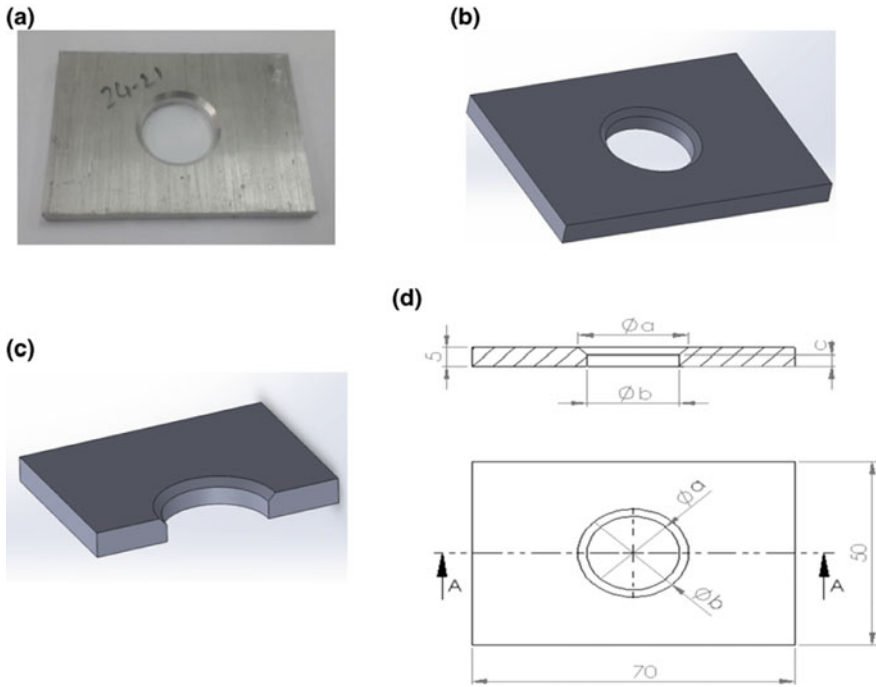


**Fig. 6** The plate used in the FWTPET method; **a, b** with weld mouth, **c** cross-section, **d** technical drawing

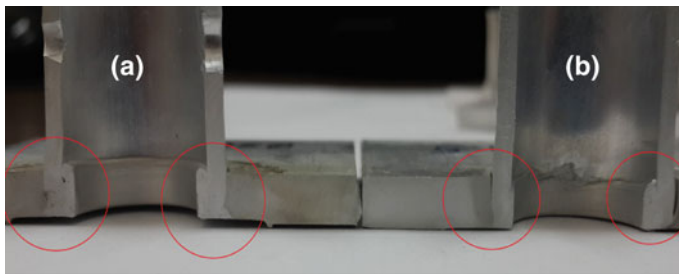


**Fig. 7** Difference between the plate-tube gap in the samples with (a), and without (b) welding mouth

plate and the tube during welding, some part of it was swept out of the plate surface. In case of groove welding, much more softened metal flowed between the tube and the plate, Fig. 6.

The welding groove was provided at an angle of 45°. It was seen that the gap between the plate and the tube was more filled as can be seen from the observations made on the scattered samples after the welding groove, Fig. 7.

**Table 2** The FWTPET welding parameters, and shear strengths of welded joints

Sample number	Sample diameter $\text{\O}a\text{-}\text{\O}b$ (mm)	Vertical load (kg)	Rotational speed (rpm)	Tube projection (mm)	Temperature ( $^{\circ}\text{C}$ )	Shear strength average, $R_m$ (MPa)
1	$\text{\O}22\text{-}\text{\O}21$	300	1180	3	440	42
2	$\text{\O}23\text{-}\text{\O}21$	325				49
3	$\text{\O}24\text{-}\text{\O}21$	280				55
4	$\text{\O}25\text{-}\text{\O}21$	310				33
<b>5</b>	<b><math>\text{\O}22\text{-}\text{\O}20</math></b>	<b>300</b>				<b>61</b>
6	$\text{\O}23\text{-}\text{\O}20$	315				59
7	$\text{\O}24\text{-}\text{\O}20$	310				54
8	$\text{\O}25\text{-}\text{\O}20$	315				55

### 3 Results

The main purpose of this study was to see the effect of the welding groove on the plate. Three of the welded samples were used to calculate the shear strength and the other two were used for inner structure analysis.

In order to increase the volume of molten metal filling between the tube and the plate, the welding groove was opened on the plates. The highest shear strength values were reached with an average of 49 MPa in samples without welding groove [22]. It had been seen that the shear strength values of the welded connections made by opening the welding groove were higher (61 MPa). When the shear strength values were compared only with the groove welded and non-welded specimens, the shear strength values of the welded specimens were increased about 20%.

The results of shear strengths were given in Table 2. When the results were examined, it was observed that the shear strength of the weldings was higher when the gap between the plate and the tube decreases.

Macro structure analysis was kept in a 10% sodium hydroxide solution for 5 min. The macro structures of the welding obtained with tool rotational speed, tube projections and welding groove was shown in Fig. 8.

The highest shear strength of 61 MPa was obtained from the weldings of specimens having an outer diameter of 22 mm and an inner diameter of 20 mm. The recrystallization of the grains in the heat-affected zone was found out to be finer than the grain size of the base metal. In addition, the region with the appearance of onion rings had undergone recrystallization of grain.

Onion rings had an apparent grain size of less than 10  $\mu\text{m}$ , while grain sizes in the heat affected zone region were below 20  $\mu\text{m}$ . As a result of the microstructure analysis, it was observed that the grains in regions near the weld interface were thinned as a result of recrystallization.

The grain size of the base metal was measured about 25  $\mu\text{m}$ , whereas the grain size was reduced to 5  $\mu\text{m}$  in the areas subjected to grain refinement, Fig. 9.

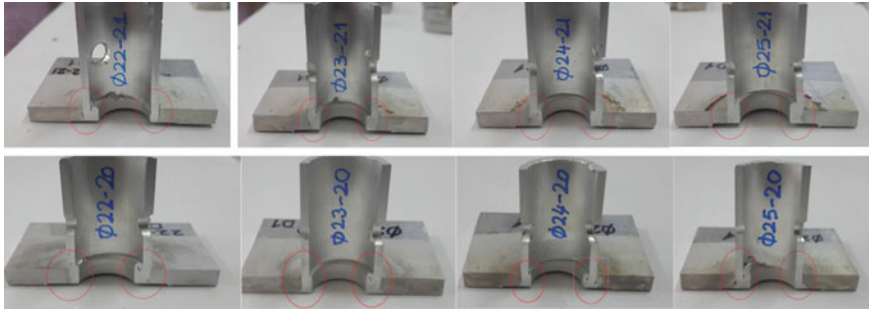


Fig. 8 Macroscopic view of cross-section of FWTPET with weld mouth

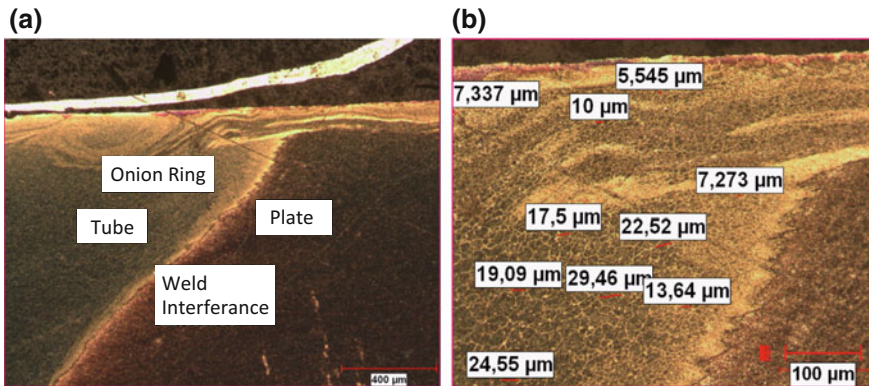


Fig. 9 The view of micro structure of welded zone (a), grain sizes (b)

The micro hardness were measured at 20 µm intervals in Fig. 10. The micro hardness of the plate was about 65 HV0.01, and tube was about 54 HV0.01. It was founded that the hardness was higher in fine grain areas.

### 4 Conclusion

In this study EN AW-6082 T6 aluminium alloy plates of 5 mm thickness and EN AW-6063 T5 aluminium alloy tubes of Ø20 mm were joined by the FWTPET. When the tool rotational speed was less than 950 rpm, and the vertical load was kept below 200 kg, the welding quality was not enough. The good looking welding could be made when the temperature reaches softening temperature of aluminium. This temperature was measured at approximately 400 °C. It had been achieved that the shear strength of the welded joints increased between 10 and 20%, when the welding groove is provided [21].



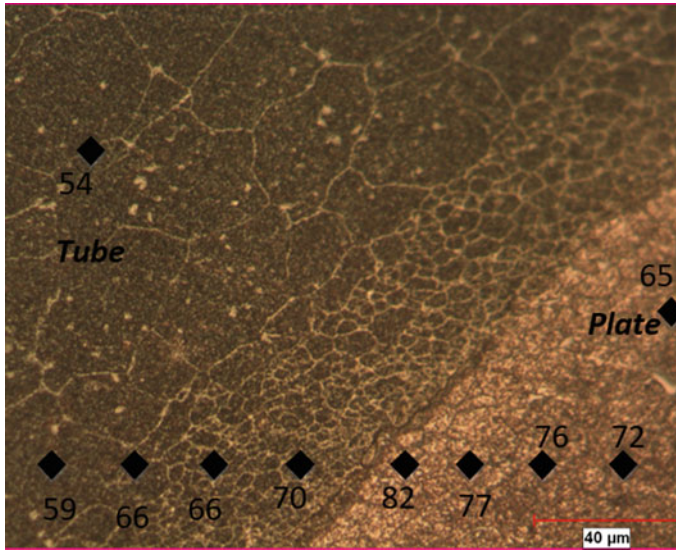


**Fig. 10** Micro hardness measurements (HV0.01)

As a result of the micro hardness measurements, the micro hardness of the tube was measured as about 54 HV0.01, whereas in the grain-thinned areas it reached to 70 HV0.01. Similarly, micro hardness of the plate material was 65 HV0.01, and it was up to 82 HV0.01 in the area with grain refinement.

## References

1. Kumaran, S.S., Muthukumar, S., Chandrasekhar, R.C.: Effect of tube preparations on joint strength in friction welding of tube to tube plate using an external tool process. *Exp. Tech.* **37**(3), 24–32 (2013)
2. Rajan, S.P., Kumaran, S.S., Kumaraswamidhas, L.A.: An investigation on SA 213 tube to SA 387 tube plate with backing block arrangement in friction welding process. *Alex. Eng. J.* **55**(2), 1255–1269 (2016)
3. Kumaran, S.S., Das, A.D.: Friction welding joints of SA 213 Tube to SA 387 tube plate boiler grade materials by using clearance and interference fit method. *Mater. Today Proc.* **5**(2), 8557–8566 (2018)
4. Kumar, C.V., Muthukumar, S., Pradeep, A., Kumaran, S.S.: Optimizational study of friction welding of steel tube to aluminum tube plate using an external tool process. *Int. J. Mech. Mater. Eng.* **6**(2), 300–306 (2011)
5. Kumaran, S.S., Muthukumar, S., Vinodh, S.: Optimization of friction welding of tube to tube plate using an external tool. *Struct. Multidiscip. Optim.* **42**(3), 449–457 (2010)
6. Kumaran, S.S., Muthukumar, S., Vinodh, S.: Optimization of friction welding of tube to tube plate using an external tool by hybrid approach. *J. Alloy. Compd.* **509**(6), 2758–2769 (2011)

7. Kumaran, S.S., Muthukumar, S., Vinodh, S.: Optimization of friction welding of tube-to-tube plate using an external tool by Taguchi method and genetic algorithm. *Int. J. Adv. Manuf. Technol.* **57**(1–4), 167 (2011)
8. Kumaran, S.S., Muthukumar, S.: Effect of projection on joint properties of friction welding of tube-to-tube plate using an external tool. *Int. J. Adv. Manuf. Technol.* **75**(9–12), 1723–1733 (2014)
9. Kumaran, S.S., Muthukumar, S., Venkateswarlu, D., Balaji, G.K., Vinodh, S.: Eco-friendly aspects associated with friction welding of tube-to-tube plate using an external tool process. *Int. J. Sustain. Eng.* **5**(2), 120–127 (2012)
10. Kumaran, S.S., Das, A.D.: An Examination of seamless ferritic tube and austenitic alloy tube plate joining by friction welding process. *Mater. Today Proc.* **5**(2), 8539–8546 (2018)
11. KaruppanaRaja, P.G., Rajkumar, M.: A study on backing block arrangement of dissimilar metal joining process of seamless ferritic and austenitic alloy by using an external tool. *J. Alloy. Compd.* **687**, 773–785 (2016)
12. Rajan, S.P., Kumaraswamidhas, L.A.: An investigation on thermal and friction effect produced by friction welding of SA 213 tube to SA 387 tube plate. *Alex. Eng. J.* **55**(1), 101–112 (2016)
13. Pandiarajan, S., Kumaran, S.S., Kumaraswamidhas, L.A., Saravanan, R.: Interfacial microstructure and optimization of friction welding by Taguchi and ANOVA method on SA 213 tube to SA 387 tube plate without backing block using an external tool. *J. Alloy. Compd.* **654**, 534–545 (2016)
14. Kumaran, S.S., Muthukumar, S., Chandrasekhar, R.C.: Suitability of friction welding of tube to tube plate using an external tool process for different tube diameters—a study. *Exp. Tech.* **37**(6), 8–14 (2013)
15. Kumaran, S.S., Das, A.D.: An investigation of Boiler Grade Tube and Tube Plate without block by using friction welding process. *Mater. Today Proc.* **(5)2**, 8567–8576 (2018)
16. Rajan, S.P., Kumaran, S.S., Kumaraswamidhas, L.A.: An investigation of metal flow during friction welding of SA 213 tube to SA 387 tube plate with backing block. *Alex. Eng. J.* **55**(2), 1187–1199 (2016)
17. Meran, C., Korkmaz, E., Küçükömeroğlu, T., Aksoy, M.A., Kestel, M., Akder, İ.: Boruların plakalara dışarıdan bir takımla sürtünme kaynak edilebilirliğinin incelenmesi. IX. Ulusal Kaynak Teknolojileri Kongre ve Sergisi, Ankara. s471–480 (2015)
18. Meran, C., Korkmaz, E., Aykanat, E., Degirmenci, S.: EN AW 6063 alüminyum alaşımı boruların plakalara dıştan bir takım yardımıyla sürtünme kaynağı yapılabilirliğinin incelenmesi. 4. Uluslararası Kaynak Teknolojileri Konferansı ve Sergisi *Gaziantep* 145–156 (2016)
19. Korkmaz, E.: Examination of the friction welding of aluminum alloy tube-plates using an external tool. MSC Thesis, Pamukkale University Institute of Science, Denizli, Türkiye (2017)
20. Muthukumar, S., Kumaran, S.S., Kumar, S.: Friction welding of Cu-tube to Al-tube plate using an external tool. *Trans. Indian Inst. Met.* **64**(3), 255–260 (2011)
21. Küçükömeroğlu, T., Meran, C.: Takım baskı kuvveti kontrollü sürtünme karıştırma kaynağı. In: 13th International Materials Symposium Denizli 1345–1349 (2010)
22. Korkmaz, E., Gülsöz, A., Meran, C.: Investigations on the joint properties of the friction welding of aluminum alloy tube to tube plate using an external tool. *J. Achieve. Mater. Manuf. Eng.* **81**(2) (2017)
23. Kannan, S., Kumaran, S.S., Kumaraswamidhas, L.A.: An investigation on mechanical property of commercial copper tube to aluminium 2025 tube plate by FWTPET process. *J. Alloy. Compd.* **672**, 674–688 (2016)

**Part XI**  
**Tribology**

# Study of the Texture Parameters Effects on the Anti-fingerprint Function



M. Belhadjamor, S. Belghith and S. Mezlini

**Abstract** In the present paper, we aim to analyze the effect of the design parameters of micro-textured surfaces on the anti-fingerprint function. For this purpose, a numerical model of the finger contact was developed to simulate the mechanical response of the finger loaded over differently micro-textured surfaces. Interestingly, this model enables the measurement of the touched area (i.e. stained area by fingerprints). A statistical analysis was conducted using a full factorial design in order to investigate the effect of the height, width and pitch describing the surface texture. The statistical significance of the parameters effects as well as the effects of their interactions was discussed. Results have shown that both the height and the interaction between the height and the pitch have significant influences on the real area of the finger contact. An optimal compromise between the height and the pitch is recommended to reduce the touched area. The obtained results highlighted by the statistical analyses can provide a guideline for the design of anti-fingerprint surfaces.

**Keywords** Numerical model · Finger contact mechanics · Anti-fingerprinting Surface micro-texture

## 1 Introduction

Anti-fingerprint surfaces have recently attracted a great deal of attention for both theoretical research and practical applications. These surfaces prevent fingerprints and achieve clean and esthetics aspects. The development of design guidelines for such surfaces requires a deep knowledge of the underlying physics. For this purpose, we have reviewed, in a previous publication, the different issues behind fingerprinting [1]. Moreover, the state-of-the-art of the design and preparation techniques of superhydrophobic and anti-fingerprint surfaces is critically revisited. Related studies

---

M. Belhadjamor (✉) · S. Belghith · S. Mezlini  
Laboratoire de Génie Mécanique, École Nationale d'Ingénieurs de Monastir, Université de Monastir, Rue Ibn Eljazzar, 5019 Monastir, Tunisie  
e-mail: [meriem.belhadjamor@gmail.com](mailto:meriem.belhadjamor@gmail.com)

© Springer Nature Switzerland AG 2019  
L. F. M. da Silva (ed.), *Materials Design and Applications II*, Advanced Structured Materials 98, [https://doi.org/10.1007/978-3-030-02257-0\\_30](https://doi.org/10.1007/978-3-030-02257-0_30)

claim that the achievement of such surfaces deals with non-wetting behavior. Indeed, anti-fingerprint surface must exhibit an amphiphobic property since the fingerprint liquid is a mixture of sweat (water), sebum (oils) and extrinsic contaminants [2]. The amphiphobicity can be achieved by lowering the surface energy and/or modifying the surface topography [3]. In addition to wettability, the mechanical behavior of the contact between the human finger and the surface (i.e. finger contact) govern fingerprinting [4, 5]. However, the finger contact response was always overlooked when evaluating the surface functionality. The evaluation of this latter, was often restricted to the surface wettability against water, hexadecane, oleic acid [2] and/or artificial fingerprint liquid [6]. It was shown that the surface texturing is an efficient strategy for enhancing amphiphobicity [7]. Nevertheless, an understanding of the effect of the surface topography on the anti-fingerprint function requires an analysis of both wettability and finger contact mechanics. In a previous study, we have highlighted an interesting correlation between the mechanics of the finger contact and the wetting behavior [8]. We have studied the effect of the texturing scale on the surface function. The bioinspired multiscale texture exhibited a potential anti-fingerprint effect. Moreover, a micro-textured surface have shown a significant effect on decreasing the finger contact area, improving the hydrophobic behavior and reducing the surface affinity to low surface tension liquids (e.g. skin oils).

In this work, we have studied the effect of the texture design parameters on the mechanics of the finger contact with the aim of enhancing the anti-fingerprint function of micro-textured surfaces. A microscopic bi-dimensional numerical model of the finger contact has been developed. A full factorial design was used in order to analyze the effect of parameters describing the micro-patterns geometry (height, width and pitch) on the real contact area. The influences of single and interactive parameters were analyzed and the more significant factor was identified. The optimized surface by the design of experiment (DOE) was compared with a micro-textured surface whose anti-fingerprint function was previously discussed [8].

## 2 Methods

### 2.1 Numerical Model

The objective of the present study is to evaluate the effect of texture parameters on the anti-fingerprint function of structured surfaces by measuring the real area of the finger contact. The contact mechanic is analyzed using a microscopic multi-layered bi-dimensional finite element (FE) model (Fig. 1). The biologically bioinspired fingertip model is composed of two skin layers (dermis and epidermis), subcutaneous tissue, bone and nail. The thicknesses of the epidermis and dermis layers are respectively 0.7 mm [9] and 0.8 mm [10].

The model geometry includes also epidermal ridges (fingerprints). The width and the height of fingerprint ridges are respectively 0.45 mm and 0.05 mm [11]. Fingertip

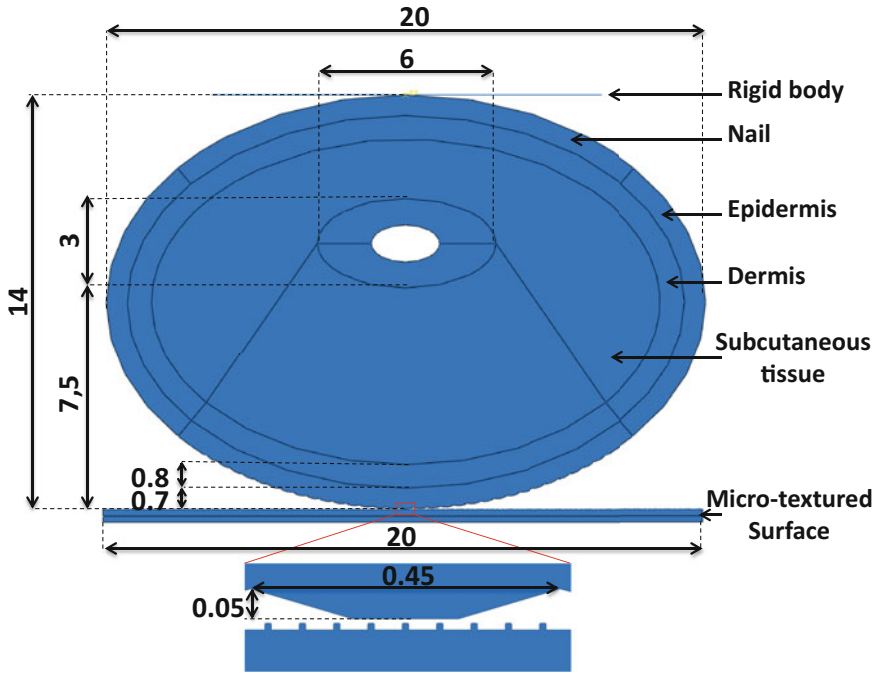


**Fig. 1** Model geometry, dimensions (mm) and boundary conditions

**Table 1** Elastic and Prony series parameters of fingertip tissues

	Elastic properties [15]		Prony series [14]		
	$E$ (MPa)	$\nu$	$g_i$	$k_i$	$\tau_i$ (s)
Epidermis	0.08	0.48	0.0332	0	1.29
Dermis	0.05	0.48	0.0282	0	17.68
Subcutaneous tissue	0.024	0.48	0.0183	0	2412
Nail	170	0.3	–	–	–
Bone	17,000	0.3	–	–	–

dimensions are assumed to be representative of a typical male index. The epidermis, dermis and the subcutaneous tissue are assumed to be viscoelastic material [12–14]. The nail and the bone are supposed to have linear elastic behaviors [15]. The viscous material parameters of the skin layers and the subcutaneous tissue, described by the Prony series, were determined by Amaied et al. [14] using the in vivo creep test. The elastic and viscous material parameters for the different tissues are illustrated in Table 1. The textured surfaces are assumed to be linearly elastic with Young’s modulus of 72 GPa and Poisson’s ratio ( $\nu$ ) of about 0.33.

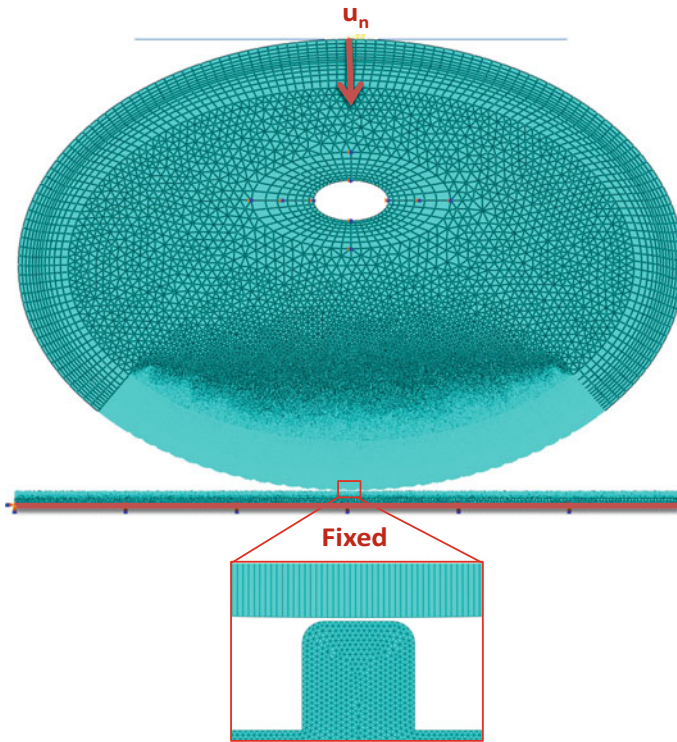


**Fig. 2** Mesh and boundary conditions

Plane strain elements were used for meshing the fingertip model. Free 3-node linear triangular elements were used to mesh the subcutaneous tissues as well as the micro-textured surfaces. Structured 4-node linear quadrilateral elements were adopted for the skin, nail and bone discretization (Fig. 2). In the contact zone, finer elements were used to improve the numerical convergence and accuracy and of the model. The size of the mesh elements in the fingerprint ridges and the surface micro-patterns is about  $0.7 \mu\text{m}$ .

For the achievement of the touch loading, a normal displacement of  $u_n = 1.3 \text{ mm}$  was applied. Such a value leads to a contact load of about  $0.05 \text{ N}$  in the 2D configuration which is equivalent to  $0.5 \text{ N}$  in the real fingertip contact (3D model). For more details about the numerical model, refer to our previous work [8].

## 2.2 Design of Experiment (DoE)

In order to investigate the effect of the texture parameters on the mechanic behavior of the finger contact, regular microscopic grooved surfaces are simulated (Fig. 3).

**Fig. 3** Topography of the micro-grooved surface

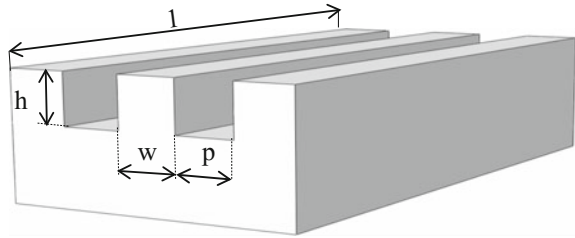


**Table 2** Factor levels

Factors: geometric parameters ( $\mu\text{m}$ )	Level 1	Level 2	Level 3
(A): height (h)	10	–	30
(B): width (w)	10	–	30
(C): spacing (p)	50	100	150

**Table 3** Full factorial design matrix

Test N°	A	B	C	$A_r/A_a$ (%)
1	10	10	50	13.44
2	10	10	100	19.45
3	10	10	150	39.29
4	10	30	50	27.75
5	10	30	100	23.73
6	10	30	150	38.73
7	30	10	50	13.44
8	30	10	100	6.04
9	30	10	150	5.43
10	30	30	50	27.75
11	30	30	100	18.58
12	30	30	150	16.86

Such surfaces were described by the height (h), the width (w) and the length of grooves (l) as well as the spacing between them (p). The length of the grooves is assumed to be equal to 1 mm.

A design of experiments (DOE) is performed based on a full factorial design considering three factors. Design factors, namely, the height (h), the width (w) and the spacing (pitch p) of the surface texture have 2, 2 and 3 levels respectively as reported in Table 2. A total of 12 ( $2 \times 2 \times 3$ ) simulations are required for the analysis (Table 3).



### 3 Results and Discussion

#### 3.1 Contact Finger Analysis and Anti-fingerprint Function

The finger contact was modeled considering the visco-elastic behavior for skin layers and the subcutaneous tissue. The fingerprint ridges were also considered in the finger model. Figure 4 illustrates the deformed shape and the strain distribution when the finger is under typical touch load of about 0.5 N.

The magnification shows a deformed finger ridge in contact with a micro-textured surface ( $w = 30 \mu\text{m}$ ,  $h = 30 \mu\text{m}$  and  $p = 50 \mu\text{m}$ ). The subcutaneous tissue between the bone and the dermis has undergone the maximum deformation since it has the lowest rigid modulus. In the contact zone, the presence of micro-patterns increases the deformation of the epidermis.

The developed model was used to predict the real area of the finger contact which corresponds to the area of the fingerprint deposit, by using the nodal contact area measurement (*CNAREA*). A node is into contact if the contact pressure CPRESS is deferent from zero. The nodal contact area is therefore the ratio of the nodal contact force to the nodal contact pressure. The real contact area of the finger contact is the sum of nodal contact areas in the interface finger/surface. Figure 5 presents the evolution of the real area ( $A_r$ ) normalized by the apparent area ( $A_a$ ) of contact as a function of the touch load. The increase of load increases the contact ratio ( $A_r/A_a$ )

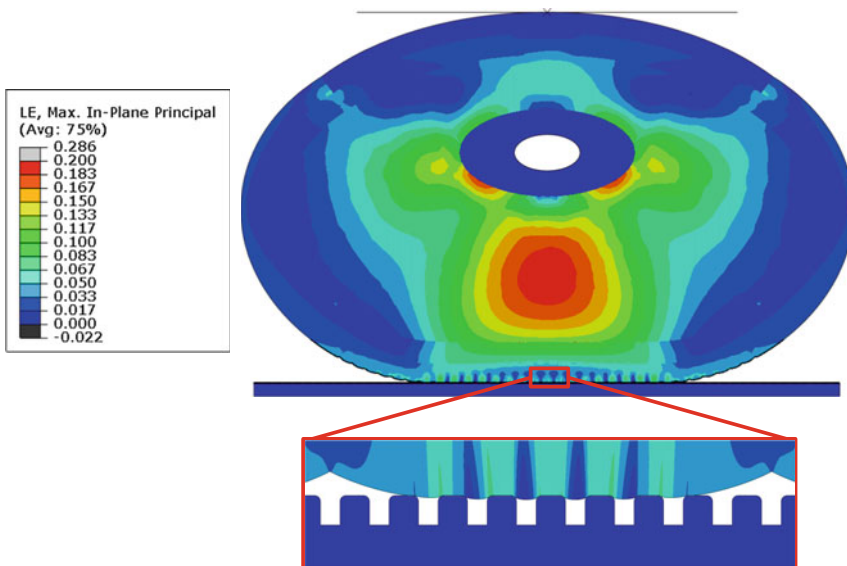


Fig. 4 The logarithmic strain (LE) distribution in the human finger during touching

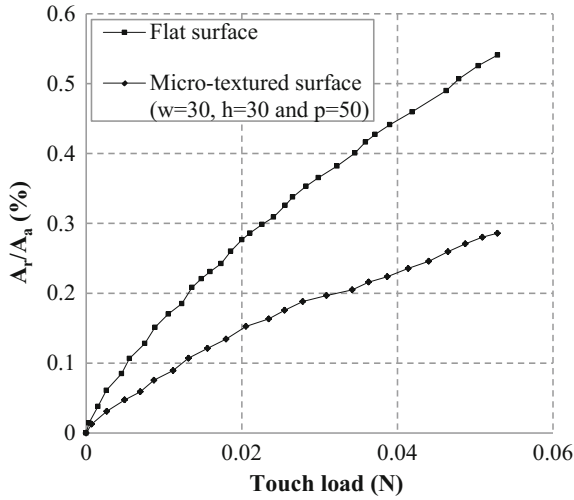


Fig. 5 Evolution of the contact ratio  $A_r/A_a$  as a function of increasing touch load

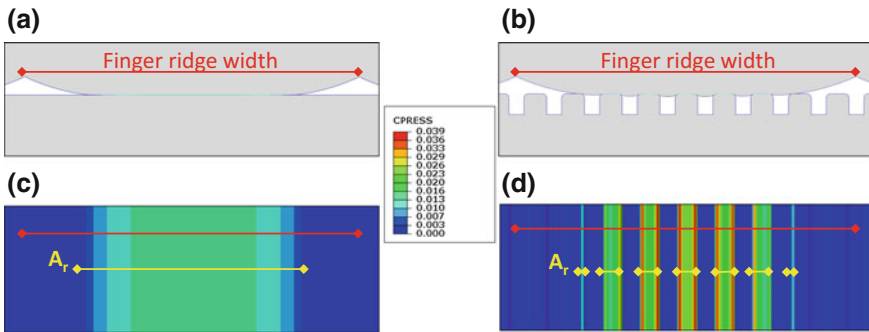


Fig. 6 The deformed finger ridge (a, b) and the contact pressure distribution (c, d) in contact with a flat surface and a micro-textured surface

due to the finger ridges deformation. It can be noted also that the surface texturing decreases the real contact area of about 47%.

Figure 6 shows a deformed finger ridge (a, b) and the contact pressure distribution (c, d) when the finger is in contact with a flat surface and a micro-textured surface. The micro-texturing leads to a discretized contact area which decreases the real area of the finger contact. Therefore, in the case of the micro-textured surface, the contact occurs with multi-contact zones for each finger ridge.

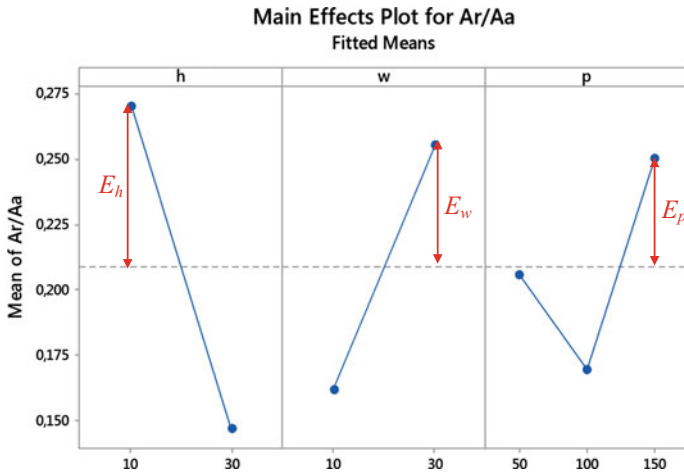


Fig. 7 Main effects of the texture parameters (h, w et p)

### 3.2 Results from the DoE: Effect of the Texture Parameters

The design matrix is shown in Table 3. The real area of the finger contact was assessed for each test. Results were analyzed using the design of experiment software, MINITAB™ (Minitab Inc.).

The influences of single and interactive factors on the contact ratio  $A_r/A_a$  were investigated based on the results of the DoE. Figure 7 illustrates the main effect plots of the different factors. The topographic parameters, the height (h), the width (w) and the pitch (p) noticeably influenced the real contact area. It can be seen that the height presents the most important effect. An increase of this parameter decreased the area of the touched surface. However, when increasing the width the real contact area was increased. Furthermore, the texture pitch has different effects. The increase of p from 50 to 100  $\mu\text{m}$  leads to a decrease of the contact ratio. Nevertheless, the latter was increased when p increases from 100 to 150  $\mu\text{m}$ .

The main effect plot of each parameter is insufficient to reveal how texturing parameters influence the contact mechanics. In order to investigate this influence, the interaction plots were presented in Fig. 8. This figure allowed us to realize high interaction between the height and the pitch but lower interactions between other parameters. Indeed, the height effect is largely affected by the change in the pitch level but slightly changed with the width.

The Pareto diagram was applied to classify the effects by their significance with a confidence interval of 95% (Fig. 9). The main effects of topographic parameters as well as the effect of the interaction between the height and the pitch are illustrated in the diagram. The most significant factor is the height of grooves. Furthermore, the interaction  $h * p$  shows a statistically significant effect on the contact ratio  $A_r/A_a$ . However, other texture parameters seem to have no significant effect.

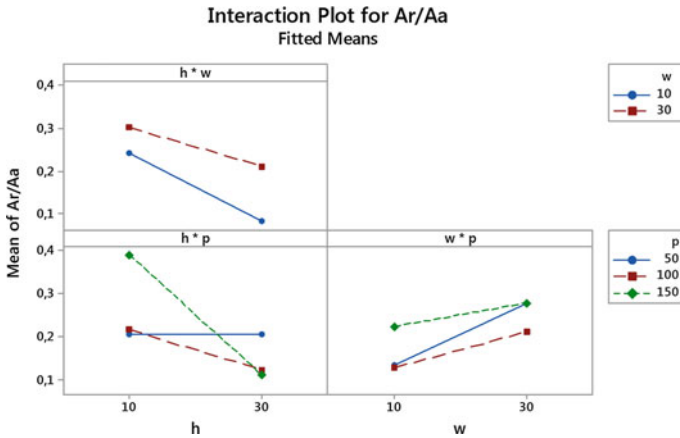


Fig. 8 Interaction effect plot

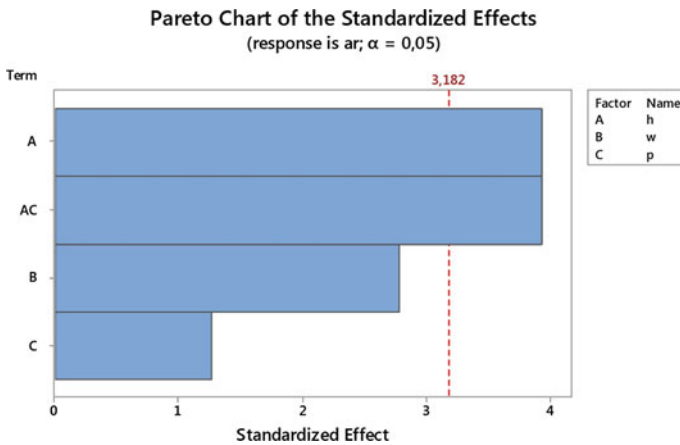
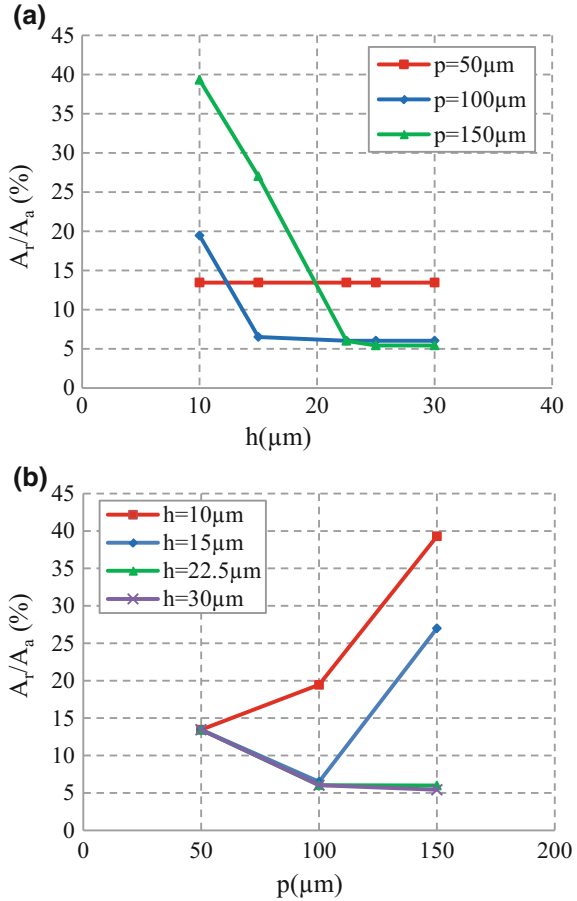


Fig. 9 Pareto diagram

Figure 10 shows the evolution of the contact ratio  $A_r/A_a$  as a function of the height (a) and the pitch (b) for a width equal to 10  $\mu\text{m}$ . Figure 10a presents the evolution of the contact ratio  $A_r/A_a$  as a function of the height for different pitch values. When the height was increased from 10 to 30  $\mu\text{m}$ , the evolution of the real contact area depend on the spacing between grooves which is consistent with the results of the statistical analysis:

- $p = 50 \mu\text{m}$ : the contact ratio  $A_r/A_a$  is independent of  $h$ .
- $p = 100 \mu\text{m}$ : when increasing the height from 10 to 15  $\mu\text{m}$ ,  $A_r/A_a$  is decreased. Further increase has no effect on the real contact area.
- $p = 150 \mu\text{m}$ : The increase of the height from 10 to 22.5  $\mu\text{m}$  leads to a decrease of  $A_r/A_a$ . When  $h$  is higher than 22.5, the contact ratio remain constant.

**Fig. 10** Evolution of  $A_r/A_a$  as a function of **a** the height, **b** the pitch between grooves



It is interesting to note that for each pitch value, there is a critical height from which further increase of  $h$  has no effect on the real contact area. When  $p$  is about  $100 \mu\text{m}$ , the critical height is  $15 \mu\text{m}$ , whereas, it is about  $22.5$  when  $p$  is  $150 \mu\text{m}$ . Figure 10b presents the evolution of the contact ratio  $A_r/A_a$  as a function of the pitch for different height values:

- For high value of  $h$  ( $h \geq 22.5 \mu\text{m}$ ), the increase of the pitch results in a decrease of the contact density and, consequently, the real contact area. This decrease is of about 61% when  $h = 30 \mu\text{m}$ .
- $h = 15 \mu\text{m}$ : when increasing the pitch from 50 to  $100 \mu\text{m}$ ,  $A_r/A_a$  is decreased. Further increase of  $p$  until reaching  $150 \mu\text{m}$  increases this ratio.
- $h = 10 \mu\text{m}$ : the real contact area increased with the pitch.

As can be seen from this figure, the lowest real contact area (5.3%) is achieved when the height is of about  $30 \mu\text{m}$  and a pitch value of about  $150 \mu\text{m}$ . The highest

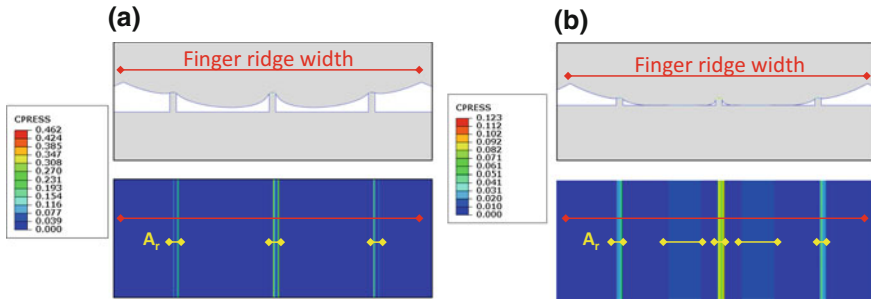


**Fig. 11** The finger contact in the case of **a** the lowest and **b** the highest contact area

one (39%) is obtained with the same pitch value but a height value equal to 10  $\mu\text{m}$ . The finger contacts in the case of these two surfaces are illustrated in Fig. 11. A closer look at the finger ridge deformation allows us to understand these results.

This figure shows that for a height value of 10  $\mu\text{m}$  (lower than the critical height value), the finger touches the bottom of the surface and the real contact area increases dramatically.

This analysis shows that the texturing parameters namely the height of the patterns and the pitch have a significant effect on the area contaminated by fingerprints.

## 4 Conclusions

The surface texture is a key parameter in the achievement of the anti-fingerprint property. In the current paper, the effect of the texture design parameters were statistically analyzed based on the design of experiment (DOE) to identify the most significant effects and determine the optimum ranges of the topographic parameters values that minimize the finger contact area (i.e. the area of fingerprint deposits). Thus, the following conclusions were drawn:

- The texture parameters namely, the height, the width and the pitch have important effects on the finger contact area. Such parameters must be fine-tuned in order to achieve the anti-fingerprint property. The decrease of the width or the height reduces the fingerprint deposits. The increase of the pitch decreases the contact density and consequently decreases the real contact area. From a critical value this trend is reversed.
- According to the design of experiments analysis, the effect of the height and the interaction between the height and the pitch are statistically significant. Therefore, the pitch effect is dependent on the height level and vice versa.

- The minimum finger contact area is reached by a texture with an optimal compromise between the height and the pitch. The micro-textured surface with  $h = 30$ ,  $w = 30$  and  $p = 50$  has been shown to improve significantly the anti-fingerprint function by reducing the surface wettability and narrowing the area of the finger touch. The optimized design parameters ( $h = 30$ ,  $w = 10$  and  $p = 150$ ) further reduces the touched area and the surface texture can be considered as more efficient.

## References

1. Belhadjamor, M., El Mansori, M., Belghith, S., Mezlini, S.: Anti-fingerprint properties of engineering surfaces: a review. *Surf. Eng.* **34**, 85–120 (2018)
2. Siriviriyannun, A., Imae, T.: Anti-fingerprint properties of non-fluorinated organosiloxane self-assembled monolayer-coated glass surfaces. *Chem. Eng. J.* **246**, 254–259 (2014)
3. Valipour Motlagh, N., Khani, R., Rahnama, S.: Super dewetting surfaces: focusing on their design and fabrication methods. *Coll. Surf. A Physicochem. Eng. Asp.* **484**, 528–546 (2015)
4. Scruton, B., Robins, B.W., Blott, B.H.: The deposition of fingerprint films. *J. Phys. D Appl. Phys.* **8**, 714–723 (1975)
5. Kent, T.: Latent fingerprints and their detection. *J. Forensic Sci. Soc.* **21**, 15–22 (1981)
6. Wu, L.Y.L., Ngian, S.K., Chen, Z., Xuan, D.T.T.: Quantitative test method for evaluation of anti-fingerprint property of coated surfaces. *Appl. Surf. Sci.* **257**, 2965–2969 (2011)
7. Peng, S., Bhushan, B.: Mechanically durable superoleophobic aluminum surfaces with microstep and nanoreticula hierarchical structure for self-cleaning and anti-smudge properties. *J. Colloid Interface Sci.* **461**, 273–284 (2016)
8. Belhadjamor, M., Belghith, S., Mezlini, S., El Mansori, M.: Effect of the surface texturing scale on the self-clean function: correlation between mechanical response and wetting behavior. *Tribol. Int.* **111**, 91–99 (2017)
9. Whitton, J.T., Everall, J.D.: The thickness of the epidermis. *Br. J. Dermatolog.* **89**, 467–476 (1973)
10. Hendriks, F.M., Brokken, D., Oomens, C.W.J., Baaijens, F.P.T.: Influence of hydration and experimental length scale on the mechanical response of human skin in vivo, using optical coherence tomography. *Ski. Res. Technol.* **10**, 231–241 (2004)
11. Shao, F., Childs, T.H.C., Barnes, C.J., Henson, B.: Finite element simulations of static and sliding contact between a human fingertip and textured surfaces. *Tribol. Int.* **43**, 2308–2316 (2010)
12. Kim, S.W., Shim, J.K., Zatsiorsky, V.M., Latash, M.L.: Finger inter-dependence: linking the kinetic and kinematic variables. *Hum. Mov. Sci.* **27**, 408–422 (2008)
13. Holt, B., Tripathi, A., Morgan, J.: Viscoelastic response of human skin to low magnitude physiologically relevant shear. *J. Biomech.* **41**, 2689–2695 (2008)
14. Amaied, E., Vargiolu, R., Bergheau, J.M., Zahouani, H.: Aging effect on tactile perception: experimental and modelling studies. *Wear* **332–333**, 715–724 (2015)
15. Shao, F., Childs, T.H.C., Henson, B.: Developing an artificial fingertip with human friction properties. *Tribol. Int.* **42**, 1575–1581 (2009)

# Mechanical Characterization of Film/Substrate Materials Using Nanoindentation Technique



Nadia Chakroun and Hedi Belhadjsalah

**Abstract** In the present paper, mechanical properties of multilayer coatings were investigated. To that end, an analytical model dedicated for characterizing the thin multilayer behaviors was considered. In this study, the nanoindentation tests on film/substrate material systems were systematically investigated using finite element modeling (FEM). Hence, the considered model of Mercier et al. is efficient for measuring meaningful mechanical properties of thin film materials up to a critical ratio  $E_f/E_s = 1.18$  (with  $E_f$  the Young's modulus of the film and  $E_s$  the Young's modulus of the substrate). But, for  $E_f/E_s \geq 1.18$  a divergence of the model was observed. The main error is caused by a wrong estimation of the contact surface  $A_c$  between the indenter tip and the film surface. As a matter of fact, for a soft film on a hard substrate ( $E_f/E_s < 1.18$ ) the deformation is almost localized at the film. However, for  $E_f/E_s \geq 1.18$  the deformation spreads at the substrate which induces a wrong value of contact surface  $A_c$ .

**Keywords** Thin films · Nanoindentation · Hard film · Soft film · Substrate effect

## 1 Introduction

Development of Thin films technology is stimulated by the industry demand for improving the effectiveness of contact surfaces. Nevertheless, the mechanical properties of thin films namely the monolayer and the multilayer are quite different to materials in bulk. In fact, for the multilayer coating this difference is more important. The improvement of the mechanical properties for multilayer films is caused by the interface presence [1]. In fact, these interfaces act as barriers to the motion of dislocations [2]. As a matter of fact, characterizing the mechanical behavior of thin film systems is quite important in order to understand the performance of these

---

N. Chakroun (✉) · H. Belhadjsalah  
Mechanical Engineering Laboratory, University of Monastir, LR99ES32 ENIM,  
5000 Monastir, Tunisia  
e-mail: [lojayna@live.fr](mailto:lojayna@live.fr)

© Springer Nature Switzerland AG 2019  
L. F. M. da Silva (ed.), *Materials Design and Applications II*, Advanced  
Structured Materials 98, [https://doi.org/10.1007/978-3-030-02257-0\\_31](https://doi.org/10.1007/978-3-030-02257-0_31)



materials in service [3]. This task is particularly relevant as it is necessary to improve the durability of coated materials [4, 5]. The nanoindentation test is the most useful technique for extracting the mechanical properties of materials with low dimensions such as thin films. This method uses an indenter that comes into contact with the surface applying a load. Therefore, using the nanoindentation technique several studies are developed to characterize thin film properties [6, 7]. In the literature, many models were developed so as to characterize surface coatings [8–12]. These models determine thin film properties taking into account especially the substrate effect.

In particular, the main objective of this paper is the characterization of thin film materials deposited on a substrate. To that end, we used an analytical model and more specifically the Mercier-2010 model [10]. The present study is focused on measuring the intrinsic film properties for different situations (hard film/soft substrate or soft film/hard substrate). Then, we evaluated the different responses by the considered model in function of film/substrate properties. Consequently, based on the interpretations of the analytical results, a discussion of the considered model depending on the stiffness of the film was conducted.

## 2 Analytical Model: Mercier-2010

In 2011, Mercier et al. [10] proposed a general analytical model for a film with  $N$  layers deposited on a substrate. This model presents an extension of the model of Bec et al. [13] which model the film/substrate system as a series of two springs. The author demonstrated the validity of his model to determine the elastic properties of multilayer thin film materials [10]. He particularly proved the effectiveness of the model for experimental sample [10]. The model is presented by the following relation:

$$E'_{f,0} = \left[ \frac{\pi a_{c,0}^2 + 2t_0 a_{c,0}}{t_0} \left[ \frac{1}{2a_{c,0} E'_s} - \left( \sum_{i=1}^N \frac{t_i}{(\pi a_{c,i}^2 + 2t_i a_{c,i}) E'_{f,i}} + \frac{1}{2(a_{c,N} + \frac{2t_N}{\pi}) E'_s} \right) \right] \right]^{-1} \tag{1}$$

where  $E'_s$  is the reduced elastic modulus of the substrate and  $E'_{f,i}$  is the reduced elastic modulus of the layer number “ $i$ ” as shown in Fig. 1.

Furthermore,  $a_{c,i+1} = a_{c,i} + \frac{2t_i}{\pi}$  where  $t_i$  and  $a_{c,i}$  are the thickness and contact radius of the “ $i$ ” layer, respectively as demonstrated in Fig. 2.

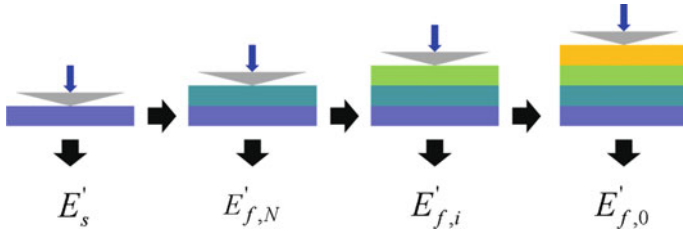


Fig. 1 Procedure for using the multilayer model [10]

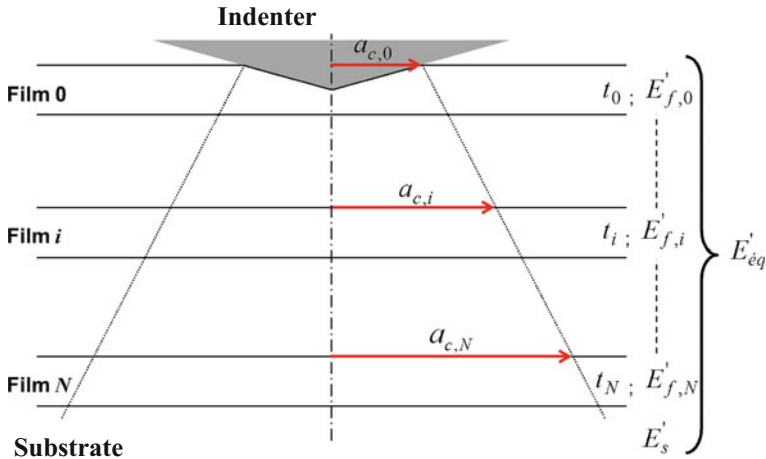
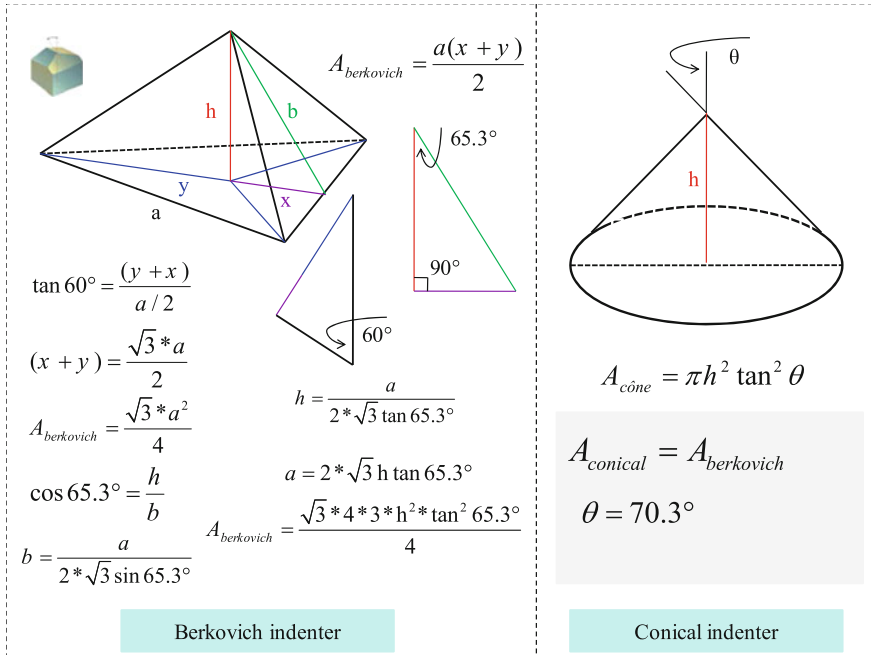


Fig. 2 Schematic of the multilayer model [10]

### 3 Results

#### 3.1 Numerical Models

The finite element analyses are carried out using the commercial code ABAQUS 6.14 [14]. Two finite element models are developed as shown in Fig. 4. The indenter is a rigid truncated cone with a half angle of  $70.3^\circ$  which makes the same projected area as the Berkovich indenter [15]. Figure 3 illustrates a geometric demonstration of the cone angle. The indentation problem is an axisymmetric owing to the conical indenter. The multilayer coating and the substrate materials are assumed to be homogenous elastic and isotropic. Fixed boundary conditions are applied to the substrate base. Contact surfaces are assumed to be frictionless since the indentation friction coefficient is a minor factor [16]. Tie constraints are applied between the layers of the coating. Evenly, for the coating and the substrate, a tie constraint is considered. For this study, the substrate was  $8 \mu\text{m}$  in width and  $10 \mu\text{m}$  in length, the thickness of the monolayer coating was  $150 \text{ nm}$  and the bilayer thickness was equal to  $300 \text{ nm}$ .



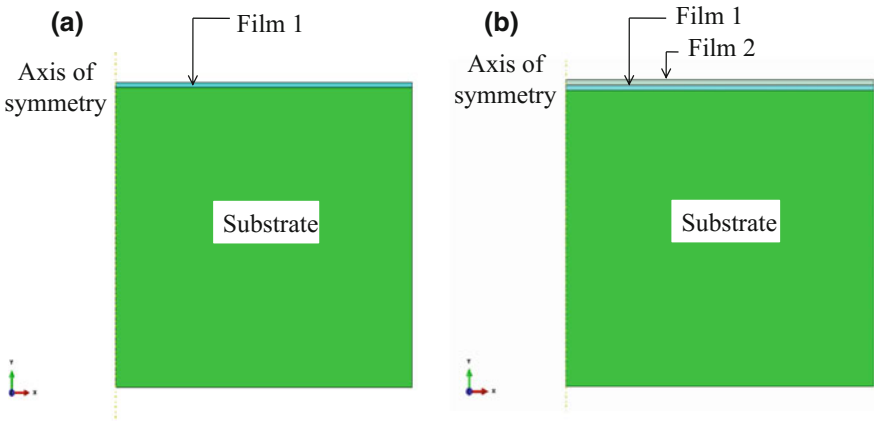
**Fig. 3** Demonstration of the choice of the cone angle to obtain the same contact area as a berkovich indenter

Figure 5 schematically illustrates the finite element meshes used for the finite element models. The film/substrate systems were modeled using four node, bilinear axisymmetric quadrilateral elements. The meshes were tested for convergence for the two finite element model. To that end, mesh studies were performed to test the numerical accuracy of the various mesh types and sizes. Consequently, a finer mesh was designed near the contact region and a gradually coarser element size further from this region was used.

### 3.2 Discussions

In order to study the responses of the analytical model of Mercier, we carried out several numerical nanoindentation tests using the two developed numerical models (the monolayer and the bilayer models).

At first, a soft substrate ( $E_s = 104$  GPa) was considered and the elastic modulus of the monolayer film  $E_{f1}$  was differently varied. Then, based on the model of Mercier, we determined the  $E_{f1}$  values using the nanoindentation curves for the different samples. Thus, Fig. 6 presents a comparison between the values of  $E_{f1}$  introduced in the numerical model and the  $E_{f1}$  values identified by Mercier for a penetration



**Fig. 4** Finite element models for multilayer film/substrate systems. **a** Monolayer thin film ( $t_{Film1} = 150 \text{ nm}$ ) and **b** bilayer thin film ( $t_{Film1} = t_{Film2} = 150 \text{ nm}$ )

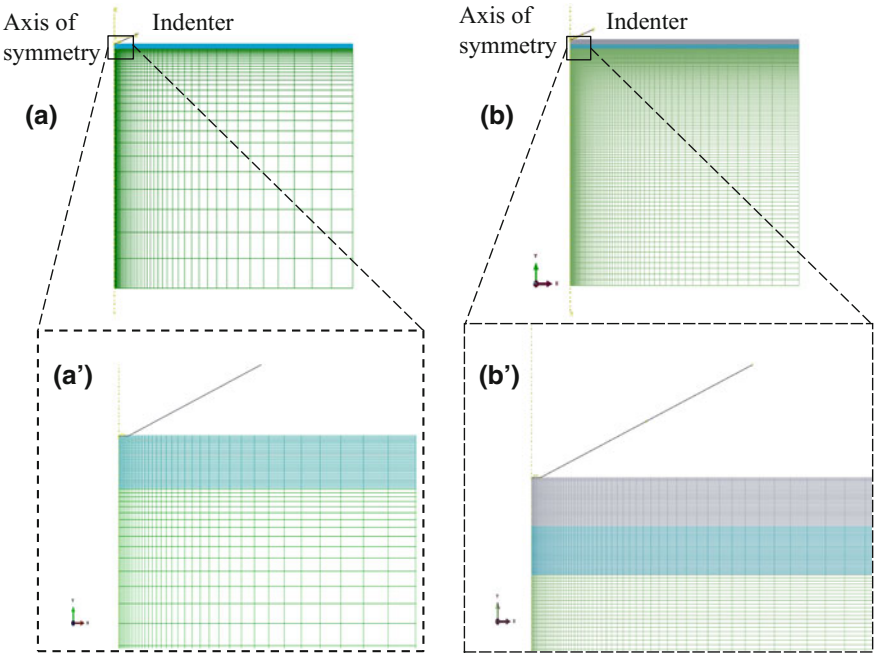


**Fig. 5** Finite element meshes of film/substrate systems. **a** and **a'** For monolayer model and **b** and **b'** for bilayer model

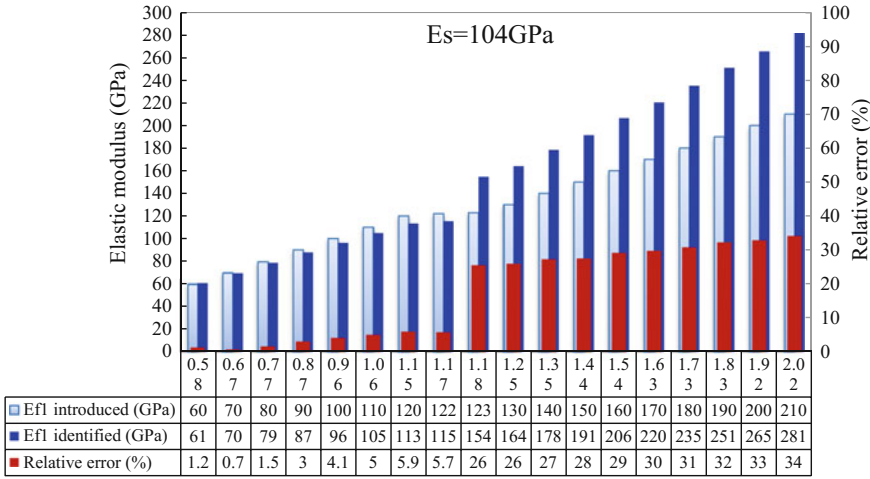


Fig. 6 Comparison between the introduced and the identified values of  $E_{f1}$  in function of  $E_{f1}/E_s$  for  $E_s = 104$  GPa and  $h = 30$  nm

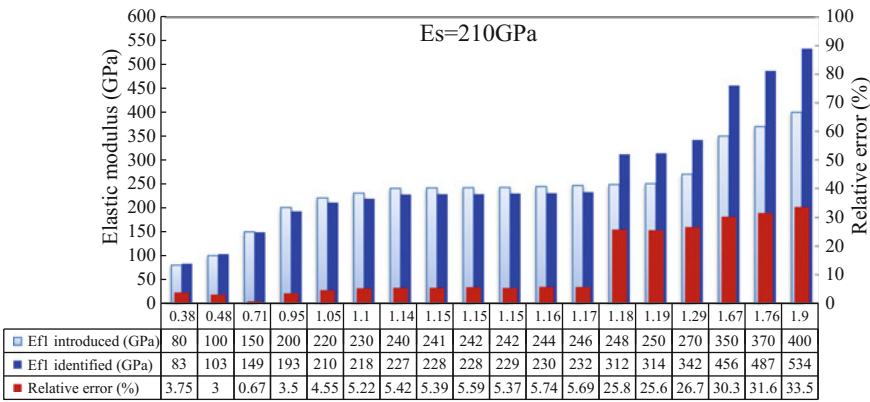
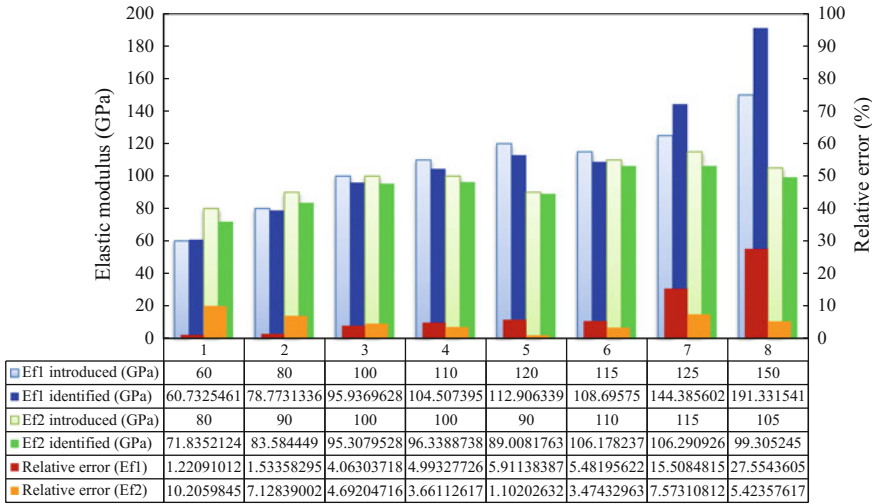


Fig. 7 Comparison between the introduced and the identified values of  $E_{f1}$  in function of  $E_{f1}/E_s$  for  $E_s = 210$  GPa and  $h = 30$  nm

depth of 30 nm. The relative error (%) is schematically shown in the same figure as a function of the ratio of two elastic modulus of the film and the substrate ( $E_{f1}/E_s$ ).

In a second step, a hard substrate ( $E_s = 210$  GPa) was considered and the elastic modulus of the monolayer film  $E_{f1}$  was also varied. Figure 7 presents a comparison between the  $E_{f1}$  values introduced in the numerical model and the  $E_{f1}$  values identified by Mercier.

Moreover, the bilayer numerical model was used to study the responses of Mercier for multilayer cases. The substrate is assumed to be a soft material with a Young's modulus equal to 104 GPa. In addition, the elastic properties of two layers ( $E_{f1}$ ,



**Fig. 8** Comparison between the introduced and the identified values of  $E_{f1}$  and  $E_{f2}$  for  $E_s = 104$  GPa

$E_{f2}$ ) were varied. Figure 8 highlights comparisons between the values of  $E_{f1}$  and  $E_{f2}$  introduced in the numerical model and the two values  $E_{f1}$  and  $E_{f2}$  identified by Mercier.

Now, we will analyze the results found by Mercier-2010 (Figs. 6, 7 and 8) in order to check the reliability of the model. In fact, Fig. 6 presents the relative error (%) between the values of  $E_{f1}$  identified by the author and that introduced to the numerical model when  $E_s = 104$  GPa. The evolution of the error is irregular. The relative error takes important values (>25%) for  $E_{f1}/E_s > 1.18$ . This observation is also observed in the case of monolayer film when the value  $E_s = 210$  GPa (Fig. 7). Figure 8 shows the case of a bilayer film on a substrate with  $E_s = 104$  GPa. We observe significant relative errors equal to 15.5% and 27.5% for sample #7 and sample #8, respectively. We notice that the ratio  $E_{f1}/E_s$  is superior to 1.18 in the case of the two samples (sample #7 and sample #8).

Consequently, comparative studies in the case of the monolayer film (Figs. 6 and 7) and in the case of bilayer film (Fig. 8) show that the Mercier model diverges if the value of  $E_f/E_s$  is superior to 1.18. This is problematic because the use of the coating is generally to protect the substrate and consequently increase its resistance ( $E_f \gg E_s$ ).

To understand these findings for the author’s model, a particular study in regards to the effects of the different parameters is necessary. As a matter of fact, we essentially studied the effects of contact surface  $A_c$  and the contact stiffness  $S$  as they are the two key parameters for the analytical model [as shown in Eq. (1)].

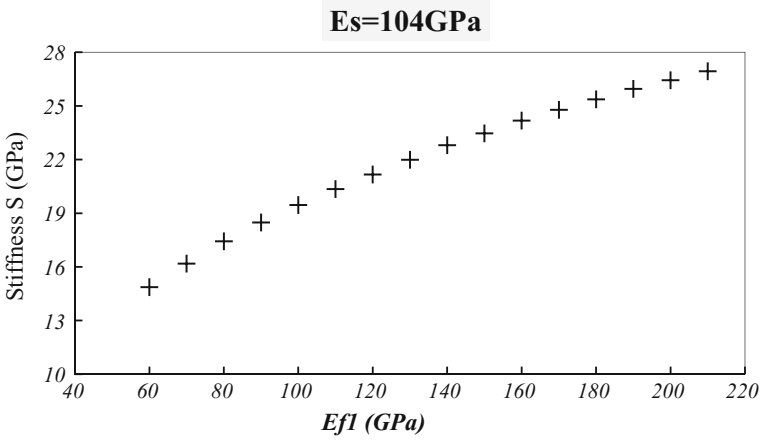


**Fig. 9** Stiffness evolution for monolayer film/substrate system for  $E_s = 104$  GPa

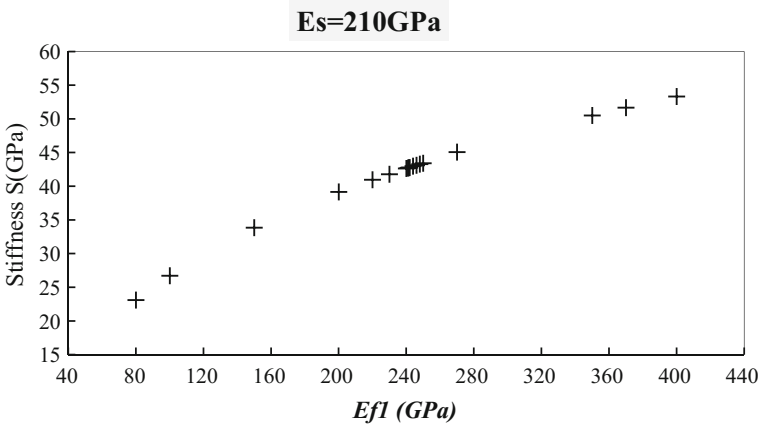


**Fig. 10** Stiffness evolution for monolayer film/substrate system for  $E_s = 210$  GPa

First, we studied the evolution of  $S$  stiffness for both monolayer (Figs. 9 and 10) and double-layer (Fig. 11) films. Indeed, the three figures, Figs. 9, 10 and 11, show that the contact stiffness  $S$  evolves upwards in a regular manner as a function of  $E_{f1}$ . Thus, the divergence of the model from the value  $E_{f1}/E_s = 1.18$  is not related to the rigidity factor  $S$  of the model.

In a second step, we studied the evolution of the contact area  $A_c$  for the case of monolayer film (Figs. 6 and 7). Indeed, Fig. 12 shows the evolution of the contact area  $A_c$  as a function of  $E_{f1}/E_s$  when  $E_s = 104$  GPa. Furthermore, Fig. 13 presents the evolution of the contact area  $A_c$  as a function of  $E_{f1}/E_s$  when  $E_s = 210$  GPa.

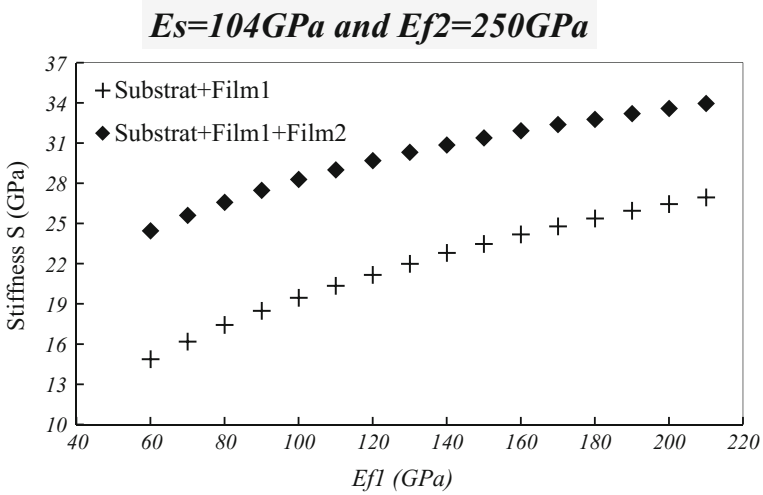


**Fig. 11** Stiffness evolution for bilayer film/substrate system for  $E_s = 104$  GPa and  $E_{f2} = 250$  GPa

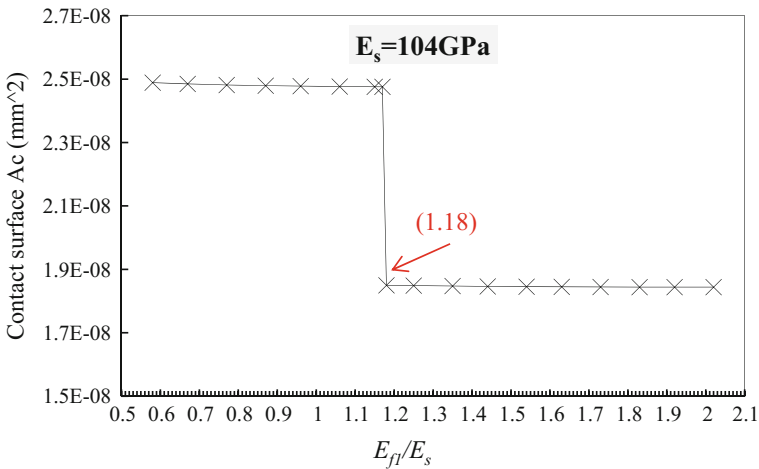


**Fig. 12** The contact surface evolution for monolayer film/substrate system for  $E_s = 104$  GPa

The evolution of the contact area is irregular for both figures (Figs. 12 and 13). It decreases sharply from the value  $E_{f1}/E_s = 1.18$  in both cases. As a result, the divergence of the model from the value  $E_{f1}/E_s = 1.18$  is related to the abrupt decrease in the contact surface  $A_c$ .



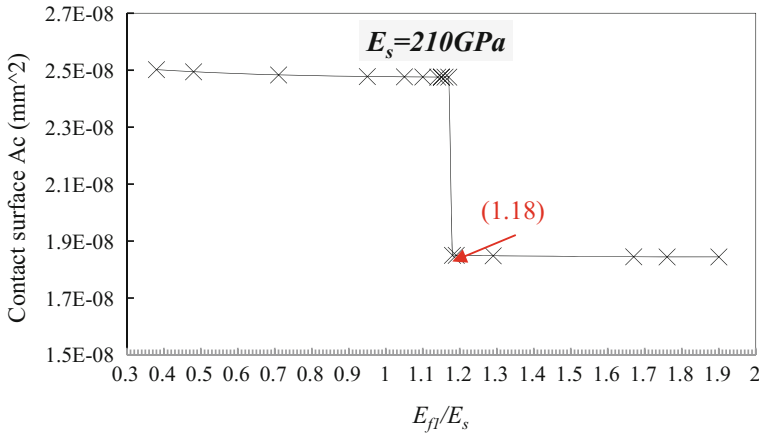


**Fig. 13** The contact surface evolution for monolayer film/substrate system for  $E_s = 210$  GPa

Figure 14 shows a simplified schematization of the contact area after the nanoindentation test and for two different situations (two samples). In situation 1 (case b Fig. 14) we consider a soft film on a hard substrate. Thus, for a given penetration, the deformation at the film is larger than the deformation at the substrate.

Furthermore, for situation 2 (case c Fig. 14) and for the same penetration the deformation at the film is comparable with the deformation at the substrate since the rigidity of the film is greater than the rigidity of the substrate. In this case, the film undergoes a displacement which generates a reduced contact area  $A_{c2}$ . Thus, the contact area  $A_{c1}$  is larger than  $A_{c2}$ .

In order to better simulate the evolution of the deformation within the film/substrate system, we considered two different samples. For the first sample, we considered that  $E_{f1}/E_s < 1.18$  whereas for the second system we assumed that ( $E_{f1}/E_s > 1.18$ ).

Figure 15 shows the evolution of the deformation at two considered film/substrate systems and along a given path.

The results highlighted in Fig. 15 show that when  $E_{f1}/E_s < 1.18$ , the response to nanoindentation is approximately related to the film. In fact, the deformation in the sample is approximately limited at the film (Fig. 16). This result is observed by Pelletier et al. [17] Nevertheless, for the case where  $E_{f1}/E_s > 1.18$ , the interface<sub>2</sub> between the film and the substrate is shifted (Fig. 15) because of the substrate effect. The deformation in this case is similarly distributed within the film and the substrate (Fig. 17). These explanations justify the divergence of the Mercier-2010 model when  $E_{f1}/E_s > 1.18$ .

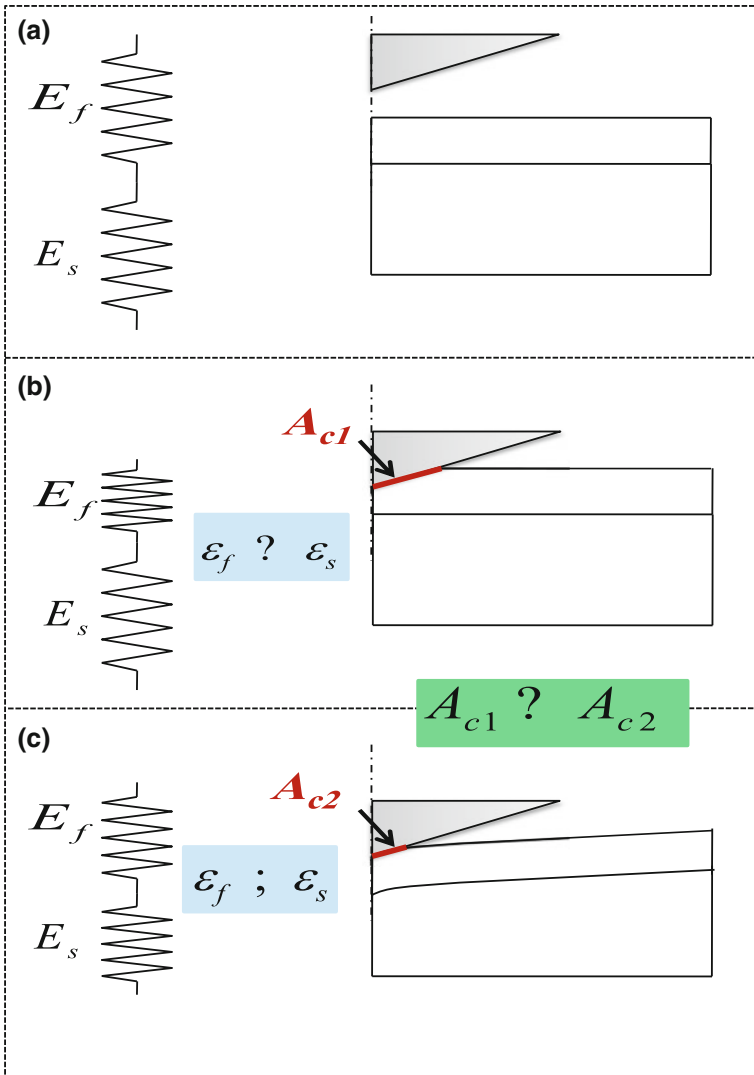


**Fig. 14** a A film/substrate system before indentation test, b indentation for soft film on hard substrate and c indentation for hard film on soft substrate

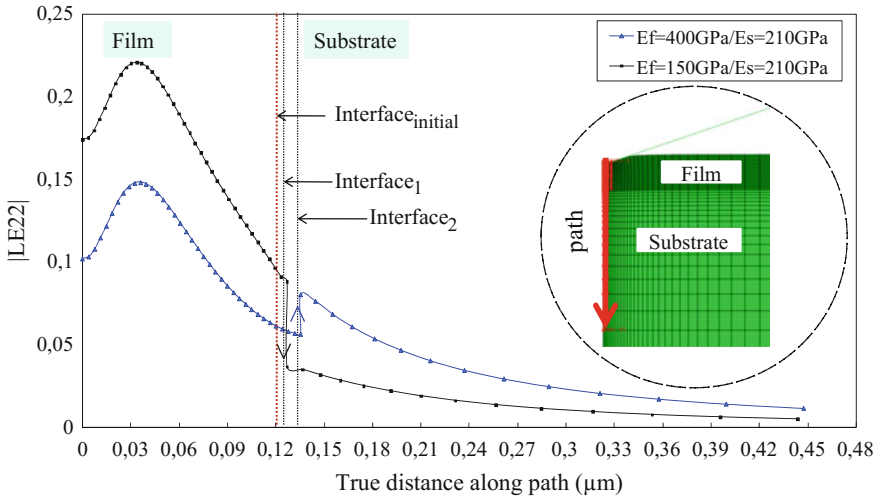


Fig. 15 Strain evolution for film/substrate systems along path

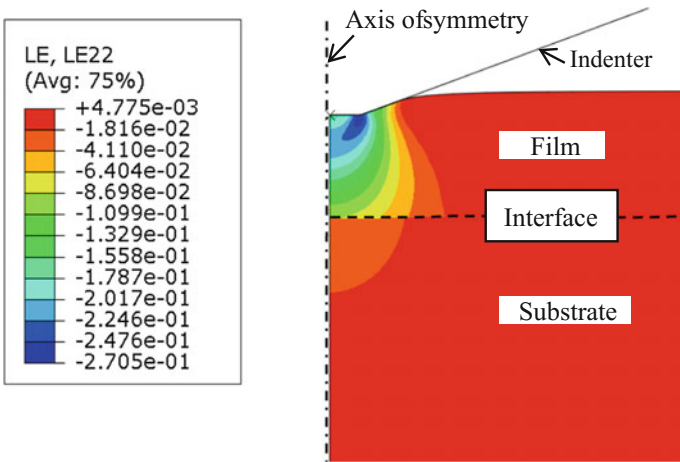


Fig. 16 Strain evolution for the film/substrate system with  $E_f = 150\text{ GPa}$  and  $E_s = 210\text{ GPa}$

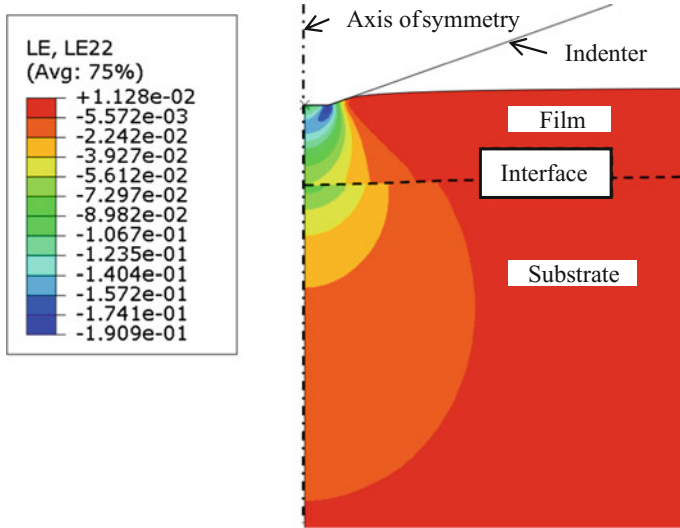


Fig. 17 Strain evolution for the film/substrate system with  $E_f = 400$  GPa and  $E_s = 210$  GPa

## 4 Conclusions

We systematically studied the mechanical properties of thin film materials using the finite element modeling (FEM). Based on the model of Mercier et al. an extensive study for measuring the elastic film properties was realized. The mechanical responses of the different film/substrate material systems have been analyzed. As a result, we demonstrate the limit of the analytical models as the model of Mercier et al. Particularly, for a hard film on a soft substrate ( $E_f/E_s \geq 1.18$ ) the response of the analytical model is quite influenced by the substrate effect. In this case, the error is mainly caused by a wrong estimation of the contact surface  $A_c$  between the indenter tip and the film surface. Therefore, it is concluded that, according to analytical models the characterization of monolayer or multilayer coatings is conditioned by the  $E_f/E_s$  ratio.

## References

1. Amaya-Roncancio, S., Restrepo-Parra, E., Devia-Narvaez, D.M., Arias-Mateus, D.F., Gómez-Hermida, M.M.: Molecular dynamics simulation of nanoindentation in Cr, Al layers and Al/Cr bilayers, using a hard spherical nanoindenter. *DYNA*. **81**, 102–107 (2014)
2. Azadi, M., Rouhaghdam, A.S., Ahangarani, S., Mofidi, H.H.: Mechanical behavior of TiN/TiC multilayer coatings fabricated by plasma assisted chemical vapor deposition on AISI H13 hot work tool steel. *Surf. Coat. Technol.* **245**, 156–166 (2014)
3. Chakroun, N., Tekaya, A., Belhadjsalah, H., Benameur, T.: Measuring elastic properties of the constituent multilayer coatings for different modulation periods. *Int. J. Appl. Mech.* **10** (2018)

4. Inui, N., Mochiji, K., Moritani, K.: A nondestructive method for probing mechanical properties of a thin film using impacts with nanoclusters. *Int. J. Appl. Mech.* **8**, 1650041 (2016)
5. Kumar, A., Zeng, K.: Alternative methods to extract the hardness and elastic modulus of thin films from nanoindentation load-displacement data. *Int. J. Appl. Mech.* **2**, 41–68 (2010)
6. Doerner, M.F., Nix, W.D.: A method for interpreting the data from depth-sensing indentation instruments (1986)
7. Oliver, W.C., Pharr, G.M.: An improved technique for determining hardness and elastic modulus using load and displacement sensing indentation experiments. *J. Mater. Res.* **7**, 1564–1583 (1992)
8. Jung, Y.G., Lawn, B.R., Martyniuk, M., Huang, H., Hu, X.Z.: Evaluation of elastic modulus and hardness of thin films by nanoindentation. *J. Mater. Res.* **19**, 3076–3080 (2004)
9. Bull, S.J.: A simple method for the assessment of the contact modulus for coated systems. *Philos. Mag.* **95**, 1907–1927 (2015)
10. Mercier, D., Mandrillon, V., Verdier, M., Brechet, Y.: Mesure de module d'Young d'un film mince à partir de mesures expérimentales de nanoindentation réalisées sur des systèmes multicouches. *Matériaux Tech.* **99**, 169–178 (2011)
11. Chakroun, N., Tekaya, A., Belhadjsalah, H., Benameur, T.: A new inverse analysis method for identifying the elastic properties of thin films considering thickness and substrate effects simultaneously. *Int. J. Appl. Mech.* **9**, 1750096 (2017)
12. Liao, Y., Zhou, Y., Huang, Y., Jiang, L.: Measuring elastic-plastic properties of thin films on elastic-plastic substrates by sharp indentation. *Mech. Mater.* **41**, 308–318 (2009)
13. Bec, S., Tonck, A., Georges, J.-M., Georges, E., Loubet, J.-L.: Improvements in the indentation method with a surface force apparatus. *Philos. Mag. A* **74**, 1061–1072 (1996). <https://doi.org/10.1080/01418619608239707>
14. ABAQUS Version 6.14, Dassault systèmes simulia corp., Providence, RI, USA (2014)
15. Jayaraman, S., Hahn, G.T., Oliver, W.C., Rubin, C.A., Bastias, P.C.: Determination of monotonic stress-strain curve of hard materials from ultra-low-load indentation tests. *Int. J. Solids Struct.* **35**, 365–381 (1998)
16. Cheng, Y.T., Cheng, C.M.: Scaling, dimensional analysis, and indentation measurements. *Mater. Sci. Eng. R Rep.* **44**, 91–150 (2004)
17. Pelletier, H., Krier, J., Mille, P.: Characterization of mechanical properties of thin films using nanoindentation test. *Mech. Mater.* **38**, 1182–1198 (2006)

# **Part XII**

## **Forming**

# Limiting Drawing Ratio and Formability Behaviour of Dual Phase Steels—Experimental Analysis and Finite Element Modelling



R. L. Amaral, A. D. Santos and S. S. Miranda

**Abstract** Three different dual-phase steels are selected (DP500, DP600 and DP780) to study and analyze the effect of microstructure on formability behaviour for this kind of materials, which are nowadays commonly used in sheet metal forming. This class of advanced high strength steels have a microstructure predominantly composed by a soft ferritic matrix, which ensures good formability, combined with hard martensite particles that give the material its strength. Moreover, the mechanical behaviour of dual-phase steels can be affected by the volume fraction of martensite present in the material matrix, thus providing different levels of formability. This paper presents a formability study and a limiting drawing ratio identification of dual-phase steel sheets, with different amounts of martensite, using a deep drawing test. Experiments and finite element simulations have been performed to analyze and compare the obtained results for this kind of advanced high strength steels. Different experimental tests have been performed with different loading conditions, such as tensile test, biaxial bulge test and Swift test in which formability can be dependent on mechanical properties of material and loading conditions. It is shown that selected materials have a decreasing formability with higher content of martensite, independently from the loading conditions or different material characteristics (e.g. different evolution of anisotropy with rolling direction).

**Keywords** Dual phase steels · Sheet metal forming · Limiting drawing ratio Swift test · Deep drawing cylindrical cup

---

R. L. Amaral (✉) · A. D. Santos · S. S. Miranda  
INEGI, Institute of Science and Innovation in Mechanical and Industrial Engineering,  
R. Dr. Roberto Frias, 400, 4200-465 Porto, Portugal  
e-mail: [ramaral@inegi.up.pt](mailto:ramaral@inegi.up.pt)

A. D. Santos  
FEUP, Faculty of Engineering, University of Porto, R. Dr. Roberto Frias, 4200-465 Porto, Portugal

© Springer Nature Switzerland AG 2019  
L. F. M. da Silva (ed.), *Materials Design and Applications II*, Advanced  
Structured Materials 98, [https://doi.org/10.1007/978-3-030-02257-0\\_32](https://doi.org/10.1007/978-3-030-02257-0_32)

469

## 1 Introduction

Advanced high strength steels (AHSS) are used nowadays in the transportation industry, in response to the tighter international emission regulations and higher safety standards [1]. One way to improve the efficiency and emissions of automobiles, as well as, the security of passengers, is to reduce the weight of vehicles while increasing their structural strength [2].

Being deep drawing a sheet metal forming process widely used in the automotive industry to produce most of the necessary components of a vehicle body, the correct selection and use of appropriate high strength materials is very important. Such AHSS materials will allow to accomplish the imposed requests, in order to produce thinner parts with similar or better properties than the previous thicker components [3, 4].

Dual-phase (DP) steels are one of these AHSS materials, which present good mechanical properties when compared to the conventional steels. Their remarkable combination of good formability, hardening behaviour and high strength allows the possibility to produce the same automotive component as before, but thinner and stronger. Another important characteristic of dual-phase steels is their high capacity of energy absorption, providing an excellent performance in the crash zones of the vehicles [5, 6]. The microstructure of DP steels is composed by a soft matrix of ferrite phase, which ensures a good formability, with hard martensite particles that give to the material their strength [7, 8].

To improve the quality and development of the final product, numerical methods are used when evaluating manufacturing processes, being an important requirement for sheet metal forming operations. This will allow an evident increase in time efficiency, as well as, in design and production cost reductions. However, the accuracy of the obtained numerical results of metal forming processes depends on the most correct material behaviour definition and the better appropriate properties characterization.

Although some research on drawability of sheet metal materials have been published, taking into account the application of numerical methods [9–11], the drawing behaviour of DP steels has still many questions to be solved, particularly the effect of martensite phase in the material mechanical properties and related formability.

Wu-rong et al. [12, 13] investigated particularly the shear fracture of different dual-phase steel grades (DP600, DP800 and DP1000) using the deep drawing cylindrical cup test. Each of these steels had different thickness (1.0, 1.2 and 1.7 mm), while the punch diameter was 32 mm and clearance and die radius was changed according to the sheet thickness. In this analysis, the authors did not consider measurement earing cup profiles and punch force evolution.

Firat [14] presented a finite element methodology to calculate FLC and stretch formability of DP600 steel in square cup drawing process. FE comparisons with experimental results showed that failure heights calculated with conventional technique were not conservative and stretch formability of DP600 was overestimated in cup drawing.



Regueras et al. [15] performed a numerical study for five dual-phase steel grades concerning the effect of the initial blank thickness ( $t$ ) and length/wide punch ratio ( $LD$ ) in the deep drawing rectangular operations. The results allowed to establish analytical relations between thickness reduction percentage and the three studied parameters ( $t$ ,  $LD$  and dual-phase steel grade). However, the validation of the numerical results was based on a limited number of experimental data using a mild steel sheet.

Tan et al. [16] studied the influence of a partially hardened zone of DP590 steel sheet to increase the limiting drawing ratio using a cylindrical cup test.

Most of the previous works that using the deep drawing cylindrical cup tests did not consider the misalignment effects on results, as well as, the pinching that occurs in cup flange, which leads to an inaccurate analysis of strain distribution and earing cup height profiles.

This paper presents a study on formability behaviour and limiting drawing ratio identification of dual-phase steel sheets, using a deep drawing cylindrical cup test. Three different dual-phase (DP) steel grades (DP500, DP600, DP780) were selected and used, in which DP grade corresponds to different amount of martensite. The novelty of this work lies on the experimental tool setup, which avoids and reduces the pinching effect at the end of drawing stage and minimizes the misalignment of circular blank relative to the tools. Also, the use of different dual-phase steels with the same initial thickness contributes to a better comparison and as overall to a more adequate and more accurate material characterization and analysis of these steels.

## 2 Material Mechanical Behaviour

To obtain the mechanical characterization of the DP steels, uniaxial tensile tests were performed for different angles ( $0^\circ$ ,  $45^\circ$  and  $90^\circ$ ) to the rolling direction. Sheet thickness is 0.8 mm for each of these selected steels.

The tensile tests were conducted according to the ASTM E8 M standard [17], using a crosshead speed of 5 mm/s at room temperature ( $23^\circ\text{C}$ ). To ensure the repeatability of results, at least three experiments for each material and direction were carried out.

Table 1 presents the obtained mechanical properties from tensile tests along the rolling direction based on the engineering stress-strain curves. The corresponding true stress-strain hardening curves for each loading direction and DP steel are shown in Fig. 1.

As expected, the material with the highest amount of martensite phase (DP780) is the material with the highest strength, although it presents a lower ductility when compared to the other DP's.

To improve the amount of information of the mechanical behaviour provided by the uniaxial tensile test, biaxial hydraulic bulge tests were performed, since with this test it is possible to achieve higher experimental values of plastic deformation [18, 19].

**Table 1** Mechanical properties of the three dual phase steels, along rolling direction

Property	Material		
	DP500	DP600	DP780
Yield stress— $R_{p0.2}$ [MPa]	356.5	416.1	526.2
Ultimate tensile strength— $R_m$ [MPa]	544.8	630.9	843.1
Uniform elongation— $e_u$ [%]	18.2	16.4	12.5
Total elongation— $e_t$ [%]	29.5	27.1	17.9

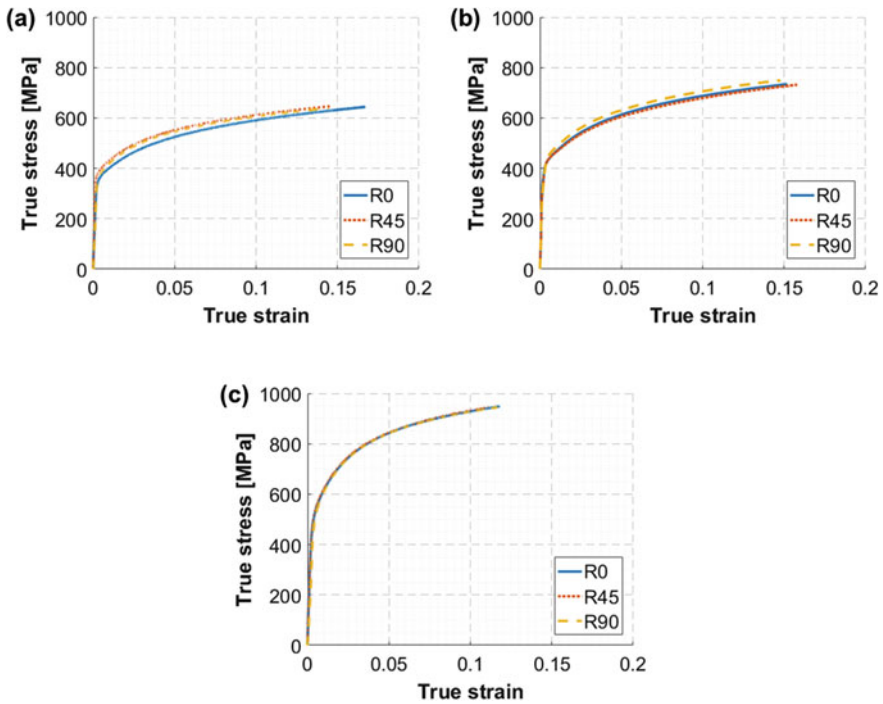


**Fig. 1** True stress-strain curves for different loading directions: **a** DP500; **b** DP600; **c** DP780

A tactile mechanical device [20] was used to measure fundamental variables in order to obtain the biaxial stress-strain curve evolution, based on the membrane theory. The measuring system is calibrated before each test, to ensure repeatability and accuracy of data acquisition [21]. The experimental bulge tests were performed using circular samples with 250 mm of diameter, at a pressure increment of 1 bar/s.

The obtained results of the hardening biaxial stress-strain curve for each dual-phase steel using the hydraulic bulge test are shown in Fig. 2.

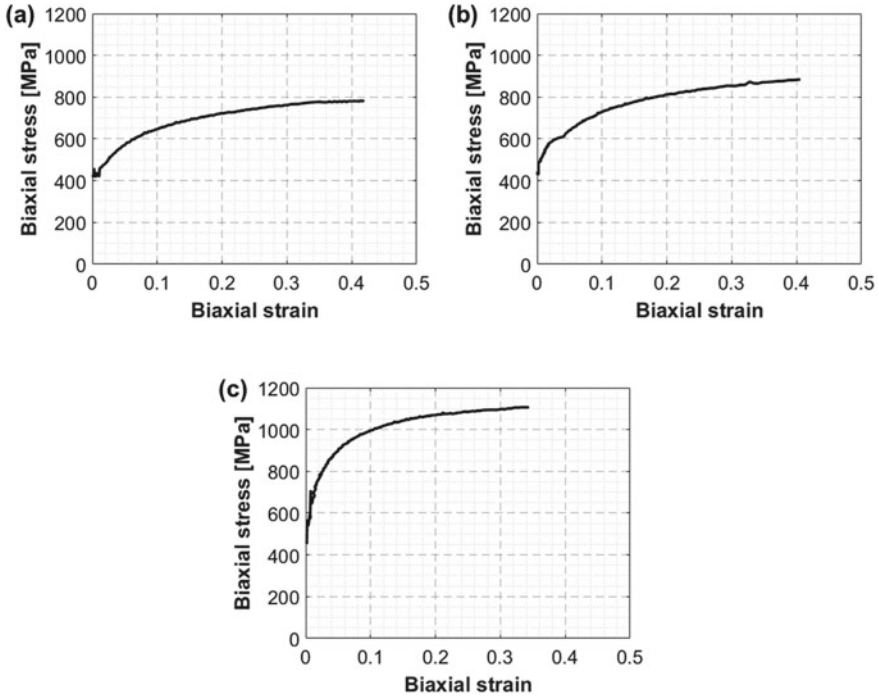


Fig. 2 Obtained biaxial stress-strain curves from hydraulic bulge test: **a** DP500; **b** DP600; **c** DP780

Taking into consideration the hardening stress-strain curves from tensile and biaxial bulge tests and assuming that both have the same plastic work to deform the material, it is possible to transform the biaxial data into an equivalent curve, because they may not be coincident (different deformation spaces).

Such transformation enables the combination of the hardening curves by including the converted bulge data in the equivalent stress-strain curve. This will allow a better identification of the constitutive law parameters that reproduce the mechanical hardening behaviour, which will be used as an input in numerical simulation. The biaxial stress-strain curve conversion into the equivalent stress-strain curve is based on the equivalent plastic work per unit of volume, considering as well the incompressibility of material [22, 23].

The extended hardening stress-strain curve using the converted biaxial is presented in Fig. 3, for each dual phase steel under study, as well as, the corresponding hardening curve representation by the combined Swift-Voce law. The identified parameters of the constitutive model are presented in Table 2.

It can be observed that implementing such methodology, there is a good continuity for the extension of hardening curve based on bulge test, for the dual-phase steels. The obtained results show also that experimental curve and Swift law evolu-

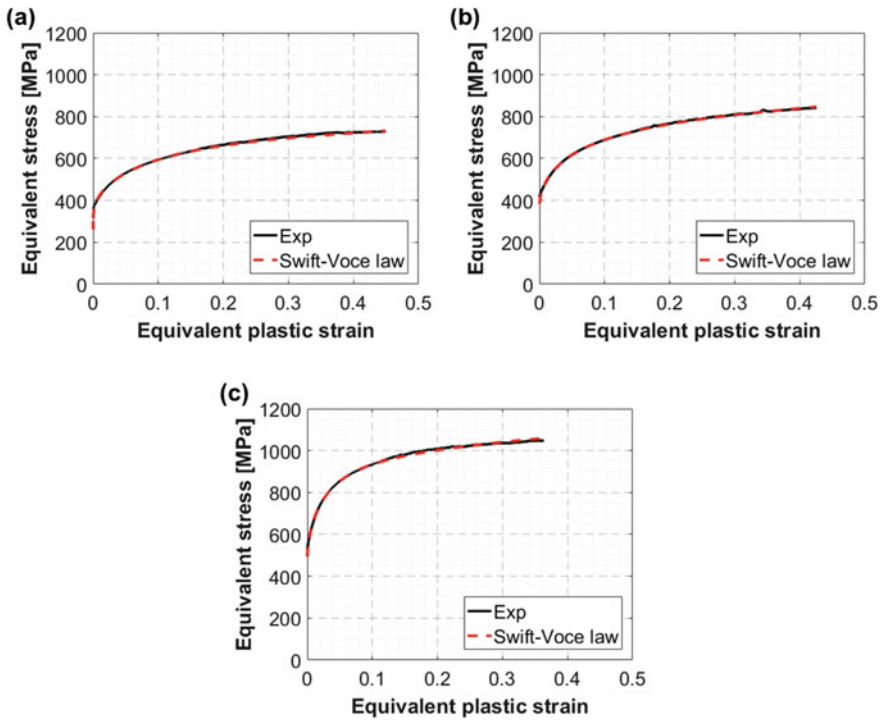


**Fig. 3** Equivalent stress-strain curves using the converted biaxial bulge data and corresponding Swift-Voce law hardening predictions: **a** DP500; **b** DP600; **c** DP780

**Table 2** Identified Swift-Voce law parameters using the combined tensile and bulge test data

Material	$\sigma = \alpha[K(\epsilon_0 + \epsilon)^n] + (1 - \alpha) \cdot [A + B(1 - e^{-C \cdot \epsilon})]$							
	$\alpha$	K	$\epsilon_0$	n	A	B	C	RSME
DP500	0.080	5403.7	-0.0001	0.228	283.7	120.7	12.10	0.32
DP600	0.401	1666.6	0.0013	0.203	124.1	124.1	15.72	0.40
DP780	0.546	1942.3	0.0011	0.103	-72.3	298.3	30.10	0.36

tion present a similar tendency, thus giving evidence to an accurate modelling of the hardening behaviour of these materials.

Lankford coefficients (anisotropy r-values) were also evaluated and measured, for the same angles relative to the rolling direction used in tensile test. Table 3 presents the obtained r-values and Fig. 4 presents the corresponding evolution with the angle relative to rolling direction for each material, based on Hill’48 yield criterion prediction.

Two distinct behaviours can be observed from r-value evolution curves, where the DP600 and DP780 show a similar tendency, having the last one the highest r-values for all the analyzed directions. The anisotropic coefficient at 45° relative to the rolling

**Table 3** Lankford coefficients of dual-phase steels obtained from different angles relative to rolling

Material	$r_0$	$r_{45}$	$r_{90}$	$\bar{r}$	$\Delta r$
DP500	1.02	0.87	1.20	0.99	0.23
DP600	0.62	1.03	0.80	0.87	-0.32
DP780	0.70	1.05	0.88	0.92	-0.26

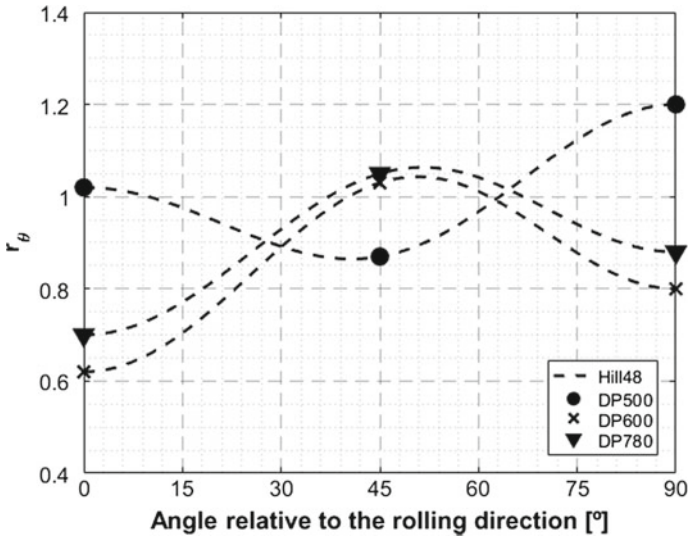


**Fig. 4** Evolution of anisotropy coefficients along different angles to rolling direction

direction has a lower value for DP500, while for DP600 and DP780 steels it has a higher value than the other two directions.

### 3 Deep Drawing Cylindrical Cup Test

In order to determine the limit drawing ratio and evaluate the drawability of the dual-phase materials, experimental deep drawing cylindrical cup tests were performed using a hydraulic testing machine, as shown in Fig. 5a. The tool setup is composed by four parts: a die, a flat blank holder, a cylindrical punch and a stopper. The punch has 60 mm of diameter while the die diameter is 62.4 mm and the radius is 10 mm (Fig. 5b).

The sheet metal blank is circular and different initial diameters were defined in order to determine the critical drawing diameter for each material. The minimum blank diameter is 105 mm and increments of 10 mm in blank diameter are considered up to the maximum diameter of 135 mm.

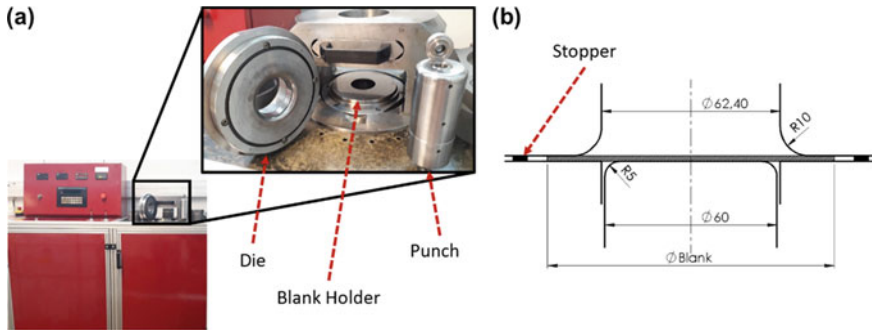


**Fig. 5** a Deep drawing cylindrical cup experimental setup; b tool dimensions in mm

**Table 4** Experimental conditions of deep drawing cylindrical cup tests

Environmental temperature	24 °C
Humidity	60%
Specimen diameters	105, 115, 125, 135 and additionally 130 mm
Punch speed	5 mm/s
Blank holder force	75 kN for 105 mm and 175 kN for 135 mm
Lubricant conditions	15 g/m <sup>2</sup> of oil (FERROCOAT N6130)

A stopper ring was produced from the same sheet material of the blank (same thickness) and the purpose is to keep a minimum gap between blank holder and die thus preventing or minimizing ironing of blank flanges at the final stage of deep drawing. To reduce the friction forces between the blank and tools contact surfaces during the experimental tests, a lubricant was applied to both sides of the circular blank.

The corresponding experimental conditions of the current study are presented in Table 4.

### 3.1 Limiting Drawing Ratio

Limiting drawing ratio (LDR) is defined as the ratio (Eq. 1) between the highest circular blank diameter ( $D_{blank\ max}$ ) that can be drawn into a cylindrical cup without fracture and the selected punch diameter ( $D_{punch}$ ).

$$LDR = \frac{D_{blank\ max}}{D_{punch}} \quad (1)$$

Different methodologies can be used to determine the material limiting drawing ratio. One method is drawing a number of cups, increasing the drawing ratio by

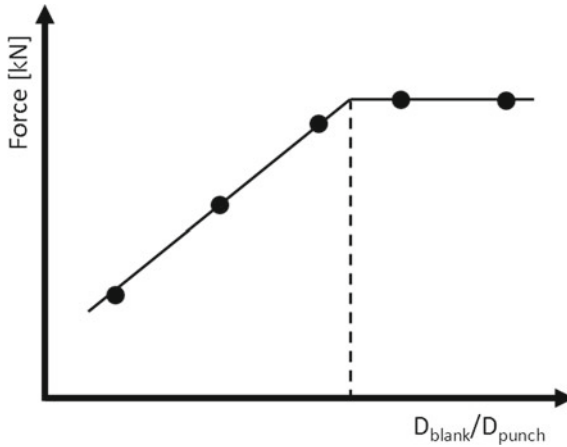


**Fig. 6** Drawing force as a function of blank and punch diameter ratio



**Fig. 7** Cylindrical cups obtained for DP780 material using a blank diameter of 105, 115 and 125 mm (left to right, respectively)

small amounts until the limiting drawing ratio is reached. Another method is using the maximum obtained drawing punch force for each defined blank diameters, as presented in Fig. 6.

The last method was used since a lower number of experiments is needed to determine the critical blank diameter. The criterion to obtain the LDR is to plot the maximum drawing force as a function of the ratio between blank and punch diameters, as well as, the maximum force attained when fracture occurs.

It is expected that the required force to draw a cup increases linearly with blank diameter until the critical value is exceeded. A horizontal line represents the maximum attained punch force when fracture will occur and the intersection point between the two lines indicates the limiting drawing ratio of the tested material.

For the first three initial blank diameters (105, 115 and 125 mm) a fully drawn cup (Fig. 7) was successfully obtained for each dual-phase steel.

The experimental evolution of punch force during the cup draw was measured, as well as, the corresponding displacement for each material and for each defined blank

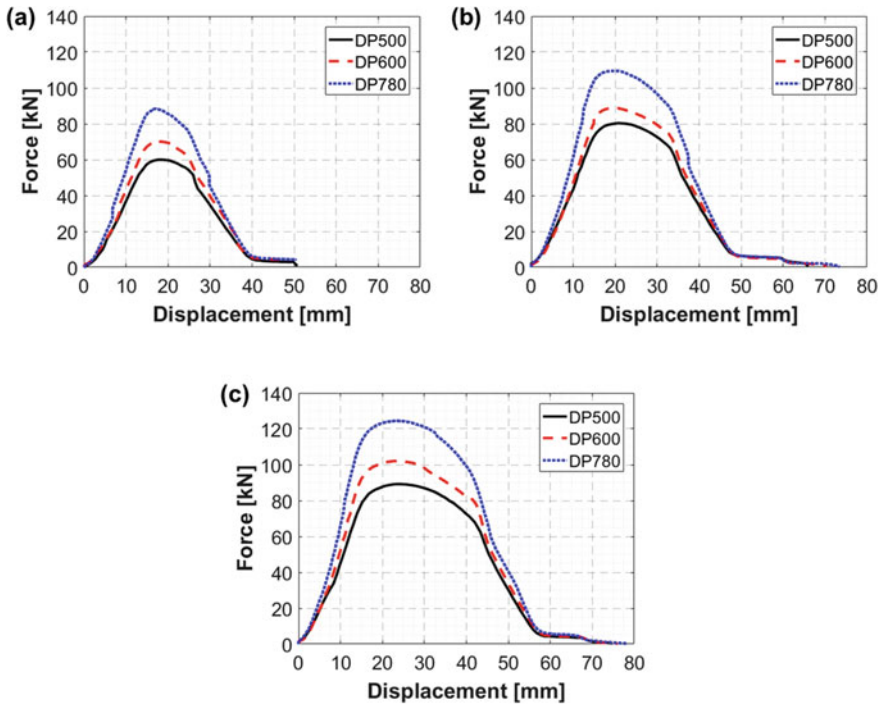


**Fig. 8** Punch force evolution with displacement of each dual-phase steel for the blank diameters: **a** 105 mm; **b** 115 mm; **c** 125 mm

diameter. The obtained punch force versus punch displacement curves are shown in Fig. 8.

As seen, all the punch force versus displacement curves show a similar behaviour, wherein DP780 needs a higher punch force in this drawing operation, due to its higher strength, as expected.

When the blank diameter is increased from 125 to 135 mm, it is not possible to draw a cup and fracture occurs near to the punch radius. To reduce the range where the critical diameter would be, the initial blank diameter was decreased from 135 to 130 mm and the same result of fracture was obtained, as shown in Fig. 9.

This means that the limiting drawing blank diameter should lie between 125 and 130 mm. The corresponding force versus displacement curves plotted for each blank diameter, are presented in Fig. 10.

Taking into account the punch force as a function of displacement curves for every case, a linear regression is fitted to the maximum punch force of the fully drawn cups, which intersects a horizontal line that corresponds to the maximum load of fracture experiments. The intersection point gives the limiting drawing ratio of the material. Figure 11 presents the obtained drawability limits based on the deep drawing cylindrical cup test for each dual-phase steel.





**Fig. 9** Fracture experimental cases when the critical blank diameter was exceeded (DP780 using the blank diameters of 135 mm and 130 mm, left to right, respectively)

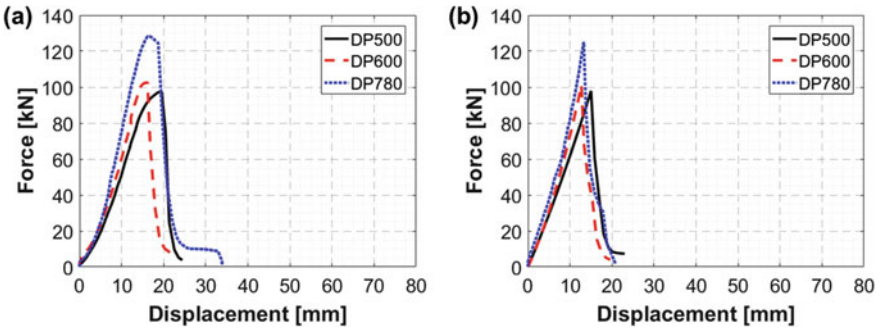


**Fig. 10** Punch force evolution with displacement of dual-phase steels for the blank diameters: **a** 130 mm; **b** 135 mm

As mentioned by ASTM E517 standard [24], the average normal anisotropy,  $\bar{r}$  parameter, is considered a measure of material drawability. With this in mind, it is possible to observe that the DP500 shows a higher limiting drawing ratio (LDR = 2.15), when compared to other DP steels (2.08 for DP600 and 2.09 for DP780), which is consistent with the higher value of planar anisotropy.

### 3.2 Earing Profile

Another evaluated result was the earing profile of the cups. The ear height was measured taking as reference the flat bottom of the cup, for five different angles relative to the rolling direction (0°, 22.5°, 45°, 67.5° and 90°). For this analysis and comparison the blank diameters of 105 and 125 mm were selected. As a complement and for a better understanding of the earing profile results, the difference between the minimum and maximum height values were also plotted for each diameter and material.

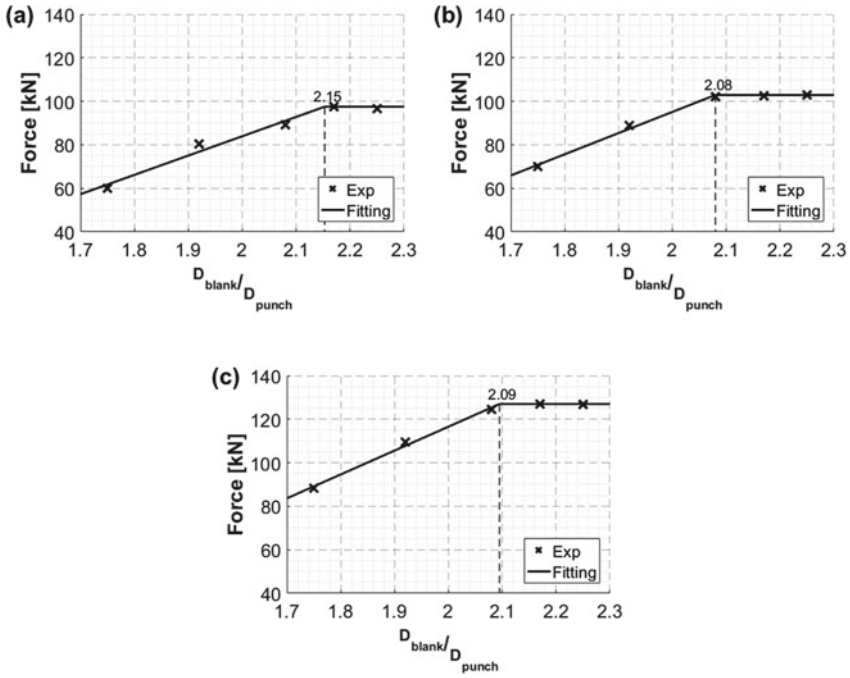


Fig. 11 Maximum drawing force as a function of blank and punch diameter ratio: a DP500; b DP600; c DP780

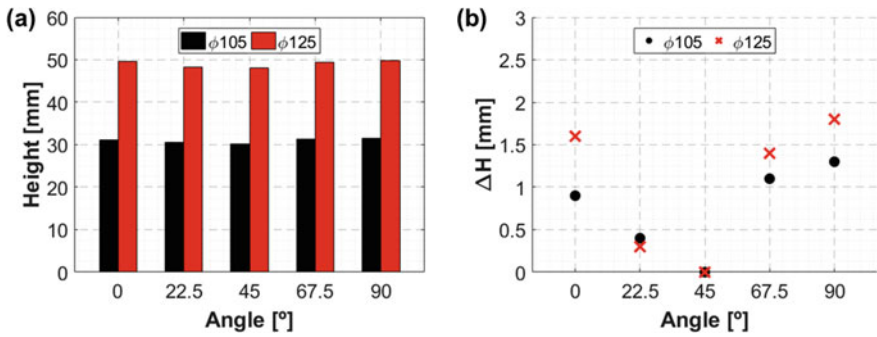
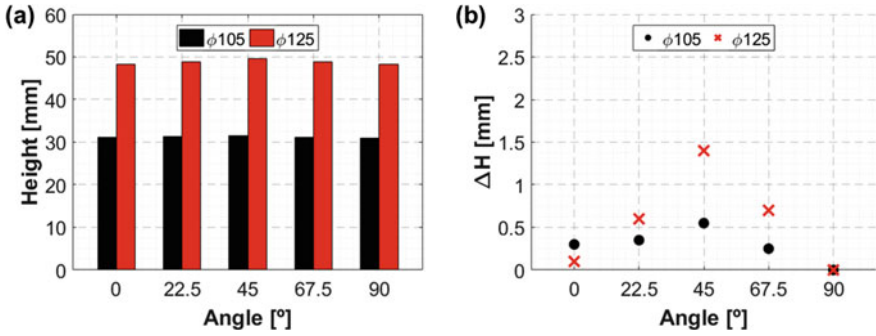
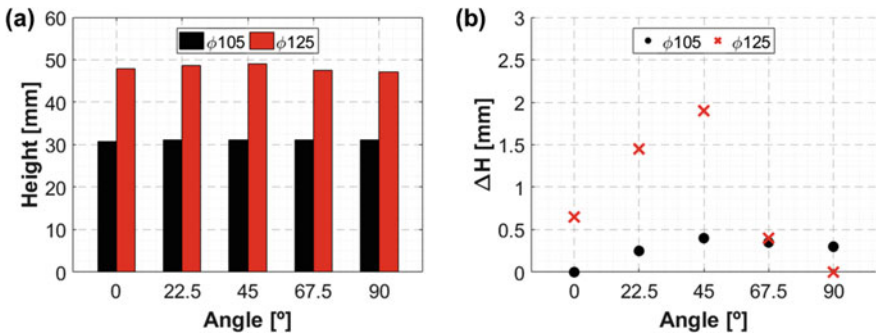


Fig. 12 Earing profile of DP500 for 105 and 125 mm blank diameters: a total ear height; b difference between maximum and minimum values

From Figs. 12, 13, 14 the obtained height of cup ears are presented, for each defined direction and material.



**Fig. 13** Earing profile of DP600 for 105 and 125 mm blank diameters: **a** total ear height; **b** difference between maximum and minimum values



**Fig. 14** Earing profile of DP780 for 105 and 125 mm blank diameters: **a** total ear height; **b** difference between maximum and minimum values

DP500 shows a lower ear height for 45° relative to the rolling direction for both drawing diameters, but the other two materials show a higher value for the same angle. This behaviour is related with the anisotropy coefficient evolution, where the DP600 and DP780 have a similar tendency as opposed to the DP500.

Being considered the planar anisotropy ( $\Delta r$ ) a measure of tendency to form ears in the cylindrical cup flange along the direction of the higher r-value [24], the obtained results show a good agreement with the experimentally obtained planar anisotropy coefficients for each material. The DP500 steel has the highest ear height at 90° relative to the rolling direction, while the both DP600 and DP780 have the highest ear at 45°.

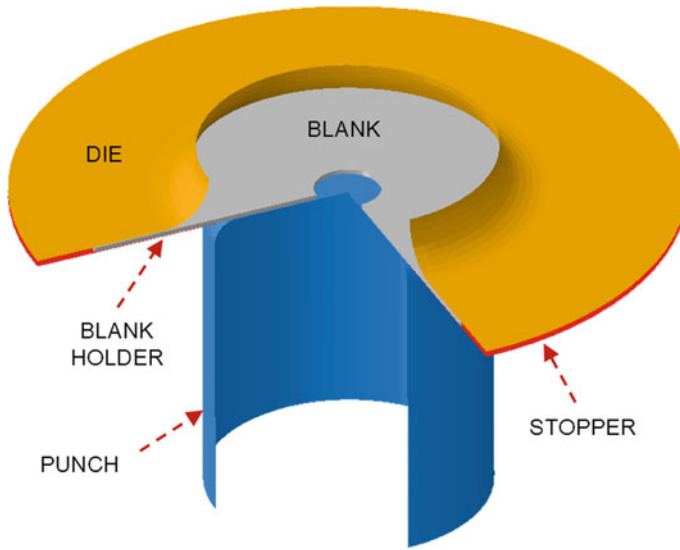


**Fig. 15** Numerical model of the cylindrical cup test

### 3.3 Numerical Simulation—FEM

To evaluate the mechanical characterization of dual-phase steels used in this work, a numerical explicit analysis of the deep drawing cup was performed using Abaqus/Explicit (Dassault Systèmes Simulia Corp., Providence, RI, USA) code. A 3D finite element model was created, defining only  $\frac{1}{4}$  of the experimental setup of the cylindrical cup test (Fig. 15), due to symmetry.

The tools were modelled as rigid analytic surfaces and the blank was discretized by deformable eight node solid elements with reduced integration (C3D8R type from Abaqus Library). The interaction between surfaces was established by a constant friction coefficient of 0.05. As for the material mechanical modelling, the sheet blank is defined with an elasto-plastic behaviour, using the Hill'48 yield criterion and an isotropic hardening defined by the constitutive model already presented in Sect. 2.

Figure 16 presents the evolution of the punch force versus displacement during forming process where experimental data and numerical results are compared.

It can be observed that the evolution of punch force predicted is very close to the experimental punch force. These results show that selected hardening law follows an appropriate description of material behaviour. Although, the attained maximum punch in numerical simulation for the DP500 material is similar to the experimental evidence, in case of DP600 the numerical punch force prediction is a little bit lower and higher for the DP780.

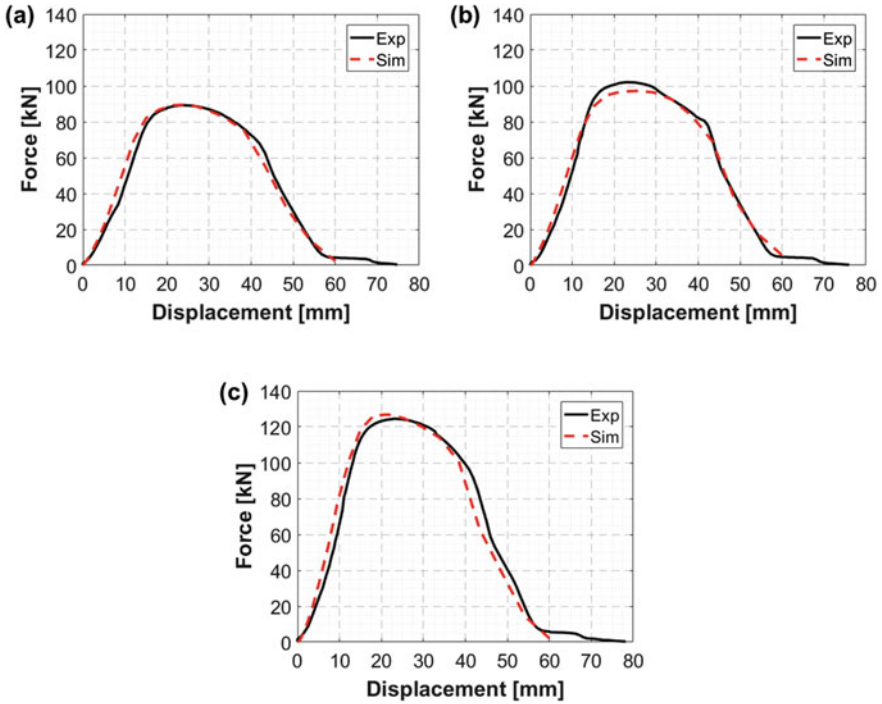


**Fig. 16** Comparison of experimental and numerical punch force versus displacement evolutions for a blank diameter of 125 mm: **a** DP500; **b** DP600; **c** DP780

As mentioned in [25] the predicted punch force evolution is very sensitive to the friction conditions, which can increase or decrease the maximum punch force, as well as, the initial slope of the evolution punch force. One other hand, the punch force evolution is not very sensitive to the selected yield criterion under this drawing operation and material.

The earing profiles for each material (Fig. 17) show a higher difference between experimental values and numerical predictions. Although the numerical evolution behaviour of the ears from 0° to 90° relative to the rolling direction is similar to the experimental data, the amplitude between maximum and minimum height ear values (Table 5) is higher.

**Table 5** Difference [mm] between maximum and minimum ears height of 25 mm blank diameter for experimental and numerical results

	DP500	DP600	DP780
Experimental	1.8	1.4	1.9
Simulation	4.54	6.55	4.87

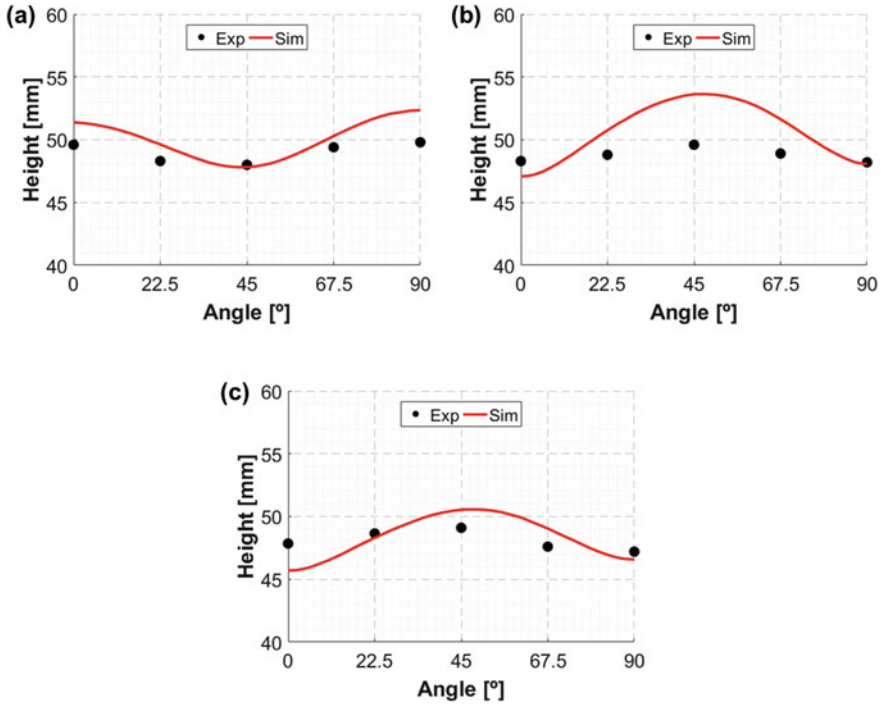


**Fig. 17** Comparison of experimental and numerical earing profiles for blank diameter of 125 mm: **a** DP500; **b** DP600; **c** DP780

The effects of the yield surface on the ear height distribution are quite significant under the deep drawing operation, meaning that an adequate and accurate description of yielding behaviour of the materials is needed in numerical simulation of sheet metal forming processes.

## 4 Conclusions

In this paper, three different dual-phase steels grades (DP500, DP600 and DP780) were selected and studied for formability analysis and limiting drawing ratio determination. The dual-phase steel DP780 shows a higher strength due to the high content of martensite phase, but it presents a lower ductility when compared to DP500 and DP600 steels. The combination of tensile test data and hydraulic bulge test results proved to be an approach that allows the improvement and an accurate hardening behaviour reproduction using constitutive models, for higher plastic strain values based on experimental data.

The use of deep drawing cylindrical cup test allowed the determination of the limiting drawing ratio for selected materials, having the DP500 the higher limit (LDR = 2.15), followed by the DP780 (LDR = 2.09) and DP600 (LDR = 2.08). These results show a good correlation with the measured experimental anisotropy coefficients, in which the planar anisotropy is higher for the DP500 steel. Earing profile predictions using numerical simulation show a greater amplitude for different angles relative to the rolling direction when compared with experimental points, meaning that some improvements should be considered on material characterization and the choice of yield criteria.

Regarding the numerical finite element modeling, further studies will include the analysis of thickness distributions in cups wall, as a complement for a better selection of the material yield criteria, and the implementation of damage models to predict the fracture occurrence. Other models to describe the friction between the contact surfaces will be also considered, since it shall play a role on obtained numerical results.

**Acknowledgements** Authors gratefully acknowledge the funding of SciTech, R&D project NORTE-01-0145-FEDER-000022 cofinanced by NORTE2020, through FEDER and the financial support of the Portuguese Foundation for Science and Technology (FCT) under project P2020-PTDC/EMS-TEC/6400/2014 (POCI-01-0145-FEDER-016876) by UE/FEDER through the program COMPETE 2020. The first author is also grateful to the FCT for the Doctoral grant SFRH/BD/119362/2016 under the program POCH, co-financed by the European Social Fund (FSE) and Portuguese National Funds from MCTES.

## References

1. Lesch, C., Kwiaton, N., Klose, F.B.: Advanced high strength steels (AHSS) for automotive applications. *Steel Res. Int.* **88**(10), 1–21 (2017)
2. Tisza, M., Lukács, Z.: Springback analysis of high strength dual-phase steels. *Procedia Eng.* **81**, 975–980 (2014)
3. Demeri, M.Y.: *Advanced High-Strength Steels: Science, Technology and Applications*. ASM International (2013)
4. Hilditch, T.B., de Souza, T., Hodgson, P.D.: In: Shome, M., Tumuluru, M. (eds.) *Welding and Joining of Advanced High Strength Steels (AHSS): Properties and Automotive Applications of Advanced High-Strength Steels (AHSS)*, pp. 9–28. Woodhead Publishing (2015)
5. Fonstein, N.: In: Rana, R. Singh, S.B. (eds.) *Automotive Steels—Design, Metallurgy, Processing and Applications: Dual-phase steels in Automotive Steels*, pp. 169–216. Woodhead Publishing (2017)
6. Belgasam, T.M., Zbib, H.M.: Key factors influencing the energy absorption of dual-phase steels: multiscale material model approach and microstructural optimization. *Mat. Trans. A* **49**(6), 2419–2440 (2018)
7. Kim, S.B., Huh, H., Bok, H.H., Moon, M.B.: Forming limit diagram of auto-body steel sheets for high-speed sheet metal forming. *J. Mater. Proc. Technol.* **211**, 851 (2011)
8. Amaral, R., Santos, A.D., Sousa, J.A., Lopes, A.B.: In: da Silva, L.F.M. (eds.) *Materials Design and Applications: The Influence of Microstructure on the Mechanical Behaviour of Dual Phase Steels*, pp. 25–35. Springer International Publishing (2017)
9. Kim, H., Sung, J.H., Sivakumar, R., Altan, T.: Evaluation of stamping lubricants using the deep drawing test. *Int. J. Mach. Tool. Manuf.* **47**(14), 2120–2132 (2007)

10. Rabahallah, M., Bouvier, S., Balan, T., Bacroix, B.: Numerical simulation of sheet metal forming using anisotropic strain-rate potentials. *Mater. Sci. Eng. A* **517**, 261–275 (2009)
11. Bandyopadhyay, K., Panda, S.K., Saha, P., Padmanabham, G.: Limiting drawing ratio and deep drawing behavior of dual phase steel tailor welded blanks: FE simulation and experimental validation. *J. Mater. Process.* **217**, 48–64 (2015)
12. Wu-rong, W., Chang-wei, H., Zhong-hua, Z., Xi-cheng, W.: The limit drawing ratio and formability prediction of advanced high strength dual-phase steels. *Mater. Des.* **32**(6), 3320–3327 (2011)
13. Wu-rong, W., Xi-cheng, W.: The effect of martensite volume and distribution on shear fracture propagation of 600–1000 MPa dual phase sheet steels in the process of deep drawing. *Int. J. Mech. Sci.* **67**, 100–107 (2013)
14. Firat, M.: A finite element modeling and prediction of stamping formability of a dual-phase steel in cup drawing. *Mater. Des.* **34**, 32–39 (2012)
15. Regueras, J.M.G., López, A.M.C.: Investigations on the influence of blank thickness ( $t$ ) and length/wide punch ratio (LD) in rectangular deep drawing of dual-phase steels. *Comput. Mater. Sci.* **91**, 134–145 (2014)
16. Tan, C.J., Aslian, A., Honarvar, B., Puborlaksono, J., Yau, Y.H. Chong, W.T.: Estimating surface hardening profile of blank for obtaining high drawing ratio in deep drawing process using FE analysis. *IOP Conf. Ser. Mater. Sci. Eng.* **103**, 012047 (2015)
17. ASTM Standard E8 M, Standard Test Methods for Tension Testing of Metallic Materials. ASTM International (2016)
18. Reis, L.C., Oliveira, M.C., Santos, A.D., Fernandes, J.V.: On the determination of the work hardening curve using the bulge test. *Int. J. Mech. Sci.* **105**, 158–181 (2016)
19. Keller, S., Hotz, W., Friebe, H.: Yield curve determination using the bulge test combined with optical measurement. In: Proceedings of IDDRG International Conference, pp. 319–330 (2009)
20. Campos, H., Santos, A.D., Martins, B., Ito, K., Mori, N., Barlat, F.: Hydraulic bulge test for stress-strain curve determination and damage calibration for Ito-Goya model. In: 11th World Congress on Computational Mechanics, 5th European Conference on Computational Mechanics and 6th European Conference on Computational Fluid Dynamics, pp. 4223–4238 (2014)
21. Campos, H., Santos, A.D., Amaral, R.: Experimental and analytical evaluation of the stress-strain curves of AA5754T4 and AA6061T6 by hydraulic bulge test. *Ciência & Tecnologia dos Materiais* **29**(1), 244–248 (2017)
22. Sigvant, M., Mattiasson, K., Vegter, H., Thilderkvist, P.: A viscous pressure bulge test for determination of a plastic hardening curve and equibiaxial material data. *Int. J. Mater. Form.* **2**, 235–242 (2009)
23. Lazarescu, L., Nicodim, I., Ciobanu, I., Comsa, D.S., Banabic, D.: Determination of material parameters of sheet metals using the hydraulic bulge test. *Acta Metall. Slovaca* **19**(1), 4–12 (2013)
24. ASTM Standard E517, Standard Test Method for Plastic Strain Ratio  $r$  for Sheet Metal. ASTM International (2018)
25. Neto, D.M., Oliveira, M.C., Dick, R.E., Barros, P.D., Alves, J.L., Menezes, L.F.: Numerical and experimental analysis of wrinkling during the cup drawing of an AA5042 aluminium alloy. *Int. J. Mater. Form.* **10**(1), 125–138 (2017)



# Characterization and Formability Analysis of a Composite Sandwich Metal-Polymer Material



S. S. Miranda, A. D. Santos, R. L. Amaral and L. T. Malheiro

**Abstract** In recent years, extensive research was carried out on the development at lightweight materials, combining metals with polymers, so-called composite sandwich metal/polymer materials, in order to face the safety and environmental requirements. These materials are composed by metal sheet skins with reduced thickness and a polymer core. However, the combination of steel with other materials poses new challenges, due to their new or different behavior and non-homogeneity of deformation, needing also a different approach to material characterization and formability analysis. This contribution presents the issues concerning material characterization and behavior for this kind of materials in addition to using and proposing appropriate approaches for traditional testing methodology. Fundamental mechanical characterization is obtained by using, not only the uniaxial tensile test, but including also hydraulic bulge test. Formability characterization for this hybrid material includes hole expansion tests and deep drawing Erichsen test, being also discussed the adequacy and differences between homogeneous and composite material results. Numerical simulations were performed to study the influence of tool geometry during the hole expansion test. For the HET to be adequate for both of types of materials, heterogeneous hybrid material and homogenous metal sheets, the increase of the die or punch radius dimensions demonstrated to be the best option to get the material formability behavior without compromising the adequacy of selected tests.

**Keywords** Composite sandwich metal-polymer · Sheet metal forming Formability · Deep drawing · Hole expansion test

---

S. S. Miranda (✉) · A. D. Santos · R. L. Amaral  
INEGI, Institute of Science and Innovation in Mechanical and Industrial Engineering,  
R. Dr. Roberto Frias, 400, 4200-465 Porto, Portugal  
e-mail: [smiranda@inegi.up.pt](mailto:smiranda@inegi.up.pt)

A. D. Santos  
FEUP, Faculty of Engineering, University of Porto, R. Dr. Roberto Frias,  
4200-465 Porto, Portugal

L. T. Malheiro  
Inapal Metal SA, Trofa, Portugal

© Springer Nature Switzerland AG 2019  
L. F. M. da Silva (ed.), *Materials Design and Applications II*, Advanced  
Structured Materials 98, [https://doi.org/10.1007/978-3-030-02257-0\\_33](https://doi.org/10.1007/978-3-030-02257-0_33)

## 1 Introduction

New and demanding global standards for vehicle safety, fuel economy and greenhouse gas emissions, due to the current environmental concerns, are the new paradigm for the transportation industry. This framework has been the opportunity for the introduction of new materials, research and development of new solutions that will help meet the imposed challenges and to balance between performance, safety and energy efficiency [1, 2].

One of these solutions, with practical interest and receiving great receptivity, is the use of hybrid materials, which have metallic skins, aluminum or steel, with a core that can be constituted by a metallic foam or alternatively by a polymeric core. The latter is also referred as a metal/polymer sandwich composite. Initially, these materials were used in automotive components with the main objective of reducing interior noise and vibration in the passenger compartment [3], due to their excellent passive damping capacity [4]. This type of material has also very high specific strength, being composed of metal sheets with reduced thickness and a polymer core. Due to their good characteristics and mass production capability, the use of thermoplastics combined with metallic materials offers advantages in the manufacturing of components by combining the high strength of the steel with the low weight of the plastic [5], allowing high flexural strength [6] and energy absorption [7].

The main advantages of sandwich composites are the excellent stiffness/weight or strength/weight ratio, ease of production and when developed for this purpose, excellent ability to absorb vibrations and noise [8]. However, current data on their formability are not sufficiently known [9], since the properties and behavior of the composite materials in metal/polymer sandwich may vary according to the thickness of the layers, chosen metal materials or even its manufacturing route.

The formability of metallic materials is an important feature in stamping processes. Tests used to identify such properties include the standard hole expansion test or the Swift test. However, the use of this test to characterize non-conventional materials, with new behaviors, non-homogeneity of deformation, poses new challenges in its applicability, due to being defined to the characterization of homogeneous materials. Therefore, the previous type of tests were considered for this selected kind of non-homogenous material in order to understand the limits and possibilities of current standard tests. Additionally, numerical simulations and models were used to complement and study the influence of testing variables, in order that more adequate testing methods can match with these “new” hybrid materials.

## 2 Material Characterization

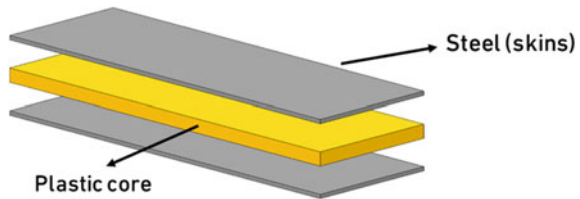
In this section, experimental results are presented for the sandwich composite material, composed by two interstitial free steel metal skins with 0.3 mm thickness and a polymeric core (polyamide combined with polyethylene) with 1 mm thickness, as shown in Fig. 1.

Table 1 presents the properties for the metal/polymer sandwich composite material given by the material supplier.

### 2.1 Tensile Test

In order to determine the mechanical behavior of the material and the fundamental corresponding constitutive model parameters reproducing such behavior, uniaxial tensile tests were performed according to the ASTM E8 M standard [10]. To ensure the repeatability of results, at least three experiments for each material and direction were carried out. It was taken into consideration the loading direction along the rolling direction of the skin sheets, being the experimental conditions shown in Table 2.

**Fig. 1** Hybrid material composed by a steel skin and polymeric core



**Table 1** Mechanical properties of the metal/polymer sandwich composite material

Property	Metallic sheets	Polymeric core
Yield strength [GPa]	210	0.98
Poisson coefficient $\nu$	0.3	0.38
Density [kg/m <sup>3</sup> ]	7800	1000
Thickness [mm]	0.3 (2×)	1

**Table 2** Experimental conditions for uniaxial tensile test

Property	Value
Width of specimens [mm]	12.5
Loading direction	0°
Test temperature [°C]	26°
Relative humidity [%]	64
Test velocity [mm/min]	5

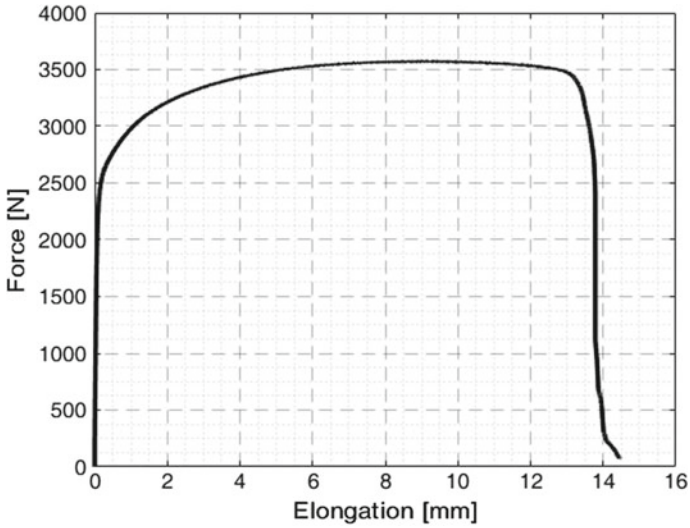


**Fig. 2** Force versus elongation curve for the composite sandwich material along the rolling direction

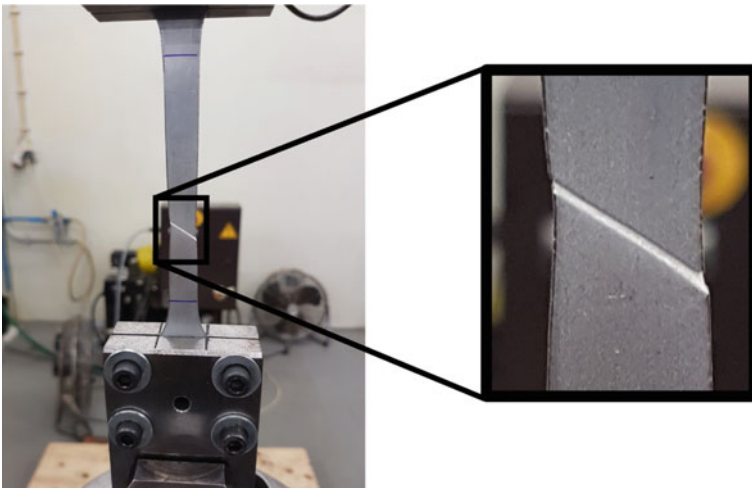


**Fig. 3** Detail of the fracture zone of the hybrid material

Figure 2 shows the force versus elongation curve, obtained from the tensile test for this composite sandwich metal/polymer material.

The plastic deformation capacity of the core is far more superior than the metal sheet skin, since the steel reaches the fracture while the plastic is still keeping its integrity, as seen in Fig. 3.

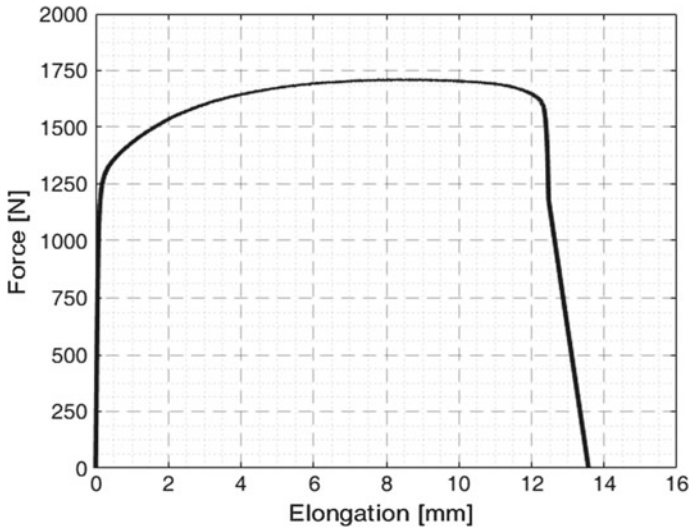


**Fig. 4** Force versus elongation curve for the steel skins along the rolling direction

**Table 3** Mechanical properties for the sheet skins of the composite metal/polymer material

Direction	Yield stress	Ultimate tensile strength	Total elongation
0°	334.4 MPa	458.9 MPa	27.6%

The determination of the actual stress-strain curve of sandwich composites is based on the mixing rule, considering the volume fractions for each constituent of the material [11]. However, since it is a sandwich structure in which the constituent materials have a very high elastic modulus differential for elastic modulus and plastic behavior ( $\approx 198\%$ ), the determination of mechanical properties of the aggregate (steel skins and plastic core) cannot be directly obtained.

Therefore, it is necessary to follow a different methodology to obtain the behavior of the material. The strategy followed herein was to separate the two outer skin steel sheets [12, 13] and to perform the tensile test for each of the steel sheets. Figures 4 and 5 show, respectively, the force versus elongation and true stress versus true strain curves for the steel sheet skins. The experimental conditions for tensile tests of the skins sheets are the same as those of the composite material, Table 2.

The mechanical properties obtained with the uniaxial tensile test of the steel skins of the sandwich material, such as yield stress ( $R_{p0.2}$ ), ultimate tensile strength ( $R_m$ ), total elongation ( $\epsilon_t$ ) along the rolling direction, are presented in Table 3.

The material at the core of the composite sandwich material is a complex material, and there is no data available in the literature allowing its characterization. In order to determine its behavior, it is considered that there is an equal distribution of the strains, both in the steel skins and in the core, ( $\epsilon_{total} = \epsilon_{skins} = \epsilon_{core}$ ). Accordingly,

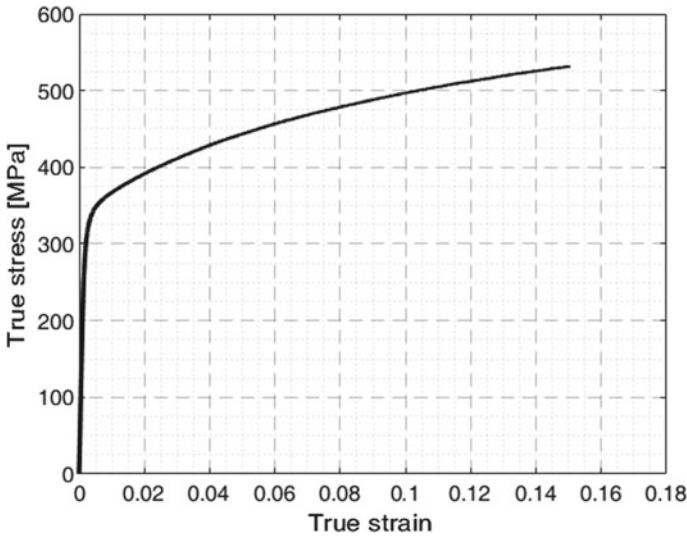
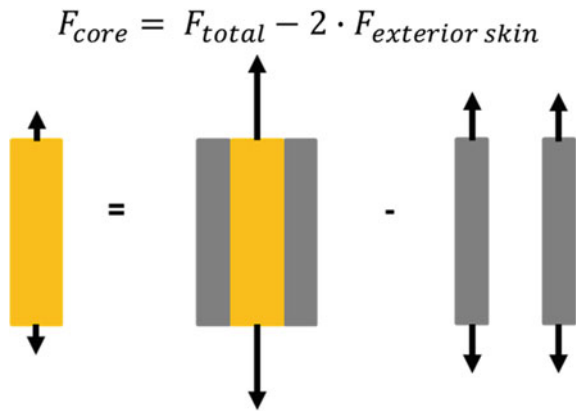


Fig. 5 True stress–strain curve for the steel skins obtained from uniaxial tensile test

Fig. 6 Drawing force as a function of blank and punch diameter ratio



the static balance ensures that the total force resulting from the application in the material is equal to the sum of the forces acting on both the skins and the core ( $F_{total} = F_{skins} = F_{core}$ ) [14], as shown in Fig. 6.

It is assumed that the core material is homogeneous and isotropic, in which the corresponding properties are unknown. With the application of the proposed methodology, it is possible to use experimental data from the tensile test of the aggregate material and its skins to obtain the force versus elongation evolution curve of the polymer core. Thus, the force differential between the two curves (Fig. 7) corresponds to the behavior of the core material.

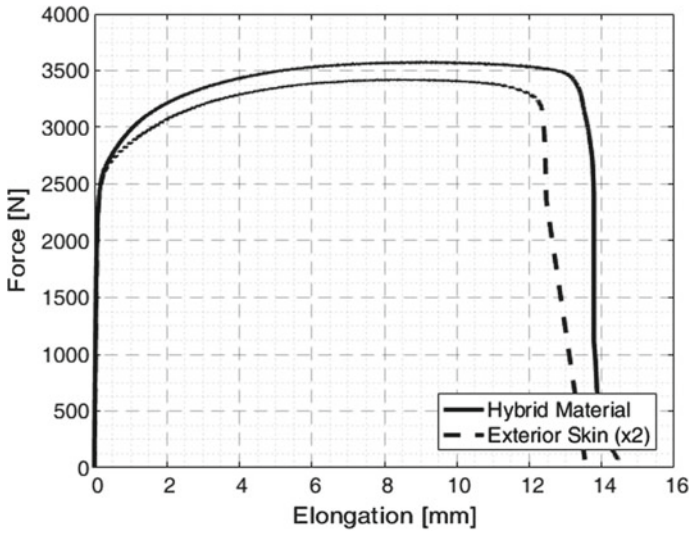


Fig. 7 Force versus elongation curves, skin and sandwich material (skins + polymer material)

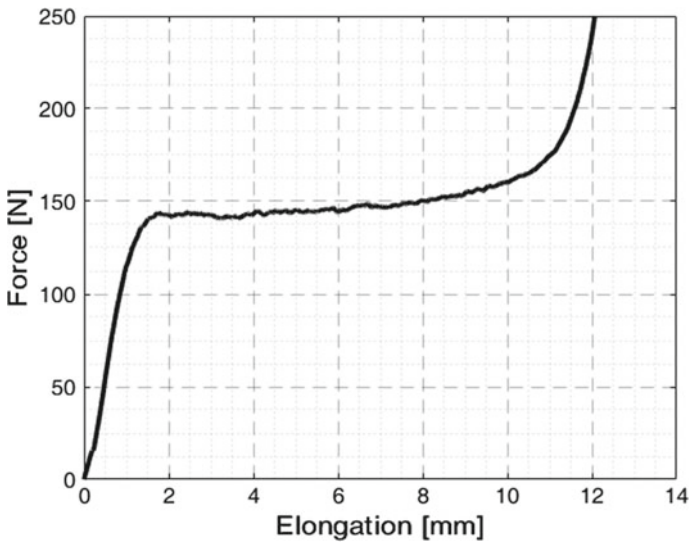


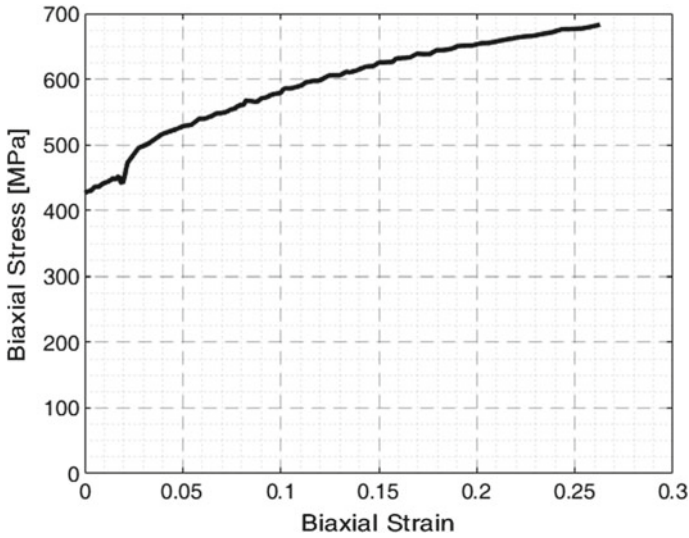
Fig. 8 Force versus elongation curve for the polymeric core

Figure 8 shows the obtained curve, which reflects the behavior of the polymer core during the uniaxial tensile test, obtained by previously described methodology.

From this Fig. 8, it is possible to see the corresponding yield stress of the core material, which is a lower value (39 MPa), when compared to steel skins (334 MPa).







**Fig. 10** Biaxial tensile-strain curve considering only the steel skin

where  $p$  is the hydraulic pressure,  $\rho$  is the radius of curvature of sheet mid surface and  $t$  is the material thickness at the pole.

The thickness at the pole is determined using the biaxial strain, assuming a constant material volume. To obtain the biaxial strain (Eq. 2) the expansion of a circle is measured, in which its initial diameter ( $D_{st_0}$ ) will increase during the test ( $D_{st}$ ) up to the fracture of the specimen. Therefore, strain can be calculated by:

$$\epsilon_b = \ln\left(\frac{D_{st}}{D_{st_0}}\right) \tag{2}$$

For this measurement, an extensometer included in the mechanical device is used, which follows deformation and the expansion of the material [19, 20].

Figure 10 shows the biaxial stress-strain curve obtained for the steel sheets skins of the hybrid material.

The membrane theory can not be applied to the composite type of material, because it is not homogeneous and therefore the determination of the biaxial tensile-strain curve can not be obtained by direct application of the theory.

However, it is possible to compare the behavior of the steel skin with the hybrid material by analyzing the evolution of the pole height (variable measured during the test) with the hydraulic pressure. The curves are shown in Fig. 11.

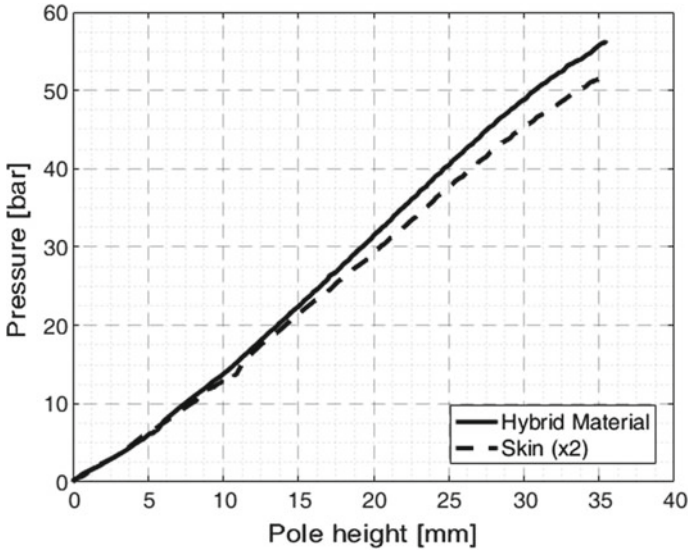


Fig. 11 Pole height evolution with hydraulic pressure, for hybrid material and also for steel skin

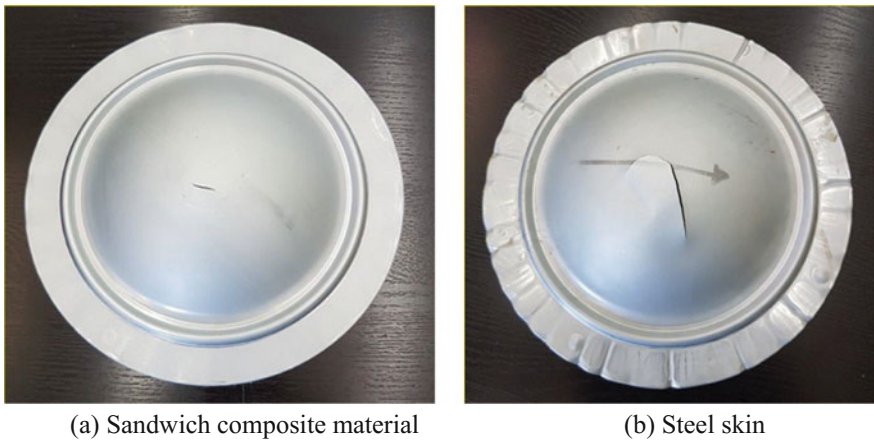


Fig. 12 Detail of the fracture zone of deformed specimens in the hydraulic bulge test

Both the specimen of steel skin and specimen of sandwich material show fracture which occurred during the process. However, due to the reduced thickness of the sheet metal (0.3 mm) and the applied hydraulic pressure, after the breakage of the material in the pole, the fracture zone propagates along the spherical cap of the deformed specimen, as shown in Fig. 12.

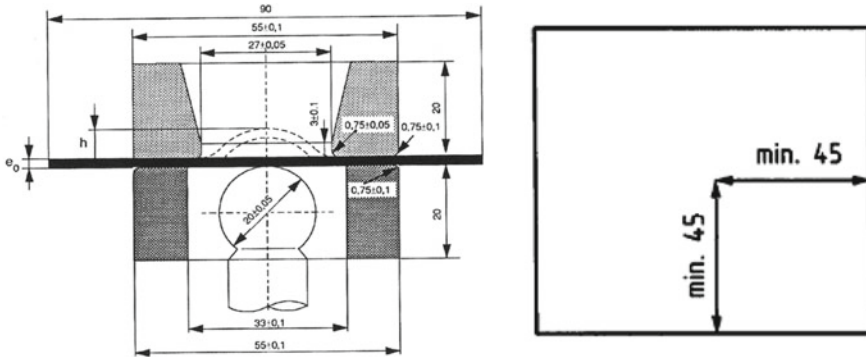


Fig. 13 Erichsen test: dimensions of the tools and the specimen

### 3 Formability Tests

Sheet metal forming processes have a significant importance in the production of metallic components. Frequently, the materials used in these processes have a limited formability, which requires an understanding of the deformation processes and the factors that limit such deformation.

The formability of a metallic material is the ability of a given metal blank to be plastically deformed in order to get the desired shape and to maintain it after forming, preserving its structural integrity and not exhibiting buckling, cracking, excessive thinning, among other defects [21]. Formability is a function of variables such as material properties, forming tool geometry, lubrication conditions, press speed, and the restrained conditions imposed by the blank holder pressure [22, 23]. As the automotive industry increasingly tends to use high strength steels due to increasing safety and environmental regulations, the likelihood of appearance of formability problems increases. Thus, in order to take advantage of all the capacity of a material to deform, it is important to know its limits of the amount of strain, thus avoiding defective parts or even breakage of the material in the forming process.

#### 3.1 Erichsen Test

Erichsen test represents one of the formability tests selected for this study. In this test the sheet blank is fixed between a die and the blank holder, being deformed by a hemispherical punch. The punch has a spherical diameter of 20 mm and the specimens are 90 mm<sup>2</sup>, as shown in Fig. 13. The stopping criterion consists in the appearance of a crack or fracture during deformation of the material [2].

Experimental tool set-up used for the Erichsen test is shown in Fig. 14. The experiments were performed on a manually operated mechanical machine.

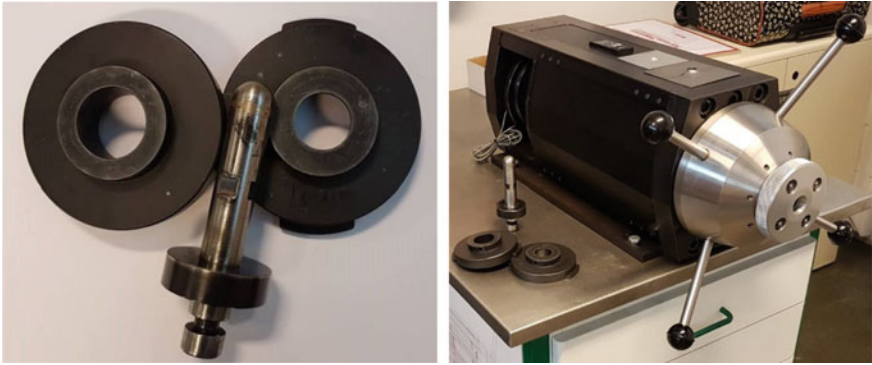


Fig. 14 Erichsen test: tools and machine used to perform the test

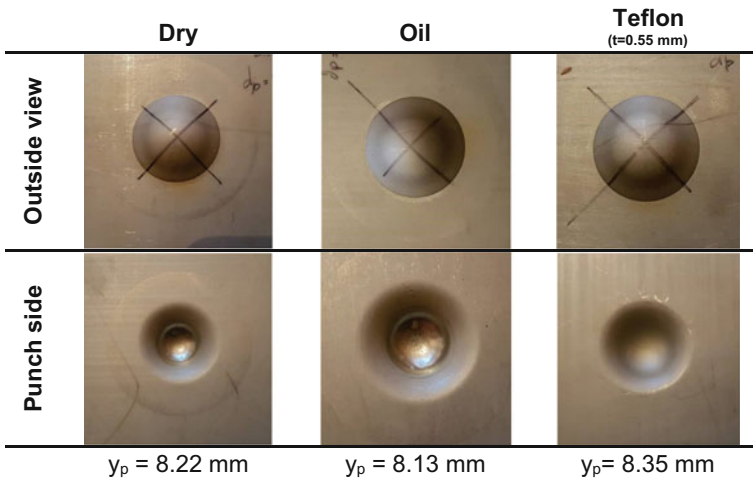
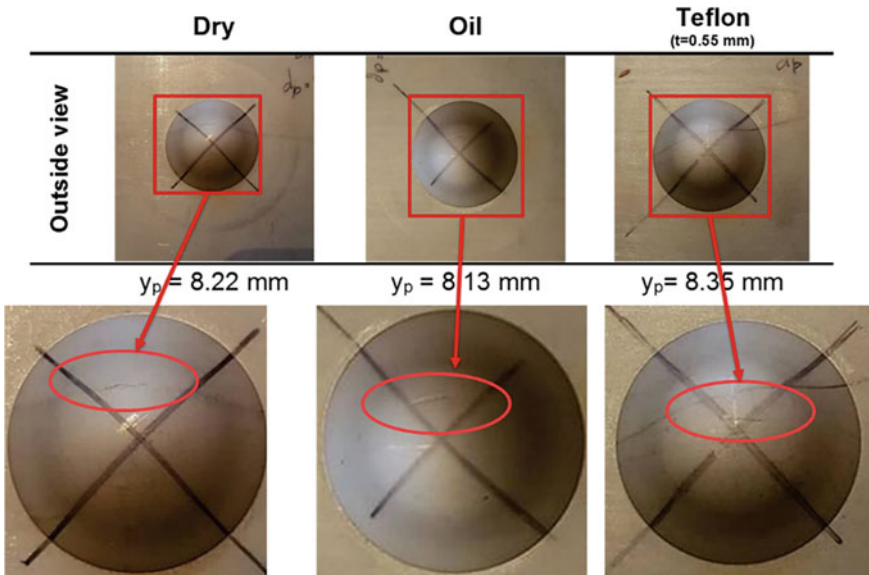


Fig. 15 Deep drawing Erichsen test results for different friction conditions ( $y_p$ —punch stroke)

The test was performed for different conditions, dry, oil and Teflon with 0.55 mm of thickness and the obtained geometries are presented in Fig. 15.

A closer view is presented in Fig. 16 and it is possible to observe the fracture on the external skin of the material.

In the contact area between sheet blank and punch it is visible a zone of friction which can be reduced by the application of oil lubricant and Teflon. However, the fracture always occurred in the upper material skin for the considered contact conditions.



**Fig. 16** Location of the crack on the outside view of the specimens provided from the Erichsen test

Although the friction conditions could affect the obtained results, the punch displacement needed to reach the material forming limit is quite similar. Taking into account these results, the Erichsen test shows being suitable for the composite sandwich metal-polymer material, since the formability limits can be obtained and detected as in case of homogeneous materials.

### 3.2 Hole Expansion Test—KWI

The KWI (Kaiser Wilhelm Institute) flat test, proposed by Siebel and Pomp [24], consists in deforming a metal sheet having a circular hole, by using a cylindrical flat head punch, as shown in Fig. 17. The sheet is centered with the punch and restrained between the die and the blank holder. The test stops when a crack starts at the edge of the hole [2].

The KWI test (Fig. 18) allows the determination of the maximum circumferential deformation at external fibers of the hole at fracture.

The hole expansion ratio, Eq. 3, is a key indicator to evaluate stretch flanging performance of steel sheets, which is usually obtained by hole expansion tests.

$$HER(\lambda) = \frac{D_f - D_i}{D_i} \times 100\% \tag{3}$$

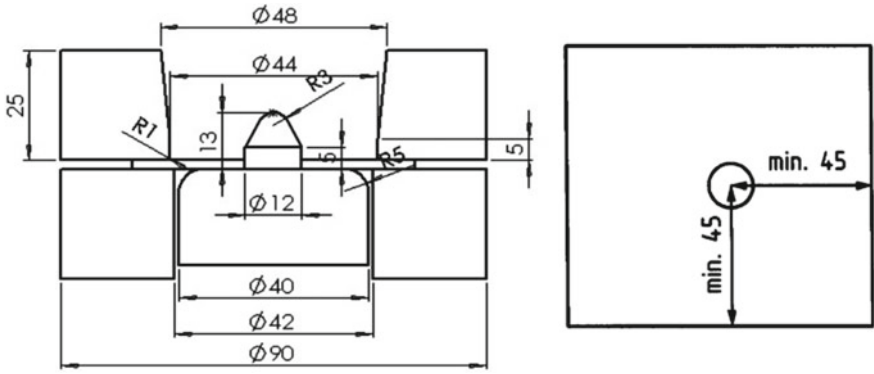


Fig. 17 Hole expansion test—KWI: dimensions of the tools and specimen

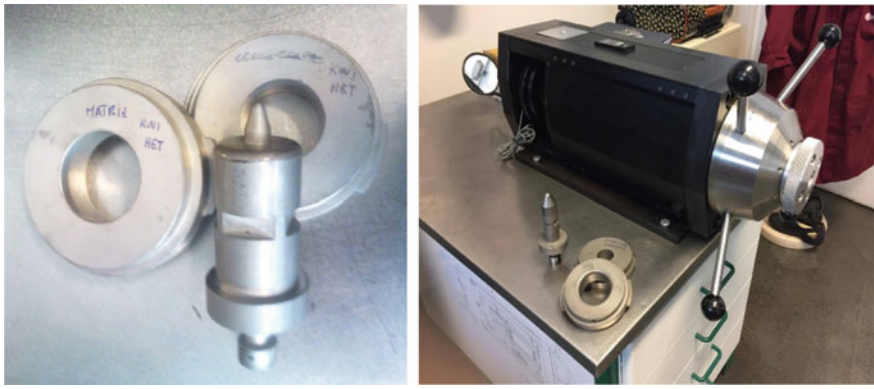


Fig. 18 Hole expansion test—KWI: tools and machine used to perform the test

where,  $D_f$  is the final diameter of the hole and  $D_i$  the initial diameter of the hole.

The results obtained in the hole expansion tests are generally sensitive to edge quality [25], the material thickness, the position of the burr relative to the punch, the mechanical properties, among other variables. In hole expansion tests, as in the uniaxial tensile tests, the surface near the hole is under uniaxial loading, since no more material on the outside exists and transverse stresses are in evidence.

To simulate different experimental conditions, the hole edges of blanks were obtained using different procedures: drilled, punched, drilled and bored. Figure 19, presents the results for these different edge conditions.

For the drilled specimen it is evident the crack visible in the edge of the hole. This is the typical result of this test. However, for the other conditions (punched, drilled and bored) the major crack occurs close to the die radius, as shown in Fig. 20.

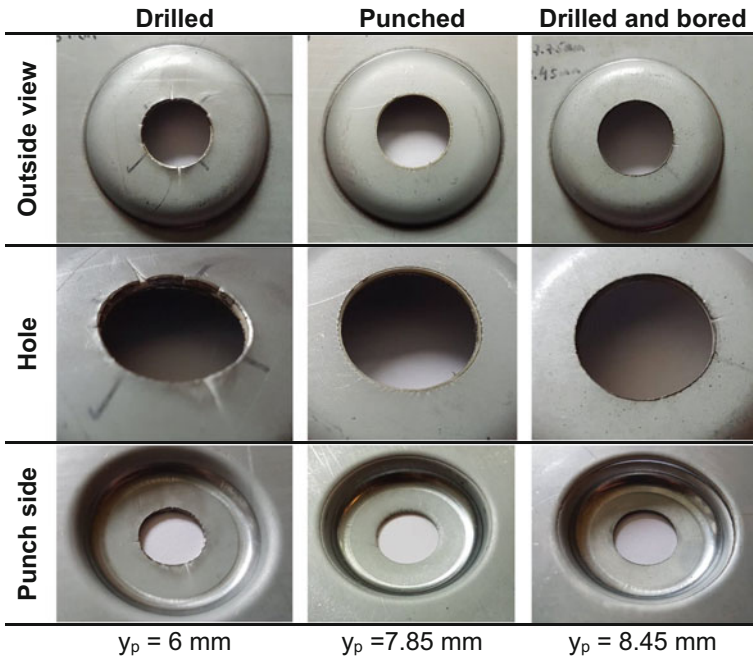


**Fig. 19** Hole expansion test—KWI results for different edge quality ( $y_p$ —punch stroke)

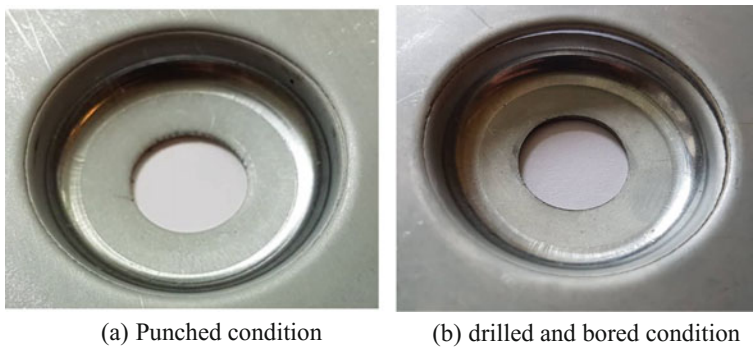


**Fig. 20** The location of the fracture for KWI hole expansion test

For a good edge quality condition (drilled and bored) this specific test shows not being adequate, since fracture occurs in a non-visible location, corresponding to the steel skin layer from the punch side. As a consequence, in this case it is not possible having control on the stop criterion for this test, since the crack appearance or fracture is not visible.

In order to get a better understanding of this experimental occurrence a numerical analysis has been performed, which is the contents of the next section.

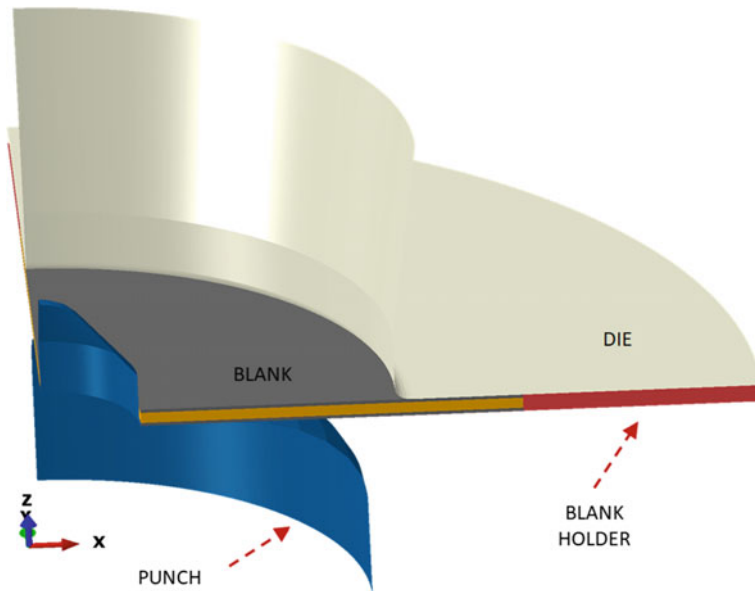


**Fig. 21** Numerical model with blank and tools (punch, die and blank holder) for KWI test

#### 4 Numerical Simulation—FEM

In this section, a numerical model has been developed for KWI test, aiming at getting details on material behavior for this kind of loading conditions, besides being possible to perform some sensitivity analysis on geometric variables of punch and die, so that KWI test could be adequate for formability analysis of hybrid materials under current study.

The numerical model was created for hole expansion KWI test using a 3D finite element (FE) explicit model and Abaqus/Explicit code. Due to the symmetry of the experimental tool system and material properties, only one-quarter of the real setup was considered, as shown in Fig. 21. The imposed boundary conditions allow the axial displacement of punch, while die and blank holder have encastre type boundary conditions with every displacement and rotation restricted.

Regarding the blank mesh discretization, eleven layers of deformable four node solid elements (C3D8R type from ABAQUS<sup>®</sup> Library) were used, in which the blank partitions represent the layers of material (steel skin+polymeric core+steel skin), as presented in Fig. 22. The tools (punch, die and blank holder) were modeled using analytic rigid surfaces.

To model the plastic hardening behavior of the blank, the constitutive Swift law was adjusted and considered for both layers (steel skin and polymeric core). The corresponding parameters were identified based on the hardening behavior of the steel skin sheets, shown in Fig. 5, as well as the polymeric core characterization.





**Fig. 22** Definition of layers and discretization implemented in the numerical model, in order to represent the sandwich material

**Table 4** Mechanical properties for the sheet skins of the composite metal/polymer material

Swift law:  $\sigma = K \cdot (\varepsilon + \varepsilon_0)^n$

Material	K	$\varepsilon_0$	n
Skin	747.04	0.0151	0.188
Core	56.1	0.006	0.068

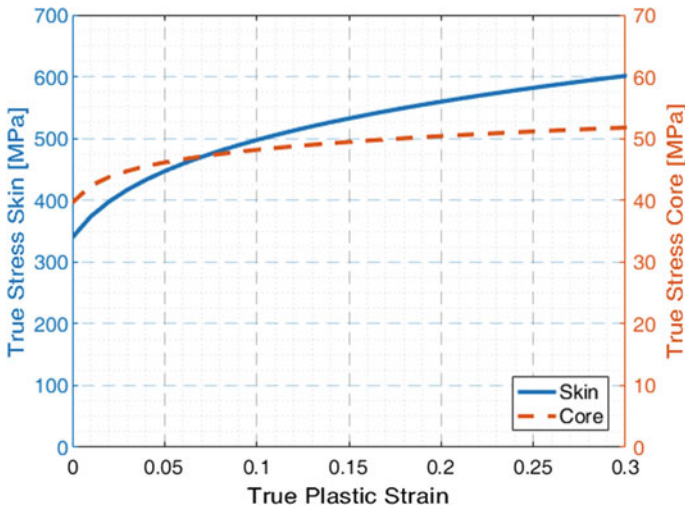


**Fig. 23** Steel skin and polymeric core hardening behavior using Swift law identified parameters

Table 4 presents the obtained parameters of Swift law and Fig. 23 the flow stress-strain curves.

### 4.1 Numerical Results

For an accurate analysis and evaluation of the obtained numerical results, a first FE simulation was performed using the same experimental conditions and tool (punch and die) geometries (Fig. 24a). The aim of such simulation is the validation of the developed and implemented numerical model, as well as, the use of a reference result for further analysis.

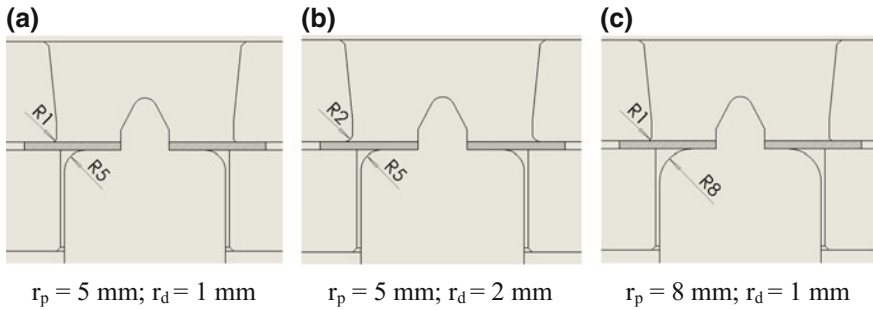


**Fig. 24** Numerical simulations proposed for sensitivity analysis of die and punch geometries

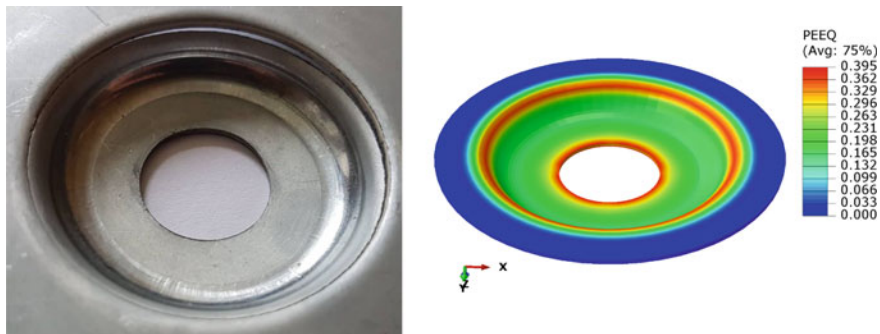


**Fig. 25** Experimental specimen and the equivalent plastic strain obtained from FE analysis

As sensitivity analysis, two geometric variables were selected and tested: die radius and punch radius, both of them aiming at promoting the fracture to occur on the hole edge during its expansion.

As for die radius ( $r_d$ ), its value was changed from 1 to 2 mm (Fig. 24b), in order to increase the contact area in the blank and consequently reducing the localized pressure.

Concerning the punch radius ( $r_p$ ), its value was increased from 5 to 8 mm, in order to allow a better material flow in the cylindrical punch head, while the hole expands during the forming process.

Figure 25 presents a comparison between the deformed experimental specimen and the corresponding numerical geometry with contours of equivalent plastic strain from FE analysis. This result corresponds to tool geometries shown in Fig. 24a, which are the standard experimental conditions. As seen, the maximum equivalent plastic strain is attained at the die radius, on the inner steel skin layer (punch side steel layer), which is the same location where the experimental fracture occurs.

As mentioned by other researchers [26, 27], the deformation path of hole edge is characterized by a pure uniaxial tensile state ( $\varepsilon_1 = -2\varepsilon_2$ ). Considering the principal strain space, the constant plastic work evolution curve represents the equivalent

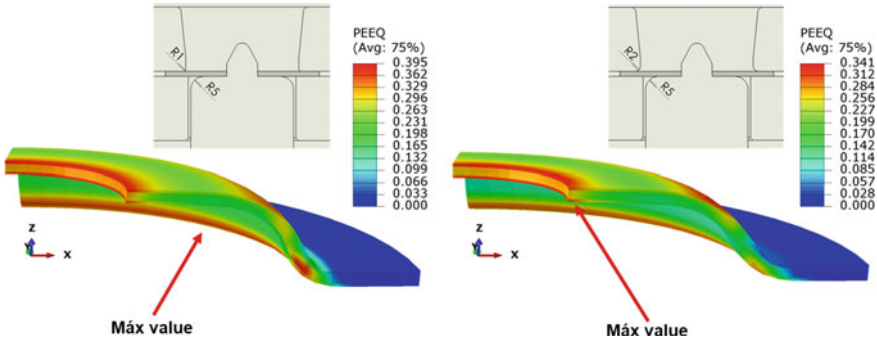


Fig. 26 Influence of die radius dimension in hole expansion test, by the numerical simulation

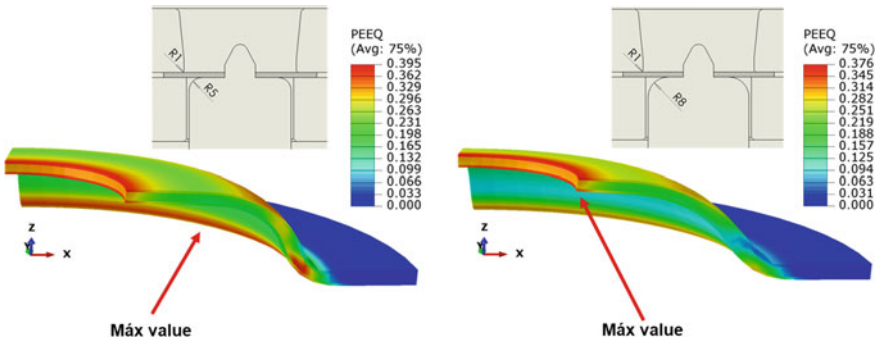


Fig. 27 Influence of change the punch radius for 1–2 mm

plastic strain. The intersection point of such curve with the linear path of the tensile test, gives a similar value than the one obtained in numerical simulation. Thus, the equivalent plastic strain variable can be used as a fracture criteria for the hole expansion test.

In this test (KWI) it is expected that a hole is expanded by adjacent material in a flat condition, as opposed to other HET (Hole Expansion Tests) [25, 28] in which the hole is expanded by a direct contact with a conical punch. The fracture being at die radius means that under these conditions, deformation and strain limits are not promoted at the right location (hole edge). Therefore, die radius ( $r_d$ ) is investigated and changed from 1 to 2 mm, as seen in Fig. 24b. Corresponding results are presented in Fig. 26 (right side), being also presented, for comparison, previous results with  $r_d = 1$  mm (left side).

As seen in Fig. 26, the maximum plastic strain was obtained in the hole edge, as expected, which promotes the strain limits at the hole and being possible to control the stop criterion, since cracks are now visible.

Besides die radius, also punch radius was investigated and changed from 5 to 8 mm, as seen in Figs. 24c and 27 shows the obtained numerical results.

When the punch radius increases from 5 to 8 mm, the deformation is concentrated in the edge of the hole, which promotes the fracture at the right location. This geometrical change shows that a better relative sliding exists, between the punch head and the inner steel skin. Moreover, the attained maximum equivalent plastic strain has similar maximum values to those obtained in the previous analysis of changing the die radius.

Results show that the KWI test can be used to perform testing of formability behavior in hybrid materials and the geometry modifications of die radius or punch radius, from standard dimensions, can be done in a simple way, thus permitting limiting strains at the edge of the hole and being possible the visibility of cracks for a stop criterion in this test.

## 5 Conclusions

The use of hybrid sheets made of different materials poses new challenges, not only in the forming processes but also in the traditional mechanical characterization.

A methodology was presented for the experimental characterization of an advanced hybrid material based on the separation of material constituents. This methodology allows the possibility of an individual characterization of the metallic skins and the polymeric core, as well as, their overall behavior. This information is important for an accurate determination of constitutive model parameters and the corresponding use in the numerical modeling of sheet metal forming processes involving this type of material.

Additionally, formability tests were performed in order to evaluate and assess the material at different loading conditions. The deep drawing Erichsen test shows to be adequate to determine the composite sandwich metal-polymer material properties. On the other hand, the hole expansion KWI test promotes prematurely the fracture on the skin layer from the punch side, not being possible to control the stop criterion.

Numerical simulations of KWI test permitted reproducing and predicting the same results as obtained by experiments. As a complement, sensitivity analysis on die and punch geometries showed that modifications on die radius or punch radius can be the solution to KWI test being completely adequate to testing formability behavior on hybrid materials.

**Acknowledgements** Authors gratefully acknowledge the funding of SciTech, R&D project NORTE-01-0145-FEDER-000022 co-financed by NORTE2020, through FEDER and the financial support of the Portuguese Foundation for Science and Technology (FCT) under project P2020-PTDC/EMS-TEC/6400/2014 (POCI-01-0145-FEDER-016876) by UE/FEDER through the program COMPETE 2020. The third author is also grateful to the FCT for the Doctoral grant SFRH/BD/119362/2016 under the program POCH, co-financed by the European Social Fund (FSE) and Portuguese National Funds from MCTES.

## References

1. Keller, S., Kimchi, M.: *Advanced High-Strength Steels Application Guidelines*. World AutoSteel, Version 5.0 (2014)
2. Santos, A.D., Ferreira Duarte, J., Barata da Rocha, A.: *Tecnologia da embutidura*. Coleção Tecnologia Mecânica, vol. 3, INEGI (2005)
3. Dickinson, R.C., Monterastelli, M.R., Vydra, E.J.: *Development of Materials for Noise and Temperature Control*, SAE Technical Paper (1995)
4. Rao, M.D.: Recent applications of viscoelastic damping for noise control in automobiles and commercial airplanes. *J. Sound Vib.* **262**, 457–474 (2003)
5. Seidlitz, H., Gerstenberger, C.: High-performance lightweight structures with fiber reinforced thermoplastics and structured metal thin sheets. *J. Mater. Sci.* **4** (2015)
6. Seidlitz, H., Kroll, L.: High-strength mixed constructions with thermoplastic fibre composites and metals. *Join. Plast.* **8**(2), 106–111 (2014)
7. Döhler, C., Hälsig, A.: Energy-efficient joining technologies to realise dissimilar joints of metal and fibre-reinforced plastics. In: Neugebauer, R., Drossel, W.G. (eds.) *3rd International Colloquium of the Cluster of Excellence eniPROD*, pp. 447–459. Chemnitz: Verlag Wissenschaftliche Scripten, (2014)
8. Moreira, R.A.S., Sousa, R.J.A., Valente, R.A.F.: A solid shell layerwise finite element for non-linear geometric and material analysis. *Compos. Struct.* **92**(15), 7–23 (2010)
9. Sokolova, O., Carradó, A., Palkowski, H.: Metal-polymer-metal sandwiches with local metal reinforcements: a study on formability by deep drawing and bending. *Compos. Struct.* **94**, 1–7 (2011)
10. ASTM Standard E8 M, *Standard Test Methods for Tension Testing of Metallic Materials*. ASTM International (2016)
11. Harhash, M., Palkowski, H., Carradó, A.: Forming potential of low-density laminates. In: Wiche, H., Wesling, V., Teichmann, C. (eds.) *Niedersächsisches Symposium Materialtechnik*, pp. 53–60. Clausthal-Zellerfeld (2015)
12. Harhash, M., Sokolova, O., Carradó, A., Palkowski, H.: Mechanical properties and forming behavior of laminated steel/polymer sandwich systems with local inlays—Part 1. *Compos. Struct.* **118**, 112–120 (2014)
13. Pimentel, A.M., Alves, J.L., Merendeiro, N.M., Oliveira, D.: Hybrix: experimental characterization of a micro-sandwich sheet. *J. Mater. Process. Technol.* **234**, 84–94 (2016)
14. Mamalis, A., Spentzas, K., Pantelelis, N., Manolakos, D., Ioannidi, M.: A new hybrid concept for sandwich structures. *Compos. Struct.* **83**(4), 335–340 (2008)
15. Mata, H., Natal Jorge, R., Santos, A.D., Parente, M., Valente, R., Fernandes, A.A.: Numerical and experimental study of the bulge test of sandwich shells with metal foam cores. In: *ECCOMAS 2012—European Congress on Computational Methods in Applied Sciences and Engineering*, Vienna, Austria, pp. 6199–6206 (2012)
16. Diehl, A., Staud, D., Engel, U.: Investigation of the mechanical behavior of thin metal sheets using the hydraulic bulge test. In: *4th International Conference on Multi Material Manufacture*, pp. 195–198. Germany (2008)
17. Martins, B., Santos, A.D., Teixeira, P.: A study on the influence of different variables for determination of flow stress using hydraulic bulge test. *Int. J. Mater. Eng. Innov.* **4**(2), 132–148 (2013)
18. Reis, L.C., Oliveira, M.C., Santos, A.D., Fernandes, J.V.: On the determination of the work hardening curve using the bulge test. *Int. J. Mech. Sci.* **105**, 158–181 (2016)
19. Amaral, R.L., Santos, A.D., Sousa, J.A., Lopes, A.B.: The influence of microstructure on the mechanical behavior of dual phase steels. *Adv. Struct. Mat.* **65**, 25–35 (2016). Springer International Publishing
20. Amaral, R., Santos, A.D., Lopes, A.B.: Mechanical properties determination of dual-phase steels using uniaxial tensile and hydraulic bulge test. *Ciência & Tecnologia dos Materiais* **27**, 239–243 (2017)

21. Campos, H., Santos, A.D., Amaral, R.: Experimental and analytical evaluation of the stress/strain curves of AA5754T4 and AA6061T6 by hydraulic bulge test. *Ciência & Tecnologia dos Materiais* **29**, 244–248 (2017)
22. Malheiro, L.: Caracterização mecânica de materiais em chapa metálica e problemas de formabilidade em componentes para automóveis. Master thesis, Faculty of Engineering, University of Porto (2012)
23. Sadagopan, S., Urban, D.: Formability characterization of a new generation of high strength steels. AISI/DOE technology roadmap program (2003)
24. Siebel, E., Pomp, A.: *Mitt. K. W. I. Für Eisenforschung*, pp. 287–291 (1929)
25. Col, A., Jousserand, P.: Mechanisms involved in the hole expansion test. International Deep Draw Research Group, IDDRG 2008 International Conference, Olofström, Sweden (2008)
26. Paul, S.K., Mukherjee, M., Kundu, S., Chandra, S.: Prediction of hole expansion ratio for automotive grade steels. *Comp. Mater. Sci.* **89**, 189–197 (2014)
27. Silva, C.M.A., Alves, L.M., Nielsen, C.V., Atkins, A.G., Martins, P.A.F.: Failure by fracture in bulk metal forming. *J. Mater. Process. Tech.* **215**, 287–299 (2015)
28. ISO 16630, Metallic materials—Sheet and Strip— Hole Expansion test. ISO Standard (2017)

# Study on Forming Tool Module with Variable Stiffness Blank-Holder for Applications in High Strength Steel and Laser Welding Parts



C. Faria, J. Magalhães, V. Blanco, N. Peixinho and S. Costa

**Abstract** This study presents experimental and numerical results of a development prototype tool that includes blank-holder plates of variable stiffness. The application is analyzed for high-strength steel parts and tailor welded blanks manufactured from dissimilar steel grades using laser welding. A numerical model was constructed within the Ansys software platform incorporating appropriate material constitutive models parameters for high-strength Dual-Phase steels. The obtained results show a positive control of springback geometries. Experimental tests were performed on the relevant geometries. The presented numerical and experimental results constitute a validation of a variable-stiffness blank-holder approach for this particular case study.

**Keywords** High strength steel · Numerical simulation · Tool design

## 1 Introduction

Metal forming of parts in advanced high strength steel grades must consider several factors such as thickness reduction and elastic springback. The control of blank-holding force in cold-forming processes is one way of addressing difficult to form parts. Although hydraulic systems can be used, careful tailoring of blank-holder plates in what regards their stiffness is a possible alternative. This implementation is analyzed in the current study recurring to a numerical model and experimental tool model of a relevant part.

Recent research in this field has identified different strategies regarding the performance of forming support forces: use of elements of variable stiffness through segmented geometry [1]; use of multi-point hydraulic actuators [2]; use of mobile

---

C. Faria · J. Magalhães · N. Peixinho  
Department of Mechanical Engineering, University of Minho, Guimarães, Portugal

V. Blanco · S. Costa (✉)  
Bairrimoldes Lda, Anadia, Portugal  
e-mail: [sergiolfc@gmail.com](mailto:sergiolfc@gmail.com)

© Springer Nature Switzerland AG 2019  
L. F. M. da Silva (ed.), *Materials Design and Applications II*, Advanced Structured Materials 98, [https://doi.org/10.1007/978-3-030-02257-0\\_34](https://doi.org/10.1007/978-3-030-02257-0_34)

hydraulic plates (shimming) [3]. It is also possible to consider the possibility of controlling the support through the gap holding (BHG) [4].

The segmented geometry approach provides simpler implementation of a variable-stiffness blank holder. In the study by Brabie and co-authors [1] tools were analyzed in which the forming support is constructed from two concentric rings of diameters that can be the same or different and realized in different materials, thus allowing to reduce the variations of thickness in components of reduced dimensions. Results were presented of reduction of variation of thickness in 35% and reduction of defects of 20%. In another implementation [5], based on the change in friction conditions the forming support, spiral springs were introduced in order to reduce the friction and facilitate the stretching of the material to be shaped, still allowing efficient lubrication between the forming and its support. The authors reported quality enhancements in the embedding of square geometry cups. The segmented geometry approach of the cushion is recognized as being of lesser simplicity but quite dependent on the geometry to conform, requiring a specific design. For example, in reference [6] is presented a double-ring shaped support of conical geometry in order to obtain variable support force in precision-forming of components with axial symmetry. The results allowed improvement in the quality and geometric and dimensional accuracy of the components produced.

The intervention on blank holding forces is also of particular importance in the shaping of multi-thickness sheets obtained by laser welding [7] or plates with varying thickness obtained in the rolling process [8]. This application is increasingly used in the automotive industry because it enables the production of optimized plate components with varying thickness. These parts poses problems of distortion, differential elastic return and localized fracture that can be solved with intervention at the level of the control force of blank support [9].

## 2 Materials and Methods

The present study presents numerical and experimental results for a validation part presented in Fig. 1. The analysis focus on an industrial component manufactured in a tool with 21 modules being one of the modules object of study: a critical geometry forming step with severe requisites in tolerances (Fig. 2).

The considered approach for the forming concept validation is illustrated in Fig. 2. In this approach a blank-holder component of the tool is divided in two parts allowing different materials to be used, which for validation purpose are conventional construction steel and Teflon. The rationale for this choice is to mix-match materials with very different Young's modulus hence stiffness behaviour. According to the legend in Fig. 2 the following combinations were analyzed: full steel (SS), full Teflon (TT) and combination of the two materials. (ST and TS).



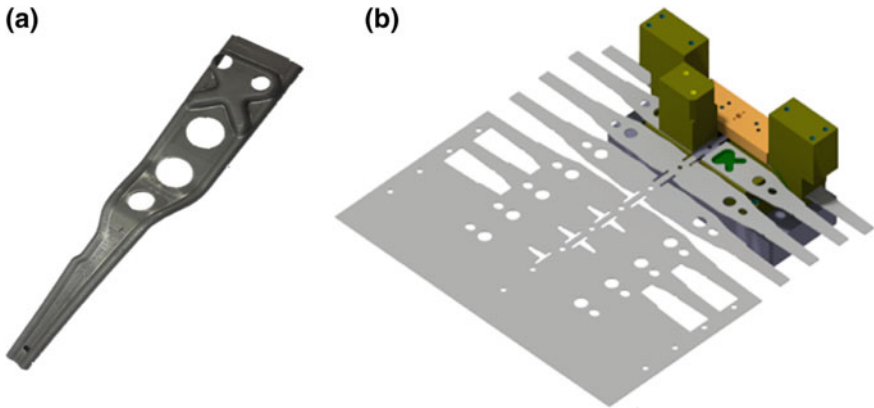


Fig. 1 Part (a) and tool design (b)

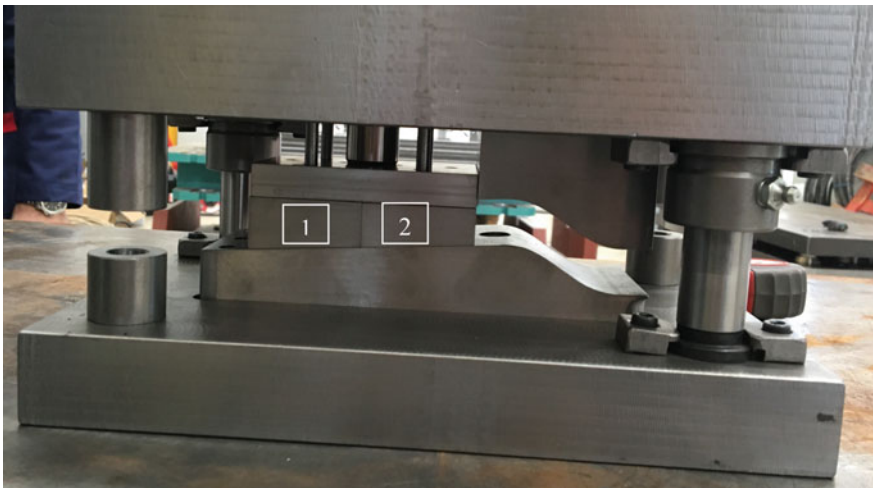
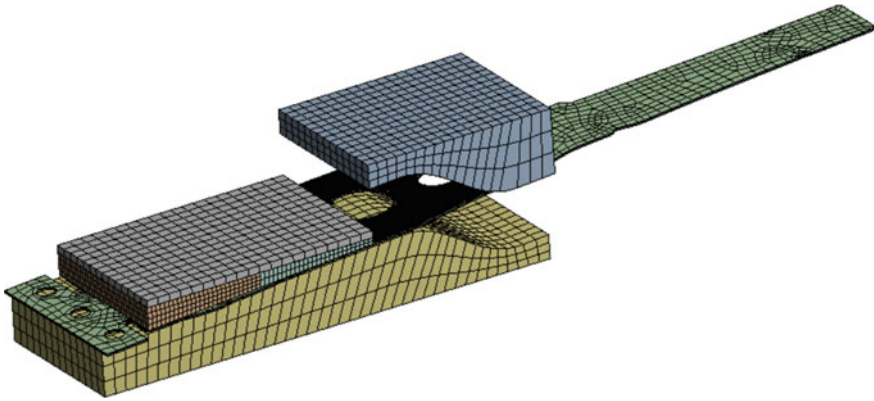


Fig. 2 Development forming tool module and position index of blank holders

The parts considered for this study were manufactured in high strength steel, namely Dual-Phase steel grades that have a ferritic–martensitic microstructure wherein a soft ferrite matrix contains islands of martensite as the secondary phase (martensite increases the tensile strength). Such microstructure provides mechanical properties of interest for automotive parts [10]. The following steel grades were supplied by ArcelorMittal: DP1000 in 1.0 and 1.75 mm thickness and DP600 in 1.0 mm thickness.



**Fig. 3** Finite element model

**Table 1** Numerical and experimental material/thickness combinations

Material	Thickness (mm)	Blank-holders
DP1000	1.75	SS/TT/ST/TS
DP1000/DP600 TWB	1.0	SS/TT/ST/TS

### 3 Numerical Model

The analysis of the manufacturing approach made use of numerical studies using the finite element method. For that purpose, a base model was constructed using Ansys tools incorporating the following options on mesh definition: automatic meshing with local refinement (mainly hexahedron elements) further analyzed in Ansys quality mesh metrics tools. Mesh refinement made use of *vertex sizing* tool with *sphere of influence* region definition type achieving a minimum of 0.5 mm element size in the main bending strain areas (Fig. 3). The contact definition included *bonded* definition between blank holders and their top load transmission plate; *frictional* contact between punch and material to be formed as well as material to be formed and blank holders. The minimum value of friction coefficient was attributed to the Teflon-steel contacts as 0.16. The geometry corresponds to the studied step in the forming tool that details a bending operation for a specific requisite geometry. Such operation was modelled through a displacement imposed in the tool punch of 22.57 mm. A static load of 11,097 N was imposed in top plate connected to the blank holders (Fig. 3) replicating the experimental conditions of the blank holder load.

Nonlinear behaviour of the Dual-Phase steel grades was included in the model through Ansys *Multilinear isotropic hardening* input options. Figure 3 presents a numerical model highlighting the mesh geometry. The overall study cases are presented in Table 1.

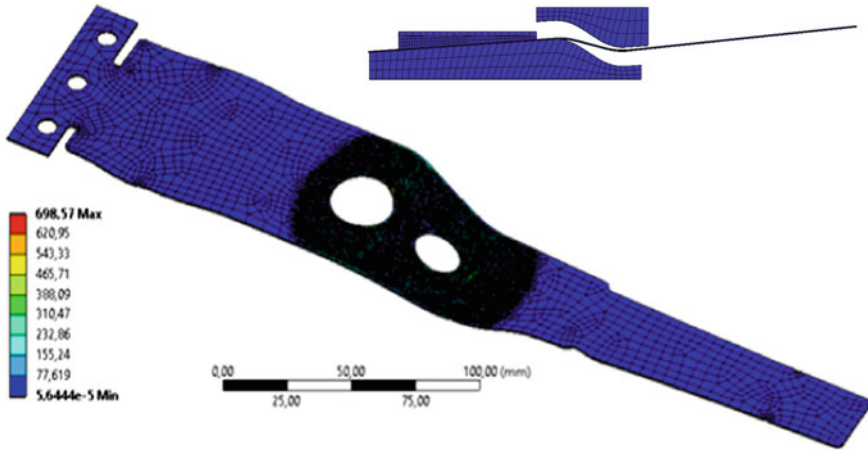


**Fig. 4** Final deformed shape and stress analysis example results (DP1000, 1.75 mm)

The Tailor Welded Blank (TWB) analysis included the two analyzed materials with DP600 in the position at larger width and DP1000 at the part tip. The weld line position in the numerical model can be observed in Fig. 6.

## 4 Results and Discussion

The presented results have focused on springback behaviour relevant to the analyzed cases. Figures 4 and 6 present an example of stress analysis and final deformed shape for reference. Figures 5 and 7 present a geometrical analysis comparing obtained final geometry for the various blank holder combinations regarding experimental and numerical results.

Regarding the results presented in Figs. 5 and 7 the line indicated as “ideal” corresponds to the desired geometry. It should be mentioned that the study tool was designed for lower strength steel grades hence while using high strength steels without any sort of punch/die adjustment or modification the springback effect is augmented.

From the analysis of results of Fig. 5 it transpires that the numerical models are capable of predicting the springback effect (negative direction) of the after-load stage with small differential amplitude. Experimental trials put in evidence problems of dimensional control and reveal improvements for the solution proposals with Teflon. The influence of the blank holder in position 2 is observed namely for the best case (TT). Numerical results are much closer amongst each other as expected and with a less clear tendency regarding the influence of the lower stiffness material in the blank holder parts but still presenting the TT option as the closest to the ideal geometry.

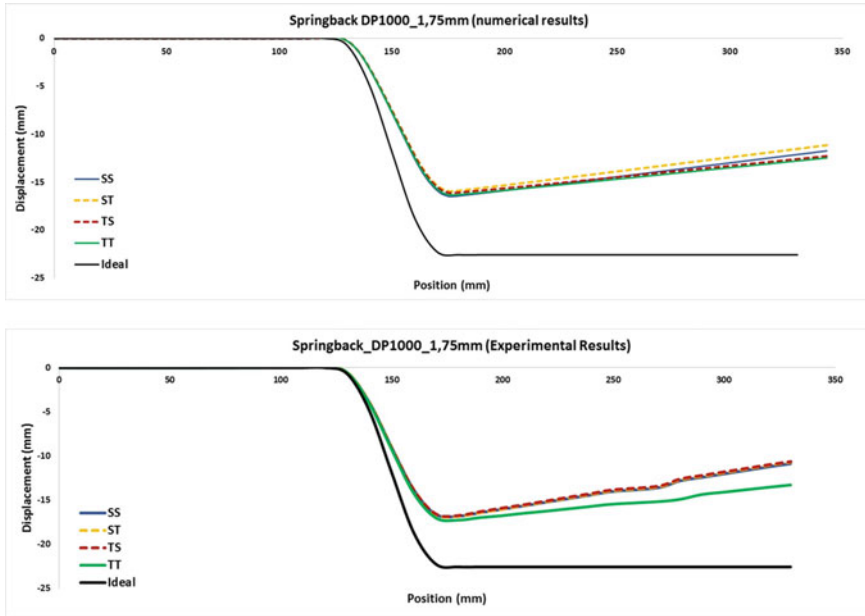


Fig. 5 Numerical (top) and experimental springback results for different blank-holder combinations (DP1000, 1.75 mm)

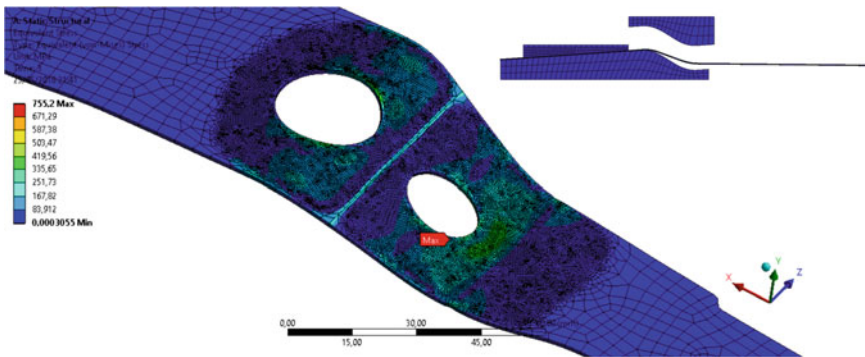
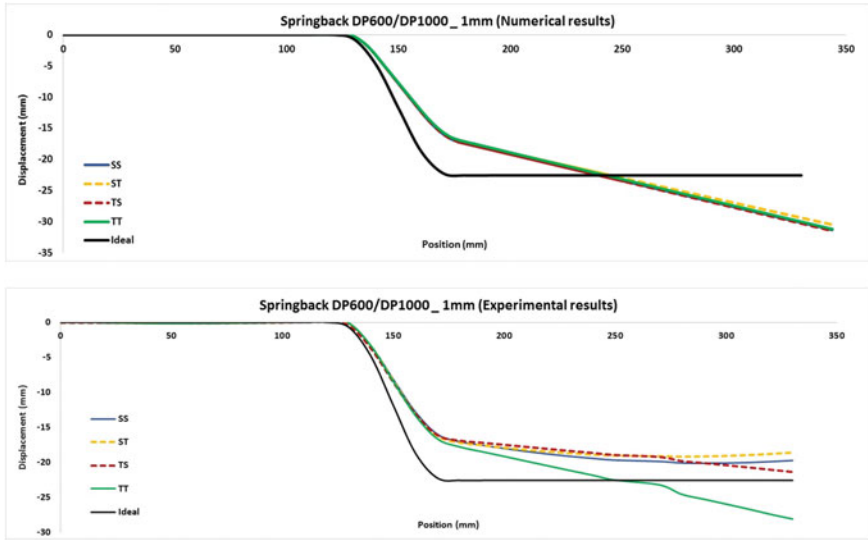


Fig. 6 Final deformed shape and stress analysis example results (DP600/DP1000, 1.0 mm)

Regarding the stamping process using a welded metal sheet composed by two different AHSS (DP600 and DP1000, back and front—Figs. 6 and 7) simulations were able to predict the overall springback effect (positive direction). The experimental tests accentuate again differences in solutions. Having Teflon in position 2 demonstrates again an interesting incremental proposal for springback reduction.

The improvements observed with the positioning of the Teflon blank-holders are associated to two factors: friction coefficient and stiffness. However, for this



**Fig. 7** Numerical (top) and experimental springback results for different blank-holder combinations (DP600/DP1000, 1.0 mm)

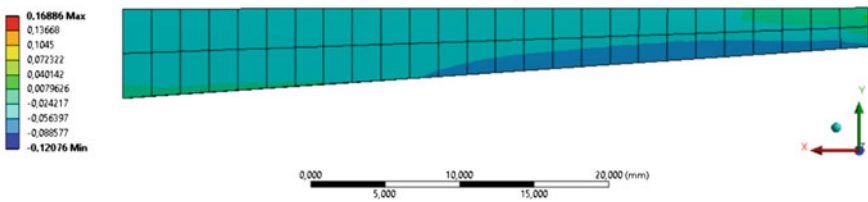


**Fig. 8** Highlight of directional deformation y of Teflon blank-holder in position 2 (DP1000; 1.75 mm TT)

particular part the friction behaviour is not as relevant due to the loading and trajectory imposed—a simple bending solicitation without significant stretching of material. The stiffness behaviour of the Teflon part contributes to the overall final geometry since its deformation reduces the clamping at the highest loaded region (Fig. 8). A maximum of 0.24 mm displacement was observed at the blank-holder extremity.

## 5 Conclusions

This study presented experimental and numerical results for parts manufactured in a development prototype tool that includes blank-holder plates of variable stiffness. The application was analyzed for high-strength steel parts and tailor welded blanks manufactured from dissimilar steel grades using laser welding. A numerical model

was constructed incorporating appropriate material constitutive models parameters for high-strength Dual-Phase steels. The obtained results indicate the possibility to influence springback behaviour through varying the stiffness of blank-holder parts in the tool. This behaviour is attributed to the localized compliance of the blank-holder that, in the present study case, was observed in the numerical simulations at the bending region of higher stress levels. The presented numerical and experimental results constitute a validation of a variable-stiffness blank-holder concept approach for this particular case study. For industrial application, the development of a metallic blank-holder part with similar local stiffness would provide similar results.

**Acknowledgements** The funding support from Project I&DT AdvancedTOOLING CENTRO-01-0247-FEDER-011399 is acknowledged.

## References

1. Brabie, G., Chirita, B., Albut, A.: Minimization of sheet thickness variation and other defects of minidrawn parts using a blank holder plate made from concentric rings. *Precis. Eng.* **42**, 311–320 (2015)
2. Altan, T., Yadav, A.: Multipoint-control die cushion systems for stamping complex parts, part I: blank holder force application. *Stamp. J.* 32–33 (2006)
3. Tommerup, S., Endelt, B.: Experimental verification of a deep drawing tool system for adaptive blank holder pressure distribution. *J. Mater. Process. Technol.* **212**(2012), 2529–2540 (2012)
4. Hosseini, A., Kadkhodayan, M.: A hybrid NN-FE approach to adjust blank holder gap over punch stroke in deep drawing process. *Int. J. Adv. Manuf. Technol.* **71**(337–355), 2014 (2014)
5. Gavas, M., Izciler, M.: Design and application of blank holder system with spiral spring in deep drawing of square cups. *J. Mater. Process. Technol.* **171**, 274–282 (2006)
6. Tian, S.-X., Feng, Y.-X., Gao, Y.-C.: Design and application of a novel cone-shaped blank holder for precision stamping process. In: *Proceedings CIRP 27, 13th CIRP Conference on Computer Aided Tolerancing*, pp. 309–312 (2015)
7. Merklein, M., Johannes, M., Lechner, M., Kuppert, A.: A review on tailored blanks—production, applications and evaluation. *J. Mater. Process. Technol.* **214**(2014), 151–164 (2014)
8. Quick, R., Träbing, O.: *The New Ford Focus*, Presented at EuroCarBody Conference, 18–20 October, Bad Nauheim, Germany (2011)
9. Kinsey, B., Cao, J.: An analytical model for tailor welded blank forming, *journal of manufacturing science and engineering. Trans. ASME* **125**(344–351), 2003 (2003)
10. Peixinho, N., Pinho, A.: Study of viscoplasticity models for the impact behavior of high-strength steels. *J. Comput. Nonlinear Dyn.* **2**(2), 114–123 (2006)